IAHR AIRH

Supported by Spain Water and IWHR, China

IAHR 2017

37th IAHR WORLD CONGRESS

13-18 August, 2017

Kuala Lumpur, Malaysia

DEVELOPMENT AND APPLICATION OF SOFT COMPUTING TOOLS IN HYDROINFORMATICS

EXPERIMENTAL ANALYSIS ON FISH SWIMMING ABILITIES AND NUMERICAL SIMULATION OF FISH SWIMMING TRAJECTORIES

RUI HAN [1], LI ZENG[2], RUONAN LI[3] & DUAN CHEN[4]

[1,2]State Key Laboratory of Simulation and Regulation of Water Cycle in River Basin, China Institute of Water Resources and Hydropower Research (IWHR), Beijing, China
hanrui_first@163.com

[3] Research Center for Eco-Environmental Sciences, Chinese Academy of Sciences, Beijing, China
[4] Changjiang River Scientific Research Institute, Wuhan, China

ABSTRACT

This research presents a comprehensive method to investigate fish swimming behavior to hydrodynamic conditions through laboratory experiments and numerical simulations. Fish swimming behavior plays a significant role in its life history, but little work has been done to describe the fundamental rules quantitatively. In this research, fish behavior is studied from two different aspects, the experimental method and the simulation way. *Myrocyprinus asianicus* juvenile is selected as an experimental object, which is a national protected species in China. In the experiments, both traditional closed water forced swimming test and open volitional swimming test are conducted. According to the results, traditional experimental method has its advantage of short duration, easily controlling and a small number of tested fish are needed to get the meaningful data. However, compared with another experiments, the outcomes obtained from the previous way amplifies the fish swimming ability. Therefore, the waste of project construction would be inevitable so as the worse fish bypass effects. Finally, the relationship between fish swimming speed and its body length is refined into regression formulations. Based on the data from the lab experiments, an individual-based fish dynamic model is developed. The model is first calibrated and validated by the experimental data, and then applied in simulating the fish performance in fish bypass which depicts the *Myrocyprinus asianicus* juvenile swimming trajectories and compared with the result gained from the experimental measurements. The result demonstrates numerical simulation could reproduce the fish behavior under micro-scale. In conclusion, this research could provide feasible experimental method and numerical simulation, and offer support to set the design velocity of fish bypass as well.

Keywords: Swimming ability; forced swimming test; volitional swimming test; numerical simulation; kinematic equation.

1 INTRODUCTION

Behaviors are essential measures for fish to accommodate changing environmental conditions (Railsback et al., 1999). However, investigation on fish behaviors in natural or laboratory systems is difficult because of multiple physiological and environmental processes and interactions, and difference between individuals. Thus, studies on fish swimming behavior, orientation of movements, flow cues for migration and swimming speeds in different environmental situations have attracted increasing interests (Coutant et al., 2000). Bailey (1983) examined predating behaviors by Aurelia aurita on early first-feeding stage larvae of the herring Clupea harengus in the laboratory. Webb (2002) conducted a series of experiments to investigate the posture, depth and swimming trajectories of various fishes under different flow perturbation and turbulence. Burrows (2001) and Gibson et al. (2002) studied juvenile plaice behaviors in relation to depth changes. These experiments mainly used regular flumes (Burrows, 2001; Bégout Anras et al., 2004) while ignored or simplified the complex flow in nature. No combination of these artificial flumes or tanks has been persuasively demonstrated to be effective enough in guiding fish movements to justify full-scale or major prototype testing in the field for application in hydroelectric projects (Coutant et al., 2000). In addition, the fish behaviors in these experiments were characterized under forced swimming. Recently, researches on fish behaviors under volitional swimming received more and more attention. Castro-Santos (2005) analyzed the volitional swimming behavior of migratory fishes when traversing velocity barriers. Li et al. (2011) studied the ethology of S. Hollandi by a laboratory physical model.

Meanwhile, the advancement of computer technology and spatial data collection (Chen et al., 2010) facilitated a variety of numerical models for fish dynamics simulation (Rose et al., 1996) including budget models of energy flows among ecosystem compartments, coupled single-species models that simulate populations through time and holistic models that incorporate features of both. These models applied an aggregated approach that use population abundances or biomass as state variables and treat individual interactions by a relatively few, lumped parameters. Limitations inherent from these aggregated models are obvious. They use the average sample to represent each individual (Crowder et al., 1992). Some of them may have biological meanings but not realistic in the nature.

Population-level behaviors of fish are usually difficult to obtain, while most species are well studied at individual level (Reed, 1983). Hence, individual-based approach could theoretically provide an alternative. Individual-based models emphasize the difference between individuals, thus they have the potential to directly overcome several limitations of the traditional aggregated models (DeAngelis et al., 1992). Although, numerical models of fish behaviors are rapidly developing (Humston et al., 2004; Li et al., 2010), problems of quantifying model performance remain difficult (DeAngelis et al., 1992). Therefore, there is a great demand to combine fish ethology study into individual-based models.

This paper presents an innovative approach to investigate fish behaviors through volitional swimming experiments in laboratory scaled model and individual-based numerical simulations. The numerical model tracked fish movements, and preferred flow conditions of individuals. *Myrocyprinus asianicus*, which is an important fish in China, was selected in the study. Once calibrated, the model was applied in simulating the fish performance in fish bypass, depicted fish swimming trajectories and compared with the result gained from the experimental measurements.

2 LABORATORY EXPERIMENTS

Fish preferential velocities are essential for ethology and simulation. Therefore, laboratory experiments on fish preferential velocities were carefully designed and conducted, using the large D-ended, flat-bottomed, fiberglass holding tank (Figure 1). In order to create a velocity gradient under laboratory conditions, an artificial baffle was attached at the bottom of the tank which had a direction of 5° against the inside wall. Thus, section areas were changed gradually and different velocities would appear in different positions in the tank. Section areas were set from 0.3 m^2 to 3 m^2. Therefore, when the water quantity was controlled around 1.4 m^3/s, velocities in this tank could have the range of 0.45 m/s to 4.5 m/s.

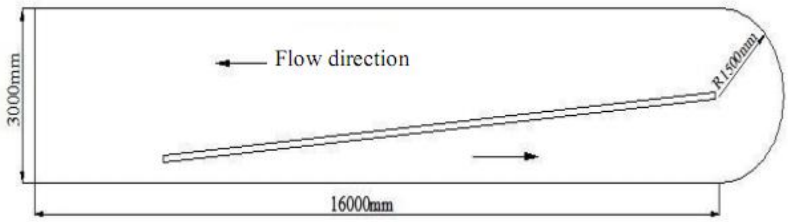

Figure 1. Layout of the experimental flume

Before experiments, all the fish were randomly divided into three groups, with 30 individuals each. During the experiments, water temperature was controlled around 21°C, pH was from 6.9 to 7.2 and the dissolved oxygen was from 5.5 mg/L to 6.5 mg/L, similar to the water quality in the river where fish lived. Fish behaviors were observed and recorded by underwater IR monitors, cameras and short-range telescopes to avoid unexpected disturbance. Velocity gradient was created by the baffle. Inflow was slightly directed against the tank wall to reduce acoustic noises.

Fish residence ratio was calculated to obtain velocity preference of *Myrocyprinus Asianicus*. Analyses on the experimental data showed that *Myrocyprinus Asianicus* preferred staying in a velocity ranging from 0.3 m/s to 0.6 m/s (Figure 2). When velocities were higher than 0.7 m/s, fish residence declined rapidly. Normally, the upmost velocity for young *Myrocyprinus Asianicus* to stay was 1.5 m/s, and very few could exceed this velocity barrier. Therefore, the preferential velocities range of *Myrocyprinus Asianicus* was from 0.3 m/s to 0.6 m/s (P_{KW}<0.05).

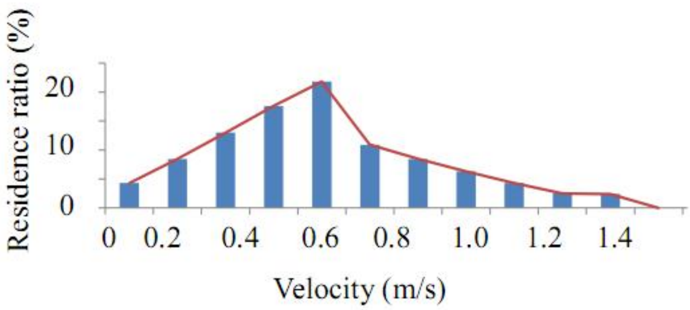

Figure 2. Relationship between residence ratio and velocity

  / ISSN 1562-6865 (Online) - ISSN 1063-7710 (Print)

3 NUMERICAL SIMULATIONS

3.1 Model overview

The need to develop more “fish-friendly” systems for hydropower facilities (Brookshier et al., 1995) motivate the studies on fish behavior. Mathematical methods linking fish trajectories to hydrodynamic patterns in terms of fish behavioral elements remain a challenge (Steel et al., 2001). In this study, a fish dynamic model using individual-based approach (DeAngelis et al., 1990) was developed, describing fish swimming behaviors and vector-based movement rules. The movement rules and larval mortality rates of the model were calibrated until species persisted at reasonable biomass, with realistic mean lengths at age by life stage. The model was integrated with a two-dimensional flow module, thus it mapped fish behaviors and flow factors.

3.2 Flow model

The flow field was simulated by SELFE, an open-source code available for computational fluid dynamics (CFD) use, solving shallow-water equations, with hydrostatic and Boussinesq approximations (Zhang et al., 2008). SELFE solves differential equation system with finite-element method. Semi-implicit schemes were applied to all equations, and the continuity and momentum equations were solved simultaneously.

3.3 Fish model

The movements of fish determine their spatial distribution in the river. Therefore, the movement rules are critical to accurate model simulations (Steven et al., 1999). Movement can be classified by whether incremental movement length (speed) and direction are interdependent or independent (Wu et al., 2000; Marsh et al., 1988). Before simulation, some reasonable assumptions were made that an individual fish was considered to be a particle, the vertical flow changes were averaged, and fish moved positively against the flow with no particular orientation.

The behavior rules in the individual-based model produced a volitional swimming vector in which speed and direction were determined interdependently for each fish at every time increment. The swimming speed was obtained through experiments and depended on its life stage (Coombs, 1999). And the direction was set against the surrounding flow. The volitional fish swimming vector (Figure 3) was first decomposed into Cartesian vector components. Then, the flow vector at present fish location was also decomposed at the same way. Finally, the fish’s location at time t was updated from the previous position after time increment ($\triangle$t):

$$\begin{aligned} x_i^t &= x_i^{t-1} + (u_{i-fish}^{t-1} - u_{i-flow}^{t-1}) \times \Delta t \\ &= x_i^{t-1} + u_i^{t-1} \times \cos\alpha_i^{t-1} \times \Delta t \end{aligned} \quad [1]$$

$$\begin{aligned} y_i^t &= y_i^{t-1} + (v_{i-fish}^{t-1} - v_{i-flow}^{t-1}) \times \Delta t \\ &= y_i^{t-1} + u_i^{t-1} \times \sin\alpha_i^{t-1} \times \Delta t \end{aligned} \quad [2]$$

The flow at any place that fish might move to was interpolated from the surrounding computation points.

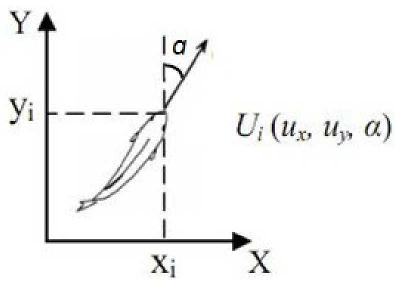

Figure 3. Sketch of fish orientation and movement

The implementation of fish movement took three-steps. First, fish was ready to move depending on its situation and flow stimuli, and then it executed a movement as a response to flow condition (Bian, 2003), and finally, it selected a place to spend the next time increment according to its flow preference obtained from the aforementioned experiments. Thus, the fish locations were determined by the current fish distribution, the flow conditions and the hydro-environmental preference.

4 MODEL APPLICATIONS

The model was applied to simulate fish swimming behavior in an experimental flume (vertical slot fishway, the flow field in fishway was simulated by the flow model and presented in Figure 4). The model parameters are listed in Table 1.

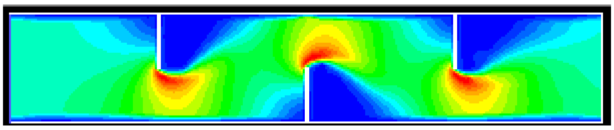

Figure 4. The simulated flow field in vertical slot fishway in laboratory

Table 1. Parameters in fish model

Parameters	Value
Life Histroy	Juvenile
Time Step	1 second
Fish Swimming Speed	0-2.93 Body Length/s
Suitable Velocity Range	0.3-0.6 m/s

Figure 5 shows the simulated result of fish swimming process. Although the movement rules for individual fish is not very obvious, with the increasing number of simulated fish, the swimming rules of fish group become apparently. We can easily reproduce the experimental result from the numerical simulation.

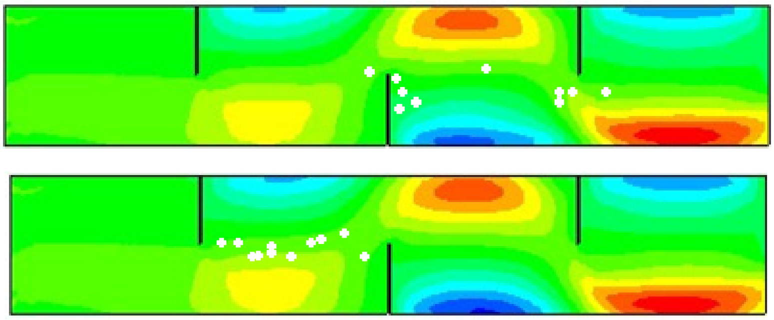

Figure 5. The distribution of swimming fish in different time (upper: T=10 s, down T=15 s, Q=20 L/s)

5 DISCUSSIONS

The heterogeneous morphology in the scaled physical model created diverse flow conditions and these could not easily be achieved by flume experiments. However, a possible change in fish behaviors with flow acceleration or turbulence in nature is a concern that may make evidence of fish behaviors in normal flow conditions a moot point. Further research will be needed to discover the relationship between flow turbulence and fish behaviors.

Fish movement is critical to realistic simulation of how individuals respond to changes of hydraulic regimes (Railsback et al., 1999). Models at a purely behavioral level can be hard to relate to known facts (Ekeberg, 1993), while vector-based movement rules were relatively straightforward to implement in the individual-based approach.

For further study, it is recommended to include turbulence intensity in the description of fish response to complex flow conditions. The fish movement behaviors could be classified into different patterns, obeying the fundamental vector-based rules while being characterized by the swimming trajectories.

The development of numerical model provides a robust interpretation from a laboratory scale to a natural world. The model could accommodate algorithms from lab observations and elaborate equations with experiment data, and then served to quantitatively explore the fish behaviors in real flows.

6 CONCLUSIONS

This research took an effort to investigate fish behaviors under volitional swimming by using a laboratory scaled model. The experimental results showed that young *Myrocyprinus Asianicus* preferred a cobble stone bed, turbulent water and a velocity ranging from 0.3 m/s to 0.6 m/s. Basing on the experimental results, numerical model at individual-level was developed and then was applied to the vertical slot fishway. The model results were later verified by real experiment which proved that this model can be used in a small-scale fish movement simulation.

ACKNOWLEDGEMENTS

The Author is grateful to the financial support of National Nature Science Foundation of China (51409242).

REFERENCES

Bailey KM, Batty RS. (1983). A Laboratory Study of Predation by *Aurelia Aurita* on Larval Herring (*Clupea Harengus*): Experimental Observations Compared with Model Predictions. *Marine Biology,* 72, 295-301.

Bégout Anras ML, Lagardère JP. (2004). Measuring Cultured Fish Swimming Behavior: First Results on Rainbow Trout using Acoustic Telemetry in Tanks. *Aquaculture,* 240, 175-186.

Bian L. (2003). The Representation of The Environment in The Context of Individual-Based Modeling. Ecological Modelling, 159, 279-296.

Brookshier PA, Flynn JV & Loose RR. (1995). 21st Century Advanced Hydropower Turbine System. *American Society of Civil Engineers: New York.*

Burrows MT. (2001). Depth Selection Behavior during Activity Cycles of Juvenile Plaice on Simulated Beach Slope. *Journal of Fish Biology,* 59, 116-125.

Castro-Santos T. (2005). Optimal Swim Speeds for Traversing Velocity Barriers: An Analysis of Volitional High-Speed Swimming Behavior Of Migratory Fishes. *Journal of Experimental Biology*, 208, 421–432.

Chen Q, Han R, Ye F & Li W. (2010). Spatio-Temporal Ecological Models. *Ecological Informatics,* 6(1), 37-43.

Chen Q, Ye F. (2008). *Unstructured Cellular Automata and the Application to Model River Riparian Vegetation Dynamics*. Lecture Notes in Computer Science, 5191, 337–344.

Coombs S. (1999). Signal Detection Theory, Lateral-Line Excitation Patterns And Prey Capture Behavior of Mottled Sculpin. *Animal Behavior,* 58, 421-430.

Coutant, C. C. & Whitney. R. (2000). Fish Behavior in Relation to Passage Through Hydropower Turbines: A Review. *Transations of the American Fisheries Society*, 129(2), 351-380.

Crowder LB, Rice JA, Miller TJ & Marschall EA (1992). Empirical and Theoretical Approaches To Size-Based Interactions and Recruitment Variability in Fishes. *Individual-based Models and Approaches in Ecology*. New York.

DeAngelis DL & Cushman RM. (1990). Potential Applications of Models in Forecasting The Effects of Climate Change on Fisheries. *Transactions of the American Fisheries Society*, 119, 224-239.

DeAngelis DL & Gross LJ. (1992). *Individual-based Models and Approaches in Ecology*. Chapman and Hall, New York

Marsh, L.M., Jones, R.E., (1988). The Form and Consequences of Random Walk Movement Models. *Journal of Theory of Biology,* 133, 113–131.

Ekeberg Ö. (1993). A Combined Neuronal and Mechanical Model of Fish Swimming. *Biological Cybernetics,* 69, 363-374.

Gibson RN, Robb L, Wennhage H & Burrows MT. (2002). Ontogenetic Changes in Depth Distribution of Juvenile Flatfishes in Relation to Predation Fish and Temperature on A Shallow-Water Nursery Ground. *Marine Ecology Progress Series,* 229, 233-244.

Humston R, Olson DB & Ault JS. (2004). Behavioral Assumptions in Models of Fish Movement and Their Influence on Population Dynamics. *Transactions of the American Fisheries Society*, 133(6), 1304-1328.

Li W, Chen Q, Huang Y. (2011). Laboratory Study On Ethology of Spinibarbus Hollandi. *Acta Ecological Sinica*, 31(5), 1404-1411. (in chinese)

Li W, Han R, Chen Q, Qu S & Cheng Z. (2010). Individual-Based Modelling of Fish Population Dynamics in The River Downstream Under Flow Regulation. *Ecological Informatics*, 5, 115-123.

Li R, Chen Q, Mynett A E, Wu S. (2008). Modelling of The Flow Changes Due To Reservoir Operations and The Impacts on Aquatic Ecosystem Downstream. *Proceedings of the 16th IAHR-APD Conference*. Nanjing. China.

Pavlov DS, Lupandin AI & Skorobogatov MA. (1994). Influence of Flow Turbulence On Critical Flow Velocity For Gudgeon (Gobio). *Doklady Biological Sciences*, 336, 215-217.

Pavlov DS, Lupandin AI & Kostin VV. (1999). Downstream Migration of Fish Through Hydropower Dams. *Russian Academy of Science*. Moscow.

Railsback SF, Lamberson RH, Harvey BC & Duffy WE. (1999). Movement Rules for Individual-Based Models of Stream Fish. *Ecological Modeling,* 123, 73-89.

Reed M. (1983). A Multidimensional Continuum Model of Fish Behavior. *Ecological Modelling*, 20(4), 311-322.

Rose KA, Tyler JA, Singhdermot D & Rutherford ES. (1996). Multispecies Modeling of Fish Populations. *Computers in Fisheries Research Chapman and Hall.* London. 194-222.

Skorobogatov MA, Pavlov DS & Lupandin AI. (1996). Effect of Current Velocity and Turbulence Intensity on The Distribution of The Roach Rutilus In A Water Stream. *Journal of Ichthyology,* 36, 654–658.

Steel EA, Guttorp P, Anderson JJ & Caccia DC. (2001). Modeling Juvenile Migration Using a Simple Markov Chain. *Journal of Agriculture Biological Environment Station*, 6(1), 80-88.

Steven F, Railsback RH, Lamberson BC & Walter ED. (1999). Movement Rules for Individual-Based Models of Stream Fish. *Ecological Modelling*, 123(2–3), 73–89.

Webb PW. (2002). Control of Posture, Depth, and Swimming Trajectories of Fishes. *Integrative Comparative Biology,* 42(1), 94-101.

Wu H, Li BL, Springer TA & Neill WH. (2000). Modelling Animal Movement as a Persistent Random Walk in Two Dimensions : Expected Magnitude of Net Displacement. *Ecological Modelling,* 132, 115–124.

Zhang Y, Baptista AM. (2008). SELFE : A Semi-Implicit Eulerian-Lagrangian Finite-Element Model for Cross-Scale Ocean Circulation. *Ocean Modelling,* 333, 26-52.

Proceedings of the 37th IAHR World Congress
August 13 – 18, 2017, Kuala Lumpur, Malaysia

DEVELOPMENT OF A LARGE-EDDY-SIMULATION FOR FREE SURFACE COMPLEX FLOWS

ADRIEN BOURGOIN[(1)], SYLVAIN GUILLOU[(2)], JÉRÔME THIÉBOT[(3)],
SOFIANE BENHAMADOUCHE[(4)] & RIADH ATA[(5)]

[(1,2,3)] LUSAC-UNICAEN, Cherbourg-Octeville, France
adrienbourgoin@gmail.com, sylvain.guillou@unicaen.fr, Jerome.thiebot@unicaen.fr
[(4,5)] EDF R&D, Chatou, France
Riadh.ata@edf.fr, Sofiane.benhamadouche@edf.fr

ABSTRACT

For the purpose of improving turbulent processes modelling for environmental flows, a large eddy simulation (LES) approach is being developed in TELEMAC-3D (Hervouet, 2007). Although it is still not widely used, LES is increasingly applied for this kind of flows, thanks to the growth of computation resources. RANS modelling, generally associated with $k - \varepsilon$ model, remains favorable for numerical modelling of natural flows, and is by the way the most popular approach for turbulence modelling. Nevertheless, as this approach neglects the transient flow characteristics, it cannot be used to analyze the turbulence induced by complex seabed morphology (abrupt bathymetric variations, macro-structures, bed roughness etc.). The development step involves the implementation of several LES turbulence models, such as the dynamic Smagorinsky (Germano et al., 1991; Lilly, 1992), and several numerical tools needed for the implementation of a LES. For example, the turbulent inlet boundary condition is achieved by a Synthetic Eddy Method (Jarrin et al., 2006) which produces a fluctuating and periodic boundary condition in order to initiate the turbulent processes. Moreover, as TELEMAC-3D uses prismatic meshes that can be strongly anisotropic, the turbulence model has to be modified by introducing two length scale filters (instead of one). An important part of the developments has been achieved. The chosen validation case is a in an open channel (Handler et al., 1993). Although first results are encouraging, they revealed lots of issues related to this kind of models (scheme order, mesh quality, mesh anisotropy, CPU time, boundary conditions, periodicity etc.). At this step, several issues have been fixed (boundary conditions, periodicity, mesh anisotropy). However, the remaining issues which can explain major gaps between numerical an experimental results (mainly scheme order and numerical diffusion) are ongoing works. Preliminary attempts show promising improvements and will be detailed in future publications.

Keywords: Turbulence; numerical modelling; large eddy simulation; free surface flows; Telemac.

1 INTRODUCTION

In environmental flows over complex bottom morphology, understanding turbulence is essential for studying processes such as sediment transport or heat transfer. A Reynolds Averaged Navier-Stokes (RANS) treatment can be used in TELEMAC-3D (Hervouet, 2007) to model an averaged turbulent flow by using for example the famous $k - \epsilon$ model. Although this kind of modelling is mostly used for natural flows, it is sometimes not accurate enough for providing specific information. The improvement of computation resources nowadays permits using Large-Eddy-Simulation (LES) for modelling environmental flows. This approach enables simulating the random aspect of turbulence, which plays an important role in transport phenomena. The method consists in introducing a sub grid model to mimic the smallest motion scales and in simulating the other scales by directly resolving the Navier-Stokes equations. The implementation of LES requires additional processing, particularly for the boundary conditions treatment. For example, contrary to RANS model, some velocity fluctuations have to be introduced in the computation domain. Moreover, near solid boundaries, wall models are required to avoid a considerable mesh refinement.

In this paper, several developments already done or being done in TELEMAC-3D are described. They are tested using a validation test case (Handler et al., 1993) representing an open channel flow at a low Reynolds number.

2 TELEMAC-3D

TELEMAC-3D is a CFD code developed by EDF R&D (Hervouet, 2007), based on a P1 finite element method on 3D extruded prismatic elements. It is mainly used to simulate environmental flows since it is able to model free surface flows and to simulate many natural phenomena, such as rain or sedimentation transport. It solves the tri-dimensional Navier-Stokes equations and for an incompressible fluid and without hydrostatic assumption, the equations are

$$\begin{cases} \frac{\partial u}{\partial x}+\frac{\partial v}{\partial y}+\frac{\partial w}{\partial z}=0 \\ \frac{\partial u}{\partial t}+u\frac{\partial u}{\partial x}+v\frac{\partial u}{\partial y}+w\frac{\partial u}{\partial z}=-\frac{1}{\rho}\frac{\partial p}{\partial x}+\nabla.(\nu\nabla u)+F_x \\ \frac{\partial v}{\partial t}+u\frac{\partial v}{\partial x}+v\frac{\partial v}{\partial y}+w\frac{\partial v}{\partial z}=-\frac{1}{\rho}\frac{\partial p}{\partial y}+\nabla.(\nu\nabla v)+F_y \\ \frac{\partial w}{\partial t}+u\frac{\partial w}{\partial x}+v\frac{\partial w}{\partial y}+w\frac{\partial w}{\partial z}=-\frac{1}{\rho}\frac{\partial p}{\partial z}-g+\nabla.(\nu\nabla w)+F_z \end{cases} \quad [1]$$

where (u,v,w) are respectively the velocities in the directions (x,y,z), p the pressure, ν the kinematic viscosity, ρ the density and F the forcing source terms. For the sake of briefness, equations of free surface and source terms (bottom frictions, wave forcing etc.) are not presented here. Interested people can refer to Hervouet (2007).

The resolution algorithm consists of three fractional steps:

(a) The first step is the advection step, which considers only the advection part of the Navier-Stokes equations. The obtained results are written f^c.

(b) Then the diffusion step uses as input the quantities from the last step and solves the diffusion term, to get f^d.

(c) At least, the pressure-continuity step gives the final quantities. It includes the resolution of the continuity equation, and updates the free surface elevation.

Each step is resolved one after the other, and the time derivative is written as:

$$\frac{\partial f}{\partial t}=\frac{f^{n+1}-f^d+f^d-f^c+f^c-f^n}{\Delta t} \quad [2]$$

3 LES METHODS

The concept of Large Eddy Simulation (LES) is to divide the energy spectrum of the flow in two parts by using a numerical filter to separate the smallest length scales from the others. As the smallest structures have a universal behavior and are hardly independent on the initial conditions, they can be modelled. In contrast, the biggest scales are directly solved by the motion equations. Mathematically, this method consists in filtering the Navier-Stokes equations and in introducing a new unknown called sub grid tensor. Thus, LES aims to simulate the filtered quantities noted $\tilde{f}$ and to evaluate this new tensor that describes the interactions between the two categories of turbulent scales.

Moreover, some appropriate boundary conditions have to be prescribed at each boundary of the domain. To prevent a too expensive computation time, some fluctuations can be introduced at the inlet in order to quickly obtain a fully developed turbulent flow. Moreover, wall laws can avoid an important mesh refinement near the solid walls.

3.1 Sub grid modelling

In order to model the sub grid tensor, the main approach is named functional modelling (Sagaut, 2006). It aims to model the action of this tensor by assuming that its effect is simply an energetic process. Most of the sub grid models are based on a sub grid viscosity ν_t that links directly the subgrid tensor τ to the filtered velocity gradients $\tilde{s}$ with a Boussinesq assumption-like formulation:

$$\tau_{ij}=\frac{2}{3}\tau_{kk}\delta_{ij}-2\nu_t\tilde{S}_{ij}$$

The development of the LES approach in TELEMAC-3D involves three sub grid models intending to evaluate the additional viscosity ν_t. They are the Smagorinsky model (Smagorinsky, 1963) with a damping function (Van Driest et al., 2003), the dynamic Lilly model (Germano et al., 1991; Lilly, 1992) and the WALE sub grid model (Nicoud et al., 1999).

3.1.1 The Smagorinsky model

The Smagorinsky model can be considered as the first sub grid model (Sagaut, 2006). It consists in evaluating simply the sub grid viscosity with the formulation:

$$\nu_t=(C_s\tilde{\Delta})^2|\tilde{S}|$$

where $\tilde{\Delta}$ is the filter with which, in practice, is directly linked to the grid size, $|\tilde{S}|$ is the norm of the velocity gradients tensor and C_s is the Smagorinsky constant. This formulation assumes a homogenous and isotropic turbulence that is obviously not relevant for complex flows. For example, the model is too dissipative near solid walls. However, it can be improved by using a damping function such as the Van Driest function (Van Driest et al. 2003). The sub grid viscosity becomes:

$$\nu_t = (C_s\widetilde{\Delta}(1-e^{-\frac{z^+}{26}}))^2|\tilde{S}|$$

where z^+ is the dimensionless distance to the solid wall.

Even if this model is suited to simulate many flows, it cannot achieve turbulent transitions. This limitation can be overcome by using a Smagorinsky constant which varies in space and in time. That's the idea of dynamic models.

3.1.2 The dynamic Lilly model

It is an extension of the standard Smagorinsky model (Germano et al., 1991; Lilly, 1992) which uses a constant variable in space and in time. The latter is expressed by using additional powers of the filtered velocity gradients tensor and by involving a second filter, larger than the first one (indexed here by the accent $\widehat{()}$).

First let us write, the filtered Navier-Stokes equations:

$$\frac{\partial \tilde{u}_i}{\partial t} + \tilde{u}_j\frac{\partial \tilde{u}_i}{\partial x_j} = -\frac{1}{\rho}\frac{\partial \tilde{p}}{\partial x_i} + \frac{\partial}{\partial x_j}\left(\nu\frac{\partial \tilde{u}_i}{\partial x_j}\right) - \frac{\partial \tau_{ij}}{\partial x_j}$$

where $\tau_{ij} = \widetilde{u_i u_j} - \tilde{u}_i\tilde{u}_j$ is the subgrid tensor.

Then, by applying the second filter operator, it becomes:

$$\frac{\partial \hat{\tilde{u}}_i}{\partial t} + \hat{\tilde{u}}_j\frac{\partial \hat{\tilde{u}}_i}{\partial x_j} = -\frac{1}{\rho}\frac{\partial \hat{\tilde{p}}}{\partial x_i} + \frac{\partial}{\partial x_j}\left(\nu\frac{\partial \hat{\tilde{u}}_i}{\partial x_j}\right) - \frac{\partial T_{ij}}{\partial x_j}$$

where $T_{ij} = \widehat{\widetilde{u_i u_j}} - \hat{\tilde{u}}_i\hat{\tilde{u}}_j$. Then, the idea is to use the turbulent stress defined by $L_{ij} = T_{ij} - \hat{\tau}_{ij}$ to build a Smagorinsky constant suitable for the instantaneous flow. So, by using the Smagorinsky model for the tensors τ and T, we get:

$$\begin{cases} \tau_{ij} - \frac{1}{3}\tau_{kk}\delta_{ij} = -2C_s^2\widetilde{\Delta}^2|\tilde{S}|\tilde{S}_{ij} \\ T_{ij} - \frac{1}{3}T_{kk}\delta_{ij} = -2\widehat{\Delta}^2\left|\hat{\tilde{S}}\right|\hat{\tilde{S}}_{ij} \end{cases}$$

and L_{ij} can be written as:

$$L_{ij} - \frac{1}{3}L_{kk}\delta_{ij} = 2C_s^2 M_{ij}$$

with

$$M_{ij} = \widehat{\Delta}^2\left|\hat{\tilde{S}}\right|\hat{\tilde{S}}_{ij} - \widetilde{\Delta}^2\widehat{|\tilde{S}|\tilde{S}_{ij}}$$

The Smagorinsky constant can be expressed using a least squares method and is written:

$$C_s^2 = -\frac{1}{2}\frac{L_{ij}M_{ij}}{M_{ij}M_{ij}}$$

3.1.3 The WALE model

The WALE model (Nicoud et al., 1999) is another Smagorinsky model designed to get a good asymptotic behavior near the solid walls where the sub grid viscosity varies linearly with z^3. The subgrid viscosity of this model is written as:

$$\nu_t = (C_w\widetilde{\Delta})\frac{\left(S_{ij}^d S_{ij}^d\right)^{\frac{3}{2}}}{\left(\tilde{S}_{ij}\tilde{S}_{ij}\right)^{\frac{5}{2}} + \left(S_{ij}^d S_{ij}^d\right)^{\frac{5}{4}}}$$

with

$$S_{ij}^d = \frac{1}{2}\left(g_{ij}^2 + g_{ji}^2\right) - \frac{1}{3}\delta_{ij} g_{kk}^2 \ , \ \ g_{ij} = \frac{\partial \tilde{u}_i}{\partial x_j}$$

and C_w a constant evaluated to 0.325.

3.2 Inlet boundary conditions

The inflow has a strong influence on the flow characteristics in the calculation domain. Indeed, in hydraulics, flows are mainly dominated by the advection. So the prescribed values of the velocity have to be as realistic as possible. The most popular approach is to prescribe Dirichlet boundary conditions over the inlet area. It is achieved by introducing a mean quantity and a fluctuating part. This technique is possible when the velocity fluctuations are known. For flows over simple bottom morphology, a common approach is to use a periodicity between the outlet and the inlet. However, when the complex geometry of the flow does not allow using periodicity, an artificial turbulence needs to be introduced at the inlet.

3.2.1 Recycling method

The recycling method is also called pseudo-periodicity. It aims at prescribing, at the time t^n, at the inlet ($x = x_0$) the velocity obtained at the outlet ($x = x_R$) at the time t^{n-1}. For each component of the velocity, it is written:

$$u_i(x_0, y, z, t^n) = u_i(x_R, y, z, t^{n-1})$$

This method is different from the real periodicity because it is explicit. Both recycling and periodicity are widely used but they have the drawback of introducing a spurious periodicity in the streamwise direction which can trigger instabilities as shown in Spalart et al. (2006). For avoiding this, a spanwise shift can be introduced at the inlet (shift with respect to the outlet).

Moreover, for channel flows, the recycling method has the disadvantage of neglecting the friction loss. Near solid walls, the thickness of the boundary layer should be bigger at the outlet δ_R than at the inlet δ_0. This overvaluation at the inlet can be compensated by imposing:

$$u_i(x_0, y, z, t^n) = u_i(x_R, y, z\delta_R/\delta_0, t^{n-1})$$

For free surface flows, a source term has to be added to the streamwise Navier-Stokes equations (Guillou et al., 2007) in order to consider the friction loss of the flow. This term is:

$$F_x = -\frac{u_\tau^2}{h}$$

where u_τ is the friction velocity and h is the water depth.

3.2.2 Synthetic Eddy Method (SEM)

The Synthetic Eddy Method (Jarrin et al., 2006) consists in injecting an artificial turbulence in the computation domain. To do that, a virtual box around the inlet is introduced, where artificial eddies are created. The dimensions of the box in each dimension x_j are defined by:

$$\begin{cases} x_{j,min} = \min\limits_{x \in S}(x_j - \sigma(x)) \\ x_{j,max} = \max\limits_{x \in S}(x_j + \sigma(x)) \\ \Delta x_j = x_{j,max} - x_{j,min} \end{cases}$$

where S is the inlet surface and σ is a length scale for the virtual eddies, given by:

$$\sigma = \max\left(\min\left(\frac{k^{\frac{3}{2}}}{\epsilon}, \kappa\delta\right), \widetilde{\Delta}\right)$$

with k the turbulent kinetic energy, ϵ the turbulent dissipation rate, κ the von Karman constant, δ the half of the water depth and $\widetilde{\Delta}$ the filter width.

N virtual turbulent structures are created in the box. Each one has a random position and a random orientation in the three dimensions of space, noted $\epsilon_j^k \in \{-1,1\}$. Then, the fluctuations at the inlet u_i' at the position $\boldsymbol{x}$ are defined by using the data of all these eddies and a shape function f_σ, such as:

$$u'_i(\boldsymbol{x}) = \frac{1}{\sqrt{N}} \sum_{k=1}^{N} c_i^k f_\sigma(\boldsymbol{x} - \boldsymbol{x_k})$$

where $\boldsymbol{x_k}$ is the position of the kth eddy, f_σ is the shape function that can be written as:

$$f_\sigma(\boldsymbol{x} - \boldsymbol{x_k}) = \prod_{j=1}^{3} \sqrt{\Delta x_j} \sqrt{\frac{3}{2\sigma}} \left(1 - \frac{|x_j - x_j^k|}{\sigma}\right)$$

and $c_i^k = a_{ij}\epsilon_j^k$ is the intensity of the k^{th} eddy in the ith direction, depending on the a_{ij} that is the Cholesky decomposition of a prescribed Reynolds tensor R_{ij}, expressed as:

$$\begin{pmatrix} \sqrt{R_{11}} & 0 & 0 \\ R_{21}/a_{11} & \sqrt{R_{22} - a_{21}^2} & 0 \\ R_{31}/a_{11} & (R_{32} - a_{21}a_{31})/a_{22} & \sqrt{R_{33} - a_{31}^2 - a_{32}^2} \end{pmatrix}$$

At each time step, the eddies are transported by the mean flow in the virtual box. When an eddy leaves the box, it is introduced again at the inlet of the box with a new random span wise and vertical positions and new intensities.

4 APPLICATIONS: FREE SURFACE CHANNEL FLOW

The developments presented in the previous section are now used and validated considering a first considering a simple free surface channel flow.

4.1 Presentation of the test case

The developments are first compared with the reference of Handler et al. (1993). This case is a DNS of a fully developed turbulent channel flow. The Reynolds number based on the bulk velocity and the friction velocity are $Re = 2340$ and $Re_\tau = 134$, respectively. The channel is rectangular; its dimensions are $[4\pi\delta, \frac{3\pi\delta}{2}, \delta]$ (which is consistent with the experimental study of Komori et al. (1983).

The simulations performed with TELEMAC use several grids which settings are given in the table 1. The water depth is such that $\delta = \frac{1}{\pi}\ m$. A Nikuradse law is prescribed at the bottom with a value of $N = 0.00273\ m$ to characterize the friction.

Table 1. Properties of meshes used with TELEMAC-3D.

Grid	$\Delta x\ (m)$	$\Delta y\ (m)$	$\Delta z\ (m)$	Δx^+	Δy^+	Δz^+
A	0.02	0.015	0.016	8.42	6.31	6.74
B	0.04	0.03	0.023	16.84	12.62	9.68

The Synthetic Eddy Method (SEM) is parametrized via the Reynolds tensor and the averaged flow field at the inlet (which transports the virtual eddies through the SEM box). The latter is determined using a Reichardt law, with the formulation:

$$U^+ = \frac{1}{\kappa}\log(1 + \kappa z^+) + 7.8\left(1 - e^{-\frac{z^+}{11}} - \frac{z^+ e^{-0.33z^+}}{11}\right)$$

where κ is the von Karman constant and z^+ the dimensionless distance to the bottom of the channel.

The prescribed Reynolds tensor is assumed to be diagonal and isotropic. It is written as:

$$\bar{\bar{R}} = \begin{pmatrix} \frac{2}{3}k & 0 & 0 \\ 0 & \frac{2}{3}k & 0 \\ 0 & 0 & \frac{2}{3}k \end{pmatrix}$$

where k is the turbulent kinetic energy, defined here by the other Reichardt law:

$$k^+ = 0.07(z^+)^2 e^{-\frac{z^+}{8}} + \frac{4.5\left(1 - e^{-\frac{z^+}{20}}\right)}{1 + \frac{4z^+}{Re_\tau}}$$

with Re_τ being the Reynolds number based on the friction velocity.

4.2 Validation of the Synthetic Eddy Method

The SEM is used for synthetizing velocity fluctuations at the inlet. Figure 1 shows the vertical profile of dimensionless turbulent kinetic energy for several grids. The comparison of the profiles to the experimental results of Komori et al. (1983) indicate that the setting of the SEM permits to introduce correct turbulence characteristics at the inlet.

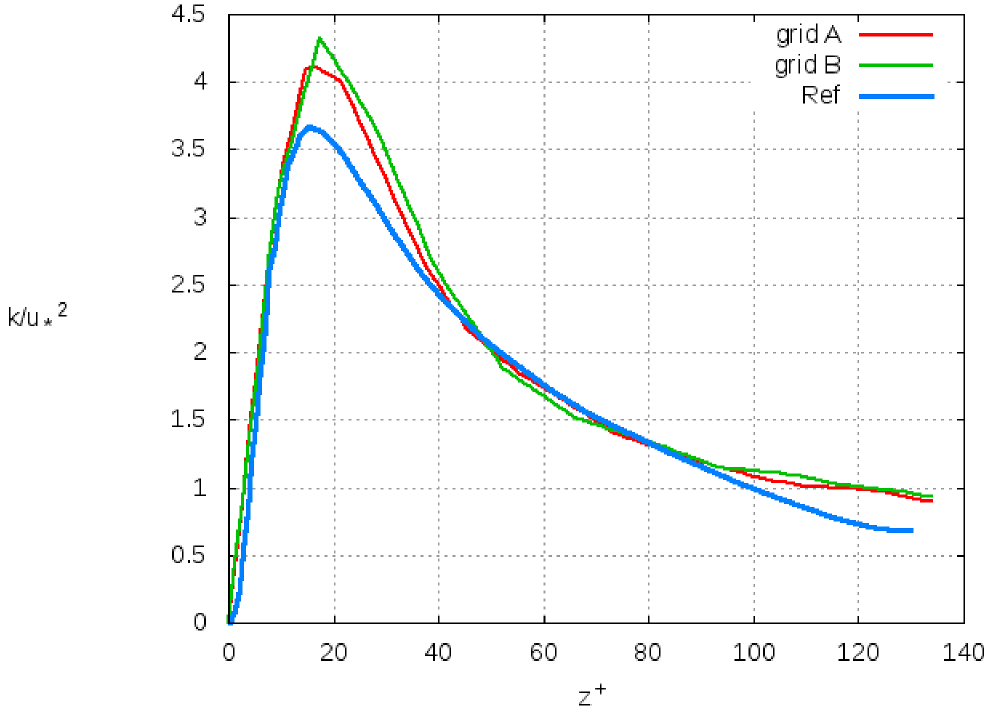

Figure 1. Vertical profile of turbulent kinetic energy at the centerline of the channel introduced with the SEM and results from experiments of Komori et al. (1983).

4.3 Turbulence evolution

Figures 2, 3, 4, and 5 illustrate the diagonal Reynolds stresses and the turbulent kinematic energy obtained in the middle of the channel (these quantities are nondimensionalized by k or by the square of the friction velocity.). Those quantities are compared to the DNS results of Handler et al. (1993).

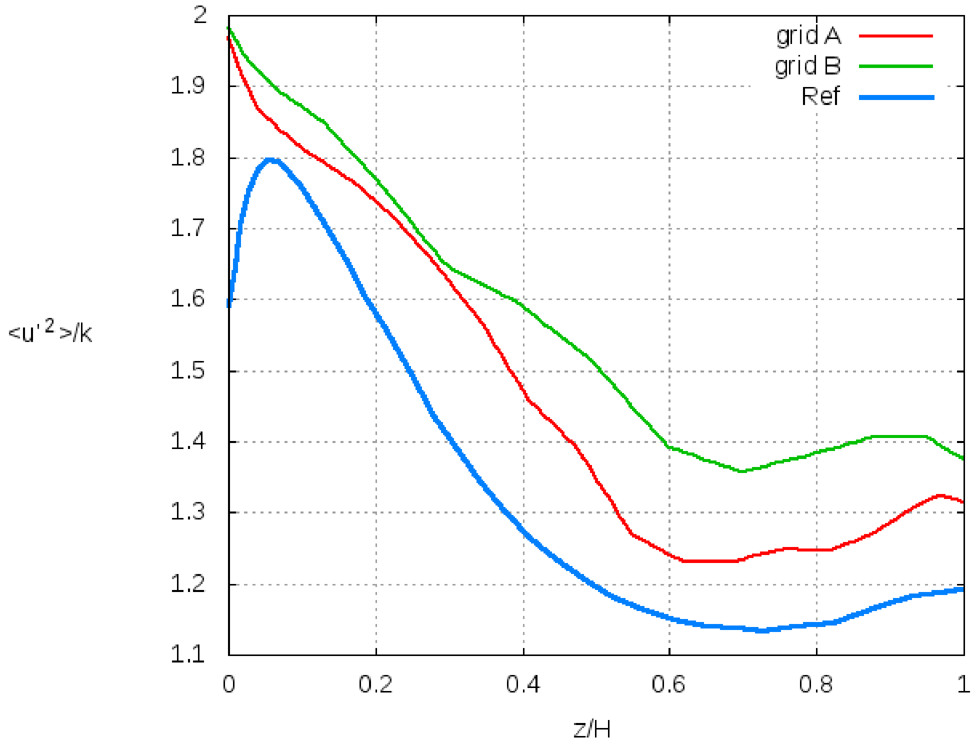

Figure 2. Vertical profile of streamwise Reynolds stress dimensionless with the turbulent kinetic energy and results from DNS of Handler et al., 1993.

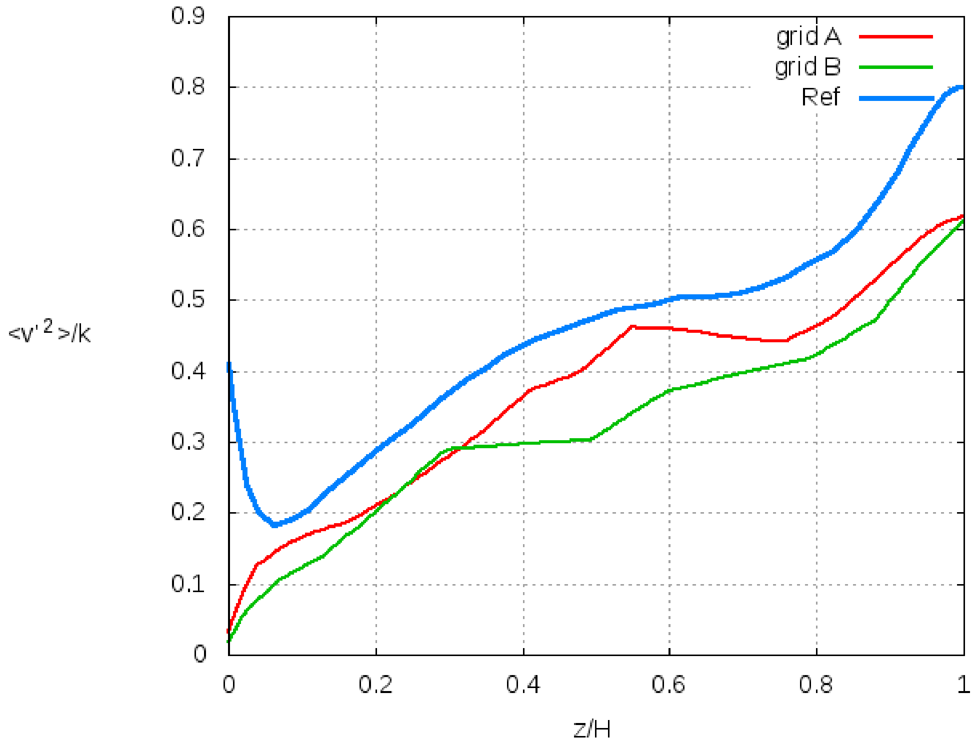

Figure 3. Vertical profile of spanwise Reynolds stress dimensionless with the turbulent kinetic energy and results from DNS of Handler et al., 1993.

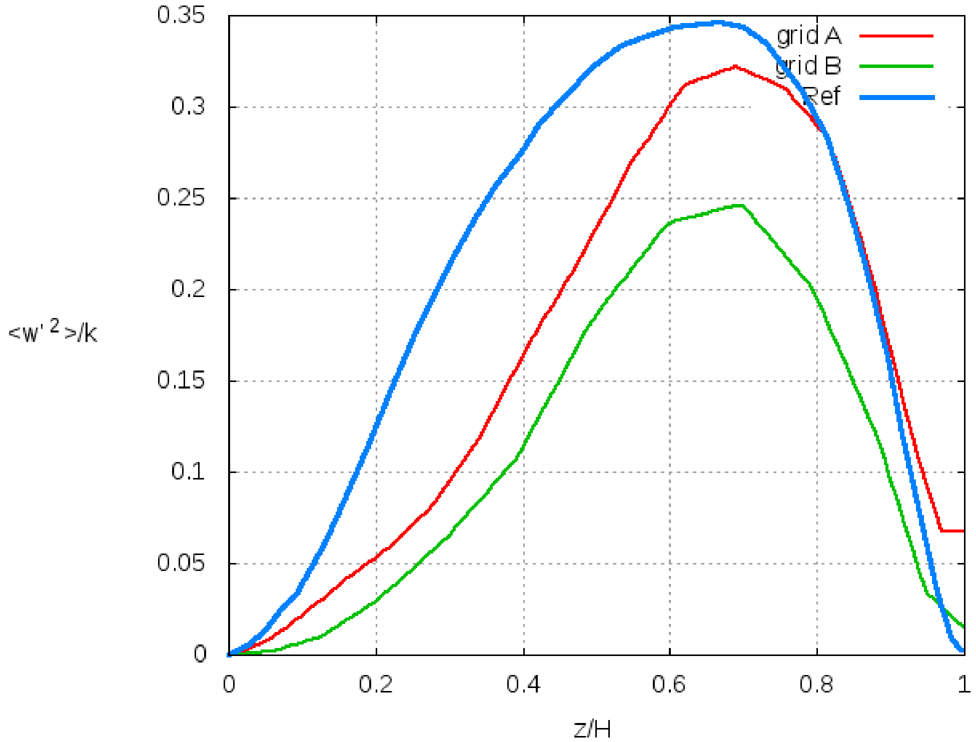

Figure 4. Vertical profile of vertical Reynolds stress dimensionless with the turbulent kinetic energy and results from DNS of Handler et al., 1993.

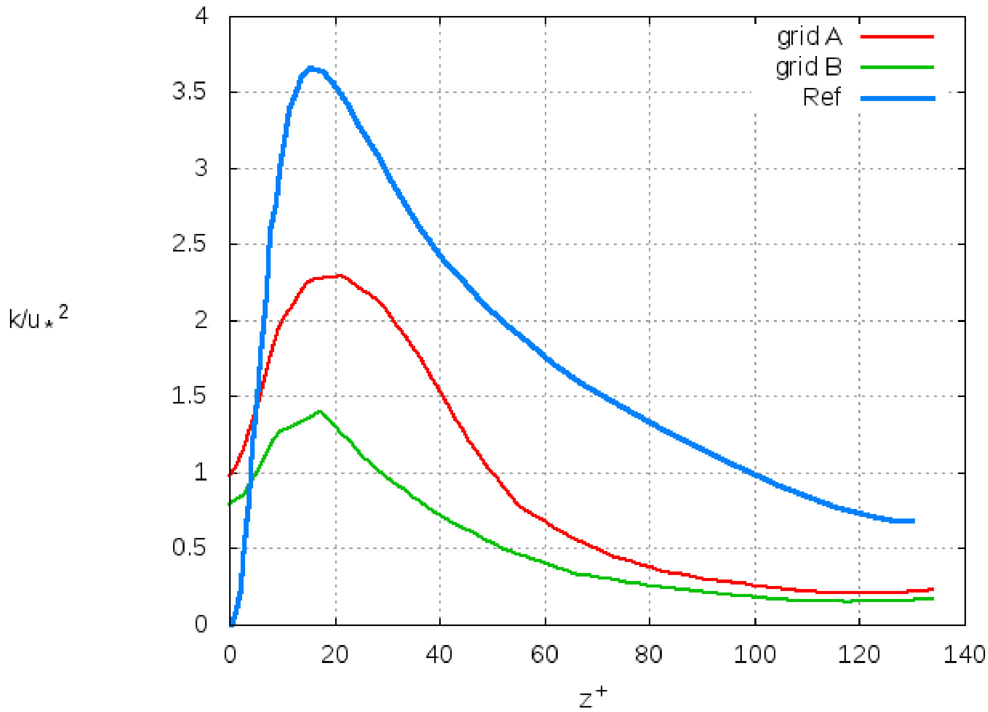

Figure 5. Vertical profile of turbulent kinetic energy dimensionless with the square of friction velocity and results from experiments of Komori et al., 1983.

Figure 1 shows that the theoretical expression of the turbulent kinetic energy compares well to the experiments of Komori et al., 1983. Indeed, the prescribed profile is consistent with the experimental reference curve. Even if the turbulence is assumed isotropic, the anisotropic behavior is recovered very quickly in the channel. As shown in Figures 2, 3 and 4, the global distribution of the fluctuations are well reproduced except near the bottom. Indeed, the streamwise and spanwise velocities show significant discrepancies with DNS results which should be imputed to the implementation of the friction.

Furthermore, in figure 5, the amplitude of the velocity fluctuations decreases sharply with the fluid progression, particularly for the coarse mesh. At this low Reynolds number, this loss of energy is quite overestimated, because the sub grid model should have a negligible effect in this case.

5 CONCLUSIONS

A Large-Eddy-Simulation approach is developed and implemented in TELEMAC-3D (Hervouet, 2007) for modelling free surface complex flows. After carrying out a state of the art of LES methods in hydraulics, three sub grid models are selected to be implemented. Since this kind of simulation requires specific boundary conditions, the Synthetic Eddy Method (SEM) (Jarrin et al., 2006)) is used at the inlet boundary for generating velocity fluctuations, and a wall model is being discussed.

The first developments allow us to get preliminary results. The SEM is a good alternative to a precursor simulation since it permits to introduce realistic velocity fluctuations with a low computation cost. By defining a simple analytical turbulence kinetic energy profile, a fully developed turbulence flow can rapidly be obtained.

The global behavior of the turbulence indicators are satisfactory but the first results show that the turbulent

kinetic energy decreases faster than expected. Indeed, a great part of the turbulence intensity introduced by the SEM is lost at the beginning of the fluid progression. We foresee that it is due to the numerical schemes used in TELEMAC-3D which are too much dissipative. Yet, the recycling method cannot be used because the turbulent energy does not reach the outlet of the computation domain.

The next step will consist in implementing high order numerical schemes, mainly for the advection term, and new wall models more appropriate for Large-Eddy-Simulation.

ACKNOWLEDGEMENTS

This work is funded by French Agence Nationale de la Recherche programme under a contract with a reference number ANR-10-IEED-0006-11

REFERENCES

Germano, M., Piomelli, U., Moin, P. & Cabot, W.H., (1991). A Dynamic Subgrid-Scale Eddy Viscosity Model. *Physics of Fluids A: Fluid Dynamics* (1989-1993), 3(7),1760–1765.

Guillou, S. & Makhloufi, R., (2007). Effect of a Shear-Thickening Rheological Behaviour On The Friction Coefficient In A Plane Channel Flow: A Study By Direct Numerical Simulation. *Journal of non-newtonian fluid mechanics*, 144(2), 73–86.

Handler, R.A., Swean, T.F., Leighton, R.I. & Swearingen, J.D., (1993). Length Scales and The Energy Balance for Turbulence Near a Free Surface. AIAA journal, 31(11):1998–2007.

Hervouet, J.-M., (2007). *Hydrodynamics of Free Surface Flows: Modelling with the Finite Element Method*. John Wiley & Sons

Jarrin, N., Benhamadouche, S., Laurence, D. & Prosser, R., (2006). A Synthetic-Eddy-Method For Generating Inflow Conditions For Large-Eddy Simulations. *International Journal of Heat and Fluid Flow*, 27(4), 585–593.

Komori, S., Ueda, H., Ogino, F. & Mizushina, T. (1983). Turbulence Structure in Stably Stratified Open-Channel Flow. *Journal of Fluid Mechanics*, 130,13–26.

Lilly, D.K. (1992). A Proposed Modification of The Germano Sub Grid-Scale Closure Method. Physics of Fluids A:Fluid Dynamics (1989-1993), 4(3), 633–635.

Nicoud, F. & Ducros, F. (1999). Sub Grid-Scale Stress Modelling Based on The Square of The Velocity Gradient Tensor. *Flow, turbulence and Combustion*, 62(3), 183–200.

Sagaut, P., (2006). *Large Eddy Simulation for Incompressible Flows: An Introduction*. Springer Science & Business Media.

Smagorinsky, J., (1963). General Circulation Experiments with The Primitive Equations: I. The Basic Experiment. *Monthly weather review*, 91(3), 99–164.

Spalart, P.R., Strelets, M. & Travin, A. (2006). Direct Numerical Simulation of Large-Eddy-Break-Up Devices in A Boundary Layer. *International Journal of Heat and Fluid Flow*, 27(5), 902–910.

Van Driest, E.R. (2003). Turbulent Boundary Layer in Compressible Fluids. *Journal of spacecraft and rockets*, 40(6), 1012–1028.

Proceedings of the 37th IAHR World Congress
August 13 – 18, 2017, Kuala Lumpur, Malaysia

CONSTRAINT SATISFACTION PROBLEM VS QUADRATIC OPTIMIZATION METHOD TO DEAL WITH THE EFFECTS OF CLIMATE CHANGE ON INLAND WATERWAYS

ERIC DUVIELLA[(1)], ARNAUD DONIEC[(2)], HOUDA NOUASSE[(3)], FRANCK TEMPET[(4)]

[(1,2,4)]Institut Mines Telecom Lille Douai, France
eric.duviella@imt-lille-douai.fr, arnaud.doniec@imt-lille-douai.fr
[(1,2,4)]Université de Lille, France
[(3)]Gipsa-lab, Domaine Universitaire - BP 46, 38402 Saint Martin d'Hères cedex
houda.nouasse@gmail.com

ABSTRACT

The domains of inland waterway transport and water resource management are two issues requiring a joint study. On one side, transport logistic approaches integrate multimodal solutions where inland navigation has more and more importance. On other side, researches on water resource consist of increasing the knowledge on hydraulic phenomena, on the impacts of global change, and in improving water resource management strategies to accommodate the navigation. It consists of controlling hydraulic structures of inland waterways to allocate available water resource amongst the network and thus keeping water levels close to their objective. An adaptive allocation planning of water resource has been proposed firstly to optimize the water allocation over a given management horizon and secondly to determine the resilience of inland navigation networks against the increase of navigation demand, drought and flood events, *i.e.* their capacity to allow the navigation. The optimal water allocation techniques can be designed as CSP (Constraint Satisfaction Problems) or QOP (Quadratic Optimization Problems). CSP consist of finding values in a finite domain with respect to a finite set of constraints. As alternative, QOP are considered as continuous domain. Both approaches are based on a dynamic directed flow graph. The main objective of this paper is to present simulation architecture on Matlab/Simulink dedicated to the implementation and test of CSP and QSP approaches. A real sub-network of inland waterways in the north of France that would be subjected to climate hazards and increase of the navigation demand should be considered. The design and implemention step of both approaches are described.

Keywords: Inland waterways; climate change; water management; constraint satisfaction problem; quadratic optimization.

1 INTRODUCTION

Inland waterway transport requires an efficient water management particularly to face an expected increase of navigation demand in a global change context. Inland navigation profits of economic and environmental interests that should lead to its future development (Brand et al., 2012). Global change will impact waterways (Bates et al., 2008; Wanders & Wada, 2015). Several studies (EnviCom, 2008; IWAC, 2009; Arkell & Darch, 2006) reached the conclusion that inland waterways will be impacted by climate hazard. In (Pant et al., 2015), a dynamic model is proposed for estimating the impact of disruptions in inland waterway networks by considering possible new multimodal transport infrastructures. It appears that new infrastructure policy is necessary to guaranty navigation conditions. This conclusion is more moderated in (Beuthe et al., 2014) which a methodology based on the NODUS transport model is proposed to study the impacts of climate change and new infrastructures on transport on the Rhine and Danube corridors. According to these studies, no serious impact due to climate change is expected but more are expecting impact due to a new multimodal transport split. From 2013 to 2016, a French project GEPET-Eau[1] aimed at contributing to the objectives of the French plan for adaptation to the global change by designing adaptive and predictive management strategies for inland navigation networks. In the framework of this project, multi-scale management architecture has proposed (Duviella et al., 2013) gathering tools that are designed for water level control (Horvàth et al., 2015; Rajaoarisoa et al., 2013), and water volume allocation (Nouasse et al., 2016a). The designed tools are used to control hydraulic structures of inland waterways to keep water levels close to their target level, and to allocate available water resource amongst the network. The methodology of adaptive allocation planning of water resource that is proposed (Nouasse et al., 2016a) consists firstly in determining the resilience of inland navigation networks against the increase of navigation demand, drought and flood events, i.e. their capacity to allow the navigation. Secondly, an optimal water allocation technique is designed to improve the water resource dispatching over a management horizon. And finally, if it is necessary, structural adaptations of the networks can be proposed to improve their resilience (Nouasse et al., 2016b). The optimal water allocation techniques are based on CSP (Constraint Satisfaction Problems) (Nouasse et al.,

[1] https://gepeteau.wordpress.com/enversion/

2016a) or on QOP (Quadratic Optimization Problems) (Duviella et al., 2016). CSP consists of finding values in a finite domain with respect to a finite set of constraints. CSP is considered as a very powerful tool for modeling, especially thanks to the support of a wide range of constraints: logical, arithmetic, temporal, lexical. But CSP is restricted to discrete problems. As an alternative, QOP is dedicated to the continuous domain. However, they require powerful optimization algorithms. Both approaches were used to improve the management of water resource of inland navigation networks by determining the optimal water allocation planning over a future time horizon. Their implementation requires the proposal of an integrated dynamic model of inland waterways to inventory interactions between navigation reaches and natural rivers, and a dynamic directed flow graph to generate the constraints on the operating conditions of the controlled hydraulic structures. To facilitate the use of these proposed approaches for the study of the increase of navigation demand and the possible impacts of global change, a software was developed (Mayet et al., 2016). It is based on a web interface where users can describe every configuration of inland navigation networks, define several scenarios of operating conditions and test them. However, the current version of the software allows only the study of one day scenario. Thus, the main objective of this paper is to present a new simulation architecture that enables the use of a simulation tool as Matlab/Simulink. The aim is to reproduce the dynamics of inland waterways on several days. This simulation tool is linked to a QSP method of Matlab or to a CSP method based on the Open Source Java Choco (Jussien et al., 2008). These new developments allow the implementation and test of CSP and QSP approaches by considering real case-studies. A real sub-network of inland waterways that is located in the north of France is thus considered. Some scenarios based on the increase of the navigation demand or extreme climate events are designed and tested.

The content of this paper is structured as follows: Section 2 is dedicated to the description of the management objectives of inland waterways, the presentation of the integrated dynamic model and finally the dynamic directed flow graph. Section 3 presents algorithms that are designed for both optimal water resource allocation planning approaches (QOP and CSP). In Section 4, the developed software and the new simulation architecture are described. In Section 5, a real inland navigation network located in the north of France is introduced to illustrate the proposed simulation architecture by considering a scenario of operating conditions. Finally, conclusions about the performed work are drawn in Section 6.

2 INLAND WATERWAYS MANAGEMENT STRATEGIES

2.1 Inland waterways management objectives

An inland waterway network is composed of several navigations reaches (NR) that are interconnected by locks (*see* Figure 1). A NR is defined as a section of the network between at least two locks.

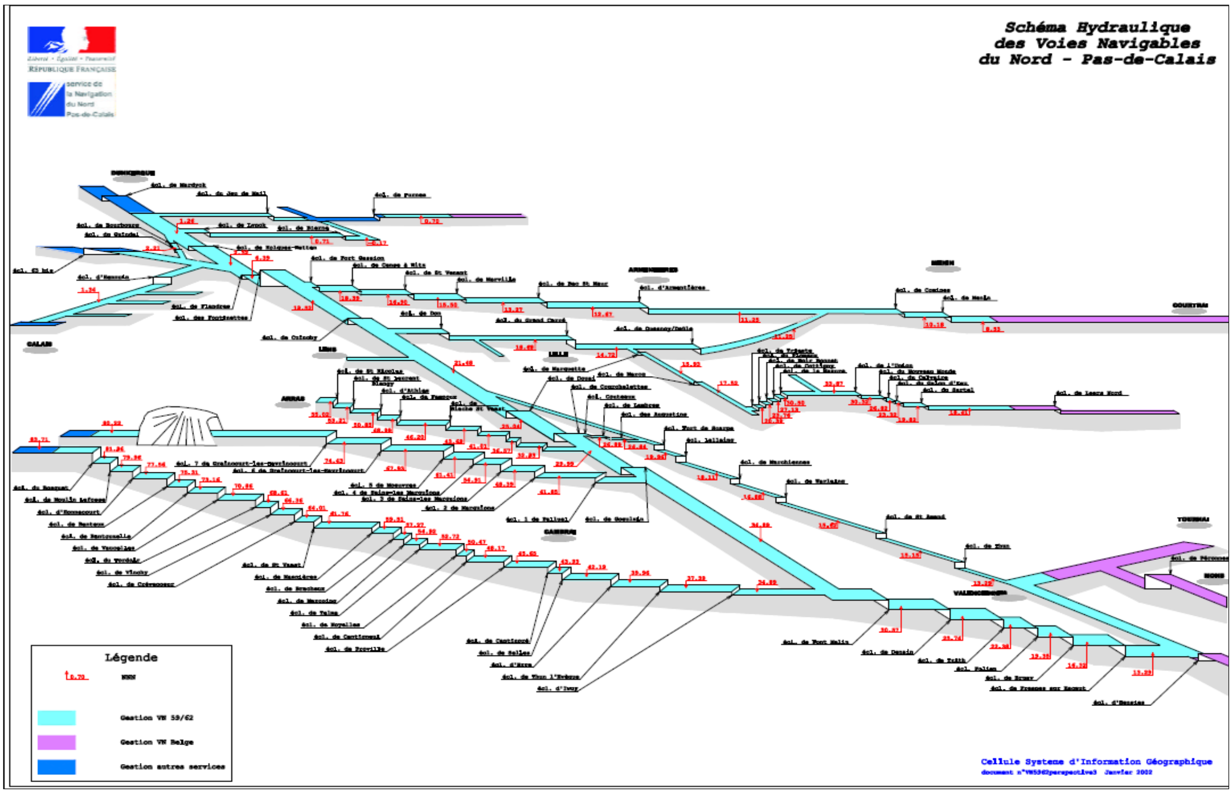

Figure 1. Inland waterway network of the north of France that is composed with more than 50 reaches.

The main management objective is to keep the water level of each NR around the Normal Navigation Level (NNL) and inside the navigation rectangle (see Figure 2). NR are equipped with gates and dams that are used to exchange water volumes between them. Locks are operated only for navigation, but they can be used without navigation demand in exceptional situations to exchange water between reaches. In addition, inland waterways are located inside watersheds and some exchanges with natural rivers can be controlled with gates. Others uncontrolled exchanges with natural rivers are often actively present. Statistical approaches can be used to determine their quantities.

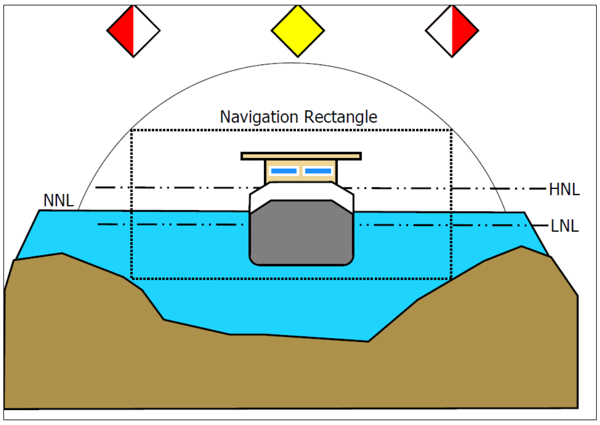

Figure 2. Navigation rectangle with the Normal Navigation Level (NNL).

Hence, the management of interconnected reaches consists in defining setpoint to the controlled gates in order to guaranty the NNL, by anticipating the navigation demand (the daily number of lock operations) and estimating the uncontrolled water exchanges.

During *normal* operating conditions, the water volume (directly linked to the water level) inside each NR is principally disturbed by lock operations (navigation demand) and uncontrolled water exchanges (natural rivers). During *flood* events, uncontrolled water exchanges have the biggest impact on NR because the water exchanges are higher. During *drought* events, uncontrolled water exchanges have low impact and it is less possible to supply the network with water from rivers thanks to controlled gates. Finally, if the navigation demand will increase, water exchanges due to lock operation will rise up, and it will be more difficult to supply the NR to compensate the water volume required for navigation.

To model inland waterways and determine all interactions between navigation reaches and natural rivers, an integrated dynamic model has been proposed in (Duviella et al., 2014). It is described in the following.

2.2 Integrated dynamic model of inland waterways

The integrated dynamic model consists in considering a water volume inside each NR during a step time. Thus, the i[th] NR is modelled as a tank containing the volume $V_i(k)$ at time *k*. This tank can be supplied and emptied by:

- a set of controlled volumes that gather the water that is coming from controlled gates and from the lock operations:
  - controlled volumes from all the upstream NR that supply the NR_i, denoted $V_i^{s,c}$ (*s*: supply, *c*: controlled),
  - controlled volumes from the NR_i that empty it, denoted $V_i^{e,c}$ (*e*: empty),
  - controlled volumes from water intakes that can supply or empty the NR_i, denoted V_i^{c}. These volumes are signed; positive if the NR_i is supplied, negative otherwise.
- a set of uncontrolled volumes that correspond to the withdrawals and supplies from water intakes located along the NR_i, and also exchanges with groundwater when they are considered:
  - uncontrolled volumes from natural rivers, rainfall-runoff, Human uses, denoted V_i^{u} (*u*: uncontrolled). These volumes are signed depending of their contribution,
  - uncontrolled volumes from exchanges with groundwater, denoted $V_i^{g,u}$ (*g*: groundwater). These volumes are also signed.

Based on these definitions, the dynamical model of the water volume $V_i(k)$ in the NR_i is expressed as:

$$V_i(k) = V_i(k-1) + V_i^{s,c}(k) - V_i^{e,c}(k) + V_i^{c}(k) + V_i^{u}(k) + V_i^{g,u}(k) \qquad [1]$$

with *k* the sample time.

  / ISSN 1562-6865 (Online) - ISSN 1063-7710 (Print)

The management objective consisting in keeping the water level close to the NNL, an objective volume for each NR is defined as V_i^{NNL}, and the navigation rectangle is taken into account by considering an interval around $V_i(k)$ such as:

$$V_i^{LNL} \leq V_i(k) \leq V_i^{HNL} \quad [2]$$

Controlled volumes that are defined above are also bounded according to the characteristics of hydraulic structures:

$$\begin{cases} \underline{V_i^{s,c}} \leq V_i^{s,c} \leq \overline{V_i^{s,c}} \\ \underline{V_i^{e,c}} \leq V_i^{e,c} \leq \overline{V_i^{e,c}} \\ \underline{V_i^{c}} \leq V_i^{c} \leq \overline{V_i^{c}} \end{cases} \quad [3]$$

with $\underline{V_i}$ and $\overline{V_i}$ the inferior and superior bounds respectively.

Then, the configuration of inland navigation networks is modelled according to links between tanks (NR) by considering as elementary links: the linear link, a tributary and a distributary. As example, a network is depicted in Figure 3.a. It is composed of 5 NR from NR_{i-2} to NR_{i+2}. The NR_i is supplied by the water volumes coming from NR_{i-1} and NR_{i-2}, and it supplies NR_{i+1} and NR_{i+2}. The corresponding integrated model is depicted in Figure 3.b.

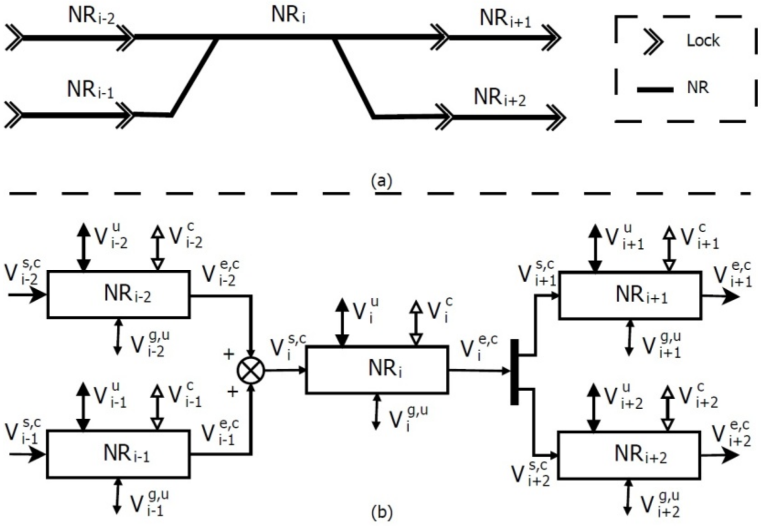

Figure 3. (a) Inland navigation network, (b) Integrated model.

2.3 Dynamic directed flow graph

Based on the proposed integrated model, a dynamic directed flow graph is designed. It consists in modelling all the possible water volume exchanges between the NR taking into account the boundaries on the controlled volumes. Network flow models are dedicated to solve problems of transportation (Silver and de Weck, 2007; Jonkeren et al., 2011), optimization of drinking water networks (Grosso et al., 2014) and flood attenuation (Nouasse et al., 2013). A network flow model is defined as a connected directed graph $G = (G_x, G_a, C)$, where G_x is the set of nodes, G_a is the set of arcs and C a set of dynamical attributes of the graph such as capacities or transit times. Each NR is representing by a node. The number of the node corresponds to the index of the NR_i, i ∈ G_x. Two additional nodes represent the source O and sink N, $\{O, N\} \in G_x$. A directed arc between two nodes is defined as a couple a=(i, j) ∈ G_a, with i the node that is leaving and j the node that is entering. On every arc a ∈ G_a, it is associated a flow variable $\square_a$ that can also be expressed by $\square_{ij}$. This flow has to respect capacities constraints $\{l_a, u_a\} \in C$, with l_a the lower and u_a the upper bound capacities of the arc a. These capacities are determined according to the bounds on controlled volumes (see relation 3) and the estimated uncontrolled volumes. Finally, on every node, it is associated the current volume $V_i(k)$ that has to respect the navigation constraints $\{V_i^{LNL}, V_i^{HNL}\} \in C$. The nodes correspond to each NR, and the arcs are directed according to the configuration of the navigation network. The node O gathers all the volumes of water that supply the navigation network from upstream and natural rivers. The node N retrieves all the volumes of water from the navigation network. The navigation network in Figure 3 is used to illustrate the design the directed flow graph that is shown in Figure 4.

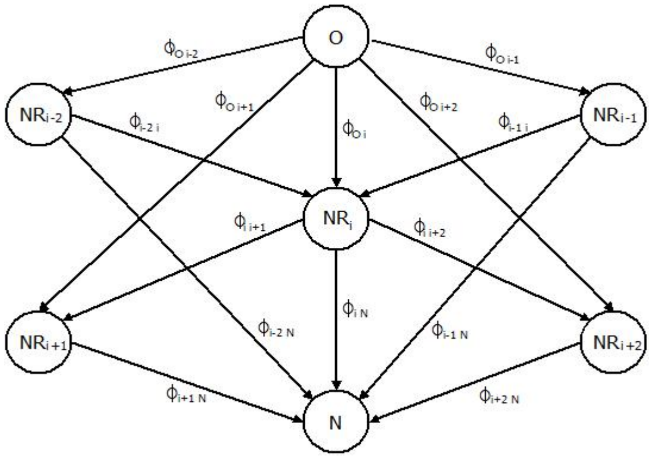

Figure 4. Directed flow graph.

The dynamic graph representing flow evolution over time is defined such as volume on node i at time k depends on volume on node i at time (k-1):

$$V_i(k) = V_i(k-1) + \phi_{a^+} - \phi_{a^-} \qquad [4]$$

with a^+ the arcs leaving the node *i* and a^- those entering. This modeling approach is then used to facilitate the design of resource allocation planning approaches.

3 OPTIMAL WATER RESOURCE ALLOCATION PLANNING

The management objective is taken into account by associating a dynamical demand $d_i(k)$ at each node of the directed flow graph. This demand is computed as:

$$d_i(k) = V_i(k) - V_i^{NNL} \qquad [5]$$

with $V_i^{NNL} - V_i^{HNL} \leq d_i(k) \leq V_i^{NNL} - V_i^{LNL},\ i \in G_x - \{O, N\}$, to respect the navigation rectangle.

The demand $d_i(k)$ has to be equal to 0 to keep the water level at the NNL. However, depending on $V_i(k)$, this demand can be positive or negative. When $d_i(k)$ is negative, the NR_i is not enough fulfilled and this NR is in demand of water. In the opposite, NR_i is too fulfilled and water volumes have to be withdrawn. Hence, the management objective consists in dispatching water volumes amongst the flow graph to keep a maximum number of $d_i(k)$ equal to 0.

3.1 Constraint satisfaction problem approach

The water resource allocation planning is defined as a constraint satisfaction problem (CSP), *i.e.* a set of variables taking their value in a finite domain and subject to a finite set of constraints. The objective is to keep all the $d_i(k)$ the closest as possible to 0 by transferring water volumes thanks to the arcs (determining the flows □$_a$). The flows take values in their domain which is consistent with all constraints, *i.e.* $\{l_a, u_a\}$. An algorithm is proposed to show how constraint programming is integrated to calculate the optimal flow, using *Choco Open Source Java library* (Jussien et al., 2008).

Table 1. Water resource allocation planning algorithm based on a CSP.

Input: Integrated Model, G	**for** $\emptyset_a$, $a \in G_a$ **do**
Output: $\emptyset$. d	declare $\emptyset_a$ as variable of the CSP, with $[l_a; u_a]$ as domain;
Local: CSP	set $d_i(k) = \phi_{a^+} - \phi_{a^-},\ i \in G_x - \{O, N\}$ as constraint of the CSP;
for $\emptyset_a$, $a \in G_a$ do	set $V_i^{NNL} - V_i^{HNL} \leq d_i(k) \leq V_i^{NNL} - V_i^{LNL}$ as constraint of the CSP;
compute l_a and u_a;	**end**
end	solve the CSP to obtain the value of the $\emptyset_a$, $a \in G_a$;
$l_{max} = \max_{a \in G_a} l_a$; $\phi_a \xleftarrow{l_a = l_{max}} l_{max}$;	**return** flow vector $\emptyset$ and demand vector d

By considering a management horizon T_M, this algorithm leads to the determination of all the discharge setpoint of each controlled gate. These values are contained in the flow vector □□ (Nouasse et al., 2016a)□

3.2 Quadratic optimization problems approach

A weight function $W(|d_i(k)|)$ is defined to penalize the gap between each current demand $d_i(k)$ and its objective. Also, a weight w_a is associated to each arc *a* with the aim to favor some of them. Managers can decide which of these arcs have the priority to supply or to empty the NR. An objective function is thus defined:

$$J(k) = \sum_{i=1}^{\eta} W(|d_i(k)|) + \sum_{a=1}^{\alpha} w_a \phi_a(k) \qquad [6]$$

with η the number of NR, α the number of arcs.

The aim is now to minimize the objective function J(k) by verifying equality constraints according to the direct flow graph (*see* relation 4), and the constraints on each flow (*see* relation 3). This objective function is minimized using the convex minimization method *fmincom*[2] in Matlab:

$$\min J(k) \ \ such\ that \begin{cases} L_b(k) \leq x(k) \leq U_b(k) \\ A.x(k) = b(k) \end{cases} \qquad [7]$$

with *x(k)* is a vector composed by elements of □□(k) and ***d***(k) (the flows and demands respectively), $L_b(k)$ and $U_b(k)$ are vectors composed by boundaries of $\phi_a(k)$ and $d_i(k)$. The last condition allows considering the dynamic relation of each node following the equation 4, where the vector *b(k)* contains the values of $d_i(k-1)$ of the previous period, and the matrix A is composed with 0 or 1 following the equation 4 and the structure of the directed flow graph.

The proposed quadratic optimization problems approach leads to the determination of the setpoint that will be assigned to the hydraulic structures of the inland waterways keeping the water levels close to their NNL (Duviella et al., 2016).

4 OPTIMAL WATER RESOURCE ALLOCATION PLANNING SOFTWARE

4.1 User's web-interface

A user's web-interface has been developed for the study of the resilience of waterways against the increase navigation demand and climate extreme events. This interface uses HTML 5, CSS and three frameworks Javascript: jointJS for the diagrams, JQuery for user's events and Bootstrap for the graphical elements: buttons, edit text, etc. The user can model inland waterways whatever is their configuration. Each NR is modeled by a cyan rectangle (*see* Figure 5). Links between NR are represented with black arrows, by considering two more elements; the tributary and distributary elements.

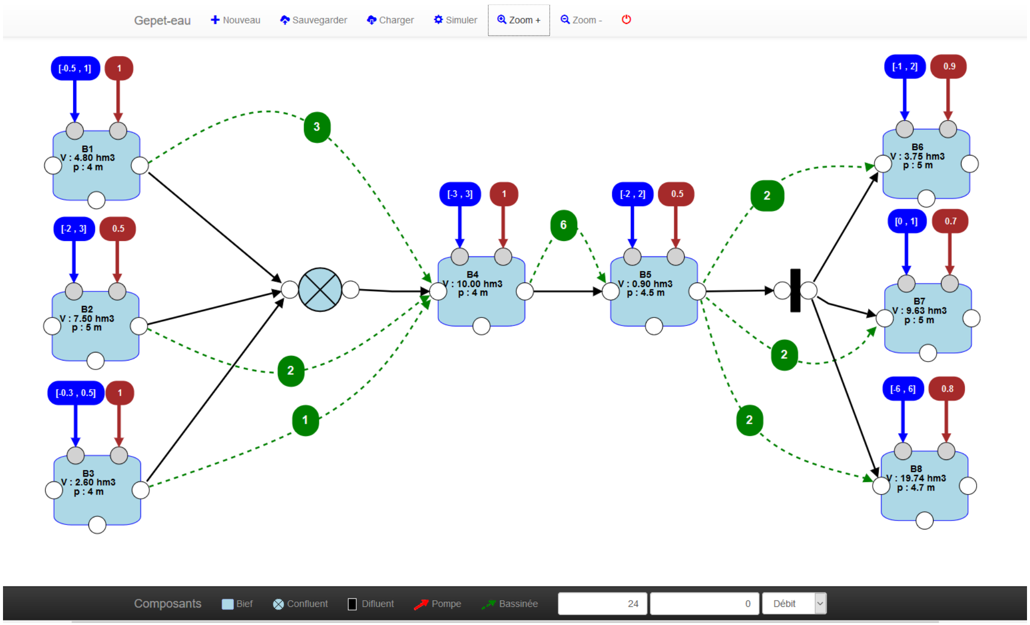

Figure 5. Screenshot of the web interface.

Once the configuration of the network is modeled, users have to specify the dimension of each NR (length, width and depth), limits that correspond to the navigation rectangle, the dimensions of the locks, *i.e.* the volume corresponding to one lock operation. They have also to indicate the controlled hydraulic structures like gates and dams and their operating range. These hydraulic structures can be located between NR or

[2] http://fr.mathworks.com/help/optim/ug/fmincon.html?requestedDomain=www.mathworks.com

between NR and natural rivers. The operating ranges of hydraulic structures from rivers are in blue rectangles up to the NR cyan rectangles. The discharge values of the uncontrolled hydraulic structures are depicted in red rectangles. Finally, the number of lock operations between each NR is indicated thanks to green arcs.

This web interface allows simulating some scenarios by modifying the management step k_M (in hours), increase or decrease the available water resource to simulate periods of drought or flood. When a scenario is defined, all the constraints are generated and the water resource allocation planning algorithm based on a CSP is used (*see* Table 1). When a solution is obtained, results are shown in discharges or in volumes on each arcs in pink rectangle (*see* Figure 6).

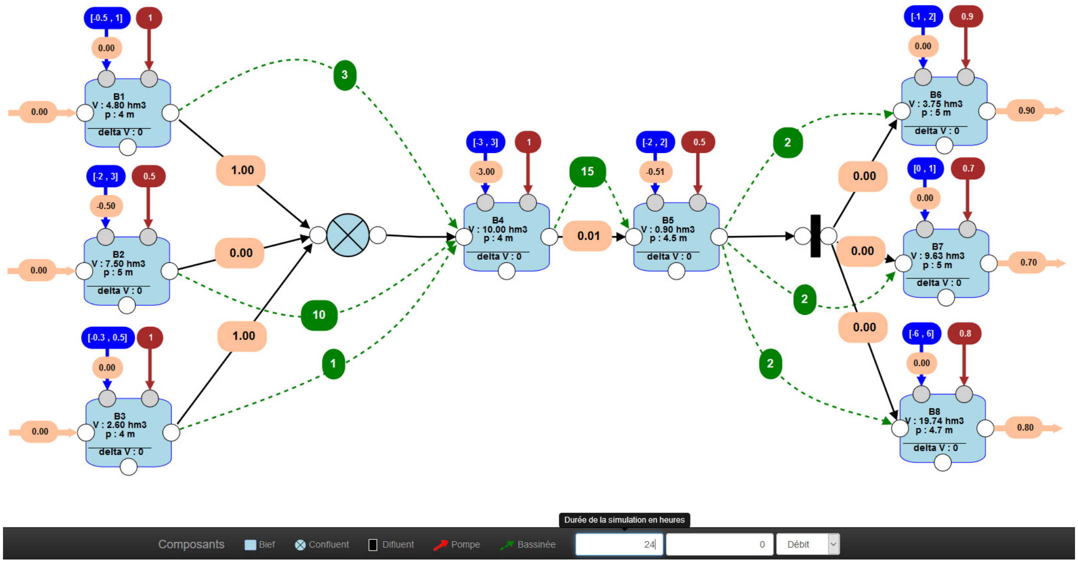

Figure 6. Screenshot of the web interface with determined setpoint .

Several case studies were studied (Nouasse et al., 2016a; 2016b). This development allows studying resilience of inland waterways with a simple and faster way. However, at this time, only the CSP approach can be used and only one step time can be considered. It is not possible to consider a large management horizon of several management steps. Improvements are proposed to be able to use others optimization approaches and to simulate the behavior of inland waterways on larger management horizons.

4.2 New simulation architecture

The objective is to propose a new simulation architecture allowing dynamical simulations of inland waterways, based on the developed user's web-interface and a simulation tool. The chosen simulation tool is Matlab/Simulink that is dedicated to simulating dynamical systems. The simulation architecture has to let the user to select the optimal water resource allocation planning approach. The simulation architecture is depicted in Figure 7. From the user's web-interface, the network, the constraints and the scenario are sent to the Matlab workspace (*see* 1 in Figure 7). A Simulink model is run at a discrete time k_M corresponding to several hours, with k_M=k.T_M, with T_M the management horizon. At each step k, the current states of the NR, *i.e.* $d_i(k)$, and the forecasted navigation demand are sent to the CSP – Choco or QOP – Matlab approaches, depending of the user choice (*see* 2 in Figure 7). Whatever is the selected optimization approach, new computed setpoint that will be sent to the controlled hydraulic structures are sent to simulink and a new simulation step is run. When the management horizon T_M is reached, all the results can be depicted or sent to the user's interface.

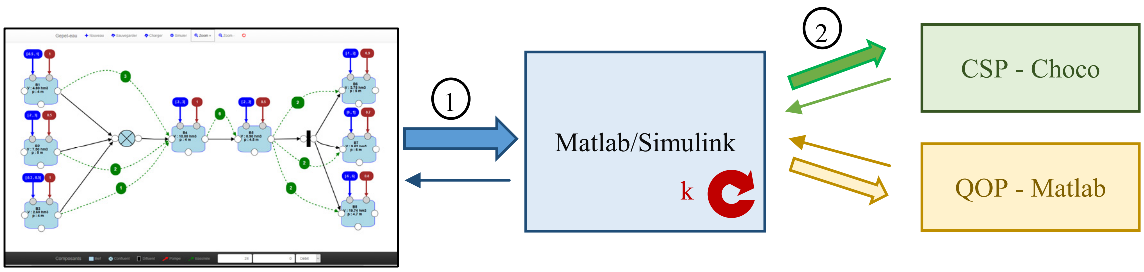

Figure 7. Simulation architecture.

5 REAL CASE-STUDY

A part of the inland waterways in the north of France is considered to illustrate the proposed simulation architecture. Both optimization approaches are tested. Because the obtained results are very similar, only results from QOP are presented. This network is composed of 3 NR from the towns of Douai to Arques and the north of Lille (*see* Figure 8). Characteristics of the NR, operating ranges of the hydraulic structures and the value of the uncontrolled discharges are given in Table 2.

Figure 8. Part of the inland waterways in the north of France.

Table 2. Characteristics of the sub-network of the inland waterways in the north of France.

	Length [km]	**Width** [m]	**Depth** [m]	**HNL(+)** [m]	**LNL(-)** [m]	**Unc. Discharge** [m^3/s]	**Cont. Input** [m^3/s]	**Up. lock sas** [m^3]	**Down lock sas** [m^3]	**Cont. gate up.** [m^3/s]	**Cont. gate Down** [m^3/s]
NR_1	56.724	41.8	3.7	0.1	0.05	6.56	[-1;-1]	6,709	-	-	-
NR_2	42.300	52	4.3	0.05	0.05	0.63	[0;0]	3,526	23,000	[0;6,4]	-
NR_3	25.694	45.1	3.3	0.05	0.05	1.2	0	5,904	7,339	[0;30]	[0;60]

The implementation of the system with the user's interface is depicted in Figure 9.a. The direct flow graph that corresponds to this network is given in Figure 9.b. Characteristics of the system allows the computation of the constraints by considering the number of lock operations and two different periods $k_M^n = 10$ hours for night period (without navigation) and $k_M^d = 14$ hours for daily period (with navigation). The average navigation demands are represented on the green arcs. Finally, a model of the network was implemented in Matlab/Simulink (*see* Figure 10).

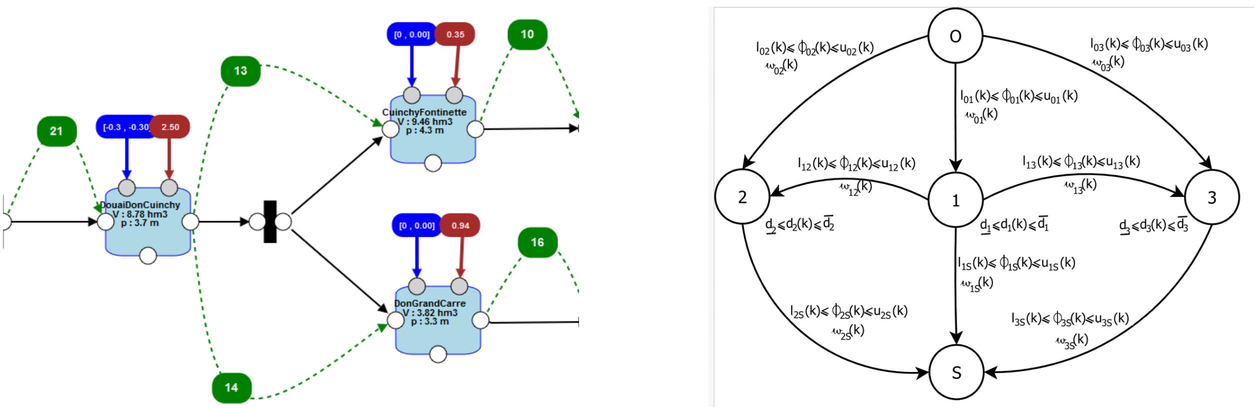

(a) (b)

Figure 9. (a) Studied network implemented with user's web interface, (b) corresponding flow graph.

The proposed scenario consists of considering a management horizon T_M = 8 days. The navigation demands vary around the average navigation demands with the exception of Sunday where no navigation is authorized. In Figure 11, water volumes in each NR are depicted. It is possible to see that whatever is the management period, volumes in NR_1 and NR_3 (*see* Figures 11.a and 11.c) are equal to the management objectives. It is not the case for NR_2 (*see* Figures 11.b) that is supplied with uncontrolled water volume during night (discharge of 0.63 m^3/s) without the possibility to withdraw this volume because this NR is not equipped with any controlled gate. Thus, the volume in NR_2 is raised up during night. During daily period, this water volume in excess is withdrawn due to the lock operations downstream.

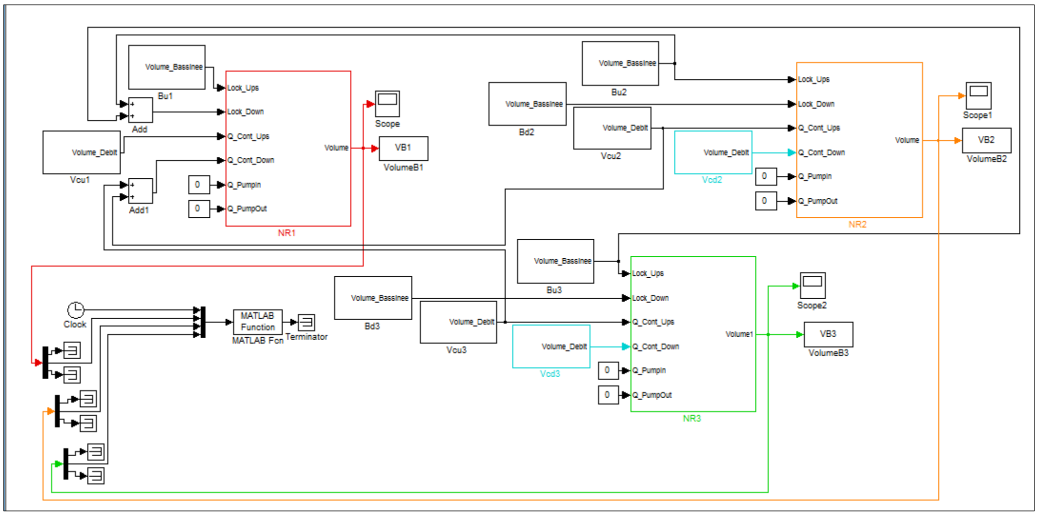

Figure 10. Simulink model of studied network.

There are only three controlled hydraulic structures (*see* Table 2); the gate between NR_1 and NR_2, the gate between NR_1 and NR_3, and the gate downstream NR_3, that are denoted G_{u2}, G_{u3} and G_{d3} respectively (u: upstream, d: downstream). Set points that are sent to these gates to guarantee the management objectives are shown in Figure 12. Gates of NR_3 are almost always controlled; that of NR_2 only during daily period.

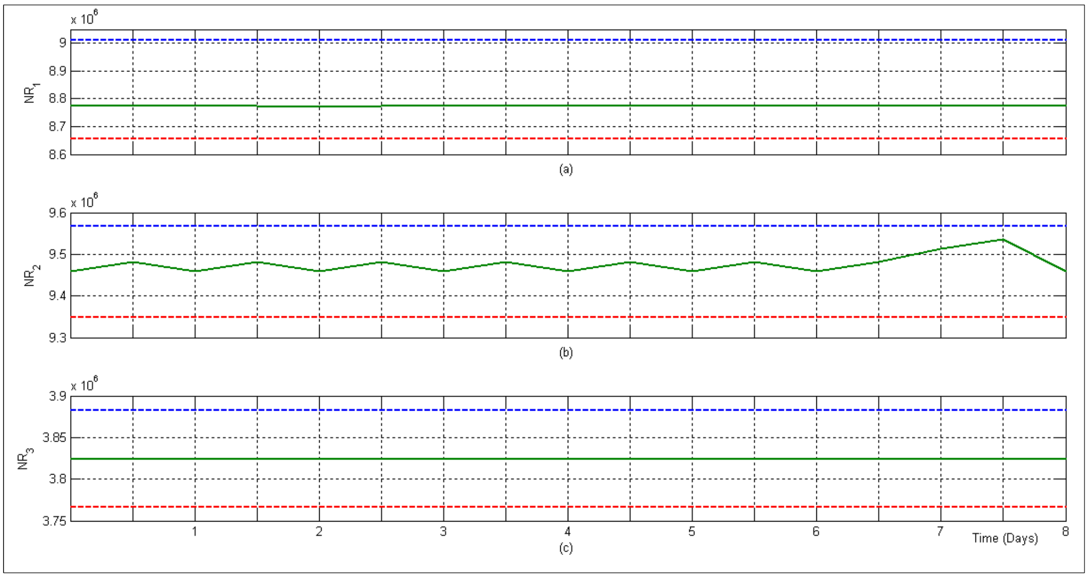

Figure 11. Volumes in (a) NR_1, (b) NR_2, (c) NR_3 (green line) with limits corresponding to navigation rectangle.

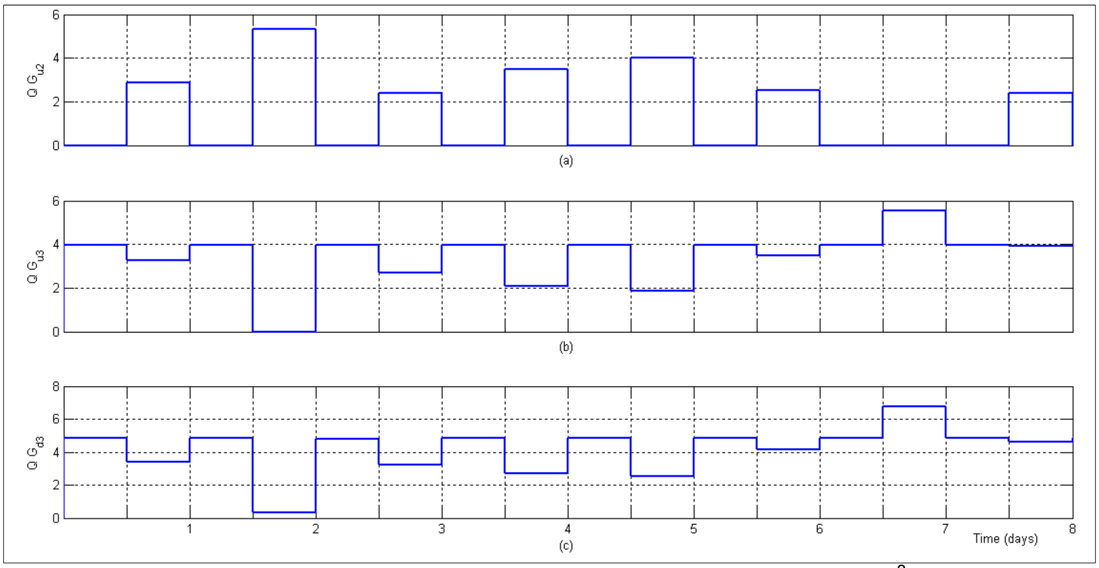

Figure 12. Controlled discharge in (a) G_{u2}, (b) G_{u3}, (c) G_{d3} in [m^3/s].

6 CONCLUSIONS

In this paper, new developments for a simulation architecture dedicated to inland waterways by considering their dynamics on management horizons of several days are proposed. These developments allow the use of Matlab/Simulink with the possibility to implement QOP or CSP optimization approaches. This architecture and associated tools are used to study the impacts of navigation demand increase and extreme events due to climate change by considering real case studies. In this paper, a real sub-network of inland waterways that is located in the north of France is presented. Future works will deal with the development of optimization approaches that takes into account uncertainties, such as large Markov decision processes.

REFERENCES

Arkell, B. & Darch, G. (2006). *Impact of climate change on London's transport326 network*. Proceedings of the ICE - Municipal Engineer, 159, 231-237.

Bates, B., Kundzewicz, Z., Wu, S. & Palutikof, J. (2008). *Climate Change and Water*. Technical Report, Intergovernmental Panel on Climate Change, Geneva.

Beuthe, M., Jourquin, B., Urbain, N., Lingemann, I. & Ubbels, B. (2014). Climate Change Impacts on Transport on the Rhine and Danube: A Multimodal Approach. Transportation Research Part D. *Transport and Environment,* 27, 6-11.

Brand, C., Tran, M. & Anable, J. (2012). The UK Transport Carbon Model: An Integrated Life Cycle Approach to Explore Low Carbon Futures. *Energy Policy*, 41, 107-124.

Duviella, E., Rajaoarisoa, L., Blesa, J. & Chuquet, K. (2013). Adaptive and Predictive Control Architecture of Inland Navigation Networks in a Global Change Context: Application to the Cuinchy-Fontinettes Reach. *IFAC MIM Conference*, Saint Petersburg, June 19-21.

Duviella, E., Horvàth, K., Rajaoarisoa, L. & Chuquet, K. (2014). *Multi-Scale Modeling Approaches of Inland Navigation Networks for Their Management in a Global Change Context*, Transport Research Arena, Paris La Défense, France, April 14-17.

Duviella E., Nouasse, H., Doniec, A. & Chuquet, K. (2016). *Dynamic Optimization Approaches for Resource Allocation Planning in Inland Navigation Networks*, ETFA’2016, Berlin, Germany, September 6-9 2016.

EnviCom (2008): Climate Change and Navigation - Waterborne Transport, Ports and Waterways: A Review of Climate Change Drivers, Impacts, Responses and Mitigation. *Journal of Climate Change*, 93(3-4), 379-388.

Grosso; J.M., Ocampo-Martínez, C., Puig, V. & Joseph, B. (2014). Chance-Constrained Model Predictive Control for Drinking Water Networks, *Journal of Process Control*, 24(5), 504-516.

Horvàth, K., Rajaoarisoa, L., Duviella, E., Blesa, J., Petreczky, M. & Chuquet, K. (2015). *Enhancing Inland Navigation by Model Predictive Control of Water Level the Cuinchy-Fontinettes Case*. Transport of Water Versus Transport Over Water, Exploring the Dynamic Interplay Between Transport and Water, 58.

IWAC (2009). *Climate change mitigation and adaptation. Implications for 399 inland waterways in England and wales*. Report.

Jonkeren, O., Jourquin, B. & Rietveld, P. (2011). Modal-Split Effects of Climate Change. The Effect of Low Water Levels on the Competitive Position of Inland Waterway Transport in the River Rhine Area. *Transportation Research Part A: Policy and Practice*, 45(10), 1007-1019.

Jussien, N., Rochart, G. & Lorca, X. (2008). *Choco: An Open Source Java Constraint Programming Library*, CPAIOR'08 Workshop on Open-Source Software for Integer and Constraint Programming (OSSICP08).

Mayet, A., Pierret, M., Nouasse, H., Tempet, F., Lozenguez, G., Doniec, A. & Duviella, E. (2016). *Outil de simulation pour l'étude de la résilience et l'optimisation de la gestion des réseaux de voies navigables*, MOSIM'16, Montréal, Québec, Canada, August 22-24 2016.

Nouasse, H., Chiron, P. & Archimède, B. (2013). A Flood Lamination Strategy Based on Transportation Network With Time Delay, *Water Science Technology Water Supply*, 68(8), 1668-1696.

Nouasse, H., Doniec, A., Lozenguez, G., Duviella, E., Chiron, P., Archimède, B. & Chuquet, K. (2016a). *Constraint satisfaction problem based on transport graph to study the resilience of inland navigation networks in a climate change context*. IFAC Conference MIM, Troyes, France, 28-30 June.

Nouasse, H., Doniec, A., Duviella, E. & Chuquet, K. (2016b). Efficient management of inland navigation reaches equipped with lift pumps in a climate change context. *4th IAHR Europe Congress*, Liege, Belgium 27-29 July.

Rajaoarisoa, L., Horvath, K., Duviella, E. & Chuquet, K. (2013). *Large-scale system control based on decentralized design.* Application to Cuinchy Fontinette Reach, *IFAC World Congress*, Cape Town, South Africa, 24-29 August 2014.

Pant, R., Barker, K. & Landers, T. L. (2015). Dynamic Impacts of Commodity Low Disruptions in Inland Waterway Networks. *Computers and Industrial Engineering Journal*, 89, 139.

Silver, M. & Weck, O. (2007). Time-Expanded Decision Networks: A Framework for Designing Evolvable Complex Systems, *Systems Engineering*, 10(2), 167-188.

Wanders, N. & Wada, Y. (2015). Human and Climate Impacts on the 21st Century Hydrological Drought. *Journal of Hydrology*, 526, 208-220.

Proceedings of the 37th IAHR World Congress
August 13 – 18, 2017, Kuala Lumpur, Malaysia

FORECASTING OF SIGNIFICANT WAVE HEIGHTS USING A HYBRID EOF-WAVELET-ANN APPROACH

JIHEE OH[1] & KYUNG-DUCK SUH[2]

[1,2] Department of Civil and Environmental Engineering, Seoul National University, Seoul, Korea,
wld12@snu.ac.kr; kdsuh@snu.ac.kr

ABSTRACT

Many studies have been established for the prediction of waves using hybridization of artificial neural networks (ANN) and other techniques to provide effective modeling. In this study, a hybrid empirical orthogonal function analysis (EOF)-wavelet transform-ANN (EOFWLNN) model is introduced and employed to forecast significant wave height simultaneously at 8 locations (Gangneung, Wangdolcho, Genkainada, Tottori, Fukui, Sakata, Aomori, Rumoi) in the East Sea of Korea using 30-min interval wave height observed data and 6 hourly meteorological data. Experiments have been conducted from October 2010 to February 2011 with training and test being conducted for 120 day period and 3 day period, respectively. The EOFWLNN model with 3 decomposition level is employed to make forecast for various lead times. The lead times are fixed as 1, 3, 12 and 24 hours. Model performance is evaluated using R, RMSE and Index of agreement. Most forecasting results show satisfactory performance except Aomori. R and I_a in Aomori are lower than other stations, but for the values of RMSE, it seems to be quite satisfactory. Although the model efficiency decreases as lead-time increases, the model results show good predictions.

Keywords: Forecasting; significant wave height; EOF; wavelet analysis; artificial neural networks.

1 INTRODUCTION

Despite of considerable advances in computational techniques, the solutions obtained by numerically solving the equations of wave growth are neither exact nor uniformly applicable at all sites and at all times due to the complexity and uncertainty of the wave generation phenomenon (Deo at al., 2001). Therefore, many studies was established for the prediction of waves using soft computing tools such as artificial neural network (ANN). Deo et al. (2001) explored the possibility of employing neural networks for wave forecasting. They mentioned that neural network modeling was proper to predict waves since it was primarily aimed at recognition of a random pattern in a given set of input values and did not require the knowledge of the physical process as a precondition. Even though ANN has flexibility, it may not be able to cope with non-stationary data without any preprocessing of the input and output data (Cannas et al., 2006). In the recent years, hybridization of ANN with other techniques was used in wave height forecasting to provide effective modeling (Deka and Prahlada, 2012; 2015; Dixit and Londhe, 2016; Shahabi et al., 2016). Deka and Prahlada (2012; 2015) used wavelet neural network (WLNN) for significant wave height forecasting up to 48 hour lead time using 3 hourly wave height observed data. Their results indicated good predictions at lower lead times but lower accuracies at higher lead times. Dixit & Londhe (2016) also used WLNN technique to predict extreme wave heights up to 36 hour lead time for five major hurricanes. Shahabi et al. (2016) developed genetic programming based wavelet transform to forecast significant wave height up to 48 hour lead time. Hybrid model results showed better prediction performance than single ANN model but their results slight deviation observed at higher lead times. There are limitations of the models: it is difficult to interpret the relationship between spatially distributed meteorological variables and waves and it is necessary to simulate the models for each location separately.

In this study, a hybrid empirical orthogonal function analysis (EOF) -wavelet transform- ANN (EOFWLNN) model is introduced and employed to forecast significant wave height simultaneously at 8 locations in the East Sea of Korea using 30-min interval wave height observed data and 6 hourly meteorological data. EOF analysis can separate spatial and temporal components in the data and it is a useful tool to interpret physical processes. Although EOF analysis has an assumption of stationarity, wavelet analysis can handle non-stationary and transient signals as well as fractal-type structures (Murguia et al., 2006). The decomposed time series are used as inputs to ANN which can handle non-stationarity and non-linearity efficiently.

2 DESCRIPTION OF DATA

Wave data were used at two different buoys (Gangneng and Wangdolcho) provided by Korea Institute of Ocean Science and Technology (KIOST) and at six different buoys (Genkainada, Tottori, Fukui, Sakata, Aomori, Rumoi) provided by Nationwide Ocean Wave Information network for Ports and Harbors (NOWPHAS). Figure 1 shows the locations of wave measurement and Table 1 presents the information of the stations. The wave data of KIOST were obtained every 30 minutes, whereas the wave data of NOWPHAS were obtained every 20 minutes, which were converted into 30 minutes.

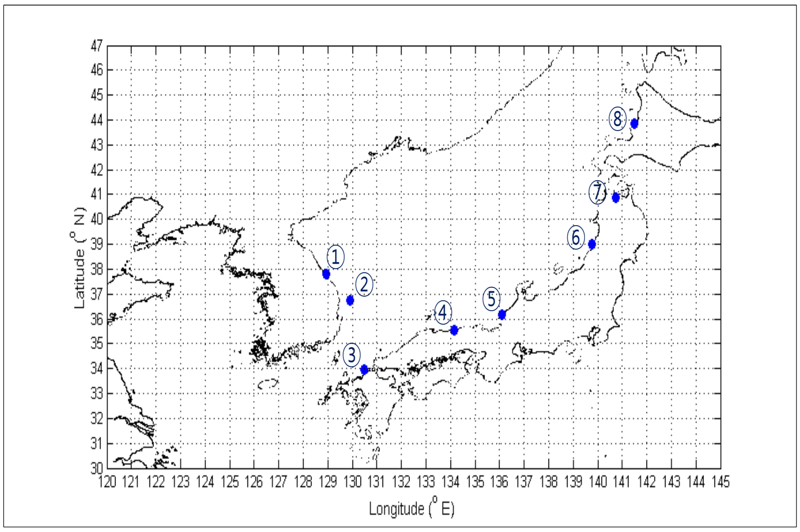

Figure 1. Wave measurement locations

Table 1. Information of wave measurement stations

Station	No.	Location	Waver depth (m)
Gangneung	1	128° 55′ 43.2″ E, 37° 47′ 50.8″ N	15.0
Wangdolcho	2	129° 43′ 52.9″ E, 36° 43′ 10.3″ N	15.3
Genkainada	3	130° 28′ 05″ E, 33° 56′ 02″ N	39.5
Tottori	4	134° 09′ 41″ E, 35° 33′ 16″ N	30.9
Fukui	5	136° 04′ 30″ E, 36° 09′ 50″ N	36.7
Sakata	6	139° 46′ 45″ E, 39° 00′ 31″ N	45.9
Aomori	7	140° 44′ 21″ E, 40° 51′ 10″ N	24.9
Rumoi	8	141° 28′ 07″ E, 43° 51′ 59″ N	49.8

Meteorological data used in this study were the National Centers for Environmental Prediction (NCEP) and National Center for Atmospheric Research (NCAR) reanalysis data provided by National Oceanic and Atmospheric Administration/Climate Diagnostics Center (NOAA/CDC). 10 m height wind speed *u*, *v* and sea level pressure were used for estimating the significant wave heights. The temporal resolution is 30-min interval by interpolation of 6 hour interval data and the spatial resolutions are 2.5 ° × 2.5 ° grid for sea level pressure data and T62 Gaussian grid for wind speed data. Figure 2 shows the region of meteorological data, which is 127° ~ 142° E, 33° ~ 46° N.

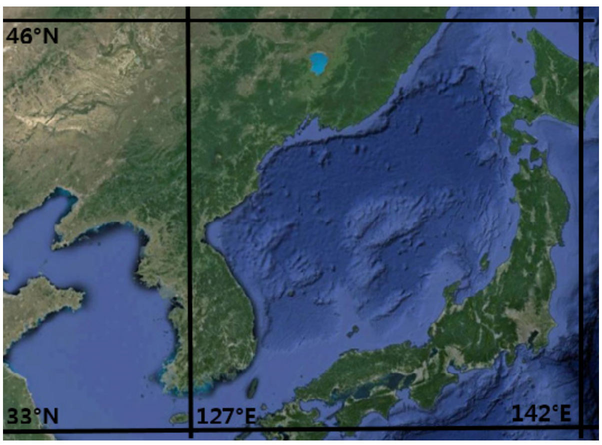

Figure 2. Region of meteorological data

Experiments were conducted for winter season from October to February. The period is 1 year period in 2010 (Oct. 2010 ~ Feb. 2011).

3 METHODOLOGY

3.1 EOFWLNN model

Neural networks combine to EOF analysis and discrete wavelet transform to obtain a powerful nonlinear ability and forecast spatially distributed wave height series, which is called EOF-Wavelet-ANN (EOFWLNN) model in this paper. Figure. 3 is the schematic diagram of the EOFWLNN model. First, EOF analysis is conducted for wave data and meteorological data to separate spatial and temporal components for training period. Each variable is decomposed into several modes, which corresponded 99.9 % variance of the series. Second, wavelet analysis is applied to each PC time series of wave data and meteorological data. The decomposed wavelet signal at level *n* is consisted of sub signals of an approximation and n details. Next, training is conducted with the decomposed wavelet signals of wind speed, sea level pressure and wave height data as input data and each PC time series of wave height data for various lead times for target. Finally, the forecasted wave height PC time series and the loading vectors (LVs) obtained in the first step are reconstructed to calculate the wave height time series at multi-stations.

In this paper, Coiflet 5 (coif5) was chosen among the several types of wavelet families. Feed forward back propagation type of ANN was selected and the Conjugate Gradient Powell-Beale (CGB) scheme was used. The ANN model implementation was carried out using MATLAB toolbox. ANN ensembles were used in order to improve the generalization ability of ANN. The simplest way for creating various ensemble members was used, which is to train each network using randomly initialized weights. After averaging the whole ensemble members, root mean square error (*RMSE*) between ensemble average result and each ensemble member was calculated. Next, the 2 largest *RMSE* cases were removed, then the remained ensemble members were averaged. The iteration is 20 times and the networks training were stopped after maximum 10,000 epochs.

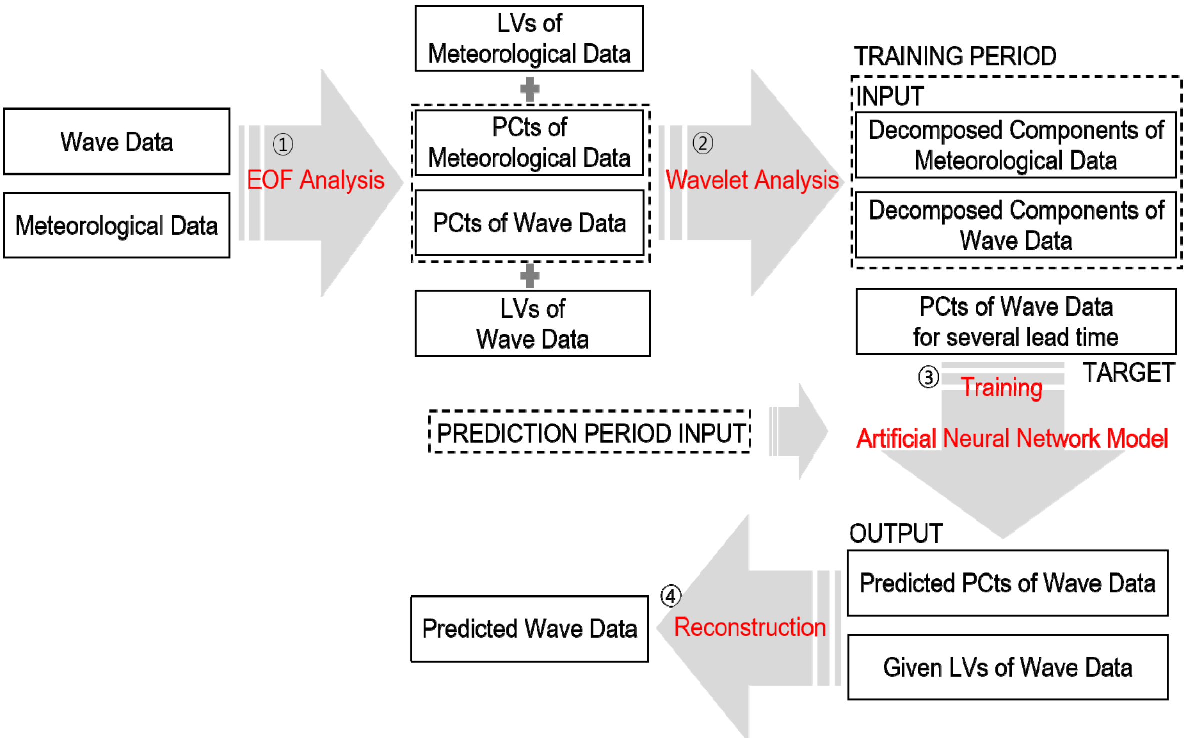

Figure 3. Schematic diagram of the EOFWLNN model

3.2 Model formulations

As mentioned above the decomposed wavelet signals of wave data and meteorological data are used as inputs of ANN, which are those of all the decomposed PC time series of significant wave height and the approximations of 90 % PC time series of meteorological data. To consider the dominance of persistence in the wave height time series and time lag effect of meteorological data, significant wave data of the previous 2 time steps (30 minute data × 2 = 1 h) from the current point and forecasted meteorological data of the previous 6 time steps (30 minute data × 6 = 3 h) were used as predictors. The scenario formed by predictor configuration to predict $H(t+n)$ is $H(t)$, $H(t-1)$, $H(t-2)$, $wnd(t+n)$, $wnd(t+n-1)$, $wnd(t+n-6)$, $slp(t+n)$, $slp(t+n-1)$, $slp(t+n-6)$. Where, H(t) is the current wave height, $H(t-1)$, $H(t-2)$ are previous time steps, $H(t+n)$ is the future significant wave data, *wnd*(*t*+*n*), *slp*(*t*+*n*) are the future meteorological data, *wnd*(*t*+*n*-1), *wnd*(*t*+*n*-6), *slp*(*t*+*n*-1), *slp*(*t*+*n*-6) are previous time steps from the forecasting point and ‘n’ denotes the lead time. The lead times were fixed as 1, 3, 12 and 24 hours.

Experiments were conducted for winter season from October to February. The period is 1 year period in 2010 (Oct. 2010 ~ Feb. 2011). There are two models of forecasting real time significant wave heights. First model is for 1 and 3 hour lead times, and next is for 12 and 24 hour lead times. In case of first model, training was conducted for 120 days (1st Oct. 2010 00:00:00 ~ 28th Jan. 2011 23:30:00) and testing was conducted for 3 days (29th Jan. 2011 00:00:00 ~ 31th Jan. 2011 23:30:00) using the weights and bias obtained from the training period (1st Oct. 2010 00:00:00 ~ 28th Jan. 2011 23:30:00). While, in case of second model, training was conducted for 120 days before each forecasting point and testing was validated for 3 day period.

4 RESULTS AND DISCUSSIONS

To evaluate the model performances, three different performance indices are employed, which are correlation coefficient (*R*), index of agreement(I_a) and *RMSE* according to Eq. [1] to Eq. [3].

$$R = \sqrt{1 - \frac{\sum_i (x_i - y_i)^2}{\sum_i (x_i - \bar{x})^2}} \qquad [1]$$

$$I_a = 1 - \frac{\sum_i (x_i - y_i)^2}{\sum_i \left(|y_i - \bar{y}| + (x_i - \bar{x}) \right)^2} \qquad [2]$$

$$RMSE = \sqrt{\frac{\sum_i (x_i - y_i)^2}{n}} \qquad [3]$$

where, x_i, y_i, $\bar{x}$, $\bar{y}$ and n are observed wave height, forecasted wave height, mean of observed wave height, mean of forecasted wave height and the number of observations, respectively.

Table 2 presents the test results of EOFWLNN model at 8 stations for several lead times. Using R, RMSE and Index of agreement, the accuracy of the results was evaluated. Most forecasting results show satisfactory performance except Aomori. R and I_a in Aomori are lower than other stations, but for the values of RMSE, it seems to be quite satisfactory. Since the waves in Aomori are very calm, RMSE is better error statistics for evaluation of model performance. Figure 4 shows the comparisons between the observed and forecasted wave heights in Sakata and Aomori for several lead times. Although the model efficiency decreases as lead-time increases, the model results show good predictions.

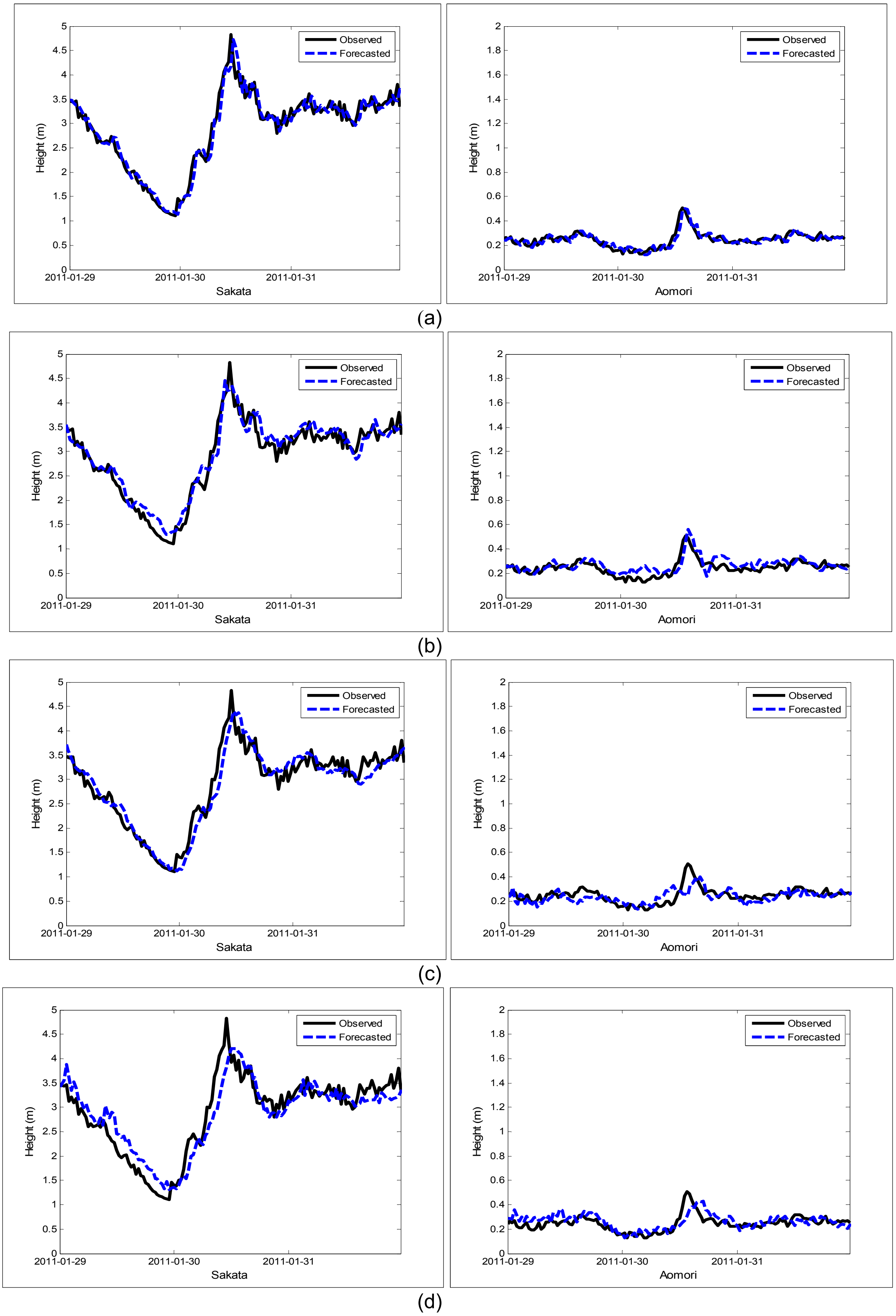

Figure 4. Comparison of observed and estimated wave height series in Sakata and Aomori (a) for 1 hour, (b) for 3 hour, (c) for 12 hour, (d) for 24 hour lead time forecasting

Table 2. Test results of EOFWLNN model for *Hs* at 8 stations for several lead times

Lead time	Station	*R*	*RMSE*	I_a
1 hr	Gangneung	0.97	0.067	0.99
	Wangdolcho	0.94	0.121	0.97
	Genkainada	0.95	0.123	0.98
	Tottori	0.94	0.163	0.97
	Fukui	0.96	0.207	0.98
	Sakata	0.97	0.189	0.99
	Aomori	0.88	0.031	0.94
	Rumoi	0.95	0.137	0.97
3 hr	Gangneung	0.95	0.103	0.97
	Wangdolcho	0.92	0.139	0.96
	Genkainada	0.95	0.150	0.96
	Tottori	0.94	0.181	0.96
	Fukui	0.96	0.222	0.98
	Sakata	0.97	0.215	0.98
	Aomori	0.74	0.050	0.83
	Rumoi	0.92	0.172	0.95
12 hr	Gangneung	0.94	0.111	0.96
	Wangdolcho	0.89	0.165	0.94
	Genkainada	0.91	0.170	0.95
	Tottori	0.91	0.202	0.95
	Fukui	0.93	0.279	0.96
	Sakata	0.90	0.355	0.94
	Aomori	0.69	0.048	0.81
	Rumoi	0.86	0.217	0.92
24 hr	Gangneung	0.90	0.145	0.94
	Wangdolcho	0.89	0.173	0.94
	Genkainada	0.92	0.158	0.96
	Tottori	0.89	0.232	0.94
	Fukui	0.93	0.297	0.96
	Sakata	0.92	0.320	0.95
	Aomori	0.62	0.056	0.77
	Rumoi	0.91	0.185	0.95

5 CONCLUSIONS

In the present study, a new approach to significant wave height forecasting based on the combination of neural network, EOF analysis and wavelet analysis is introduced. Existing data-driven models should be simulated for each location separately and cannot interpret the relationship between spatially distributed meteorological variables and waves. To overcome the limitations, EOF analysis was employed. The EOF analysis helps to forecast significant wave height simultaneously at several stations and interpret spatially distributed physical patterns.

The application of EOFWLNN model was achieved at 8 stations in the East Sea of Korea. Although there are small deviations and phase shift at higher lead times, the results show good performance of prediction. According to Dixit & Londhe (2016), WLNN results at higher decomposition level show better performance at higher lead times. Therefore, in future work, the higher decomposition level will be employed to develop the accuracy of model. In conclusion, EOFWLNN model can be used as a promising tool in forecasting.

ACKNOWLEDGEMENTS

This work was performed by a project of "investigation of large swell waves and rip currents and development of the disaster response system (No. 20140057)" sponsored by the Ministry of Oceans and Fisheries.

REFERENCES

Cannas, B., Fanni, A., See, L. & Sias, G. (2006). Data preprocessing for river flow forecasting using neural networks: Wavelet transforms and data partitioning. *Physics and Chemistry of the Earth*, Parts A/B/C, 31(18), 1164-1171.

Deka, P.C. & Prahlada, R. (2012). Discrete Wavelet Neural Network Approach in Significant Wave Height Forecasting for Multistep Lead Time. *Ocean Engineering*, 43, 32-42.
Deo, M.C., Jha, A., Chaphekar, A. & Ravikant, K. (2001). Neural Networks for Wave Forecasting. *Ocean Engineering*, 28(7), 889-898.
Dixit, P. & Londhe, S. (2016). Prediction of Extreme Wave Heights Using Neuro Wavelet Technique. *Applied Ocean Research*, 58, 241-252.
Murguia, J. & Campos-Cantón, E. (2006). Wavelet Analysis of Chaotic Time Series. *Revista Mexicana de Física*, 52(2), 155-162
Prahlada, R. & Deka, P.C. (2015). Forecasting of Time Series Significant Wave Height Using Wavelet Decomposed Neural Network. *Aquatic Procedia*, 4, 540-547.
Shahabi, S., Khanjani, M.-J. & Kermani, M.-R.H. (2016). Significant Wave Height Modelling Using a Hybrid Wavelet-Genetic Programming Approach. *KSCE Journal of Civil Engineering*, 21(1), 1-10.

LASER-POSITIONING PIV MEASUREMENT IN THE FIELD USING ANDROID DEVICES

WEN-YI CHANG(1), FRANCO LIN(2), WHEY-FONE TSAI(3), JIHN-SUNG LAI(4), CHIN-HSIUNG LOH(5) & TAI-SHAN LIAO(6)

(1,2,3) National Center for High-Performance Computing, National Applied Research Laboratories, Hsinchu, Taiwan
c00wyc00@nchc.narl.org.tw; smallsun@nchc.narl.org.tw; wftsai@nchc.narl.org.tw
(4) Hydrotech Research Institute, National Taiwan University, Taipei, Taiwan
jslai525@ntu.edu.tw
(5) Department of Civil Engineering, National Taiwan University, Taipei, Taiwan
lohc0220@ntu.edu.tw
(6) Instrument Technology Research Center, National Applied Research Laboratories, Hsinchu, Taiwan
tsliao@itrc.narl.org.tw

ABSTRACT

In this study, a laser-positioning PIV system is developed for flow surface velocity measurement in the field. By using the laser-positioning technique, the traditional ground-based survey of ground control points can be avoided, hence, a large amount of labor and time can be saved. In addition, based on own-developed APPs, the image capturing, the image ortho-rectification and the image analysis for velocity estimation can all be done on an Android camera. This laser-positioning PIV system has been installed in the field to study its capability and applicability. The preliminary result shows that this system is easy to be set up in the field and has a great potential for long-term flow monitoring.

Keywords: Laser; particle image velocimetry (PIV); android; velocity; measurement.

1 INTRODUCTION

In the last few decades, the large-scale particle image velocimetry (LSPIV) method has been developed and widely used in many hydraulic applications (Fujita et al., 1997; Muste et al., 2004; Hauet et al., 2008; Muste et al., 2011; Tsubaki et al., 2011). The conventional LSPIV method mainly comprises three steps: (1) the image capturing; (2) the image ortho-rectification; and (3) the image analysis. However, for Step (2), it usually also needs ground control points (GCPs) measured on the scene, and the GCPs survey may be difficult and labor-consuming in the field. To overcome this difficulty, the present study proposes the laser-positioning PIV (LPPIV) method for quick surface velocity measurement. This method mainly projects four laser points on the river flow in a parallel way, and these bright laser points on the flow surface can be treated as GCPs in the ortho-rectified process of images. Therefore, compared to the traditional survey of GCPs in the field, a large amount of labor and time can be saved by using the proposed LPPIV method.

Furthermore, due to the fast development of smartphone technologies, more and more researches have utilized smartphones' lens, sensors, wifi/4g and computation functions to facilitate the PIV measurement in the field (Yu et al., 2015; Tsubaki et al., 2015; Chang et al., 2016a; 2016b). In the present study, in order to increase the mobility and immediacy of the laser-positioning PIV system, the Android camera (Samsung GC-100) is adopted for the image capturing and image processing in Steps (1) and (3). Based on the APPs developed, the main components of laser-positioning PIV measurement can be quickly accomplished and displayed in a single device. Then, via the wireless communication, the flow images and measured velocity data can be transmitted to a remote monitoring center for further applications. In this study, a Laser-positioning PIV system is installed in the field to study its capability and applicability. In general, the preliminary result shows that this system can be easily and quickly installed in the field and measure the flow surface velocity with sufficient accuracy.

2 LASER-POSITIONING PIV SYSTEM

2.1 Laser-positioning technique

The framework of the laser-positioning PIV system is shown in Figure 1. An Android camera combined with a laser projector can be fixed on the bridge side for flow monitoring. Four laser points are projected in a parallel way to give GCPs on the flow surface, hence, the ground-based surveyed GCPs can be avoided. Then, the laser points on the captured flow images could be directly utilized for the image ortho-rectification to facilitate the PIV measurement in the field.

  / ISSN 1562-6865 (Online) - ISSN 1063-7710 (Print)

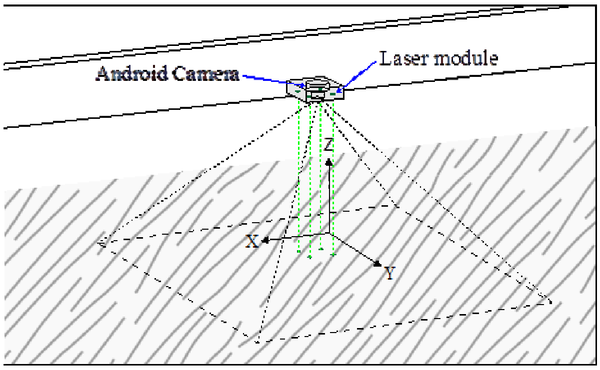

Figure 1. The framework of the Laser-positioning PIV system in the field.

According to the projecting angles of the lasers, as shown in Figure 2, the ground coordinates of laser points on the flow surface can be calculated as follows:

$$\begin{cases} (x_A, y_A) = (0,0) \\ (x_B, y_B) = (W/\cos\alpha / W\tan\alpha\tan\alpha) \\ (x_C, y_C) = (W/\cos\alpha / H/\cos\beta + W\tan\alpha\tan\alpha) \\ (x_D, y_D) = (0, H/\cos\beta) \end{cases} \qquad [1]$$

where *W* and *H* are the width and height of the laser array, respectively; □□ and □ are the yaw angle and pitch angle of the laser projector, respectively.

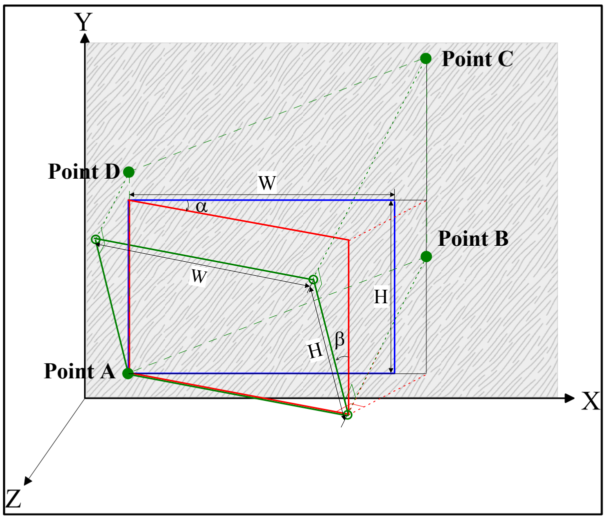

Figure 2. The ground coordinates of the laser points.

Then, a GUI APP (as shown in Figure 6(b)) is developed and used to specify the exact locations of laser points A, B, C, D on the image step by step to give their image coordinates. Since the flow surface is usually assumed flat, the mapping relations between ground and image coordinates can be represented as follows (Muste et al., 2004; Chang et al., 2016):

$$\begin{cases} x' = \dfrac{L_1 X + L_2 Y + L_3}{L_7 X + L_8 Y + 1} \\ y' = \dfrac{L_4 X + L_5 X + L_6}{L_7 Y + L_8 Y + 1} \end{cases} \qquad [2]$$

where x' and y' are image coordinates; X and Y are ground coordinates; $L_1 \sim L_8$ are the mapping coefficients to be determined. Obviously, the four laser points can just serve as the four GCPs to solve the eight coefficients of Eq. [2] and to give the required mapping relations. Then, all the flow images can be ortho-rectified by Eq. [2] for the following PIV calculation.

2.2 PIV method

After the image ortho-rectification, the laser-positioning PIV system is ready for velocity estimation. As done by the conventional PIV methods, a pair of flow images are needed for the image pattern recognition. The common cross-correlation algorithm is adopted in the present study, in which the cross-correlation coefficient is calculated as follows:

$$\phi_{fg}(m,n) = \sum_{x'=1}^{M} \sum_{y'=1}^{N} f(x',y') g(x'+m, y'+n) \qquad [3]$$

where $f(x',y')$ and $g(x',y')$ are the gray-level intensities of the image pixel at location (x',y') at time *t* and *t*+ Δt, respectively; *M* and *N* are the sizes of interrogation area (IA) window; *m* and *n* are the movement index. By searching the first image's IA window in the second image with different *m* and *n*, the obtained maximum value of $\phi_{fg}(\hat{m},\hat{n})$ at location $(\hat{m},\hat{n})$ gives the movement of surface flow particles from the location (x',y') to the location $(x'+\hat{m}, y'+\hat{n})$ within Δt. Hence, as indicated in Eq. [4], the velocity vector can be obtained by dividing the movement distance $(\hat{m},\hat{n})$ with the Δt for each IA.

$$(u,v) = (\hat{m}/\Delta t, \hat{n}/\Delta t) \qquad [4]$$

where *u* and *v* are the velocity components in x' and y' directions, respectively. In addition, in order to improve the measurement accuracy, the quadratic fitting is applied to the cross-correlation distribution to reach the subpixel accuracy.

2.3 Android-based system

Due to the fast development of smartphone technologies, performing the PIV measurement on a smartphone has become feasible (Chang et al., 2016a; 2016b). However, in order to further improve camera functions for PIV measurement in a long distance, the Android camera (Samsung GC-100) is adopted in this study. This camera has the lens with 21x optical zoom, therefore, it is more suitable for image capturing from a long distance in the field. For developing the laser-positioning PIV APP on an Android system, the Java programming language and OpenCV libraries (http:// http://opencv.org/) are used to develop the core image processing algorithms. Figure 3 shows the developed APP for the laser-positioning PIV measurement. On the screen, there are several buttons designed to control the camera functions, including zooming in & out, auto-focusing, adjusting exposure rate and taking a picture for image ortho-rectification. In addition, the sub-menus can be used to input parameters, execute image ortho-rectification, and run the PIV measurement. Based on the Android system, the proposed laser-positioning PIV APP can be easily transferred to other Android devices.

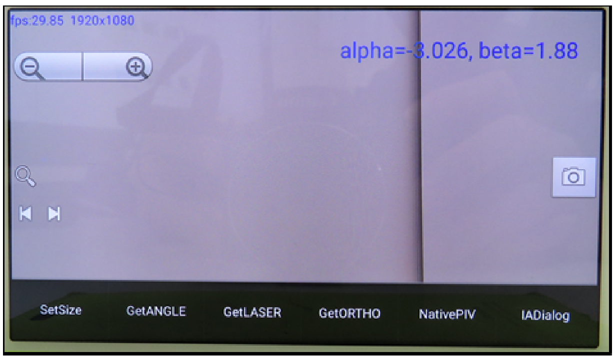

Figure 3. The laser-positioning PIV APP.

3 FIELD EXPERIMENT

In the present study, a prototype of the laser-positioning PIV system has been developed and installed at NiuDou Bridge in northern Taiwan, which is about 16m above the river. As can be seen in Figure 4, this device is quite simple; mainly consisting of an Android camera, four laser modules, a power converter and an aluminum shell for protection. Therefore, it is cheap and has a great potential for massive distribution. For our convenience, the free remote control software, AirDroid APP, was adopted and installed in the Android camera in advance. Therefore, one can easily connect to this device (Android camera) via the internet and manipulate this Android camera remotely. As can be seen in Figure 5, through AirDroid, one can easily start the LPPIV APP to have real-time flow images previewed on the screen. Then, by using the zoom-in button, the imaging area can be enlarged to any desired degree. Once the laser points on the flow surface can be seen clearly, as shown in Figure 6(a), a picture can be taken for the next step, which is the image ortho-rectification. In this step, a developed GUI APP is used to specify the locations of laser points on the image (as shown in Figure 6(b)) to give their image coordinates. Meanwhile, the ground coordinates of laser points can be calculated by Eq. [1], in which the projecting angles □ and □ are sensed by the accelerometer of the Android camera. Based on the ground and image coordinates of 4 laser points, the mapping relations, Eq. [2], could be established. Then, the flow images could be rectified as shown in Figure 6(c). After that, the system is ready for the velocity estimation. By pressing the submenu to start the PIV measurement, two consecutive images were captured into the system for the cross-correlation calculation, in which the time difference is 1/30 seconds and the interrogation area, IA is 96 pixels. As shown in Figure 6(d), the velocity vectors can be calculated and to be displayed in real-time on the screen. Due to the shallowness of water, the water, in this case, was mainly flowing on the left hand side in the imaging area. Then, this record of images and data were transmitted to the remote FTP site for future applications. After that, the next two consecutive images were captured into the system for the cross-correlation calculation. The PIV measuring loop could continue until the enough velocity data were collected. Through this preliminary test, the good applicability of the proposed LPPIV system in the field can be demonstrated. A large amount of labor and time can be saved especially in field conditions.

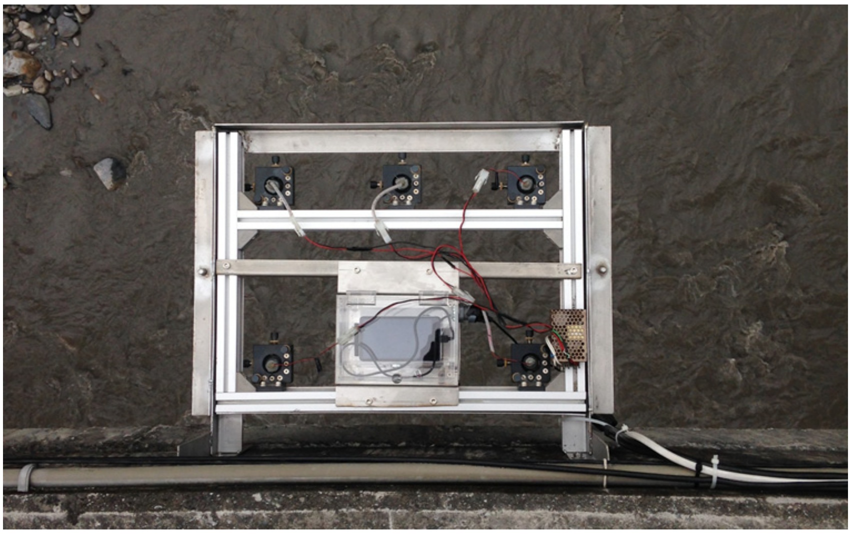

Figure 4. The laser-positioning PIV system in the field.

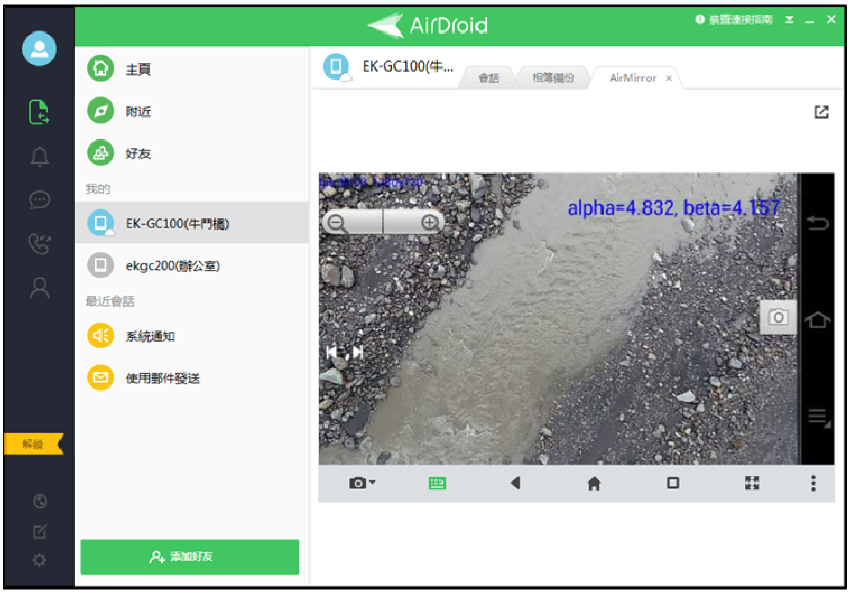

Figure 5. The remote control of the laser-positioning PIV system.

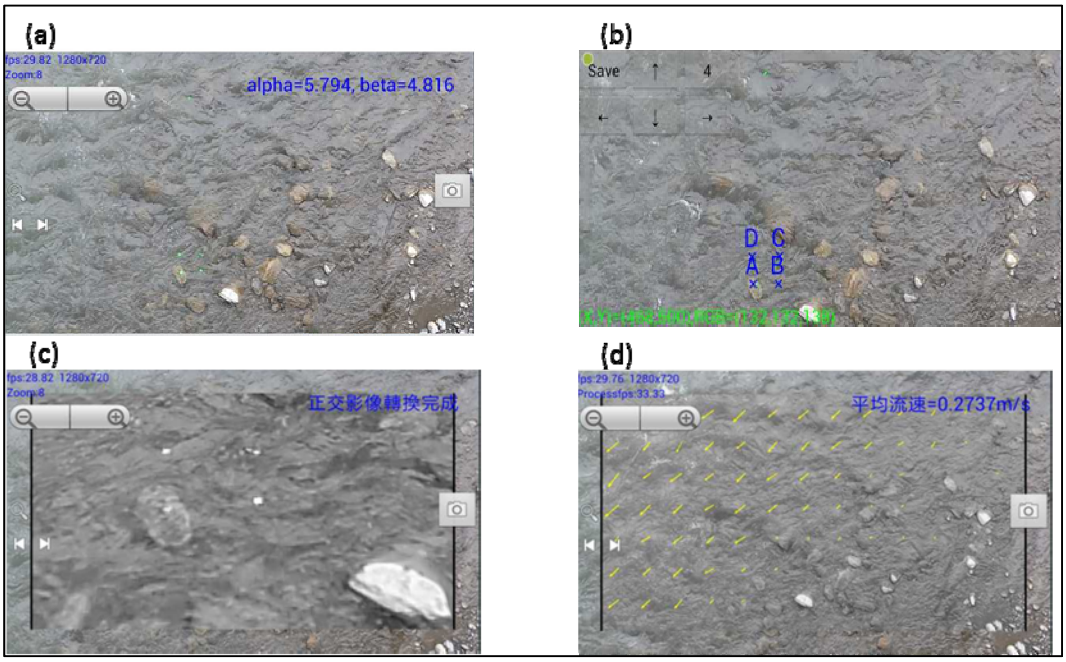

Figure 6. (a)The captured flow images; (b) A GUI APP for acquiring image coordinates of laser points; (c) The ortho-transformed flow image; (d) The measured velocity field by the LPPIV method.

4 CONCLUSIONS

In the present study, a laser-positioning PIV system has been installed in the field for flow surface velocity measurement. This system mainly integrates the laser-positioning technique together with using sensor and computation functions of an Android camera. Hence, it can solve the difficulties of surveying ground control points in the field for traditional PIV methods. Besides, based on the own-developed APPs, all the components of LPPIV measurement including the image capturing, image ortho-rectification and image analysis can be done on a single Android camera. Furthermore, all the manipulation of the LPPIV measurement can be remotely operated by a remote control software. Therefore, the labor for maintenance can be further saved. In this study, the field experiment has demonstrated the good capability and applicability of the proposed LPPIV system, which has a great potential for long-term flow of monitoring in the field. Thus, this new LPPIV method would have a great impact on hydraulic observation.

ACKNOWLEDGMENTS

Financial support from the Ministry of Science and Technology, Taiwan, under grants MOST 105-2625-M-492-004 is highly appreciated. We are also grateful to the National Center for High-Performance Computing for computer time and facilities.

REFERENCES

Chang, W.Y., Lin, F., Tsai, W.F., Liao, T.S., Lai, J.S. & Loh, C.H. (2016a). Development of Portable PIV Devices. *12th International Conference on Hydroinformatics*, Inchon, Korea, 1-5.

Chang, W.Y., Lin, F., Tsai, W.F., Lai, J.S., Loh, C.H. & Kang, S.C. (2016b). Portable Particle Image Velocimetry Measurement Using Laser-Based Technique. *Journal of Hydraulic Engineering*, 142(9), 1-9.

Fujita, I., Muste, M. & Kruger, A. (1998). Large-Scale Particle Image Velocimetry for Flow Analysis in Hydraulic Applications. *Journal of Hydraulic Research*, 36, 397-414.

Hauet, A., Kruger, A., Krajewski, W., Bradley, A., Muste, M., Creutin, J.D. & Wilson, M. (2008). Experimental System for Real-Time Discharge Estimation Using an Image-Based Method. *Journal of Hydraulic Engineering*, 13(2), 105-110.

Muste, M., Fujita, I. & Hauet, A. (2008). Large-Scale Particle Image Velocimetry for Measurements in Riverine Environments. *Water Resources Research*, 44(4), 1-14.

Muste, M., Ho, H.C. & Kim, D. (2011). Considerations on Direct Stream Flow Measurements using Video Imagery: Outlook and Research Needs. *Journal of Hydro-environment Research*, 5, 289-300.

Tsubaki, R., Fujita, I. & Tsutsumi, I. (2011). Measurement of the Flood Discharge of a Small-Sized River Using An Existing Digital Video Recording System. *Journal of Hydro-environment Research*, 5, 313-321.

Tsubaki, R., Fujita, I., Yu, K. & Muste, M. (2015). Large-Scale Particle Image Velocimeter (LSPIV) Implementation on Smartphone. *36th IAHR World Congress*, the Hague, the Netherlands, 1-7.

Yu, K., Yoon, B. & Lee, S. (2015). Surface Image Velocity Measurement System for Wide Rivers using Smartphones. *36th IAHR World Congress*, the Hague, the Netherlands, 1-3.

DEVELOPMENT OF THE STREAMFLOW AND FLOOD ANALYSIS SYSTEM USING R (SFASUR-TEC)

MAIKEL MENDEZ[(1)] & LUIS A. CALVO-VALVERDE [(2)]

[(1,2)] Escuela de Ingeniería en Construcción, Instituto Tecnológico de Costa Rica, Cartago, Costa Rica.
mamendez@itcr.ac.cr; lcalvo@itcr.ac.cr

ABSTRACT

The Streamflow and Flood Analysis System Using R (SFASUR-TEC) was developed as part of a research project focusing on hydrological modelling for operational hydropower planning and forecasting in tropical mountainous regions of Costa Rica. Since Costa Rica has an enormous hydropower potential and renewable energy markets that keep on growing, reliable estimation and assessment of river flows is imperative. SFASUR-TEC was developed to increase the understanding of natural and altered flow regimes linked to relevant physical processes with a particular interest in hydropower applications. Consequently, SFASUR-TEC is a collection of methods to identify and quantify key components of flow regimes and assess their behaviour through time. The system was completely developed using the R programming language based on various criteria, including availability of specialized libraries, open-source implementation and cross-platform compatibility. To evaluate the performance of the system, SFASUR-TEC was applied to the upper Toro River catchment in Costa Rica using a 17-year streamflow data set (1994-2010). The catchment was selected based on its predominantly mountainous and rainy conditions, its relevance in the Costa Rican hydropower generation context and the availability of temporal and spatial information. Results from the Flood Frequency Analysis Block suggest a 60 m^3/s peak flow for a 20-year return period (FFATr20) along with its 95% confidence intervals with values between 42 and 93 m^3/s. Flow Duration Curves (FDCs) show that the dry season expands from February through April, with flow values as low as 1.5 m^3/s, essentially sustained by baseflow. Baseflow Separation shows that baseflow is indeed a considerable contribution to total streamflow, with BFI values ranging from 0.12 to 0.40 between the months of May through December. Results from this study are intended to support strategic decision-making to improve the performance of the hydropower facilities currently installed in the upper Toro River catchment and elsewhere.

Keywords: Analysis; Flood; R SFASUR-TEC; Streamflow.

1 INTRODUCTION

Costa Rica is among the world's leaders in renewable energy as nearly 93% of its electricity comes from renewable sources. This has been accomplished with considerable investment in developing and expanding renewable energy capacity, particularly hydropower (WEF, 2013). Hydropower is the predominant source of energy which accounts for over 78% of the country's total generation, while geothermal represents 12%, wind 2.1%, biomass 0.25% and only 7.19% comes from thermal sources (ICE, 2011).

Many of the country's leading hydropower facilities are located in catchments with tropical mountainous conditions, which are characterized by persistent immersion in clouds, an important source of precipitation all year-round (IMN, 2008). This precipitation provides streamflow for facilities that run by water stored in reservoirs or those that are run by streamflow directly. Therefore, a reliable assessment of flow regimes in these mountainous catchments is essential to improve inflow predictions and hydropower operation, along with the development of future potentials.

Accordingly, the Streamflow and Flood Analysis System Using R (SFASUR-TEC) was developed to identify and quantify key components of flow regimes and assess their behaviour through time in mountainous tropical catchments. SFASUR-TEC was developed to increase the understanding of natural and altered flow regimes linked to relevant physical processes with a particular interest in hydropower applications.

SFASUR-TEC was applied to the upper Toro River catchment, where Insitituto Costarricense de Electricidad (ICE) operates three hydropower facilities with an installed capacity of 138 MW; approximately 10% of the Costa Rican installed capacity (ICE, 2011). This catchment was selected based on its predominantly mountainous and rainy condition, its relevance in the national hydropower generation context and the availability of temporal and spatial information.

2 STUDY AREA AND DATA SOURCES

The upper Toro River catchment (43.15 km2) is located in the province of Alajuela in north-western Costa Rica (Figure 1). The topography is mountainous with elevations ranging from 2593 to 1334 m. The slope is steep with a mean value of 23%. The mean annual rainfall of the area is 4200 mm and the mean annual temperature range is between 17.2 and 32.8 ºC. The land use in the catchment is dominated by forest (62%) and grassland (35%) with minor contributions from other uses; mainly water and urban. The catchment has a highly complex precipitation pattern and its temporal and spatial distribution is influenced by factors such as El Niño southern oscillation (ENOS), geomorphology, rugged terrain and microclimates. Daily and hourly streamflow data for the period were obtained from the ICE 12-6 gauge station. Even when the catchment has been monitored since the early 1980's, hourly records are very sparse. For this reason, only mean daily streamflow data from a 17-year dataset (1994-2010) was used in this study.

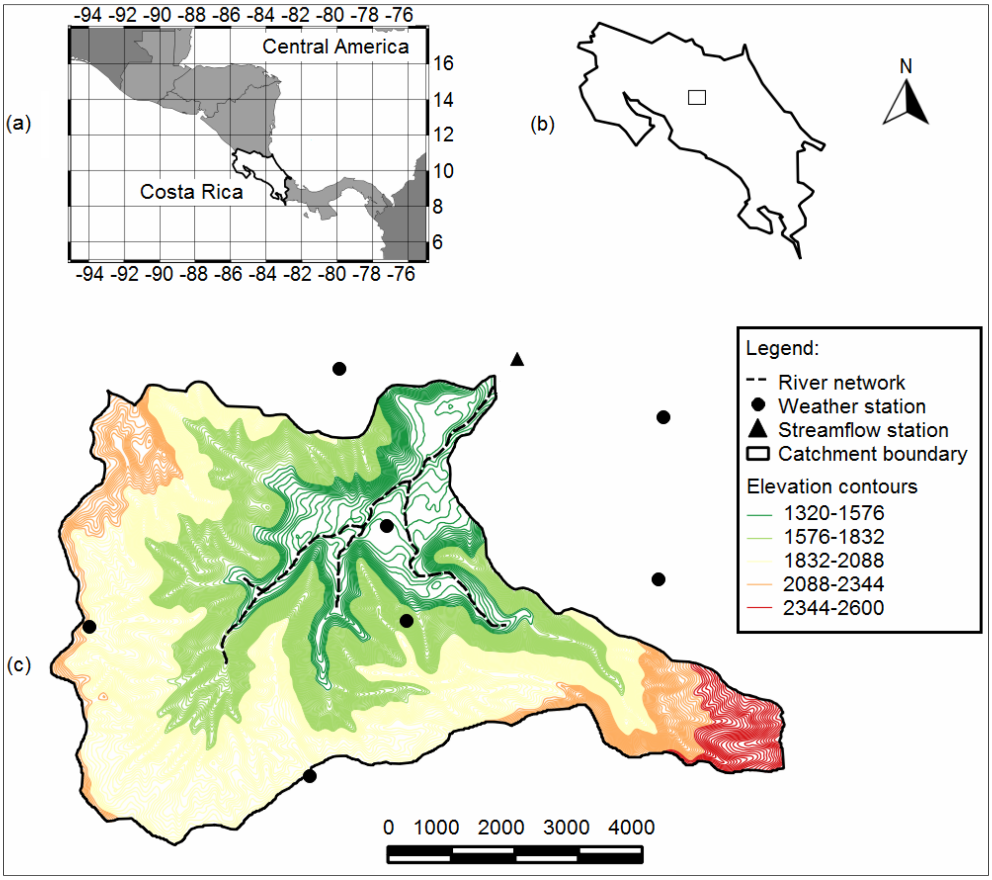

Figure 1. (a) Position of Costa Rica in Central America, (b) position of the upper Toro River catchment in Costa Rica; (c) Upper Toro River catchment boundary, river network, elevation contours, rain-gauges and streamflow gauging station.

3 SYSTEM DESCRIPTION

As coded using the R programming language (R Core Team, 2016), SFASUR-TEC is divided into various blocks (Figure 2). The authors recommend running SFASUR-TEC under RStudio-IDE (RStudio Team, 2016) as it significantly facilitates interaction with the system. Below, follows a brief description of each block. Relevant R packages used in the development of SFASUR-TEC are from now on presented in curly braces {}. For each block, the outcome of the respective analysis is displayed in tabular and graphical form.

3.1 Custom Functions - Block

One of the great strengths of R is the user's ability to add custom functions. For instance, this block includes all custom functions along with data filtering routings, descriptive statistics {*pastecs*} and temporal series manipulation {*lubridate*}, {*tidyr*} and {*dplyr*}.

3.2 Flood Frequency Analysis Block

This block along with its custom functions, fits a given extreme value distribution to an extreme value series vector (e.g. annual instantaneous maximum value). Log Pearson Type III distribution is selected by default (Maidment, 1993; Chow et al., 1988). Nonetheless, a list of distributions supported by {*lmomco*} package may also be selected (e.g. Generalized Extreme Value Distribution and Gumbel Distribution). A bootstrapping routing is also applied to randomly sample the extreme value series to estimate confidence interval for each given non-exceedance probability and return period (from 1 to 500 years).

  / ISSN 1562-6865 (Online) - ISSN 1063-7710 (Print)

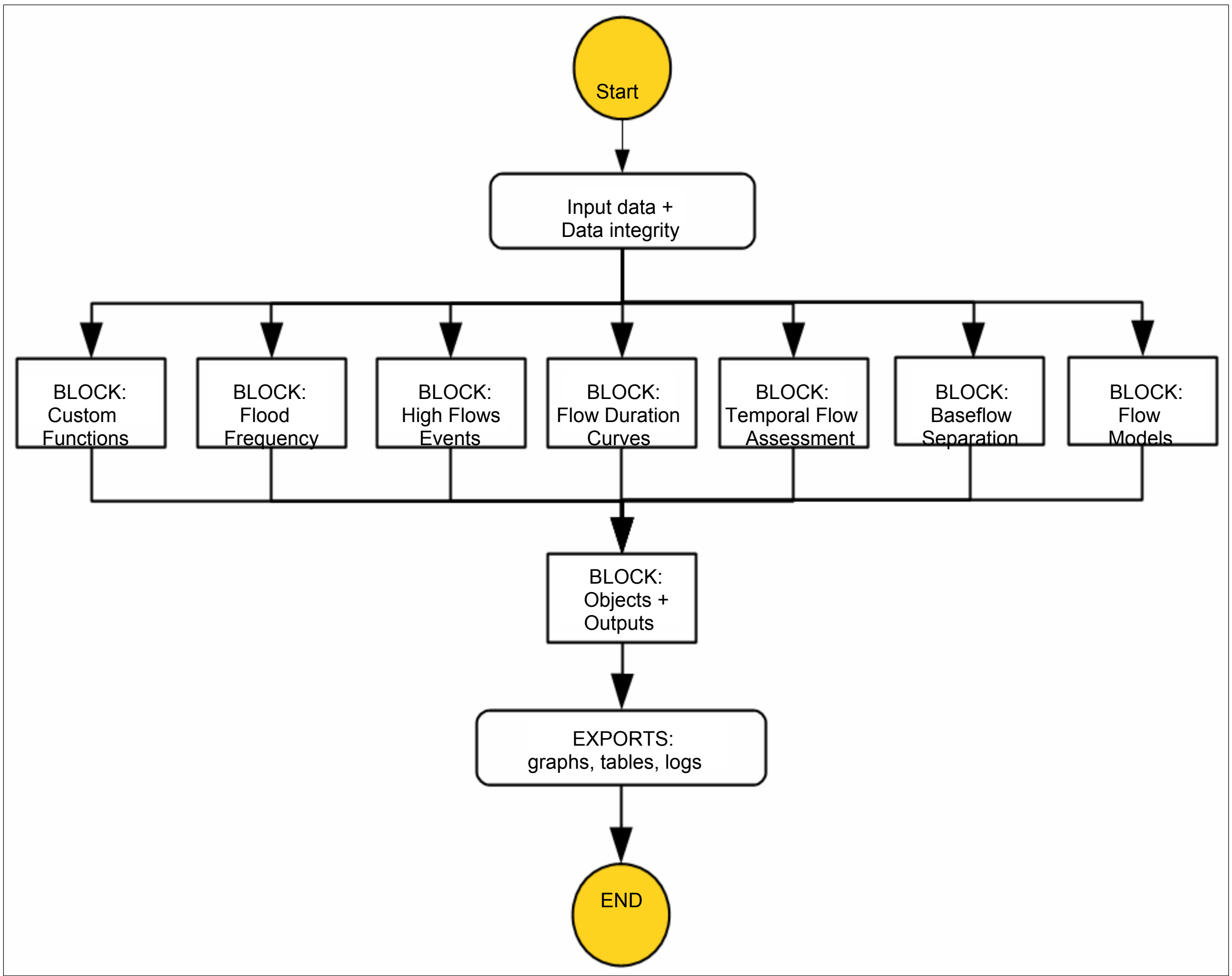

Figure 2. SFASUR-TEC model structure.

3.3 Highflow Events - Block

Based on the results from the Flood Frequency Analysis Block, highflow events with defined threshold recurrence intervals (1.5 and 10 years by default) are identified and quantified and a new subset data frame is created. Subsequently, the extreme value series vector is numerically and graphically compared with this subset. The main objective of this block is to quantify the amount and magnitude of exceedance probability highflow events included in the entire time series. Another functionality included in this block is a hydrograph explorer, which graphically displays streamflow data records in a variety of temporal aggregations (annual and monthly). The main objective is to gain a better appreciation of the entire sequence of events involved in the time series. Descriptive statistics (mainly the mean and median) are also included.

3.4 Flow Duration Curves - Block

Flow Duration Curves (FDCs) are computed using specialized functions from the {*hydroTSM*} library which follows the methods described by Vogel and Fennessey, (1994). In this method, individual FDCs are calculated for each year and month. Subsequently, a single median value is calculated for each exceedance point using the collection of values at the same exceedance taken from the multiple annual FDCs. These new median values are then plotted to create a single new FDC. The same approach is followed by Metcalfe et al. (2013). Two different temporal aggregations are supplied; one continues which includes all computed values and another one discrete, which includes user defined values for comparative purposes. A daily hydrograph discretized by year and showing the mean and median values, is also prepared by this block.

3.5 Temporal Flow Assessment - Block

The main objective of this block is to graphically show the streamflow variability using monthly and yearly box-plots and violin-plots supplied by {*ggplot2*} library. Graphs are plotted in both linear and logarithmic scales. In the case of the box-plots, the upper whisker extends from the hinge to the highest value that is within 1.5 * IQR of the hinge, where IQR is the inter-quartile range, or distance between the first and third quartiles. The lower whisker extends from the hinge to the lowest value within 1.5 * IQR of the hinge. Data beyond the end of the whiskers are outliers and plotted as points according to the Tukey criteria. These box-plots make it possible to visualize the year-to-year variation of median annual flows around the longer-term median flow for the recorded period. It is also possible to identify patterns of wet and dry years from these box-plots.

3.6 Baseflow Separation - Block

Baseflow Separation is accomplished by means of the {*EcoHydRology*} library, which reads a streamflow dataset and produces a baseflow-quickflow dataset using 1, 2 or 3 passes (Nathan and McMahon, 1990). Results are show graphically using normalized and absolute box-plots and hydrographs. The Baseflow Index (BFI), which is the ratio between baseflow and total flow, is also calculated. Therefore, a BFI of 0.5 indicates that 50% of total streamflow can be attributed to baseflow for the respective time period, either monthly or yearly.

3.7 Flow Assessment Models - Block

Taking advantages of the highly developed machine learning capabilities available in R, specialized functions from the {*stats*} library are used to compute linear models (lm) at yearly temporal resolution of the mean, median and maximum values of both total-streamflow and baseflow. The idea behind this block is to identify increasing or decreasing trends through time. A detailed summary of the model metrics, which includes coefficients and residuals, is presented both graphically and tabulated.

3.8 Exports - Block

Relevant outputs from all block are exported in csv, txt and png formats, which allows user to further manipulate data outside the R ecosystem (e.g. MS-EXCEL, STATA).

4 RESULTS AND ANALYSIS

Results from the Flood Frequency Analysis Block suggest a 60 m^3/s peak flow for a 20-year return period (FFATr20) along with its 95% confidence intervals of values between 42 and 93 m^3/s (Figure 3). Projections beyond a 20-year period show considerable uncertainty as observed record is based on a 17-year period. Highflow events on the other hand (Figure 4), show a total of 25 events exciding a 1.5-year return period (FFATr1.5 = 28.3 m^3/s) and only 2 events exceeding a 10-year return period (FFATr10 = 50.4 m^3/s). This means that the FFATr1.5 exceeds at least once every year and the FFATr10 exceeds twice in 17 years. These prove the applicability of the R methods to estimate the magnitude of low and high-frequency extreme floods can be further used in the decision-making process regarding operation of the hydropower facilities in the Upper Toro river catchment. These projections could also be used in hydrodynamic simulations of sluices, derivations and other hydraulic structures along the river bank.

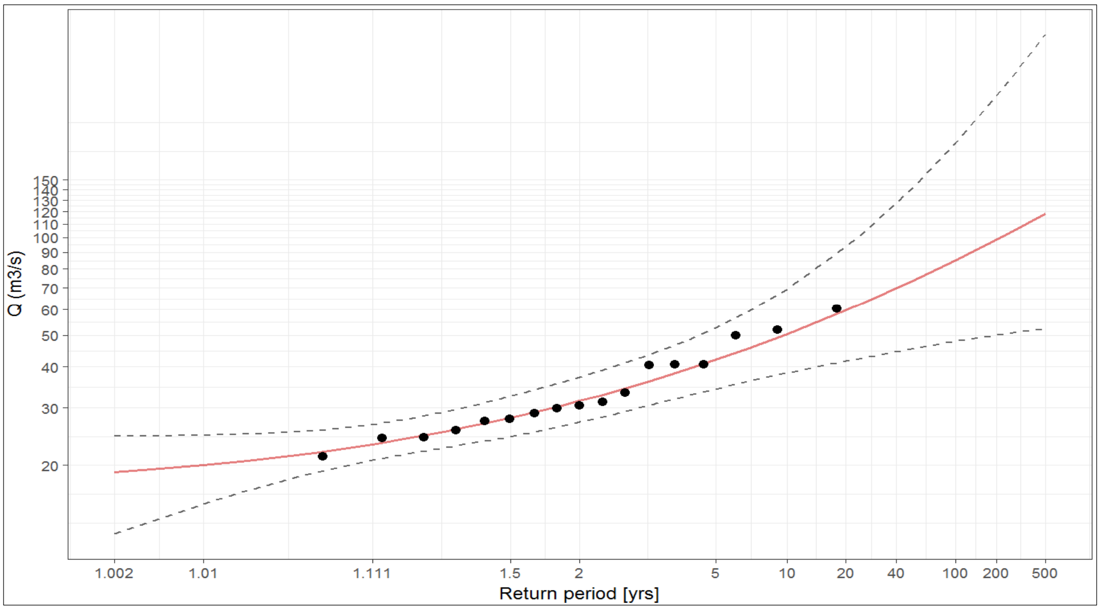

Figure 3. Upper Toro river catchment Flood Frequency Analysis (1994-2010). Log Pearson Type 3. Dotted points represent observed values, continuous red line represents the fitted model and grey dash lines represent CI at 95%.

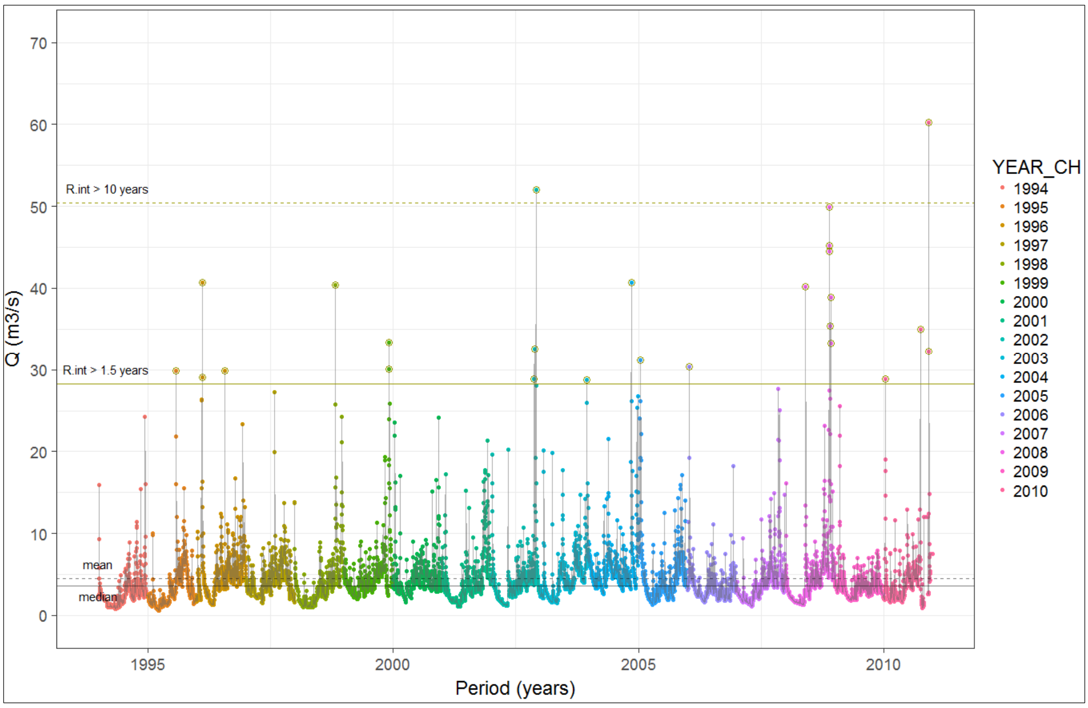

Figure 4. Upper Toro river catchment highflow events hydrograph for 1.5 and 10-year return periods.

Concerning Flow Duration Curves (FDCs), the plot shows the percentage of time that flow in the stream is likely to equal or exceed a value of interest, in this case, 80% of the time (Figure 5). It can be seen that the dry season expands from February through April with flow values as low as 1.5 m^3/s, which is essentially sustained by baseflow. From June until December nonetheless, flow recovers to values above 2.5 m^3/s. November on the other hand is the most productive month, with sustained values close to 4.0 m^3/s. This behaviour is somehow supported by the daily hydrograph discretized by year (Figure 6), where the daily mean and median trends show lower values from February through April and higher values from October through December. The shape of FDCs in their upper (above 80% of the time) and lower (below 20% of the time) regions is particularly significant in evaluating the stream and catchment characteristics (). In this case, the months of March and May are unable to sustain flow above a minimum threshold of 1.0 m^3/s. Oppositely, the months of November and December are most likely to cause flooding due to heavy precipitation, with values above 50 m^3/s.

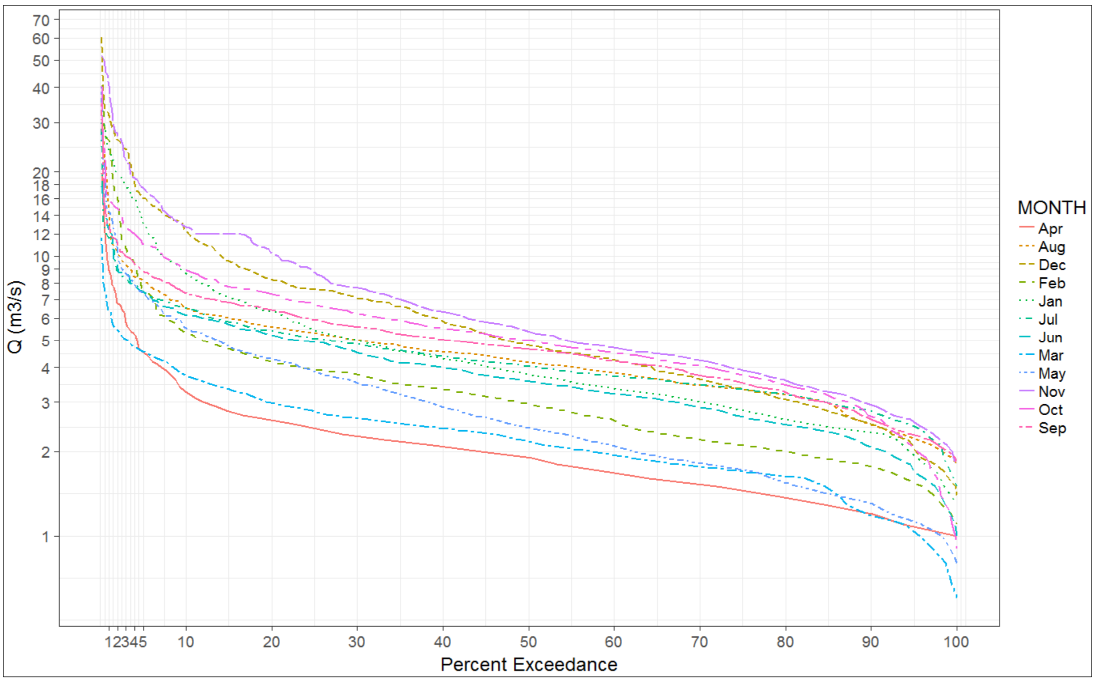

Figure 5. Upper Toro River Catchment monthly Flow Duration Curves. Continuous Values (1994-2010).

Regarding Temporal Flow Assessment, daily streamflow variability box-plots discretized by month (Figure 7) confirm what was presented by the FDCs; dry season expands from February through April. Box-plots also show extreme outlier values, either high or low. IQR for each month are clearly presented. Once more, extreme high values (beyond normality) are concentrated from November through January, and extreme low values are concentrated during the month of March. Yearly box-plots on the other hand (Figure 8), show that 1994 and 1995 were particularly dry when compared to the remaining years. This was most likely to be a consequence of El Niño of southern oscillation (ENOS). The year 2004 was however, particularly wet compared to the rest of the period.

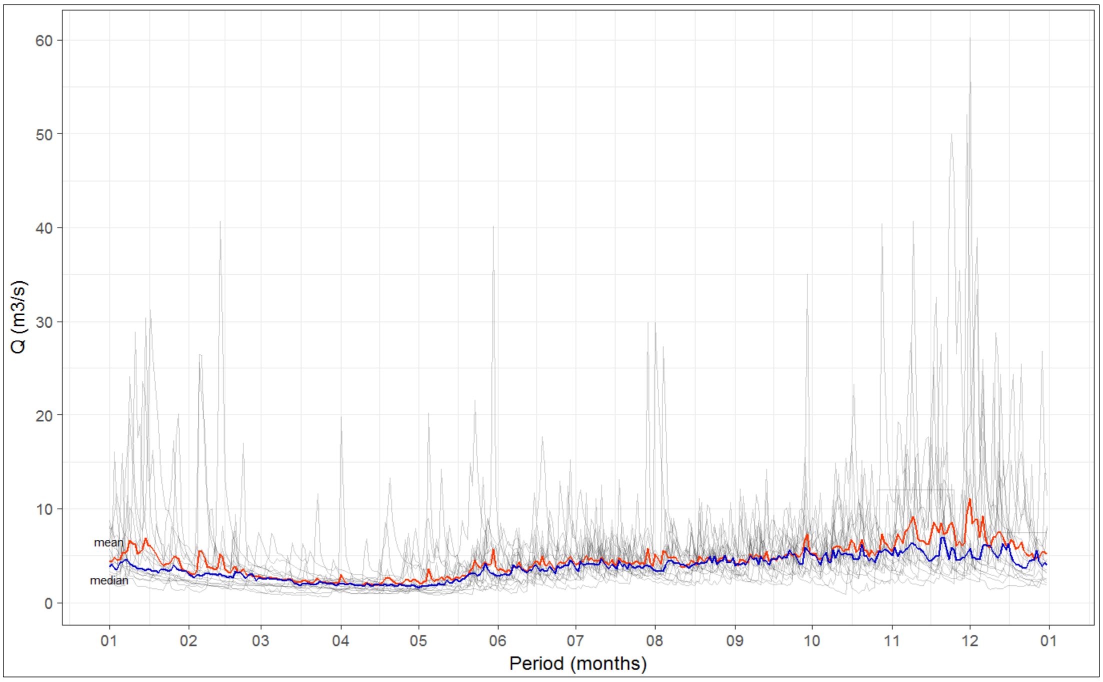

Figure 6. Upper Toro River Catchment daily hydrograph discretized by year. Red continuous line represents mean whereas the blue line represents the median.

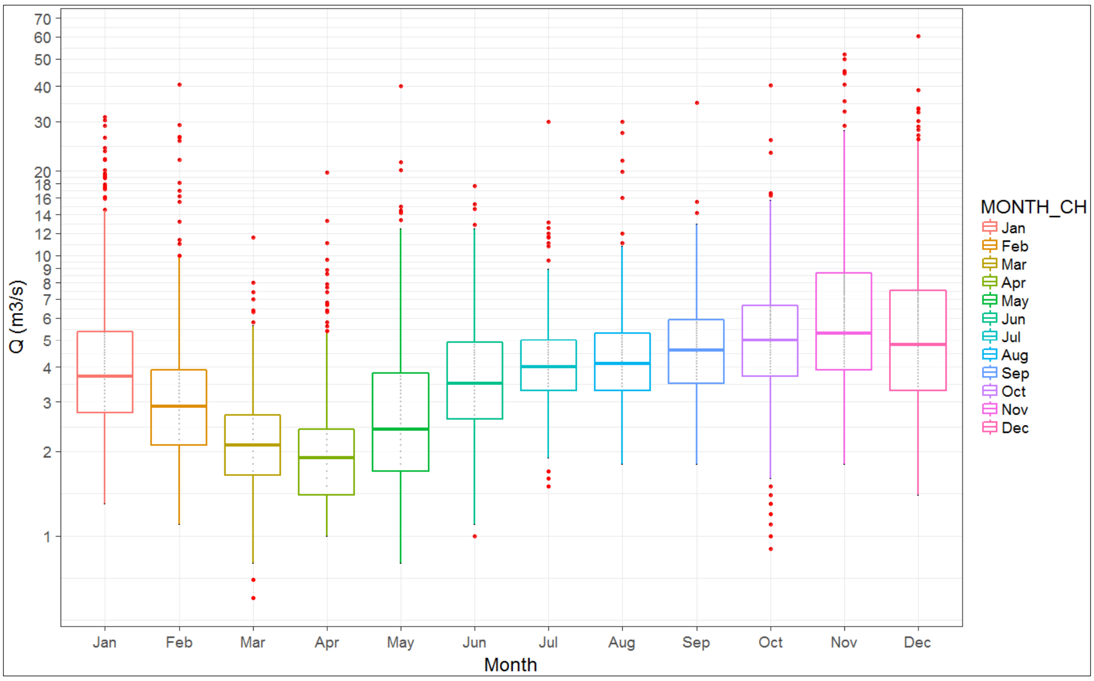

Figure 7. Upper Toro River Catchment. Daily box-plots discretized by month (1994-2010).

In relation to Baseflow Separation, the daily Baseflow Index (BFI) box-plots discretized by month (Figure 9), show how much of the total flow can be attributed to baseflow during each month. It can be seen that between the months of May through December, 50% of total streamflow (box-plots interquartile range) present BFI values ranging from 0.12 to 0.40, which are a considerable contribution to total flow. Special attention however must be paid to box-plots corresponding to the months of January through April as many observations appear as outliers (beyond normality) but are in fact, indicators of how relevant was baseflow during those observations. A daily hydrograph in logarithmic scale, along with the median and mean values for the whole period also shows the relative contribution of baseflow to total flow (Figure 10). In this case, baseflow is below the median and mean of the total flow, except during the wet season, where the relative contribution of baseflow considerably increases.

On the subject of Flow Assessment Models, an increasing trend in magnitude with time can be observed for both streamflow maximum-annual (Figure 11) and baseflow maximum-annual values (Figure 12) according to their respective linear models (LM). Even when adjusted R2 values in both cases are considerably low and the confidence intervals broad, the trends themselves are undeniable. This increasing trend could suggest changes in the catchment land use or a direct consequence of Climate Change.

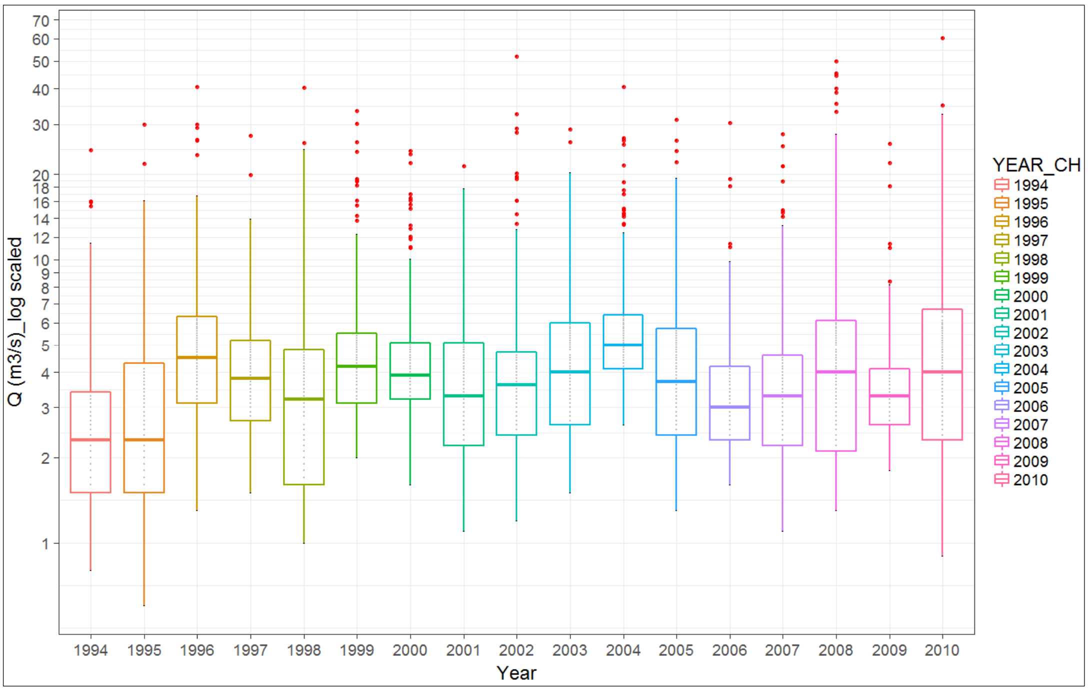

Figure 8. Upper Toro River Catchment. Daily box-plots discretized by year (1994-2010).

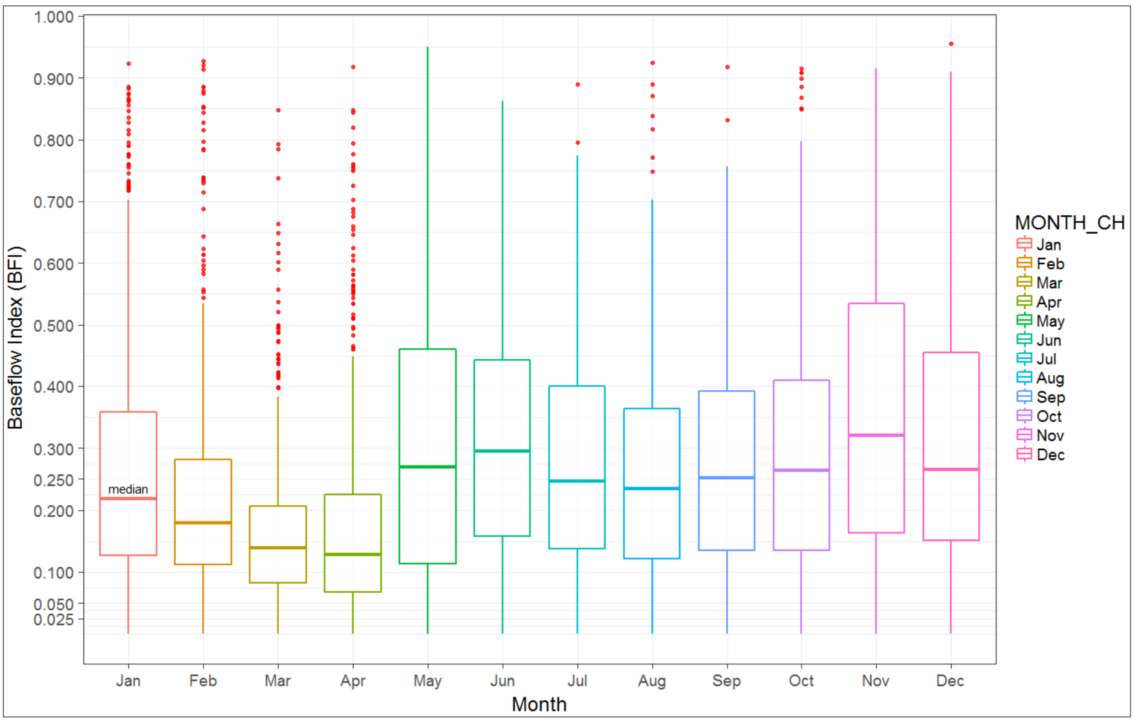

Figure 9. Upper Toro River Catchment daily Baseflow Index (BFI) box-plots discretized by month.

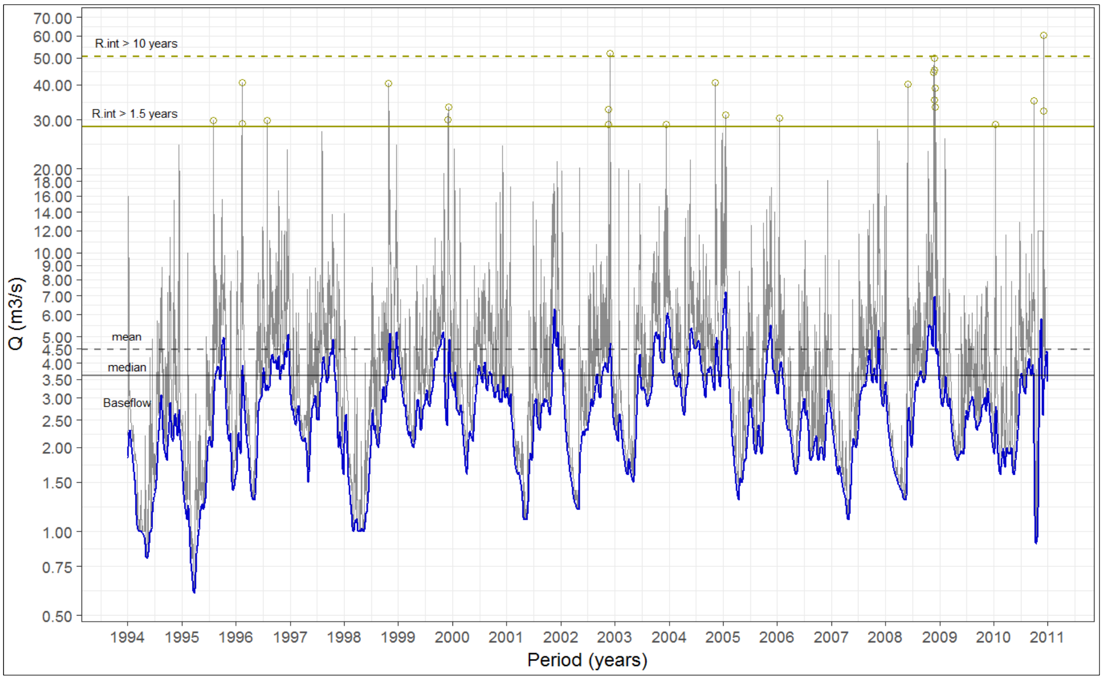

Figure 10. Upper Toro River Catchment daily hydrograph in logarithmic scale. Blue continuous line represents the baseflow contribution whereas the grey line represents total flow.

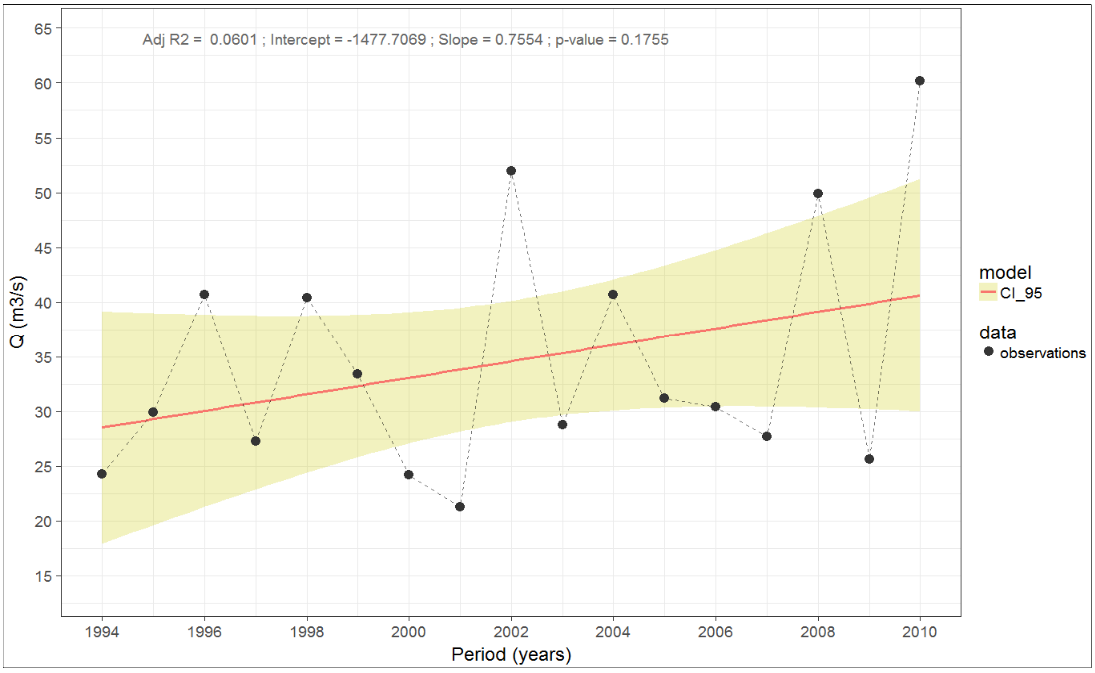

Figure 11. Upper Toro River Catchment. Streamflow Annual-Max Linear Model-LM (1994-2010).

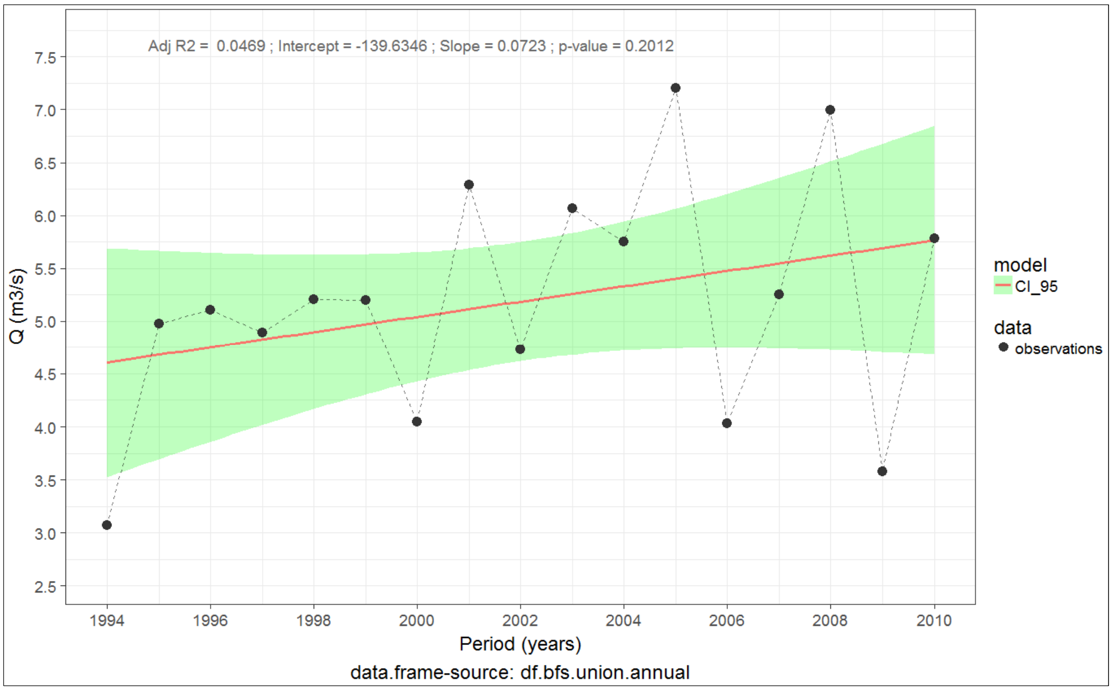

Figure 12. Upper Toro River Catchment. Baseflow Annual-Max Linear Model-LM (1994-2010).

5 CONCLUSIONS

The Streamflow and Flood Analysis System Using R (SFASUR-TEC), developed using the R programming language, was applied to for the upper Toro River catchment, Costa Rica. The following conclusions can be drawn:

a) SFASUR-TEC represents a flexible and convenient system to identify and quantify key components of flow regimes and to assess their behaviour through time.
b) The use of the R programming language allows for a flexible and robust framework that facilitates the incorporation of the data analysis and high-level visualization capabilities available in R into hydrological modelling.
c) Results from the Flood Frequency Analysis Block suggest a 60 m^3/s peak flow for a 20-year return period (FFATr20) along with its 95% confidence intervals of values between 42 and 93 m^3/s.
d) Flow Duration Curves (FDCs) show that the dry season expands from February through April, with flow values as low as 1.5 m^3/s, which is essentially sustained by baseflow.
e) Monthly Temporal Flow Assessment also supports the above conclusion, whereas Yearly Assessment indicates that 1994 and 1995 were the driest years in period considered.
f) Baseflow Separation shows that baseflow is indeed a considerable contribution to total streamflow, with BFI values ranging from 0.12 to 0.40 between the months of May through December.
g) The Flow Assessment Models exhibit an increasing trend in magnitude with time can be observed for both streamflow maximum-annual and baseflow maximum-annual values.

Future development of SFASUR-TEC will focus on:

a) Further validation over additional catchments aiming to verify the efficiency of the code and identify potential improvements.
b) Incorporation of advanced predicting and forecasting time-series analysis techniques available in R including Autoregressive Integrated Moving Averages Models (e.g. ARIMA and ARMA), Seasonal Decomposition and Neural Network Autoregression.
c) Development of an R shiny web user interface for public access.

ACKNOWLEDGEMENTS

This research was supported by Vicerrectoría de Investigación & Extensión, Instituto Tecnológico de Costa Rica (TEC). The authors are grateful to Centro de Servicio de Estudios Básicos de Ingeniería & Construcción of Instituto Costarricense de Electricidad (ICE) for providing observed data for the Upper Toro River catchment.

REFERENCES

Chow, V.T., Maidment D.R. & Mays, L.W. (1988). *Applied Hydrology*. New York: McGraw-Hill.

ICE. (2011). *Centros de Producción Peñas Blancas, Cariblanco, Toro 1 y Toro 2*. Instituto Costarricense de Electricidad (ICE), San José, Costa Rica.

IMN. (2008). *Clima, variabilidad y cambio climático en Costa Rica*. Instituto Meteorológico Nacional (IMN), San José, Costa Rica.

Maidment, D.R. (1993). *Handbook of Hydrology*. New York: McGraw-Hill.

Metcalfe, R.A., Mackereth, R.W., Grantham, B., Jones, N., Pyrce, R.S., Haxton,T., Luce, J.J. & Stainton, R. (2013). *Aquatic Ecosystem Assessments for Rivers (AEAR)*. Science and Research Branch, Ministry of Natural Resources and Forestry, Peterborough, Ontario.

Nathan, R.J. & McMahon, T.A. (1990). Evaluation of Automated Techniques for Base Flow and Recession Analysis. *Water Resources Research*, 26(7), 1465-1473.

R Core Team. (2016). *R: A language and environment for statistical computing*, R Foundation for Statistical Computing, Vienna, Austria.

RStudio Team (2016). *RStudio: Integrated Development for R*, RStudio, Inc., Boston, MA URL, 2016. URL

Vogel, R. & Fennessey, N.M. (1994). Flow Duration Curves I: A New Interpretation and Confidence Intervals. *ASCE, Journal of Water Resources Planning and Management*, 120(4), 485-504.

WEF. (2013). *The Global Energy Architecture Performance Index Report 2014*. The World Economic Forum. REF 031213.

Proceedings of the 37th IAHR World Congress
August 13 – 18, 2017, Kuala Lumpur, Malaysia

CFD ANALYSIS AND VALIDATION OF A CHLORINE DISINFECTION TANK

PABLO OURO[1], BRUNO FRAGA[2], NICOLÒ VITI[3], ATHANASIOS ANGELOUDIS[4], CARLO GUALTIERI[5] & THORSTEN STOESSER[6]

[1,2,6] Hydro-Environmental Research Centre, School of Engineering, Cardiff University, The Parade, Cardiff, UK, Stoesser@cardiff.ac.uk
[3,5] Department of Civil, Construction and Environmental Engineering, University of Napoli Federico II, Napoli, Italy, carlo.gualtieri@unina.it
[4] Faculty of Engineering, Department of Earth Science & Engineering, Imperial College London, London, UK, a.angeloudis06@imperial.ac.uk

ABSTRACT

Disinfection in contact tanks (CTs) is a treatment process applied for both drinking water and wastewater treatment systems with the purpose to inactivate micro-organisms, some of which may be pathogenic and thus preventing transmission of waterborne diseases. This paper presents the results of CFD simulations and validation of hydrodynamics and solute transport in the first two chambers of a chlorine contact tank comprised of a total of 8 compartments. Both RANS and LES methods are applied and successfully compared against experimental data for velocity and scalar concentration fields. Results outline the highly three-dimensional behaviour of the flow with the presence of recirculating and short-circuiting zones. These phenomena enlarge the flow unsteadiness and turbulence affecting the instantaneous flow field, and therefore the transport of the released passive scalar. From the analysis of the average error percentage between numerical and experimental data of both simulations, LES provides greater detail in the hydrodynamics behaviour. Although RANS is able to reproduce the time-averaged flow properties quite well, LES conveys a larger amount of information on instantaneous flow field, which makes it capable to capture the flow unsteadiness that characterise the contact tank hydrodynamics and solute transport. Finally, using velocity component quadrant analysis of LES predictions, the turbulence field is found to be non-isotropic, an aspect not acknowledged in RANS.

Keywords: Environmental hydraulics; hydrodynamics; solute transport; RANS/LES validation; disinfection contact tank.

1 INTRODUCTION

1.1 Contact tank hydraulic aspects

Contact tanks are commonly used to disinfect both drinking and wastewater prior to distribution. These tanks are usually open chambers divided by a series of baffles. Sub-dividing the chambers helps to control the flow of water through the tanks and thus improves the chlorine disinfection process. The hydraulic design of CTs has been traditionally based on the following assumptions: plug-flow condition and Complete Mixing. According to the plug-flow model, the velocity of the fluid is assumed to be constant across any cross-section perpendicular to the reactor axis. Every fluid element travels uniformly and in parallel paths from the inlet to the outlet sections of the tank, i.e. without undergoing longitudinal dispersion (Rauen et al., 2012). In this condition, the contact time for all fluid elements corresponds to the theoretical hydraulic residence time (T) which can be estimated as V/Q, where V is the volume of the CT and Q is the discharge. The second assumption considers the instantaneous mixing of all incoming fluid elements with the fluid already in the tank, which means maximum dispersion as in Continuous Stirred Tank Reactor (CSTR) conceptual model. On the other hand, previous studies (Teixeira, 1993) indicated that the flow pattern in these reactors deviates always from the theoretical condition, even in optimally designed CTs. The existence and arrangement of baffles in the tank, and the tank inlet and outlet configurations induce turbulent mixing, dead-zones and short-circuiting zones (Gualtieri, 2006; Angeloudis et al., 2014a). The flow exhibits a residence time distribution (RTD) which is often significantly different from that dictated by plug-flow. The occurrence of non-ideal plug-flow conditions result in recirculating flow zones in the horizontal or vertical planes regarded as stagnant regions, which contribute to increasing the degree of mixing in the tank with detrimental effect on the CT hydraulic performance. These regions tend to expose pathogens with disinfectant during either too short (insufficient treatment) or too long periods of time than that of T, which can result in the production of excessive disinfection by-products (Angeloudis et al., 2016).

1.2 Geometry and experimental data availability

Numerical results were validated with experimental data from Angeloudis et al. (2014b, 2015) for flow velocity and tracer concentrations in the tank. Acoustic Doppler Velocimeter (ADV) measurements were collected to characterise the hydrodynamics and turbulence behaviour in 1824 points in the area of interest. In turn, concentration readings were measured in several points using fluorescence spectroscopy, calibrated to associate fluorescence intensity with Rhodamine WT concentrations. Although the experimental tank was composed of 8 compartments, the present numerical study is focused on the hydrodynamics developed along the first two compartments, as illustrated in Fig. 1. The third compartment is also incorporated within the numerical domain to ensure that predictions in the earlier compartments are independent of the outlet boundary condition.

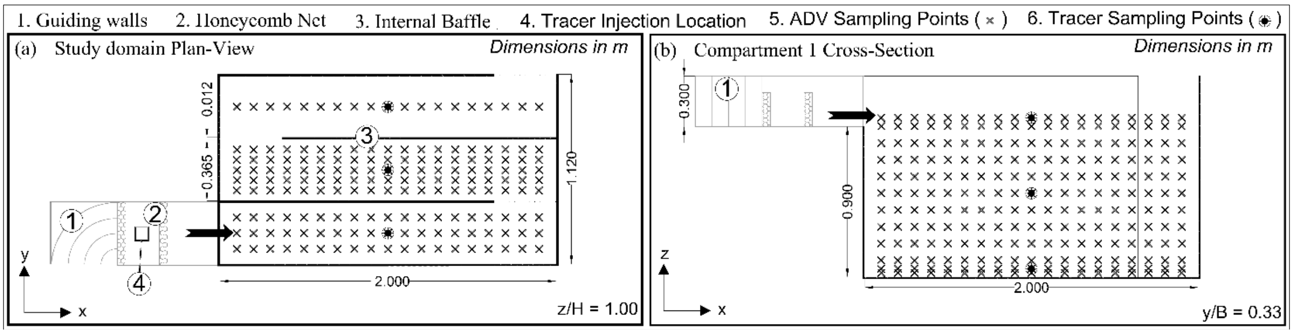

Figure 1. Numerical model geometry and the main sampling points.

A Dirichlet inflow condition with a prescribed $1/7^{th}$ power-law vertical and horizontal velocity distribution was imposed in the simulations in order to take into account the friction effects within the experimental inflow channel. The free surface was approximated as a frictionless rigid lid while no-slip conditions were imposed on the side and bottom walls of the channel. The interior solid walls were represented using the IB method. The outlet was set at the exit of the third compartment using a Neumann boundary condition ($\partial U/\partial x$ = 0). The geometry of the tank and hydraulic input data are summarised in Table 1.

Table 1. Geometry and hydraulics input data used in the computational model.

Description	Name	Value
Length	L_t	2 m
Width	W_t	1.12 m
Depth	H_t	1.2 m
Chamber width	W_c	0.365 m
Inlet flow rate	Q	0.00472 m^3/s
Theoretical residence time	$T=V/Q$	1265 s
Average inlet velocity	U_0	0.113 m/s

2 METHODOLOGY

2.1 Governing equations

In this study experimental data were compared with two three-dimensional CFD models, based on Reynolds-Averaged Navier-Stokes (N-S) and Large Eddy Simulation (LES) approaches respectively, set up to simulate the hydrodynamic and solute transport processes. Concerning N-S equations, turbulent flow characteristics can be evaluated with a time averaging operation that yield the Reynolds Averaged Navier-Stokes (RANS) equations. This suggests a statistical method where the instantaneous values of velocity and pressure are separated into mean and fluctuating components. Due to the non-linearity of the N-S equations, averaging leads to unknown correlations between scalar quantities known as Reynolds Stresses (Rodi, 1993). The determination of these parameters is achieved through the application of approximate models. For this study the standard k-ε model was adopted to compute turbulence modelling. RANS limitations include the inability of capturing instantaneous flow dynamics and the inadequacy to model anisotropic flows when an eddy-viscosity formulation is implemented.

Large Eddy Simulation (LES) has been developed considering that large-scale is strongly energetic and boundary-condition dependent motion, on the other hand small-scale is more dissipative and universal and represents only a small part of the turbulent spectrum, thus it tends to be more isotropic and boundary-condition independent (Rodi et al., 2013). Accordingly, LES simulations apply a spatial filtering procedure and calculate explicitly the motion of large-scales by solving the governing 3D time-dependent Navier-Stokes equations and treat the smaller-scale eddies with approximate models, known as Sub-Grid Scale (SGS) models.

2.2 Advection – Diffusion equation

The governing equation for the scalar transport modelling is the advection-diffusion equation. It can be solved in a similar manner to the momentum equations where, instead of the Reynolds stress term, a scalar-flux term needs to be closed. The turbulent fluctuation terms are expressed, according to the concept of Reynolds-averaging, by means of time-averaged quantities:

$$\frac{\partial \bar{C}}{\partial t} + \bar{u}\frac{\partial \bar{C}}{\partial x} + \bar{v}\frac{\partial \bar{C}}{\partial y} + \bar{w}\frac{\partial \bar{C}}{\partial z} = -\frac{\partial(\overline{u'C'})}{\partial x} - \frac{\partial(\overline{v'C'})}{\partial y} - \frac{\partial(\overline{w'C'})}{\partial z} \quad [1]$$

Here *u*, *v* and *w* are velocity components in the *x*, *y* and *z* directions, respectively, and *C* is the solute concentration. The overbar operation indicates time-averaged quantities for RANS and spatial-averaged quantities for LES, while the prime stands for fluctuating quantities. Note that molecular diffusion is neglected. Assuming the standard gradient-diffusion hypothesis (SGDH):

$$\begin{aligned} \overline{u'C'} &= -D_{t-x}\frac{\partial \bar{C}}{\partial x} \\ \overline{v'C'} &= -D_{t-y}\frac{\partial \bar{C}}{\partial y} \\ \overline{w'C'} &= -D_{t-z}\frac{\partial \bar{C}}{\partial z} \end{aligned} \quad [2]$$

where D_{t-x}, D_{t-y} and $D_{t-z}$are the turbulent diffusivities in the *x*, *y* and *z* directions, respectively, of the scalar being transported within the turbulent flow. Using Eq. [2] into Eq. [1], the advection-diffusion equation reads:

$$\frac{\partial \bar{C}}{\partial t} + \bar{u}\frac{\partial \bar{C}}{\partial x} + \bar{v}\frac{\partial \bar{C}}{\partial y} + \bar{w}\frac{\partial \bar{C}}{\partial z} = \frac{\partial}{\partial x}\left(D_{t-x}\frac{\partial \bar{C}}{\partial x}\right) + \frac{\partial}{\partial y}\left(D_{t-y}\frac{\partial \bar{C}}{\partial y}\right) + \frac{\partial}{\partial z}\left(D_{t-z}\frac{\partial \bar{C}}{\partial z}\right) \quad [3]$$

where the terms on the right hand side are related to the turbulent diffusion. The SDGH relates the advective transport of a scalar due to turbulent fluctuations to the spatial gradient of the time-averaged concentration through the turbulent diffusivity. The SDGH requires the estimation of the turbulent Schmidt number, Sc_t:

$$Sc_{t-i} = \frac{\nu_{t-i}}{D_{t-i}} \quad [4]$$

where ν_{t-i} is the eddy kinematic viscosity in the *i*-direction. This parameter is defined as the ratio of momentum diffusivity to mass diffusivity in a turbulent flow. The turbulent Schmidt number is the analogous for turbulent flow of the Schmidt number:

$$Sc = \frac{\nu}{D_m} \quad [5]$$

where *v* is the molecular kinematic viscosity of the fluid and D_m is the molecular diffusivity of the scalar within the fluid. Beside their analogy, Schmidt number and turbulent Schmidt number rely on different characteristics: *Sc* is a property of the fluid and of the substance being diffused within the fluid and it usually varies in the range 10^2–10^3, on the contrary Sc_t is a characteristic feature of the turbulent flow. The estimation of an appropriate Schmidt number has been a subject of controversy and no universally-accepted values of this parameter have been established (Combest et al., 2011; Gualtieri and Bombardelli, 2013). It is generally assumed in the range of 0.7 to1.2 or more often equal to 1 according with Prandtl analogy.A value of Sc_t equal to 0.7 was applied for this study according to the recommendations of Launder (1978) and several previous studies (Kim, 2010; Kim et al., 2013a; Angeloudis et al., 2014).

If the turbulent Schmidt number is known, the turbulent diffusivities can be estimated as:

$$D_{t-i} = \frac{\nu_{t-i}}{Sc_{t-i}} \quad [6]$$

The benefit of the SGDH lies in the lack of additional transport equations. A limitation instead is the assumption of isotropic turbulence which is not appropriate in the case in the presence of highly anisotropic flow. Additionally, the scalar-flux terms can be explicitly calculated in each direction in LES due to its eddy-resolving nature, which allows to study the reliability of the current isotropic turbulence assumption.

2.3 RANS – LES

The model SSIIM (Olsen, 2005) was applied to perform the RANS simulations. This model solves the Reynolds-Averaged Navier-Stokes equations using finite-volumes on a structured non-orthogonal grid. The SIMPLE method couples the pressure to the velocity field and the standard k-ε turbulence closure approximates the Reynolds Stresses. The Power-Law formulation is used for the interpolations of the convective term in the hydrodynamic simulation whereas for solute transport a combination of the Hybrid and the Hybrid Linear/Parabolic Approximation differentiation scheme is adopted. Real time of RANS simulations was approximately 30 minutes.

The Hydro3D code (Bomminayuni and Stoesser, 2011) was adopted to perform LES. It uses the spatially filtered Navier-Stokes equations for turbulent, incompressible, three-dimensional flow field. The SGS stresses are approximated using the Smagorinsky (1963) model. Hydro3D has been well validated in a number of other studies of complex flows ranging from tidal turbines (Ouro et al., 2015; Ouro and Stoesser, 2016), bubble plumes (Fraga et al., 2016; Fraga and Stoesser, 2016) and other hydraulic applications (Stoesser and Nikora, 2008; Stoesser, 2010; Kara et al., 2012; Kim et al., 2013).LES simulation were initially run for 400s prior to commencing the averaging of velocities, and second order statistics are collected 300s after the first order statistics averaging started. The total simulation time was equal to 2400s. The time step is variable with a CFL condition of 0.8 in order to maintain a stable simulation. Real time of LES simulations was 144 h.

3 HYDRODYNAMICS

3.1 Flow path

The hydrodynamic in contact tanks is governed by unsteady large-scale flow structures. The analysed CT featured large flow separation taking place in the junction between 1st and 2nd chamber, and vortex formation among the first two compartments. Under a plug-flow regime, the fluid flows through the reactor in an ordered manner with no fluid element overtaking or mixing with any other element ahead or behind. This theory allows lateral mixing but not longitudinal mixing or diffusion along the flow path. These conditions should ensure the same contact time in the tank for all fluid elements. The flow pattern corresponding to this regime suggests an absence of recirculation zones, a scenario that is physically unfeasible in reactor geometries featuring variable inlet and outlet conditions and baffling configurations where fluid flow meanders around them.

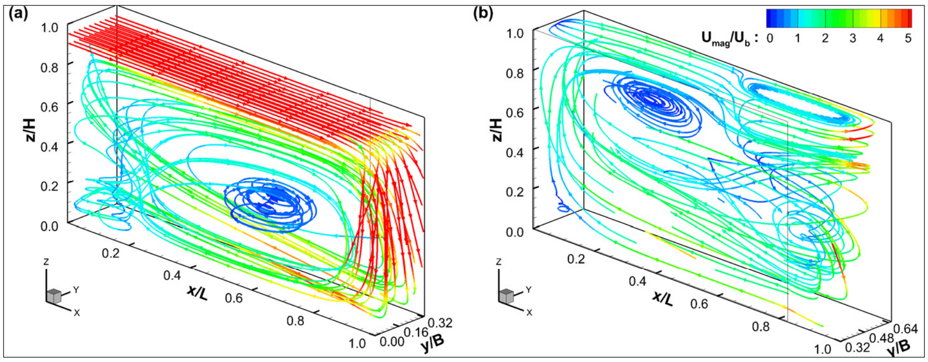

Figure 2. Three-dimensional streamlines of the mean velocity magnitude, normalised by U_b of (a) compartment 1 and (b) compartment 2, where B corresponds to the domain width in the simulations (see Fig.1a).

The generated flow path in the first two chambers of the CT is shown in Fig 2. The flow enters the first compartment and once it reaches the opposite wall it separates into two: on the one hand it turns back and it is reflected again at the bottom of the first compartment to form a large circulation zone; on the other hand it enters the second chamber where it forms another circulation zone near the surface. As the flow meanders around the first baffle, two additional vortices in the y-plane prevail. The y-plane vortex in compartment 1 is attributed to eddies formed by the sharp corner, while the second, in compartment 2, is driven by the top layer of the inflow jet. Essentially, due to the impact of the jet upon the compartment wall, the streamwise flow separates into three distinct directions. The first one remains in compartment 1 and feeds the quasi-vertical recirculation zone seen. The second feeds the quasi-horizontal vortex in the first half of compartment 2. The third drives the flow underneath the horizontal vortex towards the second half of compartment 2 and beyond.

3.2 Velocity profiles, results and validation

Both RANS and LES present a good agreement with experimental data in reproducing the flow field and main turbulent structures. Fig 3 presents the velocity distribution at the centreline of the two chambers of time-averaged values from RANS and LES, instantaneous values for LES, and experimental results from the ADV data. These velocities are normalised with the bulk velocity U_b. A notably good agreement was found for the three velocity components at the first compartment between RANS and LES with the experiments. The instantaneous values from LES compared to the time-averaged distribution suggests that there is a considerable presence of small scale turbulence, which is a major contribution to the turbulent mixing shown in the next Section 4. Similar result distribution between numerical approaches and experimental data is reported in the second compartment. Again velocity fluctuations were found along the entire water depth, indicating that in both compartments the flow was quite turbulent. The latter is relevant in the tracer transport modelling as RANS is based on time-averaged flow field whereas LES uses instantaneous velocity values.

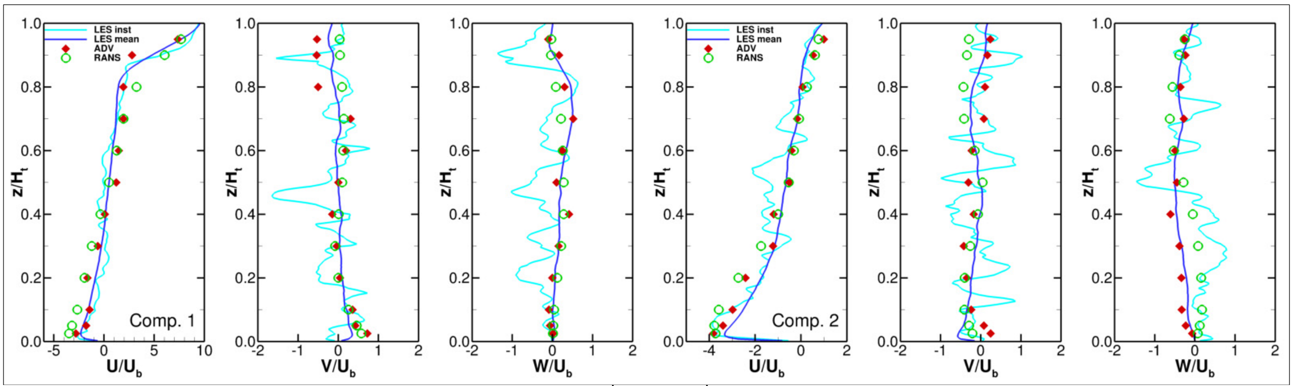

Figure 3. Velocity profiles at the central line of the1st and 2nd compartments. Comparison of the instantaneous and mean values from LES, and mean values from RANS and experiments (ADV).

Comparison between numerical data and experimental data was also calculated in reference to the average error of normalised velocity components in each section of compartments 1 and 2, which was computed as:

$$Err\ \% = 100 * (ADV - Numericaldata)/ADV \quad [7]$$

Both computational methods show errors below 2% in compartment 1 and 1% in compartment 2, both RANS and LES simulations yield feasible results. Table 2 shows the percentage of average error related to each velocity profile.

Table 2. Percentage of average velocity error for RANS and LES.

	U/U_b	V/V_b	W/W_b	
1st Compartment	+ 1.85	- 0.52	+ 1.19	Err RANS %
	- 0.85	- 0.10	+ 1.21	Err LES %
2nd Compartment	- 0.12	+ 0.66	+ 0.26	Err RANS %
	+ 0.37	+ 0.92	+ 0.16	Err LES %

3.3 Quadrant analysis

Quadrant analysis is a technique that helps identifying the presence of coherent structures in the flow and their contribution to the Reynolds stresses, and illustrates graphically the degree of anisotropy of the turbulent fluctuations. It was applied at nine locations as depicted in Fig 4a.The covariance between velocities is of particular interest for the turbulence analysis. It cannot be performed with the present RANS approach since it provides information only on the mean values of velocity field. In contrast, LES explicitly calculates velocity fluctuations. Fig 4a depicts the location of the sampling points. P1, P3 and P5 are placed at the centreline of the 1stchamber, P2, P4 and P6 are at the centreline of the 2nd chamber, and P7 to P9 are at the middle of the junction between these compartments.

For each point the quadrant analysis in both u'/u_{rms}– v'/v_{rms} and u'/u_{rms}– w'/w_{rms} planes were conducted, reflecting the strong three-dimensionality of the flow. Table 3 displays how many points out of the total fall into each quadrant. Looking at the horizontal plane of P1 in Fig 4b, under the hypothesis of isotropic turbulence, the cloud should have a circle-shape among the domain of the plots. Instead, the majority of the horizontal velocity fluctuations (u'/u_{rms}– v'/v_{rms}) fall into the first (u' and v' > 0) and third (u' and v' < 0) quadrants (36% and 30% respectively, according to Table 3), resulting in an ellipsoidal shape.

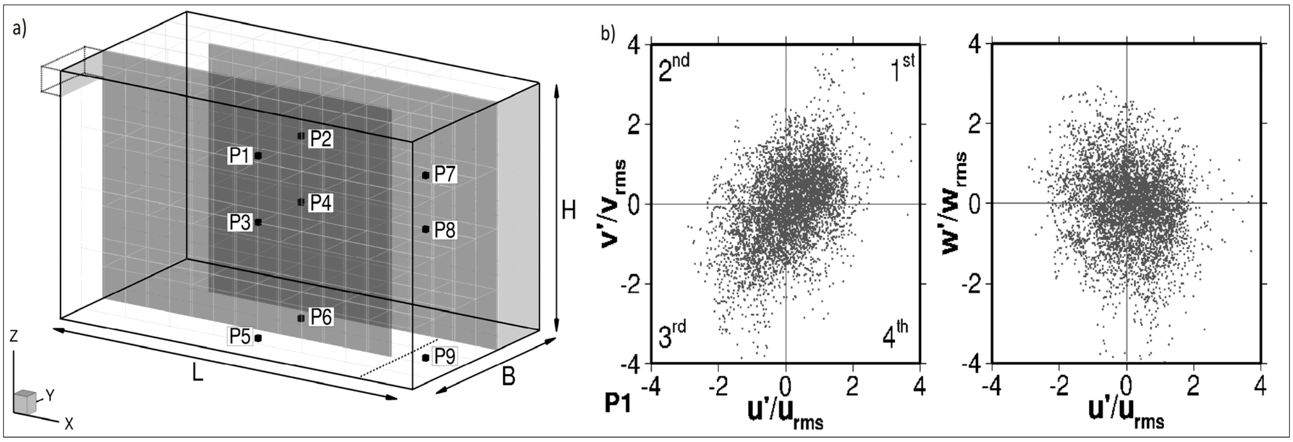

Figure 4. (a) Representation of the domain with the 9 sampling points used for the tracer and quadrant analysis. (b) quadrant plot in the axis u'/u_{rms}– v'/v_{rms} and u'/u_{rms}– w'/w_{rms} at point P1.

This indicates a prevalence of the high-momentum motion coming from the inlet near the surface. Similar observations can be done for the other points where the cloud is often ellipsoidal than circular. This confirms the anisotropic nature of the turbulence in the tank since the turbulent events are not evenly distributed among the quadrants.

Table 3. Quadrant analysis of u'/u_{rms}– v'/v_{rms} and u'/u_{rms}– w'/w_{rms} from points P1 to P9.

Plane	Quadrant	P1	P2	P3	P4	P5	P6	P7	P8	P9
$u' - v'$	1^{st}	36 %	26 %	45 %	23 %	18 %	23 %	26 %	21 %	24 %
	2^{nd}	14 %	30 %	13 %	22 %	31 %	26 %	20 %	15 %	26 %
	3^{rd}	30 %	22 %	23 %	24 %	27 %	27 %	36 %	35 %	25 %
	4^{th}	20 %	22 %	19 %	31 %	24 %	25 %	18 %	28 %	25 %
$u' - w'$	1^{st}	26 %	24 %	30 %	24 %	17 %	22 %	17 %	32 %	26 %
	2^{nd}	24 %	29 %	14 %	25 %	32 %	30 %	36 %	33 %	23 %
	3^{rd}	20 %	23 %	22 %	21 %	25 %	23 %	19 %	17 %	29 %
	4^{th}	30 %	24 %	34 %	29 %	25 %	26 %	27 %	18 %	23 %

4 SOLUTE TRANSPORT

4.1 Passive scalar dispersion

The current study demonstrates that the solute transport in contact tanks is strongly affected by hydrodynamics. Advection is identified to be the main source of tracer transport, confirming the strong interlink between hydrodynamics and solute transport. Tracer injected at the inlet is advected with the jet towards the opposite wall of compartment 1. Part of the tracer is then deflected from the wall towards the bottom of the compartment and is transported along the large recirculation zone. The phenomenon of flow separation can be also argued since it clearly affects the solute transport. When the concentration is spreading into compartment 2, the massive recirculation zone in compartment 1 (see Fig.2a) still holds the tracer for a time greater than the theoretical retention one. The tracer plume remains in the first chamber even when the tracer reaches the end of the second one, and starts spreading into the third chamber (see Fig 5). It is visible the co-existence of tracer in both compartments in Fig 6. As a result, the presence of non-ideal plug flow condition is evident.

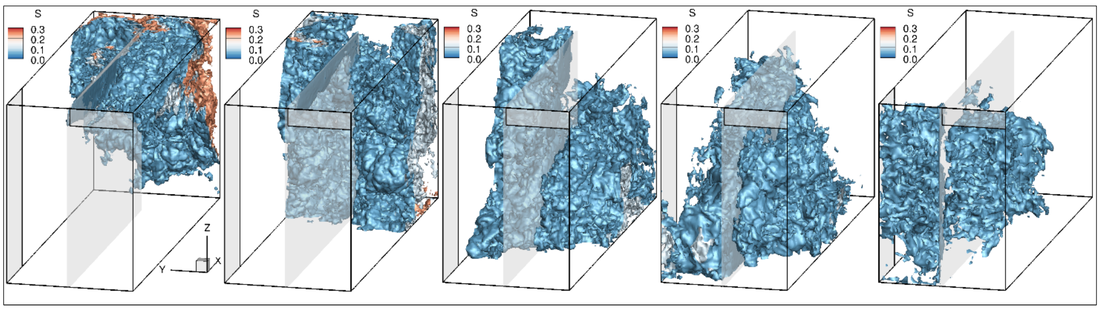

Figure 5. 3D view of iso-surfaces of instantaneous normalised concentration at different times after its initial releasing from LES.

  / ISSN 1562-6865 (Online) - ISSN 1063-7710 (Print)

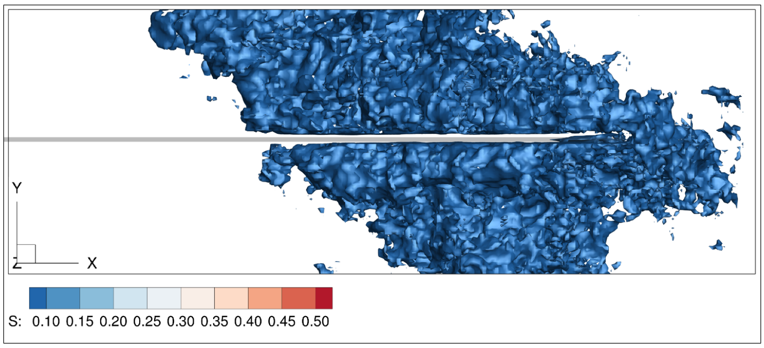

Figure 6. 2D iso-surface of instantaneous normalised concentration at t=60s (LES simulation).

4.2 Residence time distribution curves

The performance of the simulations was investigated comparing the RTD curves of numerical simulations with the experimental data at P1 to P6 sampling points located at the top, middle and bottom of each compartment (see Fig 4a).

Fig. 7 presents the normalised instantaneous tracer concentration, E(θ), at the six locations, in reference to the normalised time θ = *t/T*, where *t* denotes physical time and *T* is equal to 1265s as the theoretical retention time in the whole experimental tank. The occurrence of secondary peaks, as seen Fig. 7a, indicates moments when the tracer passes by again the same point due to the recirculation and vortex formation.

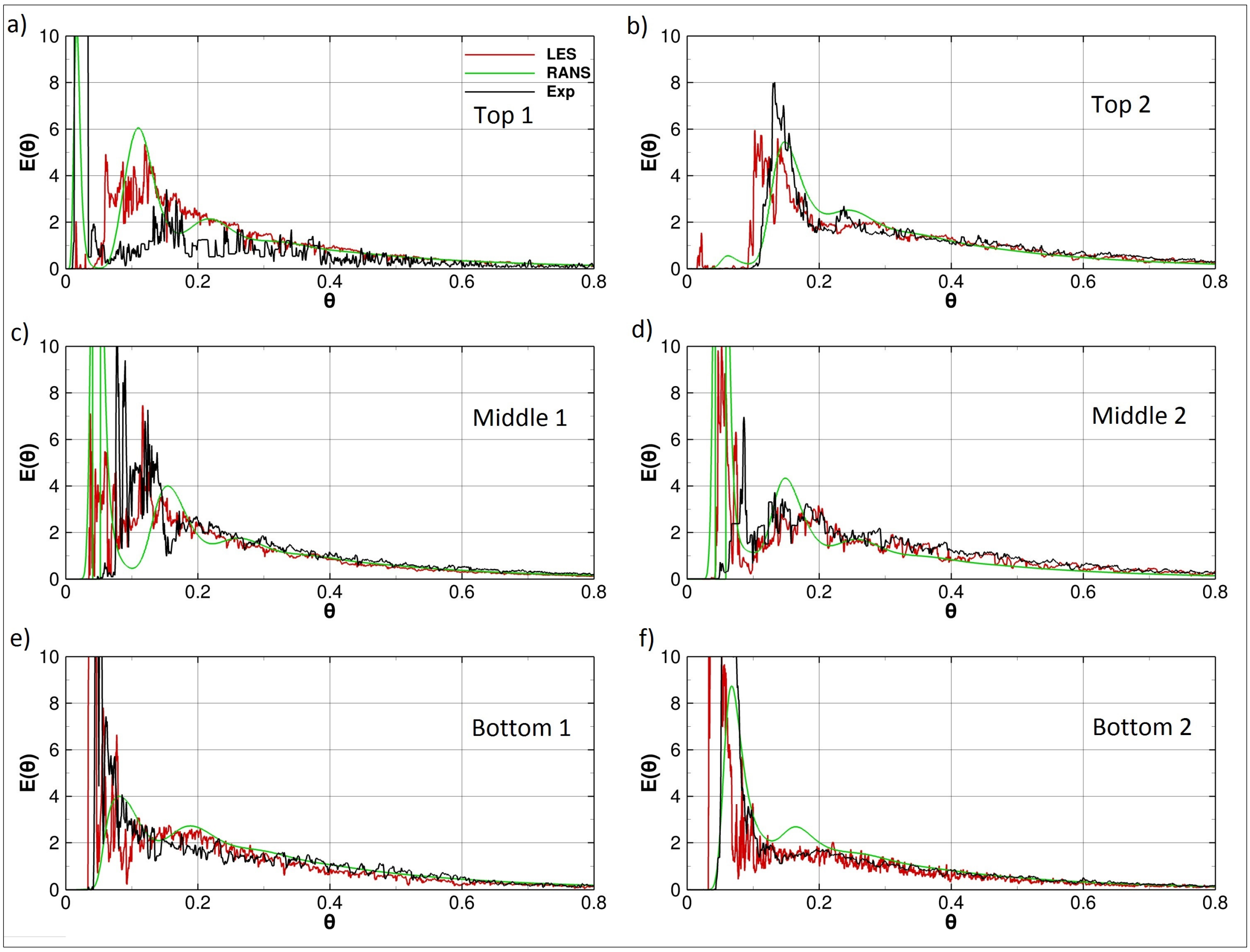

Figure 7. RTD curves from LES, RANS and experimental data at various locations: (a) P1, (b) P2, (c) P3, (d) P4, (e) P5 and (f) P6.

Both RANS and LES were able to reproduce the shape and trend of the experimental curves. In particular LES captures instantaneous concentration fluctuations which are not captured by RANS. Nonetheless, RANS was able to predict the large concentration peaks in the RTD curves fairly well, although its time-averaged nature do not resolve the unsteadiness in the flow, and exhibits a smooth distribution. Hence, the predicted RANS results slightly deviated from the ones measured in the experiments and computed by LES. In fact, the flow in contact tanks is governed by large-scale flow unsteadiness as reported recently by Kim et al. (2010b, 2013), who showed that vortex shedding originated from the baffle edges can dominate the flow and influence the transport of scalars in such tanks.

The LES RTD curves matched both the magnitude and shape of those from the experiments, and also improved RANS results. In particular, the presence of a sharp short-circuiting peak and a secondary peak that result from internal recirculation (i.e. the tracer exiting the chamber after single recirculation) are noticeable. In all the points of compartment 1, the secondary peak appears between θ= 0.1 and θ =0.2, and the same happens for points P4 and P6 (respectively middle and bottom) of compartment 2. In point P2, instead, the secondary peak appears after θ =0.2 since the spreading of the tracer in compartment 2 occurs from the bottom to the top after the separation of the flow.

5 CONCLUSIONS

This study investigated the hydrodynamic and solute transport in the first two compartments of a chlorine contact tank (CT) by means of complementary experimental and numerical techniques. RANS and LES approaches have been used to simulate the hydrodynamic and solute transport processes. The capability of these numerical methods to reproduce the actual turbulent flow conditions in the analysed CT has been assessed through comparisons with experimental data in terms of velocity fields and conservative tracer concentration readings. The velocity data has been analysed to identify short-circuiting and internal recirculation, which are accountable for disinfection performance deficiencies.

The conclusions from this research in the comparison between experimental data and numerical simulations have shown that 3D numerical models are able to reproduce the turbulent flow behavior, and the transport of a scalar throughout the CT with accuracy. From the analysis of the percentage average error between numerical and experimental data of both simulations, LES provides on average a greater accuracy in predicting hydrodynamics behaviour. Although RANS has been able to reproduce the time-averaged flow properties quite well, LES has provided a larger amount of information on instantaneous flow field, which makes it capable to capture the flow unsteadiness that characterise the contact tank hydrodynamics and solute transport.

Testament of the ability of the modelling approaches is also reflected in the good match of simulated Residence Time Distribution (RTD) curves compared to those from the experiments. Flow in CTs exhibits a RTD curves which is often significantly different from that dictated by plug flow. The correlation between the hydrodynamics and the tracer RTD curves obtained in each compartment demonstrate that advection is the main mode of tracer transport and demonstrates the strong interlink between the hydrodynamics and solute transport.

It is shown that the inlet conditions led to elevated levels of turbulence primarily as a result of interactions with bed and side boundaries and have a marked influence on the hydrodynamics in the early compartments of the tank, causing significant recirculation zones in a large portion of the compartment and leading to subsequent three-dimensionality.

Beside strictly contact tank's hydraulics aspects, the focus undertaken on the junction between the first and the second compartment and those compartment in itself, allow us to provide also an intuition on more universal phenomena that take place herewith. Following a serpentine path, the water jet crashes against the boundary wall and, in the junction between the first and second chamber a well-defined deflection of the flow is observed with the consequent occurrence of the separation of the flow. Flow separation forms secondary currents and vortices that may in turn influence the turbulent transport and interconnected processes beyond hydrodynamics. Understanding how a turbulent separated flow impacts upon the transport of a solute can be of particular interest in hydro-environmental applications.

ACKNOWLEDGEMENTS

This work was performed using the computational facilities of the Advanced Research Computing @ Cardiff (ARCCA) Division, Cardiff University and HPC Wales.

REFERENCES

Angeloudis, A. (2014). Numerical and Experimental Modelling of Flow and Kinetic Processes in Serpentine Disinfection Tanks. *PhD Thesis*, University of Cardiff.

Angeloudis, A., Stoesser, T., Kim, D. & Falconer, R.A. (2014a). Modelling of Flow, Transport and Disinfection Kinetics in Contact Tanks. *Proceedings of the ICE-Water Management*, 167(9), 532-546.

Angeloudis, A., Stoesser, T. & Falconer, R.A. (2014b). Predicting the Disinfection Efficiency Range in Chlorine Contact Tanks Through a CFD-Based Approach. *Water Research, 60, 118-129*.

Angeloudis, A., Stoesser, T., Kim, D. & Falconer, R.A. (2014). Flow, Transport and Disinfection Performance in Small- and Full- Scale Contact Tanks. *Journal of Hydro-Environment Research,* 9(1), 15-27.

Angeloudis, A., Stoesser, T., Gualtieri, C. & Falconer, R.A. (2015). Effect of Three-Dimensional Mixing Conditions on Water Treatment Reaction Process. In *Proceedings of the 36th IAHR World Congress, The Hague, the Netherlands.*

Angeloudis, A., Stoesser, T., Gualtieri, C. & Falconer, R.A. (2016). Contact Tank Design Impact on Process Performance. *Environmental Modeling & Assessment* 21(5), 563-576.

Bomminayuni, S. & Stoesser, T. (2011). Turbulence Statistics in an Open-Channel Flow over a Rough Bed. *Journal of Hydraulic Engineering,* 137(11), 1347-1358.

Bridgeman, J., Jefferson, B. & Parsons, S. (2010). The Development and Application of CFD Models for Water Treatment Flocculators. *Advanced in Engineering Software*, 41(1), 99-109, DOI 10.1016/j.advengsoft.2008.12.007.

Combest, D.P., Ramachandran, P.A. & Dudukovic, M.P. (2011). On the Gradient Diffusion Hypothesis and Passive Scalar Transport in Turbulent Flows. *Industrial & Engineering Chemistry Research*, 50(15), 8817-8823.

Fraga, B. & Stoesser, T. (2016). Influence of Bubble Size, Diffuser Width and Flow Rate on the Integral Behaviour of Bubble Plumes. *Journal of Geophysical Research*, 121(6), 3887-3904, DOI 10.1002/2015JC011381.

Fraga, B., Ouro, P. & Stoesser, T. (2016). Efficient Hybrid Parallelization of Eulerian-Lagrangian Applications in a Large-Eddy Simulation Solver. *Computers and Fluids*.

Gualtieri, C. (2006). Numerical Simulation of Flow and Tracer Transport in a Disinfection Contact Tank. *Proceedings of the 3rd Biennial Meeting of the International Environmental Modelling and Software Society*, Vermont.

Gualtieri, C. & Bombardelli, A. (2013). Parameterization of the Turbulent Schmidt Number in the Numerical Simulation of Open-Channel Flows. *Proceedings of 2013 IAHR Congress.*

Kara, S., Stoesser, T. & Sturm, T. (2012). Turbulence Statistics in Compound Channels with Deep And shallow overbank flows. *Journal of Hydraulic Research,* 50(5), 482-493, DOI 10.1080/00221686.2012.724194.

Kim, D. (2011). Large Eddy Simulation of Flow in Water and Wastewater Disinfection Reactors. *PhD Thesis*, Georgia Institute of Technology.

Kim, D., Kim, D., Kim, J.H. & Stoesser, T. (2010b). Large Eddy Simulation of Flow and Tracer Transport in Multichamber Ozone Contactors. *Journal of Environmental Engineering*, 136(1), 22-31.

Kim, D., Stoesser, T. & Kim, J.H. (2013a). The Effect of Baffle Spacing on Hydrodynamics and Solute Transport in Serpentine Contact Tanks. *Journal of Hydraulic Research*, 51(5), 558-568.

Kim, D., Stoesser, T. & Kim, J.H. (2013b). Modeling Aspects of Flow and Solute Transport Simulation in Water Disinfection Tanks. *Applied Mathematical Modelling*, (37)16, 8039-8050.

Launder, B.E. (1978). *Turbulence*. Bradshaw, P. ed., Springer, Berlin, Chapter C6

Olsen, N.R.B. (2005). *SSIIM User's Manual*. Department of Hydraulic and Environmental Engineering, The Norwegian University of Science and Technology, http://www.ntnu.no/~nilsol/ssiimwin/manual3.pdf.

Ouro, P., Stoesser, T. & McSherry, R. (2015). *CFD for Wind and Tidal Offshore Turbines. Springer International Publishing*, Chapter C5, 49-58, DOI 10.1007/978-3-319-16202-7_5.

Ouro, P. & Stoesser, T. (2016). Large-Eddy Simulation of Darrieus-type Vertical Axis Tidal Turbines. *Submitted to Computers & Fluids.*

Rauen, W.B., Angeloudis, A. & Falconer, R.A. (2012). Appraisal of Chlorine Contact Tank Modelling Practices. *Water Research*, 46(18), 5834-5847.

Rodi, W. (1993). *Turbulence Models and Their Application in Hydraulics*. 3rd ed., Taylor & Francis.

Rodi, W., Stoesser, T. & Constantinescu, G. (2013). *Large-Eddy Simulation in Hydraulics*. IAHR Monograph.

Smagorinsky, J. (1963). General Circulation Experiments with the Primitive Equations, Part I: The Basic Experiment. *Mon. Weather Rev.*, 91(3), 99-164.

Stoesser, T. & Nikora, V. (2008). Flow Structure Over Square Bars at Intermediate Submergence: Large Eddy Simulation Study of Bar Spacing Effect. *Acta Geophysica*, 56(3), 876-893, DOI 10.2478/s11600-008-0030-1.

Stoesser, T. (2010). Physically Realistic Roughness Closure Scheme to Simulate Turbulent Channel Flow over Rough Beds within the Framework of LES. *Journal of Hydraulic Research*, 136(10), 812-819, DOI 10.1061/(ASCE)HY.1943-7900.0000236

Teixeira, E.C. (1993). Hydrodynamic Processes and Hydraulic Efficiency of Chlorine Contact Units. *PhD Thesis*, University of Bradford.

Zhang, J., Tejada-Martinez, A.E. & Zhang, Q. (2014). Developments in Computational Fluid Dynamics-Based Modeling for Disinfection Technologies over the Last Two Decades: A Review. *Environmental Modelling & Software*, 58, 71-85.

Proceedings of the 37th IAHR World Congress
August 13 – 18, 2017, Kuala Lumpur, Malaysia

INVESTIGATION OF UNCERTAINTY EFFECTS ON HYDRAULIC PERFORMANCE OF WATER DISTRIBUTION NETWORKS USING THE FUZZY SETS THEORY

ADELL MORADI SABZKOUHI(1), ALI HAGHIGHI(2) & AMIN MINAEI(3)

(1,2,3) Department of Civil Engineering, Faculty of Engineering, Shahid Chamran University of Ahvaz, Ahvaz, Iran,
a-moradisabzkouhi@phdstu.scu.ac.ir; a.haghighi@scu.ac.ir; aminminaei2014@gmail.com

ABSTRACT

Water distribution networks (WDNs) are of crucial infrastructures that are required to satisfy urban water needs with desirable quality and quantity. The hydraulic performance of each WDN is highly affected by uncertainty in the system's parameters, such as nodal demands and pipe friction factors. The input uncertainties are spread out over the system and introduce uncertainty to the network responses, nodal pressures, and pipe velocities. Those uncertainties may easily violate the design criteria and significantly influence the system reliability. Hence, an important issue in the design of a WDN is to know the extent to which the imprecision of the independent input parameters affects the system output variables and hydraulic performance. Answering this question can be very complicated when the pipe network is large and complex in its configuration. Accordingly, analyzing the uncertainty effects in pipe systems has become a challenging topic for researchers in recent years. In designing a water distribution network, the system's hydraulic performance is taken into account by some indices like the reliability, resilience, and vulnerability. This study introduces a new fuzzy index represents the fuzzy behavior of system responses and its application as an alternative objective function in the multi-objective design of WDNs. The new index needs uncertainty analysis of each design scenario. Using a self-adaptive Non-Dominated Sorting Genetic Algorithm (NSGA-II), the fuzzy design is solved and the optimum trade-off between the objective functions is derived, and the solutions are discussed. Alongside the cost-fuzzy index, some other features of the solutions are analysed and the Pareto optimal front is investigated.

Keywords: Uncertainty analysis; Water Distribution Network (WDN); fuzzy sets theory; multi-objective optimization; reliability.

1 INTRODUCTION

In traditional approach of Water Distribution Networks (WDNs) design, generally, crisp values are considered for the system's input parameters, such as demands, the roughness of pipes, reservoir or pump station heads, etc. According to these crisp values, candid scenarios are further analyzed and pressure head in junctions, flow velocity in pipes, etc. are calculated as the system's responses that are inevitably crisp too. Based on this approach, the best solution(s) is/are determined while the design objective(s) and constraints would be crucial factors in the final decision taking. This is while input parameters are exposed to some level of uncertainty spread over the system and make the system's responses to be imprecise as well. In this regard, the general view is that if the most pessimistic values are simultaneously taken into account for all input parameters, accordingly the most critical values (extreme points) of responses would be modeled. The following simple example demonstrates how this presumption could be wrong in some cases when we consider looped networks. The system includes a simple 1-loop pipe network having five links and four junctions supplied by a fixed head reservoir at elevation 78m. Geometric and hydraulic properties of the system are shown in Figure 1. Except for Hazen-Williams (H-W) roughness, all other parameters are assumed to be fixed with no uncertainty. Field and laboratory tests demonstrate that Hazen-Williams roughness of pipes would averagely be 125. However, based on technical knowledge and engineering experience, a designer considers $\pm 25\%$ uncertainty associated with the roughness of pipes. In other words, the maximum and minimum values of H-W roughness are expected to be 150 and 100, respectively. According to the above general view, the designer sets H-W roughness equal to 100 for all pipes supposed to result in the worst nodal pressure head for all junctions. Figure 1a represents the nodal pressure heads calculated on the basis of this scenario. Figure 1b reveals that the previous scenario would not produce the most critical minimum nodal pressure for Node 3. If we take a probable value of 150 for H-W roughness of Pipe 3, it can be seen that more hydraulic transmission capacity for Pipe 3, results in more energy loss along Pipe 2 as well, making 1.2m decrease in the pressure head of Node 2. Whereas, the average nodal pressure for other junctions increases 0.8m as compared to the design scenario. Considering the same increase in H-W roughness, Pipe 5 has the same trend on pressure head of Node 4, in comparison to the design scenario. This is while many more

  / ISSN 1562-6865 (Online) - ISSN 1063-7710 (Print)

uncertain parameters, several loops, etc. and complexity of these parameters interaction make the uncertainty analysis much more complicated in the case of large real pipe networks.

In the present study, first, the application of fuzzy sets theory for uncertainty analysis of pipe networks is briefly pointed out. Secondly, according to the features of fuzzy uncertainty analysis, a new systematic scheme to handle the efficiency of uncertainty analysis of fuzzy systems is discussed. Further, a new fuzzy metric is introduced to the fuzzy multi-objective design of pipe networks and it is demonstrated that the new metric could effectively find better solutions, which have more resistance to uncertainty.

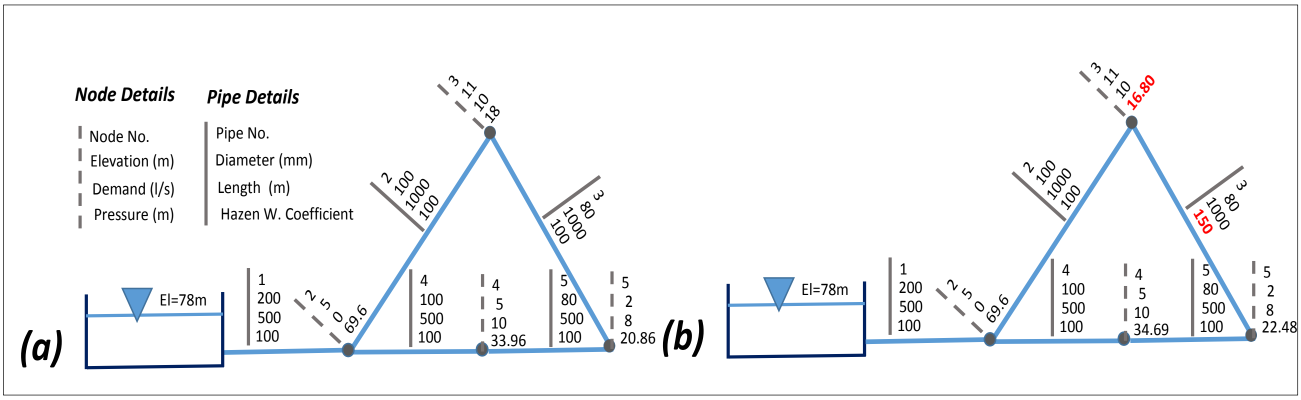

Figure 1. An illustrative example of a simple fuzzy pipe network.

2 FUZZY ANALYSIS OF PIPE NETWORKS

In a fuzzy analysis of pipe networks, the system's parameters, such as nodal demands, the roughness of pipes, etc., are not considered to be crisp. In fact, according to Figure 2a, each fuzzy parameter belongs to an interval in which the membership changes from 0 in its two extremes (named support ends) to 1 in the crisp value. Based on the level of uncertainty represented by a so-called operator a-cut (Figure 2b), the same interval of variations are determined to all sources of input uncertainties spread over the system making the responses uncertain too. In other words, according to a given level of uncertainty a-cut, each response of the system would change over the corresponding unknown interval (Figure 2c). The aim of a fuzzy analysis is to find the extremes of responses over some a-cuts and capture the fuzzy membership functions for all responses.

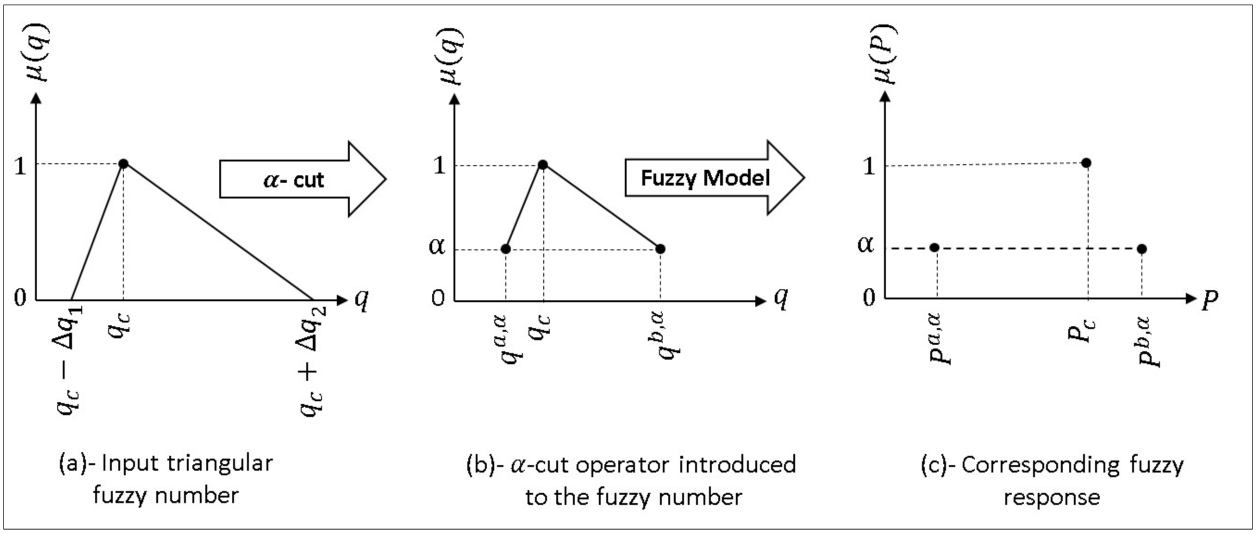

Figure 2. Fuzzy input-output model concept.

2.1 Optimization-based approach to fuzzy analysis

As mentioned above, the fuzzy analysis of pipe networks leads to finding the two extreme points for each fuzzy response. One of the practical approaches to determine these extremes is to define the problem as a mathematical problem in which the input uncertainties are decision variables and each response would be the objective function that is going to be once minimized and maximized. In this context, a many-objective optimization approach has been introduced by Sabzkouhi and Haghighi (2016). This new approach is significantly more efficient in comparison with other optimization-based approaches proposed in previous studies (Revelli and Ridolfi, 2002; Branisavljevic and Ivetic, 2006; Spiliotis and Tsakiris, 2012; Haghighi and

Keramat, 2012; Haghighi and Asl, 2014; Sivakumar et.al., 2016). For a real case study, Sabzkouhi and Haghighi (2016) reported that the many-objective PSO (MOPSO) could significantly outperform other optimization based approaches. Figure 3 shows a conceptual framework describing how the many-objective model works (Sabzkouhi and Haghighi, 2016).

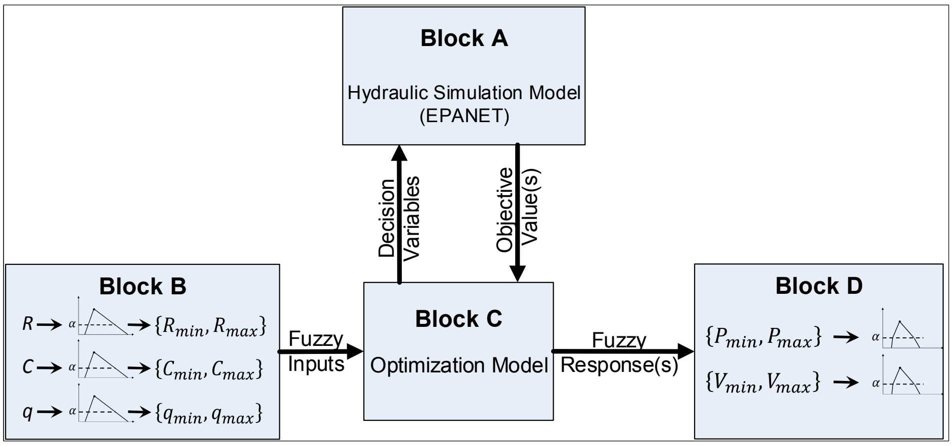

Figure 3. Conceptual description of the fuzzy model for pipe networks analysis.

- Example 1

For evaluating the many-objective approach, the results of an example used by Sabzkouhi and Haghighi (2016) is reported here. The example contains a small theoretical pipe network introduced by Revelli and Ridolfi (2002) and then, used as a benchmark by Gupta and Bhave (2007) and Haghighi and Asl (2014). The details of network's components are shown in Figure 4. To estimate the friction losses, the Chezy-Manning formula with the Gauckler-Strickler coefficient is used in this example. The reservoir head (R) and all nodal demands (q) include at most ± 0.5 m and ± 5 % uncertainty, respectively, while their crisp (most likely) values are presented in Figure 4. Also, all Gauckler-Strickler coefficients (c) include at most ± 8.33 % uncertainty and have the crisp value of $60\ m^{1/3}s^{-1}$. For fuzzy analysis of the network to find the fuzzy responses P in nodes and Q in pipes, the input fuzzy numbers R, q and c are discretized with five α-cuts including $\alpha = 0, 0.25, 0{,}5, 0.75$ and 1. For each α-cut except 1, the MO-PSO model is required to apply to the network to find the upper and lower bounds of the eight hydraulic responses $P_2, P_3, P_4, Q_1, Q_2, Q_3, Q_4$ and Q_5. Accordingly, there are totally 16 objective functions in each α-cut meaning that if the problem is supposed to be solved by a single-objective model, the optimization must be 16 times applied. Based on the membership functions of responses presented in Figure 5, the results of MO-PSO are found in a good agreement with those of the iterative single objective approach by Revelli and Ridolfi (2002) using the quadratic programming method. Also, the fuzzy analysis reveals that the input uncertainties may result in significant uncertainties in the network hydraulic responses. For instance, the pressure head at node 3 may experience -17.7 % to $+13.4$ % uncertainty due to the aforementioned input uncertainties. The uncertainty influences on the pipe discharges are much more dramatic than on the nodal pressures. For example, due to the input uncertainties the flow discharge in pipe 3 may experience -49.4 % to $+47.5$ % uncertainty with respect to its crisp value.

2.2 Optimization-free approaches to fuzzy analysis

Against optimization based approaches, there are some analytical schemes having some simplifications to eliminate the optimization process (Spiliotis and Tsakiris, 2012; Gupta and Bhave, 2007). Most of these methods assume that over the intervals of input uncertainties, system responses vary monotonically. So, nonlinear nature of governing equations of pipe network hydraulics causes these approaches to have acceptable results only for small changes in input uncertainties. This clearly reveals that these approaches have different accuracy for various uncertainty levels. It is worth mentioning that the many-objective approach is appropriate for any type of monotonic or non-monotonic input-output systems since it searches the decision space without considering the form of problem topology. This is an outstanding feature, particularly when we do not know how the system outputs change with the inputs. Moreover, when the system exposes to large input uncertainties, optimization based approaches are still reliable.

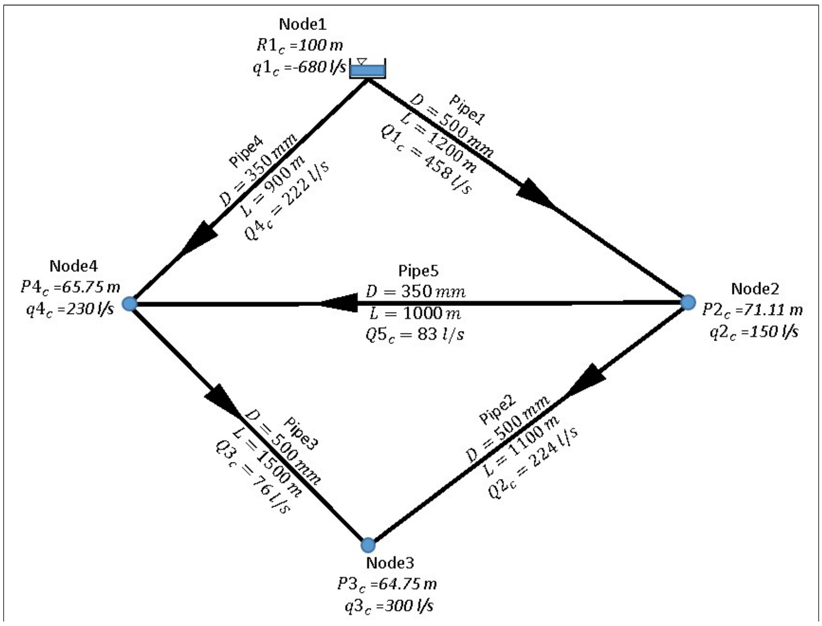

Figure 4. Network layout for Example 1 (Revelli and Ridolfi, 2002).

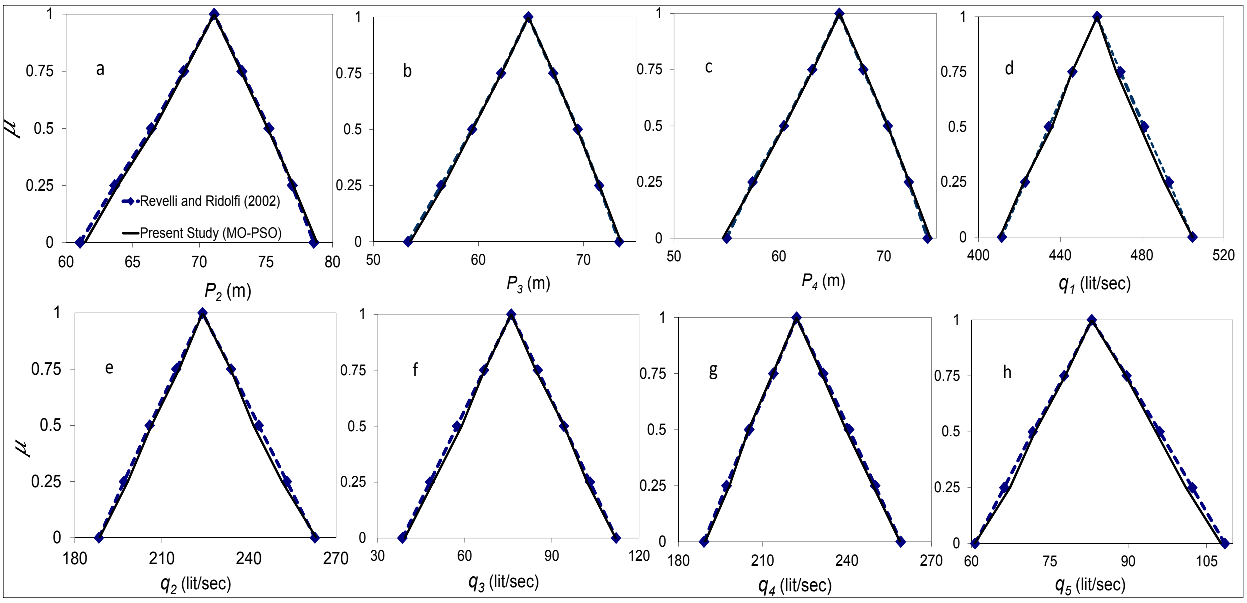

Figure 5. Membership functions of hydraulic responses for Example 1

3 FUZZY DESIGN OF PIPE NETWORKS

3.1 Master model

The fuzzy analysis approaches explained in section 2.1 and 2.2 previously are only able to assess the uncertain behavior of an existing system or a known design scenario. In the case of fuzzy design, however, we need a ***master model*** including a ***fuzzy analysis model*** (Part I) and an ***optimization solver*** (Part II) coupled to each other in order to iteratively analyze different candid solutions to satisfy design constraints while promoting the design fuzzy objective(s). This issue implies that if the MOPSO is selected to use in Part I, we require two interactive optimization processes, one includes the new many-objective approach for Part I (fuzzy analysis process) and another includes common multi-objective for Part II (design process). These two nested optimizations, however, make the fuzzy design a too complicated and time-consuming process. Hence, to have a more efficient master model in fuzzy design, we assume that the input uncertainties are small and accept the accuracy of optimization-free approach in the fuzzy analysis of pipe networks. Among the methods that benefit this approach, the present study exploits Impact Table method introduced by Gupta and Bhave (2007) to fuzzy analysis during fuzzy design procedure.

3.2 Design objective functions

The fuzzy design of pipe networks in this study includes two conflict objectives so that the trade-off between them is going to be obtained using Non-dominated Sorting Genetic Algorithm NSGA-II (Deb et.al., 2002). The first objective function is the capital cost of pipe network which is going to be minimized. The second objective is an index related to a fuzzy feature of nodal pressures as the system responses. To define this fuzzy index, imagine the general form of a fuzzy membership function of the response (P), as illustrated in Figure 6. As can be seen, for the uncertainty level of $\alpha = 0$, $P_{crisp} - P^{a,\alpha=0}$ and $P^{b,\alpha=0} - P_{crisp}$ indicate the maximum uncertainty expected to nodal pressure P, where $P^{a,\alpha=0}$ and $P^{b,\alpha=0}$ are the supports of the fuzzy number P whose crisp value is P_{crisp}. To make these uncertainties dimensionless, they are divided by P_{crisp}. So, we define a fuzzy factor demonstrating in what extent the response P is exposed to input uncertainties:

$$SFI = SFI^{+} + SFI^{-} \quad [1]$$

$$SFI^{+} = \frac{P^{b,\alpha=0} - P_{crisp}}{P_{crisp}} \ , \ SFI^{-} = \frac{P_{crisp} - P^{a,\alpha=0}}{P_{crisp}} \quad [2]$$

in which SFI is Support-based Fragility Index consisting of $SFI^{+}$and SFI^{-}, the outward and inward Support-based Fragility Indexes, respectively. The more SFI^{+} and SFI^{-} are, the more fragile the system is. Equation 1 is general form of SFI. However, based on the aim of application, we may prefer only the outward or inward SFI. Since in steady state design of pipe networks the minimum nodal pressures are more critical, in this article, we just consider SFI^{-} and instead of P_{crisp}, the minimum required design pressure P_{min-d} is defined in Equation 2. So:

$$SFI = \frac{P_{min-d} - P^{a,\alpha=0}}{P_{min-d}} \quad [3]$$

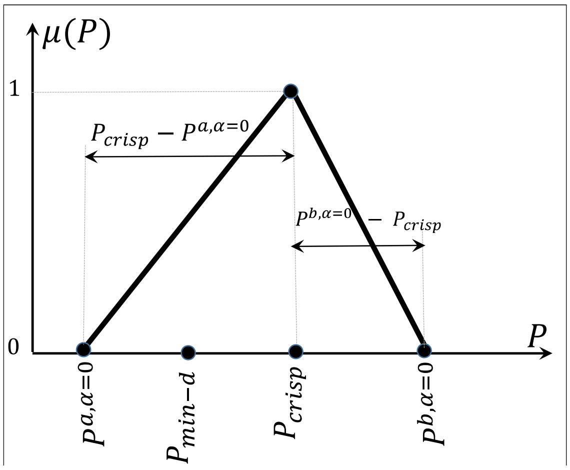

Figure 6. Components for defining fuzzy objective function ASFI.

Since negative value for SFI is not meaningful, we set $SFI = 0$ where $P^{a,\alpha=0} > P_{min-d}$. Because there are N nodal pressures in the system, in order to have a fuzzy index, the general representative of all responses, we define the Average Support-based Fragility Index ($ASFI$) as follows:

$$ASFI = \frac{\sum_{i=1}^{N} \omega_i \, SFI_i}{N} \quad [4]$$

where ω_i is the weight coefficient related to the importance of ith junction in the system. In this study, all junctions have a same order of importance. So, ω_i is 1 for all nodes.

Finally, in addition to the capital cost of the network, $ASFI$ is defined as the second objective function in NSGA-II. Both objectives are going to be minimized.

3.3 Design variables and uncertain input parameters

In the proposed multi-objective method, pipe diameters are taken into account as the design variables chosen from any available commercial list. Also, the roughness of pipes and demand of junctions are considered to be the input uncertainties. The present study assumes that uncertainty is attributed to uncertain input parameters and does not include design variables.

- Example 2

The fuzzy multi-objective design method is applied to a hypothetical two-loop network from the literature (Alprovits and Shamir, 1977). The network consists of eight pipes, six consumption nodes that gravitationally supplied by an elevated tank with 210m in total head. The system layout is depicted in Figure 7 and the nodal details are represented in Table 1. All pipes have 1000m length and 130 Hazen W. roughness. The demands and pipes roughness are exposed to the maximum $\pm 10\,\%$ uncertainty.

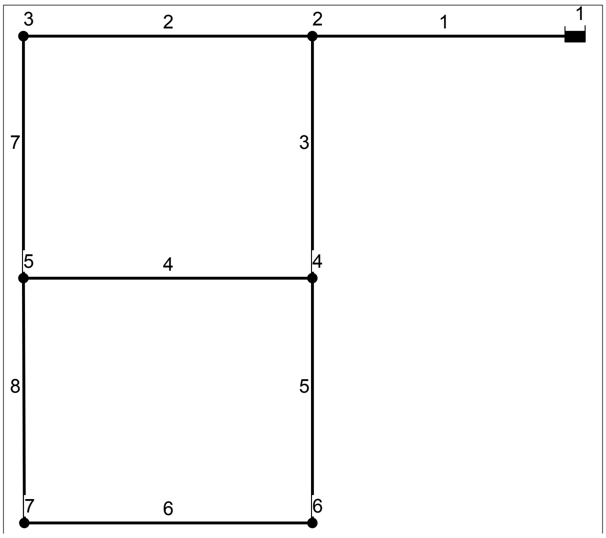

Figure 7. The layout of Example 2 (Alprovits and Shamir, 1977).

The optimal Pareto front for the Cost-ASFI indices and their corresponding maximum SFI and resilience index (Prasad and Park, 2004) are shown in Figure 8. Some optimum scenarios from the previous researches (Savic and Walters, 1997; Abebe and Solomanite, 1998; Samani and Zanganeh, 2010) have taken only the cost into account as the objective function as presented in columns 1 to 6 of Table 2. Some notable non-dominated solutions obtained here are also reported in columns 7 to 10. As seen in Figure 8 and more precisely in Table 2, there is a significant improvement in *ASFI* index for the scenario of column 8 as compared with the design scenario of column 7, *i.e.,* the least-cost scenario. For only 1 k$ change in the cost, the *ASFI*, the mean relative uncertainty of nodal pressures, decreases from 17.3 % to 8.1 %. Except for few small drops, other solutions on the Pareto front have a similar trend in *Cost-ASFI* trade-off. However, alongside *ASFI*, simultaneously considering the maximum *SFI* and *Resilience Index* reveals that the priority of solutions may change if other hydraulic features are taken into account. For example, let's assume that between the solutions 3 and 4, a decision maker would prefer solution 4 since it is slightly more expensive but with less *ASFI* as compared to solution 3. While the *Resilience Index* and the maximum *SFI* indicate that solution 3 is a better scenario with about 4.5% improvement in the probability of failure for the system's critical node.

Another benefit obtained from the fuzzy design, is to improve and diversify the multi-objective search. For example, column 2 in Table 2, presents a better solution than column 8 so that with the same cost a noticeable improvement in the ASFI, *Max. ASFI* and *Resilience Index* has been achieved.

Table 1. Junction details for Example 2.

Node No.	Elevation (m)	Demand (l/s)
3	160	27.8
2	150	27.8
5	150	75
4	155	33.3
7	160	55.6
6	165	91.7

Table 2. Results of scenarios and objectives for Example 2.

Pipe No.	Savic & Walters (1997)		Abebe & Solomanite (1998)			Samani & Zanganeh (2010)	Present Study			
	(1)	**(2)**	**(3)**	**(4)**	**(5)**	**(6)**	**(7)**	**(8)**	**(9)**	**(10)**
1	457.2	508.0	457.2	457.2	457.2	457.2	457.2	457.2	457.2	457.2
2	254.0	254.0	355.6	406.4	254.0	254.0	254.0	355.6	355.6	355.6
3	406.4	406.4	355.6	355.6	406.4	406.4	406.4	355.6	355.6	355.6
4	101.6	25.4	25.4	50.8	101.6	101.6	101.6	25.4	50.8	25.4
5	406.4	355.6	355.6	355.6	406.4	406.4	406.4	355.6	355.6	355.6
6	254.0	254.0	25.4	25.4	254.0	254.0	254.0	152.4	152.4	25.4
7	254.0	254.0	355.6	355.6	254.0	254.0	254.0	355.6	355.6	355.6
8	25.4	25.4	304.8	254.0	50.8	25.4	25.4	254	254	304.8
Cost (k$)	419	420	424	439	422	419	419	420	423	424
ASFI	0.1727	0.1721	0.0738	0.0713	0.1714	0.1727	0.1727	0.0809	0.0808	0.0738
Max. SFI	0.2857	0.3303	0.2940	0.2777	0.2877	0.2857	0.2857	0.2540	0.2517	0.2940
Resilience	0.1534	0.1579	0.2478	0.2822	0.1557	0.1534	0.1534	0.2489	0.2544	0.2478

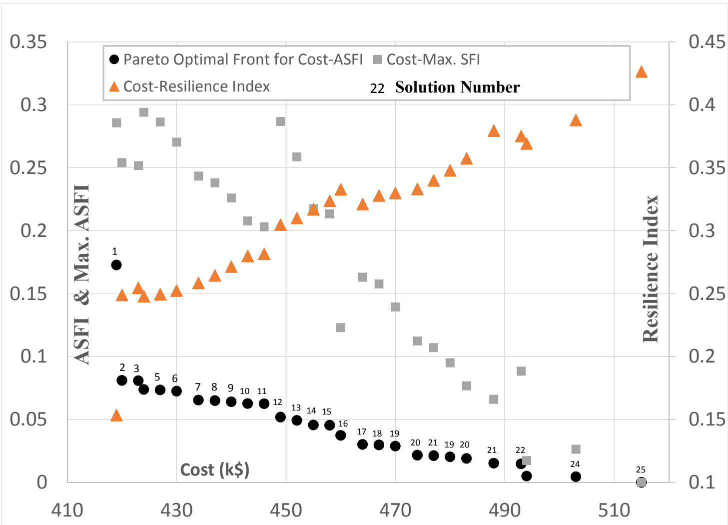

Figure 8. Pareto optimal front for Cost-ASFI and the corresponding maximum SFI and resilience index.

The above details in Example 2 show that the proposed fuzzy multi-objective approach for the design of pipe networks has two advantages over the single objective cost-effective design. First, a general benefit is related to the feature of novel fuzzy index (*ASFI*) which reveals the sensitivity of the design to the input uncertainties. The second is associated with the potential of better diversity of optimization search because of the second objective.

4 SUMMARY AND CONCLUSIONS

In this article, the optimization-based and optimization-free approaches for the fuzzy analysis of pipe networks were discussed. The optimization-based approach has less efficiency in real large networks but more accurate especially in the case of significant uncertainties. In this context, a novel Many-Objective PSO (MOPSO) model to the fuzzy analysis of pipe networks was introduced. In the fuzzy design process, however, by exploiting the MOPSO to analyze scenarios result in a two-nested optimization that makes the design very time-consuming and complicated. To make the computations efficient, some simplified assumptions were adopted to use an optimization-free model for fuzzy analysis of each design alternative. Also, for the fuzzy multi-objective design optimization, a standard version of NSGA-II was applied. In addition to the cost, a new metric named *Averaged Support-based Fragility Index* (*ASFI*) was introduced to the network design as a second objective function. The *ASFI* considers the overall uncertainty in the system responses. During the design process, the NSGA-II attempts to minimize both the *ASFI* and the cost of the network. Comparing the

  / ISSN 1562-6865 (Online) - ISSN 1063-7710 (Print)

results with those of single objective optimization in previous researches revealed that the multi-objective design based on the fuzzy metric (*ASFI*) could effectively give the designer a better insight into the system performance in existence of uncertainties. Generally, as the cost of solutions on the Pareto front decreases, the uncertainty associated with the system's responses increases. For the example pipe network, the least cost design has a cost of 419 k$ and an *ASFI* of 0.1727. While, accepting an increase of only 1 k$ in the network cost could reduce the level of system uncertainty (i.e. the *ASFI*) from 0.1727 to 0.0809, *i.e.,* 53.1% drop in overall uncertainty. Also, it seems that the new metric could improve the diversity of search and capture better solutions with the same costs as compared to the single objective optimization approaches. For instance, a solution with the cost 420 k$ has an ASFI of 0.1721 in the single objective design, but 0.0809 in the introduced fuzzy multi-objective design.

REFERENCES

Abebe, A.J. & Solomanite, D.P. (1998). Application of Global Optimization to the Design of Pipe Networks. *Proceeding of the 3rd International Conference on Hydroinformatics*, Copenhagen, Denmark, 989-996.

Alperovits, E. & Shamir, U. (1977). Design of Optimal Water Distribution Systems. *Water Resour. Res.*, 13(6), 885–900.

Branisavljevic, N. & Ivetic, M. (2006). Fuzzy Approach in the Uncertainty Analysis of the Water Distribution Network of Becej. *Civ. Eng. Environ. Syst.*, 23(3), 221–236.

Deb, K., Pratap, A., Agarwal, S. & Meyarivan, T. (2002). A Fast and Elitist Multi-Objective Genetic Algorithm: NSGA-II. *IEEE Trans. Evolut. Comput.,* 6(2), 182–197.

Gupta, R. & Bhave, P.R. (2007). Fuzzy Parameters in Pipe Network Analysis. *Civ. Eng. Environ. Syst.*, 24(1), 33–54.

Haghighi, A. & Asl, A.Z. (2014). Uncertainty Analysis of Water Supply Networks Using the Fuzzy Set Theory and NSGA-II. *Eng. Appl. Artif. Intell.,* 32, 270–282.

Haghighi, A. & Keramat, A. (2012). A Fuzzy Approach for Considering Uncertainty in Transient Analysis of Pipe Networks. *J. Hydroinf.*, 14(4), 1024–1035.

Prasad, T.D. & Park, N.S. (2004). Multiobjective Genetic Algorithms for Design of Water Distribution Networks. *J. Water Resour. Plann. Manage.*, 130(1), 73–82.

Revelli, R. & Ridolfi, L. (2002). Fuzzy Approach for Analysis of Pipe Networks. *J. Hydraul. Eng.*, 128(1), 93–101.

Sabzkouhi, A.M. & Haghighi, A. (2016). Uncertainty Analysis of Pipe-Network Hydraulics Using a Many-Objective Particle Swarm Optimization. *Journal of Hydr. Eng.*, 142(9).

Savic, D.A. & Walters, G.A. (1997). Genetic Algorithms for Least Cost Design of Water Distribution Networks. *J. Water Resour. Plan. Manage.,* 123(2), 67–77

Samani, H.M.V. & Zangeneh, A. (2010). Optimization of Water Networks Using Linear Programming. *J Water Manage, Proceedings of the Institution of Civil Engineers*, 163(9), 475–485.

Sivakumar, P., Prasad, R.K. & Chandramouli, S. (2016). Uncertainty Analysis of Looped Water Distribution Networks Using Linked EPANET-GA Method. *Journal of Water Resources Management*, 30(1), 331-358.

Spiliotis, M. & Tsakiris, G. (2012). Water Distribution Network Analysis under Fuzzy Demands. *Civ. Eng. Environ. Syst.*, 29(2), 107–122.

Proceedings of the 37th IAHR World Congress
August 13 – 18, 2017, Kuala Lumpur, Malaysia

DEVELOPMENT OF KU-STIV: SOFTWARE TO MEASURE SURFACE VELOCITY DISTRIBUTION AND DISCHARGE FROM RIVER SURFACE IMAGES

ICHIRO FUJITA(1), TAKASHI DEGUCHI(2), KIYONORI DOI(3), DAISUKE OGINO(4), YUICHI NOTOYA(5) & SAAYA TATEGUCHI(6)

(1,5,6) Graduate School of Engineering, Kobe University, Kobe, Japan,
ifujita@kobe-u.ac.jp
(2) NEWJEC Inc., Osaka, Japan,
deguchitk@newjec.co.jp
(3) Be System Co., Ltd., Sapporo, Japan,
k.doi@be-system.co.jp
(4) Concerto system Co., Ltd., Osaka, Japan,
ogino@concertosystem.co.jp

ABSTRACT

Measurement and collection of river discharge during a flood are of vital importance for a proper management of a river basin especially in huge floods when conventional flow measurement methods, such as a float method or a point by point measurement with a probe type instrument, are difficult to apply. Unfortunately, such a situation occurred several times in Japan in recent years due to the increase of high water level floods. In order not to miss such flow measurements, the use of imaging techniques has been paid attention in the past decade, *i.e.,* the use of video images recorded by a river monitoring camera installed at several locations along a river. It is because such a video recording system is hard to be destroyed even when overtopping flows takes place. Among the imaging techniques, the space-time image velocimetry (STIV) is considered as one of the most robust techniques for discharge measurements possible to apply even when the video images were deteriorated by several causes. In order to distribute the idea of using STIV technique more efficiently, software KU-STIV was developed in this research. With KU-STIV and some additional hardware installation, a real-time measurement becomes possible. The system to use a far-infrared camera in combination with an image sharpening device was introduced for establishing an all-time and real-time system including measurements during the night.

Keywords: Surface flow measurement; image-based technique; STIV; real-time discharge measurement.

1 INTRODUCTION

In establishing a flood risk management strategy, the information of river discharge as well as the rainfall intensity distribution is crucial for providing reliable prediction data. Regarding the rainfall data in Japan, high resolution rainfall information has come to be available by using a sophisticated radar technology such as the X-band MP radar, which covers the river basin with a spatial resolution of 250 meters. In fact, most of the Japanese islands are covered by twenty-six X-band radars. However, with respect to the river discharge information, the measurements are conducted at most at one or two locations along a river even in the first-class rivers, but what is worse is that the available discharge data for the smaller second-class rivers are quite rare. Considering the fact that inundation disasters tend to occur more frequently in small-scale urban rivers, flow monitoring is important to understand the runoff process, especially in smaller rivers in addition to the monitoring of larger rivers.

In order to satisfy such a requirement, the use of river monitoring cameras installed along a river is recommended and for that purpose the software capable of executing real-time flow measurements, KU-STIV, was developed. For example, the local government Hyogo Prefecture in Japan installed more than one hundred cameras within a number of river basins, but at present, those cameras are used only to provide images of river flow conditions on the web and not used for extracting quantitative information, such as flow velocity or discharge. If it would become possible to use such cameras for real-time flow measurements, the spatial density of available flow information would increase significantly and the data can be used for a more reliable flood risk management. However, the existing river monitoring systems are difficult to use for the video images during the night. In this paper, after several functions of KU-STIV are introduced, the recommended system to use a far-infrared camera in combination with an image sharpening device is introduced for establishing an all-time and real-time measurement system.

2 OUTLINE OF MEASUREMENT BY KU-STIV

The space-time image velocimetry (STIV) technique is a surface flow measurement technique developed by Fujita et al. (2007), which utilizes video images of a river surface flow mainly paying attention to streamwise

  / ISSN 1562-6865 (Online) - ISSN 1063-7710 (Print)

velocity distributions for obtaining discharge data. This feature is conceptually different from the large-scale particle image velocimetry (LSPIV) technique developed by Fujita et al. (1998), which can provide two-dimensional velocity vector distributions from obliquely viewed river surface images as in the case of LSPIV (Le Coz et al., 2010; Hauet et al., 2008; Muste et al., 2014). The process of STIV comprises five steps: (1) import video file; (2) camera calibration; (3) generation of space-time image (STI); (4) STIV analysis; and (5) discharge measurement.

2.1 Import of video files

In this step, river surface images usually taken from an obliquely viewed angle are imported to the software. The advantage of the KU-STIV is that it can import movie files as well as sequential static images with a specified time interval. The acceptable types of movie files are AVI, MP4, M2TS, MTS, and PVF and static files are JPEG, BMP, and PNG. A longer movie files can be manipulated to generate a shorter clip file. The advection feature of surface flows can be visually recognized either on the original screen or on the ortho-rectified screen to be explained later.

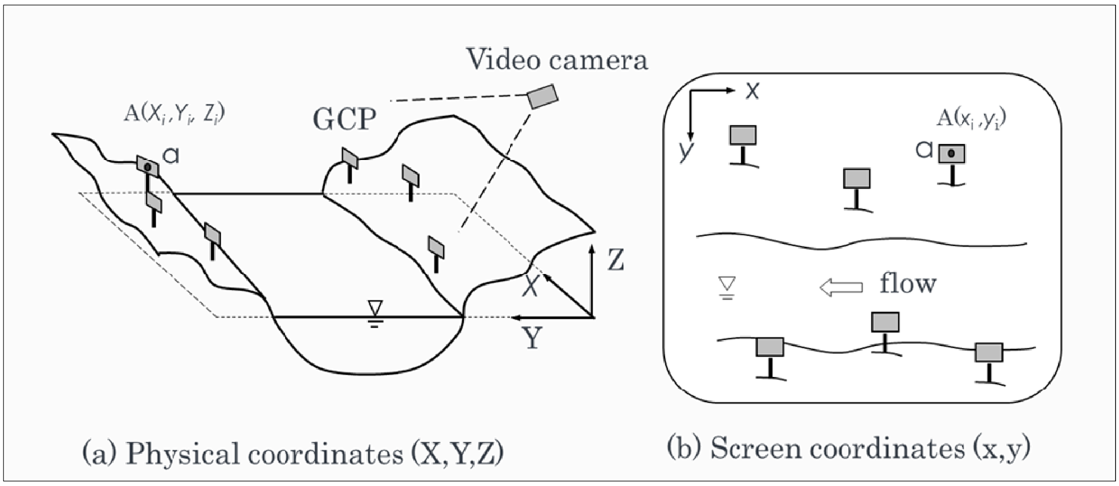

Figure 1. The arrangement of ground control points (GCP) in physical and screen coordinates.

2.2 Camera calibration

In this step, the mapping relation between two-dimensional screen coordinates (x,y) and three-dimensional physical coordinates (X,Y,Z) is established using the coordinate data of ground control points (GCPs), as shown in Figure 1. In KU-STIV, direct linear transformation (DLT) equations:

$$x = \frac{A_1X + A_2Y + A_3Z + A_4}{C_1X + C_2Y + C_3Z + 1} \quad [1]$$

$$y = \frac{B_1X + B_2Y + B_3Z + B_4}{C_1X + C_2Y + C_3Z + 1} \quad [2]$$

are used as a first guess of the mapping relationship. A_1 ~ C_3 are the coefficients to be determined by a least square method using GCP coordinates. Then, the following collinearity equations:

$$x - x_o = -f\left[\frac{a_{11}(X - X_0) + a_{12}(Y - Y_0) + a_{13}(Z - Z_0)}{a_{31}(X - X_0) + a_{32}(Y - Y_0) + a_{33}(Z - Z_0)}\right] \quad [3]$$

$$y - y_o = -f\left[\frac{a_{21}(X - X_0) + a_{22}(Y - Y_0) + a_{23}(Z - Z_0)}{a_{31}(X - X_0) + a_{32}(Y - Y_0) + a_{33}(Z - Z_0)}\right] \quad [4]$$

are used to finally determine the mapping relationship with some trial and error procedure. (X_0, Y_0, Z_0) is the physical coordinate of a camera lens, (x_0, y_0) is the principal point coordinates in the screen coordinates, f is the focal length, and a_{ij} are coefficients related to camera angles. In order to generate an ortho-rectified image, a water level data is required, which can be given manually or transmitted via a web network at a specific time interval in the real-time system.

In the first place, the accuracy of the image transformation can be visually confirmed, as shown in Figure 2. The confirmation is executed by drawing a line segment from each GCP to the assumed water surface level using the calibrated data of image transformation. If the camera calibration is successfully executed, the green lines will be drawn vertically towards the water level point from each panel center, as indicated in Figure 2a and at the same time a transformed ortho-rectified image will be displayed, as shown in the Figure 2b. If the camera calibration fails, the green lines will start from different points other than GCPs and the lines will be drawn obliquely. In that case, the camera calibration process has to be repeated until it reaches a stable converged state by changing the initial guess value of camera parameters. The size of the transformed image can be controlled by specifying the pixel size and its display area can be determined by setting the vertical and horizontal coordinate ranges, as indicated in Figure 2b. Quantitative evaluation of image transformation can be performed by comparing the measured GCP coordinates with those calculated by using the inverse relation of Eq. [1] and Eq. [2]. As an example, the calculated length errors in both directions (dX, dY) are shown in Figure 3, indicating that errors at farther points from the camera on the right bank are larger than the left bank data. This is because the spatial image resolution is much lower at far points, but considering the river width is about 150m, the error of less than one meter seems to be negligible and the generated transformed image shown in Figure 2b can be used in STIV analysis.

(a) Original image (b) Transformed ortho-rectified image

Figure 2. Confirmation process of image transformation; vertical green line segment connects GCP to the assumed plane of water surface.

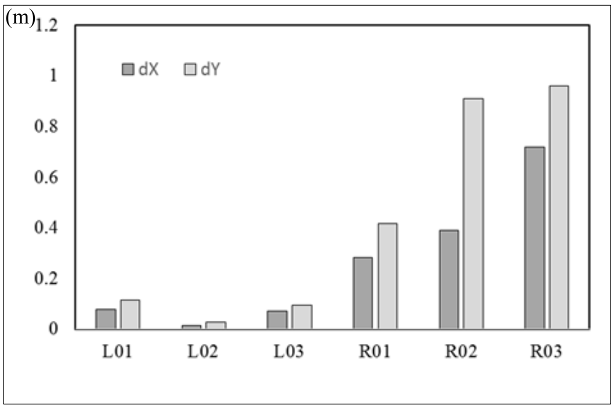

Figure 3. Evaluation of image transformation.

2.3 Generation of space-time image (STI)

In this step, search lines for the STIV analysis are first set in the direction of main flow, as shown in Figure 4. For the purpose of discharge measurement, the search lines with the same spacing are first drawn in the ortho-rectified image and corresponding lines are displayed in the original image. In Figure 4, fifteen search lines with a length of 11.3m and a spacing of 8.6m are prepared, which covers a spanwise width of 120.4m. Space-time images are then generated by stacking the image intensity distribution along a search line in the downward direction. It should be noted that since the original image is generally distorted, simple stacking of search line would produce erroneous STI because the length scale varies continuously along a search line. In order to generate an STI with a constant scale along a search line direction, the pixel length of

  ISSN 1562-6865 (Online) - ISSN 1063-7710 (Print)

a search line in the original image is first obtained as L_s pixels. Then, start and end coordinates of a search line, $S_S(x_s,y_s)$ and $S_E(x_e,y_e)$ shown in Figure 5, are converted into physical coordinates, $P_S(X_s,Y_s)$ and $P_E(X_e,Y_e)$. The distance between P_S and P_E is the physical length of the search line L_p. Next, L_p is divided by L_s to obtain the unit pixel length (D_L) along the search line and the physical coordinates along the search line with a unit length of D_L are converted into screen coordinates $S_P(x_p,y_p)$. Since the calculated pixel location of S_P does not always an integer value, the image intensity at S_P is obtained by a two-dimensional interpolation of pixel intensities close to S_P. These steps are repeated until the interpolated point reaches the end of the search line, thereby image intensity distribution along a search line with no distortion is obtained. This process is repeated until the end of the frame to generate an STI. In STIV analysis, since a conventional measurement time is about ten to twenty seconds, the vertical image size becomes 300 to 600 pixels if an NTSC video standard is used. The horizontal image size depends on the resolution of the original image but a size comparable to a vertical size is preferred for the analysis.

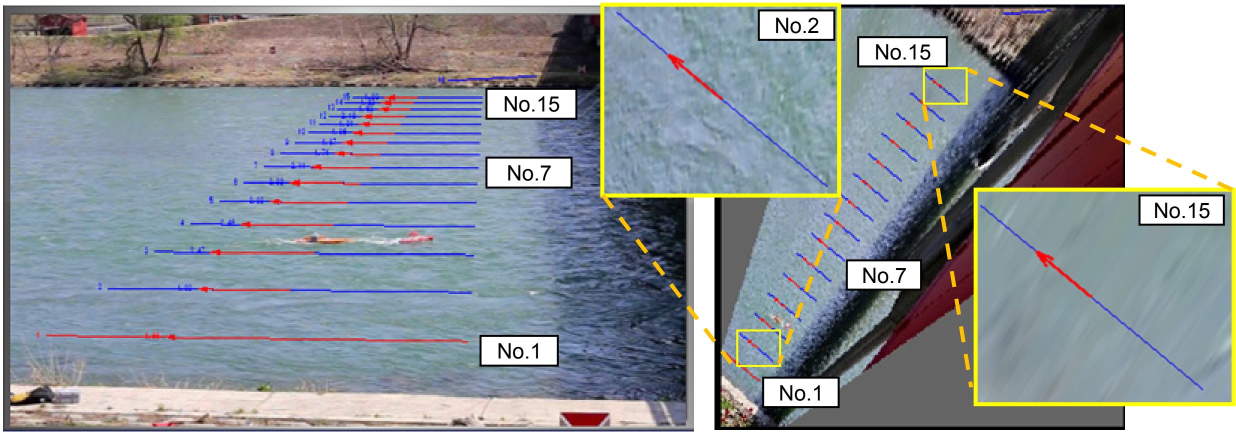

(a) Original image (b) Transformed ortho-rectified image

Figure 4. Setting of search lines before and after image transformation.

As an example, three STIs generated from the original video image presented in Figure 4 are shown in Figure 5. Since the measurement time was fifteen seconds, the vertical size is 450 pixels and with an increasing distance from the camera location, the apparent horizontal length decreases from 799 pixels to 246 pixels although the actual physical length is the same as 11.3m. To compare the image features appeared in each STI, the original STIs as well as horizontally stretched STIs are demonstrated in Figure 5. It is obvious that oblique patterns appear in each STI indicating the advection feature of irregular surface pattern. It should be noted that even the farthest STI, measured at more than 120m from the camera, includes a pattern indicating the surface flow. If LSPIV is used in this condition, it would be quite difficult to obtain reliable data because the quality of a rectified image deteriorates as the distance from the camera increases. As an example, local surface area around the search line No.15 is shown in Figure 4b, indicating that the surface feature is significantly blurred and LSPIV would yield erroneous data. Conversely, the local pattern around No.2 shown in Figure 4b includes detailed surface features capable to use in LSPIV. Another advantage of STIV over LSPIV is that the sequential ortho-rectified images are not required as in LSPIV, which needs a large amount of recording space. On the other hand, STIV records only the STIs for the search lines, which requires a little data storing space.

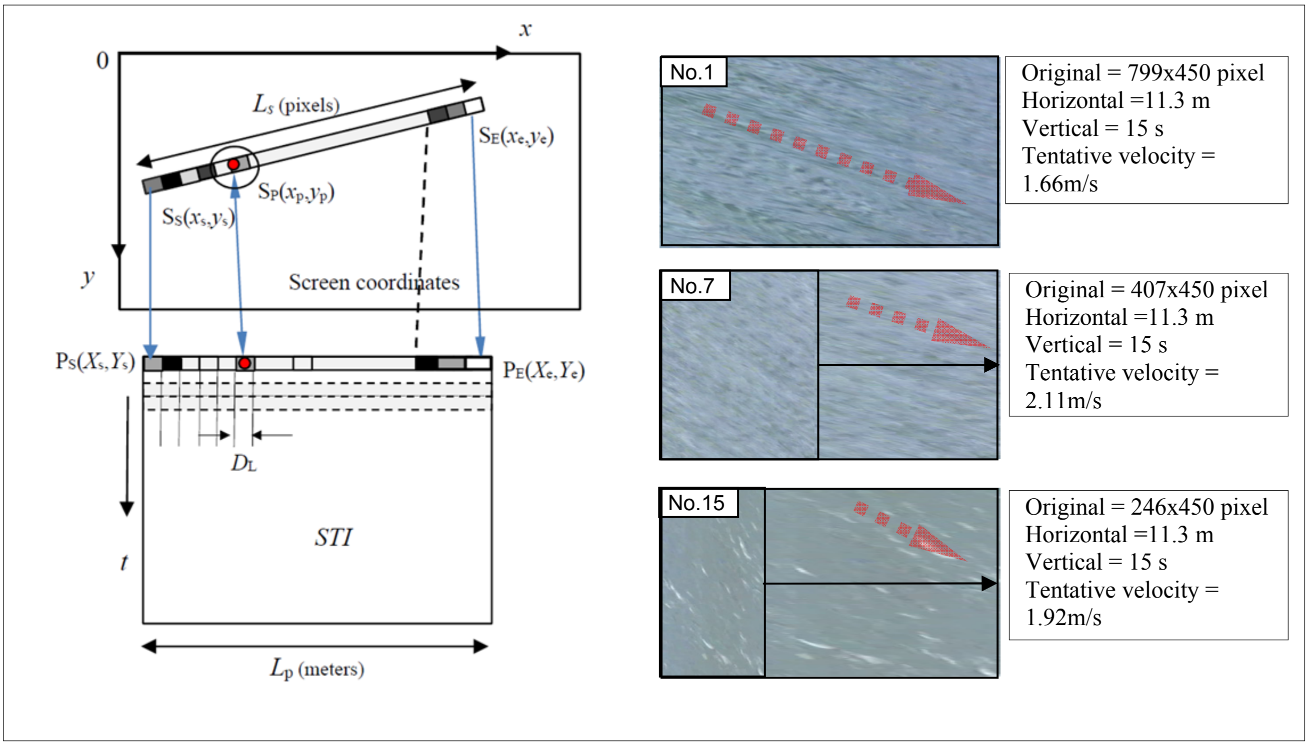

Figure 5. Generation of STI and examples.

2.4 STIV analysis

It is obvious from Figure 5 that an STI contains enough information about the velocity flowing along a search line by displaying almost uniform oblique pattern. The significant point is how to extract the average pattern gradient accurately and efficiently from an STI. In KU-STIV, a gradient tensor method (GTM) (Fujita et al., 2007) is used as a default method. In GTM, the pattern gradient can be calculated by:

$$\tan\phi = \frac{2J_{xt}}{J_{tt} - J_{xx}} \quad [5]$$

where:

$$J_{pq} = \int_A \frac{\partial g}{\partial x_p}\frac{\partial g}{\partial x_q} dxdt, \quad [6]$$

$g(x,t)$ is image intensity distribution of STI and A is a small window area to calculate a local gradient within it. The velocity obtained by STIV is a time and line average velocity calculated by the following equations:

$$U = \frac{S_x}{S_t}\tan\bar{\phi} \quad [7]$$

where:

$$\bar{\phi} = \frac{\int \phi C d\phi}{\int C d\phi}, \quad [8]$$

and:

$$C = \frac{\sqrt{(J_{tt} - J_{xx})^2 + 4J_{xt}^{\ 2}}}{J_{xx} + J_{tt}} \quad [9]$$

S_x and S_t are the length scales in horizontal and vertical directions, respectively, and C is an image coherency, which takes zero for white noise and one for clear pattern (Jähne, 2005). In the gradient tensor method, local gradients calculated for a number of windows are averaged by taking coherency as a weigh parameter. In the default condition, a square with 30 by 30 pixels is shifted at a spacing of 10 pixels in each direction to cover the entire STI and the calculated mean gradient by Eq. [8] is displayed in a form of parallel lines, as indicated in Figure 6a to visually check the accuracy. It can be noted that darker coherency area corresponds to clear pattern in STI. Figure 6 shows the calculated gradient agrees fairly well with the feature pattern.

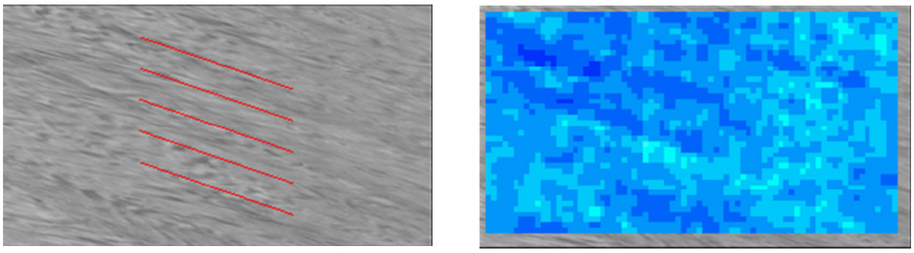

(a) calculated pattern gradient (b) coherency distribution

Figure 6. STIV result by KU-STIV for search line No.1; (a) calculated pattern gradient, (b) coherency distribution, darker color is for larger coherency.

On the other hand, when the feature pattern is not clearly visible as in the case of the search line No.15 shown in Figure 5, the calculated gradient occasionally yields obviously an erroneous result, as indicated in Figure 7a. In such a case, the original image can be processed by a histogram equalization filter to enhance the feature included in the original image, as provided in Figure 7b. In KU-STIV, the pattern gradient can be measured manually by drawing appropriate oblique lines in the processed image, as shown in Figure 7b, in which seven lines are tentatively drawn. The averaged velocity in this case is 1.14 m/s, which is smaller than the default value of 1.92 m/s. The newly obtained value is more reliable considering the agreement with the pattern slope. Figure 8 is the surface velocity distribution thus obtained by KU-STIV.

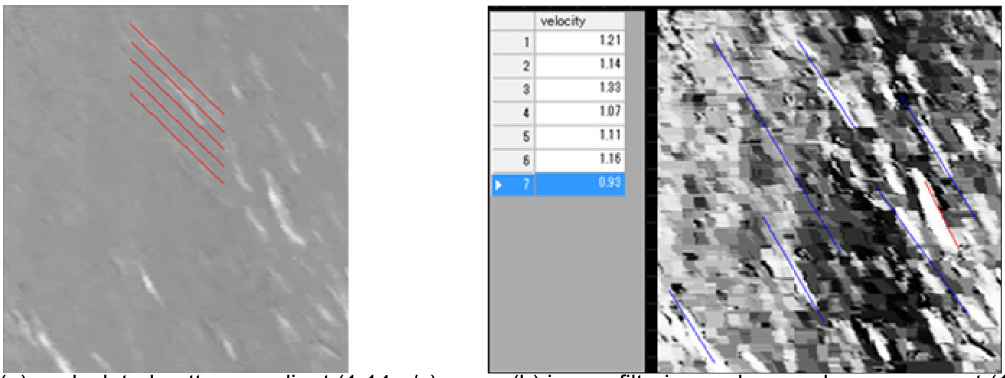

(a) calculated pattern gradient (1.14m/s) (b) image filtering and manual measurement (1.92m/s)

Figure 7. STIV result by KU-STIV for search line No.15; (a) calculated pattern gradient, (b) manual measurement using image after histogram equalization; horizontal length is 11.3m and vertical scale is 15 seconds.

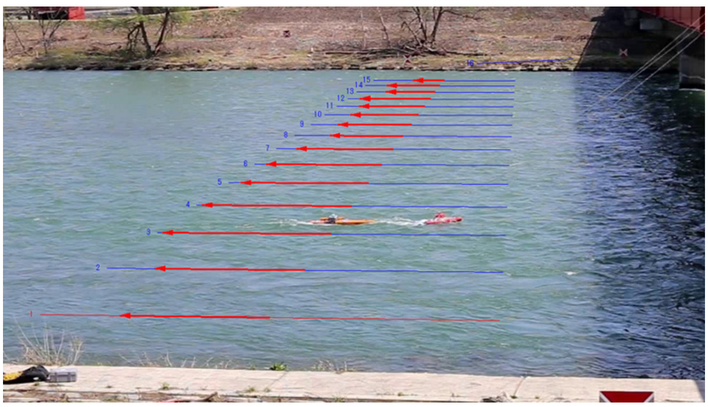

Figure 8. Calculated surface velocity distribution by KU-STIV.

2.5 Discharge measurement

The discharge flowing at the cross-section of search lines is obtained by summing up the piecewise discharge for a search line by estimating a local depth-averaged velocity (U_m) from the surface velocity (U_s). A conventional coefficient converting U_m from U_s is 0.85, which would become smaller for a rougher bottom condition. The more reliable coefficient value can be obtained by comparing it with a more detailed measurement by an ADCP if available. In the previous example, the bathymetry data is given, as shown in Figure 9 with the water level of 78.7m at the time of measurement. The discharge thus obtained by using a conventional velocity coefficient was 352.1m^3/s.

To show the measurement accuracy of STIV, another measurement example of a small flood at the Ishikari River in Hokkaido Japan is provided in Figure 10. The discharge measurement results by STIV with the converting coefficient of 0.85 are compared with those measured by an ADCP tagged along the Ishikari-gawa Bridge. The results by STIV by using a normal high-definition video camera and a far-infrared camera show excellent agreements with ADCP data within the relative accuracy of 5%.

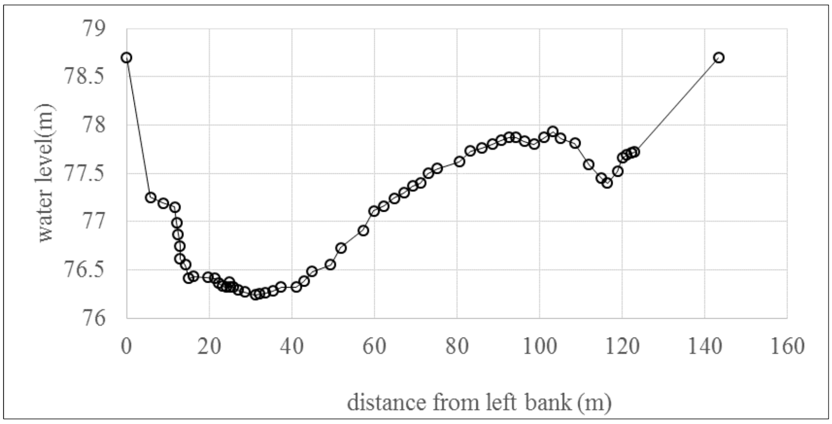

Figure 9. The bathymetry at a cross-section; the water level was 78.7m at the time of measurement.

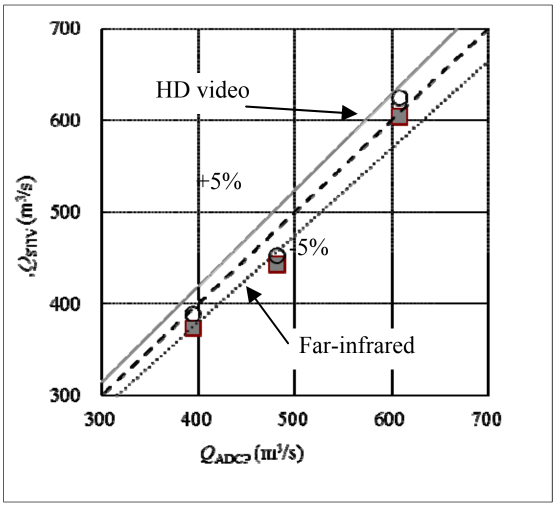

Figure 10. Comparison of discharge measurements at the Ishikari River.

3 SYSTEM FOR SEQUENTIAL MEASUREMENT AND REAL-TIME MEASUREMENT

3.1 Sequential measurement

Once the camera parameters were determined, measurements at other timing can be conducted by simply replacing the water level data. In order to analyze a sequential video images previously obtained, it is required that an input csv file listing a movie file name, water level, and measurement time line by line is prepared in the same folder where the video files are stored, as depicted in Figure 11. After KU-STIV reads the csv file, the program starts automatically by reading the file name and the water level from the csv file. Once the first video file is analyzed, the next video file is analyzed and so on until the end of the csv file. The analyzed data for one video file is saved into a newly generated folder with the same name as the video file.

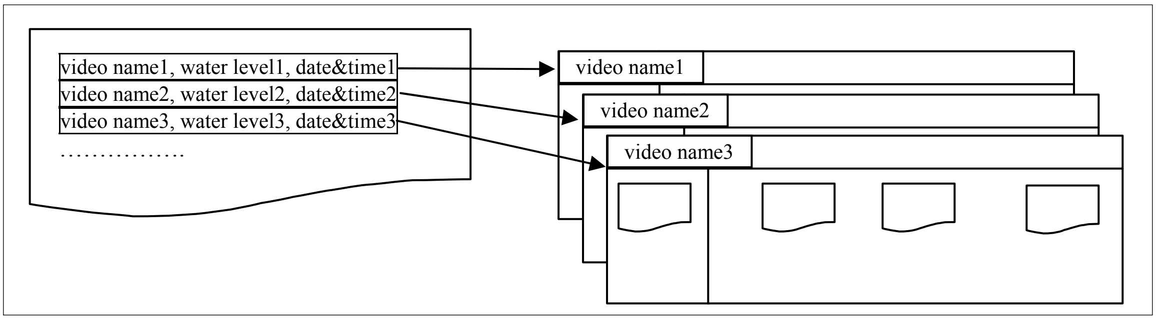

Figure 11. Sequential analysis for previously obtained video data.

3.2 Real time measurement

For establishing a real-time measurement, a set of hardware equipment has to be installed at the measurement site, as illustrated in Figure 12. Basically, the video data are recorded on a digital video recorder (DVR), capable to record all the image data consecutively for more than a month with 2 TB of data storing capacity, installed at the local site. KU-STIV and an image data management (IDM) software are installed on a micro server locally set at the site. The IDM controls the image sampling timing from the DVR while also controlling the KU-STIV. For example, the IDM can extract a ten seconds of video image at a time interval of ten minutes and the video files thus extracted are stored in a newly created folder with the name indicating the sampling time of day. IDM software can detect the creation of a new folder and activate KU-STIV to execute STIV analysis. Once the analysis has completed, while generating analyzed data, as shown in Figure 11, the IDM shuts down the KU-STIV software waiting for the next timing of STIV analysis. This process is repeated continuously until the administrator quits the software. The KU-STIV can be controlled remotely via an internet using the virtual private network (VPN) protocol. The water level information can be obtained either by a locally installed water level gauge or from the official web site containing water level data. The important feature of the system is that video image data are stored locally at the measurement site in order to avoid sending large amounts of image data via an internet, which sometimes overloads the signal traffic.

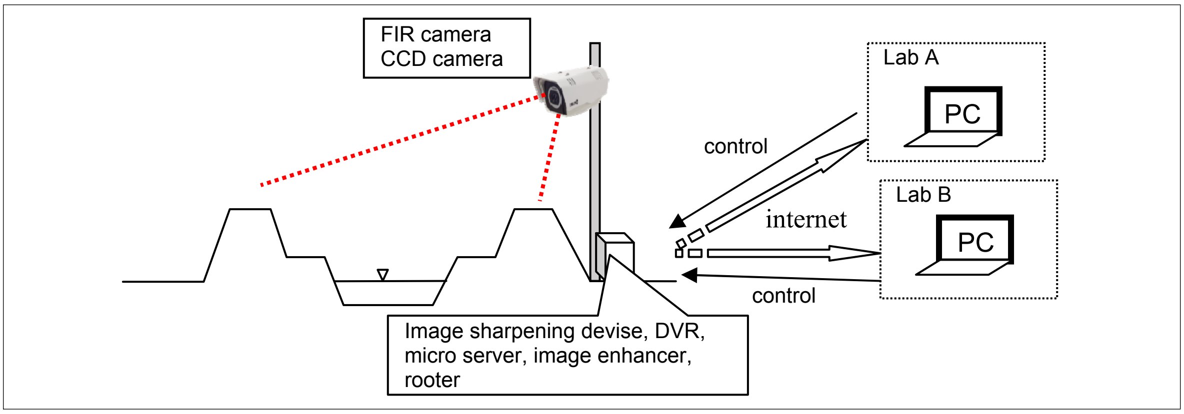

Figure 12. General system of real-time measurement.

4 EFFICIENT MEASUREMENT DURING THE NIGHT

In order to establish a real-time and all-time measurements, a high-performance camera capable to capture images even during the night or under a worse weather condition is indispensable. One of the imaging devise satisfying this requirement is a far-infrared (FIR) camera, which receives far-infrared light with the wave length of 6 to 15 μm much longer than that of visual light. With a far-infrared camera, it becomes possible to obtain bright images even during the night, as shown in Figure 13. However, the image quality sometimes deteriorates under some heat environment or weather conditions, making it difficult to detect surface advection features even on an STI. For solving such problems, KU-STIV system recommends to use an image sharpening device (ISD). An example demonstrating the effect of ISD is also shown in Figure 13. It is obvious that water surface features become much clearer by using ISD. It is also possible to use a high sensitivity camera instead of a FIR camera, but as long as visible lights are used by enhancing them, it would become difficult to detect detailed surface features under very little light. Moreover, rain drops may hinder the sight in rainy condition, which is not affected significantly in the image by FIR camera.

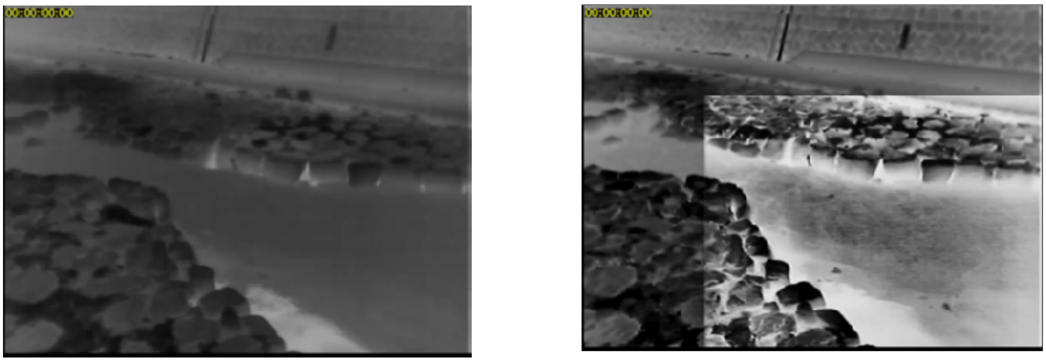

(a)No.1 iNo.7 aNo.15 eNo.2 No.15 (b) with image sharpening device

Figure 13. Effects of far infrared camera and image sharpening device at the Toga No.1 No.7 bNo.15e.

5 CONCLUSIONS

The paper describes the performance of the software KU-STIV for measuring river surface velocity distributions and discharge efficiently by using an image-based technique STIV and sophisticated imaging devises. The performance of STIV has been evaluated in the practical application of flood measurements in Japan for a number of major rivers, although not shown in this paper. The advantage of imaging techniques is that it can measure the flow safely even in a peak flow condition, in which other methods such as a float method becomes impossible to carry out. Since the proposed real-time system introduced in this research has just been installed in several rivers in Japan, it would yield a discharge hydrograph when the next flood occurs. For constructing a stable real-time measurement system, a proper numerical evaluation of the quality of STI is needed.

ACKNOWLEDGEMENTS

We are grateful to the support from Mr. Masuda from the FLIR Systems Japan who provided us the detailed information of far-infrared cameras and helped us decide a specific camera model. The study was supported by a research grant from the Foundation of River and Basin Integrated Communications Foundation (FRICS) and Grants-in-aid for Scientific Research in collaboration with International Centre for Water Hazard and Risk Management (ICHARM). The data other than imaging data were provided through ICHARM. I am grateful to their support of the present research.

REFERENCES

Fujita, I., Watanabe, H. & Tsubaki, R. (2007). Development of a Non-Intrusive and efficient Flow Monitoring Technique: The Space Time Image Velocimetry (STIV). *International Journal of River Basin Management*, 5(2), 105-114.

Fujita, I., Muste, M. & Kruger, A. (1998). Large-Scale Particle Image Velocimetry for Flow Analysis in Hydraulic Engineering Applications. *Journal of Hydraulic Research*, 36(3), 397-414.

Hauet, A., Creutin, J.D. & Belleudy, P. (2008). Sensitivity Study of Large-Scale Particle Image Velocimetry Measurement of River Discharge Using Numerical Simulations. J*ournal of Hydrology,* 349(1),178–90.

Jähne, B. (2005). *Digital Image Processing*. Springer.

Le Coz, J, Hauet, A., Pierrefeu, G., Dramais, G. & Camenen, B. (2010). Performance of Image-Based Velocimetry (LSPIV) Applied to Flash-Flood Discharge Measurements in Mediterranean Rivers. *Journal of Hydrology,* 394(1), 42-52.

Muste, M., Hauet, A., Fujita, I., Legout, C. & Ho, H.C. (2014). Capabilities of Large-Scale Particle Image Velocimetry to Characterize Shallow Free-Surface Flows. *Advances in Water Resources*, 70, 160-171.

NUMERICAL STUDY OF THE HYDRAULIC BEHAVIOR IN A TUNNEL

CECIA MILLAN-BARRERA[(1)], GILBERTO SALGADO-MALDONADO [(2)] & VÍCTOR ARROYO-CORREA[(3)]

[(1,2,3)] Mexican Institute of Water Technology (IMTA), Jiutepec, Morelos, México,
cmillan@tlaloc.imta.mx; gsalgado@tlaloc.imta.mx; vmarroyo@tlaloc.imta.mx

ABSTRACT

This work deals with the hydraulic performance of a long tunnel called "Tecorito", which is part of an irrigation main channel known as Canal Principal Humaya. It is located in the state of Sinaloa, Mexico and has a circular section of 6.5 m in diameter and a length of around 1200 m. Due to the irrigation needs in agricultural areas, it is required that the system channel-tunnel leads 120 m^3/s, however, its functioning becomes problematic when it is driving higher water volumes to 90 m^3/s. One of the difficulties to drive this flow rate is the water level that remains downstream, provoked by the operation of some hydraulic structures located forward of the tunnel. The current geometry of the system has some asymmetries, both, the entrance and exit of the tunnel are sloping, the first one has an abrupt contraction of section and the exit has an abrupt expansion with an adverse slope in the bottom. The data given for this study in conjunction with data obtained in a physical model, will form the basis to find the answers to issues such as: improve the geometry of the entrance and the exit, the flow depth in the channel under which flows at 120 m^3/s, taking into account that at downstream, there is a water strut that obstruct the free flowing in the canal. Two designs of entry and exit were proposed, based on the trajectories of the streamlines obtained running the original case. A significant improvement in the hydraulic behavior of the system is observed after running these geometries. Regarding the capabilities of CFD software to predict the hydraulic depths downstream, was good considering that the measurement site had not the hydraulic conditions to carry out an appropriated measurement, however, such place is one of the point of interest to know the hydraulic performance of the hydraulic structure in study.

Keywords: Numerical forecasting; free surface; hydraulic design; numerical data; experimental data.

1 INTRODUCTION

The distribution net of which the Main Channel Humaya is part in Irrigation District No. 10, is formed by a series of principal, lateral, sublateral, and branch channels which are made of soil and/or concrete. On the one hand, due to its great length and its composition, high losses of water by infiltration is produced, affecting the volume of water available for crops, which makes it difficult to apply the irrigation service and reduces the flexibility of irrigation by extending irrigation intervals; (Castillo, J., 2011) on the other hand, this channel has a large number of hydraulic structures such as floodgates and siphons, rapids, etc. which together with its deterioration caused by important floods and lack of maintenance which is observed among other things in the lifting of slabs in some lengths of the channel and a large amount of sediment and weeds, lead to a reduction of hydraulic area and the loss of effective driving capacity of the canal.

The flow in channels has the characteristic of having a free surface and presents a series of forces such as gravity, friction, static and dynamic pressure, surface tension and turbulent effects among the most important, which make this type of flow very complex. This condition is aggravated when dealing with channels of composite sections, with different slopes, or when there are hydraulic or control structures, such is the case of this revision by numerical modeling.

In some events, like extreme rainfall, the flow regime in sewer systems may change from free surface to pressurized flow or vice versa, in such cases, flows in pipes are categorized as mixed flows. There are various types of flow conditions in transitional regimes, one of these is flow depressurization that produces a shock surface (Bashiri-Atrabi et al., 2016). Although this was observed during the experiments to calibration of numerical model, the present study does not focus on monitoring the air cavity as in the works of (Bashiri-Atrabi et al., 2015; Bashiri-Atrabi et al., 2016), but rather on the identification of turbulent structures that affect the discharge capacity of the tunnel.

This work deals with the study of the hydraulic operation of the Tecorito tunnel, which is of circular section and is located between the stations 07 + 924 - 09 + 124 of the system known as Humaya main channel. It has a length of approximately 1200 m, and was designed to conduct a flow rate of 100 m^3/s, however, its operation is problematic when it is driven greater than 90 m^3/s. The channel joins to the tunnel abruptly from a trapezoidal section to a circular one without a transition; it also has a (descending) step at the entrance to the tunnel; in the same way at the end of the tunnel, it is abruptly joined to the trapezoidal channel and there is also a step, in this case ascending.

The objective of this work is to locate the flow structures that are formed by channel-tunnel-channel interconnections and the presence of abrupt slopes at bottom (descending and ascending) to present geometric alternatives that improve the hydraulic operation of the system (channel-tunnel-channel) and even, that allow to increase its capacity of conduction to 120 m^3/s.

2 METHODOLOGY

The first step was to calibrate the numerical model. The CFD FLOW-3D™ software was used to simulate the hydraulic behavior in the tunnel. To carry out the simulation, information collected in field (flow rate - flow depths) and data from other 1D- hydraulic software were used. The measurements were taken at around 13 m from the entrance and 13 m from the end of the tunnel, and they are shown in the following table:

Table 1. Field data measurements* and the HEC-RAS Software **

Q, m^3/s	h ups, m	h dws, m
34.536 *	3.719	4.16
79 *	4.095	5.061
85 *	4.668	5.197
90 **	5.041	5.411
91.5 **	5.171	5.475
92.5 **	5.245	5.504

With these data, the above software was fed in order to calibrate it. Several simulations with different roughness of channel-tunnel surfaces (n = 0.017, n = 0.018 and n = 0.020) were carried out. The results closest to the field data was obtained with n = 0.017. The results and the error evaluation related to the field measurement data, are shown in Table 2. The error obtained is less than 3%, so we can consider that the model and the input parameter to the software are suitable.

Table 2. Hydraulic depths obtained with CFD software FLOW-3D ™ and its error in percent

Q, m^3/s	h ups num, m	h dws num, m	Error %, ups	Error %, dws
34.536	3.6262	4.1376	2.4952	0.5385
79	4.0533	5.037824	1.0183	0.4579
85	4.62411	5.1579	0.9402	0.7523
90	5.0527	5.3988	-0.2321	0.2254
91.5	5.1424	5.4753	0.5527	-0.00673
92.5	5.2127	5.3945	0.6158	1.9894

The simulation results show that when circulating volume flow around 90 m^3/s, the tunnel works intermittently: free surface - pressure. On the other hand, due to the topography and the presence of some hydraulic structures used in the operation of the main canal, it is often that water level remains downstream at a certain height. This standing water prevents the free passage of flow causing what is known as "hydraulic plug".

The initial results demonstrate the presence of certain turbulent structures that adversely affect the hydraulic behavior of the tunnel when it is not pressurized, and in the other hand, the current transversal channel geometry is not large enough to conduct 120 m^3/s. The goal of this study is to propose modified geometries in such a way that the hydraulic functioning improves and to determine the hydraulic load on the tunnel roof and freeboard height of the side slopes needed to drive the flow rate mentioned through the information above, numerical modeling and experimental data.

3 NUMERICAL MODELING

3.1 Equations

The numerical modeling software used is the FLOW-3D™, a tool based on the theory of Computational Fluid Dynamics which has been proven to be robust in solving engineering problems related to hydraulic and versatile in their applications. The problem was solved using the average Navier-Stokes:

Continuity Equation:

$$\frac{\partial \overline{U_J}}{x_j} = 0 \quad [1]$$

Momentum Equation:

$$\frac{\partial \overline{U_\iota}}{\partial t} + \overline{U}_J \frac{\partial U_i}{\partial x_i} = -\frac{1}{\rho_N}\frac{\partial \bar{P}}{\partial x_i} + g_i + \nu_N \frac{\partial^2 \overline{U}_i}{\partial x_j^2} - \frac{\partial(\overline{u_\iota u_J})}{\partial x_j} \quad [2]$$

  / ISSN 1562-6865 (Online) - ISSN 1063-7710 (Print)

Many turbulence models employ the concept of turbulent viscosity or turbulent diffusion to express turbulent stresses and the flow itself.

3.1.1 RNG closure model

The RNG model approach is similar to k-ε model but includes an additional term in the equation of ε, modeling the dissipation of turbulence and average shear stress incorporates the effect of swirling turbulence, an analytical formula for the Prandtl number of turbulent and a differential formula to calculate the effective viscosity. In this model, Reynolds tensor is schematized manner analogous to the expression of molecular stresses such that:

$$-\overline{u_\iota u_J} = \nu_T \left(\frac{\partial U_i}{\partial x_j} + \frac{\partial U_j}{\partial x_i}\right) - \frac{2}{3}\,\delta_{ij}\kappa \qquad [3]$$

wherein ν_T, is turbulent viscosity coefficient based on the space and time and which in turn is assessed:

$$\nu_T = C_\mu \frac{\kappa^2}{\varepsilon} \qquad [4]$$

where κ, is the kinetic energy of turbulence and ε, its dissipation, evaluated with the following transport equations, respectively:

$$\frac{\partial \kappa}{\partial t} + \overline{U}_J \frac{\partial \kappa}{\partial x_j} = \nu_T \left(\frac{1}{2}\left(\frac{\partial U_i}{\partial x_j} + \frac{\partial U_j}{\partial x_i}\right)\right)^2 + \frac{\partial}{x_i}\left(\alpha_k \mu_{eff} \frac{\partial \kappa}{\partial x_i}\right) + B - \varepsilon \qquad [5]$$

$$\frac{\partial \varepsilon}{\partial t} + \overline{U}_J \frac{\partial \varepsilon}{\partial x_j} = C_{1\varepsilon}\left(\frac{\varepsilon}{\kappa}\right)\left(\frac{1}{2}\left(\frac{\partial U_i}{\partial x_j} + \frac{\partial U_j}{\partial x_i}\right)\right)^2 + \frac{\partial}{x_i}\left(\alpha_\varepsilon \mu_{eff} \frac{\partial \kappa}{\partial x_i}\right) - C_{2\varepsilon}\left(\frac{\varepsilon^2}{\kappa}\right) - R_\varepsilon \qquad [6]$$

where $C_{1\varepsilon}$, $C_{2\varepsilon}$, α_k, α_ε, are explicitly derived in the RNG process. The main difference between the RNG model and the κ-ε standard model, is in the additional term $R\varepsilon$, which includes experimentally obtained constant values that make the model more sensitive to the effects of high deformations and curvatures of the streamlines that the κ-ε standard model, which explains its best performance in certain types of problems where vorticity is presented. *B* is a term that includes the effects of flotation, but this paper does not consider important temperature changes, hence, the influence of this term is negligible.

With respect to the coefficients in the RNG model which are shown in Eqs. [5] and [6], values are assigned as follows (Yakhot et al., 1992). The coefficient of C_μ = 0.0845, $C_{1\varepsilon}$ equal to 1.42, η_o equal to 4.38 and β = 0.012 (obtained from experiments) diffusion constants, σ_k and σ_ε are both considered equal to 0.7194.

4 RESULTS

4.1 Preliminary results

Simulation results were presented when circulating in the tunnel at 120 m^3/s to see the influence of the transition of the entrance, which is an extension of the channel width of approximately 13 m length, it has a steeper slope than the main channel at the beginning of the tunnel entrance, and on the other hand, to know the influence of the outlet transition which is an extension of the tunnel to the channel about 18 m length, with adverse slope. The edges of the tunnel's walls are straight. In the above simulations, the height of canal walls were raised with respect to the actual geometry to determine the required freeboard both upstream and downstream so that the channel could conduct the flow rate tested.

It is pertinent to note that the results shown in Figures 1 to 6 correspond to the pressurized tunnel operation, is considered a freeboard of the slopes of the channel in order to drive 120 m^3/s. Note that in Figure 2, it can be seen that the crown edges of the tunnel causes the development of the boundary layer, the effect is seen in the delay of the flow patterns near the walls, being more pronounced in the upper corner. In Figure 3, the influence of topography at outlet is notorious, causing the flow to be asymmetric and have some oscillation, which can also be verified in Figure 5.

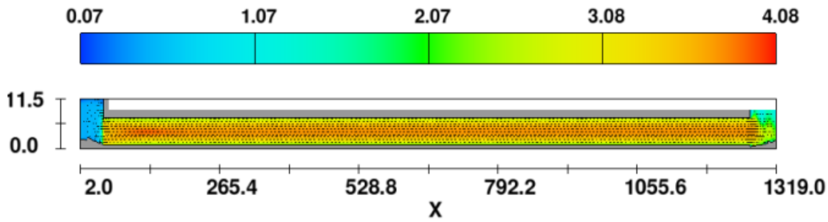

Figure 1. Plane *x-z* of velocities in tunnel and entrance / outlet transitions

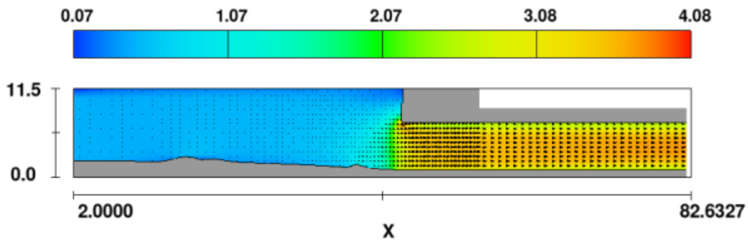

Figure 2. Plane *x-z* of velocities, detail in tunnel's entrance.

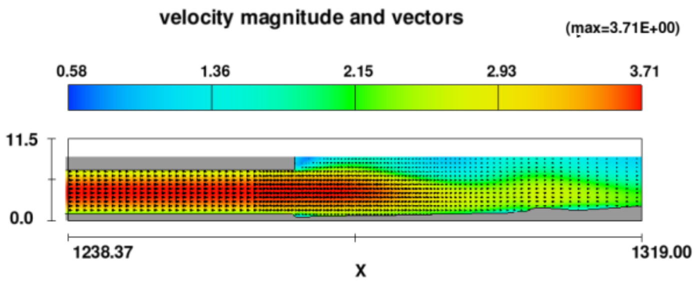

Figure 3. Plane *x-z* of velocities, detail in tunnel's outlet.

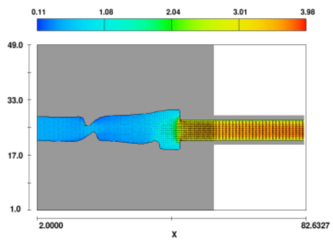

t = 900 s, *z* = 3.0 m

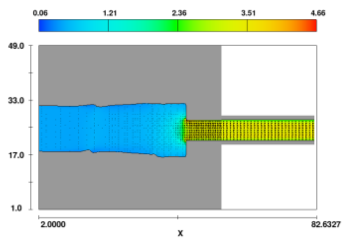

t = 900 s, *z* = 5.25 m

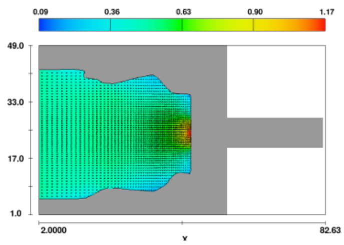

t = 900 s, *z* = 8.0 m

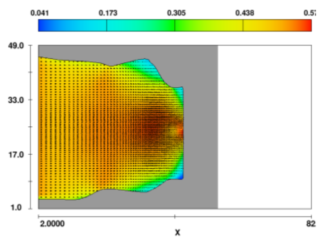

t = 900 s, *z* = 9.3 m

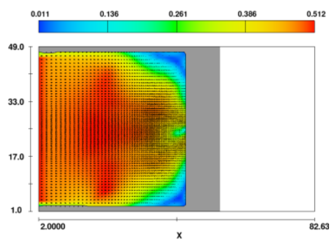

t = 900 s, *z* = 10.3 m

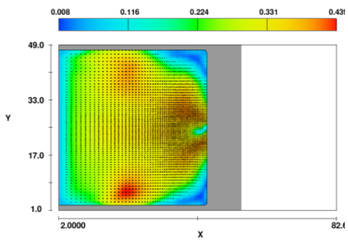

t = 900 s, *z* = 11.3 m

Figure 4. Planes *x-y* of velocities to different heights in *z*, in tunnel's entrance.

  / ISSN 1562-6865 (Online) - ISSN 1063-7710 (Print)

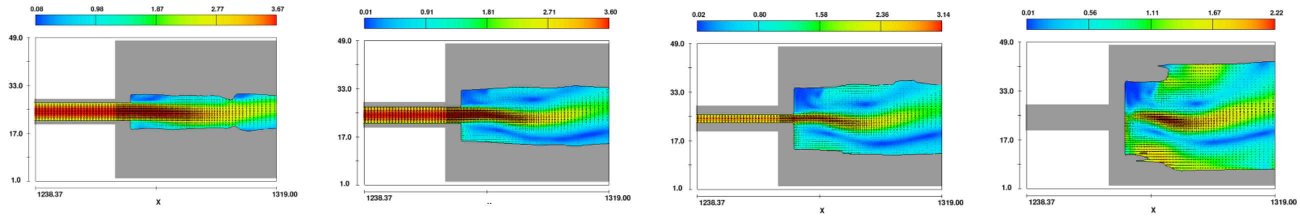

t = 900 s, *z* = 3.0 m | *t* = 900 s, *z* = 5.25 m | *t* = 900 s, *z* = 7.0 m | *t* = 900 s, *z* = 8 m

Figure 5. Planes *x-y* of velocities to different heights in *z*, in tunnel's outlet.

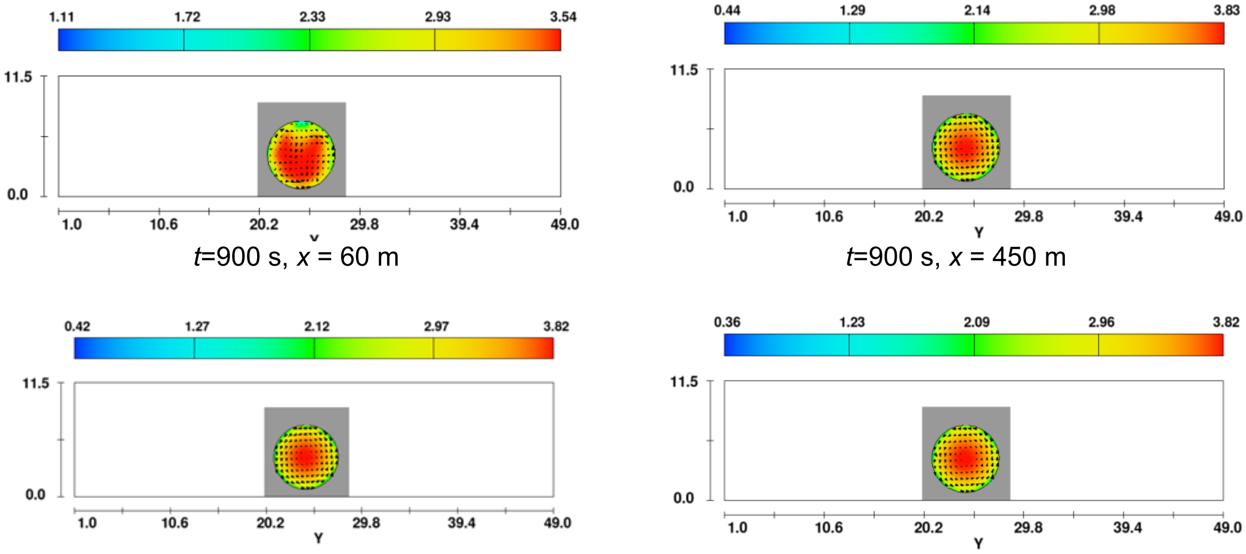

t=900 s, *x* = 60 m | *t*=900 s, *x* = 450 m

t=900 s, *x* = 800 m | *t*=900 s, *x* = 1200 m

Figure 6. Planes *y-z* of velocities to different points in *x*, in tunnel.

4.1.1 Proposed geometries

When the tunnel works are pressurized, the problematic areas are the entrance and outlet. In Figures 4 and 5, such parts can be seen, in which there are areas with turbulence and other areas of stagnation. Therefore, the modifications to these two structures based on the trajectories of the streamlines was proposed and they are shown below. Also, the straight edges of the tunnel entrance were smoothed to reduce the development of the boundary layer. To test their performance, some numerical tests were carried out, which are described in Table 3.

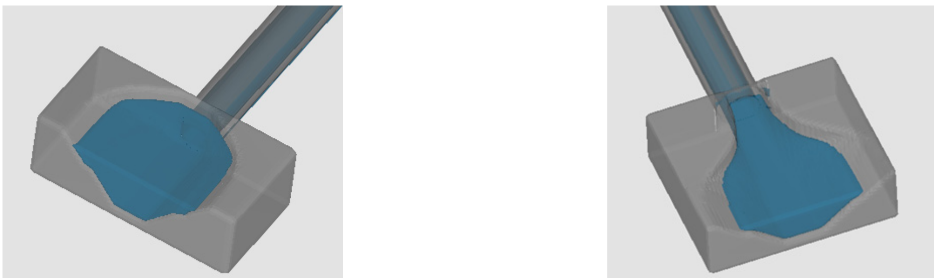

Figure 7. Alternative 1, series 1. Redesign of the entrance and outlet areas.

Figure 8. Alternative 2, series 2. Redesign of the entrance and outlet areas.

Table 3. Descriptions of performance tests of alternatives proposed.

Serie 1

Test	**Description**	***Q*, m^3/s**	***n***	**H_1, m**	**H_2, m**
GAS14.1	Flow rate is simulated in a geometry that follows the streamlines at the entrance and exit, with vertical slope walls.	120.0	0.016	8.087	6.387

Serie 2

Test	**Description**	***Q*, m^3/s**	***n***	**H_1, m**	**H_2, m**
GS24.1	Flow rate is simulated in a geometry that follows the streamlines at the entrance and exit, with gradual slope walls.	120.0	0.016	8.087	6.387

To save computational time, a gradually tighter mesh was used in the channel-tunnel and tunnel-canal (0.47 x 0.75 x 0.49) connections and another coarser along the tunnel (1 x 0.47 x 0.76). The simulation time was 900 s, but in some cases, the steady state is reached at approximately t = 450 s.

4.1.2 Results of geometry of alternative 1

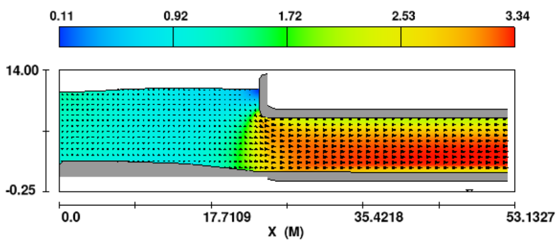

Figure 9. Plane *x-z* tunnel's entrance

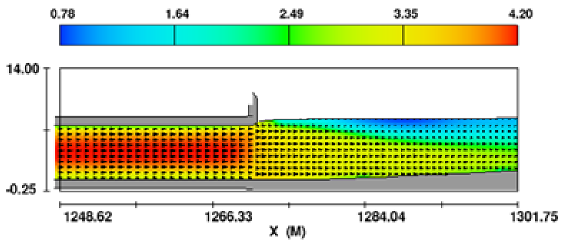

Figure 10. Plane *x-z* tunnel's outlet

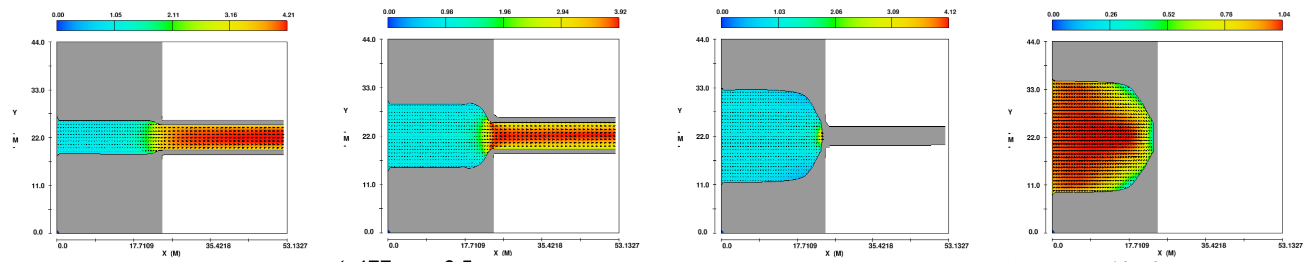

t=477 s, *z*=4 m | *t*=477 s, *z*=6.5 m | *t*=477 s, *z*=9.0 m | *t*=477 s, *z*=10.56 m

Figure 11. Planes *x-y* transitions of tunnel's entrance to different elevations in *z* axis.

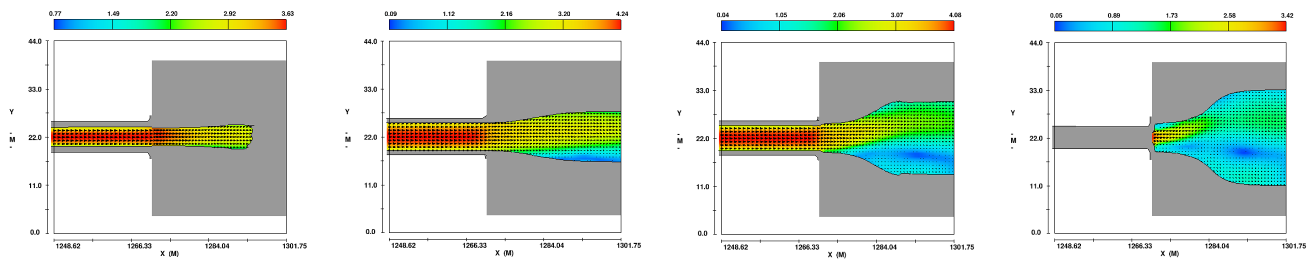

t=477 s, *z*=2 m | *t*=477 s, *z*=4.0 m | *t*=477 s, *z*=6.0 m | *t*=477 s, *z*=7.3 m

Figure 12. Planes *x-y* transitions of tunnel's outlet to different elevations in *z* axis.

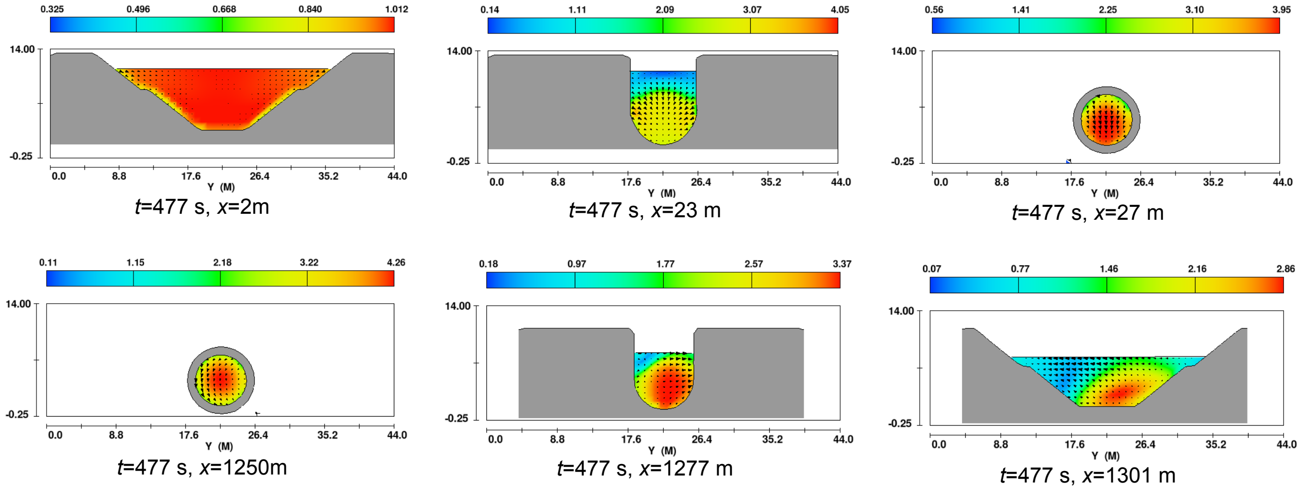

Figure 13. Transversal planes *y-z* of velocity contours developing along the channel.

4.1.3 Results of geometry of alternative 2

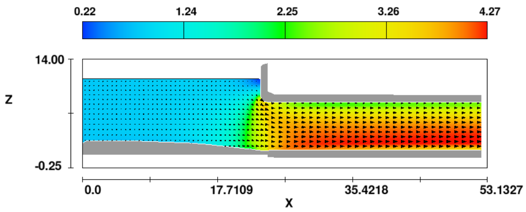

Figure 14. Plane *x-z* of tunnel's entrance.

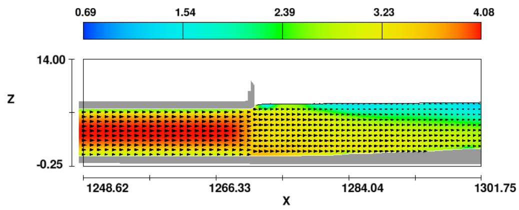

Figure 15. Plane *x-z* of tunnel's outlet.

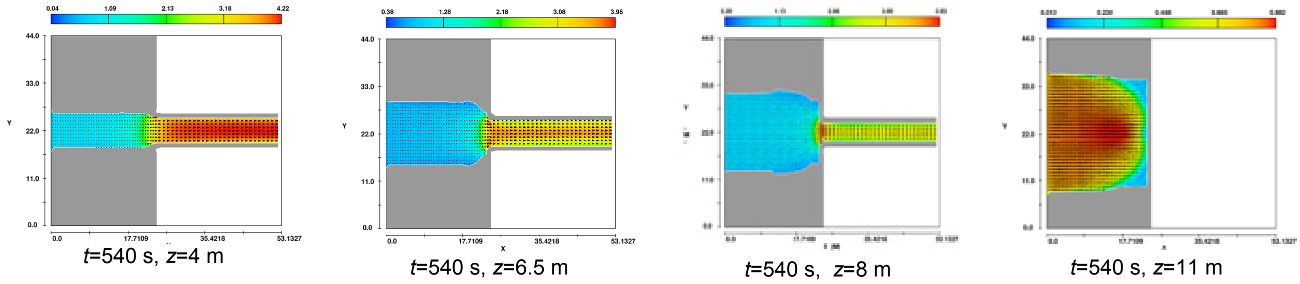

Figure 16. View of *x-y* plane of the tunnel entrance transition to different elevations.

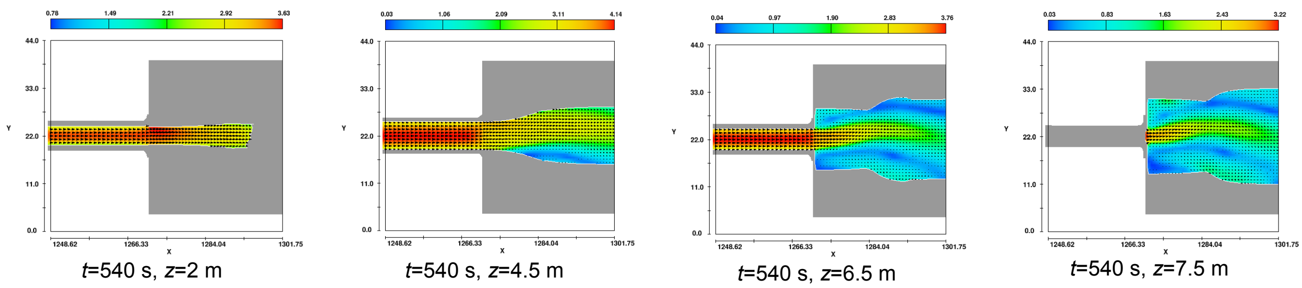

Figure 17. View of *x-y* plane of the tunnel outlet to different elevations.

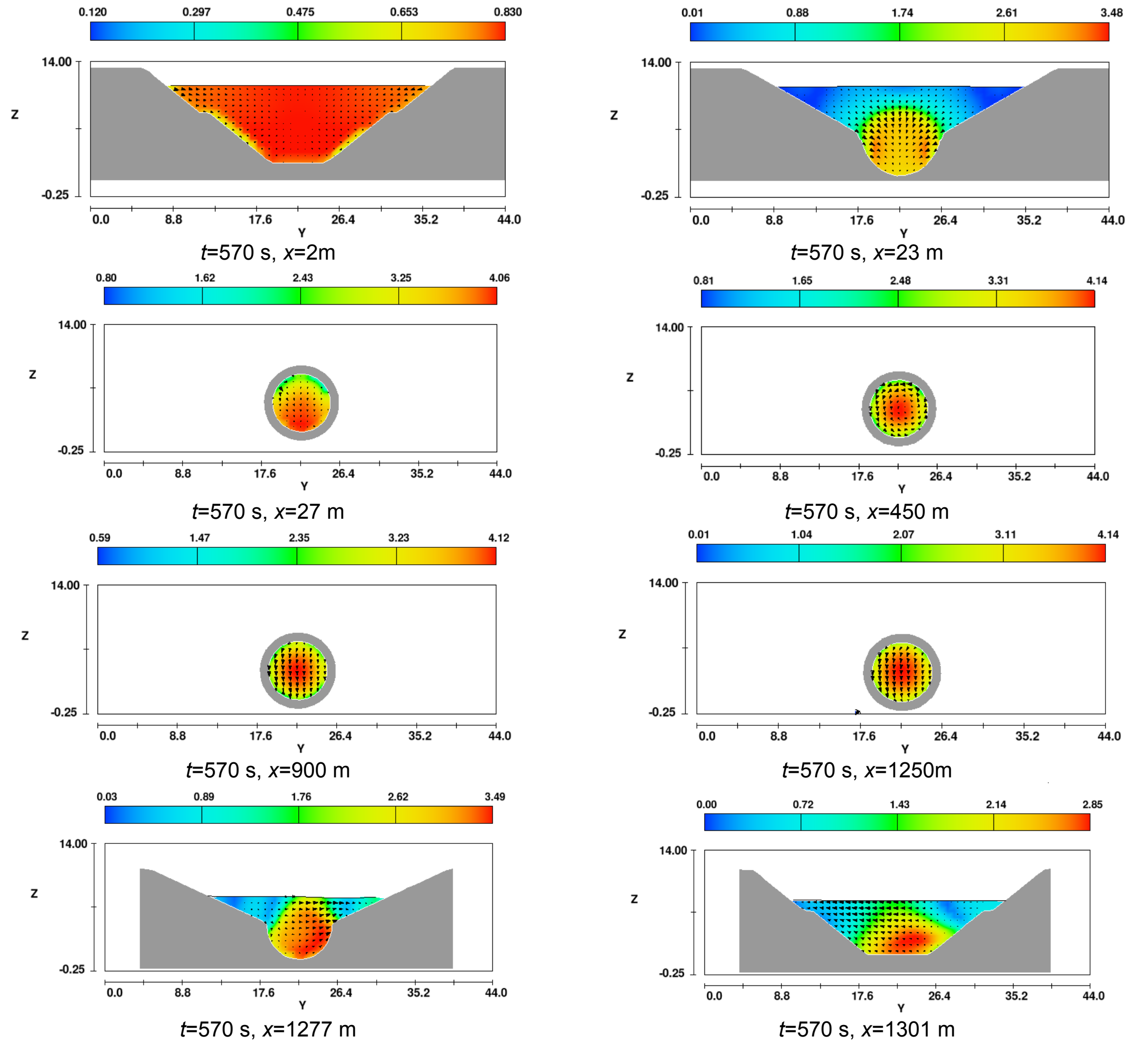

Figure 18. Transversal planes *y-z* of velocity contours developing along the tunnel and channel.

In the previous figures, it is shown that the two designs improve hydraulic operation, for example, upstream, eliminating the stagnation zones, the influence of the boundary layer at the tunnel entrance, and downstream lessening the oscillation of the flow patterns at the outlet. For comparison purposes with the measurements in the physical model, the data extracted from alternative 2 were used.

4.1.4 Measurements in physical model

After obtaining these results, it was proceeded to compare hydraulic depths obtained with the numerical model and the ones measured on a physical model of the system under study for different volumes flow. In relation to the conditioning of numerical model, the flow rate tested is introduced into the upstream boundary, while in the downstream boundary, initially (t=0) is the hydraulic depth corresponding to the backwater level due to operation of the channel. It was made as such to allow the model to predict the water depths for the circulating volume flow, as happens in the physical model.

In all of them and next graphics, MN* is related to the data obtained by numerical model, MF** to data measurement in the physical model and MC*** to data measurement in field. There are three measurements of volume flow and water depths made in the prototype, they will be included in the comparison of results. Results are shown in tables below.

  ISSN 1562-6865 (Online) - ISSN 1063-7710 (Print)

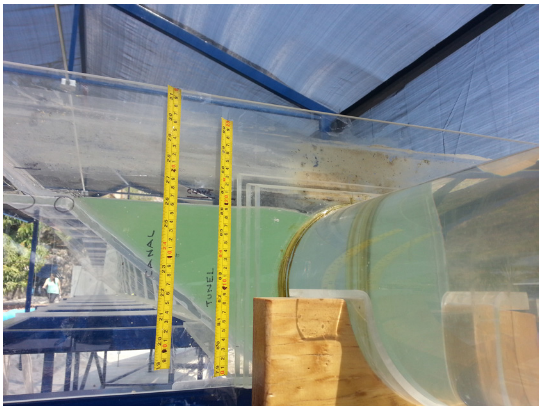

Figure 19. Measurements in tunnel's entrance in physical model.

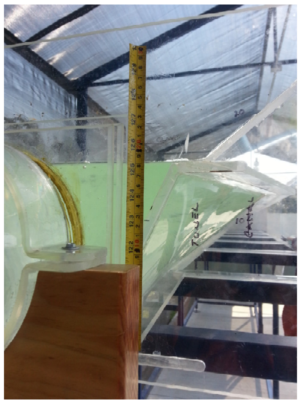

Figure 20. Measurements in tunnel's outlet in physical model

Table 4. Comparison of hydraulic depth among numerical and physical modeling for Q=34.54 m^3/s.

Q 34.54 MN *		Q 34.54 MF **		Q 34.54	
h ups, m	**h dws, m**	**h ups, m**	**h dws, m**	**Error %, h ups**	**Error %, h dws**
2.57	2.11	2.5558321	2.0753219	-0.5543361	-1.6709745
2.97	2.31	2.9388421	2.188807	-1.0602101	-5.5369432
3.17	2.38	3.1227477	2.2542937	-1.5131642	-5.5763053
4.22	3.04	4.1748538	3.0142441	-1.0813840	-0.8544729
5.48	4.13	5.4384947	4.5193243	-0.7631763	8.6146573

Table 5. Comparison of hydraulic depth among numerical and physical modeling for Q=79.20 m^3/s.

Q 79.2 MN*		Q 79.2 MF **		Q 79.2	
h ups, m	**h dws, m**	**h ups, m**	**h dws, m**	**Error %, h ups**	**Error %, h dws**
3.4171124	4.4390588	3.47	4.16	1.5241383	-6.7081442
4.5587959	4.615756	4.62	4.62	1.3247641	0.0918615
5.0235133	5.1310759	5.05	5.07	0.5244891	-1.2046529
6.1297908	5.917222	6.17	6.17	0.6516888	4.0968882
6.4639006	6.2116656	6.5	6.5	0.5553754	4.4359138

Table 6. Comparison of hydraulic depth among numerical and physical modeling for Q=85.72 m^3/s.

Q 85.72 MN*		Q 85.72 MF **		Q 85.72	
h ups, m	**h dws, m**	**h ups, m**	**h dws, m**	**Error %, h ups**	**Error %, h dws**
4.1143737	4.7916265	4.16	4.59	1.0967861	-4.3927342
4.6767225	4.8677363	4.72	4.95	0.9168962	1.6618929
5.0829883	5.3886046	5.15	5.36	1.3011981	-0.5336679
6.1972628	6.1776834	6.27	6.44	1.1600829	4.0732391
7.3839726	7.8752951	7.43	7.49	0.6194805	-5.1441268

Table 7. Comparison of hydraulic depth among numerical and physical modeling for Q=120 m^3/s.

Q 120 MN *		Q 120 MF**		Q 120	
h ups, m	**h dws, m**	**h ups, m**	**h dws, m**	**Error %, h ups**	**Error %, h dws**
4.6268	6.2259	4.62	6.27	-0.1471861	0.7033493
5.8296824	7.2693124	5.87	7.33	0.6868416	0.8279345
6.1520748	8	6.2	7.99	0.7729871	-0.1251564
7.5025115	9.375	7.59	9.31	1.1526812	-0.6981740

5 CONCLUSIONS

Regarding the super elevation of embankments needed to increase the conducting capacity of the tunnel, it was found that it is necessary to increase 1.70 m upstream and 0.5 m in downstream in order that the channel is driven to 120 m^3/s.

With respect to the proposed geometries, it is shown that by designing them in base of streamlines improved the hydraulic performance in this case, eliminating the stagnation zones, the influence of the boundary layer at the tunnel entrance, and downstream lessening the oscillation of the flow patterns at the outlet.

The conditioning of the numerical model for calibration was appropriated because the error in data was less than 3% in such case where Dirichlet type boundaries were used in both ends, however, when the flow rate was imposed on the upstream boundary in order that the model predicts water depths downstream, results obtained were not so good although the error is within the allowable (±10 %) (Tamari et al, 2010), as shown in Tables 4, 5, 6 and 7.

According to the information given in Tables 4-7 and as it can be seen in Figure 21, larger errors occur in the numerical model forecasting of the downstream strap. However, in this respect and judging from Table 7, the data obtained from numerical and physical models seem to agree when volume flows are increased. On the other hand, in the graph shown above (Figure 21), the few measurement data obtained in the field, are less than those thrown by the numerical model and physical model.

As for the future of this study, the next step would be to find another upstream boundary condition that improves prognosis downstream hydraulic depth which is where the largest discrepancies occur.

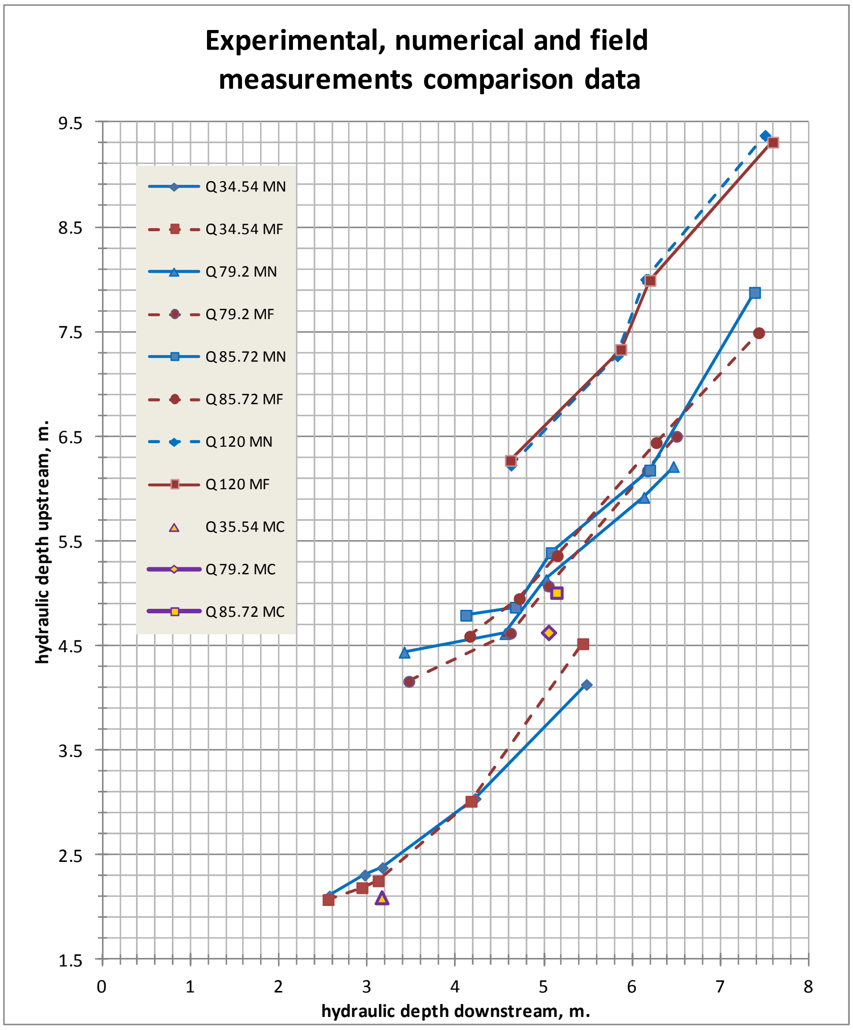

Figure 21. Data comparison between numerical data and physical measurements

REFERENCES

Bashiri-Atrabi, H., Hosoda, T. & Tada, A. (2015). Simulation of Air Cavity Advancing into a Straight Duct. *Journal of Hydraulic Engineering*. 10.1061/(ASCE)HY.1943-7900.0000953,04014068.

Bashiri-Atrabi, H., Hosoda, T. & Shirai, H. (2016). Propagation of an Air-Water Interface from Pressurized to Free-Surface Flow in a Circular Pipe. *Journal of hydraulic Engineering*. 10.1061/(ASCE)HY.1943-7900.0001200,04016055.

Castillo González, Jorge A. (2011). Ficha Informativa del Proyecto RD0928.3 Proyecto Ejecutivo para la Modernización Integral del Riego en el Módulo de Riego V-II, del Distrito de Riego 010, Culiacán-Humaya, Sinaloa. *Instituto Mexicano de Tecnología del Agua*. México, 2011. Disponible para World Wide Web:http://www.imta.gob.mx/historico/instituto/historial-proyectoswrp/rd/2010/fi-rd0928-3.pd.

Tamari S., Aguilar A. (2010). *Aforo en Canales y Presas: Selección de una Técnica*. Instituto Mexicano de Tecnología del Agua. México. Guía técnica. 12-14

Yakhot, V., Orszag, S.A., Thangam, S., Gatski, T.B. & Speziale, C.G. (1992). Development of Turbulence Models for Shear Flows by a Double Expansion Technique, *Physics of Fluids A*, 1992, 4(7), 1510-1520.

Proceedings of the 37th IAHR World Congress
August 13 – 18, 2017, Kuala Lumpur, Malaysia

DETERMINING TIDAL MIXING ZONE USING NUMERICAL AND DATA-DRIVEN MODEL IN MALACCA STRAIT

ALAMSYAH KURNIAWAN[(1)], SERENE H.X. TAY[(2)], SENG KEAT OOI[(3)] & VLADAN BABOVIC[(4)]

[(1)] Ocean Engineering Program, Institut Teknologi Bandung (ITB), Bandung, Indonesia,
alamsyah@ocean.itb.ac.id
[(2,4)] Department of Civil and Environmental Engineering, National University of Singapore (NUS), Singapore,
serenetay@nus.edu.sg; vladan@nus.edu.sg
[(3)] Tropical Marine Science Institute, National University of Singapore (NUS), Singapore,
sk.ooi@nus.edu.sg

ABSTRACT

The Malacca Strait, a shallow passage that connects South China Sea and Andaman Sea, offers serious challenges for ocean weather modeling. Prediction of tidal changes using regional ocean models and data based linear time series models are often inadequate for accurate forecasting. Previous studies have indicated that tidal mixing zone in the Malacca Strait might influence the sea level anomalies propagation from South China Sea to Andaman Sea. Present work analyzes the location of tidal mixing zone in the Malacca Strait using numerical modeling and data driven model. Average Mutual Information (AMI) based on the data driven modeling provides an alternate opportunity in understanding tidal with complex behavior. This work studies the efficiency of AMI as a potential hydroinformatics tool. Prediction of tidal variations using numerical model around Malacca Strait is adopted as case study. Historical tide datasets at predefined geographical locations are used to build the non-linear time series models to determining the tidal mixing zone. The results are compared with the predictions obtained using linear time series models (*e.g.,* Formzahl Number).

Keywords: Hydroinformatic; tidal mixing zone; Average Mutual Information (AMI); Formzahl Number; Malacca Strait.

1 INTRODUCTION

As an international shipping route, the Malacca Strait is among the busiest and most important waterways in the world (Figure 1). The understanding of the generating mechanisms and the ability to generate forecasts of tidal and non-tidal (wind-induced water level, waves) flow phenomena and their forcing mechanisms for practical application in this environment are of both scientific and economic importance. A major step in their analysis and forecasting is the development of an accurate hydrodynamic model to predict the barotropic and non-barotropic water levels and currents (Kurniawan et al., 2011; 2015; Tay et al., 2016). Relevant issues are model domain and grid resolution, sensitivity to model formulation (robustness), accuracy and predictability.

Previous studies have indicated that tidal mixing zone in the Malacca Strait might influence the sea level anomalies propagation from South China Sea to Andaman Sea (Kurniawan et al., 2015; Tay et al., 2016). The strong tidal dynamics in the Malacca Strait is primarily due to the fact that here the main interaction takes place of the tidal signals that enter the region from the two oceans, *i.e.,* Indian, mainly semi-diurnal and Pacific, mainly diurnal (Wyrtki, 1960). It is further complicated by factors such as sharply varying bottom topography toward the predominant shallow Sunda Shelf, which acts as a separator of two deep basins (South China Sea/Pacific Ocean and Andaman Sea/Indian Ocean) and the complicated coastal geometries due to the narrow straits and numerous small islands. Prior analysis carried out of observational data showed the Malacca Strait is the area with the highest spring/neap tides in the entire model domain, with much tidal mixing (Zijl and Kernkamp, 2004).

Modeling of ocean dynamics around the Malacca Strait is a challenging task due the presence of strongly non-linear tidal interactions, meteorological effects on different scales, and complex local bathymetry. The flows experience the effects of nonlinear dynamical interactions between the large water bodies of South China Sea, Andaman Sea and Java Sea. The complex shallow water hydrodynamics resulting from multiple ocean currents moving into and out of this region combined with sharply varying short term meteorological effects leads to a very high variability of the water level along the Malacca Strait.

In addition, complex governing mechanisms, multi-scale, multi-dimensional, time varying, and highly non-linear dynamics of marine systems make oceanographic modeling efforts much more challenging. Conventional numerical models provide primary solution to this challenging task of characterizing and forecasting ocean weather (mainly water level and flow) by representing the underlying physics in terms of solvable equations. Yet, capturing the ocean dynamics in totality, accounting for the non-tidal anomalies calls for rigorous tuning of the models for further improvement. Such an exercise demands detailed domain knowledge and heavy computational effort. Hence, there is an increasing need for alternate approaches which can provide vital information leading to better domain knowledge and reduced time and effort required to tune the numerical models. To determine uncertain parameters in numerical model to be calibrated, an understanding of the sources of these uncertainties is needed. Such information may help to reduce the number of uncertain parameters to be calibrated. Information that can help in the reduction of uncertainty is of particular interest in the present work.

Previous studies on data modeling and data driven techniques have shown the utility of one of the important data driven analysis tools based on mutual information theory (Babovic and Keijzer, 1999; Babovic et al., 1999; Kurniawan et al., 2014; 2015). The present study explores feasibility of applying average mutual information (AMI) theory by evaluating amount of information contained in prediction of tidal numerical modeling by relating them to variables that reflect the physics such as spatial distribution of tidal constituents. To give a proper distinction from the previous studies, the present study focuses on comparing the information between the computed using numerical modeling and data-driven modeling using AMI whereas previous studies focused on prediction errors of non-tidal barotropic numerical modeling to improve numerical model prediction.

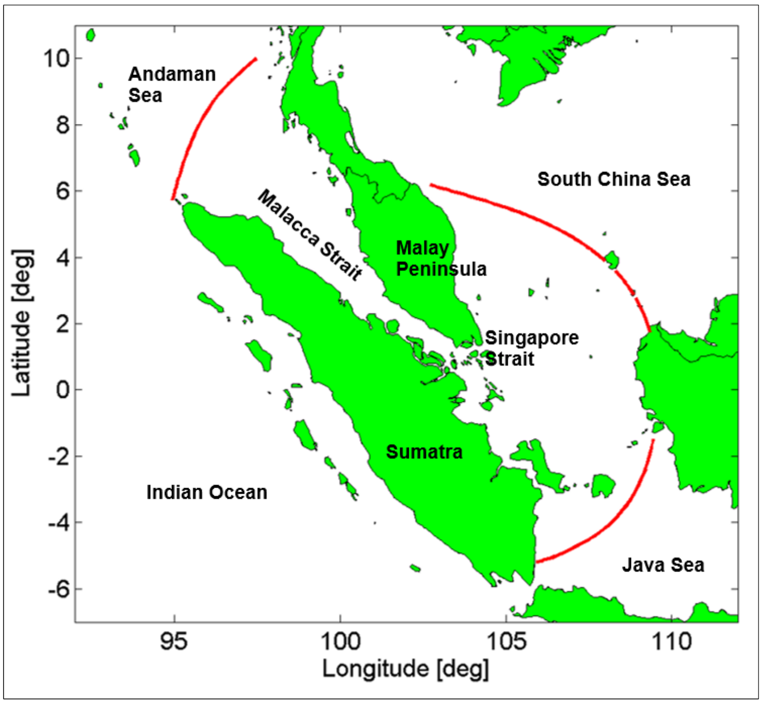

Figure 1. Area of interest showing the location of the Malacca Strait and the numerical model open boundary location (red line).

2 METHODOLOGY

Present work analyzes the location of tidal mixing zone in the Malacca Strait using numerical modeling and data-driven model.

2.1 Numerical model

The numerical model in this study solves the 2D depth averaged shallow water flow equations (Deltares, 2011). For embedded sub-domains covering coastal areas and straits with complex topographic features in the Malacca Strait, a fine resolution tidal model is used (Figure 2). The tidal model uses a boundary-fitted orthogonal spherico-curvilinear grid which reduces potential modeling errors from representing the coastal geometry, especially when compared to a rectangular grid. The model domain covers the region, stretching from northern Sumatra to the eastern coast of Borneo. The total number of grid cells in the model is approximately 38,500 and the grid cells vary smoothly in size from approximately 20 – 40km^2 at the open sea boundaries to approximately 150 – 200m^2 in the interior waters. The model has open water boundaries across the Andaman Sea, Java Sea and the South China Sea. Along these open boundaries, best estimates of tidal constituents are prescribed, which are expanded during computations to provide tidal water level forcing of the model. The eight main tidal constituents Q1, O1, P1, K1, N2, M2, S2 and K2 are prescribed (phases related to GMT+8) at the three open sea boundaries, while tide generating forces are included in the interior domain. The bathymetry in the model domain ranges from a maximum depth of about 2000m in the Andaman Sea to approximately 40 – 50m depth in the Singapore Strait. A Manning friction coefficient of 0.022m$^{-1/3}$s has been applied for bed friction. A detailed description of the model including tidal sensitivity analysis and improved tidal representation can be found in Kurniawan (2014).

  / ISSN 1562-6865 (Online) - ISSN 1063-7710 (Print)

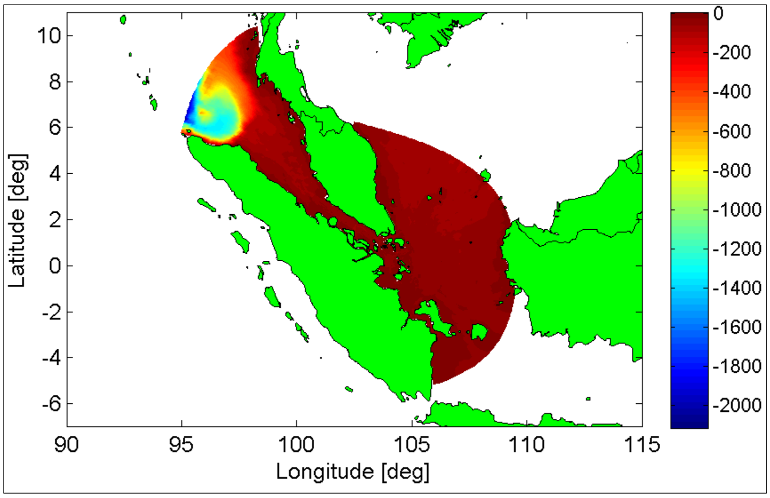

Figure 2. Tidal model domain computation showing its extent and bed level.

2.2 Tidal constituents

For large scale tidal flow models, the numerical model is equipped with a facility to perform online Fourier analysis on computational results (Deltares, 2011). This enables the generation of computed co-tidal maps which can be compared with co-tidal maps from literature. Present study analyses 4 (four) tidal constituents as shown in Table 1.

Table 1. Tidal constituents.

	Angular Frequency (degree/hour)	Type
M_2	28.9841042	Semi-Diurnal
S_2	30.0000000	Semi-Diurnal
K_1	15.0410686	Diurnal
O_1	13.9430356	Diurnal

In order to classify the tides of a locality, present work adopts three principal types of tides based on the ratio of the sum of the amplitudes of the diurnal constituents (K1+O1) to the sum of the amplitudes of the semi-diurnal constituents (M2+S2). This ratio increases when the diurnal inequality of the tides increases. It attains a maximum when there is only one high water a day. Therefore, F = (K1+O1)/ (M2+S2) is designated as the "Formzahl" of the tides, which has given the following classification in Defant (1960) as follows:

- F: 0.00 – 0.25; semi-diurnal type; two high waters and two low waters daily of approximately the same height. The interval between the transit of the moon and high water at a locality is nearly constant;
- F: 0.25 – 1.50; mixed, mainly semi-diurnal type. There are daily two high and two low waters, which however, show inequalities in height and time, which attain their maximum when the declination of the moon has passed its maximum;
- F: 1.50 – 3.00; mixed, mainly diurnal type. Occasionally only one high water a day, following the maximum declination of the moon. At other times there are two high waters in the day, which however, show strong inequalities in height and time, especially when the moon has passed through the equator;
- F: 3.00 – ∞; diurnal type. Only one high water daily and the semi-diurnal almost vanish. At neap tide, when the moon has passed through the equatorial plane, there can also be two high waters.

2.3 Average Mutual Information (AMI)

Mutual information has been found to be a more suitable measure of dependence for analyzing the non-linear systems (Gallager, 1968; Abarbanel, 1996; Babovic and Keijzer, 1999; Babovic et al., 1999; Abebe and Price, 2004; Kurniawan et al., 2015). Mutual information makes no assumption regarding the structure of the dependence between variables. It has also been found to be robust due to its insensitivity to noise and data transformations (Abarbanel, 1996; Abebe and Price, 2004).

Average Mutual Information (AMI) based on data driven modeling provides an alternate opportunity in understanding tidal with complex behavior. It is a measure of information that can be learnt from one set of data having knowledge of another set of data. The AMI does not depend on any particular function and therefore can help to detect both linear and non-linear correlations. It simply connects two sets of data with each other and established a criterion for their mutual dependence based on the notion of information between them (Abarbanel, 1996).

Fundamental of the notion of information among data Shannon's idea (Shannon, 1948) described in Gallager (1968). Given a random output variable Y, there will be some uncertainty surrounding an observation y ∈ Y, which can be defined using Shannon entropy (Shannon, 1948). Following Abarbanel (1996), present work uses this connection to give precise definition to theoretic fashion to the data *s(t+T)* at time *t+T*. To compute the AMI between a time series *s(t)* and its time delayed *s(t+T)*, average mutual information with regards to time delay is defined as in Eq. [1]:

$$AMI(T) = \sum_{s(t),s(t+T)} P(s(t),s(t+T)) \log\left[\frac{P(s(t),s(t+T))}{P(s(t))\,P(s(t+T))}\right] \qquad [1]$$

where *P(s(t))* and *P(s(t),s(t+T))* are probability density functions (PDF), whereas *P(s(t),s(t+T))* is joint PDF. From this formulation, it can be seen that when *T* becomes large, chaotic behavior of the signals makes the data *s(t)* and *s(t+T)* become independent in a practical sense and *AMI(T)* will tend to be zero (Abarbanel, 1996). AMI between the original signal and the time lagged signal can be computed for each time lag values. The nature of AMI variations for different T values is used as basis for establishing the individual tidal and non-tidal temporal patterns. Interpretation of AMI values can be found in Babovic and Keijzer (1999) and Abebe and Price (2004).

3 RESULTS AND DISCUSSIONS

3.1 Spatial distribution of model results

In this work, spatial distribution from numerical modeling and temporal distribution from data-driven modeling of tidal constituents are assessed and analyzed to determine the location of tidal mixing zone in the Malacca Strait.

3.1.1 Spatial distribution of tidal constituents

Figure 3 to 4 show spatial distribution of semi-diurnal and diurnal tidal constituents in the model domain, respectively. As can be seen, semi-diurnal tidal constituents are dominated in the Malacca Strait, whereas diurnal tidal constituents are dominated in South China Sea and Java Sea. The results support the basic and general properties of the waters and circulations in the Malacca Strait, which are provided by Wyrtki (1961) and Zu et al. (2008).

3.1.2 Formzhal Number

The spatial distribution in Figure 3 to 4 also highlights that semi-diurnal and diurnal tidal constituents are collided at the south end of the Malacca Strait before the Singapore Strait. To give a proper distinction, the Formzhal Number is then calculated and its spatial distribution in the model domain can be seen in Figure 5 (left). As can be seen, mixed tidal zone, mainly semi-diurnal type (F = 0.25 – 1.50) can be located at the south end of the Malacca Strait before the Singapore Strait, whereas mixed tidal zone, mainly diurnal type (F = 1.50 – 3.00) can be located mainly at the South China Sea.

In more detail, Figure 5 (right) shows spatial distribution of Formzhal Number between 0.25 and 0.50. This indicates a strong mixed tidal zone, mainly semi-diurnal type is occurred at the south end of the Malacca Strait. The results support the indication of the previous studies that the mixed tidal zone phenomenon observed in the narrow channel between Malacca Strait and Singapore Strait, which may introduces a blockage effect. Furthermore, the results supports the indication that the mixing zone would be most sensitive to any depth or parameter variation but that significant variation in depth or friction in this region could also alter the incoming tide characteristics at the boundaries of the numerical model. The results also indicate the important role of the Malacca Strait in tidal and non-tidal dynamics propagation between Indian and Pacific Ocean.

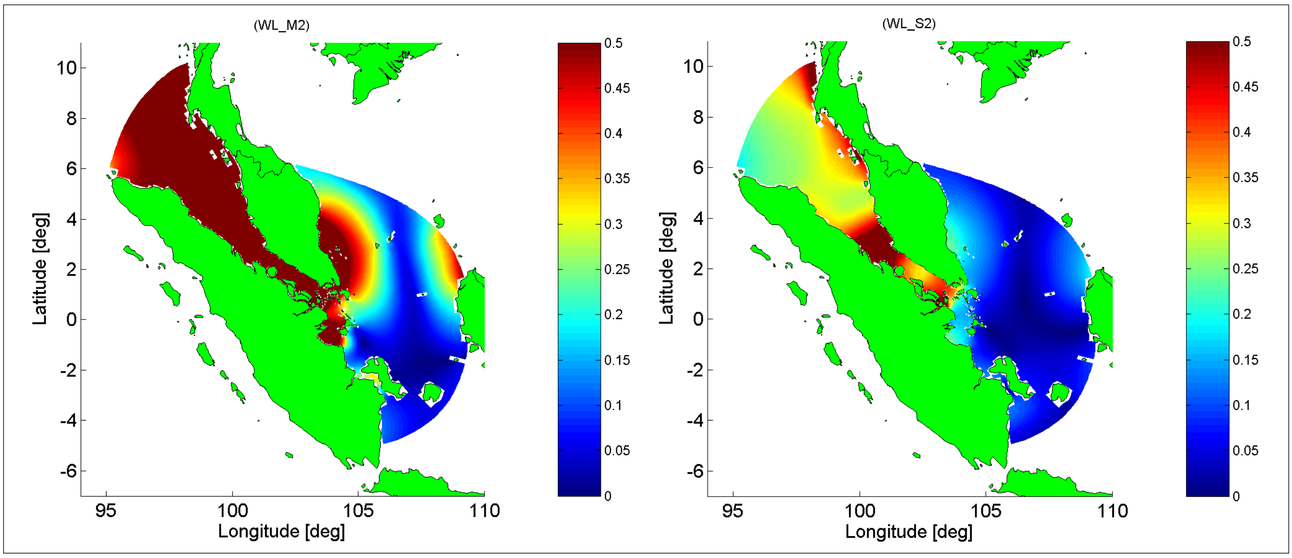

Figure 3. Spatial distribution of semi-diurnal tidal constituents in the model domain showing magnitude of M2 (left) and S2 (right).

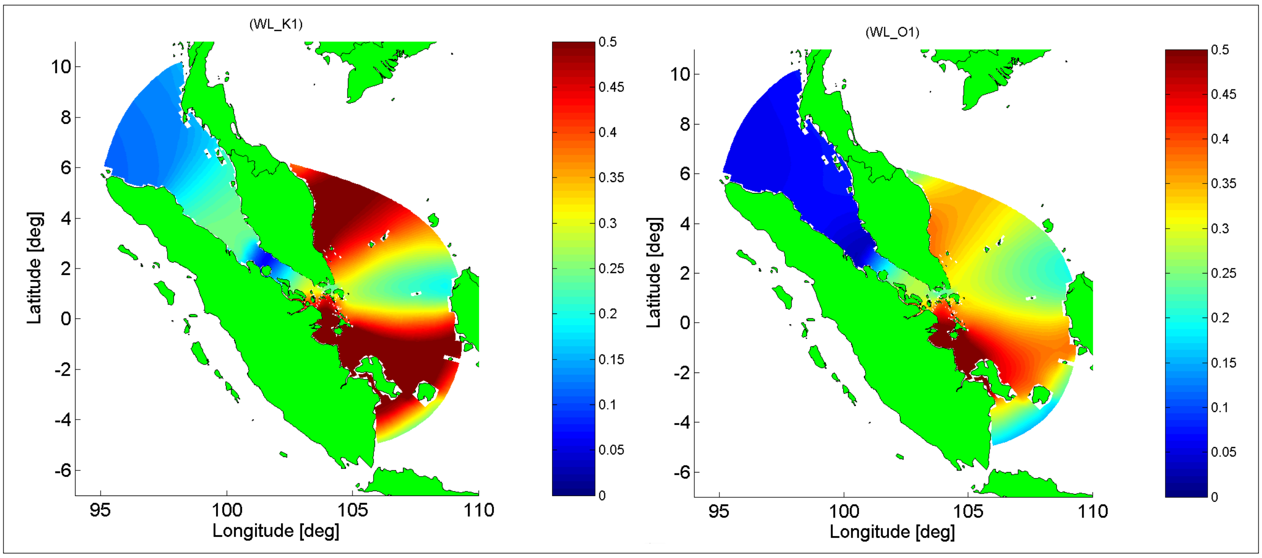

Figure 4. Spatial distribution of diurnal tidal constituents in the model domain showing magnitude of K1 (left) and O1 (right).

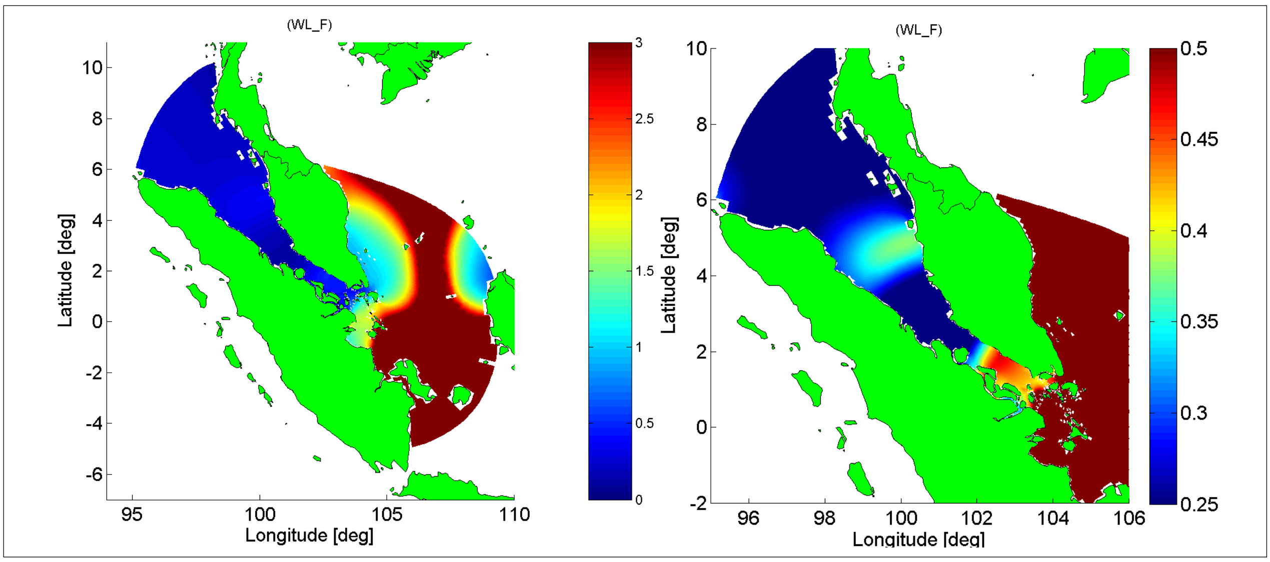

Figure 5. Spatial distribution of Formzhal Number showing at the model domain (left) and more detail at the Malacca Strait (right).

3.2 Temporal distribution of mutual information

Data-driven modeling is carried out at 5 (five) different locations, as shown in Figure 6 (left). The locations are chosen as the representative of each tidal constituents based on numerical modeling results. For example, p1 is semi-diurnal tidal component, p2 and p3 represent mixed, mainly semi-diurnal type and p4 is diurnal tidal component whereas p5 represent mixed, mainly diurnal type.

Figure 6 (right) shows the AMI results for all locations. As can be seen, AMI is able to give a proper distinction between 4 (four) tidal classification. Although the trends are quite the same, AMI at p1 is higher than at p2 and p3. These indicates that AMI can give more information on signal strength at each location to support more general spatial distribution of Formzhal Number. The AMI results suggest that tidal mixing zone in the Malacca strait is dominated by semi-diurnal tidal constituents.

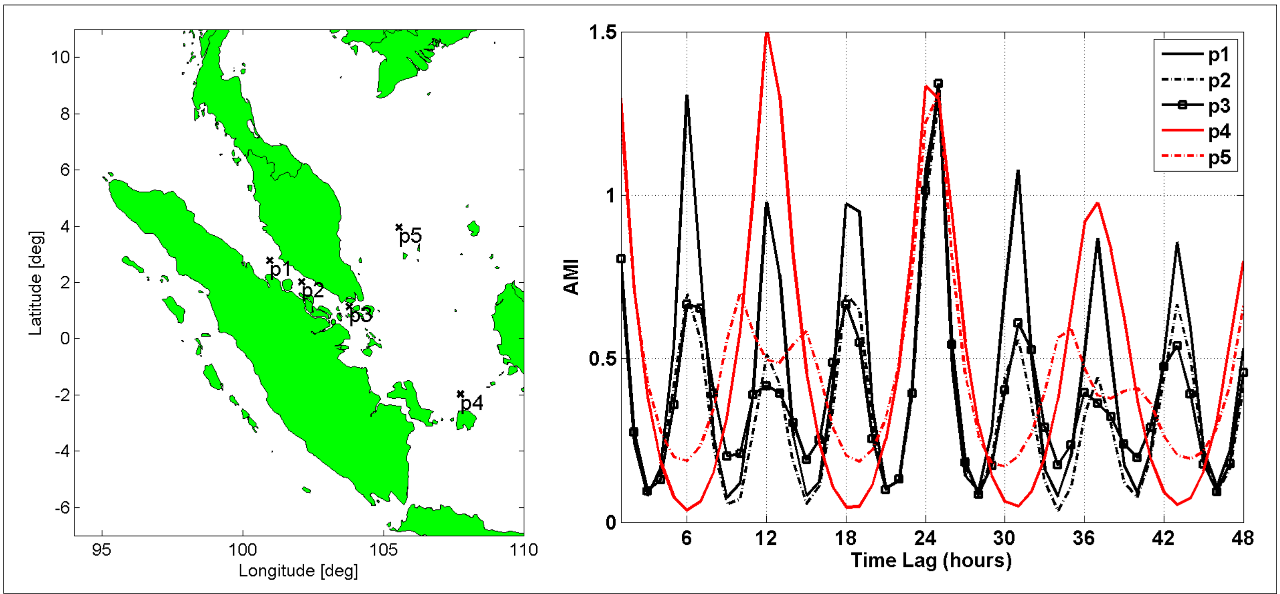

Figure 6. AMI showing analysis location (left) and temporal distribution of AMI (right).

4 CONCLUSIONS

The results of the present work in this paper illustrate that the tidal mixing zone location in a local region like the Malacca Strait can be effectively analyzed by using combination of numerical modeling and data-driven model. The results support the indication that the mixed tidal zone phenomenon observed in the narrow channel between the Malacca Strait and the Singapore Strait which may introduces a blockage effect for the propagating sea level anomalies generated in South China Sea or Java Sea. The present work shows the efficiency of AMI as a potential hydroinformatics tool. Future work is recommended to compute AMI for the entire domain in a spatial map to have spatial distribution of AMI in the area of interest.

ACKNOWLEDGEMENTS

The authors gratefully acknowledge the support and contributions of the Ocean Engineering Program, Faculty of Civil and Environmental Engineering, Institut Teknologi Bandung, National University of Singapore and Deltares' open source software for the numerical modeling.

REFERENCES

Abaranel, H.D.I. (1996). *Analysis of Observed Chaotic Data*. Springer-Verlag, New York.

Abebe, A.J. & Price, R.K. (2004). Information Theory and Neural Networks for Managing Uncertainty in Flood Routing. *Journal of Computing in Civil Engineering,*18(4), 373-380.

Babovic, V. & Keijzer, M. (1999). *Forecasting of River Discharges in the Presence of Chaos and Noise*. In Marsalek, Jiri (Ed.), Coping with Floods: Lessons Learned from Recent Experiences, NATO ARW Series, Kluwer, Dordrecht, 405-420.

Babovic, V., Keijzer, M. & Mahbub, R. (1999). *Analysis and Prediction of Chaotic Time Series*. D2K Technical report 0399-2, Danish Hydraulic Institute, http://www.d2k.dk.

Defant, A. (1961). *Physical Oceanography*. Pergamon Press, New York, 729.

Deltares, D.F. (2013). *Delft3D-FLOW - Simulation of Multi-Dimensional Hydrodynamic Flows and Transport Phenomena, Including Sediments*, User Manual, Deltares, the Netherlands.

Gallager, R.G. (1968). *Information Theory and Reliable Communication*. John Wiley and Sons, New York.

Kurniawan, A., Ooi, S.K. & Babovic, V. (2014). Improved Sea Level Anomaly Prediction Through Combination of Data Relationship Analysis and Genetic Programming in Singapore Regional Waters. *Computers & Geosciences*, 72, 94–104.

Kurniawan, A. (2014). Improved Tidal and Non-Tidal Representation of Numerical Models through Data Model Integration, *PhD Thesis*. National University of Singapore, Singapore.

Kurniawan, A., Ooi, S.K., Hummel, S. & Gerritsen, H., (2011). Sensitivity Analysis of the Tidal Representation in Singapore Regional Waters in a Data Assimilation Environment. *Ocean Dynamics*, 61(8), 1121–1136, DOI: 10.1007/s10236-011-0415-6.

Kurniawan, A., Tay, S.H.X., Ooi, S.K., Babovic, V. & Gerritsen, H. (2015). Analyzing the Physics of Non-Tidal Barotropic Sea Level Anomaly Events Using Multi-Scale Numerical Modeling in Singapore Regional Waters. *Journal of Hydro-environment Research*, 9(3), 404-419, DOI: 10.1016/j.jher.2014.10.005.

Shannon, C.E., (1948). The Mathematical Theory of Communication, *Bell System Technical Journal*, 27(4), 623-656.

Tay, S.H.X., Kurniawan, A., Ooi, S.K. & Babovic, V. (2016). Sea Level Anomalies in Straits of Malacca and Singapore. *Applied Ocean Research* 58,104-117, DOI: 10.1016/j.apor.2016.04.003.

Wyrtki, K. (1961). Physical Oceanography of the Southeast Asian Water. NAGA Report. In Scientific Result of Marine Investigation of the South China Sea and Gulf of Thailand 1959-1961, vol. 2. *Scripps Institution of Oceanography*, La Jolla, California, 195.

Zijl, F. & Kernkamp, H.W.J. (2004). *Further Hydraulic Model Studies for Pulau Ubin & Pulau Tekong Reclamation Scheme*, Delft Hydraulics Report Z3437 for Housing and Development Board (HDB).

Zu, T., Gan, J. & Erofeeva, S.Y. (2008). Numerical Study of the Tide and Tidal Dynamics in the South China Sea. *Deep Sea Research I,* 55(2), 137-154.

Proceedings of the 37th IAHR World Congress
August 13 – 18, 2017, Kuala Lumpur, Malaysia

FORCE SIMULATION FOR GRAVEL AND ROCK TRANSPORT

PEIWEI XIE[1], SHOOKA KARIMPOUR[2] & VINCENT H. CHU[3]

[1,3] Department of Civil Engineering, McGill University, Montreal, Canada,
peiwei.xie@mail.mcgill.ca
[2] CIRAIG, Université du Québec à Montréal, Montreal, Canada,

ABSTRACT

The force on gravels and rocks in mountain streams on a steep slope is studied for the role of the flood waves on the transport process. The numerical simulation using the shallow-water equations determines the height of the flood wave and the reflection of the wave by a single hemispherical rock. The goal of the simulation is to find the relevant wave parameters to replace the classical description based on Shields' critical stress for the mobility of gravels and rocks susceptible to the wave forces. The flow is constantly changing from subcritical to supercritical and back through the formation of surge waves. The flux-limiting scheme MINMOD controls the spurious oscillations across the depth and velocity discontinuity in the waves. The dimensionless parameters identified for the wave effect are the wave-force coefficient and the surge-wave Froude number. The peak values of the wave-force coefficient for the hemispherical rock are nearly constant varying from $C_{WF} \approx 1.1$ to 1.0 over a range of Froude number varying from $Fr_s = 0.1$ to 2.0. The critical sliding and tipping forces determine the threshold discharge for the mobility of the gravels and rocks.

Keywords: Mountain stream; flood waves; gravel and rock mobility; shock waves; numerical simulation.

1 INTRODUCTION

Classical turbulence and transport models are based on the experimental data obtained in shear flow of small Froude numbers. The numerical simulation of the shear flow in shallow waters often uses the rigid-lid approximation. The dynamics of the surface waves ignored in the classical models are the dominant influence in many important river engineering problems including the routing of flood waves on mountain streams and the diversion of water in the events of a dam failure. At low Froude number, the exchanges of mass and momentum across the shear flow are by vortex street. At higher Froude numbers, on the other hand, the exchanges are by the radiation and reflection of the gravity waves. We will show through a series of numerical simulations how high-order accurate numerical schemes may capture the dynamics of the waves and how the direct numerical simulations are used to find the transport of gravels and rocks in rivers on a steep slope that is not describable by the conventional sediment transport formulation.

Gravels and rocks in mountain streams are immobile most of the time, but during flooding stage, they may become mobile and contribute to the intermittent transport of sediments along the channel on a steep slope. The high-speed currents interacting with the gravels and rocks are continuously in the transition from subcritical to supercritical and then back to subcritical flow (Figure 1). The waves and the breaking of the waves determine the forces on the gravels and the rocks. The transport process by the waves is beyond the classical description of the critical stress by Shields (1936). The wave effect nevertheless has been included semi-empirically in predicting bed load transport on gravel bed streams on steep slopes (Bathurst et al., 1987; Yang, 1996; Recking, 2009; Ma et al., 2014; Prancevic et al., 2014; Schneider et al., 2016). To understand the fundamentals of the mechanics, one has to consider the wave resistance and the critical conditions for the mobility of the gravels and the rocks. Figure 2 delineated the idealized simulation problem. The arrival of the flood is a surge wave of height (H_s), celerity (c) and inflow rate (q_s) approaching a hemispherical block of radius (R). The goal of this simulation is limited but specific. The flow structure around the block is determined from the numerical solution of the shallow-water equations. The pressure on the block is integrated to find the wave force for a range of surge-wave Froude number from $Fr_S = 0.1$ to 2, the radius-to-depth ratio from R/H = 0.2 to 0.8 and the channel width-to-diameter ratio $W/2R$ = 2 to 8. The results are the introduction of a wave-force coefficient and the correlation of the coefficient with the surge-wave Froude number.

Figure 1. Subcritical-supercritical-subcritical transition in a mountain stream on a steep slope. Gravels and rocks are immobile most of the time, but may become mobile during the flood stage.

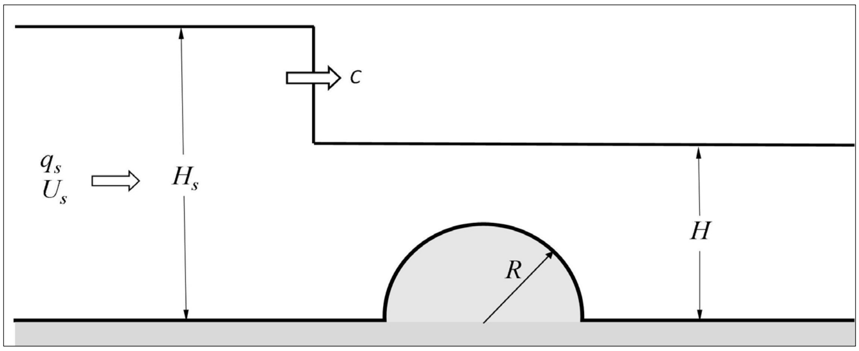

Figure 2. The surge wave of height (H_s) and celerity (c) produced by the flooding flow rate (q_s) approaching a hemispherical block of radius (R).

2 FORMULATION

The direct simulation for the water depth (*h*), the velocity components (*u, v*), and the discharge components (*qx, qy*) = (*uh, vh*) of the flow and the waves around the block is obtained as numerical solutions of the shallow water equations:

$$\frac{\partial h}{\partial t}+\frac{\partial q_x}{\partial x}+\frac{\partial q_y}{\partial y}=0 \qquad [1]$$

$$\frac{\partial q_x}{\partial t}+\frac{\partial}{\partial x}\left(\frac{q_x\,q_x}{h}\right)+\frac{\partial}{\partial y}\left(\frac{q_x\,q_y}{h}\right)=-gh\frac{\partial(h+z_o)}{\partial x} \qquad [2]$$

$$\frac{\partial q_y}{\partial t}+\frac{\partial}{\partial x}\left(\frac{q_y\,q_x}{h}\right)+\frac{\partial}{\partial y}\left(\frac{q_y\,q_y}{h}\right)=-gh\frac{\partial(h+z_o)}{\partial y} \qquad [3]$$

where g is gravity and z_o is the elevation of channel bottom elevation. The finite-volume approximation of the shallow-water equations is implemented on a staggered grid. The flux-limiting scheme MINMOD is used to suppress overshot and undershot across any sharp discontinuity such as the hydraulic jump as the flow changes from supercritical to subcritical state. The fluxes are modified in the MINMOD flux limiting scheme by lowering the order using the first-order upwind (FOU) scheme to gain computational stability. A fourth-order Runge-Kutta method estimates the advancement in time. The numerical method for the implementation on a staggered grid was described by Karimpour and Chu (2014; 2015; 2016).

The simulation starts with an inflow discharge (q_s). This produces a surge of height (H_s) and celerity (c) of surge wave front. Undisturbed downstream depth of submergence, *H*, is set from f 1.25*R* to 5*R*, at *t* = 0s. The results presented in this paper were obtained using the grid size of $\Delta x/R = \Delta y/R = 0.1$. The length of the channel relative to the diameter of the hemisphere is $L/2R = 40$. Our grid-refinement study shows the wave force obtained have a better than 1% accuracy.

3 THE UNSTEADY SUBCRITICAL AND SUPERCRITICAL FLOW

Figures 3 gives the height (H_s), the velocity (U_s) and the celerity (c) of the surge wave as a function of the surge-wave Froude number (Fr_S) before the arrival of the surge wave impacted on the hemispherical block. The definition of the surge-wave Froude number base on the height and velocity of the surge is:

$$\mathrm{Fr_s} = \frac{q_s}{\sqrt{gH_s^3}} \qquad [4]$$

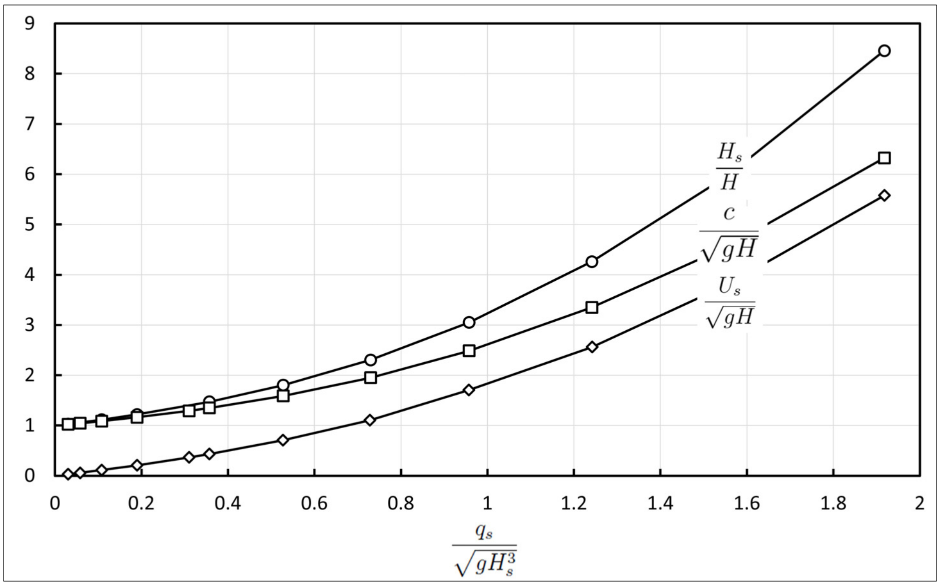

Figure 3. The height, the velocity and the celerity of the surge wave before the impact of the wave on the hemispherical block.

Figures 4, 5 and 6 show the flow for the surge-wave Froude number $\mathrm{Fr_s}$ = 1.2, 0.8 and 0.4, respectively. The (a), (b) and (c) parts of these figures shows the flow at the instant when the force on the hemispherical block reaches a peak value at time $t = t_p$. The (c) (d) and (f) parts show the flow at a later time when $t = t_p + 8R/U_S$. In parts (a) and (c) of the figures, the color of red defines the supercritical flow when the local Froude-number (Fr) is greater than unity and the color of blue defines when the local flow the subcritical flow. The local Froude number is defined by the local velocity and the local depth of the flow as follow:

$$Fr = \sqrt{\frac{u^2 + v^2}{gh}} \qquad [5]$$

The flow is shown at two instants of time in Figures 4, 5 and 6, at time $t = t_p$ and at the later time $t = t_p + 8R/U_S$. For $\mathrm{Fr_s}$ = 1.2 and R/H = 0.5, the flow shown in Figure 4 (a), (b) and (c) is supercritical only in the upstream at time $t = t_p$ while the entire flow is supercritical at the later time $t = t_p + 8R/U_S$. This flow pattern for $\mathrm{Fr_S}$ = 1.2 in Figure 4 is to compare with the flow in Figures 5 and 6 where the flow is subcritical upstream. There is a depression in the depth of water behind the block and a corresponding increase in local Froude number. The variability in space produces the pressure difference between the front and back of the hemisphere. The force on the hemisphere is obtained by integration of the pressure over the surface as the flow around the sphere is changing rapidly with time. The flow at high surge-wave Froude number is characterized by rapid change in depth from supercritical flow to subcritical flow through the discontinuity across the hydraulic jump. Forces are evaluated from the simulations to find the wave-force coefficients and then correlate the coefficient with the surge-wave Froude numbers. The forces reach their peak value at time $t = t_p$. The nearly quasi-steady states occur at a later time when $t = t_p + 8R/U_S$.

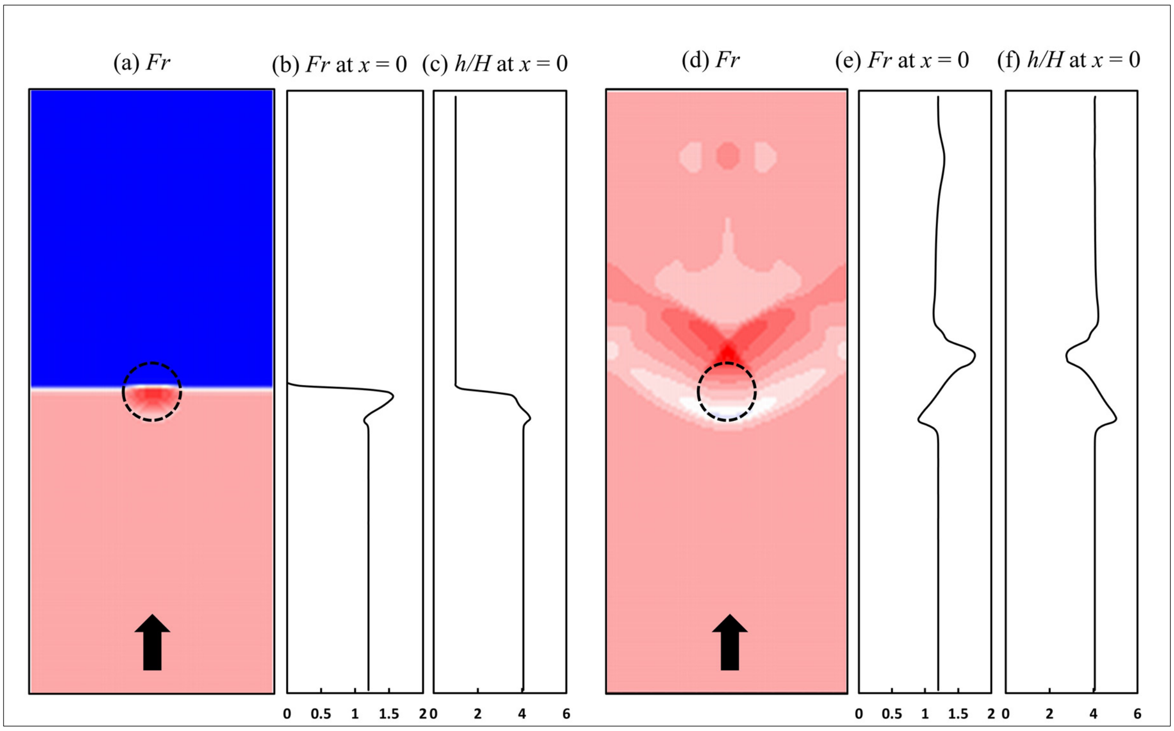

Figure 4. The Froude-number and depth profiles for the surge-wave Froude number of Fr_S = 1.2 and the hemispherical block of radius, *R/H* = 0.5. (a) Froude-number (*Fr*) contour, (b) center plane *Fr* profile and (c) center plane depth (*h*) profile when the wave force on the block reaches its peak at time at time $t = t_p$; (d) Froude-number (*Fr*) contour, (e) center plane *Fr* profile, and (f) center plane depth (*h*) profile as the wave force on the hemispherical block reaches a quasi-steady state at time $t = t_p + 8R/U_S$. The arrows in (a) and (b) show the flow direction. The contours show the subcritical flood flow in blue and the supercritical flow in red.

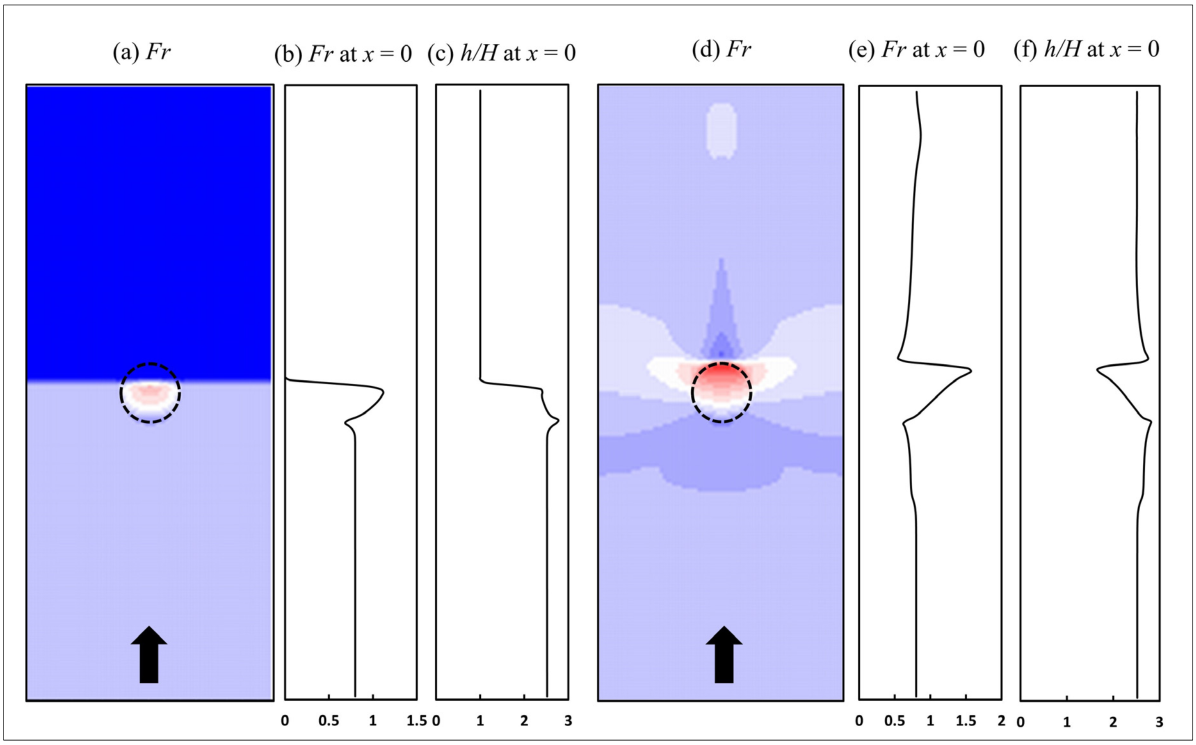

Figure 5. The Froude-number and depth profiles for the surge-wave Froude number, Fr_S = 0.8 and the hemispherical block of radius, *R/H* = 0.5. Captions for (a), (b), (c), (d), (e), and (f) are the same as Figure 4.

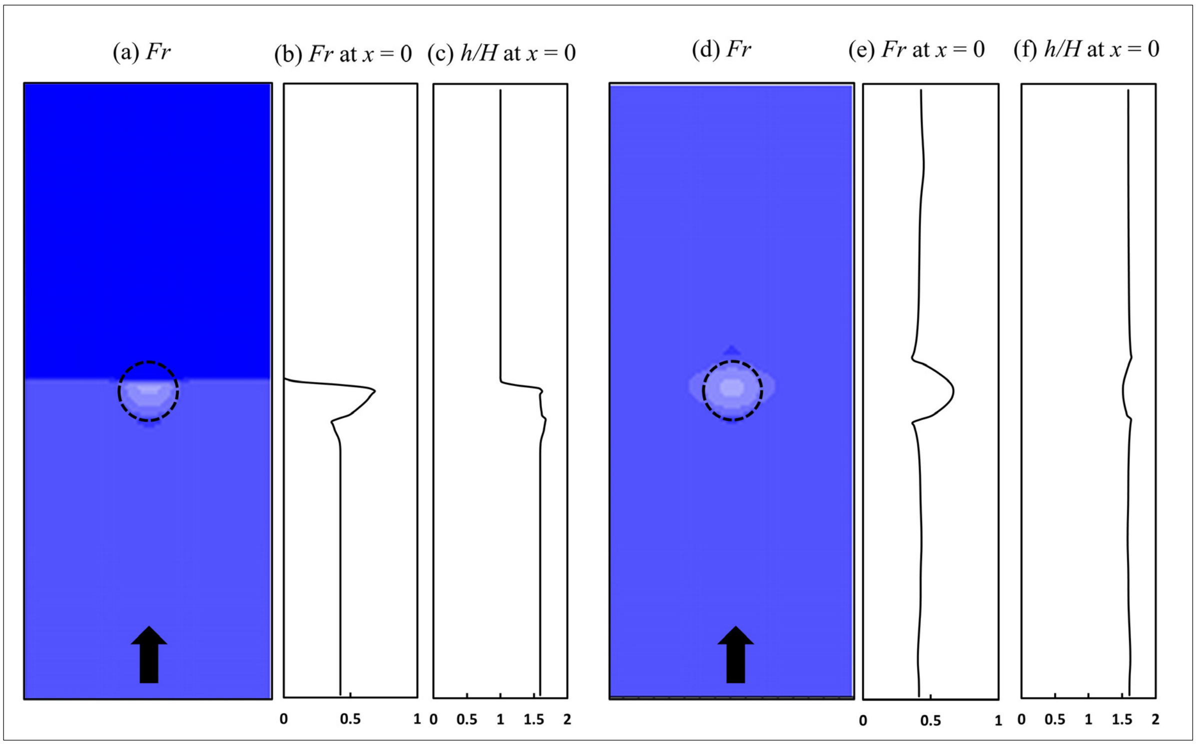

Figure 6. The Froude-number and depth profiles for the surge-wave Froude number, Fr_S = 0.4 and the hemispherical block of radius, *R/H* = 0.5. Captions for (a), (b), (c), (d), (e), and (f) are the same as Figure 4.

4 WAVE FORCE AND WAVE-DRAG COEFFICIENT

The difference in the pressure between the flow upstream and the flow downstream gives rise to a wave force on the block. The integration of the pressure over the surface is carried out in the polar coordinate shown in Figure 7. The wave force in the longitudinal direction, *i.e.,* flow direction, is:

$$F_W = \int_0^{\frac{\pi}{2}} \int_0^{2\pi} \rho g h R^2 \cos\alpha \sin\alpha \cos\beta \, d\beta \, d\alpha \quad [6]$$

The corresponding wave-force coefficient is:

$$C_{WF} = \frac{F_W}{\rho g A_S (H_S - H)} \quad [7]$$

where $A_s = ½\,\pi R^2$ is the frontal projection area of the hemisphere. The wave-force coefficient is a dimensionless parameter associated with the gravity. This is in contrast to the drag coefficient below defined by the stagnation pressure:

$$C_D = \frac{F_W}{\frac{1}{2}\rho {U_S}^2 A_S} \quad [8]$$

The wave force rises to a peak shortly after the arrival of the surge wave and then drops to a quasi-steady state over a period of time from $tU_S/2R$ = 2 to 3. Figure 8 shows the variation of the wave-force coefficient (C_{WF}) with the dimensionless time $tU_S/2R$. The rise of the force on the hemisphere to a peak value occurs shortly after the arrival of the surge wave front. The force then drops sharply to a minimum at time $t = t_m$. The flow can be considered to reach approximately a quasi-steady state at time $t = t_p + 8R/U_S$. Figure 9 shows the duration of the force from the time of occurrence of the peak $t = t_p$ to the time of the force minimum $t = t_m$. The peak wave-force coefficient is relatively constant. The duration of the force increases with the surge-wave Froude number. The impulse on the gravels and rocks is the integration of the wave force over the period of time from $t = t_p$ to $t = t_m$.

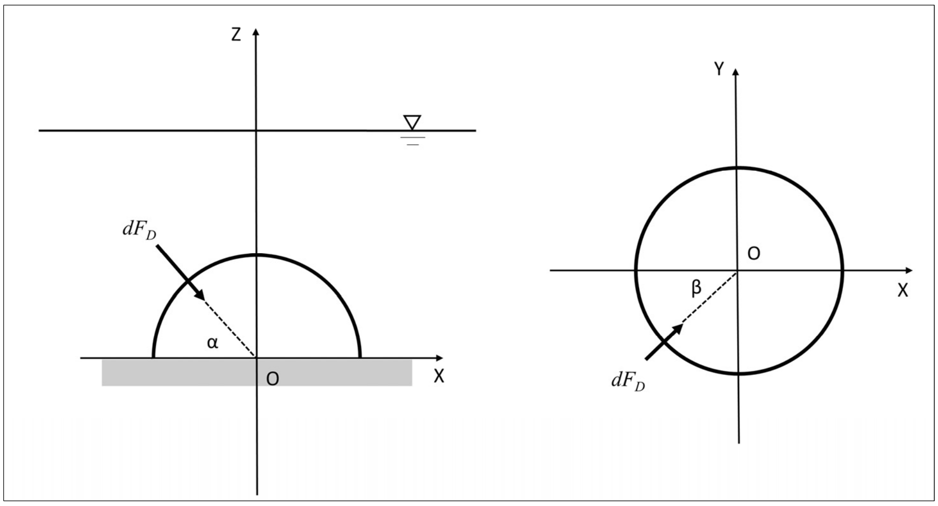

Figure 7. The integration of the pressure on the surface of the hemispherical block in the polar coordinate for the force on the block.

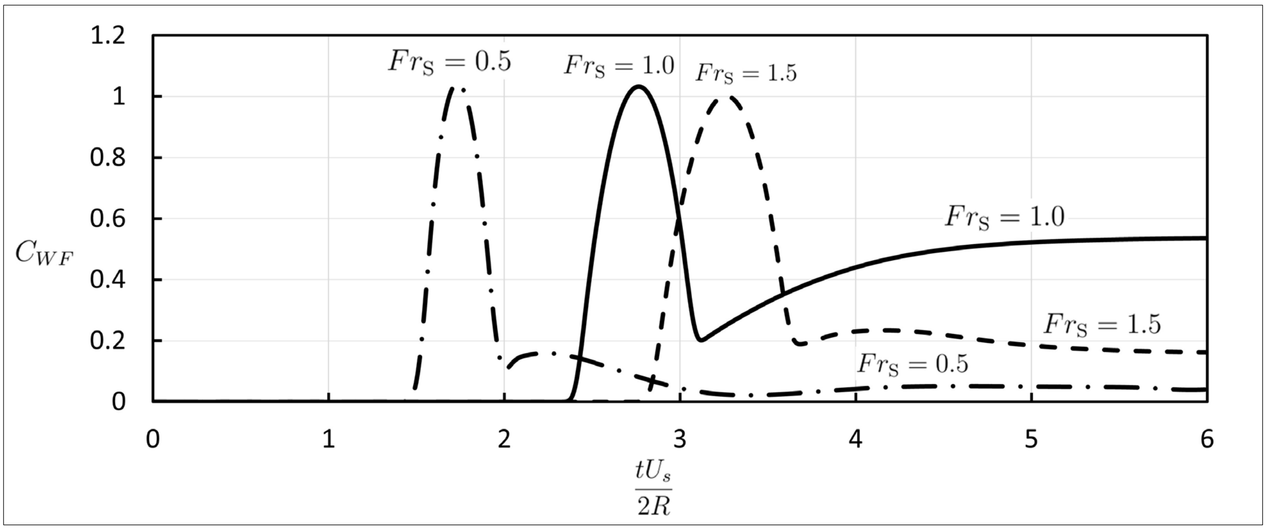

Figure 8. The time-dependent variation of the wave-force coefficient (C_{WF}) with the dimensionless time $tU_S/2R$ for R/H = 0.5. The wave-force data are for the surge-wave Froude number of Fr_S = 0.5, 1.0 and 1.5.

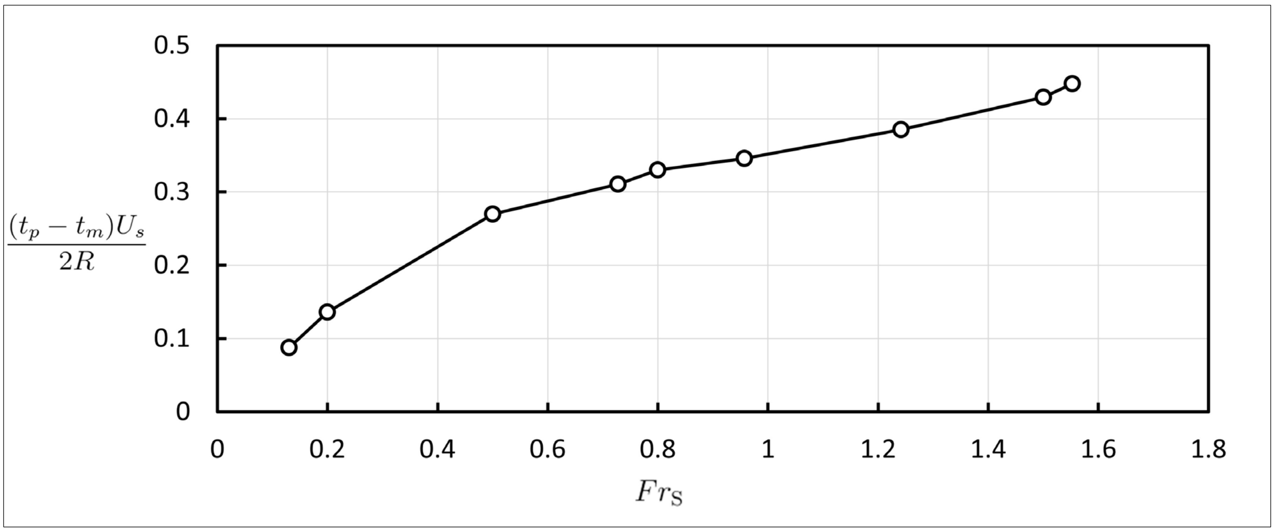

Figure 9. The time lapse between the arrival of the force peak at time $t = t_p$ and $t = t_m$, when the force declines from the peak to a minimum value.

5 THE WAVE-FORCE COEFFICIENT VERSUS THE DRAG COEFFICIENT

The numerical simulations are conducted for very different depth of the submergence. The depth of water is five times greater than the radius of the hemisphere in one case with *R/H* = 0.2 and is nearly the same as the radius in the other case with *R/H* = 0.8. Despite the difference in the depth of the submergence, the wave-force coefficient for *R/H* = 0.2, 0.5 and 0.8 is remarkably constant and is relatively independent of the surge-wave number (Fr_s), as shown in Figure 10. The value of C_{WDp} is varying from 1.1 to 1.0 in the range of surge-wave Froude number from Fr_S = 0.1 to 2.0 for the radius-to-depth ratio, *R/H* = 0.2, 0.5 and 0.8. The wave-drag coefficient should be therefore considered as the universal dimensionless parameter for the flood wave force. This drag coefficient, on the other hand, is highly dependent on surge-wave Froude Number. The variation of the drag coefficient with the Froude number is remarkable. As shown in Figure 11, over the range of the surge-wave Froude number, Fr_S = 0.1 to 2.0, the value of the drag coefficient drops from C_{Dp} = 16 to 0.5, respectively. The force on the hemispheric block in shallow waters is due to the waves. The force associated with the formation of the vortex in the wake behind the block is negligible by comparison. Without the waves, the typical value of the drag coefficient would be $C_D \approx 1$.

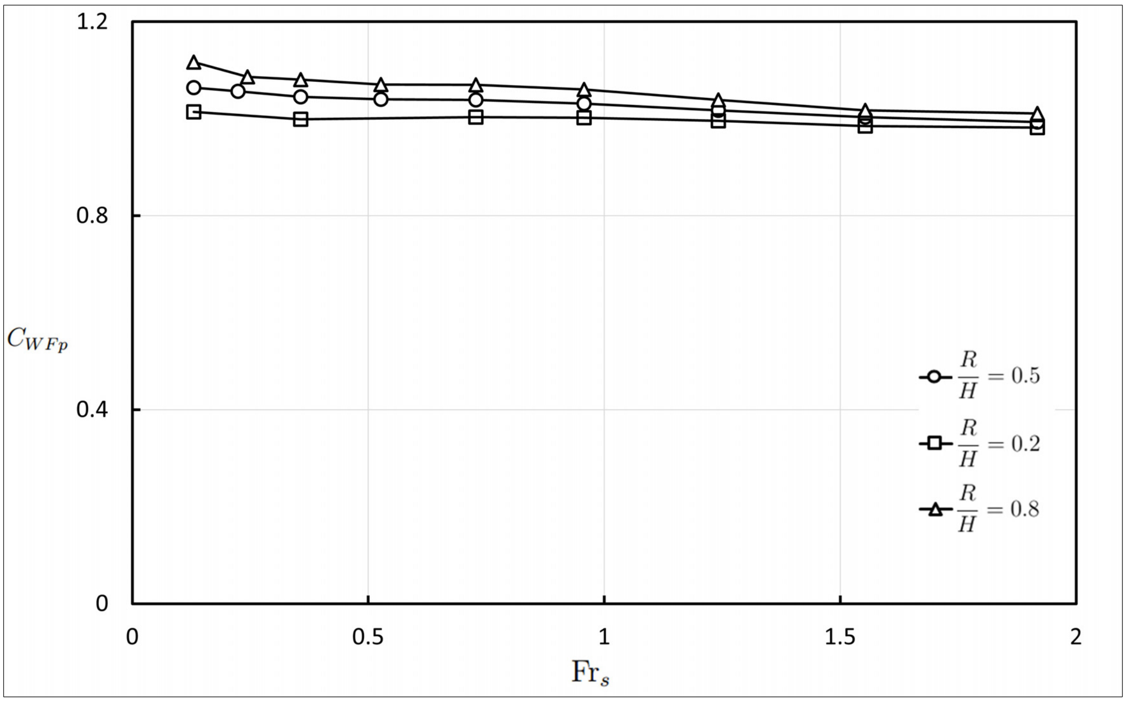

Figure 10. Peak wave-force coefficient at time $t = t_p$ and its dependent on the surge-wave Froude number. The square, the circle, and the triangle symbols denote the correlation for the radius-to-depth ratio, *R/H* = 0.2, 0.5 and 0.8, respectively.

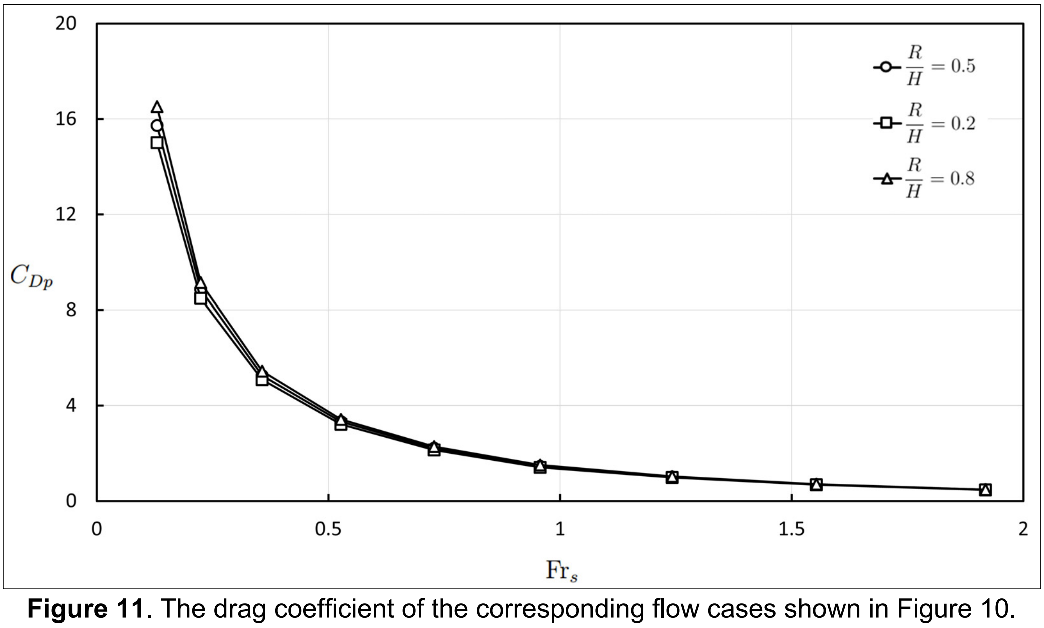

Figure 11. The drag coefficient of the corresponding flow cases shown in Figure 10.

6 CRITICAL DISCHARGE FOR MOBILITY OF GRAVELS AND ROCKS

One method to determine the mobility of the hemispherical block is to find the moment of force about the downstream edge of the block as shown in the inset of Figure 12. The critical moment of force is the balancing of the submerged weight with the force on the block. The contribution due to the submerged weight is:

$$\mathrm{M}_{\mathrm{Wcritical}} = (\rho_s - \rho) g \frac{2}{3} \pi R^4 \qquad [9]$$

This gives a critical value of $\mathrm{M}_{\mathrm{Wcritical}}/(\rho g R^4) = 3.35$ for the tipping over of the block. The moment of the wave force from the simulation is the integration of the pressure over the surface of the block:

$$\mathrm{M}_W = \int_0^{\frac{\pi}{2}} \int_0^{2\pi} \rho g h R^3 \cos\alpha \sin^2\alpha \cos\beta \, d\beta \, d\alpha \qquad [10]$$

Figure 12 shows the dimensionless correlation of this moment of the wave force obtained from the simulation with the discharge coefficient. The simulation results for the three submergence ratios with R/H = 0.2, 0.5 and 0.8 fall essentially onto the same curve. The critical value of $\mathrm{M}_{\mathrm{Wcritical}}/(\rho g R^4) = 3.35$ is obtained from Eq. [9] by letting the specific weight of the sediment, $\rho_s/\rho = 2.6$. This critical value is marked as the dashed line in the figure. The intersection of the dashed line with the solid lines in the figure gives critical discharge coefficient varying from $q_{\mathrm{critical}} / \sqrt{g R_s^{\,3}} \cong 20$ to 21.5. With this critical value, the critical discharge for the tipping over of the hemispheric rock is given in Figure 13 to depend on the size of the rock, R. A similar derivation for the sliding of the block would give the critical wave force to be $F_{\mathrm{Wcritical}}/(\rho g R^3) = 3.35\,\mu$ relating the force to the coefficient of sliding friction, μ. A sliding friction coefficient of μ = 2.4 would give the same critical discharge as the situation of tipping over. In reality, however, the sliding friction coefficient is unlikely to be greater than 0.5. Therefore, sliding would be the most likely mode of motion for the hemispherical block. By taking the sliding coefficient, μ = 0.5, the critical discharges of sliding of the hemispheric block as a function of the block radius are plotted in Figure 14. According to Figure 14, the hemispherical block of 0.4m radius, for example, would slide with the flow if the discharge exceeds the critical value of about 3.5m^2/s. The hemispherical block of 0.8m radius, for example, would slide with the flow if the discharge exceeds the critical value of about 9.3m^2/s. The critical discharge is sensitive to the value of the coefficient of the sliding friction. It also depends on the shape of the gravels and rocks. The concept of the critical discharge nevertheless is a significant extension of the classical method of Shields. The concept will set the goal of the future numerical and laboratory investigations. The mobility of the gravels and rock therefore will be decided in these future investigations by the critical discharge rather than the critical stress.

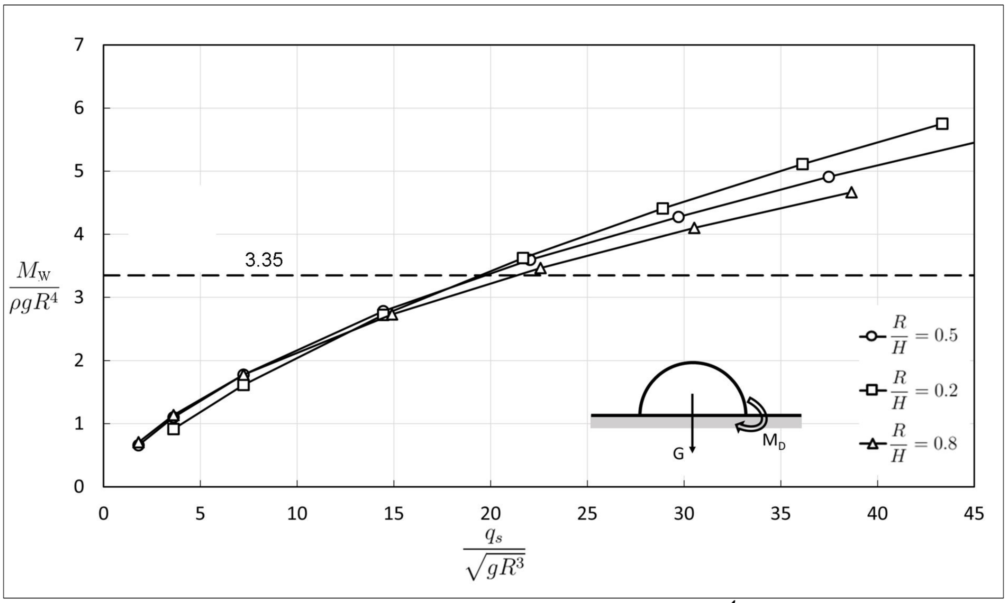

Figure 12. Dimensionless moment of wave force, $M_W/\rho g R^4$ as a function of the discharge coefficient, $q_s/(gR^3)^{1/2}$. The rectangular symbol, circular symbol, and triangular symbol denote the submergence of R/H = 0.2,0.5 and 0.8, respectively. The dashed line defines the critical moment of the force, $M_{W\mathrm{critical}}/\rho g R^4 = 3.35$.

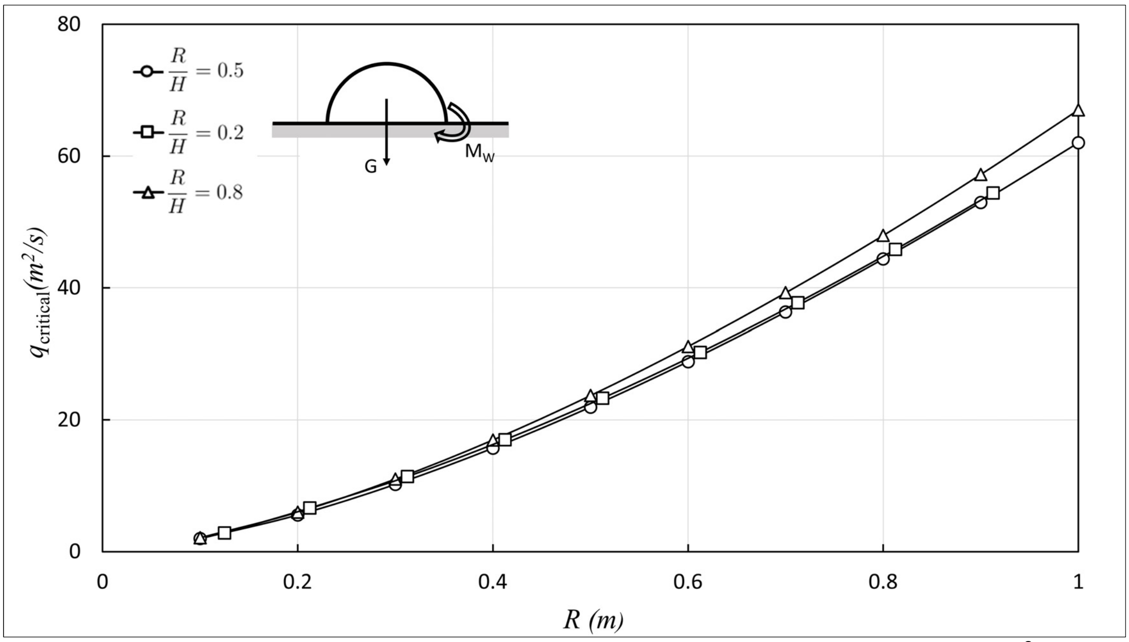

Figure 13. The critical discharges for tipping over of the hemispherical block, $q_{critical}$ (m^2/s) as a function of the radius, *R* (m). The submergence of *R/H* = 0.2, 0.5 and 0.8 are denoted by the square, circle and triangle symbols, respectively.

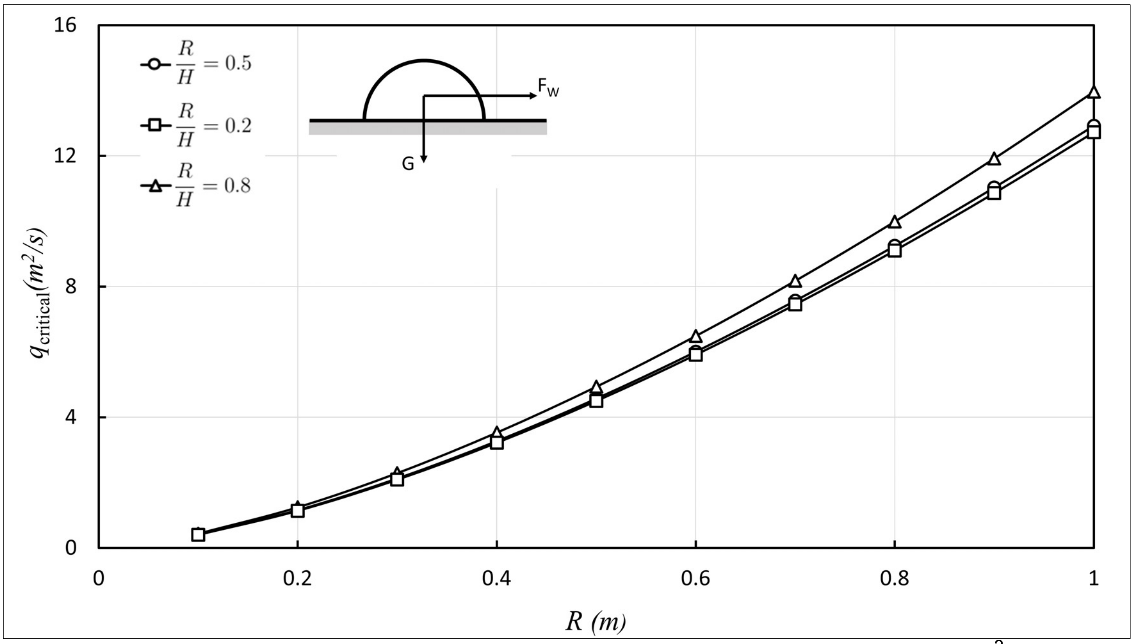

Figure 14. The critical discharges for sliding of the hemispherical block, $q_{critical}$ (m^2/s) as a function of the radius, *R* (m) if the coefficient of the slide friction is μ = 0.5. The submergence of *R/H* = 0.2, 0.5 and 0.8 are denoted by the square, circle and triangle symbols, respectively.

7 CONCLUSIONS

The wave force produced by the surge waves on a hemispherical block is determined for a range of surge-wave Froude number from Fr_s = 0.1 to 2.0. The wave force rises to a peak value and lasts for a period of time before dropping onto a quasi-steady value. The wave-force coefficient (C_{WF}) is introduced to correlate the wave force with a surge-wave Froude number (Fr_s). The peak value of the wave-force coefficient is relatively constant varying from $C_{WFp} \approx 1.1$ to 1.0 for the range of surge-wave Froude number from Fr_s = 0.1 to 2.0. The corresponding drag coefficient, however, is over a very wide range of value from $C_{Dp} \approx 16$ to 1. The value of $C_{Dp} \approx 16$ for the case of small Froude number of Fr_s = 0.1 is many times greater than the typical value of one. The significance of the waves clearly is not negligible even in the limiting case when the surge-wave Froude number is very small. This result is not obvious but is significant. It shows that the wave force calculated by the conventional simulation model based on rigid-lid approximation is not correct under any circumstance.

The present simulation for the idealized hemispheric block also introduced the critical discharge for the mobility of the sediment as an extension of the classical method of the critical stress by Shields (1936). The existence of the critical discharge is conceptually significant. The specific of the critical discharge for the individual or the cluster of gravels and rocks of different sizes and shapes may be determined by either numerical simulation or laboratory experiment.

REFERENCES

Bathurst, J.C., Graf, W.H. & Cao, H.H. (1987). Bed Load Discharge Equations for Steep Mountain Rivers, in *Sediment Transport in Gravel-Bed Rivers*, edited by Thorne, C.R., Bathurst, J.C. & Hey, R.D., 453–491, John Wiley, New York.

Prancevic, J.P., Lamb, M.P. & Fuller, B.M. (2014). Incipient Sediment Motion across the River to Debris-Flow Transition. *Geology*, 42(3), 191-194.

Karimpour Ghannadi, S. & Chu, V.H. (2015) High-Order Interpolation Schemes for Shear Instability Simulations. *International Journal of Numerical Methods for Heat & Fluid Flow*, 25(6), 1340-1360.

Karimpour Ghannadi, S. & Chu, V.H. (2016). Instability of Unbounded Transverse Mixing Layer in Shallow Waters. *Canadian Journal of Civil Engineering*, 43(6), 504-510.

Karimpour Ghannadi, S. & Chu, V.H. (2014). Transverse Dam-Break Waves. *Journal of Fluid Mechanics*, 758, 12.

Recking, A. (2009). Theoretical Development on the Effects of Changing Flow Hydraulics on Incipient Bed Load Motion. *Water Resour. Res.*, 45(4), 16.

Schneider, J.M., Rickenmann, D., Turowski, J.M., Schmid, B. & Kirchner, J.W. (2016). Bed Load Transport in a Very Steep Mountain Stream (Riedbach, Switzerland): Measurement and Prediction. *Water Resour. Res.*, 52(12), 20.

Ma, H., Heyman, J., Fu, X., Mettra, F., Ancey, C. & Parker, G. (2014), Bed Load Transport over a Broad Range of Timescales: Determination of Three Regimes of Fluctuations. *J. Geophys. Res. Earth Surf.*, 119(12), 2653–2673.

Shields, A. (1936). Anwendung der Ähnlichkeitsmechanik und der Turbulenzforschung auf die Geschiebebewegung: Mitteilungen der Preußischen Versuchsanstalt für Wasserbau und Schiffbau, Heft 26, Berlin, Germany (in German). English translation by Ott, W.P. & van Uchelen, J.C. available as Hydrodynamics Laboratory Publication No. 167, Hydrodynamics Lab., California Institute of Technology, Pasadena, California, p.1–36.

Yang, C.T. (1996). *Sediment Transport: Theory and Practice*. McGraw-Hill, New York.

Proceedings of the 37th IAHR World Congress
August 13 – 18, 2017, Kuala Lumpur, Malaysia

PRESSURE MANAGEMENT OF WATER DISTRIBUTION NETWORKS FOR INCREASING WATER AVAILABILITY AND DECREASING WATER LOSS

FARHAD YAZDANDOOST(1) & ARDALAN IZADI(2)

(1,2) Department of Civil Engineering, K. N. Toosi University of Technology, Tehran, Iran
yazdandoost@kntu.ac.ir; a.izadi@mail.kntu.ac.ir

ABSTRACT

Pressure Management (PM), as a key strategy for reducing water distribution networks leakage and water demand management (WDN) has commonly been a practical point of attention. While the effects of PM on the performance of WDNs have received enough attention from academics, it is often nominated as the earliest and the most practical approach in many water utilities to reduce water leakage and manage demand. Therefore, managing WDNs pressure, in a manner that can optimise water leakage while ensuring consumer demands, is an important goal. In this study, implementing PM in a WDN located near the southwest of the City of Isfahan, Iran is considered as the case study. While this network has high daily average pressure head, it suffers from high rate of leakage and unmet desired water demands. Different scenarios of PM at inlet of network are proposed and evaluated based on two objectives namely; the total WDN's water leakage and the system's water availability. Pressure Dependent Demand and Integrated Model for evaluating losses are used to simulate water consumption and pipe water leakage respectively. The results show that with minor modifications in the pressure at inlet of the network, the system's water availability and the leakage rate may be optimised. The more conformity is available between pressure variation and consumption pattern, the more advantages can be gained from PM practices.

Keywords: Water distribution network (WDN); pressure management (PM); leakage, availability.

1 INTRODUCTION

Nowadays, many international communities and countries have paid special attention to the problem of limited available water resources and presented various solutions or policies to deal with water shortages. One of these policies associated with Water Distribution Networks (WDNs), have especially focused on reduction of water losses. Pipe leakage, as the intrinsic feature of every WDN, can lead to significant amount of water losses. In fact, water leakage is nominated as one of the barriers for sustainable performance of WDNs (Puust, 2010). Generally, leakage of WDN is a function of available pressure head. In this regard, it can be stated that there is a physical relationship between leakage and pressure head in WDN (Gomes, 2011). During the last decades, several studies have been conducted in order to clarify this relationship. Consequently, some well-known theories and models have been developed during these studies. Some of these models, presently subject to wide usage, are described in Lambert (1994), May (1994), Tabesh et al. (2011), Gupta et al. (2016) and Islam (2011). Most of these researches showed that using Pressure Dependent Demand (PDD) has the best results in order to simulate water leakage (Germanopoulos, 1985; Martinez et al., 1999; Tabesh et al., 2011) and nodal consumptions. Furthermore, their results demonstrate that the more pressure head is available the more water loss can be observed. Pressure Management (PM) as one of the earliest approaches among Best Management Practices (BMPs) for reducing WDNs leakage has been a practical point of attention. Not exposing water utilities to additional costs, rapid effectiveness and its high efficiency for water loss reduction are the main incentives of using PM in WDNs. In earlier WDN literature, PM is usually associated with pressure reduction. However, if the reduced pressure head becomes less than the desired pressure head, the desired water demand and water availability cannot be sustained.

Therefore, PM not only can manage leakage but also has indisputable role in demand management of WDN (Vicente et al., 2015). In other words, determining the minimum required pressure in order to provide customer demands (with suitable quantity and quality) is the most essential factor in appropriate operation of WDN. Therefore, whenever the PM is used as a policy to manage WDN leakage and consumption, this question is revealed that, what is the best acceptable condition of PM, which can optimise water leakage while preserving consumer rights. In this study, implementing PM in a WDN located near the southwest of the City of Isfahan-Iran was considered as the case study. While this network has high daily average pressure head, it suffers from high rate of leakage and unmet desired water demand. Therefore, to remediate these problems and achieve a balance between objectives (maximizing water availability and minimizing water leakage) in the study area, the final course of PM was selected as the main goal of this study.

2 METHODOLOGY

Aiming to achieve the most suitable PM conditions in the study area, many different scenarios for time pressure variation at inlet of the WDN were investigated. These scenarios are modelled by using a combination of intelligent Pressure Reducing Valve (PRV) and a Pump to create different time series of pressure at inlet of the network. It is worth noting that, each suggested scenario must satisfy the minimum required pressure head in the network. The suitability of each proposed scenario for the WDN is judged based on two identified indices; the total WDN's water leakage and the system's water availability. Here, the system water availability is considered as the ratio of the total supplied water demand to the total desired water demand during the day. The system water availability is calculated based on nodal water availability calculated for all the system nodes (equations 1 and 2). The amount of supplied water demand for each node was simulated with the Pressure Dependent Demand model. For assessing the system's water leakage distribution, the integrated model of evaluating water losses (Tabesh et al., 2009) in WDNs was used. Brief description of each these of the two models are presented as follows. It is worth noting that the analyses were performed using a developed MATLAB code incorporated within the EPANET toolkit.

$$AV_{node\ i} = \frac{\sum_{t=1}^{t=T} Q_{i,t,sup}}{\sum_{t=1}^{t=T} Q_{i,t,req}} \qquad [1]$$

$$AV_{sys} = \frac{\sum_{t=1}^{t=T} \sum_{i=1}^{i=N} Q_{i,t,sup}}{\sum_{t=1}^{t=T} \sum_{i=1}^{i=N} Q_{i,t,req}} \qquad [2]$$

Where AV_{node} and AV_{sys} is availability of node and system respectively. Q_{sup} and Q_{req} is the supplied and required water demand in each time step (t) and each node (i). N is the number of nodal junction and T is the total duration of analysis.

2.1 Pressure Dependent Demand

There are many methods for assessing actual nodal consumption in WDN literatures. Among them, Pressure Dependent Demand (PDD) modelling is one of the most prevalent method in which it is supposed that nodal water consumption is a function of nodal available pressure head. When the nodal pressure head is equal or greater than the reference pressure head, the nodal water demand can be supplied completely. Otherwise, nodal water consumption will not be satisfied. Here the relationship between nodal pressure and demand proposed by Wagner (1988) is used according to equation 3.

$$\begin{cases} Actual\ Demand = Nodal\ Demand & if \quad CPH \geq RPH \\ Actual\ Demand = Nodal\ Demand \times \left(\dfrac{CPH - MPH}{RPH - MPH}\right)^{0.5} & if \quad MPH < CPH < RPH \\ Actual\ Demand = 0 & if \quad CPH \leq MPH \end{cases} \qquad [3]$$

In which, Actual Demand is the actual supplied nodal consumption obtained from PDD modelling, Nodal Demand is the base required demand for nodal consumption. CPH, RPH and MPH are Calculated EPANET Pressure Head, Local Reference/desired Pressure Head (18 m) and Minimum Pressure Head (0 m) respectively.

2.2 Integrated Model for pipe leakage

This proposed model provides the advantage of integrating nodal and pipe leakages where the amount of nodal leakage is initially assumed and then this amount of water leaks through the many hypothetical orifices located on the pipe length. The pressure of all orifices in half part of the pipe is equal to the pressure of upstream node and the leakage from other orifices is related to the pressure of downstream node. Having the estimated network leakage rates, the proposed procedure can lead the simulation to converge to the calibrated hydraulic model in which the amount of pipe leakage can be determined as equation 4.

$$Q_{L,ij} = Q_{L,i} \times \frac{L_{ij}}{\sum L_i} + Q_{L,j} \times \frac{L_{ij}}{\sum L_j} \qquad [4]$$

Where, $Q_{L,ij}$ is the leakage of pipe ij. $Q_{L,i}$ and $Q_{L,j}$ are the nodal leakage rates and L_i and L_j are the total pipe lengths connected to nodes i and j, respectively. For the sake of brevity, more details on proposed procedure of evaluating Integrated Model for losses can be found in Tabesh et al. (2009).

3 CASE STUDY

The existing WDN of the city, aged more than 30 years, serving a population of around 20000 people comprising three municipal districts (Figure 1) is selected here as the study area. This network is located near the southwest of Isfahan City. The water demands of city are supplied through four reservoirs with constant water level. Based on the local regulation, the minimum pressure head that must be satisfied in network is 18 m. Table 1 represents some relevant data of the study network in a condensed format.

Table 1. Some important data of the study network.

Type of Data	Quantity
Average Pressure Head	40 (m)
Minimum Night Flow (MNF)	13 (lit/s)
Minimum Night Uses	2.6 (lit/s)
Maximum Hourly Consumption Factor	1.45 (at 14 PM)
Minimum Hourly Consumption Factor	0.32 (at 4 AM)
Daily Water Supplied	3359 (M^3)
Daily Water Demand	3525 (M^3)
Estimated Water Losses (Pipe Leakage)	12.66 (%)

As seen in Table 1, in spite of high daily average pressures, instigating higher potentials for water consumption and leakage, daily pressure head seems insufficient to satisfy the desired pressure head (18 m) and consequently water demands in all areas of districts D and N. Therefore, the pressure management can be used as a key strategy in leakage and demand/consumption management (Karadirek, 2012) to face with these challenges and to address how study network can achieve its minimum leakage and maximum consumer water availability.

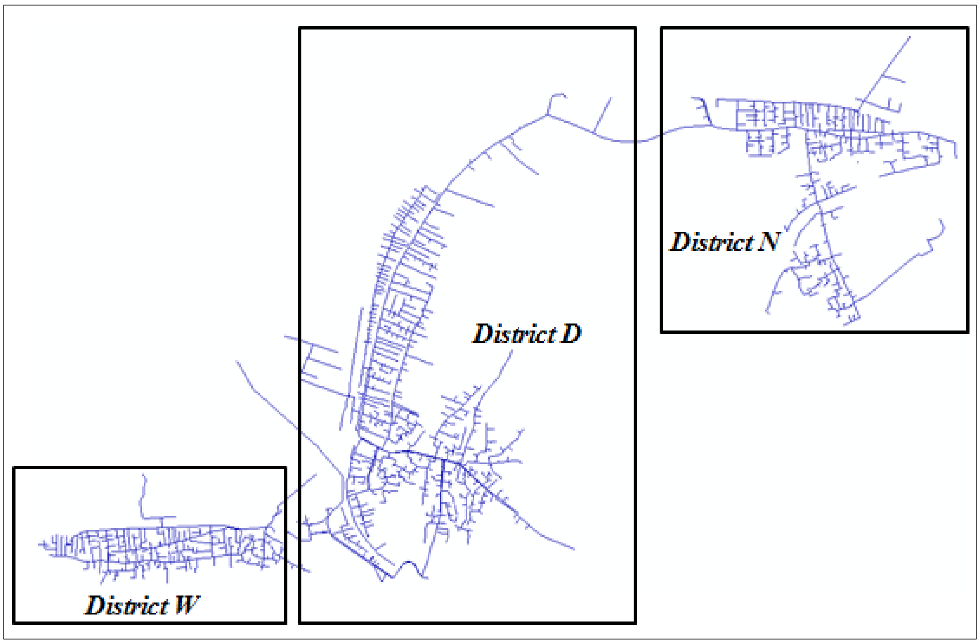

Figure 1. Study network layout with its three municipal districts.

4 RESULTS

4.1 Analysing current state of network

The results of the calibrated model show that, nodal demand in many parts of district D are faced with pressure deficits and consequently with water shortage between 09:00 and 21:00. On the contrary, between 22:00 and 08:00, all the nodal junctions in the network have high excess pressure head. Frequency distribution of pressure head for all the nodal junctions during the peak (14:00) and MNF hours are shown in Figure 2.

Based on figure 2, more than 13% of the nodal junctions in network are faced with a pressure less than the desired allowable pressure head (18 m) during the peak hours. In the worst nodal condition, there is a node accessing water only 14.74 hours during the day. Existence of more than 70 and 60 percent of nodal pressure heads greater than 40 m at MNF and peak hours respectively is the other noticeable fact in this figure. This amount of pressure is around twice (2 times) the desired pressure head. According to the obtained results, the least water availability of system (around 92%) is detected in 14:00. In addition, the highest water leakage rate (around 10.38 lit/s) is during the MNF hour. It is worth noting that, total water loss is computed around 12.2% indicating only about 3.6% error in computation of water losses. In the following the results of two different ideal scenarios planned to minimize water leakage (scenario 1) and maximise water availability (scenario 2) through PM, are discussed in details.

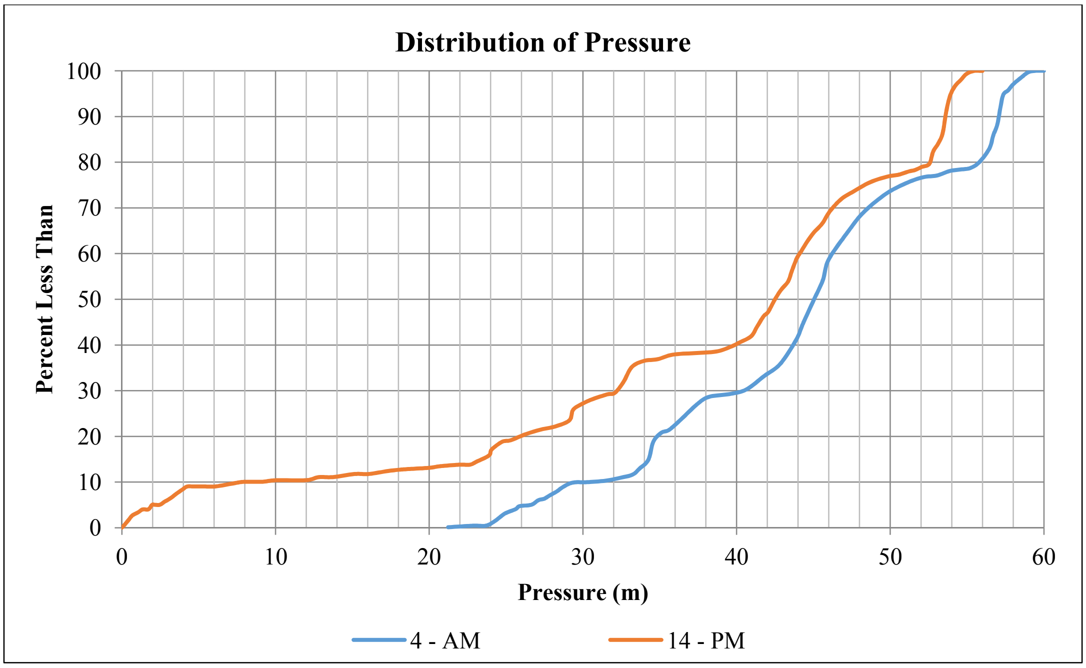

Figure 2. Frequency distribution of pressure head in network for peak and MNF hours.

4.2 Analysing PM at inlet of Network

In this stage, different scenarios of PM implemented through a combination of PRV and a pump at inlets of network were investigated. The results show that, setting the variation of pressure at the inlet of the network proportional to the consumption patterns can have the best results in practice. In other words, the inlet pressure must increase and decrease in peak and MNF hours respectively (according to the consumption pattern). Table 2 and Figure 3 present the comparison of the hourly leakage and average hourly pressure heads for two ideal proposed scenarios (the first one aimed at minimizing the leakage and the second one aimed at maximizing the water availability) with the current condition of the WDN respectively.

Table 2. Comparison of hourly leakage between 2 ideal proposed PM scenarios with current condition of network.

Hour	Hourly Leakage (l/s)			Hour	Hourly Leakage (l/s)		
	Scenario 1	Current State	Scenario 2		Scenario 1	Current State	Scenario 2
0-1	7.09	9.65	8.11	12-13	6.27	8.95	8.91
1-2	7.64	10.10	8.01	13-14	6.27	8.95	8.91
2-3	7.87	10.29	8.23	14-15	6.16	8.85	8.79
3-4	7.94	10.35	8.31	15-16	6.54	9.19	9.19
4-5	7.97	10.38	8.34	16-17	6.81	9.42	9.48
5-6	7.94	10.35	8.31	17-18	6.81	9.42	9.48
6-7	7.91	10.32	8.28	18-19	6.54	9.18	9.19
7-8	7.76	10.20	8.13	19-20	6.27	8.95	8.91
8-9	7.27	9.80	8.29	20-21	6.27	8.95	8.91
9-10	6.81	9.42	9.48	21-22	6.39	9.05	9.03
10-11	6.39	9.05	9.03	22-23	7.10	9.66	8.12
11-12	6.27	8.95	8.91	23-24	7.18	9.73	8.21

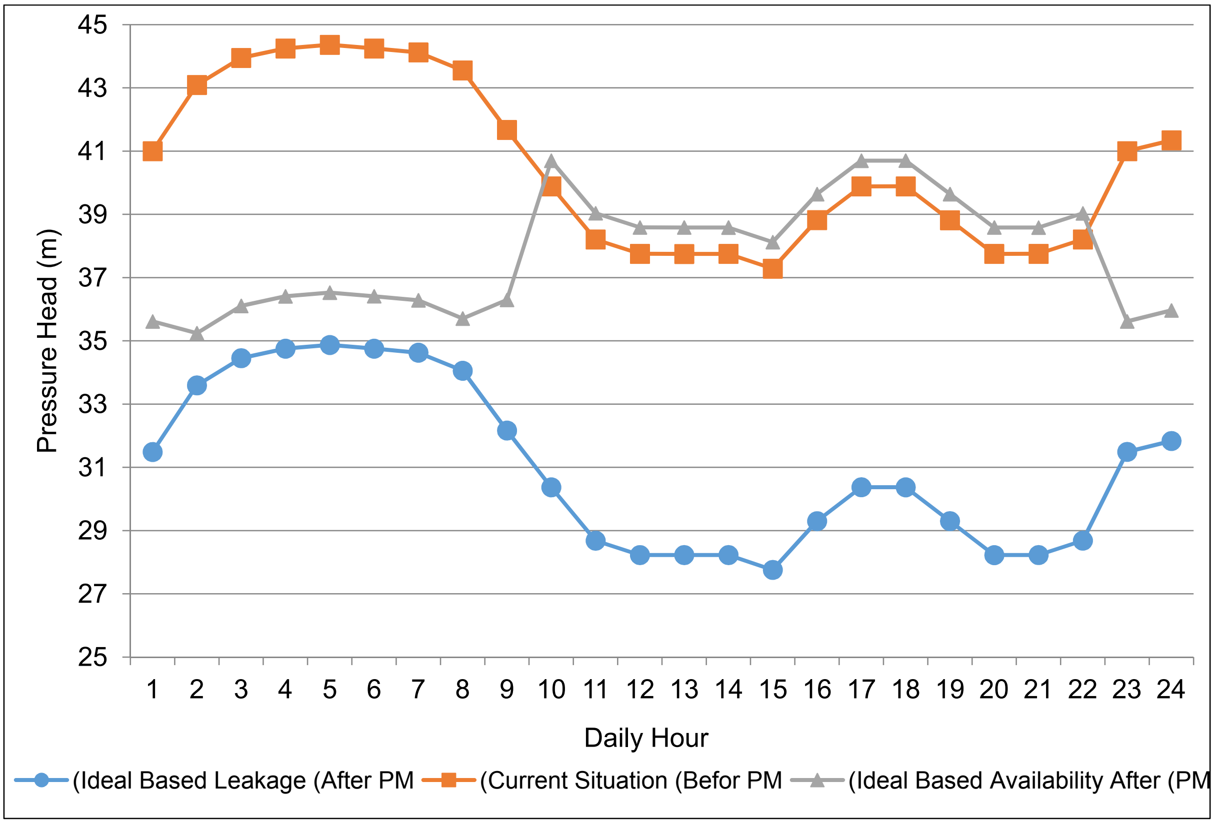

Figure 3. Comparison of average pressure head between 2 ideal proposed PM scenarios with current condition of network.

Examination of scenario 1 indicates that reducing the pressure head by about 23% would reduce the water loss by 24.5%. In this scenario, the maximum daily pressure head would be limited to 47 m and more than 90% of nodal junctions would have pressures less than 40 m at MNF hour. Furthermore, in this scenario system availability would increase up to 97.8%. Similarly, in scenario 2, a reduction of 7% in the pressure head would reduce water leakage by 6% while maximising the water availability (system availability is 100%). In this scenario, the maximum daily pressure (around 52 m) is higher than the scenario 1 and the current condition of network. This increase in pressure of network is due to extra pressure in providing head to ensure appropriate supplying of all the daily demands especially in peak hours. In this regards, the pressure head and consequently water leakage in scenario 2 would have higher amount than the current condition of network during 10:00 and 22:00. It is worth noting that, the hourly pressure head in scenario 2 has narrower domain of variation compared to the other PM conditions. This uniform distribution of pressure head in scenario 2, can provide better PM practices within the network in future. These results confirm that current condition of network with about 12.2% water leakage and 97.3% system availability is not acceptable in comparison with the proposed scenarios.

5 CONCLUSIONS

Existence of excess pressure head in Water Distribution Networks (WDNs) may usually lead to increase of mechanical failure, excessive water consumption, pipe leakage etc. Hence, Pressure Management (PM) can be nominated as one of the Best Management Practices in operation of WDNs. Using the EPANET software linked to a designed MATLAB code, Pressure Dependent Demand model for water consumption, and the Integrated Model for pipe water leakage, this study tried to evaluate effect of PM in performance of WDNs. The approach was examined for a network located in the southwest of Isfahan Province - Iran suffering from high rate of leakage, pressure deficits and consequently unmet demands. Different scenarios of PM were assessed to minimize leakage rate and to maximise the system's water availability. The results confirm that the best scenarios are the ones whose pressure variations are matched twith the consumption pattern. It may be further emphasised that the proper management of pressure in the network is rightly considered as one of the prerequisites for the proper performance of WDNs. In regards to the obtained results, designing District Metering Area (DMA) and implementing PRV within the network can be proposed as the further actions in the study area.

REFERENCES

Germanopoulos, G. (1985). A Technical Note on the Inclusion of Pressure Dependent Demand and Leakage Terms in Water Supply Network Models. *Civil Engineering Systems*, 2(3), 171-179.

Gomes, R., Sá Marques, A. & Sousa, J. (2011). Estimation of the Benefits Yielded by Pressure Management in Water Distribution Systems. *Urban Water Journal*, 8(2), 65-77.

Gupta, R., Nair, A.G.R. & Ormsbee, L. (2016). Leakage as Pressure-Driven Demand in Design of Water Distribution Networks. *Journal of Water Resources Planning and Management*, 142(6), 1-14.

Islam, M.S., Sadiq, R., Rodriguez, M.J., Francisque, A., Najjaran, H. & Hoorfar, M. (2011). Leakage Detection and Location in Water Distribution Systems using a Fuzzy-Based Methodology. *Urban water journal*, 8(6), 351-365.

Karadirek, I.E., Kara, S., Yilmaz, G., Muhammetoglu, A. & Muhammetoglu, H. (2012). Implementation of Hydraulic Modelling for Water-Loss Reduction through Pressure Management. *Water Resources Management*, 26(9), 2555-2568.

Lambert, A.O. (1994). Accounting for Losses: The Bursts and Background Concept. *Water and Environment Journal*, 8(2), 205-214.

Martinez, F., Conejos, P. & Vercher, J. (1999). Developing an Integrated Model for Water Distribution Systems Considering Both Distributed Leakage and Pressure-Dependent Demands. In *WRPMD'99: Preparing for the 21st Century*, 1-14.

May, J. (1994). Pressure Dependent Leakage. *World water environmental engineering*, 17(8), 10.

Puust, R., Kapelan, Z., Savic, D.A. & Koppel, T. (2010). A Review of Methods for Leakage Management in Pipe Networks. *Urban Water Journal*, 7(1), 25-45.

Tabesh, M., Jamasb, M. & Moeini, R. (2011). Calibration of Water Distribution Hydraulic Models: A Comparison between Pressure Dependent and Demand Driven Analyses. *Urban Water Journal*, 8(2), 93-102.

Tabesh, M., Yekta, A.A. & Burrows, R. (2009). An Integrated Model to Evaluate Losses in Water Distribution Systems. *Water Resources Management*, 23(3), 477-492.

Vicente, D.J., Garrote, L., Sánchez, R. & Santillán, D. (2015). Pressure Management in Water Distribution Systems: Current Status, Proposals, and Future Trends. *Journal of Water Resources Planning and Management*, 142(2), 1-13.

Wagner, J.M., Shamir, U. & Marks, D.H. (1988). Water Distribution Reliability: Simulation Methods. *Journal of Water Resources Planning and Management*, 114(3), 276-294.

Proceedings of the 37th IAHR World Congress
August 13 – 18, 2017, Kuala Lumpur, Malaysia

DEVELOPING NEW INDICES FOR ASSESING RESILIENCY IN WATER DISTRIBUTION NETWORKS

ROZA RANJBAR(1), ARDALAN IZADI(2) & FARHAD YAZDANDOOST(3)

(1,2,3) Department of Civil Engineering, Khajeh Nasir Toosi University of Technology, Tehran, Iran,
rranjbar@mail.kntu.ac.ir; a.izadi@mail.kntu.ac.ir; yazdandoost@kntu.ac.ir

ABSTRACT

Water Distribution Networks (WDNs), as one of the most vital infrastructures in cities, have been associated with many disruptive events, such as pipe breaks, damages, pipe leakages, inaccessibility and pressure deficits. Failure consequences in these networks may cause chaos in cities and expose citizens to significant risks. Resilient risk management is adopted here as a novel approach in minimizing the consequences of these events. Despite conventional assessment of resiliency in WDN, which are usually system-based, this study aims at introducing a new perspective for measuring resiliency of WDN, entitled Asset-Based. In this study, five new indices have been presented to cover insufficiency of the previous indices proposed for resiliency measurement of risks in a WDN. Herein, Graduality, Recovery Rate, Water Outage Time, Hydraulic Critical Index (HCI) and Regret Cost are the new identified resilient indexes measuring resiliency of each pipe asset due to the failure risk. The EPANET software linked to a designed MATLAB suit code, are employed here to assess proposed indices for a real case study suffering from high rate of pipe failure. The results show that the new indices can truly assess the asset's role in system resiliency. Thus, the consequences of failures and the priority of assets for facing with the disruptions can be better determined. Furthermore, the Water Outage Time and Regret Cost indices have more importance as they are related to the social and financial issue, respectively.

Keywords: Water Distribution Network (WDN); ssset-based; resilient risk management; water outage time; regret cost.

1 INTRODUCTION

Water Distribution Networks (WDNs) are among the vital infrastructures that consist of many assets. Failure of each asset can cause multi aspects of risks and eventually lead to the operational disruptions or serious consequences. Understanding the nature of risks and reducing the level of them are the most important role in risk management. The risks in water distribution systems can originate from natural incidents and/or operational incidents (CIPAC Workgroup, 2009). Supporting WDNs against these incidents may require exorbitant costs to implement reactive and proactive actions.

In order to minimize resources costs needed to face with the WDN risks, establishing some risk management approaches with their corresponding criteria and measurement indexes are traditionally developed. Reliability, flexibility and resiliency are some of the most well-known approaches of risk management. Amongst many approaches presented, there has always been an incontrovertible role for resilient approach in management of WDN risk. Characteristics of a resilient system are known as preparedness, absorption, adaptation and recovery (Klise, 2015). Description of resilience has evolved through time. However, a unique definition has not been provided yet and every researcher has added a novel explanation into the definition of resiliency.

Holling (1973) presented his theories on resilient management of a system based on an ecological approach. The concept of resilience in WDNs were presented by various interpretations, such as increasing the total pressure head in networks (Todini, 2000), developing a framework for increasing resilience characteristics (Yazdani, 2011; Francis, 2014), increasing availability of systems (Zhuang, 2012), and supplying the necessary water demand after failure occurrences (Cimellaro, 2010). Generally, resilience may be measured based on the whole system or on every single asset of the system individually. The former can be termed as a system based method and the latter as the asset based one. The majority of work presented previously (Nazif, 2009; Dziedzic, 2014) have focused on the system based approach for WDNs, where the proposed indexes of resiliency are measured for the whole system without considering the role of each asset failure in WDNs operation. The asset-based approach is employed here in order to establish a tool for measuring the resilience of each asset in WDNs. For this purpose, special indexes have been introduced and each index represents a special feature of resilience. Subsequently, the quantity of each index must vary in a way to improve the value of resilience.

To end this, five indexes for quantifying WDNs resilience were introduced where each index represents a particular aspect of the system. The corresponding values of indexes for a real case study suffering from high rate of pipe failure were computed. A developed code linked to EPANET, the commonly used software for hydraulic and water quality simulations (Rossman, 2000), was used for simulating the WDN conditions and assessing the role of the proposed indexes. By comparing the quality and quantity of the indexes, the present condition of the WDN in the study area was evaluated. The most resilient system was determined as the most capable to absorb, endure and recover within a specified time and cost limits (Gay, 2012).

2 METHODOLOGY

This study aims to assess the resilience of WDNs in a new perspective. This proposed sighting of resilience is evaluated by five indexes measuring the role of each pipe asset failure in the operation of WDNs. These presented indexes are established based on some specific abilities previously defined and characterized for a resilience system. These selected features are based on the ability to reduce the magnitude and/or the duration of disruptive events, the ability to minimize the costs of a disaster and returning to the status quo in the shortest feasible time (McAllister, 2013), the ability to propagate disruption in a gradual manner (Yazdandoost, 2008), and the ability to recover from an unsatisfactory condition as soon as possible (Hashimoto et al. 1982). In a very simplified form, ure 1 illustrates the functional state of a system before, during, and after a failure. The vertical axis of the diagram in Figure 1 can represent any system performance measure, such as the amount of water supplied for customers, provided the higher values indicate the higher performance and the horizontal axis represents the time.

Different regions of this figure may imply normal condition of WDN performance (before the failure – part a), drop in performance (loss of performance – part f), allocating resources in order to repair the system (part b), and recovery of the WDN performance (increase of WDN performance – part e).

In this figure, it is supposed that, at time t0, a disruptive event occurs and the system performance deteriorates until it reaches a stable condition at time t1 (this duration corresponds to the part f). At time t1, the water utility interventions start and end at t2 for repairing the WDN. In other words, t2 – t1 is the repairing time of the failed asset (part b). After completing the repairs, the system begins to recover and reaches a new stable recovered condition at time Te (part c). On many occasions, returning exactly to the condition before failure might not be feasible, although the parts (s) and (e) in Figure 1 may not have the same characteristics (Chang, 2010) as they stay on the same line, as presented in Figure 1. In this study, it is assumed that the part (s) and (e) would have the same WDN performance.

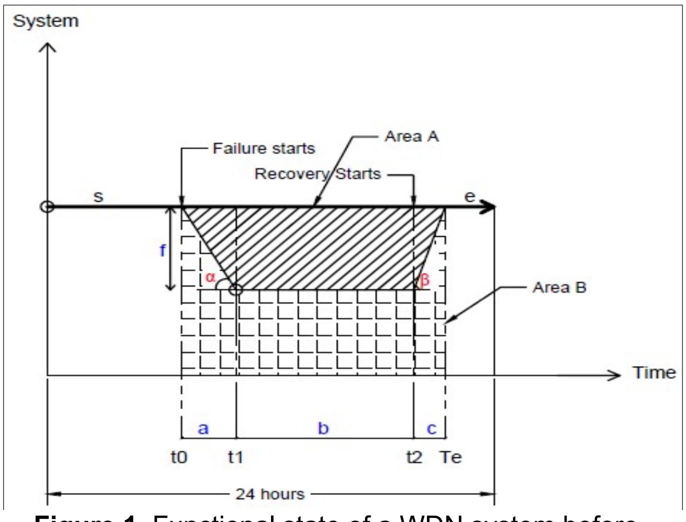

Figure 1. Functional state of a WDN system before, during and after a failure.

The five indexes of Graduality, Recovery Rate, Water Outage Time, Hydraulic Critical Index (HCI) and Regret Cost with their corresponding features in Figure 1 are condensed in Table 1. In the following subsections, more details about each of these indexes are described.

Table 1. Indexes introduced for the study.

Index	Section in Figure 1	Unit
Graduality	α	Lit/s²
Recovery Rate	β	Lit/s²
Water Outage Time	Te – t0	hour
HCI	-	percentage
Regret Cost	A/(A+B)*Water sales income	IR.Rial

Corresponding units for each index is based on the proposed characteristics specified for the vertical axis in Figure 1.

2.1 Graduality

This index represents the speed of a failure occurrence. The relative increase of propagation is directly related to the rate of number of casualties. Therefore, the more gradual extension of disruption is desired. This index is introduced as the ratio of performance loss to the corresponding time, in which the reduction of WDN's performance occurs:

$$Graduality = \frac{Rate\ of\ Loss}{Loss\ Time} \qquad [1]$$

where Rate of Loss and Loss time are equivalent to part (f) and (t1-t0) in Figure 1, respectively.

2.2 Recovery rate

The other feature of resilience in the system can be dependent on how quickly the system recovers from a failure, once failure has occurred. According to Eq. [2], as the denominator of this equation is getting smaller, the higher the Recovery Rate can be achieved. It is worth noting that the unit of this index is similar to that of the Graduality.

$$Recovery\ Rate = \frac{Rate\ of\ Rise}{Rise\ Time} \qquad [2]$$

where Rate of Rise is expected to be equal to Rate of Loss (see Eq. [1]), Rise Time implies (Te-t2) in Figure 1.

2.3 Water outage time

The time when water users remain out of water supply in the case of each failure is known by Water Outage Time index. In other words, the water outage time measures the duration of unsatisfactory condition in the WDN performance. This time consists of a rise time (from the Eq. [2]), Mean Time to Repair a pipe (MTTR) and loss time (form the Eq. [1]), as Eq. [3].

$$Water\ Outage\ Time = a + b + c \qquad [3]$$

where "a", "b" and "c" are shown in Figure 1.

2.4 Hydraulic Critical Index (HCI)

The Hydraulic Critical Index (HCI) of each pipe (as an asset) indicates the ratio of total water demands supplied after the failure to the amounts supplied before the failure (Eq. [4]). The higher value of this index shows the greater importance of an asset in supplying required water demands of network. Actually, it defines which assets' failure is more serious in network's operation. This index is very sensitive to the position of the asset in a network.

$$HCI = \frac{Total\ suplied\ demands\ of\ network\ after\ the\ failure}{Total\ suplied\ demands\ of\ network\ before\ the\ failure} \qquad [4]$$

2.5 Regret cost

This index represents the revenue that water utility may lose if it cannot provide the required demands of consumers. This condition may occur when the performance of system is unsatisfactory. In other words, when the network is incapable to supply the total required demand, the water utility cannot earn its income totally.

According to Figure 1, the ratio of A/ (A+B) can be regarded as a measure of unsatisfactory condition as compared to the normal operation of the system. Thus, by multiplying this quantity by the average water price (in a specific year), the regret cost (the amount of income/revenue lost) can be computed as Eq. [5].

$$Regert\ cost = \frac{Unsatisfactroy\ Area\ (A)}{Total\ Area\ (A+B)} * 100 * Water\ Price \qquad [5]$$

where water price includes annual inflation rates.

3 CASE STUDY

The methodology has been applied to a WDN in south-west of Isfahan, Iran. The cities' area is around 36km² and its population is estimated at 20000. The area is divided into three main districts, namely N, D, and W.

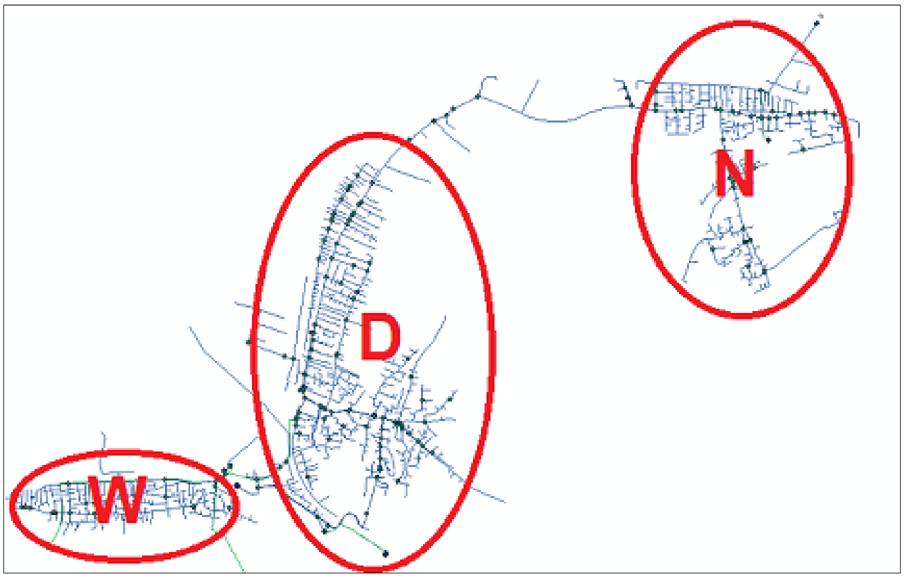

Figure 2. Case study's schematic water distribution network.

In this WDN, water is supplied through four reservoirs. The pipes diameters vary from 25 millimeters to 250 millimeters. Due to the high groundwater level and region's soil condition, the pipes' depth of installation is low and sometimes about 30 centimeters. This condition makes the probability of pipes' breakage greater. Based on recorded data, there are two pipe failures in study area every day on an annual basis. Here, the main question is, "is the study network resilient with regards to the high rate of pipe failure". To answer this question, it is necessary to probe the weakness of the network.

4 RESULTS

In order to quantify the proposed resilience indexes for the existing condition of the WDN, a MATLAB suit code linked to EPANET toolkit was used. This code is able to simulate failure of each pipe and then assesses the indexes. This process is regarded as the failure analysis of each asset. It is obvious that failure of all pipe assets do not have the same impacts on the WDN function. Those pipes whose failures can create more unmet demand are the critical ones. Table 2 shows the measured indexes for some of the most critical pipes. It is worth noting that while the higher amounts of recovery rate are desired, the lower amounts for the other indexes are favorable. Pipes 1 to 3 are those linked directly to the main reservoirs and Pipes 4 to e 6 are the connectors between the two main districts of the WDN. The pipes are arranged in order of their HCI level (criticality).

Table 2. Indexes and features of the critical pipes of the existing WDN.

FEATURE	UNIT	PIPE1	PIPE2	PIPE3	PIPE4	PIPE5	PIPE6
DIAMETERE	(Millimeter)	60	250	150	150	150	150
LENGTH	(Meter)	8.4	90.5	11.3	32.2	229.6	47.4
GRADUALITY	(Lit/s²)	17.66	0.28	6.06	1.41	0.15	0.46
RECOVERY RATE	(Lit/s²)	0.59	0.5	0.52	0.56	0.71	0.52
WATER OUTAGE TIME	(Hour)	6.07	6.18	6.06	6.07	6.22	6.1
HCI	(%)	16.67	12.77	12.68	11.42	10.96	9.86
REGRET COST	(MIR.Rial)	8.66	6.97	7.00	6.47	6.20	5.80

As shown in Table 2, the criticality of pipes is not relevant to their diameters or lengths. For instance, Pipe1 with a smaller diameter and length than Pipe 2 may be more critical based on a higher percentage of HCI and Graduality. On the contrary, Pipe1 has better condition than Pipe 2 when the Recovery Rate and Water Outage Time are the only criteria for judgment. In other words, when Pipe2 fails, its consequences are less gradual and it recovers slower than the situation when Pipe1 fails. Furthermore, in case of Pipe 2 failure, access of users to satisfactory conditions of water supply is more time consuming. It must be noted that 16.67% HCI of Pipe 1 is equal to the lack of 163 liters per second demand in supply of the WDN. Although no specific relationship may be deducted for the proposed criteria, it appears that the variation of Regret Cost index is directly proportional to the variation of the HCI index.

According to Figure 1, the degree of α which represents the Graduality index, must decrease to cause lower intensity of disruption and makes the emergence of failure consequences more gradual. On the other hand, the degree of β refers to the Recovery Rate and has to be a maximum in order to increase the speed of recovery. Water Outage Time index is principally desired to be the least. The percentage of HCI index as the ratio of total supplied demands of the network after failure to its quantity before failure is sought to be at its minimum value. Regret Cost index is obviously desired to be at its minimum.

Quantifying proposed indexes have been performed in case of all pipes' failure. The average value of these indexes is presented in Table 3. Existence of plenty of pipes with low water flow in the network has led to smaller average values of indexes than those for the critical pipes (previously given in Table 2). Apparently, the Graduality index doesn't follow this rule for its variable nature with regards to the location of the pipes and their responsibility for water transportation.

Table 3. The average values of indexes of the existing WDN.

INDEX	GRADUALITY (Lit/s^2)	RECOVERY RATE (Lit/s^2)	WATER OUTAGE TIME (HOUR)	HCI (%)	REGERT COST (IR.RIAL)
AVERAGE	1.4	0.7	5.33	5	4,003,492

As Table 3 shows, the Graduality and Recovery Rate indexes have similar units while the Graduality index has lower values than the Recovery rate. An analogy between these average values reveals that the existing WDN's current situation is not acceptable. In fact, in this situation, the disruption and failure consequences appear more quickly than the process of system recovery. If a usual disruption in the network occurs, the system will suffer from 5% unmet demand, 5 hours and 20 minutes of water outage for users and financial losses of 4,003,492 IR.Rials.

5 CONCLUSIONS

Resilience risk management of Water Distribution Networks studies have been debated since last decades. In these studies, many approaches and criteria have been developed. Usually the WDN is analyzed in its entirety without referring to the role of individual asset failure in the disruption of the system. This study aims to propose a methodology for evaluating impact of each asset failure based on the resiliency of the WDN. This approach is termed asset based. Based on this approach, the system's weak points can be evaluated from different sights and any undesirable effect of asset failure can be highlighted. In this approach, it is assumed that any unfavorable feature of a single asset would result in the descent of the resiliency of the whole system. Here, five indexes were proposed and their efficiencies were examined for a real case in Isfahan Province suffering from high rate of pipe failure. The results show that the novel indexes introduced in this research are efficient enough to cover the economic (Regret Cost), social (Graduality, Recovery Rate and Water Outage Time), and technical (HCI) perspectives of WDNs operation simultaneously. By taking into account the enhanced scenarios, the WDN can prosper into a more resilient system. The proposed approach in quantifying resilience for WDNs would help stakeholders in making the best management decisions on repairing, replacing and maintaining the system.

REFERENCES

Chang, Y., Wilkinson, S., Seville, E. & Potangaroa, R. (2010). Resourcing for a Resilient Post-Disaster Reconstruction Environment. *International Journal of Disaster Resilience in the Built Environment*, 1(1), 65-83.

Cimellaro, G.P., Reinhorn, A.M. & Bruneau, M. (2010). Framework for Analytical Quantification of Disaster Resilience. *Engineering Structures*, 32(11), 3639-3649.

Dziedzic, R.M. & Karney, B.W. (2014). Water Distribution System Performance Metrics. *Procedia Engineering*, 89, 363-369.

Francis, R. & Bekera, B. (2014). A Metric and Frameworks for Resilience Analysis of Engineered and Infrastructure Systems. *Reliability Engineering & System Safety*, 121, 90-103.

Gay, L.F. & Sinha, S.K. (2012). Novel Resilience Assessment Methodology for Water Distribution Systems. In *Pipelines 2012: Innovations in Design, Construction, Operations, and Maintenance, Doing More with Less*. 61-69.

Hashimoto, T., Stedinger, J.R. & Loucks, D.P. (1982). Reliability, Resiliency, and Vulnerability Criteria for Water Resource System Performance Evaluation. *Water Resources Research*, 18(1), 14-20.

Holling, C.S. (1973). Resilience and Stability of Ecological Systems. *Annual Review of Ecology and Systematics*, 4(1), 1-23.

Nazif, S. & Karamouz, M. (2009). Algorithm for Assessment of Water Distribution System's Readiness: Planning for Disasters. *Journal of Water Resources Planning and Management*, 135(4), 244-252.

Klise, K.A., Murray, R. & Walker, L.T.N. (2015). *Systems Measures of Water Distribution System Resilience* (No. SAND2015-20746R), Sandia National Laboratories (SNL-NM), Albuquerque, NM (United States).

McAllister, E.W. (2013). *Pipeline Rules of Thumb Handbook: A Manual of Quick, Accurate Solutions to Everyday Pipeline Engineering Problems*. Gulf Professional Publishing.

Preparedness, Emergency Respond, and Recovery CIPAC Workgroup (2009). *All-Hazard Consequence Management Planning for the Water Sector*, Department of Homeland Security Washington DC Critical Infrastructure Partnership Advisory Council.

Rossman, L.A. (2000). *EPANET 2: Users Manual*, U.S. Envir. Protection Agency, Cincinnati, Ohio.

Todini, E. (2000). Looped Water Distribution Networks Design Using a Resilience Index Based Heuristic Approach. *Urban Water*, 2(2), 115-122.

Yazdani, A., Otoo, R.A. & Jeffrey, P. (2011). Resilience Enhancing Expansion Strategies for Water Distribution Systems: A Network Theory Approach. *Environmental Modelling & Software*, 26(12), 1574-1582.

Yazdandoost, F. & Bozorgy, B. (2008). Flood Risk Management Strategies Using Multi-Criteria Analysis. In *Proceedings of the Institution of Civil Engineers-Water Management.* 161(5), 261-266.

Zhuang, B., Lansey, K. & Kang, D. (2012). Resilience/availability Analysis of Municipal Water Distribution System Incorporating Adaptive Pump Operation. *Journal of Hydraulic Engineering*, 139(5), 527-537.

Proceedings of the 37th IAHR World Congress
August 13 – 18, 2017, Kuala Lumpur, Malaysia

WALL FUNCTIONS FOR BOUNDARY ROUGHNESS PREDICTION IN UNIFORM CHANNEL FLOWS

ISMAIL AYDIN[(1)]

[(1)]Civil Engineering Department, Middle East Technical University (METU), Ankara, Turkey
ismaydin@metu.edu.tr

ABSTRACT

Boundary roughness is an important hydraulic parameter in describing dynamics of free surface flows. There is no direct method to estimate the possible boundary resistance in natural environment. Available empirical formulations are based on the particle size on the river bed. However, other factors such as shape and size of flow section are also effective in the development of boundary resistance. Accurate prediction of boundary roughness can only be made by in situ hydraulic measurements for each specific flow domain. This paper use the experimental and computational approaches together to calculate the discharge and the boundary roughness. Flow is assumed to be uniform and velocity at the free surface is measured to be applied as boundary conditions of a numerical solution. Computational model uses a non-linear turbulence model that is capable of producing complete velocity field including turbulence driven secondary flows. Numerical solution requires repeated iterations for variable values of boundary roughness to adjust the velocity field to fit the measured values at the free surface. An explicit wall function is proposed for efficient calculation of the wall shear stresses and also for evaluation of the boundary roughness. The method is verified by a large number of data set obtained from a tilting flume in the laboratory.

Keywords: Wall functions; bed roughness; channel flows; uniform flow; discharge.

1 INTRODUCTION

In the numerical analysis of free surface flows in natural environment, a parameter to represent the boundary resistance on the flowing fluid is required. The roughness parameter should specify the amount of resistance from the solid boundary which has a decisive influence on the flow characteristics. Mathematical model used in the solution may use 1D, 2D or 3D formulation depending on type of problem and detail of solution required. Manning roughness *n* is the well-known parameter used in 1D and 2D depth integrated computations. The error in estimation of roughness value used in the computation is proportionally reflected in the flowrate and water depth. In other words, the accuracy of roughness estimated determines the accuracy of the computation. In practice, roughness value may be determined from field observations based on particle size of the bed material. In all textbooks, there are tables listing recommended values based on engineering experience and observations. However, there are many other effects such as size and shape of flow section that should be considered in final tuning of the roughness value. Some research have also been carried out to evaluate roughness from the field measurements of water surface profiles using 1D solutions to fit the measured data (Atanov et al., 1999; Ramesh et al., 2000). Measurement of flood flows is also a difficult task where non-intrusive techniques (Baud et al., 2005; Bradley at al. 2002) are becoming more popular.

Combined use of experimental and computational approaches was proposed in recent studies (Gharahjeh and Aydin 2016; Gharahjeh 2016). Flow is assumed to be uniform at the working section where a local balance between gravity component as the driving force and the boundary resistance force is considered. For a fixed cross section geometry, there are two types of flow boundaries: the bed and the free surface. No-slip boundary conditions can be applied on the bed. The flow velocity just on the free surface is a result of dynamic equilibrium between the driving and resisting forces and the secondary flows driven by turbulence un-isotropy. In other words, free surface velocity has a unique value for a given equilibrium condition in uniform channel flow. Thus, the measured free surface velocity can be applied as a boundary condition in the numerical solution of the governing equations. This study is based on the idea of computing the velocity field, the discharge and the boundary roughness from the measured free surface velocity for a given cross-section geometry and the bed slope. Such a procedure requires measurement of free surface velocity by some appropriate methods and then a computational tool which can reproduce velocity distribution in the flow section including the secondary flow contributions. It is also required that the boundary conditions applied on the solid wall should be appropriate for prediction of wall roughness, while the computed velocity field satisfies the measured free surface velocity. Such a solution procedure involves additional iterations to find the appropriate roughness value while the numerical solution of the governing equations is enforced to satisfy the conditions of convergence.

At the early stages of this study (Gharahjeh and Aydin 2016; Gharahjeh 2016), the classical wall functions were employed to calculate the wall shear stresses and also to determine the boundary roughness.

It was noticed that an explicit solution of the wall functions for the wall shear stresses would noticeably increase the speed of convergence and also improve the stability of computations. Such a novel, explicit wall function is proposed in the following sections together with the mathematical model and applications in channel flows.

2 MATHEMATICAL MODEL

Uniform flow assumption in river flows is a common approach to describe the local flow conditions. As a result of this assumption all variations in the flow direction are ignored. Thus, flow in a section can be described as two-dimensional. However, all three velocity components have to be computed due to secondary flows around corners induced by turbulence un-isotropy. Most of the turbulence models are not capable of reproducing secondary flows and therefore computations with such models will fail to calculate the correct velocity field especially in narrow channels where corners are most effective in development of un-isotropy in turbulence.

Uniform flow in prismatic open channels can be formulated in terms of vorticity transport equation in the plane of flow section, the stream function to express the continuity and the stream wise momentum equation. Reynolds averaged momentum equation for fully developed, steady, incompressible, turbulent, uniform flow is written as

$$\frac{\partial u}{\partial t}+\frac{\partial (uv)}{\partial y}+\frac{\partial (uw)}{\partial z}=g\sin\theta+\nu\left(\frac{\partial^2 u}{\partial y^2}+\frac{\partial^2 u}{\partial z^2}\right)+\frac{\partial \tau_{yx}}{\partial y}+\frac{\partial \tau_{zx}}{\partial z} \qquad [1]$$

where u, v, w are the mean velocity components in x, y, z-directions respectively, x is the stream wise direction of the flow, t is time, g is gravitational acceleration, θ is the angle of channel bed with horizontal, ν is kinematic viscosity and τ is turbulent kinematic stresses. The stream wise vorticity transport equation in the flow section is written as

$$\frac{\partial \xi}{\partial t}+\frac{\partial (v\xi)}{\partial y}+\frac{\partial (w\xi)}{\partial z}=\nu\left(\frac{\partial^2 \xi}{\partial y^2}+\frac{\partial^2 \xi}{\partial z^2}\right)+\frac{\partial^2 (\tau_{zz}-\tau_{yy})}{\partial y\partial z}+\frac{\partial^2 \tau_{yz}}{\partial y^2}-\frac{\partial^2 \tau_{yz}}{\partial z^2} \qquad [2]$$

where ξ is the vorticity in the flow section (y-z plane) and is defined as

$$\xi=\frac{\partial w}{\partial y}-\frac{\partial v}{\partial z} \qquad [3]$$

The time derivative in Eqns. [1] and [2] is kept simply to facilitate an iterative solution of the equations. Poison equation for stream function (ψ) is used to imply continuity:

$$\frac{\partial^2 \psi}{\partial y^2}+\frac{\partial^2 \psi}{\partial z^2}=-\xi \qquad [4]$$

Stream wise velocity is computed directly from the momentum solution whereas the velocity components normal to stream wise direction are obtained from the stream function solution.

$$v=\frac{\partial \psi}{\partial z} \qquad [5]$$

$$w=-\frac{\partial \psi}{\partial y} \qquad [6]$$

Computational approach can be successful if the turbulence structure of the flow field is appropriately described by a suitable turbulence model to be combined with the above set of governing equations. A turbulence model named as Nonlinear Mixing Length Model (NMLM) tuned for uniform flow situations was proposed and tested in Aydin (2009). The mixing length is obtained from a distance weighting function for boundary proximity and the model has no additional transport equations to be solved. Turbulent stresses are expressed in terms of nonlinear correlations of strain rates and vorticity. Computation of turbulence kinetic energy is not required when vorticity transport equation is solved for uniform flow. It was shown (Aydin, 2009) that the model is able to reproduce secondary flows with significant savings in computing cost. The model was improved to accurately compute the free surface velocities by introduction of a specific damping function for the free surface boundary (Gharahjeh, 2016). Turbulence anisotropy was taken into account using nonlinear correlations of the strain rates in describing the turbulent stresses. Model is robust since it requires no additional differential equations. The model aims to capture the secondary flow patterns in detail by computing the 3D velocity field of uniform channel flow with minimum complexity of modeling and thus requiring less computational effort for the solution. In NMLM the turbulent stresses are defined as

$$\tau_{ij} = -\overline{u_i' u_j'} = l_m^2 \begin{bmatrix} |\Omega| S_{ij} - \frac{2}{3} k_t \delta_{ij} \\ - C_1 (S_{ik} S_{jk} - \frac{1}{3} S_{kl} S_{kl} \delta_{ij}) \\ - C_2 (S_{ik} \Omega_{jk} + S_{jk} \Omega_{ik}) \\ - C_3 (\Omega_{ik} \Omega_{jk} - \frac{1}{3} \Omega_{kl} \Omega_{kl} \delta_{ij}) \end{bmatrix} \quad [7]$$

in which $S_{i,j}$ is the rate of strain, Ω is vorticity vector and $|\Omega|$ is the magnitude of vorticity vector defined as follows

$$S_{ij} = \frac{\partial u_i}{\partial x_j} + \frac{\partial u_j}{\partial x_i} \quad [8]$$

$$\Omega_{ij} = \frac{\partial u_i}{\partial x_j} - \frac{\partial u_j}{\partial x_i} \quad [9]$$

$$|\Omega| = \sqrt{\Omega_{12}^2 + \Omega_{13}^2 + \Omega_{23}^2} \quad [10]$$

In Eq. [7] k_t is turbulent kinetic energy, $\delta_{i,j}$ is Kronecker delta, C_1, C_2 and C_3 are constants adjusted by numerical experiments and l_m is the turbulent mixing length. The mixing length represents a weighted distance from all boundaries and is defined as:

$$l_m = \kappa l_v f_\mu \quad [11]$$

in which $\kappa = 0.41$ is Karman constant, l_v is volumetric mixing length defined by

$$l_v = \frac{\pi}{\int_w \frac{\mathrm{d}A_r}{r^3} + \lambda \int_s \frac{\mathrm{d}A_r}{r^3}} \quad [12]$$

where λ=0.41, subscript w indicates integration over solid wall, subscript s indicates integration over water surface and f_μ is a damping function given by:

$$f_\mu = \min\ (f_s, f_w) \quad [13]$$

where f_w is the damping effect from the solid wall boundary and f_s is the same effect coming from free surface boundary. The damping functions are expressed in terms of dimensionless distances:

$$f_w = 1 - \exp(-l^+ / A^+) \quad [14]$$

$$l^+ = l_v u_\tau / \nu \quad [15]$$

  ISSN 1562-6865 (Online) - ISSN 1063-7710 (Print)

$$f_s = 1 - \exp(-D^+ d / l_v) \quad [16]$$

where d is vertical distance from the free surface, D^+ is a parameter that controls the surface damping rate and subsequently has an effect on the free surface velocity distribution, A^+=26 is a dimensionless constant and u_τ is local shear velocity computed from

$$u_\tau = \sqrt{\left|\nu \frac{\partial u}{\partial y} + \tau_{yx}\right| + \left|\nu \frac{\partial u}{\partial z} + \tau_{zx}\right|} \quad [17]$$

The free surface damping parameter D^+ is found to be a function of channel aspect ratio and relative roughness at the channel bed. It has been defined based on surface velocity measurements in rectangular and compound channels in a recent study (Gharahjeh and Aydin, 2016).

$$D^+ = 0.35 \ Log\left(\frac{k_s}{6\,D_h} + 0.035\,\frac{A}{T^2}\right)^{-2} \quad [18]$$

The governing equations combined with turbulence closure provided by NMLM are solved numerically (via finite volume method) over a staggered grid.

3 WALL FUNCTIONS

The computer code uses wall functions to calculate the wall shear stresses. In earlier runs, the classical logarithmic wall function, which is implicit in wall shear velocity, was used in wall shear stress determination. It consumes longer CPU times when numerical iterations are performed for inverse solution of the wall roughness. To speed up the numerical solution, a new form of wall function is proposed. The most important property of the new function is its explicit form for the computation of shear velocity. Formulation considers the wall layer composed of viscous sublayer, the transition and fully turbulent layers. The dummy argument y in the equations is the distance from the solid boundary. The new wall function is given as:

$$u^+ = \sqrt{y^+} \quad \text{for} \quad y^+ < 12 \quad [19]$$

$$u^+ = f_w(A \ln(y^+) + B - E) \quad \text{for} \quad 12 < y^+ < 700 \quad [20]$$

$$u^+ = A \ln(y^+) + B - E \quad \text{for} \quad y^+ > 700 \quad [21]$$

$$u^+ = u / u_* \quad [22]$$

$$y^+ = yu / \nu \quad [23]$$

$$u_* = \sqrt{\tau_w / \rho} \quad [24]$$

$$f_w = 1 - \exp\left[-\left(\frac{y^+ + 25}{40}\right)^{0.63}\right] \quad [25]$$

where A=2.2, B=0.1 are universal constants, E is boundary roughness parameter, ρ is fluid density, τ_w is the wall shear stress and u_* is the shear velocity. It should be noted that the new wall function uses local velocity in the definition of dimensionless distance. Therefore, Eqns. [19], [20] or [21] can be used for computation of shear velocity explicitly whichever is relevant depending on zone of the velocity profile. The function given by Eq. [25] is used to encompass the transition zone between the viscous sublayer and the fully turbulent layer which was developed by utilizing the pipe flow solutions. A comparison of the classical log-law and the new one is shown in Fig.1 for the same solution. The horizontal axis, y^+, is defined by Eq. [23] for the new formulation whereas the dimensionless distance for the classical log-law is given by $y^+ = yu_*/\nu$. The dashed lines show the log-laws and the circles are representing data of the same numerical solution in a wide channel.

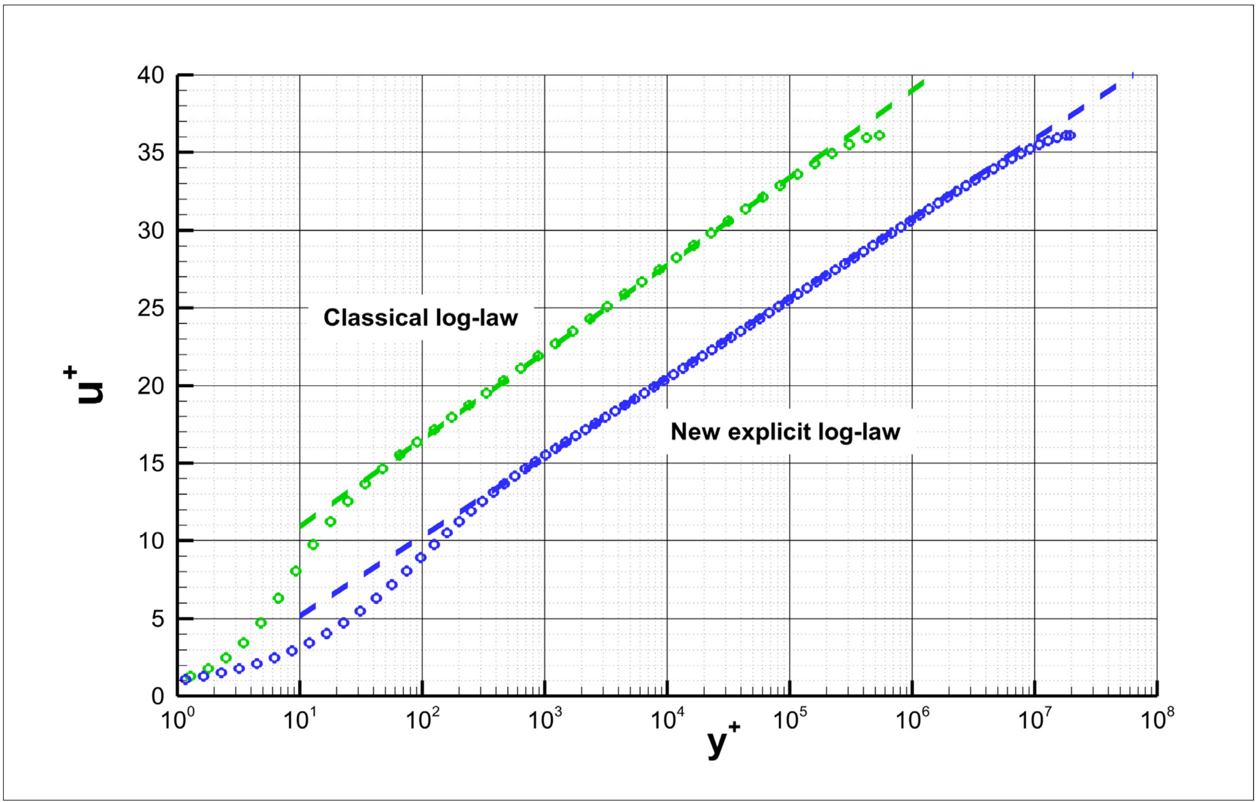

Figure 1. Comparison of the classical and new logarithmic velocity profiles in a wide channel.

In the case of rough beds, data of Nikuradse (Schlichting, 1979) has been used to calculate boundary roughness parameter *E* (Fig.2).

$$E = 0. \quad \text{for} \quad R_k < 3.43 \qquad [26]$$

$$E = f_e\left[\frac{1}{\kappa}\ln(R_k) - 3\right] \quad \text{for} \quad R_k \geq 3.43 \qquad [27]$$

$$f_e = 1 - \exp\left[-\left(\frac{R_k}{11.3}\right)^{0.82}\right] \qquad [28]$$

$$R_k = k_s u_* / \nu \qquad [29]$$

where k_s is the Nikuradse's equivalent sand roughness. The function given by Eq. [28] is provided to encompass the transition from smooth to hydro dynamically rough cases. Eqns. [19]~[29] describe the wall layer which can be used to calculate the wall shear stress from the first grid point velocity or the boundary roughness, k_s, in an iterative manner.

The above formulation (Eqns. [1]~[29]) gives a complete mathematical description of uniform flow in a prismatic channel. Numerical solution requires cross-section geometry, bed slope and boundary roughness as input data. The output will be the velocity field as function of space in the flow section. Then, the discharge can be easily obtained by integration of the stream wise velocity over the cross sectional area. The challenging power of the proposed formulation becomes obvious if some velocity measurements on the water surface are available. Then, the unknown bed roughness can be inversely computed by applying the measured surface velocity data as boundary conditions of the numerical solution. The boundary roughness is varied to affect the computed velocity field such that the computed surface velocity fit to the measured data. There is no need for any empirical prediction or assumption for the bed roughness, it is computationally determined based on experimentally measured surface velocity data of the specific flow domain. This approach removes the uncertainty in bed roughness estimation when a few velocity measurement on the water surface is available. This formulation and the inverse solution algorithm for the wall roughness has been successfully tested and verified in pipe flow.

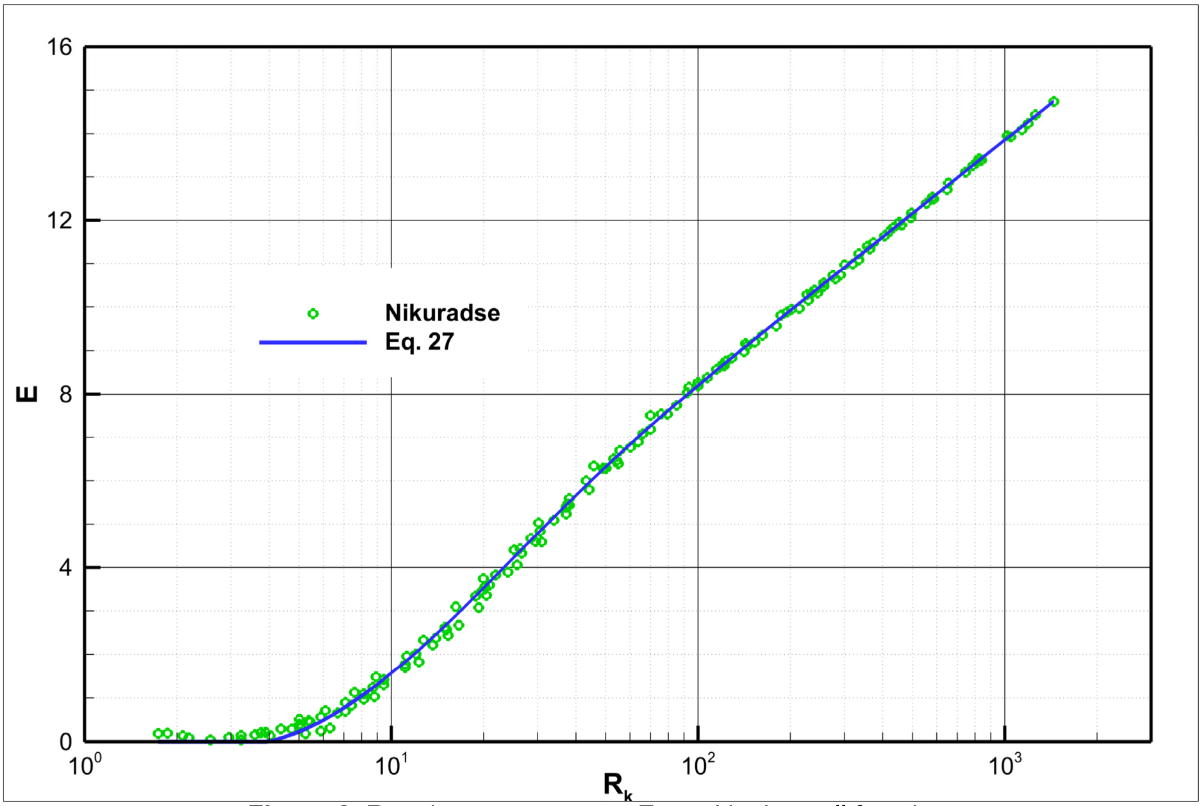

Figure 2. Roughness parameter E used in the wall function.

4 EXPERIMENTS

The experimental setup consists of a 12 m long, 60 cm wide and 35 cm deep tilting channel. The side and bottom surfaces are made up of glass. The channel is supported by a steel structure connected to a reservoir in the upstream end. The downstream end of the channel is a free fall where water discharges back into underground reservoir. Water is recirculated via a pump having discharge capacity of 170 l/s. The schematic representation of the set-up is depicted in Fig. 3 below.

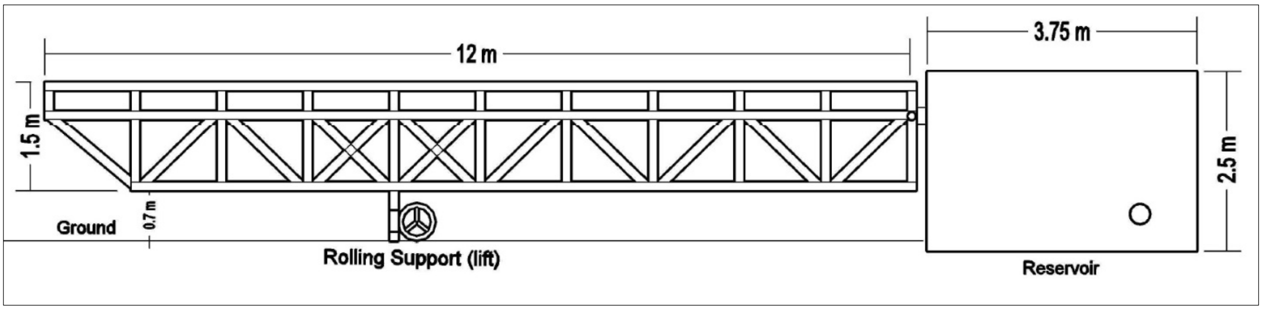

Figure 3. The schematic view of the set-up.

Water surface velocity is measured by Particle Tracking Velocity (PTV) method. PTV is considered as the most promising technique to measure water surface velocity, since it is non-intrusive, low–cost and easy to apply without preparation in natural environment. The main aim of the study was to illustrate the applicability of PTV-CFD combination to determine the discharge and bed roughness. At the beginning surface velocities are measured in smooth rectangular channel just to calibrate the turbulence model to calculate the free surface velocities accurately. For this purpose a parameter that determine the amount of damping at the surface has been tuned based on experimental data. After verifying the turbulence model and the computational code, the channel bed was covered by square ribs (Fig. 4) to produce bed roughness. Various roughness cases were created by changing the rib size and spacing between the rib elements on the bed. The experimental cases in regard to bed roughness are listed in Table 1.

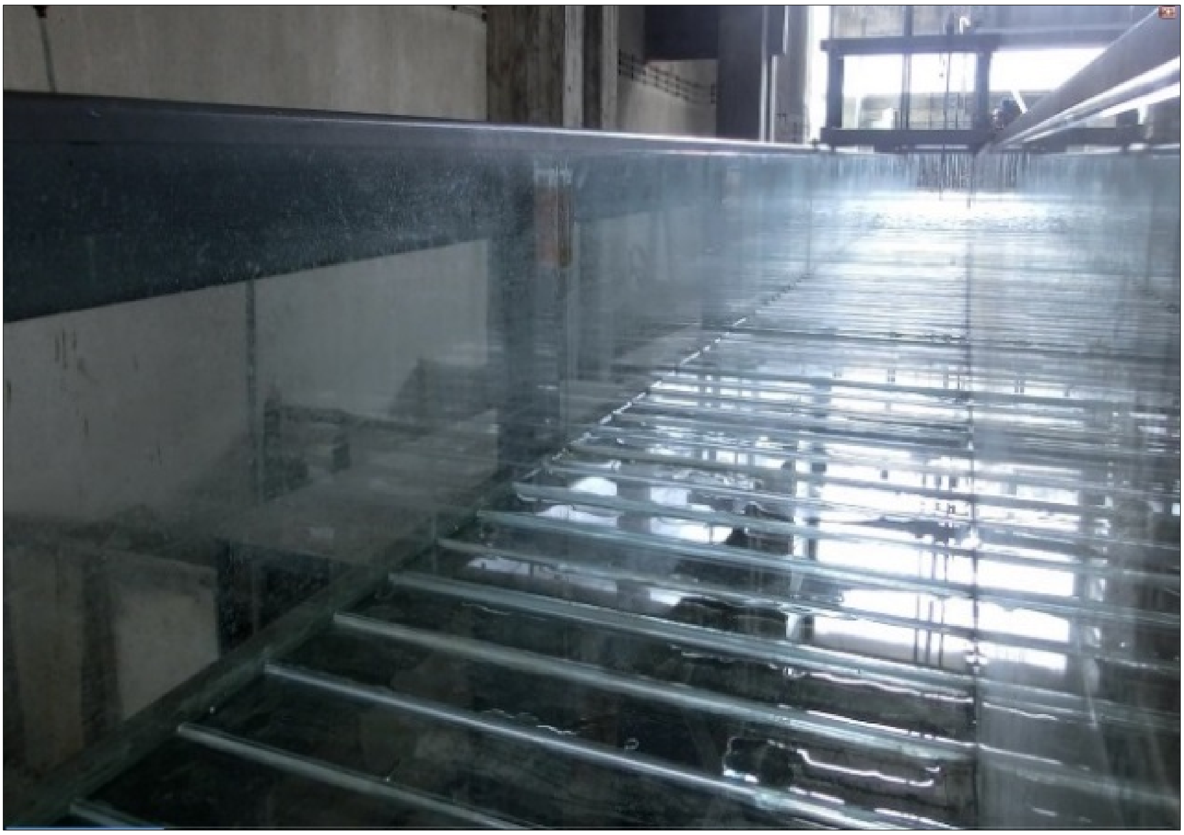

Figure 4. Ribs on the channel bed as roughness elements.

Table 1. Roughness types studied for rectangular channels.

Test case	Roughness symbol	Rib spacing (cm)	Rib dimensions (cm)
1	k_{s1}	20	1 x 1
2	k_{s2}	10	1 x 1
3	k_{s3}	40	0.6 x 0.6
4	k_{s4}	20	0.6 x 0.6
5	k_{s5}	10	0.6 x 0.6

Once the bed is covered with a given roughness pattern about 10 experiments with different flow depth and bed slopes have been done to investigate the resistance shown by the roughness pattern under study. In each experiment a number of surface velocity measurements have been repeated to collect enough number of data to compare with the computed values. A sample plot of computed water surface velocity in comparison to measured data is shown in Fig. 5. Different colors of point data indicates the video recording speed (frames per second, fps) that is used in the PTV analysis. Channel width to normal depth ratio (B/Z_n) is also indicated in the legend of the figure. Contours of the normalized stream wise velocity computed from the numerical solution is shown in Fig.6 (left) together with the streamlines of secondary flows (right) for the same test case. Streamlines describe the surface and the bed vortices clearly, which cause the velocity dipping.

The computer code uses the wall functions described by Eqns. [19] to [29]. In the iterative solution process for the rough beds, the roughness height, k_s, is varied until the computed water surface velocity matches the measured values with minimum averaged error for all point velocity data available. When solution is converged with no more changes in the roughness height, the discharge is computed by integration of the computed velocity field. The same computation has been repeated for the same roughness case for different flow conditions and the computed roughness heights are averaged to represent the bed roughness measure for that rib configuration. Similar study has been repeated for the 5 roughness pattern described in Table 1 and the results are summarized in Table 2. The manning roughness parameter n (computed from Manning's equation) is also shown in the last column of the table.

  / ISSN 1562-6865 (Online) - ISSN 1063-7710 (Print)

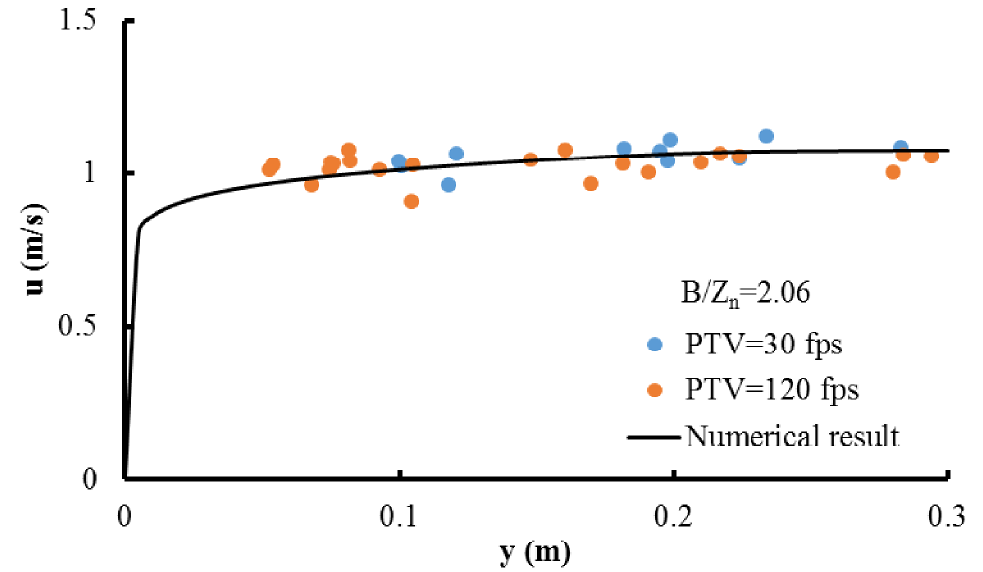

Figure 5. Numerical and experimental surface velocities for S_o=0.001, Z_n=0.29 m, Q=171 l/s.

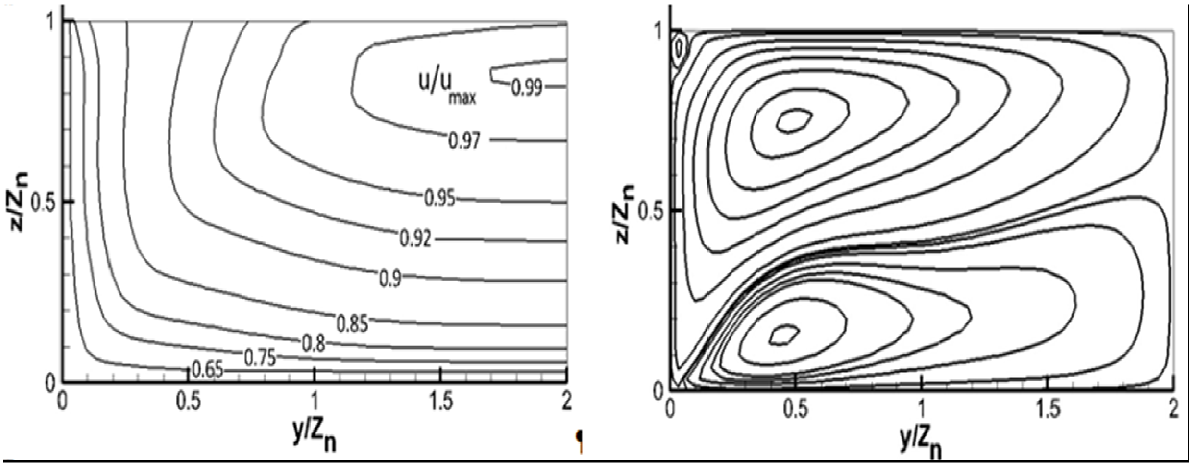

Figure 6. Computed velocity contours (left) and streamlines of secondary flows (right) (S_0=0.004, Z_n=0.15 m, Q=0.136 m^3/s).

Table 2. Numerical predictions of bed roughness.

Test case	Roughness symbol	Roughness height (cm)	Manning n (cm)
1	k_{s1}	3.29	0.0242
2	k_{s2}	4.78	0.0263
3	k_{s3}	0.56	0.0161
4	k_{s4}	1.29	0.0193
5	k_{s5}	1.99	0.0214

5 CONCLUSIONS

A combined experimental and computational approach is described to compute the discharge and bed roughness in channel flows. The method requires measurement of water surface velocity to be applied as boundary conditions at the free surface for the numerical solution. The free surface velocity measurements have been accomplished using PTV technique. The complete 3D velocity field is obtained from the numerical solution describing the secondary flows also. Computational tool uses a nonlinear turbulence model that is capable of reproducing the secondary flows. Major contribution of this study is the development of the new wall functions to speed up the numerical solution and cover all ranges of boundary roughness from smooth to hydro dynamically rough. Wall functions are made explicit for the shear velocity by defining the dimensionless distance in terms of local velocity. The method is found to be successful in computing discharge while predicting the boundary roughness with satisfactory accuracy in rectangular channels. This approach removes the uncertainty in roughness determination in free surface flows.

ACKNOWLEDGEMENTS

The research reported herein is funded by TÜBİTAK (Türkish national foundation for scientific and technical research) by the project numbered 113M435. The author would like to thank TÜBİTAK for the financial support provided in realization of this study.

REFERENCES

Atanov, G.A., Evseeva, E.G. & Meselhe, E.A. (1999). Estimation of Roughness Profile in Trapezoidal Open Channels. *Journal of Hydraulic Engineering*, 125(3), 309-312.

Aydin, I. (2009). Nonlinear Mixing Length Model for Prediction of Secondary Currents in Uniform Channel Flows. Journal of Hydraulic Engineerong. 135(2), 146-153.

Baud, O., Hager, W.H. & Minor, H.E. (2005). Toward Nonintrusive Flood Discharge Measurement, Journal of Hydraulic Engineering. 131(12), 1031-1035.

Bradley, A. A., Kruger, A., Meselhe, E. A. & Muste, M. V. (2002). Flow Measurement in Streams using Video Imagery. *Water Resource Research*. 38(12), 1315–1322.

Gharahjeh, S. (2016). Flow Measurement in Open Channels by Combined use of Free Surface PIV and CFD, *PhD dissertation*, Middle East Technical University, Ankara, Turkey.

Gharahjeh, S. & Aydin, I. (2016). Application of Video Imagery Techniques for Low Cost Measurement of Water Surface Velocity in Open Channels. *Flow Measurement and Instrumentation*. 51, 79-94.

Ramesh, R., Datta, B., Bhallamudi, S.M. & Narayana, A. (2000). Optimal Estimation of Roughness in Open Channel Flows. *Journal of Hydraulic Engineering*. 126(4), 299-303.

Schlichting, H. (1979). *Boundary-Layer Theory*. McGraw-Hill, New York.

NUMERICAL SIMULATION FOR TYPHOON AND WAVE OF QIONGZHOU STRAIT

YANAN XU(1), HANBAO CHEN(2), CIHENG ZHANG(3) & WENJUN SHEN(4)

(1,2,3,4) Tianjin Research Institute of Water Transport Engineering, Ministry of Transport, Tianjin, China,
xyn_tiwte@126.com

ABSTRACT

Southern China has been subject to some of the deadliest typhoons in history with records going back over a thousand years. Before the large waves associated with a typhoon reach the mainland of China, there is a delay between the typhoon reaching landfall and the time of the extreme waves arriving. This paper focuses on an approach to simulate this lag in the waves reaching landfall in the Qiongzhou Strait in southern China. A numerical approach has been adopted to simulate the typhoon and wave processes using a parametric typhoon model and the SWAN wave model. Two typhoon events are simulated (typhoon Kai- Tak in 2012 and typhoon Jebi in 2013) and used to tune the parameters for the numerical models. The simulated wind speeds and significant wave heights of the typhoon are compared with measured data. For the simulation of typhoon Kai-Tak, the correlation coefficient gives an 87% agreement between the simulated and measured values of wave height with a standard deviation of 0.29m. For typhoon Jebi, the fit is less good (66%). However, the simulation results have provided insight into improving the parametric typhoon model.

Keywords: Typhoon waves; wind field; SWAN wave model; Qiongzhou Strait; numerical simulation.

1 INTRODUCTION

Qiongzhou Strait is located in South China Sea. It goes E-W direction, and connects China mainland and Hainan Island. The strait is on average 30km wide associate with a maximum water depth of approximately 120m. The location of Qiongzhou Strait is shown in Figure 1

The typhoons in the Qiongzhou Strait have characteristics such as frequent activities and serious harms. These typhoons are usually generated during the summer in the South China Sea or the Northwest Pacific Ocean near the Philippine islands, resulting in extensive loss of life and property.

With more than ten years of feasibility research, a sea-crossing project of the Qiongzhou Strait will be planned and constructed in future. The strong wind and huge waves are significant factors in the construction. Since the measured data of typhoon waves are extremely limited, the preliminary research on typhoon waves with the numerical simulation technology is a good supplement.

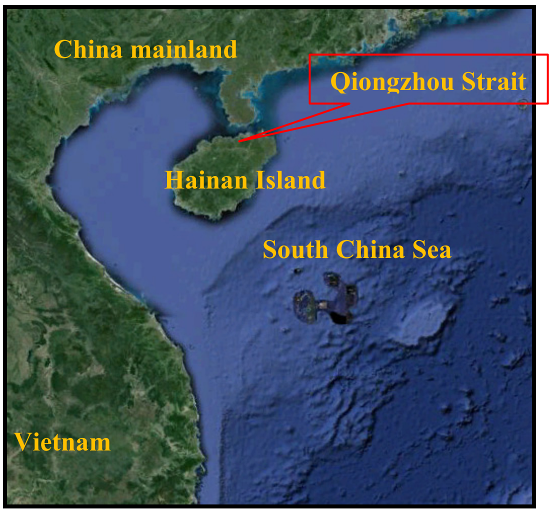

Figure 1. Location of Qiongzhou Strait.

In particular, the SWAMP Group (1985) developed the third-generation wave simulation models, such as the WAM model by WAMDI Group (1988) and the WAVEWATCH-Ⅲ model by Tolman (1989) for global scale applications. For nearshore applications, the most recent SWAN wave model by Delft University of Technology (Booij et al., 1996) was modified from third-generation models, especially from the WAM model. It includes more flexible options on the parameters for processes such as nonlinear wave–wave interactions, wind wave generation, energy dissipation by breaking, and friction and frequency shifting due to current and local topographical conditions. After being satisfactorily verified with field measurements, it is considered to be a reliable simulating model of typhoon waves in the waters of Qiongzhou Strait once a typhoon's cyclonic wind field is determined. Holthuijsen et al. (2003) added the diffraction effect in the SWAN model based on the mild-slope equation and further developed the model. Ou et al. (2003) applied the SWAN wave model to simulate typhoon waves in the coastal waters around Taiwan Island. Hsu et al. (2005) applied it to the Bay of Bengal, and Kim et al. (2008) applied it to the coastal waters of Korea. Zhao and Xu (2010) studied the numerical simulation of typhoon waves in the South China Sea based on the SWAN model.

With the sea surface driving winds obtained from the parametric models as the input for the SWAN wave model, one representative typhoon waves are simulated and the results are compared with the measured data from the wind-and-wave observation stations which are specially established at the Qiongzhou Strait, and typhoon wave numerical simulation method applied to the Qiongzhou Strait is studied and verified in the paper.

2 EQUATIONS

The information of the typhoon is prepared before the numerical simulation of typhoon waves. Wind field models mainly include numerical models and parametric models. Although numerical models, such as MM5, WRF and other mesoscale atmospheric model, accurately describe the dynamic mechanism of wind fields, for practical applications the wind fields are always represented in terms of relatively simple parametric models. In this paper, the parametric wind models are adopted. This parametric model contains two parts, which are cyclone circulation field and typhoon movement field. The typhoon movement field is based on the equations (Takeo, 1981) as follows:

$$\vec{V}_{sm} = V_x \exp\left(-\frac{\pi}{4} \cdot \frac{|r-R|}{R}\right)\vec{i} + V_y \exp\left(-\frac{\pi}{4} \cdot \frac{|r-R|}{R}\vec{J}\right) \quad [1]$$

where V_x, V_y are x-component and y-component of wind speed, respectively. r is the distance from the computed points to typhoon center, R maximum velocity radius. Thus, the expression for cyclone circulation field can be expressed as:

When $0 < r < 2R$,

$$\begin{aligned} W_x &= C_1 V_x \exp\left(-\frac{\pi}{4} \cdot \frac{|r-R|}{R}\right) \\ &- C_2 \left\{-\frac{f}{2} + \sqrt{\frac{f^2}{4} + 10^3 \frac{2\Delta P}{\rho_a R^2}\left[1 + 2\left(\frac{r^2}{R^2}\right)\right]^{-\frac{3}{2}}}\right\} \cdot \left[(x-x_0)\sin\theta + (y-y_0)\cos\theta\right] \end{aligned} \quad [2]$$

$$\begin{aligned} W_y &= C_1 V_y \exp\left(-\frac{\pi}{4} \cdot \frac{|r-R|}{R}\right) \\ &+ C_2 \left\{-\frac{f}{2} + \sqrt{\frac{f^2}{4} + 10^3 \frac{2\Delta P}{\rho_a R^2}\left[1 + 2\left(\frac{r^2}{R^2}\right)\right]^{-\frac{3}{2}}}\right\} \cdot \left[(x-x_0)\cos\theta - (y-y_0)\sin\theta\right] \end{aligned} \quad [3]$$

When $2R < r < \infty$,

$$\begin{aligned} W_x &= C_1 V_x \exp\left(-\frac{\pi}{4} \cdot \frac{(r-R)}{R}\right) \\ &- C_2 \left\{-\frac{f}{2} + \sqrt{\frac{f^2}{4} + 10^3 \frac{\Delta P}{\rho_a \left(1 + r/R\right)^2 Rr}}\right\} \cdot \left[(x-x_0)\sin\theta + (y-y_0)\cos\theta\right] \end{aligned} \quad [4]$$

$$\begin{aligned} W_y &= C_1 V_y \exp\left(-\frac{\pi}{4} \cdot \frac{|r-R|}{R}\right) \\ &+ C_2 \left\{-\frac{f}{2} + \sqrt{\frac{f^2}{4} + 10^3 \frac{\Delta P}{\rho_a \left(1 + r/R\right)^2 Rr}}\right\} \cdot \left[(x-x_0)\cos\theta - (y-y_0)\sin\theta\right] \end{aligned} \quad [5]$$

where, W_x,W_y are the are x-component and y-component of typhoon circulation velocity, $\Delta P = P_\infty - P_0$ is pressure difference of peripheral pressure and typhoon-center pressure. x_0, x-coordinate of computed point and typhoon tracks. y_0, y-coordinate of computed point and typhoon tracks. f Coriolisforce coefficient, ρ_a is air density, r is the distance from the computed points to typhoon center, R maximum velocity radius.

3 SWAN WAVE MODEL

SWAN (Simulating Waves Nearshore) is the third-generation research on the numerical model for nearshore shallow water wave, which was developed by the Delft University of Technology, Holland. The model simulates the wave propagation and transformation process by solving the spectral action balance equation, and now it is widely used in the wave numerical study. In Cartesian coordinates, the spectral action balance equation is as follows:

$$\frac{\partial}{\partial t}N + \frac{\partial}{\partial x}C_x N + \frac{\partial}{\partial y}C_y N + \frac{\partial}{\partial \sigma}C_\sigma N + \frac{\partial}{\partial \theta}C_\theta N = \frac{S}{\sigma} \qquad [6]$$

The first term on the left-hand side of (6) represents the local rate of change of action density in time, the second and third term represent propagation of action in geographical space (with propagation velocities Cx and Cy in x and y space, respectively). The fourth term represents shifting of the relative frequency due to variations in depths and currents (with propagation velocity Cs in s space). The fifth term represents depth-induced and current-induced refraction (with propagation velocity Cu in u space). The expressions for these propagation speeds are taken from linear wave theory (Whitham, 1974; Dingemans, 1997). The term S at the right-hand side of the action balance equation is the source term in terms of energy density, representing the effects of generation, dissipation, and nonlinear wave-wave interactions.

4 CALCULATED PARAMETERS

Some representative typhoons passing nearby the Qiongzhou Strait are chosen for the simulation. The tracks of these typhoons are shown in Figure 2, according to the China Meteorological Administration (CMA)'s tropical cyclone database which includes not only the best-track dataset but also tropical cyclone induced wind and precipitation data (Ming, 2014).

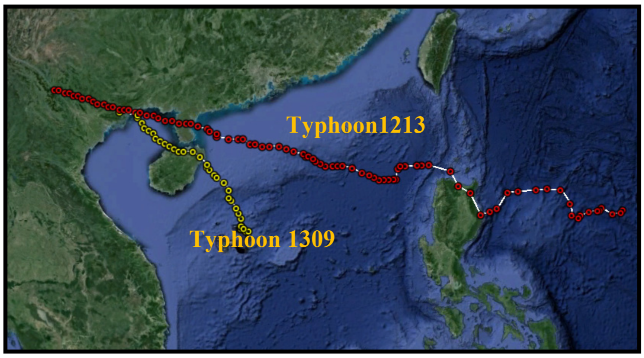

Figure 2. Tracks of Typhoon1213 and Typhoon 1309.

The SWAN wave model is used for numerical simulation of typhoon waves. The area of size is from 105.5°E~113°E and 6°N~16°N, and the triangular grid with local refinement in the waters of Qiongzhou Strait is adopted and the resolution is from 20m to 20km as shown in Figure 3, the region water depth using ETOP2 global terrain database and the resolution is 1′ ×1′ also as shown in Figure 3.

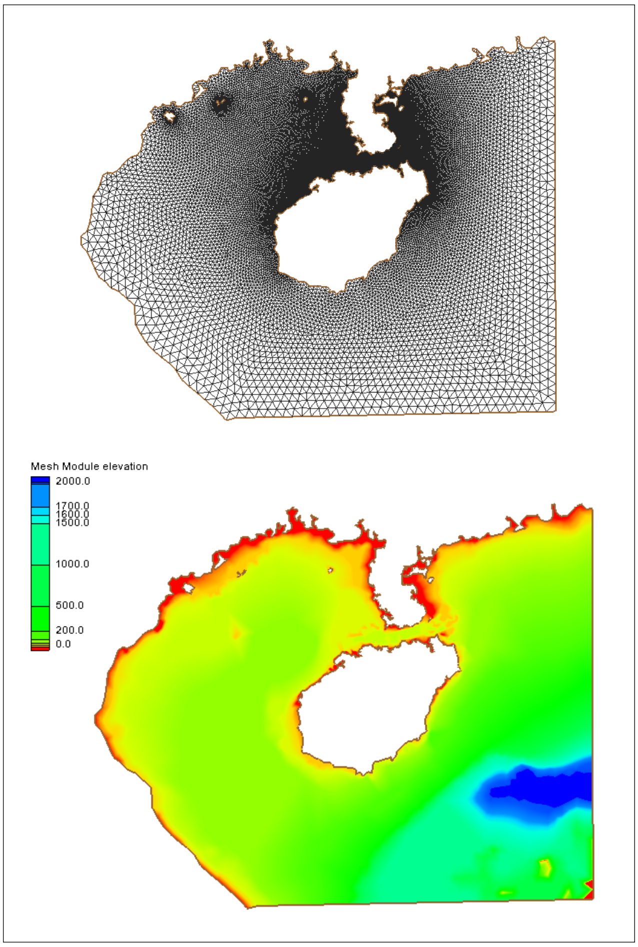

Figure 3. Mesh and bathymetry.

5 SIMULATED RESULTS

In order to obtain the real field data of wind and wave, the wind and wave observation stations are established in the waters of Qiongzhou Strait since 2012 and three years wind and wave data have been collected, including the wind and wave data during the nine typhoons passing by the Qiongzhou Strait.

The locations of observation stations are shown in Figure 4. The water depth of the wave observation point is measured as 47.6m.

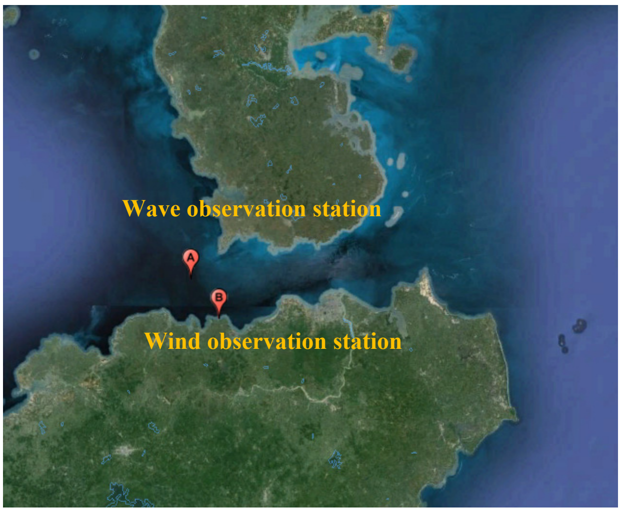

Figure 4. The location of observation station.

The simulation duration for the typhoon is from 00:00, August 16, 2012 to 00:00, August 18, 2012. The calculated and observed values of wind speed and wind direction are compared as shown in Figure 5 and Figure 6, and the values of wind speed are converted to normalized values for security requirements of ongoing research program. The wind speed is the 10-minute mean wind speed.

It can be seen from the Figure 5 that the calculated and observed values of wind speed have good consistency in all. The curve shapes and peak values have small deviations. Actually, the consistency of initial curve shapes is not very good, mainly because the wind observation tower is far away from the typhoon center and which is a little affected by the typhoonfield. If the edge of the wind field is simulated more accurately, the background winds from some reanalysis data, such as CCMP, QuickSCAT, NCEP, EAR and other re-analysis wind fields, can be added into the parametric wind models.

In Figure 5, the calculated peak value of wind speed is bigger than observed value correspondingly, mainly because the land terrains, detailed spatial variation of typhoon structure is not considered in parametric wind models, and the detailed typhoon parameters existing error either. In order to obtain the more accurate wind field, some half-empirical and half-numerical typhoon wind models, such as Shapirowind field (Shapiro, 1983), Yang Meng wind field (Meng et al., 1995) and CE wind field (Tompson et al., 1996), are developed especially instructural wind engineering or typhoon hazard analysis.

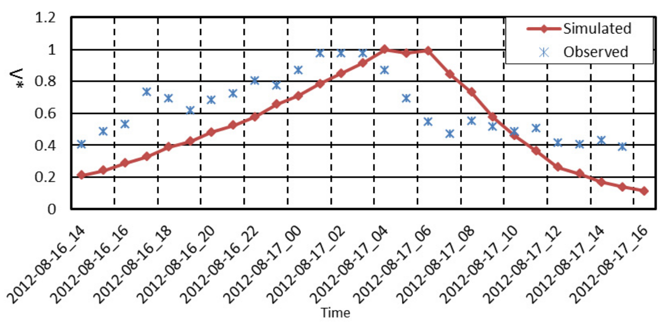

(a) Typhoon 1213

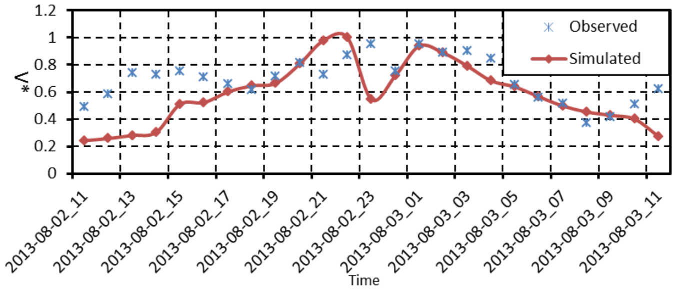

(b)Typhoon 1309

Figure 5. Wind verification.

It also can be seen from Figure 6 that the calculated and observed values of wave height have good consistency in all, and the curve shapes and peak values also have small deviations, which is similar with the wind field simulation.

The observed and computed comparison between wind and wave are showed in Figure 7 and Figure 8. From Figure 7 the delay hours for typhoon 1213 is 4 hours, and the simulated results show the delayed time is 2 hours. And from Figure 8, for observed data there is no delayed hour between wind and wave extreme value, the simulated result shows the delay time is one hour. It is considered time difference between observed and computed wind process is due to the time error in wind simulation. The typhoon moving velocity is different in land and sea area, if the model considers the real terrain changes, the time differences can be improved.

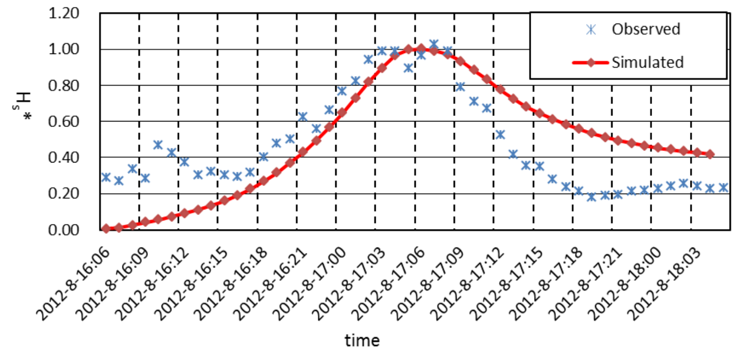

(a)Typhoon 1213

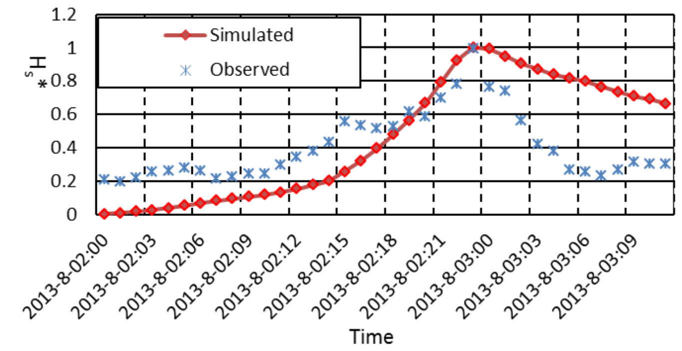

(b)Typhoon 1309

Figure 6. Wave verification.

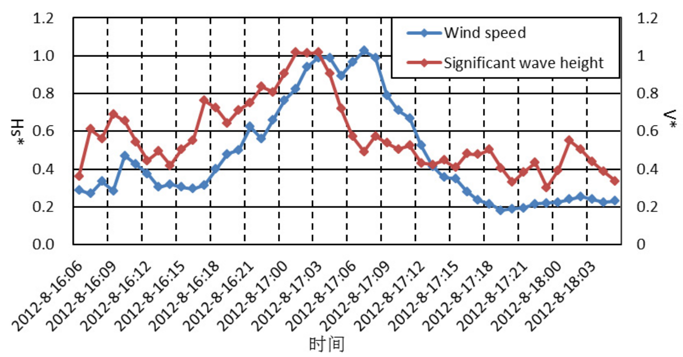

(a) Observed values

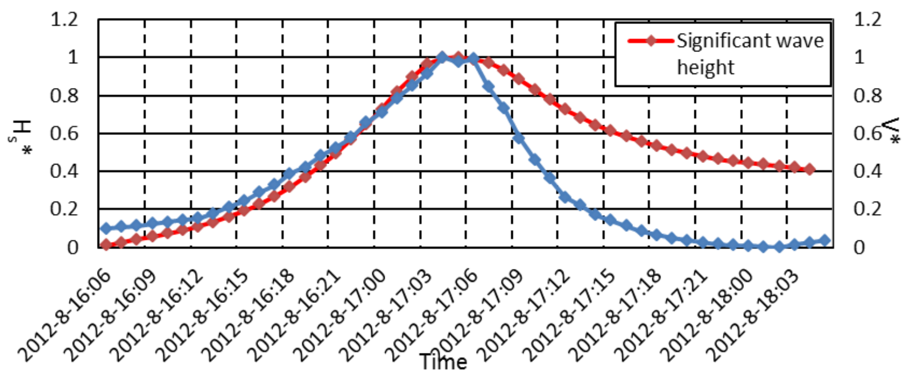

(b) Calculated values

Figure 7. Comparison between wind and wave for typhoon 1213.

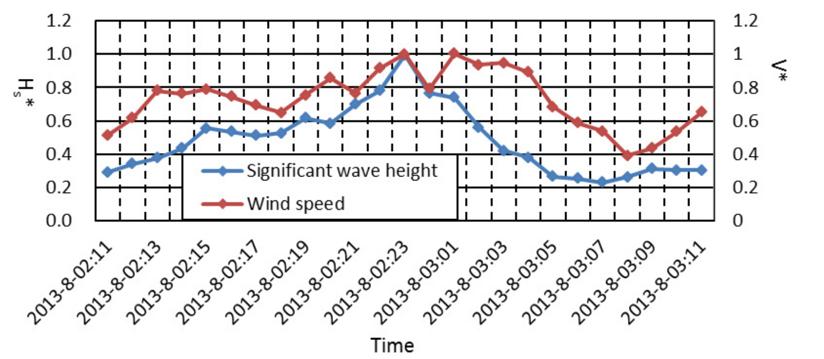

(a) Observed values

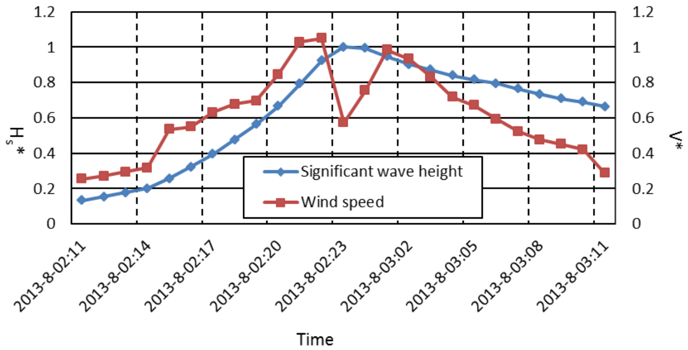

(b)Calculated values

Figure 8. Comparison between wind and wave for typhoon 1309.

6 CONCLUSIONS

The parametric typhoon model and the SWAN wave model are selected to simulate the typhoon waves in the waters of Qiongzhou Strait. The Takahashi and Fujita nested pressure model, Gradient wind equation and Ueno equation construct the wind field model, and the comparison between the simulated results and the measured data showed that the selected parametric typhoon model is efficient and feasible.

The SWAN wave model is used for numerical simulation of typhoonwaves. With no consideration of tidal level, wave-current coupling effects and other factors, the simulation results of typhoon waves have a small deviation with the measured data, but holistic characteristics of typhoon waves have good consistency. It ascertains this simulation method applicable for coastal engineering practices or activities. Furthermore, this numerical simulation method of typhoon waves and the related simulation conclusions could provide the research references with the determination of the wind and wave designed parameters in planned sea-crossing project of the Qiongzhou Strait.

In this study, the delayed time between wind and wave extreme value affected by typhoon processes is simulated. There is difference between the observed results and simulated results. It is considered the difference is due to the wind moving velocity changes on land and sea area. The empirical typhoon model is better to consider the terrain changes.

ACKNOWLEDGEMENTS

The authors would like to acknowledge the support of National Natural Science Foundation of China (Grant No.51309127), Tianjin Applied Basic and Frontier Technology Research Project (Grant No. 15JCQNJC07300), Central Commonweal Research Institute Basic R&D Special Foundation of TIWTE (Grant No.TKS160206), Central Commonweal Research Institute Basic R&D Special Foundation of TIWTE (Grant No.TKS160219). I am grateful for advices from the Meteorological observatory, especially Lin Yi, to the numerical model for wave conditions of Qiongzhou Strait and thanks for providing the meteorological datum. Both reviewers are thanked for their detailed comments on the manuscript.

REFERENCES

Graham, H.E. & Nunn, D.E. (1959). *Meteorological Conditions Pertinent to Standard Project Hurricane*, Atlantic and Gulf Coasts of United States, National Hurricane Research Project, Report No. 3, US Weather Service.

Holthuijsen, L.H., Herman, A. & Booij, N. (2003). Phase-Decoupled Refraction-Diffraction for Spectral Wave Models. *Coastal Engineering*, 49(4), 291-305.

Hsu, T.W., Ou, S.H. & Liau, J.M. (2005). Hindcasting Nearshore Wind Waves Using a Fem Code for SWAN. *Coastal Engineering*, 52(2), 177-195.

Kim, S.Y., Yasuda, T. & Mase, H. (2008). Numerical Analysis of Effects of Tidal Variations on Storm Surges and Waves. *Applied Ocean Research*, 30(4), 311-322.

Meng, Y., Matsui, M. & Hibi, K. (1995). An Analytical Model for Simulation of the Wind Field in a Typhoon Boundary Layer. *Journal of Wind Engineering and Industrial Aerodynamics*, 56(2-3), 291-310.

Ying, M., Zhang, W., Yu, H., Lu, X., Feng, J., Fan, Y., Zhu, Y. & Chen, D. (2014). An Overview of the China Meteorological Administration Tropical Cyclone Database. *Journal of Atmospheric and Oceanic Technology*, 31(2), 287-301.

Ou, S.H., Liau, J.M., Hsu, T.W. & Tzang, S.Y. (2002). Simulating Typhoon Waves by SWAN Wave Model in Coastal Waters of Taiwan. *Ocean Engineering*, 29(8), 947-971.

Shapiro, L.J. (1983). The Asymmetric Boundary Layer Flow Under a Translating Hurricane. *Journal of the Atmospheric Sciences*, 40(8),1984-1998.

SWAMP Group (1985). *Ocean Wave Modeling*. Plenum Press, NY, 256.

Tolman, H.J. (1992). Effects of Numerics on the Physics in a Third-Generation-Wind-Wave Model. *Journal of Physical Oceanography*, 22(10), 1095-1111.

Tompson, E.F. & Cardone, V.J. (1996). Practical Modeling of Hurricane Surface Wind Fields. *Journal of Waterway, Port, Coastal, and Ocean Engineering*, 122(4), 195-205.

Takeo, U. (1981). Numerical Computations of Storm Surges in Tosa Bay. *Journal of Oceanographical Society of Japan*, 37(2), 61-73.

Wang, X.N., Ying, Q.J. & Zhang, B.M. (1991). Research and Applications of a Forecasting Model of Typhoon Surges in China Seas. *Advances in Water Science*, 2(1), 1-10, (in Chinese).

WAMDI Group (1988). The WAM Model - A Third Generation Ocean Wave Prediction Model. *Journal of Physical Oceanography*, 18(12), 1775-1810.

Zhao, H.J., Song, Z.Y., Xu, F.M. & Cheng, C. (2010). Numerical Simulation of Typhoon Waves in the South China Sea – A Case Study of Typhoon Chanchu. *The Ocean Engineering*, 28(3), 128-134, (in Chinese).

PREDICTION OF FECAL CONTAMINATION LEVEL IN NAKDONG RIVER USING DATA-DRIVEN MODEL

IL WON SEO(1) & SOO YEON CHOI(2)

(1,2) Department of Civil and Environmental Engineering, Seoul National University, Seoul, Korea,
seoilwon@snu.ac.kr; jjasa1103@snu.ac.kr

ABSTRACT

The level of fecal contamination in rivers is one of major concerns when it comes to safety of contact recreation in rivers, since fecal contamination is related to presence of pathogen in rivers. Therefore there is a need to predict the level of fecal indicator bacteria in real-time through fast and simple method. In this study, the level of fecal coliform among various fecal indicator bacteria was predicted in real-time using logistic regression model which is one of data-driven models. Using logistic regression model, it is possible to predict directly whether the concentration of fecal coliform exceeds 200 CFU/100ml, which is the safe water quality criteria for contact recreation in terms of fecal contamination. Nakdong River was selected as a study site, since Nakdong River is becoming popular for recreational activity facilities thanks to Four Major River Restoration Project from 2010 to 2012. In this study, monitoring stations were classified into four groups, G1, G2, G3 and G4, according to their locations and hierarchical clustering results in order to reduce heterogeneity in datasets. Logistic regression models were developed using datasets from monitoring stations in three groups, G2, G3, and G4. G1 was excluded because exceedance of fecal coliform safe criteria was a rare event in G1 section. Developed models were tested using test datasets. As results, three models show relatively high accuracy of more than 80% in terms of total classification, specificity and sensitivity.

Keywords: Contact recreation; fecal coliform; Nakdong River; logistic regression model; hierarchical clustering method.

1 INTRODUCTION

Recently, Nakdong River, which is one of the major rivers in South Korea, has become a popular place for riverine contact recreation such as waterskiing and boating. It is because spaces for riverine recreation were created along the Nakdong River as part of river restoration project from 2010 to 2012. This popularity caused concerns about the level of fecal contamination in Nakdong River when it comes to safety of contact recreation, since contact recreation in fecally contaminated water can lead to gastrointestinal, respiratory, and skin illnesses (Byappanahalli et al., 2012). Thus, it is important to check if the level of fecal contamination exceeds certain safe level in real-time. The level of fecal contamination can be examined by measuring fecal indicator bacteria. However, fecal indicator bacteria cannot be measured in real-time and it takes at least 18 hours to measure (Byappanahalli et al., 2012). Therefore, there is a need to predict the level of fecal contamination in real-time.

There are two ways to predict the level of fecal contamination: physics-based model and data-based model. Data-based model is more preferable for the use of real-time prediction, since data-based model tends to take less time to run and does not need any geometry data or nonpoint source pollutants data which are usually necessary to physics-based model. On the contrary, input data of the data-based model such as water quality and hydro-meteorological data can easily be measured in real-time using the existing auto-monitoring system. However, when data-based model is applied to spatially large scale such as Nakdong River, spatial heterogeneity of data can exist, which can weaken the prediction accuracy. Therefore, there is need to classify sections according to similarity and develop separate models for each classification.

In this study, prediction model of the level of fecal contamination in Nakdong River was developed using data-driven model. Among data-based model, logistic regression model was used because it can predict the exceedance and compliance of safe criteria for fecal indicator bacteria rapidly to indicate the level of fecal contamination. Herein, fecal coliform was used as fecal indicator bacteria since it is measured periodically in Korea. Furthermore, hierarchical clustering method was applied to group sections with similar water quality characteristic.

2 METHODOLOGY

2.1 Hierarchical clustering method

Clustering methods are used to find subgroups, or clusters in datasets. Clustering methods partition datasets into groups so that the datasets within each group are similar to each other, while datasets in different groups are different from each other (James et al., 2013). Hierarchical clustering method is the most common approach of clustering methods. Hierarchical clustering method provides intuitive similarity relationships between datasets by illustrating dendrogram (McKenna, 2003). Dendrogram provides a summary of clustering results visually. In hierarchical clustering method, similarity between datasets can be measured by various ways. Among them, Euclidean distance, which considers similarity as distance of two dataset, is mostly used. In hierarchical clustering method, clustering process starts from n clusters when there are n datasets. Then, similarities between clusters are calculated and the most similar two clusters are fused to one cluster. This process was repeated until whole datasets belong to one cluster.

2.2 Logistic regression model

Logistic regression model is linear regression model for categorical response variable. It models the probability of Y belonging to a particular category (James et al., 2013). Log-odds is introduced in order to calculate the probability of certain response variable. When response variables are given as 0 and 1, the odds can be defined as the ratio of (probability of response variable, 1 at a given explanatory variables, $\mathbf{X}$) to (probability of response variable, 0 at a given explanatory variables, $\mathbf{X}$) as Eq. [1].

$$odds = \frac{p(\mathbf{X})}{1-p(\mathbf{X})} \quad [1]$$

where, $p(\mathbf{X}) = \mathrm{prob}(Y=1|\mathbf{X})$. $\mathbf{X} = (X_1, ..., X_n)$ are n explanatory variables.

Then relationship between log-odds and explanatory variables is figured out as Eq. [2].

$$\log\left(\frac{p(\mathbf{X})}{1-p(\mathbf{X})}\right) = \beta_0 + \beta_1 + ... + +\beta_n X_n \quad [2]$$

where, β_0 is the intercept and $\beta_1, ..., \beta_n$ are the slope coefficients of each explanatory variables.

The Eq. [2] can be expressed as following Eq. [3].

$$p(\mathbf{X}) = \frac{\exp(\beta_0 + \beta_1 X_1 + ... + +\beta_n X_n)}{1+\exp(\beta_0 + \beta_1 X_1 + ... + +\beta_n X_n)} \quad [3]$$

The coefficients were achieved by maximum likelihood method. For selecting explanatory variables to be included in the model, stepwise variable selection methods can be used. Stepwise selection methods is performed by adding and removing variables one by one until variables in the model have the best fit to data. Logistic regression showed prediction results as probability, which requires cut-off value which is used as threshold to determine that result can be determined as a certain response variable. The cut-off value from 0 to 1 should be adjusted through cross validation. Proper cut-off value can solve the problem of unbalance between the numbers of datasets for response variables which can increase prediction inaccuracy.

2.3 Model assessment

Developed models were tested in terms of three error measurement, Total Correct Classification Rate (TCCR), sensitivity and specificity. TCCR is the percentage of correctly predicted exceedance and compliance datasets. Sensitivity is percentage of exceedance datasets that can be predicted correctly. Specificity is percentage of compliance datasets that can be predicted correctly (Thoe et al., 2014). In this research, TCCR, sensitivity and specificity can be calculated as following Eq. [4] – [6].

$$TCCR = \frac{n_{GG} + n_{PP}}{n_{GG} + n_{GP} + n_{PP} + n_{PG}} \quad [4]$$

$$Sensitivity = \frac{n_{PP}}{n_{PP} + n_{PG}} \quad [5]$$

$$Specificity = \frac{n_{GG}}{n_{GG} + n_{GP}} \quad [6]$$

where, n_{ij} is the number of data which is observed as i class and predicted as j class.

  / ISSN 1562-6865 (Online) - ISSN 1063-7710 (Print)

3 STUDY SITE

The Nakdong River is located in the southeastern part of the Korean peninsula. The river is about 510.36 km long, has a drainage area of 23,384 km^2 (MOLIT, 2009). Within the Nakdong River watershed, Busan and Daegu, which are the second and fourth largest cities in South Korea, are located and more than 13 million people reside. The Nakdong River basin has distinct seasons. Summer (from June to August) is hot and humid, whereas winter (from December to February) is cold and dry. The average annual temperature is 11.1 ℃ from 1981 to 2010. The average seasonal temperatures show a cyclic variation between -2.5 ℃ in summer and 23.6 ℃ in winter. The average annual precipitation is 1,104 mm in the Nakdog River basin and about 60% of annual rainfall is concentrated in the summer (MOLIT, 2009). The water quality of the Nakdong River is generally good in the upstream (Lee et al., 2010). However, water quality in mid and downstream is worse than that in the upstream, since large industrial complexes and urban area are located in Daegu, Gumi, Jinju and Changwon at the mid and downstream of Nakdong River. Agriculture and livestock farming, which are practiced over the watershed, can also be the major source of fecal pollution and nutrients into the river.

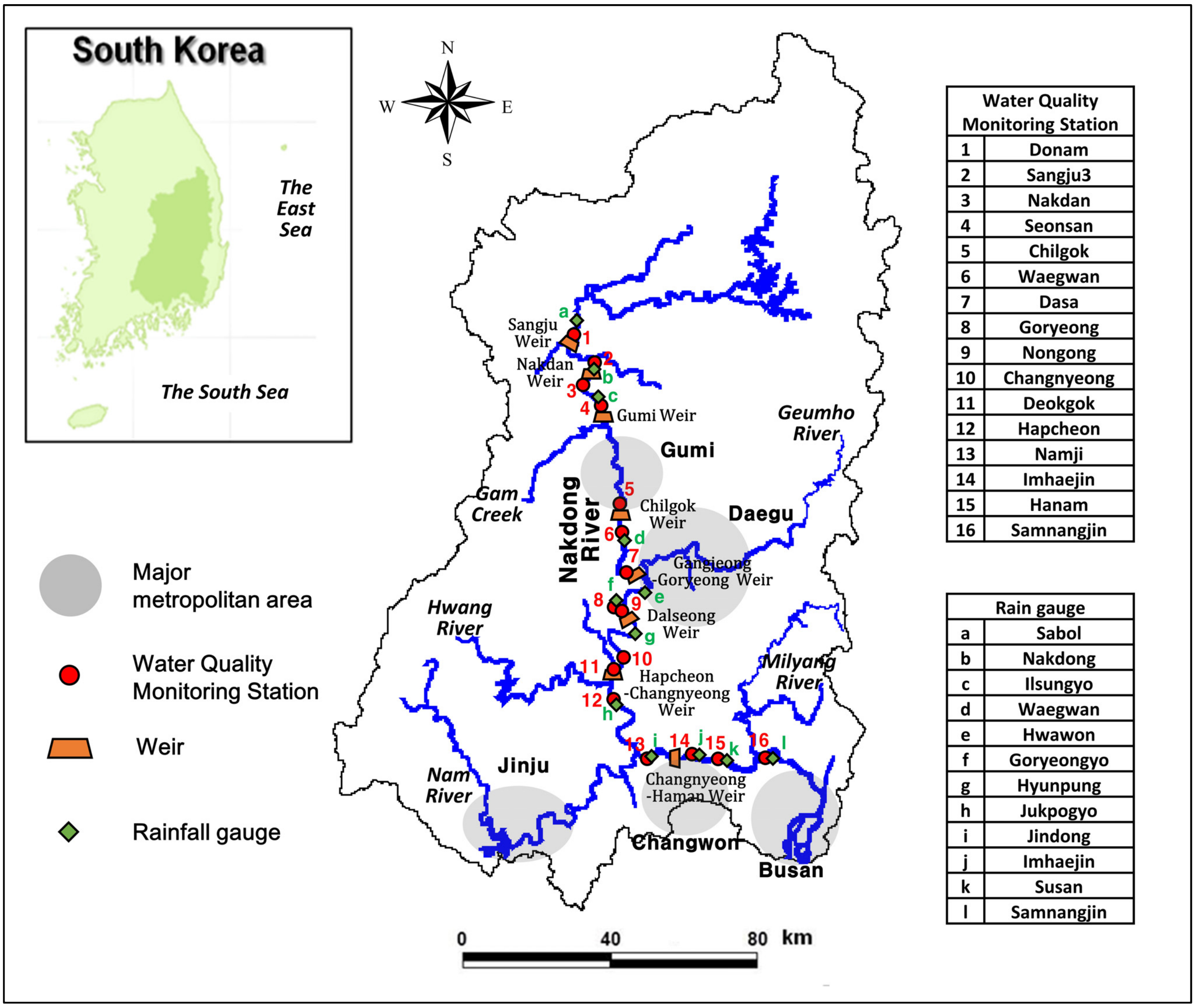

Figure 1. Nakdong River basin.

4 DATA DESCRIPTION

In this research, response variables of the model are categorical types which mean fecal coliform concentration would violate safe criteria for river recreation at a given situation. Safe criteria for contact activities was determined as 200 CFU/100mL. If fecal coliform concentration was less than 200 CFU/100mL, categorical response variables became "Good". In opposite case, "Poor" was given. Potential explanatory variables were selected for model development. Potential variables should satisfy the following standards: 1) whether variables have some relationships with fecal coliform, and 2) whether variables measured in real-time through auto monitoring station. Following these standards, water temperature (WT), pH, dissolved oxygen (DO), electric conductivity (EC), total nitrogen (TN), total phosphorus (TP), chlorophyll-a (Chl-a), and rainfall-related factors such as antecedent rainfall (AR3), antecedent rainfall duration (ARD3), antecedent rainfall intensity (ARI3) were chosen. The relationships with these variables and fecal coliform were reviewed based on literature.

Water quality and rainfall data were collected from 2013 to 2016, since river environment changed after river rehabilitation project in 2009 to 2012. Water quality data included were WT, pH, DO, EC, TN, TP, Chl-a and fecal coliform. These water quality data were acquired from 16 water quality monitoring stations (Fig. 1) via Water Resources Management Information System (WAMIS) which is run by Korea Ministry of Land, Infrastructure and Transport. Cold seasons (October - April) data were discarded since riverine recreation activities are rare during cold seasons and water quality characteristics are different depending on seasons. Collected fecal coliform data was transformed into “Good” and “Poor” classes. Furthermore, in order to make AR3, ARD, and ARI3 data corresponding to collected water quality data, rainfall volume and duration data were also gathered from 12 rain gauges adjacent to 16 water quality monitoring stations. Created AR3, ARD, and ARI3 data were combined with water quality data to compose one dataset.

5 RESULTS

5.1 Grouping sections

In this study, 16 water quality monitoring stations representing water quality characteristics of each section were clustered using hierarchical clustering method. Herein, similarity of stations was determined whether stations have similar values of fecal coliform and other explanatory variables, such as WT, pH, DO, EC, TN, TP, Chl-a, ARV3, ARD3, and ARI3. Not only that, correlation pattern of fecal coliform with other explanatory variables was also considered to determine similarity of stations. For that, medians of all variables and correlation coefficients of fecal coliform concentration with other explanatory variables were calculated for each station and are as shown in Table 1 and Table 2.

Table 1. Medians of fecal coliform and other explanatory variables.

Station	FC (CFU/ 100ml)	pH	DO (mg/L)	TN (mg/L)	TP (mg/L)	WT (℃)	EC (µS/ cm)	Chl-a (mg/ m^3)	ARV3 (mm)	ARD3 (hr)	ARI3 (mm/ hr)
1	4	8.5	9.2	1.931	0.0330	24.2	213	14.1	3.0	2	1.00
2	4	8.2	8.5	1.906	0.0340	24.3	220	13.6	3.0	2	1.00
3	4	8.0	8.5	1.979	0.0345	24.6	222	12.2	2.0	1	1.00
4	4	8.2	8.7	1.875	0.0340	24.4	220	11.9	1.0	1	1.00
5	6	8.1	8.2	2.233	0.0450	24.8	268	12.3	4.0	2	1.50
6	11	8.2	8.5	2.282	0.0400	25.2	261	15.9	4.0	2	1.50
7	5	7.9	7.3	2.139	0.0500	23.9	250	10.6	3.0	2	1.32
8	6	8.4	8.9	2.853	0.0540	26.0	352	27.1	5.0	3	1.38
9	6	8.0	8.4	2.947	0.0650	24.7	353	15.6	4.0	3	1.33
10	20	8.2	9.9	2.541	0.0560	26.0	294	20.3	7.0	3	1.80
11	6	8.0	8.3	2.724	0.0660	24.7	339	14.3	6.5	3	1.61
12	15	7.9	8.8	2.607	0.0500	25.0	300	16.7	7.0	3	1.75
13	28	8.3	10.5	2.047	0.0560	25.7	217	30.8	5.0	3	1.33
14	13	8.1	9.2	2.186	0.0490	25.0	245	23.0	3.0	2	1.50
15	24	8.4	9.6	2.220	0.0530	25.3	239	22.7	3.0	2	1.13
16	28	8.3	9.7	2.154	0.0550	25.3	225	23.3	5.0	2	1.14

Table 2. correlation coefficients of fecal coliform with other explanatory variables.

Station	pH	DO	TN	TP	WT	EC	Chl-a	ARV3	ARD3	ARI3
1	-0.570	-0.277	0.378	0.675	-0.019	-0.545	-0.280	0.453	0.503	0.269
2	-0.609	-0.085	0.317	0.678	-0.088	-0.471	-0.025	0.482	0.517	0.261
3	-0.415	0.027	0.337	0.558	-0.156	-0.448	-0.211	0.557	0.589	0.102
4	-0.512	-0.049	0.277	0.545	-0.086	-0.435	-0.089	0.555	0.482	0.221
5	-0.329	-0.106	0.057	0.554	0.005	-0.378	-0.094	0.617	0.560	0.431
6	-0.213	0.080	0.160	0.416	-0.045	-0.212	-0.057	0.484	0.372	0.325
7	-0.273	0.028	0.130	0.420	-0.012	-0.273	-0.193	0.461	0.423	0.170
8	-0.373	-0.144	-0.031	0.481	-0.052	-0.358	-0.169	0.615	0.507	0.280
9	-0.442	-0.133	-0.082	0.459	-0.014	-0.424	-0.164	0.664	0.650	0.224
10	-0.320	-0.272	0.205	0.568	-0.163	-0.254	-0.098	0.519	0.488	0.085
11	-0.389	0.048	0.076	0.501	-0.077	-0.434	-0.148	0.400	0.408	0.060
12	-0.262	-0.226	0.113	0.474	-0.082	-0.284	-0.051	0.447	0.438	0.106
13	-0.406	-0.397	0.286	0.679	-0.207	-0.207	-0.194	0.606	0.510	0.333
14	-0.354	-0.191	0.139	0.512	-0.037	-0.330	-0.221	0.548	0.451	0.312
15	-0.422	-0.371	0.347	0.716	-0.139	-0.209	-0.147	0.575	0.486	0.539
16	-0.411	-0.390	0.292	0.692	-0.205	-0.236	0.002	0.700	0.597	0.443

Hierarchical clustering was conducted on data shown in Table 1 and 2. Medians of all variables were scaled because variables have different units. Hierarchical clustering results were shown in Fig. 2. According to clustering results, stations were divided into four groups from G1 to G4. G1 included stations from S1 to S4, which are all located in upper stream. G2 covered stations from S5 to S7 which are located at downstream of Gumi industrial complex and at upstream of confluence of Geumho River. Geumho River, which is a major tributary of Nakdong River, flows through metropolitan area and industrial complexes in Daegu. From S8 to S12 belong to G3, which are located at downstream of confluence of Geumho River and at upstream of confluence of Nam River. Nam River is also important tributary of Nakdong River and is affected by metropolitan area and industrial complexes in Jinju. Remaining stations from S13 to S16 are located in downstream of Nakdong River belongs to G4.

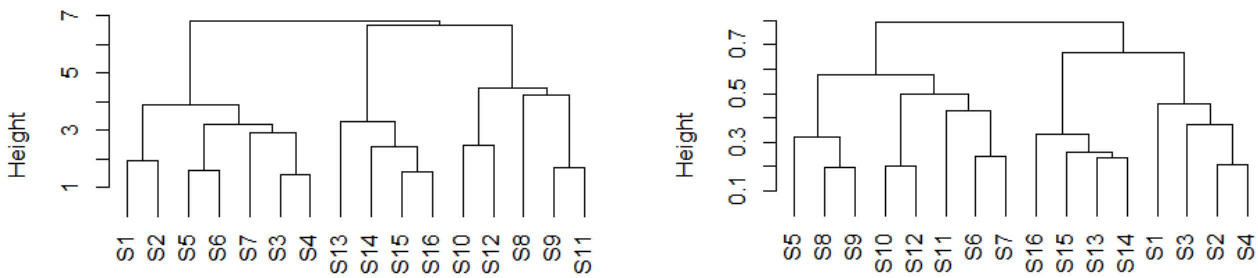

(a) Clustered by medians (b) Clustered by correlation coefficients

Figure 2. Dendgram of hierarchical clustering result.

5.2 Model training and testing

Logistic regression models for predicting FCG were developed based on clustered groups of water quality monitoring stations. However, model of G1 was excluded because the occurrences of “Poor” class were rare. Collected datasets of G2, G3, and G4 were divided into training and test datasets using stratified sampling. 70% of “Good” and “Poor” class were sampled as training datasets. The remaining datasets were used as test datasets. Application of logistic regression model resulted in Eq. [7] - [9] for each group, G2 - G4, respectively. By these equations, probability at which response variable is classified as “Poor” class can be calculated.

$$p_{G2}(Poor) = \frac{\exp(-9.31 + 46.79TP + 0.01EC + 0.15ARD3)}{1 + \exp(-9.31 + 46.79TP + 0.01EC + 0.15ARD3)} \quad [7]$$

$$p_{G3}(Poor) = \frac{\exp(9.76 - 1.11pH + 0.26DO + 34.06TP - 0.20WT + 0.04ARV3)}{1 + \exp(9.76 - 1.11pH + 0.26DO + 34.06TP - 0.20WT + 0.04ARV3)} \quad [8]$$

$$p_{G4}(Poor) = \frac{\exp(6.84 - 1.14pH + 0.06ARV3 - 0.09ARD3)}{1 + \exp(6.84 - 1.14pH + 0.06ARV3 - 0.09ARD3)} \quad [9]$$

The optimal cutoff value which represented threshold for “Poor” class was selected before the model test. 5-fold cross validation method was applied to compare cutoff value in terms of TCCR, sensitivity and specificity as shown in Fig. 3. Cutoff value, 0.10, 0.15 and 0.15 were chosen for G2, G3 and G4, respectively, since these values show similar high values of TCCR, sensitivity and specificity. In this study, relatively low cutoff value were chosen since bias exist between the number of training datasets for “Good” and “Poor” classes. The number of datasets corresponding to “Good” is 5 to 10 times larger than the number of datasets for “Poor”. Using chosen cutoff value, developed models were tested. Model test results are shown in Fig. 4. All three models show more than 80% of prediction accuracy in terms of TCCR, Specificity and Sensitivity.

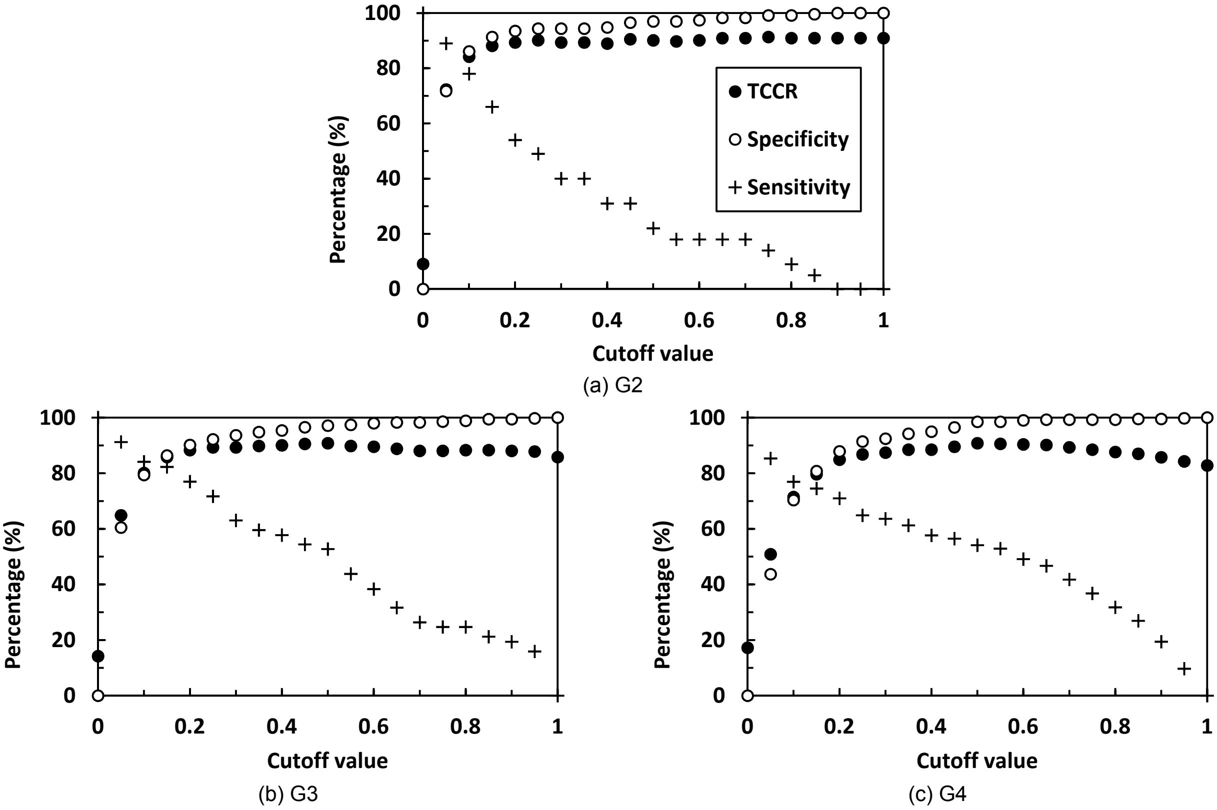

Figure 3. Result of 5-fold cross validation method for choosing optimal Cutoff value.

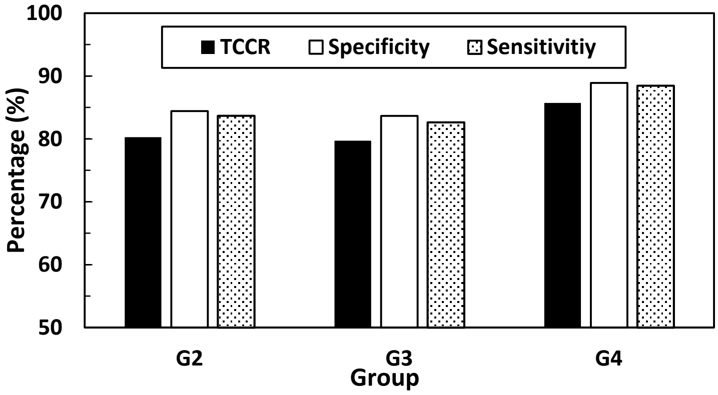

Figure 4. Test of developed models for G2, G3 and G4

6 CONCLUSIONS

In this research, logistic regression models were developed for reaches with different water quality characteristics in Nakdong River. All developed model showed relatively high prediction accuracy, i.e. more than 80%. Nakdong River reaches were divided into four groups using hierarchical clustering. Clustered groups corresponded to their location and effect of industrial and domestic waste water. It was shown that G1, which is located in upstream of Nakdong River, has had rare event of “Poor”. Therefore, there is a need to apply other data-based model for rare event prediction. In case of G2, G3, and G4, logistic regression models could be applied and shown differently trained model. However, all three models show that rainfall related explanatory variables such as ARV3 and ARD3 are significant to predict the exceedance of fecal coliform.

ACKNOWLEDGEMENTS

This research is supported by a grant (11-TI-C06) from Advanced Water Management Research Program funded by Ministry of Land, Infrastructure and Transport of Korean government.

REFERENCES

Byappanahalli, M.N., Nevers, M.B., Korajkic, A., Staley, Z.R. & Harwood, V.J. (2012). Enterococci in the Environment. *Microbiology and Molecular Biology Reviews*, 76(4), 685-706.

James, G., Witten, D., Hastie, T. & Tibshirani, R. (2013). *An Introduction to Statistical Learning* (Vol. 6). New York: springer.

Lee, H.W., Bhang, K.J. & Park, S.S. (2010). Effective Visulalization for the Spatiotemporal Trend Analysis of Water Quality in the Nakdong River of Korea. *Ecological Informatics*, 5(4), 281-292.

McKenna, J.E. (2003). An Enhanced Cluster Analysis Program with Bootstrap Significance Testing for Ecological Community Analysis. *Environmental Modelling & Software*, 18(3), 205-220.

MOLIT (Korea Ministry of Land, Intrastructure and Transport). (2010). *River Maintenance Planning Report: The North Han River. (In Korean)*

Thoe, W., Gold, M., Griesbach, A., Grimmer, M., Taggart, M.L. & Boehm, A. B. (2014). Predicting Water Quality at Santa Monica Beach: Evaluation of Five Different Models for Public Notification of Unsafe Swimming Conditions. *Water Research,* 67, 105−117.

FLOWCV - AN OPEN - SOURCE TOOLBOX FOR COMPUTER VISION APPLICATIONS IN TURBULENT FLOWS

DANIEL B. BUNG[(1)] & DANIEL VALERO[(2)]

[(1,2)] FH Aachen University of Applied Sciences, Aachen, Germany,
University of Liège, Liège, Belgium,
bung@fh-aachen.de;valero@fh-aachen.de

ABSTRACT

Despite the continuous advances in numerical modeling methods and the continuous increase of computer power and storage capacities in the last decades, physical modeling remains a common technique for evaluation of flow processes. One major advantage of this classical approach is given by the transparency of experiments as the flow can be easily observed in the laboratory and effects of changing boundary conditions may be better understood. Nowadays, the flow is commonly captured in most experiments with means of digital cameras or high-speed cameras to get a better insight and for further analyses after the model test. Besides some well-known techniques such as Particle Image Velocimetry, some new methods can be found in Computer Vision disciplines allowing for more detailed investigation of the images. This paper presents two modules of the new open-source toolbox FlowCV which has been developed to be applied in hydraulic laboratories. The first module is given by a synthetic particle image generator which provides the user with particle images of a predefined motion and turbulence. The second module implements different Optical Flow methods for determination of obstacle movement (here: particle movement). The Farnebäck method, which is presented in this paper, gives dense velocity fields, i.e. velocity data for every image pixel with moving particles. The Optical Flow results based on the synthetic images are then benchmarked against their predefined particle velocity. It will be shown that even the smallest turbulent flow structures are adequately detected.

Keywords: Imaging techniques; computer vision; optical flow; turbulence; particle images.

1 INTRODUCTION

Physical modeling is still a common technique to evaluate flow features of complex flows. Investigation of flow parameters, such as velocity and turbulence intensity profiles are typically gathered by means of intrusive probes, e.g. 1D flow anemometers or 3D ADV probes in clear water or dual-tip phase detection probes in air-water flows. Most of these probes provide point measurement data only, thus requiring multiple measurements to obtain some idea about complete velocity fields in a given area of interest.

A complementary technique is given by non-intrusive imaging techniques, with the Particle Image Velocimetry (PIV) being the most recognized method among the fluid mechanics community. It has reached a maturity stage (Adrian and Westerweel, 2011) and is commonly employed in almost every hydraulic laboratory nowadays. For PIV, the flow is seeded with neutrally buoyant particles and captured with a (high-speed) camera. The field of view is then divided into several smaller interrogation windows of a pre-defined size. By application of a cross-correlation technique (in spatial or frequency domain) to two subsequent frames and a certain peak finding method, the most likely average movement of the particles within the interrogation area is obtained. It is obvious that particles within a given interrogation window must not leave this window from one frame to the next in order to be taken into account for cross-correlation. This requirement leads to a minimum feasible interrogation window size for a given field of interest and camera sample rate, thus to a limited spatial resolution of the resulting velocity fields. Although the temporal resolution may be sufficiently high when a high-speed camera is employed, small-scale flow structures are still difficult to visualize.

It was recently shown that the so-called Optical Flow (OF) method may help to overcome this problem. Bung and Valero (2016a; 2016c) and Zhang and Chanson (2017) presented velocity and turbulence intensity profiles for complex air-water flows while Corpetti et al. (2006), Liu and Shen (2008), Liu et al. (2015) and Bung and Valero (2016b) applied this method to common particle images from PIV. Optical Flow is a well-recognized technique in the Computer Vision (CV) community and has become essential in many industrial applications (Fortun et al., 2015). It helps to determine obstacle displacements in a series of images on the basic assumption of pixel intensity (brightness) conservation:

$$\frac{\mathrm{d}I}{\mathrm{d}t} = \frac{\partial I}{\partial t} + \frac{\partial I}{\partial X}\frac{\partial X}{\partial t} + \frac{\partial I}{\partial Y}\frac{\partial Y}{\partial t} = 0 \tag{1}$$

In Eq. [1], I is the pixel intensity, X and Y are the pixel coordinates and t is the time. With the temporal derivative I_t, and the spatial derivatives I_x and I_y, it yields

$$I_t + I_X U + I_Y V = 0 \tag{2}$$

where U and V are the unknown spatial displacements of a pattern in X and Y directions. Eq. [2] is the so-called spatial term which needs to be extended by an additional constraint (i.e. the data term) to become iteratively solvable. The most classical proposals for such data terms are those given by Horn and Schunck (1981), yielding a dense velocity field (with information for every pixel), and Lucas and Kanade (1981), providing sparse velocity data at selected locations only. Numerous more advanced approaches have been developed in the recent past. A comprehensive overview is presented in Sun et al. (2010), Wedel and Cremers (2011) and Fortun et al. (2015). One of these novel techniques was introduced by Farnebäck (2003) assuming that the pixel intensity in a pixel neighborhood can be approximated by a quadratic polynomial:

$$I_1(X,Y) \approx \begin{bmatrix} X \\ Y \end{bmatrix} A_1 [X \quad Y] + b_1^T [X \quad Y] + c_1 \tag{3}$$

$$I_2(X+U, Y+V) = I_1(X,Y) = \begin{bmatrix} X+U \\ Y+V \end{bmatrix} A_2 [X+U \quad Y+V] + b_2^T [X+U \quad Y+V] + c_2 \tag{4}$$

with 1 and 2 the indices related to image 1 and image 2, A a symmetrical matrix, b a vector and c a constant. By a simple polynomial expansion, Farnebäck (2003) shows that the unknown displacement vector may be determined as:

$$\begin{bmatrix} U \\ V \end{bmatrix} = -0.5 A_1^{-1} (b_2 - b_1) \tag{5}$$

Thus, requiring A_1 to be invertible. It must be noted that Eq. [5] holds only for absolute pixel intensity conservation ($A_1 = A_2$), i.e. an ideal condition which is rarely met in practice. By consequence, the symmetrical matrix in Eq. [5] may be replaced by $0.5(A_1 + A_2)$ as a reasonable approximation. Eq. [5] can be solved pixelwise. However, Farnebäck (2003) describes the results to be affected by noise and proposes to solve Eq. [5] for an ensemble of pixels within a neighborhood while applying a weighting function for the pixels involved. This step is reasonable if it is assumed that the displacement field is only slowly varying. Eq. [5] turns then into a more complex minimization problem which needs to be solved iteratively. For more detailed information, the reader is referred to the original literature (Farnebäck, 2003). One drawback of this technique is that the local polynomials are likely exposed to spatial variance, thus involving some error which increases for large displacements. If a rough estimate of an a priori displacement would be known, the final displacement could be determined by adding the solution of above method to this a priori displacement. Such a priori displacement may be obtained by application of a multi-scale approach where the first rough estimate is obtained by solving above equations for a coarser scale of the image (with lower resolution). This technique is known as image pyramid in the Computer Vision community. Bung and Valero (2016a) demonstrated the significant influence on the quality of results. More detailed information on the image pyramid technique can be found in Adelson et al. (1984) and Burt and Adelson (1983). The above mentioned Optical Flow methods, and more than 2,500 other Computer Vision methods, are implemented in OpenCV, being an Open Source computer vision and machine learning software library (Bradski and Kaehler, 2008). OpenCV is natively written in C++, but APIs for Python, Java and Matlab are also available.

The first aim of the present paper is to present the new FlowCV Python toolbox, which is an easy-to-use work-around combining the OpenCV library with other useful scientific Python libraries for pre- and post-processing. FlowCV allows for estimation of various hydraulic parameters, such as flow velocity and turbulence, flow depth and void fraction, on basis of images taken during hydraulic model tests. The second aim of this paper is then to demonstrate and quantify the capabilities of OF. Hereby, the current paper is limited to the Farnebäck method. In order to quantify the accuracy of velocity estimation, exact values for both are necessary. To obtain such exact data, another toolbox module has been implemented, namely a synthetic particle image generator, which provides the user with artificial images of a specified particle density, mean velocity and turbulence.

2 FLOWCV

2.1 General remarks

The herein presented Open Source toolbox FlowCV has been developed in Python (2.7) and is primarily based on OpenCV libraries. Further important libraries are NumPy for scientific computing (van der Walt et al.,

2011) and Matplotlib for post-processing (Hunter, 2007). A preformatted Excel spreadsheet serves as an easy-to-use user interface (using the openpyxl library) and allows the use of Computer Vision methods in Python without requiring any Python skills of the user. FlowCV is distributed under the GNU GPLv3 license and is freely available at https://github.com/FlowCV. The toolbox has been developed using Enthought Canopy, but has also been successfully tested with other Python installations on different operating systems. In this paper, only the Optical Flow module (FlowCV-OF) and the synthetic particle image generator (FlowCV-SPIG) are presented.

2.2 FlowCV-OF: Optical Flow estimation

2.2.1 Pre-processing

The Excel interface allows selection of some image pre-processing techniques. For instance, contrast enhancement can be conducted by means of standard histogram equalization as well as contrast limited adaptive histogram equalization (CLAHE). With histogram equalization, the pixel intensity values of the histogram are spread out to the extreme values. CLAHE is more suitable to improve local contrast as it divides the full image into smaller subareas and locally equalizes the pixel intensities. By consequence, a very dark area in a single part of the image does not affect the resulting contrast of over all the image. In order to avoid over-amplification of noise in homogenous areas of the image, the resulting contrast is limited to a certain threshold value.

As OF is known to be better suitable to continuous patterns instead of particle images due to its differential nature (Liu et al., 2015), a Gaussian blur option has also been implemented. It is a low-pass filter using a Gaussian transfer function in frequency domain. Image restoration, i.e. removing of blur due to noise or long exposure times, can be applied using a Wiener filter (Wiener, 1949).

For detailed information and mathematical descriptions on the implemented pre-processing techniques, the reader is referred to Bung and Valero (2015).

2.2.2 Solver

Besides the Farnebäck (2003) method, the Horn-Schunck and Lucas-Kanade methods can be selected in the current version 1.0. To execute the Farnebäck method, which will be tested subsequently, the function “cv2.calcOpticalFlowFarneback” is called from the OpenCV library. This function allows different settings, such as the averaging window size, the size of the pixel neighborhood to find the polynomial expansion, the number and scale of image pyramid levels and the number of iterations to solve the problem. Input and variation of all settings can be easily conducted via the Excel interface.

2.2.3 Post-processing

The post-processing module allows the generation of different types of plots as well as the export of ASCII files. Spatial and temporal scales can be specified to scale the calculated displacements from [px/frame] to [m/s]. Moreover, videos can be directly exported. In addition to the calculation of displacements between specified images, the mean or median results can be determined. Divergence of velocity fields is checked. All output parameters can be selected and specified via the Excel interface.

2.3 FlowCV-SPIG: Synthetic particle image generation

2.3.1 Motivation

In order to test the accuracy of a new optical technique, PIV seems to be the model of reference (Bung and Valero, 2016b). However, errors may occur also and the accuracy of the new technique will always be related to that of the employed PIV method. Another alternative would be to test the proposed technique against canonical flows (where analytical solution is available) reproduced in the laboratory. In such case, the velocity fields would be subject to particle slip and other sources of error (Adrian and Westerweel, 2011) yielding velocity differences and inescapable mistakes in the experimental facilities. Thus, a third option emerges as an alternative: the use of synthetic particle images. In this case, the exact velocity of each particle can be known but focus must be put in the accurate generation of the velocity fields to ensure that conclusions can apply to other types of flows.

2.3.2 Particle generation

Particles are generated with different fraction rates (f_p, ratio between particles area and the total image area). Their center location is then randomly initialized by using a uniform distribution. Particle radiuses are also randomly generated by specifying a mean and standard variation normal distribution (r_m and r_{std} correspondingly). Negative radiuses are avoided by taking the absolute values of the generated sample. Pixels within the radius of the particle are assigned 1.0 whereas the partially filled pixels receive a fractional value. Additionally, a “shadow” mask is applied. This shadow mask aims to reproduce the pixel errors commonly happening for a camera by modelling it as a white noise. The illumination of the experimental setup also enters into this shadow mask altogether with the aforementioned white noise by using a normal distribution with center s_m and standard deviation s_{std}. Values larger than 255 are restricted in order to keep image values as integers between 0 and 255. An exemplary generated image is shown in Fig. 1.

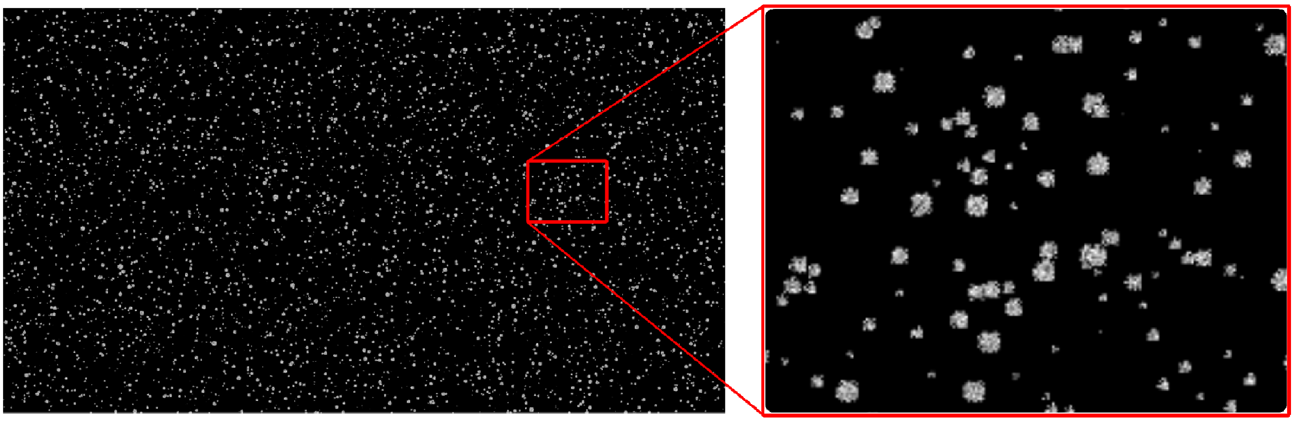

Figure 1. Synthetic image generated for $f_p = 0.05$, $r_m = 2.5$ px, $r_{std} = 1.25$ px, $s_m = 170$, $s_{std} = 40$ and high-resolution (HD).

2.3.3 Stochastic particle displacement: simulating isotropic turbulence

Particles displacement $(x_2 - x_1)$ can be computed by integrating the instantaneous velocity of a particle between t_1 and t_2:

$$x_2 = x_1 + \int_{t1}^{t2} U\, dt \qquad [6]$$

with U is the instantaneous velocity in the x coordinate, which can be expressed in terms of its mean and fluctuating component as:

$$U = \langle U \rangle + u \qquad [7]$$

with $\langle U \rangle$ being the expected value of U and u the instantaneous fluctuation. For $\langle U \rangle$, many experimental and analytical solutions exist (i.e.: boundary layer flow, mixing region, wake), which can be easily found in classic literature of fluid mechanics as Pope (2000) and White (2006). By definition, the expected value of u would be zero, so that it is common to study $\langle u^2 \rangle$. Herein, it becomes necessary to simulate the behavior of u to define a realistic turbulent velocity for each particle.

With this purpose, Langevin equation can be used. Langevin equation was first proposed as a stochastic model for the velocity of a particle subject to Brownian movement (Langevin, 1908) just three years after Einstein (1905) initiated the modern study of random processes. The stochastic process u^* generated by the Langevin equation is known as Ornstein-Uhlenbeck process and its probability density function is governed by the Fokker-Planck equation (Pope, 2000). Thereby, it is here modelled the instantaneous quantity u by means of a stochastic differential equation for u^* $(u(x,y,z,t) \approx u^*)$:

$$du^*(t) = -u^*(t)\frac{dt}{T_L} + \left(\frac{2\sigma^2}{T_L}\right)^{\frac{1}{2}} dW(t) \qquad [8]$$

where T_L is the time scale defined by the Lagrangian velocity autocorrelation function $\rho(s) = \exp\left(-s/T_L\right)$ as:

$$T_L = \int_0^\infty \rho(s) ds \qquad [9]$$

In the stochastic differential equation (Eq. [8]), σ is a measurement of the velocity fluctuation scale and $W(t)$ represents a Wiener process. Equation [8] can be approximated by the following finite difference equation (Pope, 2000):

$$u^*(t+\Delta t) = u^*(t) - u^*(t)\frac{\Delta t}{T_L} + \left(\frac{2\sigma^2 \Delta t}{T_L}\right)^{\frac{1}{2}} \xi(t) \qquad [10]$$

where $\xi(t)$ is a standardized Gaussian random variable (mean zero and unit standard deviation).

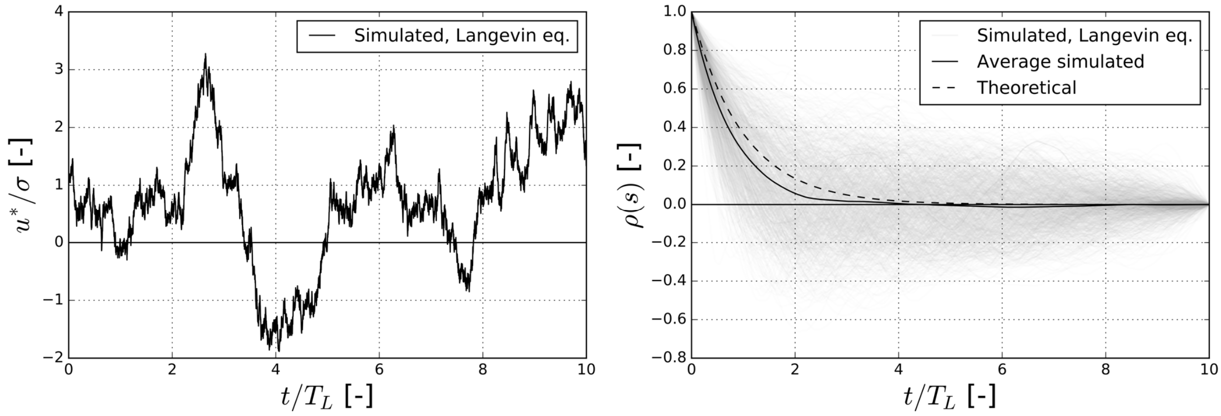

Figure 2. Left: exemplary u^* generated with Eq. [10] for one particle; and right: autocorrelation of 1,000 generated particles.

Eq. [10] represents a diffusion equation which is consistent with Kolmogorov (1941) hypotheses for the turbulence inertial subrange, thus:

$$\tau_\eta \ll \Delta t \ll T_L \qquad [11]$$

with τ_η the Kolmogorov time scale. It can then be demonstrated that, instead of the two parameters σ and T_L, Eq. [8] can be written in terms of the turbulent kinetic energy k, its dissipation ε and a model coefficient C_0 (Pope, 2000):

$$du^*(t) = -\frac{3}{4}C_0\frac{\varepsilon}{k}u^*(t)dt + (C_0\varepsilon)^{\frac{1}{2}}dW(t) \qquad [12]$$

While the choice of C_0 value is not completely clear (Pope 2000; Pope 1994), Lien and D'Asaro (2002) studied a broad range of DNS and experimental results concluding that $C_0 = 6 \pm 0.5$ is consistent. Consequently, a value of $C_0 = 6.0$ is used in this study. In FlowCV, $\langle U \rangle$, $\langle V \rangle$, k and ϵ can be varied at the Excel interface.

3 CASE STUDIES

Eq. [6] has been integrated, both for x and y direction, by using a fourth order Runge-Kutta method as described by White (2006). A mean velocity $\langle U \rangle$ of 5 px/frame is assumed for each case and the velocity fluctuation u is modelled by using Eq. [12] for each particle and time step. In order to advance from one frame to another, Δt is chosen to be small enough to satisfy Eq. [11] and the Courant-Friedrich-Lewy (CFL) condition (Hirsch, 2007). Main features of the synthetic velocity fields generated can be found in Table 1, altogether with the corresponding turbulence intensity (T_u). Exemplary, instantaneous velocity fields for all cases are shown in Fig. 3 by using the synthetic velocity information.

Table 1. Turbulence information on the generated particles synthetic images.

Case	$\langle U \rangle$ [px/frame]	$\langle V \rangle$ [px/frame]	k [px^2/frame^2]	ε [px^2/frame^3]	T_u [%]	Resolution
U01	Uniform (5.0)	Null	0.094	0.004	5.0	1920x1080
U02	Uniform (5.0)	Null	1.500	0.067	20.0	1920x1080
U03	Uniform (5.0)	Null	6.000	0.267	40.0	1920x1080
U04	Uniform (5.0)	Null	13.50	0.600	60.0	1920x1080
U05	Uniform (5.0)	Uniform (5.0)	27.00	1.200	60.0	1920x1080

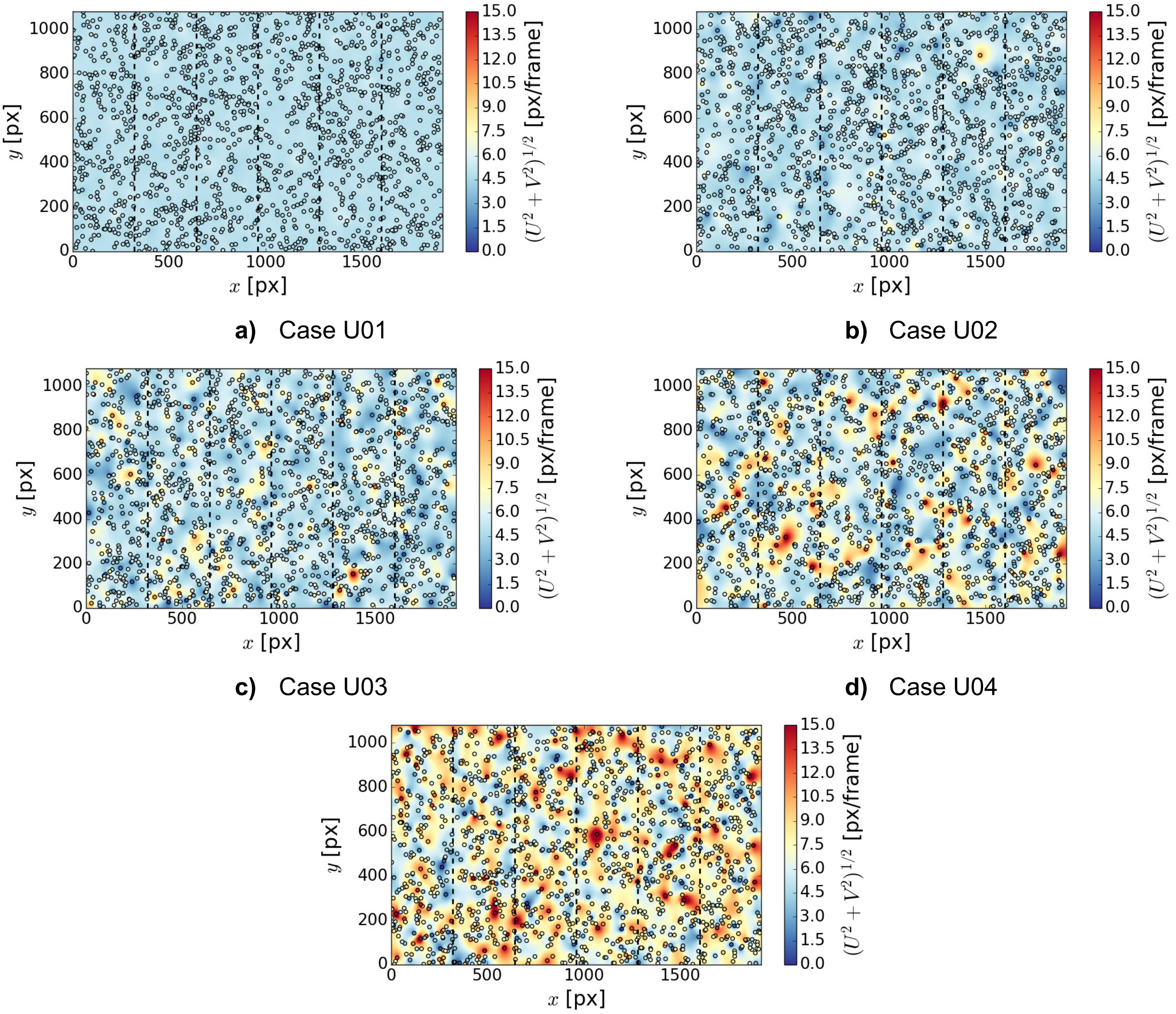

a) Case U01

b) Case U02

c) Case U03

d) Case U04

e) Case U05

Figure 3. Exemplary, instantaneous velocity fields; interpolated by using the synthetic velocity information generated for the particles of all cases U01 to U05. Particles are marked with circles; dashed lines indicate location of extracted velocity profiles in Fig. 5.

4 RESULTS

4.1 General remarks

As the focus of this study is to generally demonstrate velocity estimation applying FlowCV and the Farnebäck method to synthetic particle images, no parameter sensitivity study was conducted. All results were generated with an averaging window size of 3 x 3 px, a pixel neighborhood size of 5 x 5 px and a maximum of 7 iterations. As it is known from earlier studies (Bung and Valero, 2016a), the image pyramid essentially enhances the quality of results. Accordingly, this multi-resolution approach was applied here as well. Three different level numbers were tested, namely a single level (no image pyramid), three levels and five levels. The level scale was set to 0.5 for all cases, corresponding to an image resolution decrease of 50 % between two pyramid levels.

4.2 Image pyramid

The effect of the image pyramid technique is illustrated in Fig. 4 for an exemplary, instantaneous OF velocity field obtained for case U04. Obviously, most of the local velocity peaks from the synthetic image (see Fig. 3d) were not detected when this multi-resolution approach was not applied (Fig. 4a). The related histogram confirms that particularly velocities between 8 and 10 px/frame are underestimated while even higher velocities up to 15 px/frame are totally missed. On the other hand, low velocities up to about 2 px/frame tend to be overestimated by OF. When a multi-resolution approach was chosen, the OF method was first applied with same settings to a coarser copy of the image. In the given example with a level scale factor of

0.5, the maximum distance or velocity of 15 px/frame was reduced to about 4 px/frame for the coarsest image pyramid level when three pyramid levels were chosen. Starting from the coarsest level, the calculated displacement was refined according to the new results from the next finer level. As shown in Fig. 4b, three image pyramid level are sufficient for this study to accurately determine the velocities. More pyramid levels do not further improve the results (this finding was consistently found for all other cases).

It is pointed out that some higher deviation between synthetic and calculated velocities appear at the left and right image edges. The presented case U04 considers a translatory particle movement from left to right. Thus, particles suddenly appear at the left image edge and disappear at the right image edge and cannot be correctly detected. However, the results in Fig 4b and 4c compare well with expected data shown in Fig. 3d.

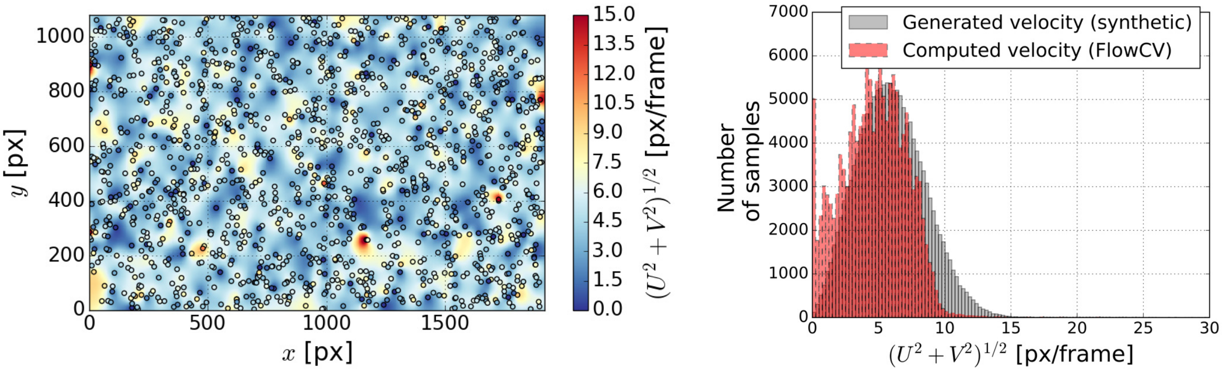

a) No image pyramid

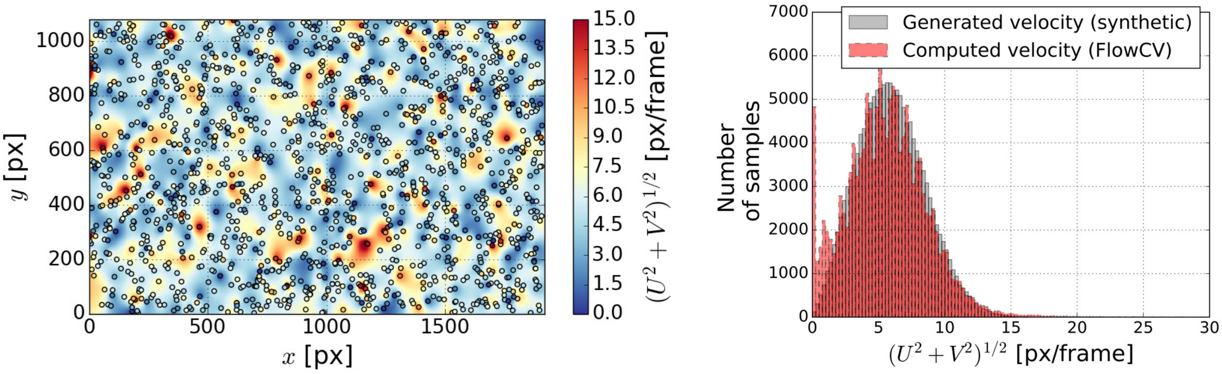

b) 3 pyramid levels

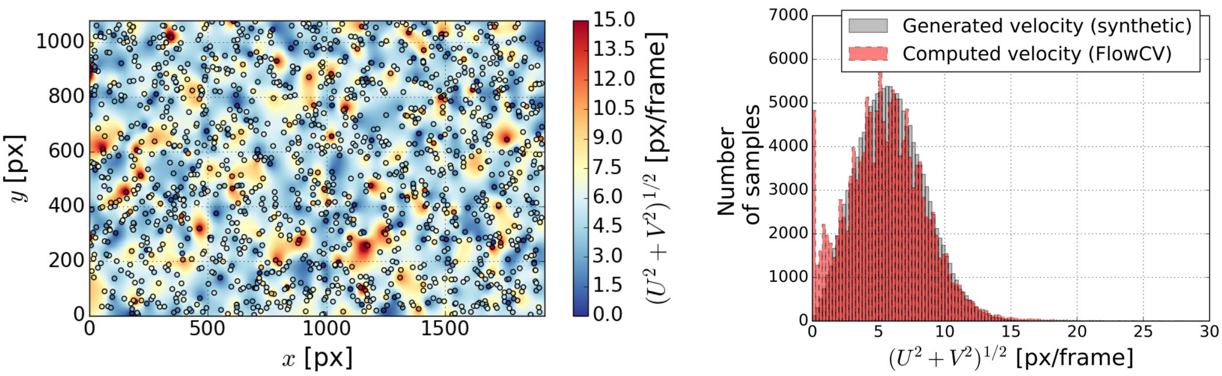

c) 5 pyramid levels

Figure 4. Effect of the multi-resolution approach (image pyramid) on the instantaneous velocities, exemplarily for case U04; results to be compared with synthetic particle velocities from Fig. 3d; left: OF velocity fields, right: related OF velocity histograms (from FlowCV) in comparison to synthetic velocity histogram.

4.3 Velocity profiles

Fig. 5 shows some extracted, instantaneous velocity profiles for all tested cases. All profiles are taken from the velocity fields shown in Fig. 3 (note that the profile locations are indicated in Fig. 3 as dashed lines).

It is found that the velocity data from OF compares fairly well with the expected velocities from the synthetic images. Some higher deviation is found for higher turbulence intensity cases. However, an adequate accuracy is still obtained as even local velocity peaks are detected. It must be noted that the Farnebäck method provides velocity data at image coordinates where a moving obstacle (here: particle) was found and null velocity elsewhere. A high-resolution velocity profile from OF may be obtained by averaging numerous velocity fields taken from a long series of images or interpolating the data.

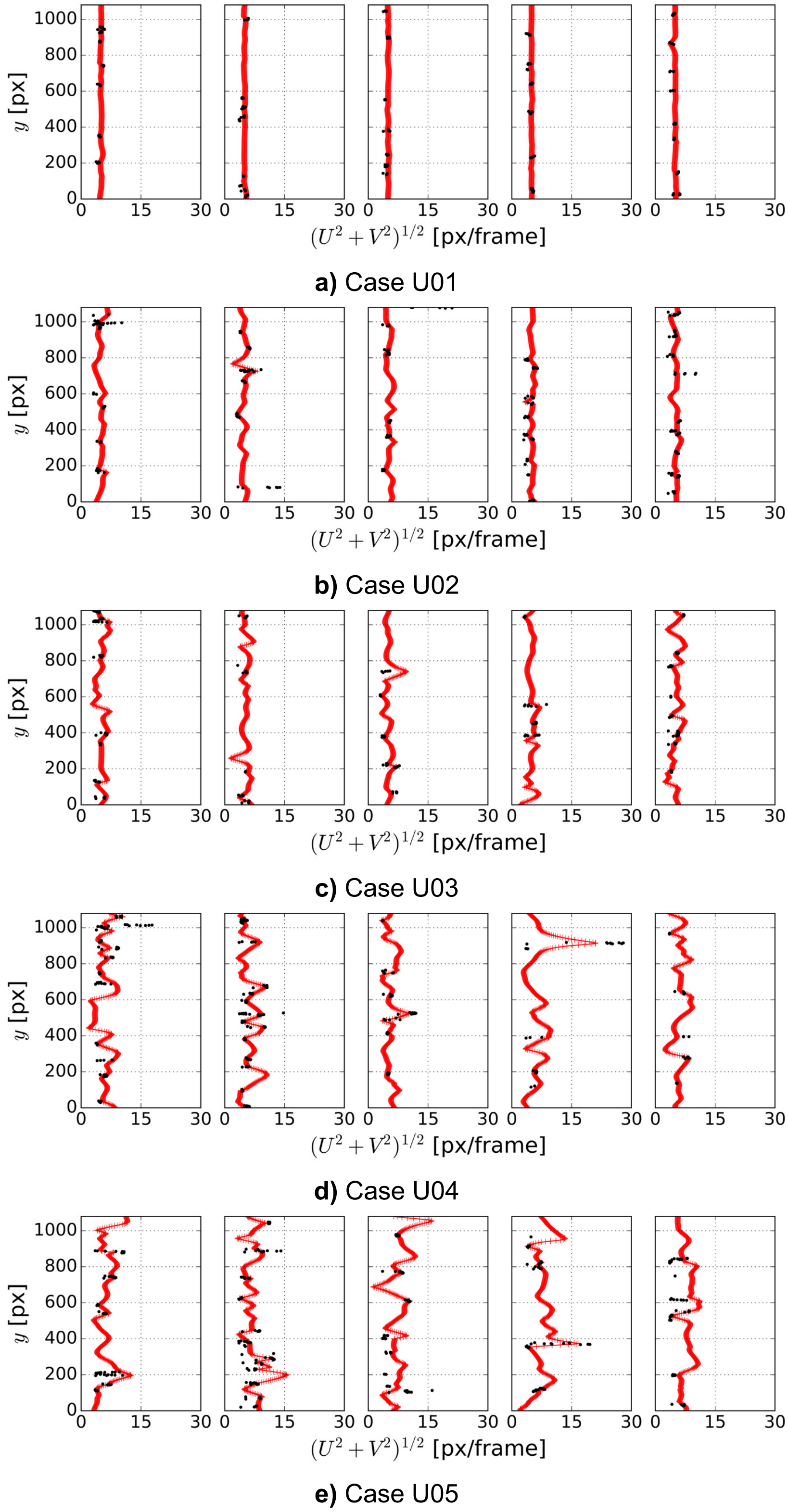

Figure 5. Extracted, instantaneous velocity profiles from OF (black markers) compared to synthetic data (red markers), locations and order of velocity profiles as indicated in Fig. 3.

4.4 Discussion

The extracted velocity profiles compare well with the expected data from the synthetic particle images. Thus, it can be concluded that the Farnebäck method, which was developed for detection of obstacle displacements in a series of images, may be applied to fluid problems as well without any further modification of its original formulation. The processing time for an image pair with full HD resolution using 5 pyramid levels and 7 iterations is about 1.5 s only and thus, about two orders of magnitude faster than the classical Horn-Schunck scheme (run in Matlab on the same computer) and about 5 times faster than PIV (run in Matlab on the same computer), though yielding more of a much denser velocity dataset (see Bung and Valero, 2016b). The high resolution of velocity data may be used for some turbulence analysis (Zhang and Chanson, 2017). It is pointed out that the results in this paper are obtained without any image pre-processing or OF parameter optimization, although both steps are known to potentially improve the results.

5 CONCLUSIONS

In this paper, two modules of the new Open Source toolbox FlowCV are presented. FlowCV is based on the OpenCV libraries and has been developed to help analyzing videos or images captured during hydraulic model tests and extracting relevant flow parameters. It is freely available under the GNU GPLv3 license at https://github.com/FlowCV.

The first presented module FlowCV-SPIG allows to generate synthetic particle images for benchmarking of imaging techniques for velocity estimation. Particles with a realistic appearance can be generated and a stochastic particle motion is simulated based on a Langevin equation. Knowledge of exact particle position and velocity is essential to evaluate the performance of velocity estimation, such as Optical Flow.

The second module FlowCV-OF computes flow velocities on basis of the Optical Flow method. The presented results are obtained using the Farnebäck method. A major advantage of this approach when compared to classical PIV is given by the resulting dense velocity data. i.e. a velocity information for every image pixel computed. This high-resolution data allows to detect small-scale turbulent flow structures. It is shown that the results compare fairly well with the expected data from synthetic particle images.

Additonal FlowCV modules include water surface extraction for flow depth estimation and void fraction estimation based on pixel intensity distributions. A continuous future development and improvement of the FlowCV toolbox is planned.

REFERENCES

Adelson, E., Anderson, C.H., Bergen, J.R., Burt, P.J. & Ogden, J.M. (1984). Pyramid Methods in Image Processing. *RCA Engineer*, 29(6), 33-41.

Adrian, R. J. & Westerweel, J. (2011). *Particle Image Velocimetry* (No. 30). Cambridge University Press.

Bradski, G. & Kaehler, A. (2008): Learning OpenCV Computer Vision with the OpenCV Library. O'Reilly, O'Reilly Media, Inc.".

Bung, D.B. & Valero, D. (2015). Image Processing for Bubble Image Velocimetry in Self-Aerated Flows. *36th IAHR World congress*, The Hague, Netherlands, 6594-6601.

Bung, D.B. & Valero, D. (2016a). Optical Flow Estimation in Aerated Flows. *Journal of Hydraulic Research*, 54(5), 575-580.

Bung, D.B. & Valero, D. (2016b). Application of the Optical Flow Method to Velocity Determination in Hydraulic Structure Models. *6th IAHR International Symposium on Hydraulic Structures*, 240-249.

Bung, D.B. & Valero, D. (2016c). Image Processing Techniques for Velocity Estimation in Highly Aerated Flows: Bubble Image Velocimetry vs. Optical Flow. *4th IAHR Europe Congress*, 151-157.

Burt, P.J. & d Adelson, E.H. (1983). The Laplacian Pyramid as a Compact Image Code. *IEEE Transactions on Communications*, 31(4), 532–540.

Corpetti, T., Heitz, D., Arroyo, G., Memin, E. & Santa-Cruz, A. (2006). Fluid Experimental Flow Estimation Based on an Optical-Flow Scheme. *Experiments in Fluids*, 40(1), 80-97.

Einstein, A. (1905). On the Movement of Small Particles Suspended in Stationary Liquids Required by the Molecular-Kinetic Theory of Heat. *Annalen der Physik*, 17, 549-560.

Farnebäck, G. (2003). Two-Frame Motion Estimation based on Polynomial Expansion. *13th Scandinavian Conference*, SCIA 2003 Halmstad, Sweden.

Fortun, D., Bouthemy, P. & Kervrann, C. (2015). Optical Flow Modeling and Computation: A survey. *Computer Vision and Image Understanding*, 134, 1-21.

Hirsch, C. (2007). Numerical Computation of Internal and External Flows. Butterworth-Heinemann.

Horn, B.K.P. & Schunck, B.G. (1981). Determining Optical Flow. *Artificial Intelligence*, *17*, 185-203.

Hunter, J.D. (2007). Matplotlib: A 2D Graphics Environment. *Computing In Science & Engineering*, 9(3), 90-95.

Kolmogorov, A.N. (1941). The Local Structure of Turbulence in Incompressible Viscous Fluid for Very Large Reynolds Numbers. *Dokl. Akad. Nauk SSSR* 30, 299-303. (In Russian)

Langevin, P. (1908). Sur la théorie du movement Brownien. *Comptes Rendus Acad. Sci.*, 146, 530-533.

Liu, T., Merat, A., Makhmalbaf, M.H.M., Fajardo, C. & Merati, P. (2015). Comparison between Optical Flow and Cross-Correlation Methods for Extraction of Velocity Fields from Particle Images. *Experiments in Fluids*, 56(8), 166.

Liu, T. & Shen, L. (2008). Fluid Flow and Optical Flow. *Journal of Fluid Mechanics*, 614, 253-291.

Lucas, B.D. & Kanade, T. (1981). An Iterative Image Registration Technique with an Application to Stereo Vision. *IJCAI*, 81(1), 674-679.

Pope, S. B. (1994). Lagrangian PDF Methods for Turbulent Flows. *Annual review of fluid mechanics*, *26*(1), 23-63.

Pope, S.B. (2000). Turbulent Flows. Cambridge University *Press*.

Sun, D., Roth, S. & Black, M. J. (2010). Secrets of Optical Flow Estimation and their Principles. *IEEE Conf. on Computer Vision and Pattern Recognition (CVPR)*, San Francisco, USA.

Walt, S. V. D., Colbert, S. C. & Varoquaux, G. (2011). The NumPy array: A Structure for Efficient Numerical Computation. *Computing in Science & Engineering*, 13(2), 22-30.

Wedel, A. & Cremers, D. (2011). *Stereo Scene Flow for 3D Motion Analysis*. Springer Science & Business Media.

White, F. M. & Corfield, I. (2006). *Viscous Fluid Flow* (Vol. 3). New York: McGraw-Hill.

Wiener, N. (1949). *Extrapolation, Interpolation, and Smoothing of Stationary Time Series* (Vol. 7). Cambridge, MA: MIT press.

Zhang, G. & Chanson, H. (2017). *Application of local Optical Flow Methods to High-Velocity Air-Water Flows: Validation and Application to Skimming Flows on Stepped Chutes*. The University of Queensland, School of Civil Engineering, Report CH105/17.

Proceedings of the 37th IAHR World Congress
August 13 – 18, 2017, Kuala Lumpur, Malaysia

PREDICTION OF TIDES OFF MITHIVIDI, GUJARAT – WEST COAST OF INDIA

PRASHANTH JANARDHAN [1], HARISH NARAYAN [2] & SUKOMAL MANDAL [3]

[1] Department of Civil Engineering, National Institute of Technology Silchar, India
prashnitk.hsn@gmail.com
[2] Department of Civil Engineering, East West Institute of Technology, Bengaluru, India
harishnnitk.hsn@gmail.com
[3] Department of Civil Engineering, PES University, Bengaluru, India
smandal12341@rediffmail.com

ABSTRACT

Tides are the rise and fall of water level caused by gravitational forces exerted by the sun, moon and earth. Understanding sea level variation and its impact on currents is very important, especially in coastal regions. Traditional methods such as harmonic analysis, least mean squares method, and hydrodynamic models have disadvantages in that they require excessive data, are time consuming, and are tedious to carry out. Artificial Neural Network (ANN) has been widely applied in the coastal engineering field in the last two decades for solving various problems related to time series forecasting of waves and tides; predicting sea-bed liquefaction and scour depth; and estimating design parameters of coastal engineering structures. In the present study, an attempt was made to predict the tides in the area off Mithividi which is north of Alang ship breaking yard, Gujarat, west coast of India using tidal harmonic analysis and ANN. Predictions were carried out for various durations using the daily and weekly data sets. The harmonic analysis predicted mixed semidurinal dominant tide which was same as the field data. The results were compared and it was observed that ANN can be a good alternative tool for tidal prediction. Results obtained were encouraging with ‘r’ value greater than 0.94.

Keywords: Tidal current; harmonic analysis; tidal constituents; artificial neural network.

1 INTRODUCTION

The phenomenon of oceanic tides has been observed and studied by humanity for centuries. Success in localized tidal prediction and in the general understanding of tidal propagation in ocean basins led to the belief that this was a well understood phenomenon and no longer of interest for scientific investigation. However, recent decades have seen a renewal of interest for this subject by the scientific community.

Monitoring and prediction of tidal level are thus important so that activities that are controlled by it are planned and operated properly. Tidal ranges are largely affected by the gravitational pull of the sun and moon on the oceanic water body, the component of tide being called ‘the astronomical tide.’ Other factors such as bottom topography, sea-level atmospheric pressure, and wind speed also contribute to the other component called ‘non-astronomical tide.’

The tide can be predicted at any location on the earth as a sum of a number of harmonic terms contained in the polynomial expansion representation of the tide-producing forces. The harmonic analysis of tides is based upon an assumption that the rise and fall of the tide in any locality can be expressed mathematically by the sum of a series of harmonic terms having certain relations to astronomical conditions. Many researchers have adopted this technique successfully to predict the long term tide data (Cheng and Gartner, 1985; Foreman and Henry, 1989; Pawlowicz et al., 2002; USACE, 2002).

A new model based on the working of human brain has been conceptualized to meet the objective of learning the relationship between complex parameters involved in the interaction without having to know the underlying physics behind it. As it is an attempt to mimic the capabilities of human neural system, it is called Artificial Neural Network (ANN). It imbibes the qualities of exploiting non-linearity, adaptability to adjust free parameters (in this case the connection weights, comparable to synaptic connections in the human nervous system) by mapping input/output data sets using various learning algorithms and fault tolerance. Also, compared to the available techniques in majority of the cases, it gives accurate results. It has been extensively used for solving problems in coastal engineering ever since it was used for stability analysis of rubble mound breakwaters. Some of the studies that implemented the ANN for tide predictions are reviewed in the following section.

The back propagation neural network method was applied for accurate prediction of tides (Mandal, 2001). Their neural network model predicted the time series of hourly tides using quick learning process called quick prop. The correlation coefficient between predicted tides and measured tides was found to be 0.998. Large data requirement by the traditional method for prediction tidal level can be avoided by adopting neural network with little dataset (Lee and Jeng, 2002). To predict long term water levels in a coastal inlet a Regional Neural Network–Water Level (RNN-WL) model using feed forward, back propagation neural network structure was developed by Huang et al. (2003). The results of the model indicated that RNN-WL model could be used as a supplement for the long-term historical water level data. Lee (2004) developed a back propagation neural network model using short term on site tidal level data obtained from Taichung Harbor in Taiwan. Model predicted results were compared with conventional harmonic methods, indicates that the back propagation neural network efficiently predicted the long term tidal levels. The feed forward neural network was used to predict hourly sea level variations for 1/2, 1, 5 and 10 days mean sea level (Makarynskyy et al., 2004). The functional and sequential learning neural networks were applied for accurate prediction of tides using very short-term observations (Rajasekaran et al., 2005; 2006). The comparison between the measured and predicted tidal levels for 3 days and 1 month's prediction using 1 day observation showed the correlation coefficients, 0.981 and 0.999, which were higher than the values obtained by Tsai and Lee (1999).

The present study focuses on creating a model that requires minimum amount of data for the satisfactory prediction of month long half hourly tide-level predictions to overcome the disadvantage of excessive data requirement in the existing methods. This can be further developed to create a regional neural network for the prediction of tides where similar conditions exist and will help in obtaining a preliminary but reliable tide data for greenfield projects at places where permanent tide gauge stations are not established.

2 STUDY AREA AND DATA DIVISION

The study is carried out for station of Mithividi, Gujarat. The tides in the Mithividi region are mixed semi-diurnal dominant. The average tidal range at Mithividi is 1.90 m. ANN has been used for the prediction of tides at Mithividi, located on the west coast of India. One month of observed half hourly tide-level data (from February 2011 to March 2011) were obtained from the National Institute of Oceanography; Goa is used in the present study. The success of ANN largely depends on the amount and quality of the data that are used for training purposes. The present data used at the Mithividi region are void of any missing values. Also, being observed/measured real time data obtained from tide gauge station, the information regarding the meteorological parameters is built in.

The data are divided into daily and weekly data sets for the prediction of tides using various durations of data sets. In daily data sets, a row in the input data matrix comprises 48 data points corresponding to an equal number of half hours in the week. These rows represent a single node in the input and output layer of the network. Similarly, in weekly data sets, a single row (or a node) consists of 336 data points corresponding to7 days.

3 METHODS

3.1 Harmonic analysis

The traditional method of tide prediction is done by the harmonic method, which accounts for the parameters or constituents of astronomical tide. When studying variations in tidal levels at a location, it is possible to decompose them into harmonic components with specific periods. A harmonic component has the form of cosine function whose argument increases linearly with time according to known speed criteria. If the expansion terms of the tide-producing forces are combined according to terms of identical period (speed), then the tide can be represented as a sum of a relatively small number of harmonic constituents. Each set of constituents of common period are in the form of a product of an amplitude coefficient and the cosine of an argument of known period with phase adjustments based on time of observation and location. Observational data at a specific time and location are then used to determine the coefficient multipliers and phase arguments for each constituent, the sum of which are used to reconstruct the tide at that location for any time. This concept represents the basis of the harmonic analysis, i.e., to use observational data to develop site-specific coefficients that can be used to reconstruct a tidal series as a linear sum of individual terms of known speed. Tidal height at any location and time can be written as a function of harmonic constituents according the following general relationship,

$$H = H_o + A\cos(at + \alpha) + B\cos(bt + \beta) + C\cos(ct + \gamma) \qquad [1]$$

where H is the height of the tide at location; H_o is the MSL; A, B, and C are the amplitudes of the constituents; and (at+ □), (bt+□) and (ct+□) are the phase constituents.

The combination of the two sytems, earth-moon and sun-earth, gives rise to four basic periods, called the basic tidal constituents, *viz.*, M2, S2 (semi-duirnal lunar and solar respectively) and O1, K1 (duirnal lunar and solar respectively). For an almost complete estimation, about 390 harmonic components are needed. To reach a high degree of accuracy about 115 semi-diurnal, 160 diurnal and 100 long periodic components are needed to be considered.

The relative importance of the semidiurnal constituents against the diurnal constituents is measured by a non dimensional number called the Form Factor (F),

$$F = \frac{(O_1 + K_1)}{(M_2 + S_2)} \quad [2]$$

Here, the letters indicate the amplitude of the constituents. In other words, the form factor is defined as the ratio of the combined amplitudes of the diurnal constituents against the combined amplitudes of the semidiurnal constituents. Four categories are distinguished:

Table 1. Values of F and its classification.

Values of F	Classification
0 – 0.25	Semidurinal
0.25 – 1.5	Mixed, manily semidurinal
1.5 – 3	Mixed, mainly durinal
> 3	Durinal

3.2 Artificial neural network (ANN)

The artificial neuron mimics the characteristics of the biological neuron. The artificial neuron basically consist inputs, each inputs represents the output of another neuron (Figure 1). The amount of information about the input that is required to solve a problem is stored in the form of weights. Each input is multiplied with an associated weight before it reaches to the summing node. In addition, the artificial neuron has a bias term, a threshold value that has to be reached or extended for the neuron to produce a signal, a nonlinear function (f) that acts on the produced signal net and output (Y) after the nonlinearity function. Figure 1 shows the basic mathematical model of ANN where, x_1; x_2; ……. x_n are the input parameters; w_1; w_2; ……. w_n are the weights associated with the connections; i.e., synaptic weight connections from input neuron 'i' to neuron 'k' and i = 1 to n. The 'k' neuron is the summing junction where net input is given by

$$u_k = \sum_{i=1}^{n} w_{ki} . x_i \quad [3]$$

$$v_k = u_k + b_k \quad [4]$$

where b_k is the bias value at the 'k^{th}' node. The final output y_k is the transformed weighted sum of v_k, or in other words, y_k is the function of v_k represented by

$$y_k = \Phi(v_k) \quad [5]$$

where Φ is the transfer function used to convert the summed input. A non-linear sigmoid function, which is monotonically increasing and continuously differentiable, is the commonly adopted transfer function.

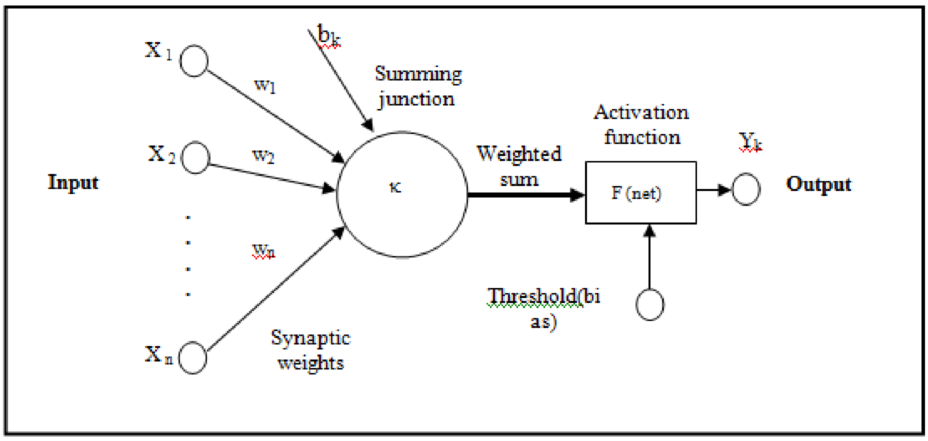

Figure 1. Basic structure of ANN.

3.3 Network performance indicators

The performance of the network is measured in terms of various performance functions such as sum squared error (SSE), mean squared error (MSE), root mean squared error (RMSE) and Correlation coefficient (r) between the predicted and the observed values of the quantities. In the present study, 'mse' and 'r' are used as performance indicators; the lower value of MSE and higher value of CC indicate better performance of the network.

The root mean squared error (RMSE) is given by,

$$rmse = \sqrt{\sum_{i=1}^{n} (x_i - y_i)^2 / n} \quad [6]$$

Correlation coefficient measures the strength of association between the variables and is given by the formula

$$r = \frac{\left(\sum_{i=1}^{n} x_i . y_i\right)}{\left(\sqrt{\sum_{i=1}^{n} x_i^2 . \sum_{i=1}^{n} y_i^2}\right)} \quad [7]$$

4 RESULTS AND DISCUSSION

4.1 Harmonic analysis

The maximum tidal range during the measurement period was 1.90 m at Mithividi station. Predominant tidal constituents are M2, S2, K1, M4 and O1 with constituent M2 (2.61 m) having the highest magnitude followed by S2 (0.91 m) constituent (Table 2). The form factor is 0.256 and hence, classified as mixed with predominantly semidiurnal in nature. The mean spring tide range i.e., 2(M2+S2) is 7.16 m and the mean neap tide range is 1.836 m. The comparison of the harmonic analysis and with observed data and ANN is shown in Figure 2. The prediction is good with R^2 of 0.922 and 0.996 respectively.

Table 2. Harmonic analysis.

Constituent	A (m)	A_ci (m)	g (degrees)	g_ci (degrees)	Percent Energy
M2	2.61	0.136	200	3.61	80.11%
S2	0.97	0.166	244	9.62	11.08%
K1	0.569	0.0314	315	3.85	3.82%
M4	0.405	0.0507	231	7.11	1.92%
O1	0.349	0.0302	296	5.12	1.45%
MS4	0.285	0.0611	282	11.2	0.95%
MSF	0.194	0.0481	12.2	12.3	0.45%
2SM6	0.0619	0.0128	166	11.6	0.06%
2MS6	0.0593	0.0121	44.8	12.7	0.04%
M3	0.0568	0.0153	201	17.4	0.04%
S4	0.0566	0.0583	287	61.3	0.03%
M8	0.0416	0.0106	333	13	0.02%
SK3	0.0404	0.0173	69.6	26.2	0.02%
M6	0.033	0.014	292	22.4	0.01%
2MK5	0.0219	0.0111	105	25.8	0.01%
2SK5	0.0209	0.0101	327	31.8	0.00%
3MK7	0.0112	0.00774	121	39.7	0.00%

Where, A = Amplitude, A_ci =95% confidence interval for A, g = Greenwich phase lag, g_ci = 95% confidence interval for g

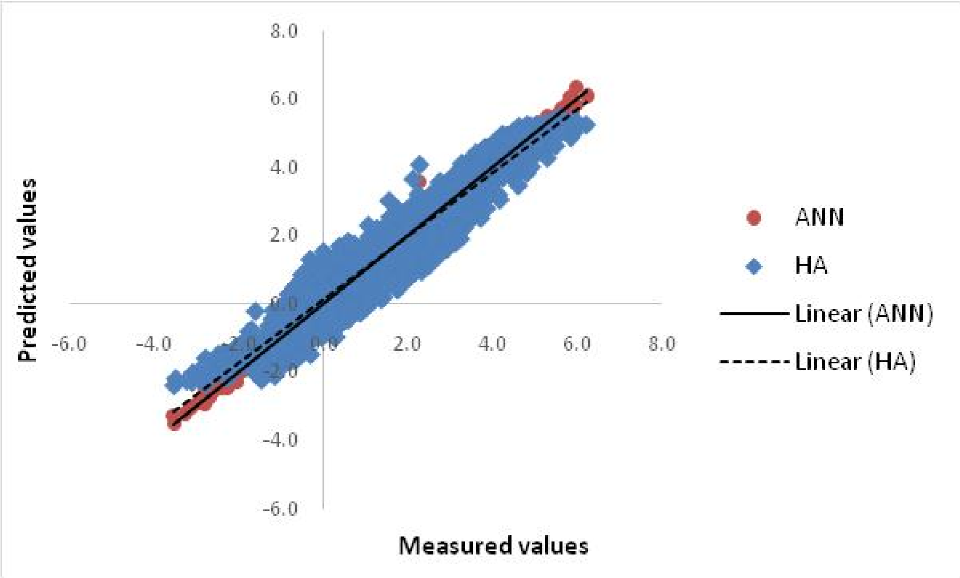

Figure 2. Comparison of measured and predicted values.

4.2 Daily Predictions

In the present study, daily predictions are carried out using single day data to predict tide levels for 1, 7, 14 and 30 days, respectively. The results obtained for training and testing data in terms of 'rmse' and 'r' values are shown in Table 3. The accuracy of the prediction for testing data is good with 'r' ranging from 0.977 to 0.9533 and 'rmse' ranging from 0.044 to 0.0206 for 1 to 30 days respectively. A typical plot for 30 days prediction for testing is shown in Figure 3.

Table 3. Statistical measures for daily predictions.

	Days	1	7	14	30
Training	R	0.997	0.995	0.994	0.998
	Rmse	0.0018	0.0022	0.0016	0.0020
Testing	r	0.977	0.9832	0.959	0.9533
	Rmse	0.044	0.018	0.0154	0.0206

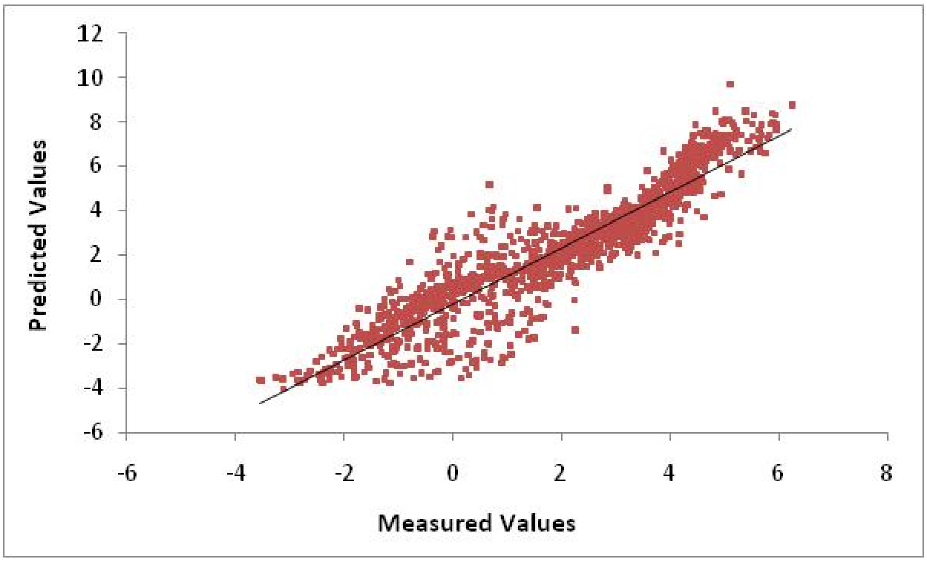

Figure 3. Comparison of measured and predicted values for 30 day prediction.

4.3 Weekly Predictions

Weekly predictions were carried out in similar lines to that of weekly predictions. One week data were used as input for predictions of one month tide levels. The results are tabulated in Table 4. The accuracy of the prediction for testing data is good with ‘r’ ranging from 0.983 to 0.941 and ‘rmse’ ranging from 0.024 to 0.0406 for 1 to 3 weeks respectively. A typical plot for 3 weeks prediction for testing is shown in Figure 4.

Table 4. Statistical measures for weekly predictions.

	Weeks	**1**	**2**	**3**
Training	r	0.9979	0.9972	0.9975
	rmse	0.0028	0.0031	0.003
Testing	r	0.9832	0.9547	0.9413
	rmse	0.024	0.0383	0.0406

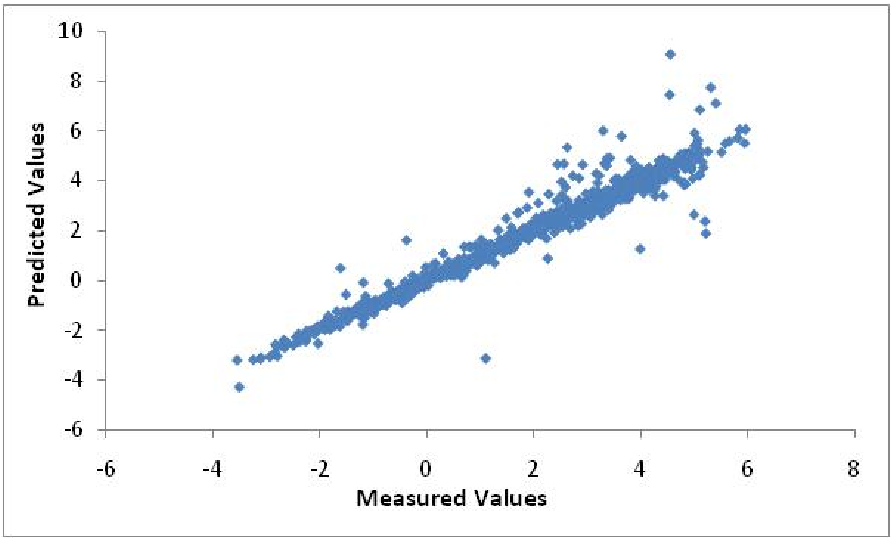

Figure 4. Comparison of measured and predicted values for 3 week prediction.

4 CONCLUSIONS

Conventionally, tide-level predictions are carried out using harmonic analysis, which is data-intensive and does not account for the ‘non astronomical’ component of the observed tide levels. From the harmonic analysis, predominant tidal constituents obtained were M2, S2, K1, M4 and O1 with constituent M2 (2.61 m) having the highest magnitude. The form factor 0.25 also confirms the mixed with predominantly semidiurnal tidal nature. The comparison of measured values with Harmonic analysis and ANN showed good prediction with R^2 of 0.922 and 0.996. The present study makes use of ANN modeling, which has been tried and tested in solving various problems related to coastal engineering applications. Predictions carried out using one day tide level gave satisfactory results for 30 days prediction with ‘r’ value of 0.953; whereas excellent results were obtained for equal length prediction of one week with ‘r’ value reaching up to 0.977. Week predictions done using one week data sets also gave very high ‘r’ value of 0.941. The predictions of one-week tide level using one week’s tide level also gave ‘r’ greater than 0.983.

ACKNOWLEDGEMENTS

The authors would like to thank the National Institute of Oceanography, Goa for providing us with the data required for the execution of this study. Also, the authors would like to thank Codiga D. L. for developing UTide Matlab program which was utilized to perform harmonic analysis.

REFERENCES

Cheng, R.T. & Gartner, J.W. (1985). Harmonic Analysis of Tides and Tidal Currents in South San Francisco Bay, California. *Estuarine, Coastal and Shelf Science*, 21(1), 57-74.

Foreman, M.G.G. & Henry, R.F. (1989). The Harmonic Analysis of Tidal Model Time Series. *Advances in water resources*, 12(3), 109-120.

Huang, W., Murray, C., Kraus, N. & Rosati, J. (2003). Development of a Regional Neural Network for Coastal Water Level Predictions. *Ocean Engineering*, 30, 2275-2295.

Lee, T.L. (2004). Back Propagation Neural Network for Long Term Tidal Predictions. *Ocean Engineering*, 31, 225-238.

Lee, T.L. & Jeng, D.S. (2002). Application of Artificial Neural Networks in Tide Forecasting. *Ocean Engineering*, 29, 1003-1022.

Makarynskyy, O., Kuhn, M., Makarynska, D. & Featherstone, W.E. (2004). The use of Artificial Neural Networks to Retrieve Sea-Level Information from Remote Data Sources. *In Proceedings of International Association of Geodesy International Symposium: Gravity, Geoid and Space Missions* (GGSM2004).

Mandal, S. (2001). Prediction of Tides using Back-Propagation Neural Networks. *Proceedings of the International Conference in Ocean Engineering*, ICOE, 499-504.

Pawlowicz, R., Beardsley, B. & Lentz, S. (2002). Classical Tidal Harmonic Analysis including Error Estimates in MATLAB using T_TIDE. *Computers & Geosciences*, 28(8), 929-937.

Rajasekaran, S., Jeng, D.S. & Lee, T.L. (2005). Tidal Level Forecasting during Typhoon Surge using Functional and Sequential Learning Neural Networks. *Journal of Waterway, Port, Coastal and Ocean Engineering*, ASCE, 131(6), 321-324.

Rajasekaran, S., Thiruvenkataswamy, K. & Lee, T.L. (2006). Tidal Level Forecasting using Functional and Sequential Learning Neural Networks. *Applied Mathematical Modeling*, 30, 85-103.

Tsai, C.P. & Lee, T.L. (1999). Back-Propagation Neural Network in Tidal-Level Forecasting. *Journal of Waterway, Port, Coastal, and Ocean Engineering*, 125(4), 195-202.

USACE, C. (2002). *Coastal Engineering Manual,* Engineer Manual 1110-2-1100, US Army Corps of Engineers.

EXPERIMENTAL AND NUMERICAL INVESTIGATION OF PIANO KEY WEIRS

METE KOKEN(1), ISMAIL AYDIN(2), EMRE HASPOLAT(3) & AHMET NAZIM SAHIN(4)

(1,2,3,4) Civil Engineering Department, Orta Dogu Teknik Universitesi, Ankara, Turkey,
mkoken@metu.edu.tr; ismaydin@metu.edu.tr; haspolat@metu.edu.tr; sanazim@metu.edu.tr

ABSTRACT

Piano Key Weirs (PKW) are useful overflow structures to increase discharge capacity per unit length of spillway crest for relatively small heads over the weir compared to a standard straight weir crest. PKW can be used as a side or frontal weir in many circumstances to regulate reservoir levels with small changes in water surface elevation. Nearly constant reservoir level has many advantages in optimum operation of water reservoirs for instance in maximizing hydropower production. There are several empirical formulations available in the literature to find the discharge over the PKW for a given head. However, because of large number of geometric parameters involved in the weir design, available experimental data gathered from different sources do not overlap showing significant variations indicating dependence on specific experimental conditions of each data source. There is a physical model at 1/30 scale used in this study involving three units of PKW which was constructed as a part of hydraulic model testing for the spillway of Aşağı Kaleköy Hydropower Plant which is under construction in Turkey. Head-discharge data was measured for the specific design available. Then, Flow-3D was used to numerically solve flow over PKW for different configurations, one configuration being identical to that of the physical model, at the model scale. The experimental results are compared to numerical ones to validate the CFD code. It was noticed that CFD solution is very sensitive to mesh size and quality. After validation, Flow 3D was used to investigate various design configurations at prototype scale to maximize the discharge capacity of the PKW. Compared to the flat shape, having curved parapet walls increases the discharge capacity of the system by approximately 3%.

Keywords: Piano Key Weir; spillway; discharge capacity; CFD solutions.

1 INTRODUCTION

Piano Key Weirs are overflow structures which are preferred because of their increased discharge capacity within the same crest length compared to the conventional weirs (Machiels et al., 2011; Anderson and Tullis, 2012; Riberio, 2012). This is a rather recent design where only several applications are available all over the World. Therefore, no sufficient research has been conducted on PKW's up to date. There are a number of geometric parameters which affect the discharge capacity of a piano key weir like: length of the PKW, B; upstream and downstream overhang crest lengths B_o and B_i; base length, B_b; height of the outlet and inlet entrance measured from the PKW crest, P_o and P_i; total width of the PKW, W; outlet and inlet key widths W_o and W_i; and the sidewall thickness T_s (Figure 1). Although several researches worked on obtaining a discharge relationship (Kabiri-Samani and Javaheri, 2011; Machiels et al., 2014), there is not a unique discharge expression valid for all PKW designs.

Aşağı Kaleköy Dam is built on Murat River in eastern Anatolia region. It is an RCC dam 125m high from the foundation. The spillway inlet is equipped with 24 Piano Key Weirs (PKW) overlaying the 240m long crest which will be the first PKW application in Turkey. The PKW is planned to operate together with 6 orifice type bottom outlets to pass the maximum flood discharge. The outlet channel is designed as stepped spillway which is contracted to 130m at the bottom from the 240m at the crest. The flip bucket type outlets of the 6 orifice units are located at the central portion of the spillway and assumed to discharge as water jets into the stilling basin.

The design discharge is 5773m^3/s that corresponds to flood discharge of 10000-year return period. The total capacity of the bottom outlets is expected to be 1460m^3/s which will be discharged as water jets from the flip buckets as the orifice outlets. Remaining 4313m^3/s will be spilled over the 24 units of PKW and flow over the stepped channel until it reaches to the stilling basin.

The main source of uncertainty in the design is the discharge capacity of PKW on the spillway crest. This type of weir design is preferred to pass the required flowrate over a 240m long spillway crest for the maximum reservoir operation level of 1102.5m in an uncontrolled manner, without any gates. The main idea is to minimize the reservoir level variations in spite of large variations in the discharge so that the maximum power production is achieved from the hydroelectric power plant (HEPP). The weir formulae available in the literature for the PKW are not collapsing to a single curve, indicating strong dependency on the experimental conditions from which they are derived. Therefore, the discharge capacity of PKW system formed by 24 units needs to be verified.

It was not practical to construct a comprehensive hydraulic model including complete spillway at a valid scale for model studies because of large space and flowrates required. Therefore, an investigation involving 3D numerical simulations is aimed. In this case, precise computation of overflow discharge from such a large and complicated geometry involving 24 units of PKW from 3D simulations would require a very fine mesh size that would be another practical limitation as a source of uncertainty again. Finally, it was decided to construct a truncated hydraulic model involving 3 units of PKW only and validate the computational tool by the experimental data and then perform 3D numerical simulations to study all aspects of flow over the PKW's.

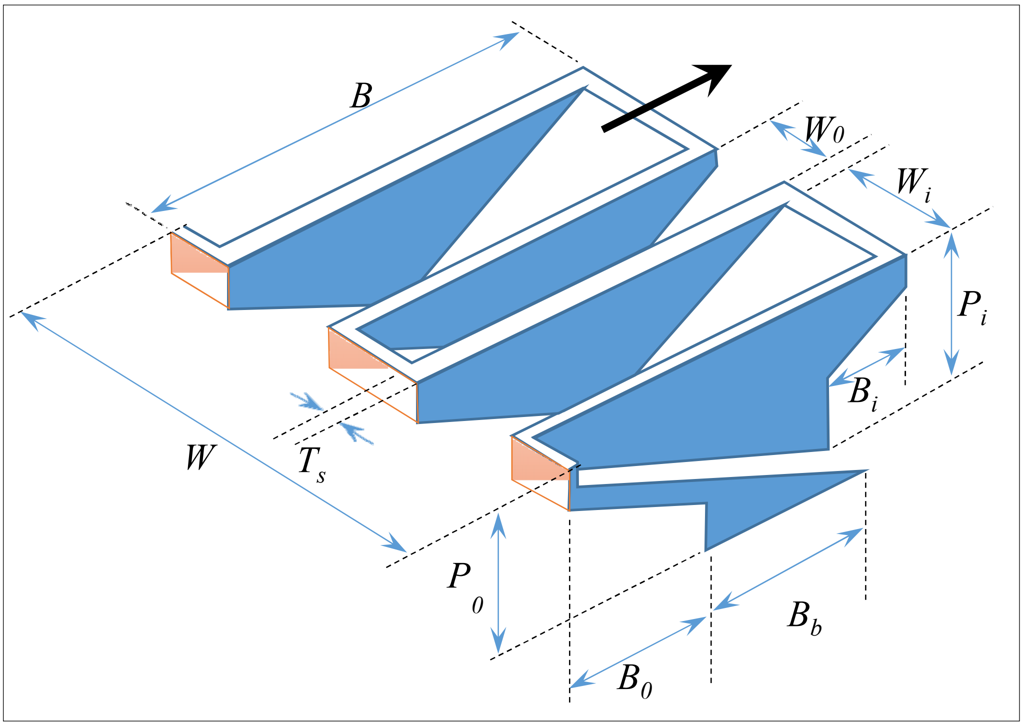

Figure 1. Geometric parameters for a PKW.

2 EXPERIMENTAL AND NUMERICAL MODEL

Hydraulic model was constructed in Hydromechanics Laboratory of Civil Engineering Department at METU (Figure 2). Model-prototype similitude is based on Froude number and model scale is 1/30. The main purpose of the hydraulic model is to measure the discharge capacity of the specific PKW design. The model reservoir is an elevated tank 4m wide and 6m long. Three units of PKW are installed at the spillway crest (Figure 2). Discharge was measured by an electromagnetic flow meter before entering the model reservoir. The stepped outlet channel has the same width as the PKW units modeling only a unit strip of the prototype spillway and the stilling basin. Thus, the 3D effects that should occur in the prototype at the entrance from the reservoir was not observed in the model. The model scale (1/30) is satisfactory for the measurement of discharge capacity of PKW as there is sufficiently large flow depth of 5 cm over the PKW crest to eliminate the surface tension effects (Erpicum et al., 2016). Characteristic dimensions of one PKW unit in the prototype scale are given in Table 1. During the experiments water was pumped to the elevated tank from a reservoir via a supply pipe where discharge was measured using an electromagnetic discharge measuring device that is connected to the pipe. Waited until the water level in the model reservoir remains unchanged, then the discharge reading from the electromagnetic discharge measurement device and the water depth in the model reservoir are recorded. This procedure was repeated for different water levels and thus for different discharges.

Table 1. Characteristic PKW dimensions given in meters.

B	*Bo*	*Bi*	*Bb*	*Po*	*Pi*	*W*	*Wo*	*Wi*	*Ts*
24.05	6.20	6.20	11.65	8.75	8.75	240	4.18	5.02	0.40

Flow-3D software was used in the numerical simulations which solves incompressible Reynolds Averaged Navier Stokes equations on orthogonal structured meshes. The code uses volume of fluid method for tracking the free surface deformations. RNG k-ε type turbulence model was used in the calculations which utilizes wall functions close to the solid surfaces. A hydrostatic pressure distribution was assumed at the inlet section with a specified water depth. No slip boundary condition was used along all the solid surfaces.

Two separate numerical models were generated one for simulating the physical model which contains three PKW units and one for simulating one PKW unit in the prototype scale (Figure 3). For the model in the prototype scale symmetry, boundary condition was used on both sides of the model which assumes an infinite number of PKW's are in operation side by side. Two separate mesh blocks were used in the numerical simulations: a finer mesh block to resolve the PKW's and a coarser block to solve the reservoir part of the domain. In the model scale simulations, the mesh sizes were selected as 0.01m and 0.04m whereas in the prototype simulations the corresponding mesh sizes were 0.20m and 0.40m. The total number of grid points were approximately 1.3 million and 1.8 million in the model and prototype scale simulations, respectively. Note that these mesh sizes were selected after a grid dependence test. The grid used in the simulations was refined until the difference within the discharge values calculated with different meshes drop below 1%.

Figure 2. Hydraulic model (left) and the PKW details (right) used in the experiments.

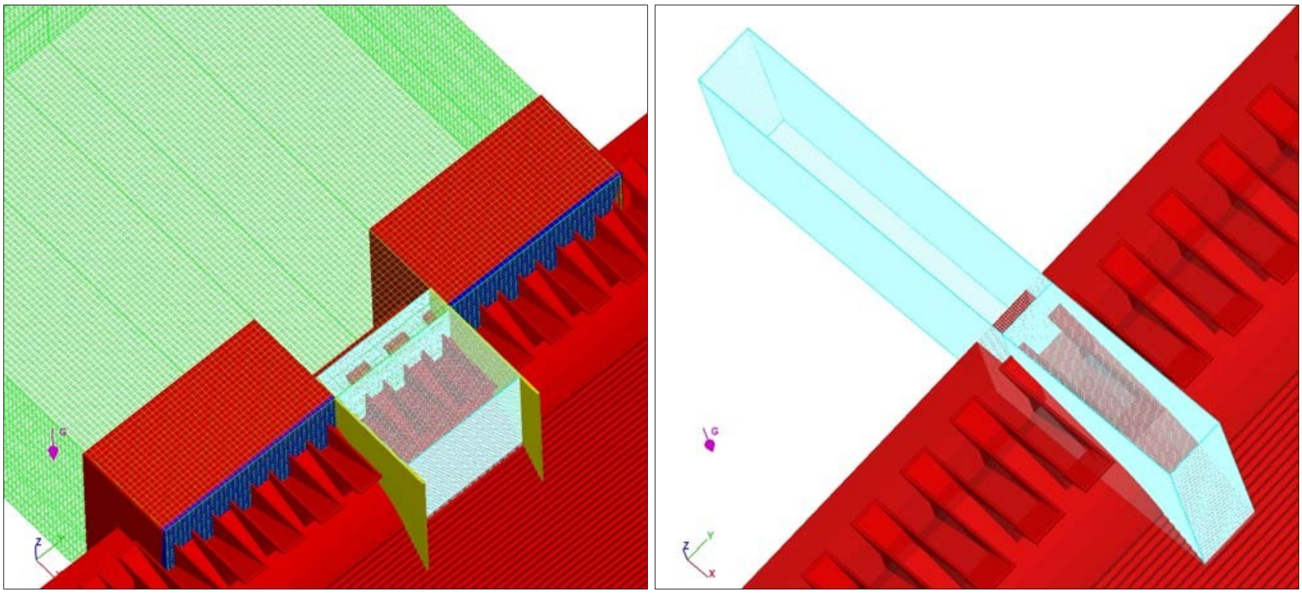

Figure 3. Numerical model and the computational mesh used in the validation study conducted in the model scale for three PKW units (left) and in the prototype scale for one PKW unit (right).

3 RESULTS

3.1 Validation

There were three units of PKW in the model constructed. The discharge capacity of PKW units at both ends were significantly reduced due to 3D contraction effects at the entrance from the reservoir. Therefore, it was not possible (in the physical model) to correctly measure the unaffected discharge of single unit. Instead, the total discharge of the three units was measured. In the numerical solution, the same configuration was simulated in the model scale with completely the same boundary conditions. Therefore, the comparison of the two approaches were done for the same geometry and flow conditions.

After completion of the hydraulic model construction, the discharge over the PKW design was measured for variable water levels in the reservoir. The results are shown in Figure 4, discharge as function of head over weir. Experiments were repeated four times by different engineers and each experiment set is shown with different colors in Figure 4. All readings were averaged over one minute recording time. A continuous line is also shown on this figure to represent the best fit to measured data.

In Figure 4, the numerical simulation results are also shown by squares for three different water levels in the reservoir. When compared to the best fit curve, the deviations of the computed discharge values are very similar to that of experimental data. In the numerical simulations in the model scale, the difficulty is related to the computational grid used to describe the weir crest. To represent the semi-circular weir crest accurately, more grid points have to be placed. But, small mesh size then reduces the computational time step that resulted in some convergence problems. It was possible to perform the numerical simulation with finer mesh sizes in the prototype scale without any convergence problems. Therefore, numerical simulations in prototype scale are expected to be more confident.

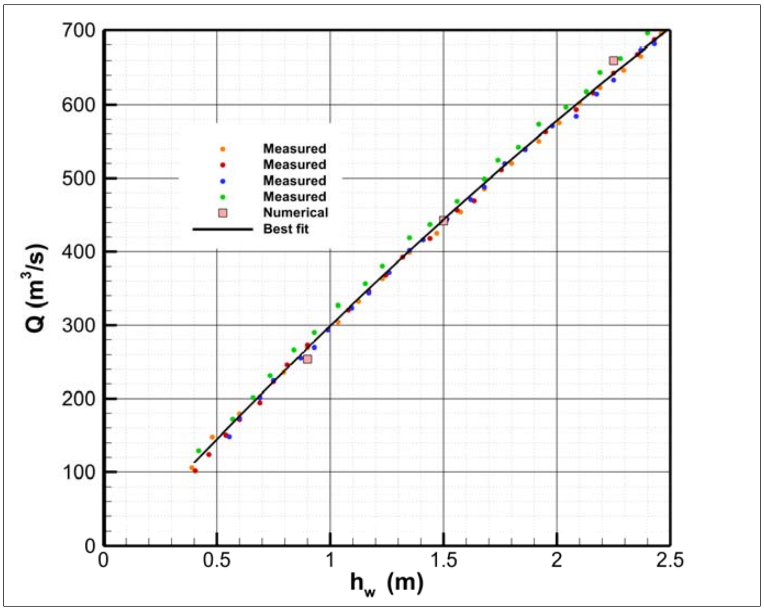

Figure 4. Discharge over the PKW as function of head over weir (three units of PKW).

3.2 Discharge calculations for a single PKW

In order to obtain the head-discharge relationship for one PKW unit under parallel approach flow conditions, simulations at prototype scale were run. A numerical model was developed as shown in Figure 5. In the numerical model one full inlet key and two half outlet keys on both sides of the inlet key was used as shown in Figure 5. Effect of the domain size on the solution was investigated. Different domain lengths and heights within the reservoir were tested and it was decided to have a domain height of 35m and a length of 58m inside the reservoir was sufficient to not to be affected from the boundary conditions.

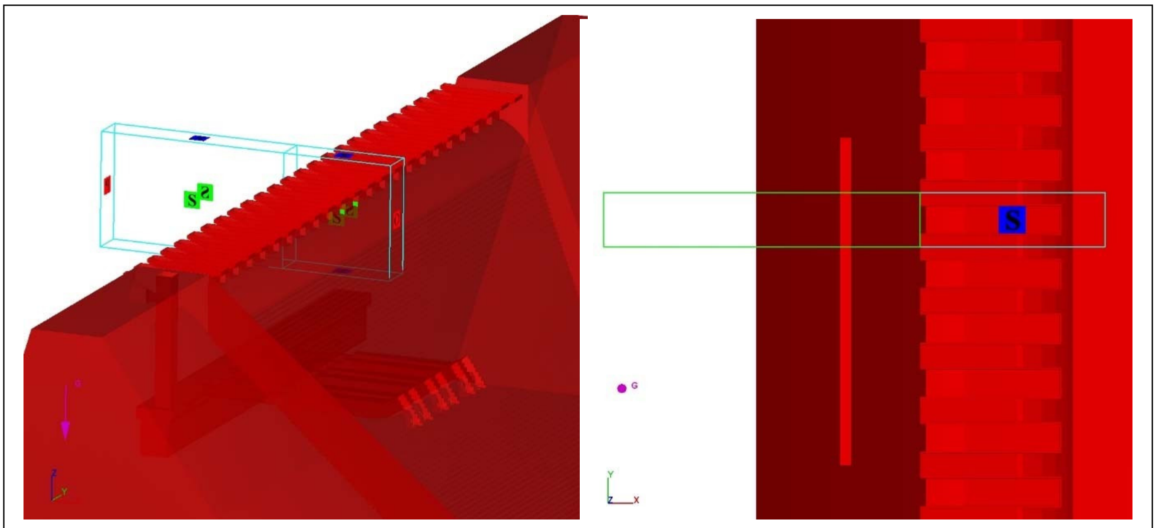

Figure 5. The perspective view (left) and top view (right) of the numerical model for single PKW simulations.

At the maximum reservoir level of 1104m, one piano key weir of the initial design (Table 1) offered by the designer was run at different piano parapet shapes of flat, half circular and circular. Parallel to the findings of Anderson and Tulis (2013), it was observed that for half-circular and circular parapet shapes the piano discharge was 3-4% larger than the flat parapet shape. Considering the hydraulic conditions and the possibility of wear of the parapet walls, it was decided to use circular parapet walls. From this point on, all the results given corresponds to a circular parapet shape. At the maximum reservoir level, one piano key weir was only able to discharge 152m^3/s which was not sufficient to pass the corresponding portion of the required 10000-year return period design discharge. A revision was proposed by increasing the upstream and downstream overhang crest lengths, Bo and Bi by 1 meter each which was called as the modified model.

In the modified model, at different flow depths simulations are run for one piano key. The following head discharge relationship was obtained as in Figure 6. It was observed that at the maximum reservoir level of 1104m (net head of h_{net} = 1.5m) approximately 166m^3/s discharge was passing through one PKW unit. Velocity magnitude contours were given for the simulation run at maximum reservoir level in Figure 7. Velocity magnitudes are largest along the outlet key and goes up to values of 15m/s. Each simulation was run for a 75 second duration which lasted for 24-60 hours of computation on a 16 core 2.00GHz Intel Xeon processor workstation.

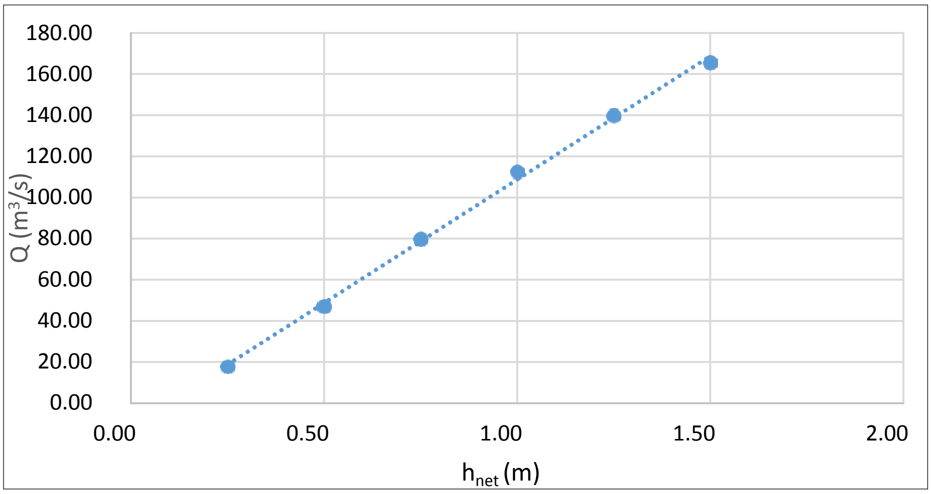

Figure 6. Discharge vs net head over the piano crest.

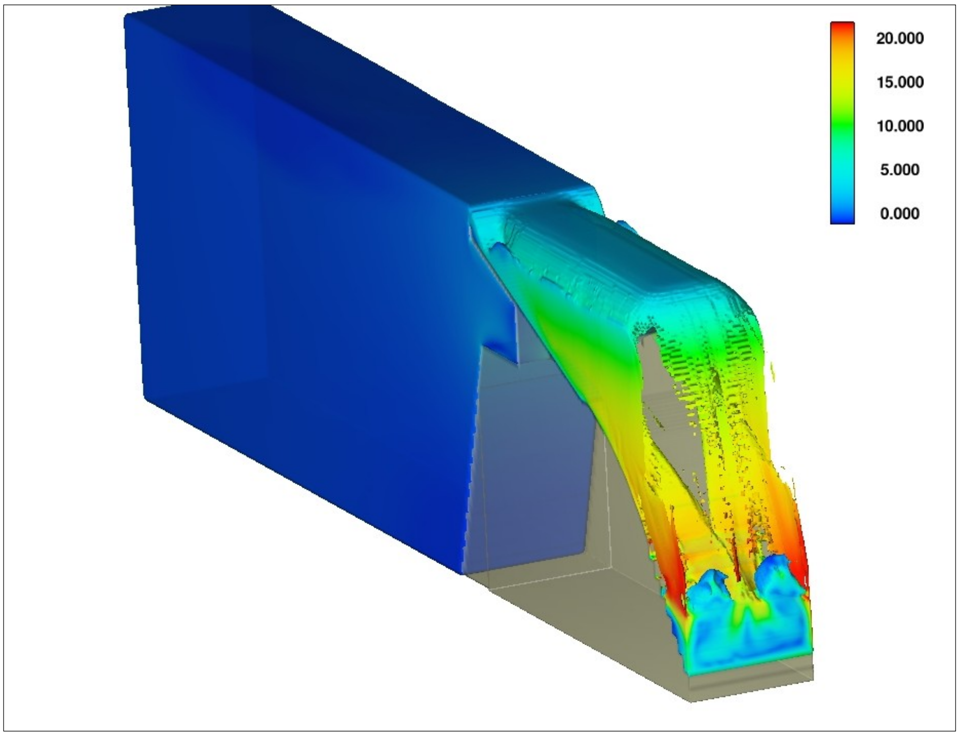

Figure 7. Velocity magnitude contours in m/s for flow over one PKW unit at maximum reservoir water level of 1104m.

3.3 Discharge calculations for all PKW units

In order to investigate the effect of approach flow conditions on the PKW performance, all PKW units should be modeled with the reservoir. However, because of the huge mesh requirement, it was not possible to simulate this case with the 24 PKW units. Instead, the reservoir and the weir part was modeled such that piano keys were taken out of the model (Figure 8). Approximately 250m of length in the streamwise direction within the reservoir was modelled containing the actual topography of the dam site. The system was modeled such that approximately the same amount of discharge that was supposed to pass through the 24 PKW units (~4000m^3/s) was discharged from a broad crested weir along the same crest length of 240m. Having 24 PKW units along the 240m crest length, at every 10m of the broad crested weir discharge is measured. Each measurement recorded here was then linked to the corresponding PKW unit in the original design. Applying this methodology indirectly, the effect of the approach flow conditions on the individual PKW units were evaluated.

Three mesh blocks were used in this model: the first mesh block along the weir part; the second mesh block on the reservoir part which is adjacent to the weir and the third mesh block at the far upstream part of the reservoir as shown in Figure 8. Similar to the single PKW unit model, a grid dependence study was conducted and the mesh sizes used for blocks one to three were selected as 0.1m, 1m and 4m, respectively. The total number of grid points used in this simulation was around 21 million. The simulation was run until steady state conditions were reached at approximately 1400 seconds.

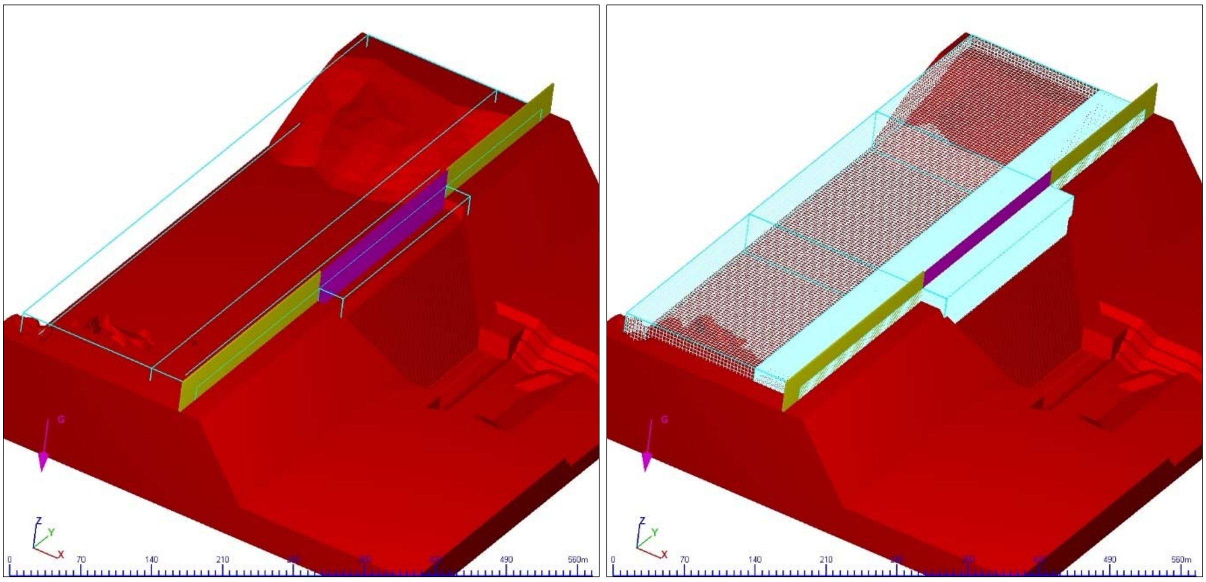

Figure 8. The perspective view of the reservoir numerical model with (right) and without (left) the mesh.

Streamline patterns in the reservoir are drawn at 1400 seconds in Figure 9. As it can be seen from this figure, at the middle portion of the weir streamlines were parallel to each other suggesting that the symmetrical approach flow assumption made in single PKW unit calculations was reasonable for these piano keys. On the other hand, at both sides of the weir the streamlines were not parallel to each other. Especially on the right-hand side of the reservoir in the streamwise direction, there was a big recirculation region close to the shore line which affects the flow entering the PKW unit on this side. These flow features affected the discharge capacity of the PKW units close to the two sides. This observation was confirmed from the discharge measurements on the weir which is given in Table 2. Here, PKW units were numbered from right hand side towards left hand side in the streamwise direction as PKW-1 to PKW-24. Discharge passing at each 10m width of the weir (which corresponds to one PKW unit) is calculated and normalized with the discharge passing through the opening where PKW-12 would lay. Obtained discharge values at each PKW were given as a percent of PKW-12 which is given in Table 2. It was clear that symmetrical approach flow assumption made in the single PKW unit calculations was reasonable for PKW-3 to PKW-22 as they passed the same discharge. However, the first two piano keys both on the right and left were affected from the reservoir inflow conditions. PKW-1 and PKW-24 have a discharge capacity reduction of 21% and 12%, respectively, whereas PKW-2 and PKW-23 have an increase in discharge by 2%. Overall the whole system has a discharge capacity loss of 29% of one PKW unit which corresponds to 48m^3/s as a result of the asymmetrical approach flow conditions.

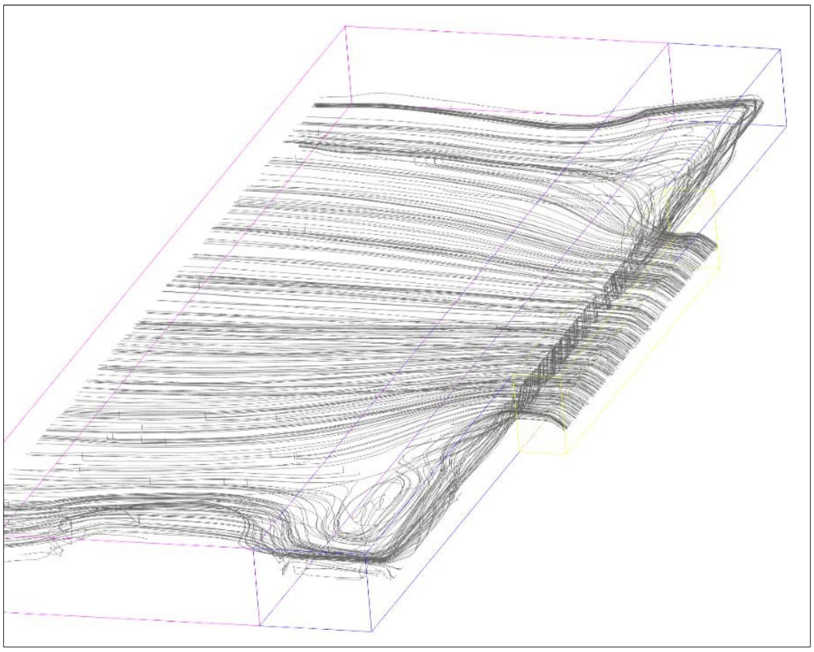

Figure 9. Streamline patterns in the reservoir.

Table 2. Discharge passing through individual PKW units.

PKW unit	discharge (%)	discharge (m^3/s)
PKW 1	79	131
PKW 2	102	169
PKW 3	100	166
.	.	.
.	.	.
.	.	.
PKW 22	100	166
PKW 23	102	169
PKW 24	88	146

4 CONCLUSIONS

Aşağı Kaleköy Dam spillway which contained 24 PKW units was investigated experimentally and numerically. Three out of twenty-four units were constructed within the physical model was is completed based on Froude similitude. On the other hand, Flow-3d software was used in the numerical simulations. Initially, to assess the predictive capabilities of Flow-3d software, a numerical model is created which has identical flow conditions with the physical model. Simulation results showed that the discharge values observed at the maximum reservoir level in both experimental and numerical model were in good agreement.

Since it was not computationally possible to model all the PKW units because of the huge grid requirement, it was decided to model only one PKW unit assuming symmetrical approach flow conditions in the reservoir. Single PKW unit was tested in the prototype scale and a head-discharge relationship was obtained. It was observed that using circular or half circular crest shape instead of a flat crest on the PKW units increased the discharge efficiency by 3-4%.

The effect of approach flow conditions on the PKW capacity was also tested. The whole reservoir width for a length of 250m in the streamwise direction was modelled as a broad crested weir eliminating the PKW units. Approximately the same amount of discharge was passed through the weir and the discharge passing through the opening of each PKW unit is calculated. It was observed that because of the recirculating flows forming on the sides of the reservoir the first and last PKW units were not working at full capacity. The decrease in their capacity were in the order of 10-20%. It is shown that numerical simulations can be used as a useful tool in design of hydraulic structures.

REFERENCES

Anderson, R.M. & Tullis, B.P. (2012). Comparison of Piano Key and Rectangular Labyrinth Weir Hydraulics. *Journal of Hydraulic Engineering*, 138(4), 358-361.

Anderson, R.M. & Tullis, B.P. (2013). Piano Key Weir Hydraulics and Labyrinth Weir Comparison. *Journal of Irrigation and Drainage Engineering*, 139(3), 246-253.

Erpicum, S., Tullis, B.P., Lodomez, M., Archambeau, P., Dewals, B.J. & Pirotton, M. (2016). Scale Effects in Physical Piano Key Weirs Models. *Journal of Hydraulic Research*, 54(6), 692-698.

Kabiri-Samani, A. & Javaheri, A. (2012). Discharge Coefficients for Free and Submerged Flow Over Piano Key Weirs. *Journal of Hydraulic Research*, 50(1), 114-120.

Leite Ribeiro, M., Bieri, M., Boillat, J.L., Schleiss, A.J., Singhal, G. & Sharma, N. (2012). Discharge Capacity of Piano Key Weirs. *Journal of Hydraulic Engineering*, 138(2), 199-203.

Machiels, O., Erpicum, S., Dewals, B.J., Archambeau, P. & Pirotton, M. (2011). Experimental Observation of Flow Characteristics Over a Piano Key Weir. *Journal of Hydraulic Research,* 49(3), 359-366.

Machiels, O., Pirotton, M., Archambeau, P., Dewals, B.J. & Erpicum, S. (2014). Experimental Parametric Study and Design of Piano Key Weirs. *Journal of Hydraulic Research*, 52(3), 326-335.

COMPUTATIONAL FLUID DYNAMICS MODELLING OF A ROMAN DROP SHAFT

HALLIE THORNBURROW[(1)], PAUL RODRIGUE[(2)] & VINCENT H. CHU[(3)]

[(1,2)] CDM Smith, Massena New York
[(3)] Department of Civil Engineering, McGill University, Montreal, Canada
rodriguepd@cdmsmith.com

ABSTRACT

A drop shaft is typically characterized by a vertical connection between two pipes at different elevations which facilitates the conveyance of water from one elevation to another. The hydraulic analysis associated with the design of a drop shaft is complex due to the entrainment of air, the loss of energy throughout the structure and the region where the water jet enters the lower pool. A poorly designed drop structure can lead to drastically reduced lifespans of the structures caused by erosion, in addition to very serious safety concerns. Smaller scale physical models have been used to develop the hydraulic design criteria associated with these structures and predict flow patterns of various designs. This procedure is very expensive and time consuming, particularly if modifications are required, even if the modifications are minor. This research compares the physical model of a drop shaft with a computational fluid dynamics (CFD) model of the same structure. The physical scale was completed by Hubert Chanson. The flow regime simulated by these models consists of a free jet which emanates from the inlet channel and hits the opposite wall. This jet travels vertically down the opposite wall creating a “film” or a curtain in front of the outlet pipe. Results of this work show that when identical inflow conditions are set, very similar flow behaviors, water levels and hydraulic residence times results were produced by both types of models. This suggests that CFD software can be used as a tool to evaluate drop shaft model designs. All the salient data sets produced from the Chanson’s work could be duplicated. In addition, other information can be extracted from the CFD model such as air content, pressure, velocity at any point throughout the flow regime.

Keywords: Computational fluid dynamics (CFD); drop shaft; energy dissipation; air entrainment; residence time.

1 INTRODUCTION

A drop shaft is a vertical connection between two pipes at different elevations. This arrangement poses a myriad of analytical problems with respect to loss of kinetic energy, volume of air entrainment and water surface elevations in the drop shaft. These hydraulic structures have been used since ancient times and are very commonly used in managing combined sewer overflows. Proper design implementation of these structures is crucial for economic, maintenance and safety reasons. Improper dissipation of energy can lead to rapid deterioration or damage to the structure itself, thus drastically reducing the useful lifespan and increasing maintenance costs (Anderson, 1961). Additionally, excessive residual downstream energy, resulting from poor design, can result in a large flow surge which can be very dangerous. Excessive accumulated entrained air from the drop can create excess pressure downstream of the structure and produce large hydraulics forces at unanticipated locations (Anderson, 1961). Blowbacks and blowouts which are the release of highly pressurized air in the opposite and same direction of flow, respectively, are common results of poor design and can be very hazardous (Williamson, 2001).

Due to the complicated hydraulics and the negative impacts associated with them, drop shafts are commonly overdesigned with large factors of safety (Anderson, 1961). Most of the past research on these structures has been based on experimental data and scaled hydraulic models, noting the difficulty and inaccuracy associated with evaluations involving air entrainment and aeration behaviors with traditional flow mechanics (Williamson, 2001). While studies using physical models have been applied with great success, it has been found that slight variations in the structure dimensions can cause large unexpected variations in flow behavior (Williamson, 2001). The literature also indicates that air entrainment behaviors cannot be accurately correlated between model and a full-scale structure (Williamson, 2001).

Computational fluid dynamic (CFD) modelling is a useful tool and facilitates the potential to minimize many of the problems associated with scale up of physical models. This is because it has the ability to model hydraulic structures at full scale, air and water simultaneously and the ability to easily incorporate changes to the model dimension in supplemental simulations.

2 PURPOSE

The purpose of this work is to use ANSYS Workbench 16.2, a CFD platform, to model the hydraulic performance of a drop shaft and compare it to an identical physical model. The results from this computational model are compared to results and observations from the physical hydraulic model of the same dimensions and flow conditions as evaluated in Hubert Chanson's "An Experimental Study of Roman Dropshaft Operation: Hydraulics, Two-Phase Flow, Acoustics" (Chanson, 2002). In Chanson's work flow measurements were made using pointer gauges, rulers and total head tubes. These values were extracted from the CFD model by setting up surface monitors which reported the average velocity and phase composition for each mesh cell intersecting the set plane.

3 COMPUTATIONAL FLUID DYNAMIC MODEL

The ANSYS Workbench platform was used to perform the CFD analysis. Workbench includes several different components which can be linked to perform different CFD analyses. In this project, four different components were used. Design Modeler was used to generate the 3D geometry, ANSYS mesher was used to generate the mesh, ANSYS Fluent was used to process the model for some post-processing purposes and CFD-Post was used to produce additional graphics. To process the model ANSYS fluent uses the three fundamental fluid flow equations, conservation of mass, conservation of energy and conservation of momentum to predict fluid flow properties

In ANSYS Workbench, the mesh is used to divide the model volume into a discrete domain so each governing equation can be solved. In a discrete domain, the flow variables are only defined at each grid node. The flow equations are solved at a specific node defined by a boundary condition, and then these values are interpolated to predict these values at undefined nodes (Oxford University, 2014).

The mesh representation of the drop shaft geometry was generated using the assembly meshing algorithm. In this process, the mesh for the entire geometry was generated in one step using the cutcell algorithm. This algorithm uses the volume meshing approach, while other meshing algorithms generate the mesh from the body surface and then generate the interior mesh from the generated surface mesh.

With assembly meshing, a Cartesian grid mesh is generated within the body. This grid mesh is constrained by the user input max mesh size (ANSYS, 2016c). As the name suggests, the cutcell algorithm divides or cuts the inner mesh cells to almost perfectly fit the geometry limits. With this method the elements are not stretched or compressed to trace the model extents, resulting in a high quality mesh. The cutcell meshing method generates a large proportion of hexahedron (or brick) mesh cells. When comparing similar comparable number of elements in the mesh, hexahedral meshes produce the most accurate solution (ANSYS, 2016c). The mesh layout for this model is shown in Figure 1. The model contains 264,574 mesh cells.

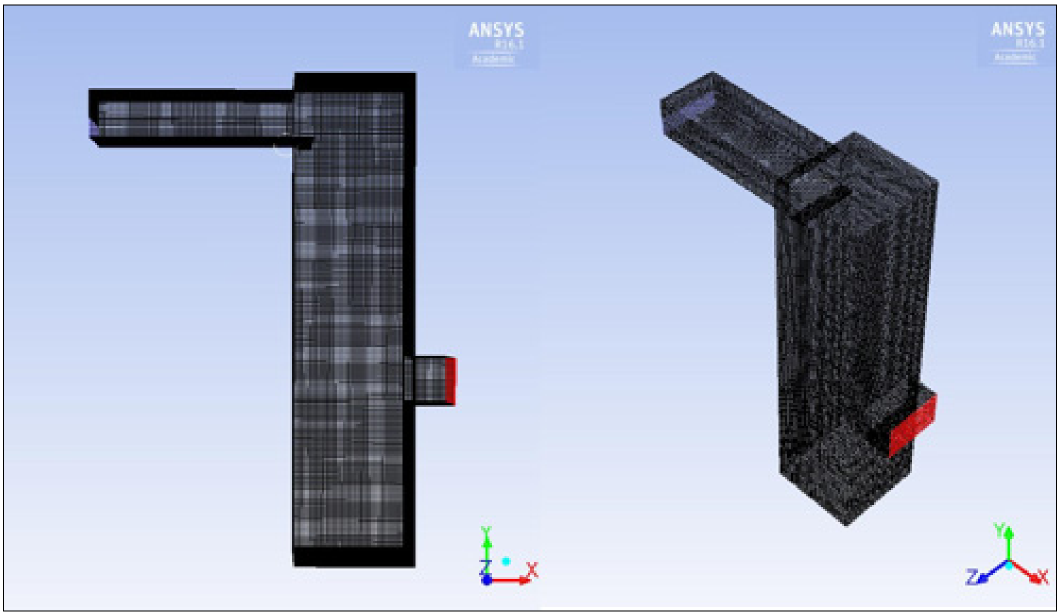

Figure 1. Model mesh.

3.1 Volume of Fluid Model

A volume of fluid model can model the flow behaviors of multiple independent phases by solving a single set of momentum equations. This model is most commonly selected when the interface between the two phases is of specific importance. In this model the volume fraction of each phase (in this case water or air) is tracked in each mesh cell (ANSYS, 2016a), by solving the volume fraction equations are for the secondary phase only (in this case water). The volume fraction for the secondary equation is solved assuming the volume fraction of both phases sums to one.

3.2 Turbulence Model

In a plunging drop structure, the turbulence model is important in this simulation since turbulence is the major cause of air entrainment (Hirt, 2012). The realizable k-Ɛ model was specifically chosen because it is known to be more robust than most turbulence models (ANSYS, 2016b).

Type	Pressure Based
Velocity Formulation	Absolute
Time	Transient
VOF	
Formulation	Explicit
Body Force Formulation	Implicit Body Force
Viscous	
Model	k-epsilon
K-epsilon Model	Realizable
Operating Condtions	
Operating Pressure (pa)	101325
Reference Pressure Location	x=0.755, y=3.08, z=0
Specified Operating Density (kg/m^3)	1.225
Solution Methods	
Pressure-Velocity Coupling	Coupled
Spatial Discretization	
Gradient	Least Squares Cell Based
Pressure	PRESTO!
Momentum	FOU
Volume Fraction	Geo-Reconstruct
Turbulent Kinetic Energy	FOU
Turbulent Dissipation Rate	FOU
Transient Formulation	First Order Implicit
High Order Term relaxation	0.25 - Flow Variables only
Solution Controls	
Flow Courant Number	200
Explicit Relaxation Factors	
Momentum	0.25
Pressure	0.25
Under-Relaxation Factors	
Density	1
Body Forces	0.5
Turbulent Kinetic Energy	0.5
Turbulent Dissipation Rate	0.5
Turbulent Viscosity	0.5
Time Step (s)	0.01

Note : FOU - First Order Upwind

Figure 2. CFD model set-up.

3.3 Solution Methods

The coupled algorithm is much faster than the alternative segregated algorithm when pressure based is chosen. In addition to added speed, this method also tends to produce a more stable solution (ANSYS, 2016a). A pressure based solver was chosen since this solver was historically designed for low speed incompressible flows (ANSYS, 2016a). In general, solver decisions were made to improve stability and model convergence.

3.4 Convergence

In general, convergence shows the imbalance in the principle equations which Fluent used, summed over each cell. The two of the convergence criteria used to access convergence of this model were the consistency of water surface height in the drop shaft, stability of surface monitor input and outputs and mass flux at the inlet and outlet.

3.5 Model Outputs

Various surfaces were created in ANSYS Fluent to act as data output planes. Automatic export of data was generated for the depths, impact points and velocity outputs. These outputs report the average value for each specified parameter (in this case, velocity and phase fraction) for each mesh cell associated with the surface. The depth and velocities were taken from the mesh cells aligned center point of the plane (z=0.382m) and averaged to present an output value. Only mesh cells with a volume fraction of water greater than 0.5 were used in the average calculation.

3.6 Model Work Flow

It must be stated that the CFD model was completed without constantly comparing back to the physical model results, rather the team relied on Hallie Thornburrow's experience to model as if the physical results were not available. After that the comparisons were made.

4 RESULTS

Much of this work in terms of comparison between the CFD model and physical model is focused on the subset of Chanson's work that he describes as the R3 regime. Under this flow regime:

1) The jet from the upper pipe is supported partially by a small lip;
2) The orientation of the inlet and outlet pipes are at a 180º angle;
3) The jet from the upper inlet pipe strikes the opposite wall of the drop shaft;
4) The wall opposite of the inlet channel acts as a deflector;
5) The flow downward along the far wall forms what Chanson describes in his literature as a 'film' this acts as a barrier causing higher water surface elevations in the pool, than if the water plunged directly into the pool;
6) The flow jet wall spreads as it travels reaching a width greater than that of the vertical shaft before it reaches the opposite wall;
7) Air is entrained in the jet flow; and
8) Air is entrained at the water surface in the drop shaft.

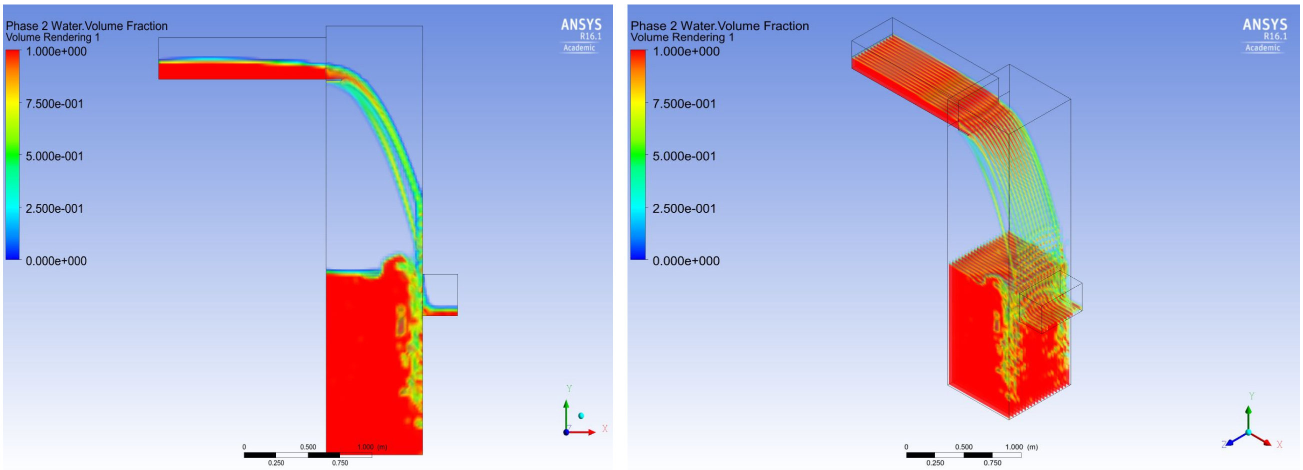

Figure 3. Three dimensional CFD volume rendering.

Figure 3 shows volume rendering of the CFD model results showing these features. In this figure, water is depicted as solid red while air is shown as blue, green indicates a 50% mixture. The figure accurately depicts the flow pattern described in the physical model ran in Chanson's experiment. The rendering on the right of this figure is an isometric view which shows the flow pattern at the corners of the vertical drop is different from that directly beneath the invert of the outlet pipe, where no bubble swarm present It should be noted that the portion of the physical model below the invert of the outlet was built with plywood, therefore no visual comparison could be made.

Figure 4 shows the air-water rendering through progressive cross-sections through the CFD model. The cross-section of the far wall, x=0.755, shows the spreading of the flow is evident and it clearly shows that there is no significant bubble swarm beneath the invert of the outlet pipe. The fact that air is being entrained in the downward flow but it being absent beneath the invert suggests that the portion of the jet that strikes the wall directly above the outlet pipe is not entering the pool.

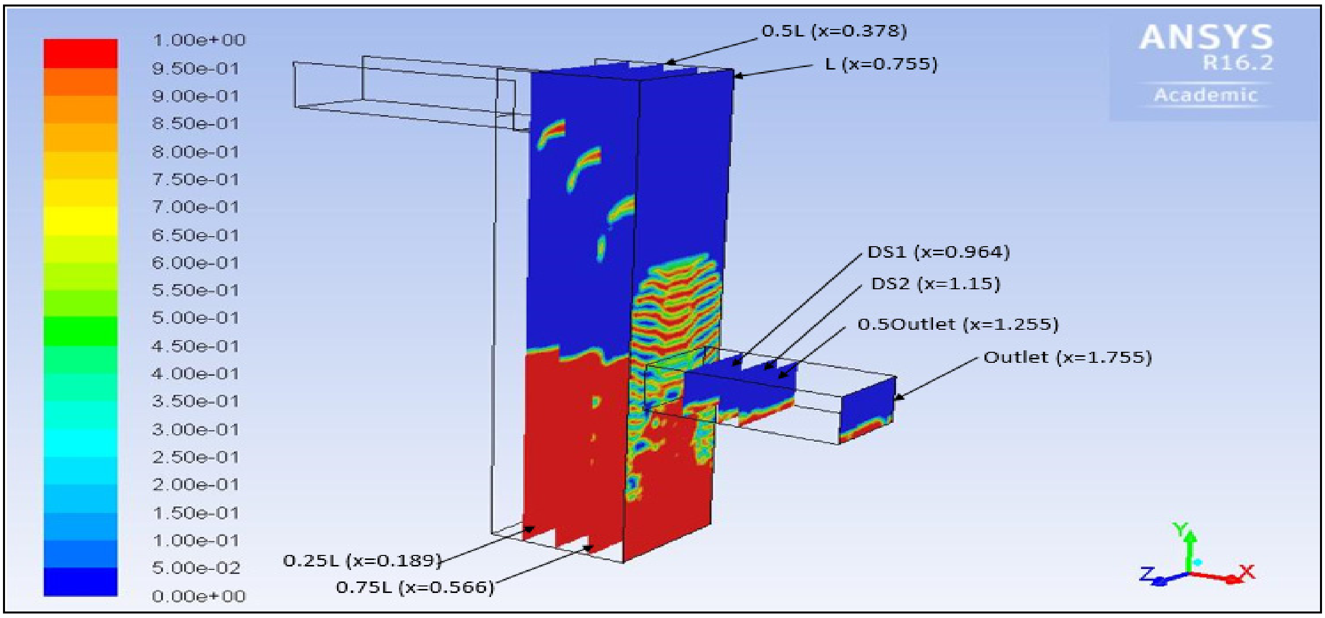

Figure 4. Contours colored by phases at various section.

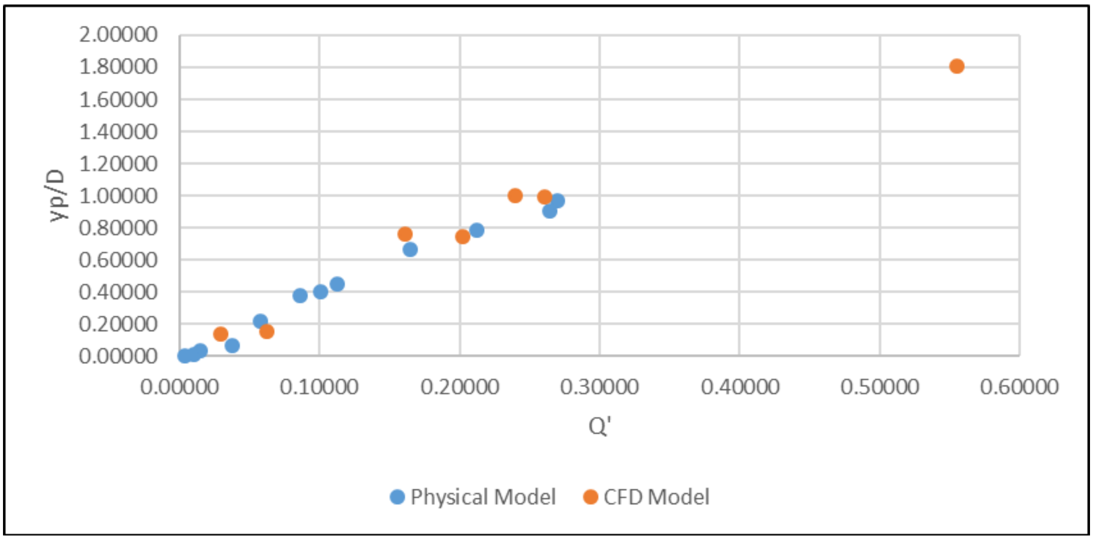

Figure 5. Pool height verses dimensionless flow.

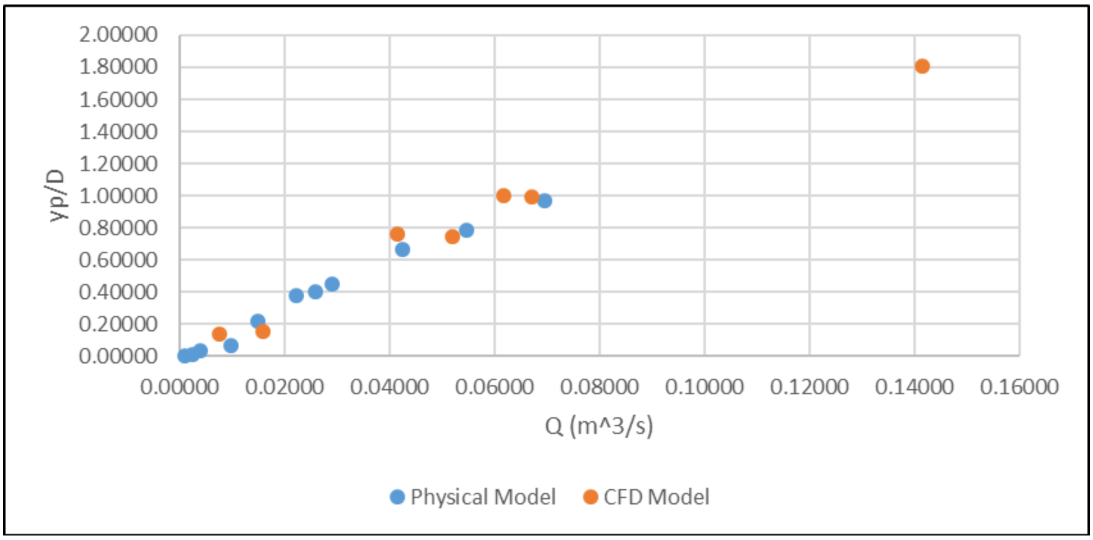

Figure 6. Pool height verses flow.

The next point of comparison between the physical and CFD model was the y_p variable, which is the measured distance between the outlet invert and the pool height. Figure 5 shows the pool depth versus flow in terms of yp/D & Q' from Chanson's work. In this case, Q' is a dimensionless discharge number, calculated by $Q'=Q/(g*b^2*D3)^{0.5}$. It must be noted that the Q (flowrate) had to varied significantly to obtain this data set and the data points to the left were not all from the R3 regime. Figure 6 shows the identical results except the x-axis is flow (Q) measures in cubic meters per second.

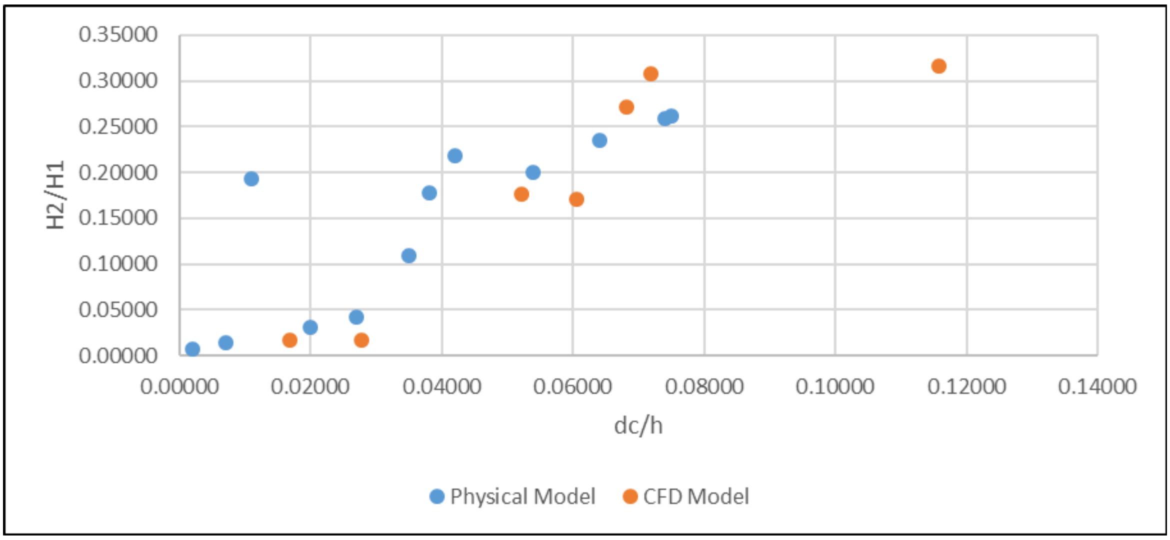

Figure 7. Head loss verses critical depth.

Another point of comparison between the physical and CFD model was completed for the variable H_2/H_1, where H_1 represents the total head at the inlet, and H_2 is the residual head, both measured in meters. This is a measurement of the energy loss, this data is shown in Figure 7. These results show an excellent correlation between the CFD and physical model results.

The next area of comparison was between the hydraulic retention time of particles that were dropped into the pool. Chanson did this by dropping 3.3 to 15 mm diameter particles that were neutrally buoyant into the upper pipe at the end of the inlet channel, also referred to as the brink. The time it took for each particle to exit the model was measured. This was repeated to complete his data set. Chanson reported his results in terms of a dimensional parameter $T*v_c/d_c$ where T is the time the particle spent in the model (in seconds), v_c is the critical velocity and d_c is the critical depth. The results of the physical model are shown in Figure 8. Note the comparison to be made is for prototype P2 and the CFD results.

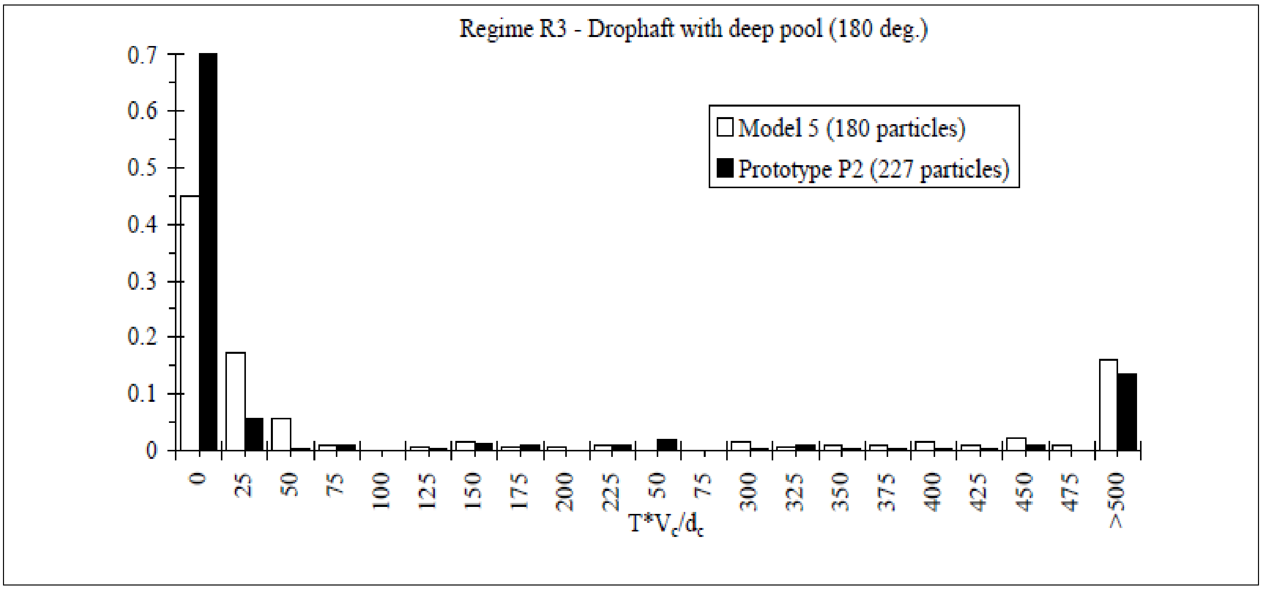

Figure 8. Particle residence time – physical model.

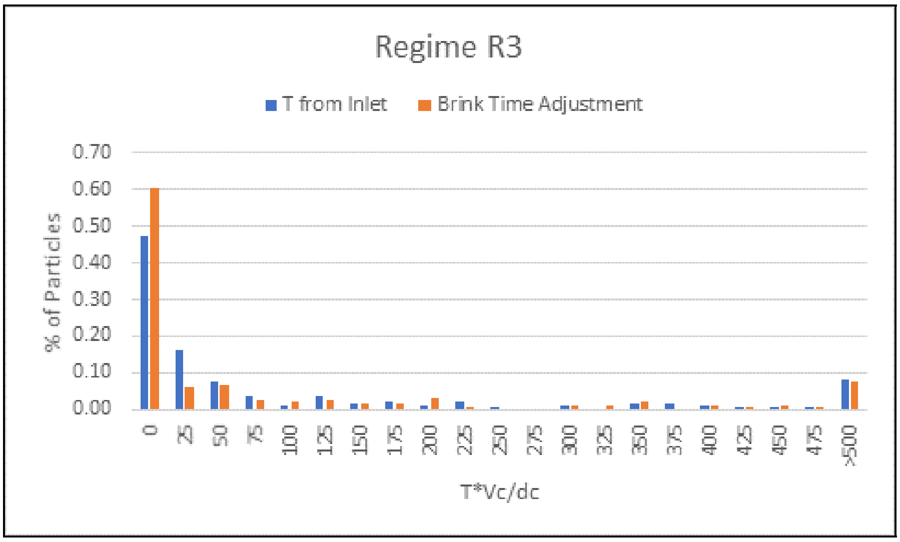

Figure 9. Particle residence time – CFD model.

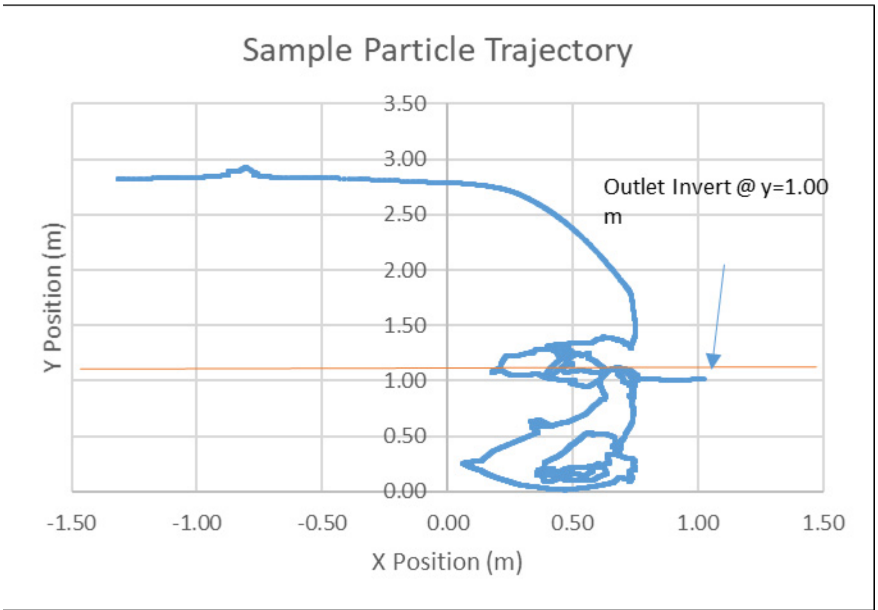

Figure 10. Particle track data of a trapped particle.

The CFD analysis of the particle hydraulic retention time was completed slightly differently. In the CFD analysis, all the particles were released from the inlet (far left, shown in Figure 3) of the model simultaneously. The reported T was calculated by subtracting the travel time to the brink location to obtain similar data sets. This calculated value is reported as 'Brink Time Adjustment' in Figure 9 in terms of the dimensional parameter T^*v_c/d_c. While the release point of the particles was different, the CFD results also showed the same bimodal distribution as the results from the physical model. That is both data sets show most particles leave the model very quickly, although there are nearly 10% of the particles that have very high detention times that get trapped in the pool. Figure 10 shows the tracked flow path of one of these few particles that gets trapped in the pool.

These two data sets can be explained again by the flow pattern shown in Figure 3. The majority of the flow and the particles do not enter the pool, but instead travel down the far wall and enter the outlet channel near its invert, this accounts for no bubble swarm beneath the air vent.

5 DISCUSSION AND IMPLICATIONS

The results produced from the CFD model agreed to those obtained from the physical model. The CFD results show that the bubble penetration (bubble swarm) is not even across the far wall of the vertical shaft as would be expected if the jet was just plunging into a pool without hitting the far wall. The CFD model clearly shows very little of the bubble swarm directly beneath the outlet even though there is a significant amount of air in the plunging flow. This indicates that most the flow from the inflow channel in conveyed directly into the outlet channel. This accounts for the bimodal distribution of the particle hydraulic detention time. The hydraulics of the drop shaft specifically in the R3 regime are controlled by the downward 'film' across the inlet of the outlet pipe.

The full-scale implications of this work are very important in relation to air entrainment. A drop shaft must have provisions for the handling air under great pressure. As earlier research has noted, air entrainment does not scale up accurately, therefore CFD modelling done at the full scale of the proposed structure might be used to overcome this limitation.

3 CONCLUSION AND FUTURE WORKS

The results presented in this paper show that the CFD software platform ANSYS Workbench can accurately represent the hydraulics associated with a vertical drop structure across varying flow conditions.

In the future, the most practical use of the work described in this paper might be in accounting for the air entrained in the flow. The CFD software can account for air quantity in each cell but there is an expectation that this might be improved by the refining of the mesh in certain zones. Since air entrainment is so important, an important next step would be to analyze a full-scale drop shaft to quantify the air entrainment scale up factor.

ACKNOWLEDGEMENTS

The authors would like to thank Dr. Hubert Chanson of the University of Queensland for all his timely help.

REFERENCES

Anderson, S (1961). *Model Studies of Storm Sewer Drop Shaft*, Technical Paper No. 35, Series B. St. Anthony Falls Hydraulic Laboratory, University of Minnesota.

ANSYS, Inc. (2016a). *ANSYS Fluent Theory Guide*, ANSYS Inc., Canonsburg, PA, 780 pp.

ANSYS, Inc. (2016b). *ANSYS Fluent User's Guide*, ANSYS Inc., Canonsburg, PA, 2428 pp.

ANSYS, Inc. (2016c). *ANSYS Meshing User's Guide*, ANSYS Inc., Canonsburg, PA, 55 pp.

Chanson, H. (2002). *An Experimental Study of Roman Dropshaft Operation: Hydraulics Two-phase Flow,* Acoustics (No. CH50/02, pp. 1-50). University of Queensland, Department of Civil Engineering.

Hirt, C (2012). *Modelling Turbulent Entrainment of Air at a Free Surface*, Technical Note 61, Flow Science, Inc (FSi-03-TN61) 48. Hirt CW, Nichols BD.

Oxford University (2014). Introduction to CFD. Oxford University Department of Engineering and Science. http://www.eng.ox.ac.uk/thermofluids/research/computational-fluid-dynamics

Williamson, S (2001). *Drop Structure Design for Wastewater and Stormwater Collection Systems*. Parsons Brinckerhoff Inc, 126.

DECISION-SUPPORT SYSTEM FOR UNDERPINNING COLLABORATIVE PLANNING FOR MULTI-HAZARD MITIGATION

HAOWEN XU(1), HAIDER HAMEED(2), MARY WINDSOR(3), MARIAN MUSTE(4), IBRAHIM DEMIR(5), JASON SMITH(6), TOBY HUNEMULLER(7) & MARYBETH STEVENSON(8)

(1, 2, 3, 4, 5) IIHR—Hydroscience & Engineering, University of Iowa, Iowa City, IA, USA,
marian-muste@uiowa.edu
(6, 7) U.S. Army Corps of Engineers, Rock Island District, Rock Island, IL, USA
(8) Iowa Department of Natural Resources, Iowa City, IA, USA

ABSTRACT

The increased stress on the natural landscape due to human impacts and climate change has triggered an increase in water-related hazards (e.g., floods, river pollution), which in turn impose direct and immediate implications for the sustainability, resilience, and security of our watersheds. Because of their complexity, hazards are typically studied in isolation, as stand-alone processes. Moreover, the interconnections between different types of hazards are vast and not fully known. In most of the cases, however, the primary difficulty to simultaneously address hazards stems from our limited capabilities to integrate and handle the vast amount of data needed for solving the problem at the appropriate scale, i.e. the full size of the drainage area converging to the point of interest. The lack of the technological capability precludes not only the thorough the understanding of the feedback dynamics between the multiple hazards, but also accounts for the synergies and tradeoffs among the possible solutions used to address them. Overcoming the status-quo requires the development of evidence-based decision support systems (DSS) that are focused on the end-user interests. A DSS typically provides users with interfaces that are easy to understand and use by all stakeholders using the DSS tools for problem-solving and decision-making. This paper presents a prototype DSS used for a Multi-Hazard Tournament (MHT) organized by the US Army Corps of Engineers' Institute for Water Resources in the state of Iowa (U.S.A.). The computational environment, referred to as IoWaDSS, provides data insights for problem solving and supports decision-making for the mitigation of multiple hazards. The platform was developed using single-page application while implementing serious gaming concepts in order to enhance social learning. The platform was built with open source technologies that make the system light-weight, low-cost, and flexible. The objective of this paper is to present the IoWaDSS software architecture and its components while illustrating the interfaces used for collaborative planning in the game-like environment.

Keywords: Natural hazards; integrated water resources management; flood mitigation; decision support systems; web-based.

1 INTRODUCTION

In recent decades, increased anthropogenic interventions in the natural landscape (e.g., agriculture and urbanization) have aggravated the water-related hazard frequency and intensity affecting the security, resilience and sustainability of our watersheds (Dibike and Coulibaly, 2005; Crossman et al., 2013; Luo et al., 2013). In effect, hazards have appeared in a wide variety of forms such as flood, sedimentation, water quality, and ecological habitat deterioration causing considerable devastating social and economic negative impacts. One of the notable examples is Iowa's great flood of 2008. As a result of this event, 85 of Iowa's 99 counties were declared a Federal Disaster Area and the total statewide damage was estimated at $10 billion. Many of those hazards produce risks that are assessed using diverse disciplines (e.g. hydrology, meteorology, ecology, and socioeconomics), and over multiple scales (e.g., physical and socio-political). In some of these events, multiple hazards (e.g., flood, water pollution, soil loss) occur simultaneously, hence they have to be addressed simultaneously (Kappes et al., 2012). The planning associated with multi-hazard mitigation faces multiple challenges, such as: (1) assemblage of large amounts of data for covering the holistic view of the watershed; (2) ensuring close collaboration and clear communication between multiple heterogeneous actors (e.g. decision makers, analysts, stakeholder) with diverse expertise and interests (Andrienko et al., 2007) and (3) capturing the feedback among multiple hazard drivers. The massive amount of data and information required to develop plans for multi-hazard mitigation is time- and labor-intensive if tackled with conventional methods. Beginning in the past decades, hazard mitigation plans have been increasingly approached with customized Decision Support Systems (DSS) that adopt the architecture and technologies developed in other socio-economic domains (e.g., banking, e-commerce, etc). DSS focused on watershed management have been already tested by government agencies, academic institutions, and consulting firms (Zhang, et al., 2011).

DSSs are defined as interactive computer-based systems and subsystems intended to assist decision makers' use of communication technologies, data, documents, knowledge and/or models to identify and solve problems and make decisions (Power and Kaparthi, 2002). In many applications, DSSs are powered by modern Geographic Information System (GIS) technologies to solve problems with spatial data (e.g. watershed management, resource management). The DSSs with spatial capability are also known as Spatial Decision Support System (SDSS) according to Power and Kaparthi (2002). Most of the initial SDSSs target one aspect of watershed management by integrating data and models specific to one or few disciplines (Watson et al., 2002). Advancement in computer and information technologies have promoted the extensive use of web-based SDSS. The web-based SDSSs have the capability to discover, access share, and integrate data and resources in an automated and systematic fashion using the Internet, hence having direct access to a multitude of resources using machine-to-machine communication.

An alternative definition for domain-specific SDSS is Problem Solving Environment (PSE). Typical PSE features include users-defined problems, strategies selection, results in visualization and analysis, and problem solving tasks extension and coordination (Rice and Boisvert, 1996). The Iowa Watershed Decision Support System (IoWaDSS) is designed in conformity with the principles of a web-based PSE for: (1) automating data resource integration, (2) evaluating of the best management practices from multi-hazard perspectives through competitive gamification techniques, and (3) facilitating collaboration and results communication between different actors. The IoWaDSS was originally designed to address floods, droughts, and water quality hazards. The system is designed to accommodate multiple actors with well-defined roles, i.e., players, referees, team facilitators, and announcers. Each individual user operates the system through a registered user-account. Described below are the system design considerations and selected interfaces of the IoWaDSS.

2 SYSTEM DESIGN

2.1 PSE design

Conceptually, the PSE structure entails four modules: (1) the watershed characterization (offering a digital representation of the existing data about the watershed), (2) the watershed planning (new data and information created with multi-domain modeling), (3) the competitive gaming environment (enabling game-like competitions), and (4) the plan evaluation (entailing a metric for evaluation of the proposed alternatives and scoring of the competitors). Figure 1 illustrates the PSE modules and associated components.

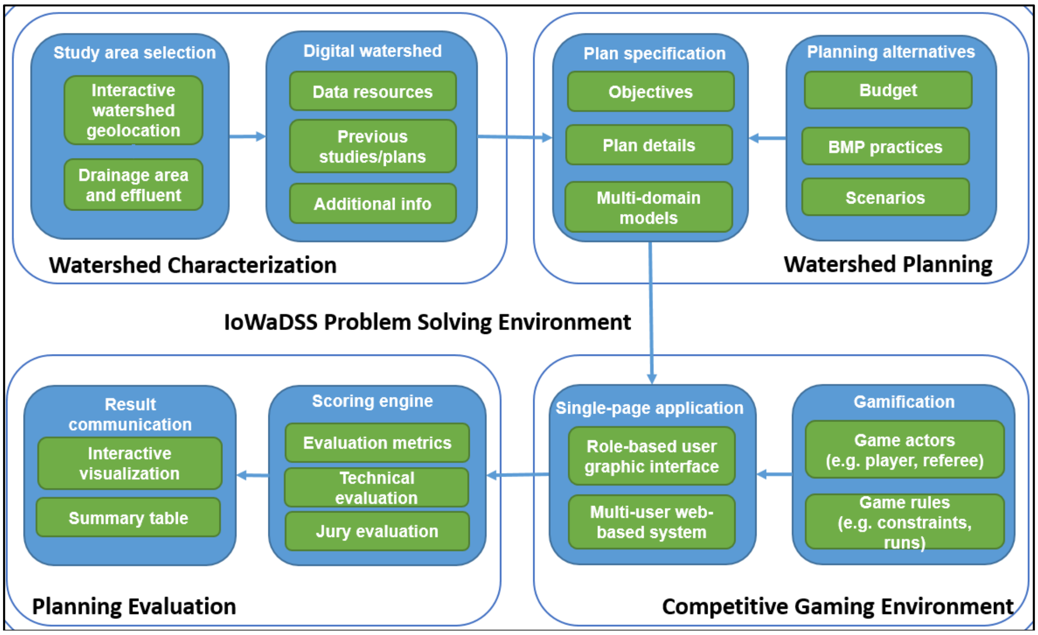

Figure 1. Problem Solving Environment structure for the IoWaDSS prototype

2.1.1 Watershed characterization.

The watershed characterization module is the foundation of the PSE as it has the background data and information about the watershed existing at a given instant. The sub-components within this module include the Digital Watershed (DW) and tools to select the watershed of interest. The DW concept was introduced by Maidment (2006) to define the comprehensive digital characterization of the eco-hydrologic systems residing in a given watershed. The IoWaDSS architecture uses DW as a spatial unit for assembling multi-scale, multi-domain data acquired in-situ or resulting from models produced by various agencies. The selection tool offers multiple choices for the search (e.g., HUC or administrative key words) and subsequently triggers visualization of the selected watershed with the upstream drainage areas and downstream effluents associated with the watershed. Using the spatial boundary of the delineated drainage area, the IoWaDSS dynamically generates a DW of the area entailing the data and information stored in the system's database. Organization of the data in DW is made by indexing the data with a watershed identifier and relating data with watershed connectivity.

The backbone of the watershed characterization module is the National Hydrography Dataset Plus (NHDPlus), which provides physical (e.g. shapefiles of rivers, catchments, and watershed boundaries) and topological (e.g. river connectivity, hierarchy of tributaries, hydrologic unit code system) descriptions of the real-world hydrologic system in a digital environment. The physical description includes features, such as streams, catchments, and hydrologic unit code (HUC) watersheds that are either displayed on map or spatially indexed with the data resources (e.g. raster data, point-observation) associated with them. Results of previous models and additional information relevant to planning studies are also spatially indexed. The use of this approach from the watershed data and info (generically labeled as resources in the planning process) can be easily discovered and retrieved for each indexed watershed (e.g. by watershed name, hydrologic unit code, river name). The topological description of the watershed search engine defines the upstream-downstream relationship among the individual physical features. The NHDPlus covers hydrologic features at a national level, and it is widely used among hydrologic research groups and watershed management communities in the U.S. The dataset can be easily extended in terms of spatial coverage and new attributes.

2.1.2 Watershed planning.

This module provides users with diverse management options to be used for mitigating hazards. The module was developed on the top of the watershed characterization module. The IoWaDSS application presented in this paper entails data and options associated with the Middle Cedar River watershed in central Iowa (U.S.A). The module contains two sub-components: planning specification and planning alternatives. The planning specification enables users to specify the objectives of the plan and existing constraints (e.g., limitations in the available data and budget). The sub-component also retrieves from DW results of available multi-domain models. The planning alternative module allows users to place best management practices in targeted control points (such as urban areas) or upstream in the watershed for mitigating the hazards. The practices are spatially distributed within the watershed and visualized for convenience on the map. The such-defined planning alternatives are converted into inputs for the models used for exploration of the alternative scenarios.

The scenarios simulated for the IoWaDSS initial implementation in the Middle Cedar River watershed were obtained with 8 different multi-domain models (physical and socio-economic). The watershed based simulations used 40 different alternative practice combinations (IWR, 2016; Muste et al., 2017). Each combination was applied for four climate scenarios (historic, flood, drought, composite) to build a landuse change database. Watershed based actions were combined with localized practices based on their flow, stage and/or temperature relationships to generate a numeric database of localized and watershed actions. These numeric results were then tied to a suite of economic, social and environmental metrics by normalizing the numbers. The input and output data associated with the pre-run simulations were stored in the IoWaDSS relational database along with information on how each of these pre-run simulations, if selected in different combinations by the teams, would interact with each other and ultimately impact the environmental, economic, and social scores. The models used for simulations are provided in Table 1. Figure 2 provides the links between the various models leading to the results targeted by the risk analysis module.

2.1.3 Competitive gaming environment.

This module utilizes the concept of gaming to facilitate collaborative planning and communication. It creates an environment where users with different interests and backgrounds can share and discuss planning experiences through competition towards a consensus management plan. The module consists of two sub-components: gamification and single-page application (SPA). Gamification, also known as gaming science, is defined as the application of game-design elements and game principles in solving scientific problems (Deterding et al., 2011). By using a competitive gaming environment, the traditional watershed planning process is converted into a competitive game by defining the game actors and rules. The implementation of the gaming science concept results in a computational environment with capabilities to support multiple users and to render Graphic User Interface (GUI) based on different users-roles. SPAs are web applications that load, cache and dynamically update information and views in one HTML page. The application of SPAs in the gaming environment has made the planning process smoother and the user experience more interactive, without interrupting the flow of information visualization. Behind the SPA, a multi-user web-based system manages users' activities through user registered accounts. It stores the user's information, ongoing and past plans, and their performances (i.e. scores) generated from the planning evaluation module. The module enables user to share, compare plans, and even to learn from previous plans.

Table 1. List of the multi-domain models used in the IoWaDSS initial implementation.

Model Name	Domain	Output type
North American Regional Climate Change Assessment Program (NARCCAP)	Climatology	Climate scenarios
SWAT: Soil & Water Assessment Tool	Hydrology	Discharge and water quality at control points
Agricultural Conservation Planning Framework (ACPF)	Agroecology	Screening of various conservation practices
Hydrologic Engineering Center's (HEC) Statistical Software Package (HEC-SSP)	Hydrology	Flood frequency analysis
Hydrologic Engineering Center's (HEC) River Analysis System (HEC-RAS)	Hydraulics	Stage at control points
Hydrologic Engineering Center's (HEC) Flood Impact Analysis (HEC-FIA)	Risk Management	Socio-economic impacts of hazardous events
Hydrologic Engineering Center's (HEC) Geospatial River Analysis System (HEC-GeoRAS)	Hydraulics & Geoinformatics	Inundation map and visualization
Integrated Valuation of Ecosystem Services and Tradeoffs (InVEST)	Ecology	Hazards impact on ecosystem and benefits of the ecological services

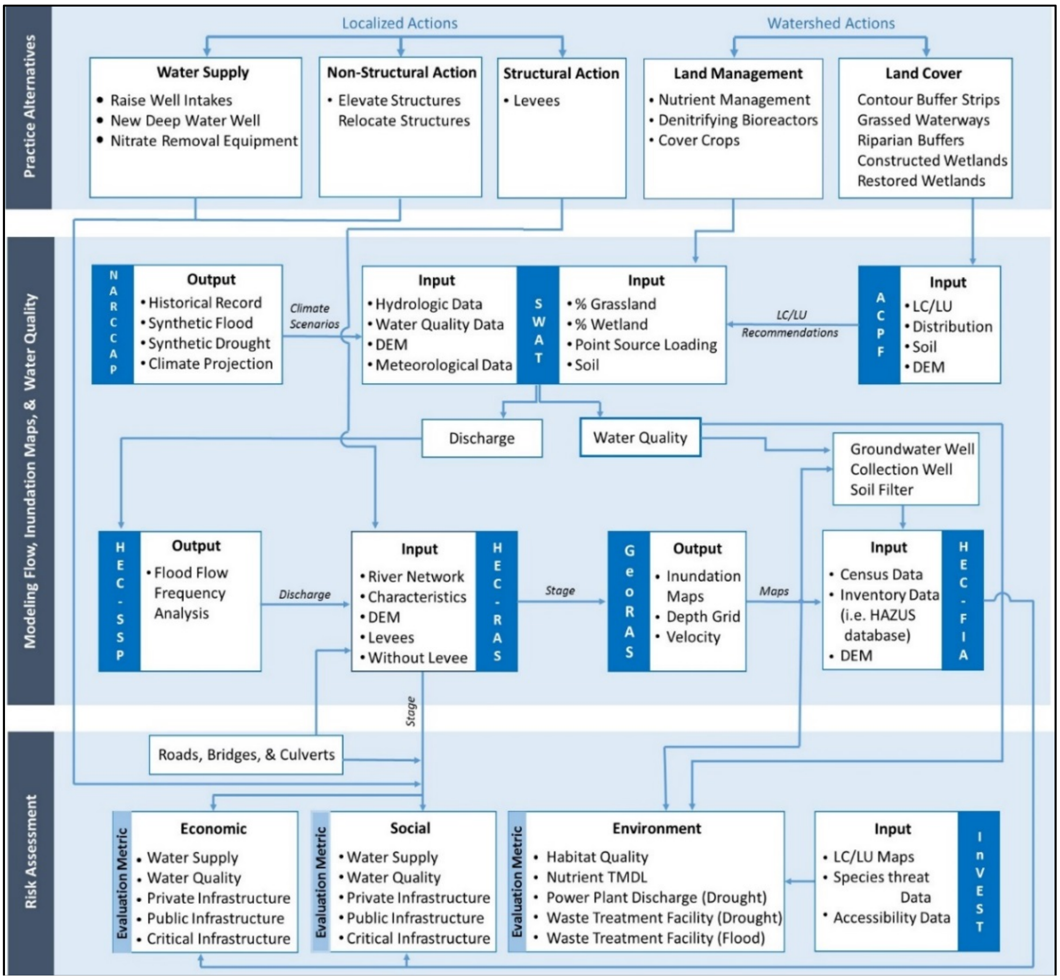

Figure 2. Flow of data and information among the models used in the scenario analysis.

2.1.4 Planning evaluation.

The module evaluates all plans created by users through a scoring system, and communicates the scores through dedicated graphics. A scoring engine and a result communication sub-component are also included in this module. The scoring engine has built-in evaluation metrics as the criteria for evaluation, and produces scores with both technical evaluation and jury evaluation. The technical evaluation is solely driven by watershed modeling results in the watershed planning module. It calculates scores of individual plans based on the modeling outputs (e.g. maximum flood peak reduction) of the simulation. The jury evaluation is an expert system that brings human expertise into the loop. As mentioned earlier in the section, in addition to the player role, the IoWaDSS accommodates the judge role, which is designed for watershed experts to oversee and evaluate the performance of individual players. An administration system is provided within the module so that judges can create an expert score for each plan based on their technical experiences.

The IoWaDSS was originally developed for the Middle Cedar watershed as a delivery means for a Multi-hazard Tournament (MHT) hosted by the US Army Corps of Engineers' Institute for Water Resources in collaboration with other federal, state, and local agencies involved in water resources management (IWR, 2016). The tournament brought together a diverse group of multi-sector participants including representatives of local/regional government offices; resource management agencies; the private sector; interest groups; and universities. The objective of the MHT is to promote multidisciplinary preparedness and strategies for addressing hazards in a competitive and collaborative game-like environment. The MHT also helps participants to better understand their risk in their watershed and the feasible hazard mitigation options. Even more importantly, it promotes the building of relationships and understanding of interests between basin participants.

2.2 Software architecture and & technologies

Following the modern web-application templates, the IoWaDSS, adopts a three-tier architecture that includes the following components: (1) presentation, (2) logic, and (3) data. To ensure the platform reliability, flexibility, extendibility, modularity, and maintainability, industrial design patterns and architecture patterns (e.g. MVC and MVVM) were applied in the system development. Figure 3 illustrates the overall architecture, along with the web, informatics, and GIS technologies that are associated with each tier.

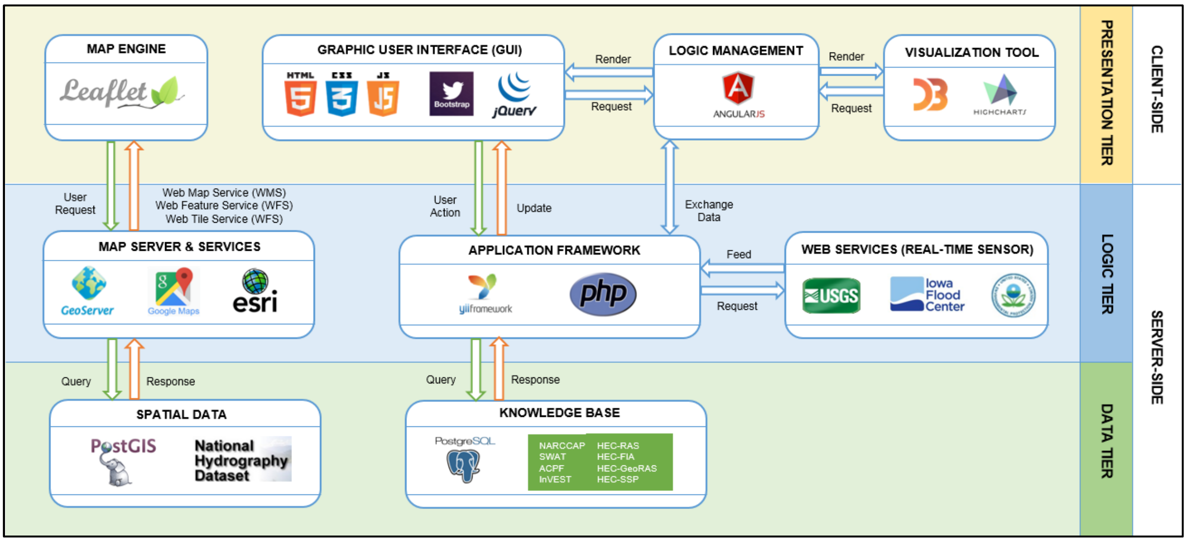

Figure 3. Overall architecture.

The presentation tier is primarily rendered at the front-end in user's web or mobile browser. It contains platform elements that a user can see and interact with. This tier provides users with Graphic User Interfaces (GUI), a map engine, and visualization tools to facilitate map operations, information retrieval, workflow control, watershed planning, and result communication. The presentation tier in IoWaDSS entails four components: (1) the map engine, (2) the GUI, (3) logic management, and (4) the visualization tools. The map engine is the means to visualize geo-spatial information, such as basemaps, river networks, watershed boundaries, locations of BMPs, and modeling results (e.g. soil maps, inundation maps). For IoWaDSS, the presentation tier is developed with Leaflet JavaScript library and its extensions. The GUI provides a media for users to navigate through the platform, to manage and control tools, and to retrieve information. The GUI is developed using JQuery and the Bootstrap library, which guarantees both the user interactivity and mobile compatible for multiple screen sizes.

The logic management component contains a front-end Model–view–controller (MVC), that improves fluid web page design and two-way data-binding. The main reason to have a logic management component is that our platform contains Single-Page Applications (SPAs), which make the front-end very heavy. The front-end

MVC, a JavaScript library itself, helps structure and optimize the front-end developments with practical industrial conventions, which increases the maintainability and extendibility at the front-end. Visualization tools are primarily responsible for visual communication and representations (e.g. plots, chart). They are developed with D3JS and Highchart libraries, both of which are data-driven and user-responsive. The entire presentation tier is developed using popular front-end technologies (e.g. JavaScript, HTML, and CSS). To perform multiple system operations (e.g. updating data & information, displaying spatial features on a map, user log-in, saving user-defined watershed plans), the presentation tier sends Asynchronous JavaScript and XML (AJAX) requests to exchange information with the server-side applications in the form of JSON, XML, and images.

Unlike the presentation tier, the logic tier and data tier are deployed on the server-side (i.e., "back-end" of the platform). The logic tier is responsible for organizing the data, assembling the services according to relationships between the user scenarios and the models, and for providing the necessary information requested by the presentation tier. The logic tier consists of three sub-components: (1) the map server & map services, (2) the application framework, and (3) the web services for real-time sensors. The map server and the web services prepare and manage spatial information, as well as handle request from the presentation tier for the map visualization. The IoWaDSS uses Geoserver, an open-source map server application, to host spatial information that is stored locally on the server (e.g. river, watershed boundaries). The Geoserver is in complying with a number of open standards, such as Web Feature Service (WFS), Web Map Service (WMS), and Web Coverage Service (WCS), which improve the interoperability of spatial data effectively. Third-party map services, such as Google maps, ESRI, USGS, are also used to increase the diversity of the basemaps (e.g. satellite imagery, topo-maps, and NHD basemap) within the platform. The application framework components manage the overall back-end logics (e.g. scientific models, PSE design, and data integration) and user-scenarios (e.g. multi-user web-based system).

Many of the platform's tool and applications (e.g. watershed search engine) that are too heavy to be hosted in the presentation tier, were hosted in the application framework module. This module hosts and is responsible for managing the local web services. The system design adopts a Service Oriented Architecture (SOA) to bring multiple web services in one place. There are two types of web services in the IoWaDSS: (1) local web services (that are developed within the application framework on the local server), and (2) external web services (that are hosted on third party servers). External web services in IoWaDSS are mainly third-party data providers (e.g., USGS, EPA). The web services are important components for the presentation tier as they facilitate the communication between the presentation tier and the logic tier. The backbone of the application framework module is Yii (a PHP framework that also follows the MVC pattern).

The data tier is located on the bottom of the architecture. This tier consists of databases and datasets. The spatial data are stored in the PostGreSQL database with its PostGIS library, which adds support for the use and management of spatial objects. The knowledge base is the customized database that stores results of simulations with the 8 multi-domain models and their relationship as entities (as a computational term). Details of model connection and information flow are illustrated in the Figure 2.

3 IOWADSS INTERFACES

The IoWaDSS was developed, and hosted under the "iowawatersheds.org" domain as a web-based platform for assisting the MHT delivery. The IoWaDSS is launched from a landing page that provided users guidance and tutorials pertaining to the platform, as well as the navigation to several platform features. The landing page entails an introduction, a map of watershed management authorities in Iowa, a Menu bar, and a navigation bar in the lower middle of the page. The Menu bar contains the IoWaDSS title and three tabs: about, support, and contact. The user can access the full introduction page through the "About" tab, and the platform tutorial videos through "Support" tab. The "Contact" tab provides the user contact information of the development team of the platform. The navigation bar includes four tabs: (1) decision support platform, (2) watershed infrastructure, (3) water resources management, and (4) communities & collaboration. By clicking the "decision support platform" tab, the user can launch the actual PSE. The "water resource management" tab presents the user with relevant management concepts, policies, and guidance in watershed management. While the "Communities & collaboration" tab directs user to the webpage of Iowa-Cedar watershed interagency coordination team and several watershed organizations. Figure 4 shows the overview of the landing page.

The "Decision-support platform" contains three workflows: (1) watershed -search, (2) watershed-info, and (3) watershed-planning. The Decision-support platform landing page is shown in Figure 5. The decision-support web page contains four functional blocks (1) the Menu bar, (2) the Workflow bar, (3) the functional panel, and (4) the web map, as illustrated in Figure 5. Similar to the landing page, the Decision-support platform carries the title of the platform and three tabs that lead user to the landing page, the DSS introduction page, and the tutorial page. The "Task bar" supports various aspects of the decision-making process by providing the user with the needed resources to carry out a watershed plan. For this purpose, four workflows have been designed: a) Search Watershed, b) Overview, C) Data resources, d) Planning. A "Help" button opens for the guidelines for using the platform.

The "Search Watershed" interface corresponds to the "Watershed characterization" module in the PSE design. The objective of this workflow is to define the study area on the map as well as the drainage area upstream (from where does the water come) and the main effluent leaving the watershed. Multiple search criteria are enabled: state level, HUC 8 watershed, HUC 12 watershed, city, county, and Point of Interest (POI) such as an address or a point on the map. Figure 6A presents the interface for the search criteria using as a point of interests the "Iowa state" (Figure 6A). Figure 6B shows the same for a HUC 8 watershed search. After the desired study area is identified, the user can access the DW by activating the "Load POI" button.

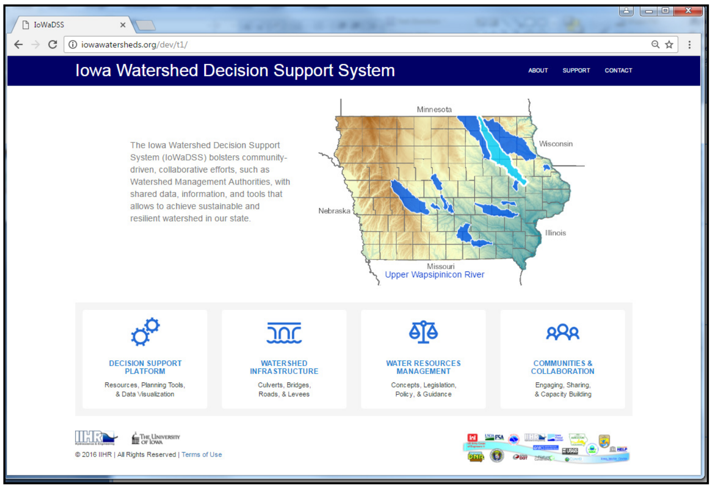

Figure 4. IoWaDSS landing page.

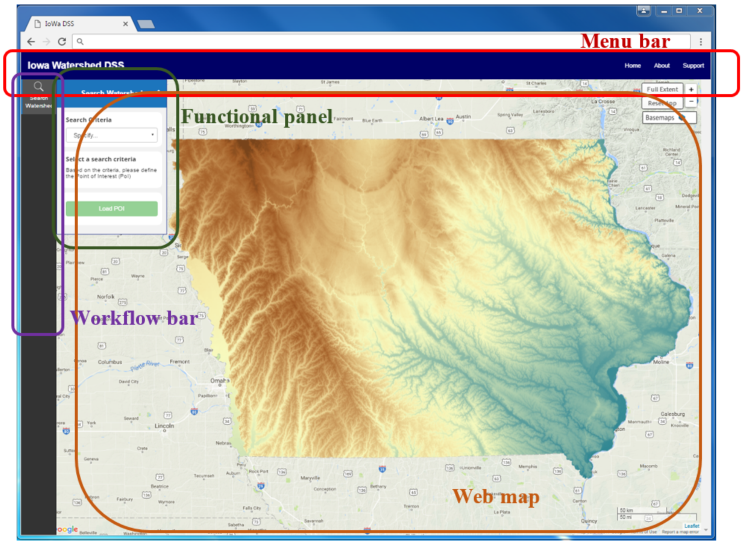

Figure 5. IoWaDSS customized interfaces

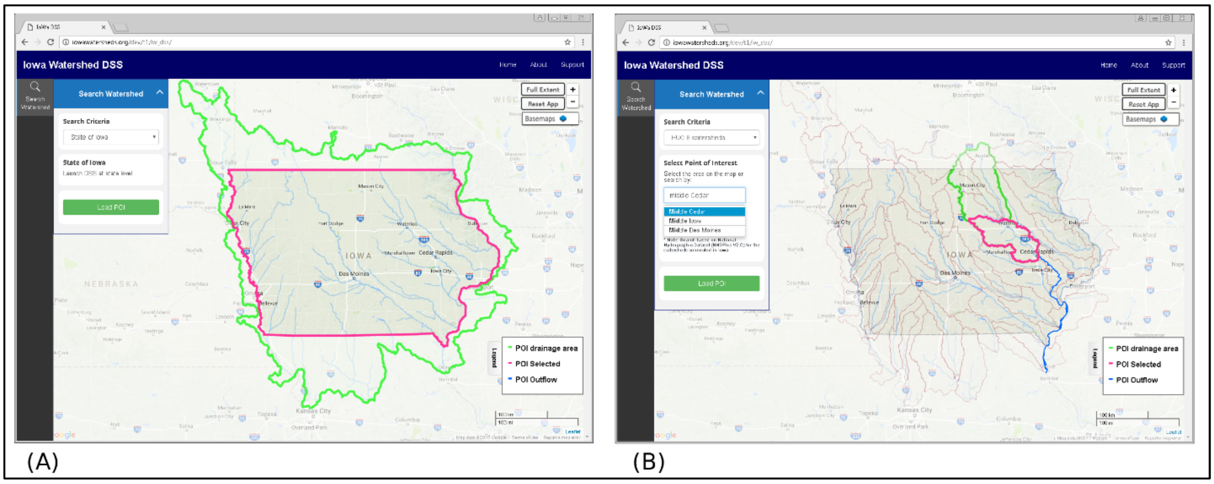

Figure 6. Search Watershed workflows using as criteria: a) the state of Iowa, and b) HUC 8 watershed.

Additional functions in the Workflow bar includes “Overview” and the “Data resources” options. These workflows assemble, synthesize and visualize important watershed data and information regarding the study area. The “Overview” workflow displays summary geographic information, displays dynamically the type of data available in the watershed including their providers (see Figure 7A), and lists the previous studies conducted in the watershed (see Figure 7B). The data resources tool displays the locations of different sensors grouped by their domain: hydrology, geomorphology, water quality, meteorology, land and water habitat, and socio-economic. Each domain contains selected variables. For example, hydrology contains:

stream discharges, stream stages, lake levels, runoff potential. The extension of the number of domains and variables for each domain can be increased if more on-line data is available. Uniformly-designed windows allow to view data for the variables acquired at various locations using two sub-interfaces. The first sub-interface shows the last recorded data and essential information about the source of the data that was selected for visualization (see Figure 7A). The second sub-interface shows the location of the sensor in an interactive map along with the time series for the variable plotted for a pre-established time window as illustrated in Figure 7D. Essential statistics of the visualized time series is also shown in this visualization sub-interface. This window is fitted with functions that allow to compare multiple time series acquired at other location and to download the data for further analysis.

The watershed-planning interfaces can be accessed from the "Planning" tab in the workflow bar (see Figure 8). This workflow is the most complex one in the platform and cannot be described fully in the present context. More details are provided in IWR (2016), Muste et al. (2017) and in the interactive tutorials published on the platform's website (iowawatershed.org/iowadss/support.php). The workflow provides users with options to either manage previous watershed plans or to create new plans. The "Planning" workflow entails a phased sequence of seven steps: 1) Objectives, 2) Resources, 3) Alternatives, 4) Asessment, 5) Selection, 6) Implementation, and 7) Evaluation. The progress of the plan development is visually displayed as the work advances. Each of the planning steps has multiple sub-menus and interfaces that will be not described in this paper. The work on the plans can be interrupted and continued at the pace of the user's availability. The Content Management System (CMS) developed behind the planning tool using PHP Yii framework allows simultaneous access of multiple contributors to the development of the plan. They all can store data and information, share, and manage the plans within the PSE.

Figure 9 illustrates the interface for the "Alternative" step (#4 in the upper part of the figure) of the "Planning" workflow. The choices of planning alternatives illustrated in this figure are those developed for the Multi-Hazard Tournament delivered in the Middle Cedar River watershed using the sequence of models shown in Figure 2 (IWR, 2016). The interactive interface asks the user to assemble an integrated hazard mitigation strategy using best management practices (BMP's) deployed locally ("Localized Actions") or within the watershed ("Watershed Actions"). The BMPs can be selected in in multiple combinations to accommodate various hypothetical climate scenarios and budget limitations, which are the constraints in the game-like environment. The finalized plan is stored under the user's account, and is submitted for evaluation in the "Assessment" step. The interface for the "Assessment" step is basically the front-end representation of the planning evaluation module (described in Section 2.2.

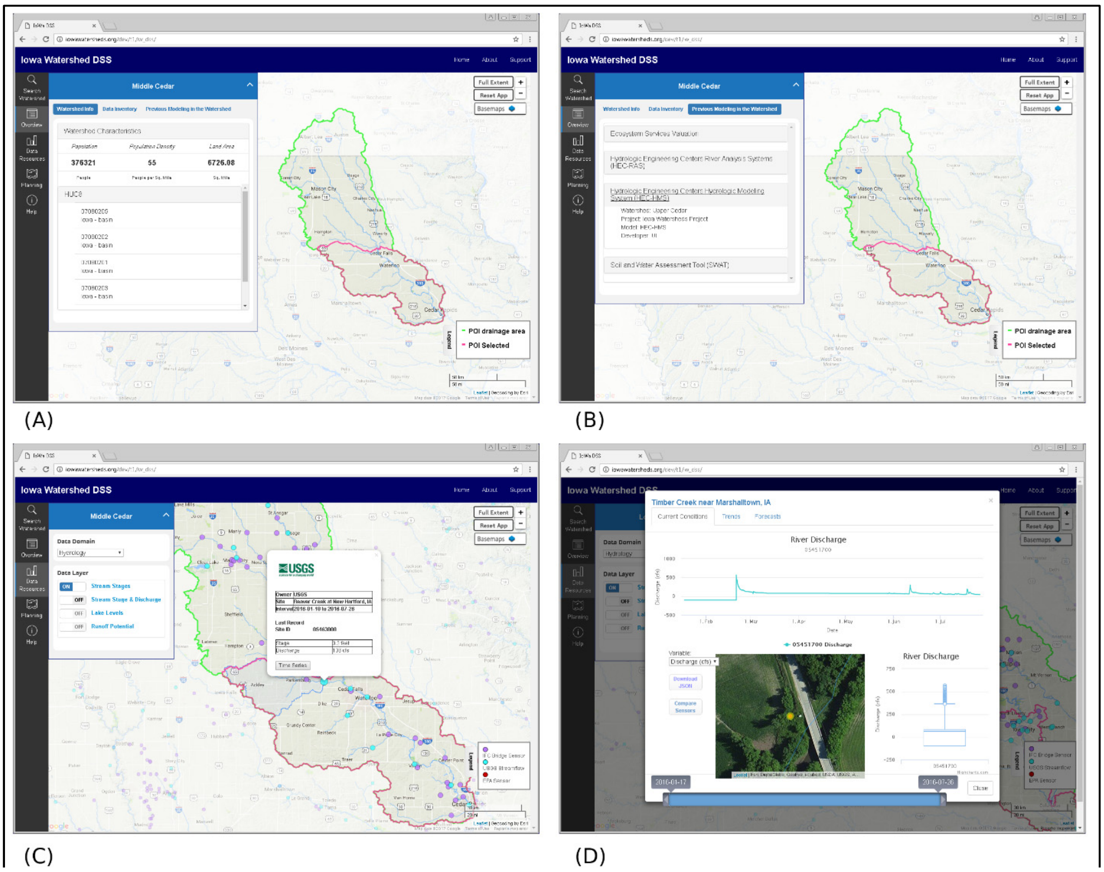

Figure 7. Interfaces for IoWaDSS workflows: A, B "Overview"; C) "Data resources", and D) viewer for the discharge time series

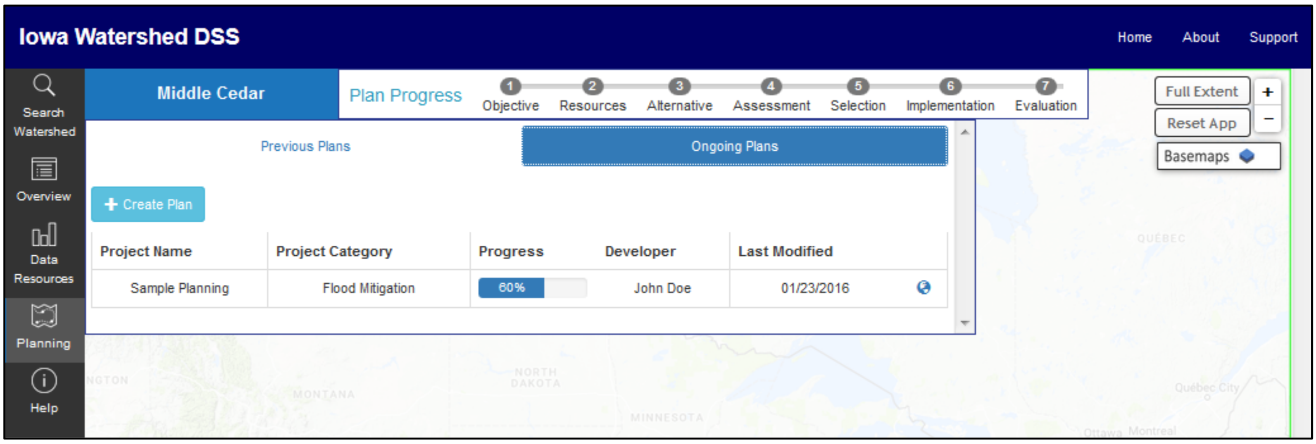

Figure 8. Watershed “Planning” initial interface

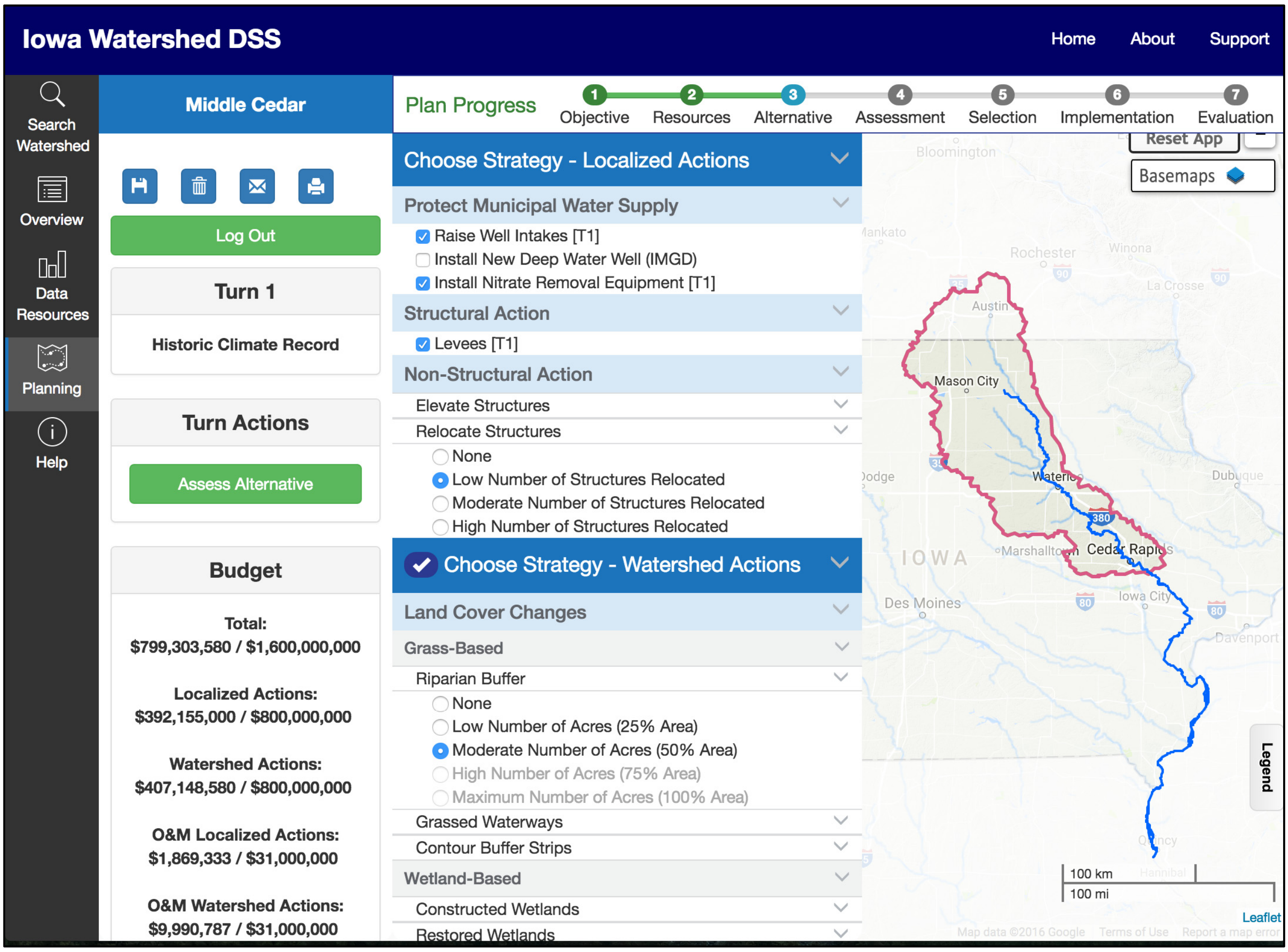

Figure 9. The interface for the “Alternative” step (#4) of the Planning workflow.

4 CONCLUSIONS

A growing number of researchers have recognized that technical solutions do not always perform well in addressing sustainability and adaptability strategies for practical situations, and thus have proposed role-playing games where the stakeholders are the decision makers. The co-production of the decision making with the involvement of management agencies and local stakeholders has the potential to improve the quality and efficiency of the decision-making process. By transferring the roles in the actual decisions, this approach increases considerably the viability of the plan implementation as the local stakeholders are co-owners of the plan. The IoWaDSS used for delivery of the MHT serious-gaming prototype presented in this paper is one of the possible paths to engage the community in the planning process by hiding the complexity of the technical aspects and providing a problem-solving environment that is understandable and adapted to the technical skills of the local watershed stakeholders. A user-friendly and interactive prototype of IoWaDSS was developed by seamlessly integrating open-source Web GIS tools, multi-domain models, real-time sensor network, and other open-source components and libraries. Compared with other generic watershed decision system, the IoWaDSS has two unique computational concepts: the single-page application and gamification implemented in collaborative watershed planning.

ACKNOWLEDEGMENT

The IoWaDSS has been built atop of a large dataset produced by a large interagency team coordinated by the USACE Flood Risk Management Program, Collaboration and Public Participation Center of Expertise, Asset Management Program, and ICIWaRM. Partners involved: U.S. Army Corps of Engineers Rock Island District, Portland District; Institute for Water Resources; Sandia National Laboratories; University of Iowa IIHR; the City of Cedar Rapids; the National Drought Mitigation Center at University of Nebraska-Lincoln; the Natural Resources Conservation Service; U.S. Geological Survey; the National Integrated Drought Information System; Iowa State University; and The Nature Conservancy. The authors are thankful for this large amount of collective work that made IoWaDSS development possible.

REFERENCES

Andrienko, G., Andrienko, N. & Jankowski, P. (2007). Geovisual Analytics for Spatial Decision Support. *International Journal of Geographical Information*, 21(8), 839-857.

Crossman, M.N., Futter, S.K., Oni, P.G., Whitehead, L., Jin, D., Butterfield, H.M., Baulch, P.J. & Dillon, J., (2013). Impacts of Climate change on Hydrology and Water Quality: Future Proofing Management Dtrategies in the Lake Simcoe Watershed, Canada. *Journal of Great Lakes Research,* 39(1),19-32.

Deterding, S., Dixon, D., Khaled, R. & Nacke, L. (2011). From Game Design Elements to Gamefulness: Defining "Gamification". *15th International Academic MindTrek Conference: Envisioning Future Media Environments*, 9-15.

Dibike, B.Y. & Paulin C. (2005). Hydrologic Impact of Climate Change in the Saguenay Watershed: Comparison of Downscaling Methods and Hydrologic Models. *Journal of Hydrology*, 307(1), 145-163.

IWR (2016). Institute for Water Resources (IWR), *USACE Rock Island District, National Drought Mitigation Center, Sandia National Laboratories, City of Cedar Rapids, and US Geological Survey (2016). "Playbook for the Cedar Rapids and Surrounding Area Multi-Hazard Tournament,"* Collaboration & Public Participation Center of Expertise, U.S. Army Corps of Engineers, Alexandria, VA, U.S.A.

Luo,Y., Darren, L., F., Liu, X.M. & Zhang, M.H. (2013). Assessment of Climate Change Impacts on Hydrology and Water Quality with a Watershed Modeling Approach. *Science of the Total Environment*, 450, 72-82.

Kappes, M.S., M. Keiler, K., Von, E. & T. Glade (2012). Challenges of Analyzing Multi-Hazard Risk: A Review, *Natural Hazards,* 64(2), 1925-1958.

Maidment,D. (2006). Hydrologic information system. *CUAHSI Workshop*. Austin, TX: Consortium of Universities for the Advancement of Hydrologic.

Muste, M., Smith, J., Demir, I. & Carson, A. (2017). "*Serious Gaming for Community Engagement in Multi-Hazard Mitigation" Hydrolink,* International Association of Hydro-Environment Engineering and Research, Madrid (IAHR), Spain.

Power, J.D. & Kaparthi, S. (2002). Building Web-Based Decision Support Systems. *Studies in Informatics and Control*, 11(4), 291-302.

Rice, R.J. & Boisvert, F.R. (1996). Environments, from Scientific Software Libraries to Problem-Solving. *IEEE Computational Science & Engineering*, 3(3), 44-53.

Watson,T.L. , Lohani, K.V. , Kibler, F.D. , Dymond, L.R. , Ramakrishnan, N. & Shaffer, C. (2002). Integrated Computing Environments for Watershed Management. *Journal of Computing Environments for Watershed Management*, 16(4), 259-268.

Zhang, Y., Sugumaran, R., McBroom, M., DeGroote, J., Kauten, R.L. & Barten P.K. (2011). Web-based Spatial Decision Support System and Watershed Management with a Case Study. *International Journal of Geosciences*, 2(3), 195-203.

Proceedings of the 37th IAHR World Congress
August 13 – 18, 2017, Kuala Lumpur, Malaysia

VERIFICATION OF HINDCASTING FOR HIGH WAVE AND STORM SURGE DUE TO EXPLOSIVE CYCLONE

TAKUTO HAGA[(1)], KATSUMI SEKI[(2)] & TARO ARIKAWA[(3)]

[(1,2,3)] Chuo University, Tokyo, Japan,
takuto-h@civil.chuo-u.ac.jp; seki-k@civil.chuo-u.ac.jp; arikawa@civil.chuo-u.ac.jp

ABSTRACT

In winter, duration and strength of explosive cyclones, whose development is rapid and strong winds with low pressure ranges are shown to be on an increasing trend in the last few years around Japan and they are becoming important factor affecting high wave and storm surge. Global Spectral Model (GSM) climate distribution data set by Japan Meteorological Agency (JMA) is applied to the wave and storm surge estimation around Hokkaido and Tohoku for explosive cyclone in January 2016. Wind and atmospheric pressure condition for the wave and storm surge estimation is obtained by two ways using GSM data set. One way is that GSM data set is interpolated linearly while another is Myers method based on the data set. Comparison between calculation and observation for the time variations of significant wave height and mean wave period and mean sea level departure from normal is conducted at observation points. The applicability of the data set to wave and storm surge estimation is verified. The main results are summarized as follows; 1) Maximum wind speed value by Myers method approximately matches the value of observation, but timing does not match. On the other hand, the fluctuation by liner interpolation is approximately equal to the observation fluctuation. 2) Significant wave height, mean wave period and mean sea level departure from normal of calculation by Myers method are underestimate as compared with observation values. 3) Significant wave height of calculation by linear interpolation is approximately equal to observation values, but the maximum values are a little underestimate. Mean wave period, mean sea level departure from normal and maximum them of calculation by linear interpolation are approximately equal to observation values.

Keywords: Storm surge; high waves; explosive cyclone; SWAN and STOC-ML; GSM winds.

1 INTRODUCTION

There are concerns regarding the risk of high waves and storm surge disasters due to global warming in recent years. Explosive cyclone in winter due to global warming causes high wave and storm surge around Japan. World Meteorological Organization (WMO) defines explosive cyclone as extratropical cyclone where the central pressure is required to decrease more than 24hPa×sin(φ)/sin(60°) at φ latitude in 24 hours. It causes strong wind and low atmospheric pressure over a wide range. In winter, duration and strength of explosive cyclones are shown to be on an increasing trend in the last few years around Japan (Saruwata et al., 2015). On the other hand, climate is an important factor of wave and storm surge estimation. Around Japan, Grid Point Value (GPV) climate distribution data set by Japan Meteorological Agency (JMA) is often used by the estimation. GPV data set includes several kinds of data sets which are divided based on analysis method. One of them, Meso Scale Model (MSM) climate distribution data set is the highest resolution and wave estimation by using highly precise without mesoscale numerical weather prediction system around Japan. (Nonaka et al., 2016) However, fetch and duration of wind are related to wave estimation, the estimation for explosive cyclones which reach peaks around Hokkaido and Tohoku needs range of climate data wider than MSM. Therefore, Global Spectral Model (GSM) climate distribution data set by Japan Meteorological Agency (JMA) where the range is wider and resolution is lower than MSM data set is applied to the wave and storm surge estimation around Hokkaido and Tohoku for explosive cyclone in January 2016 and comparison between calculation and observation by PARI (Port and Airport Research Institute) for the time variations of significant wave height, mean wave period and mean sea level departure from normal is conducted at observation points.

2 CONDITIONS OF OCEANOGRAPHIC AND ATMOSPHERIC PHENOMENA

2.1 Atmosphere phenomena

Explosive cyclone on January 2016 occurred in northern Taiwan and approached Japan while developing rapidly. When the cyclone passed over the Japan Alps, center of it divided to two centers. The lowest pressure was 974.1hPa off the Pacific coast of Hokkaido. Observation values of the maximum instantaneous wind speeds by Japan Meteorological Agency (JMA) were 45.1m/s at Erimo, 33.3m/s at Nemro in Hokkaido and 35.4m/s at Enoshima in Miyagi. Figure 1 is a weather chart made from GSM data set when the pressure was the lowest.

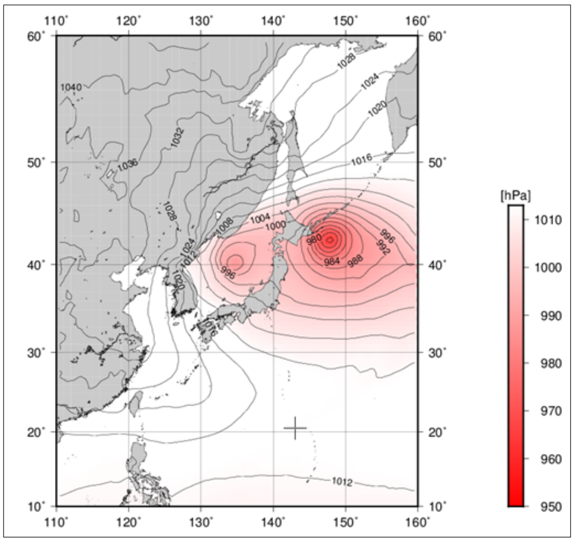

Figure 1. Weather map at 1/19/2016 15:00.

2.2 Oceanographic phenomena

The explosive cyclone caused high wave and storm surge off the Pacific coast of Hokkaido and Tohoku. Ports and harbors were damaged by wave overtopping. Observation values of the maximum significant wave heights by PARI (Port and Airport Research Institute) were 6.6m/s at Tokachi in Hokkaido, 9.4m/s at Kuzi in Aomori and 11.1m at off northern Iwate. The values of maximum mean sea level departure from normal were 0.67m at Nemuro, 0.45m at Muroran and 0.34m at Shiraoi in Hokkaido. Observation values for the time variations of maximu wave height and maximum wave period at Tomakomai are shown in Figure 2. The values of mean sea level departure from normal at Nemuro are shown in Figure 3.

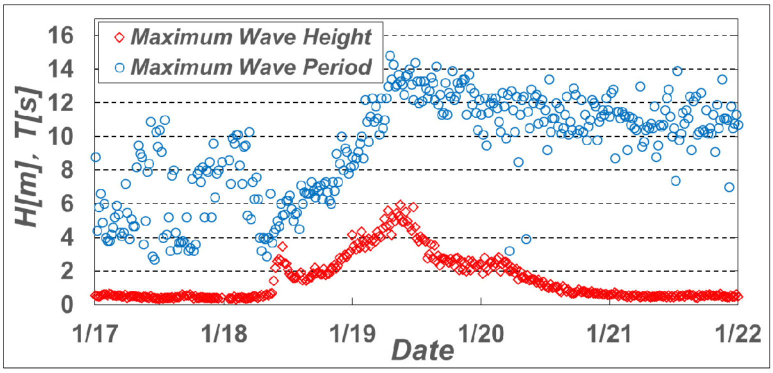

Figure 2. Observation values of maximum wave height and period at Tomakomai.

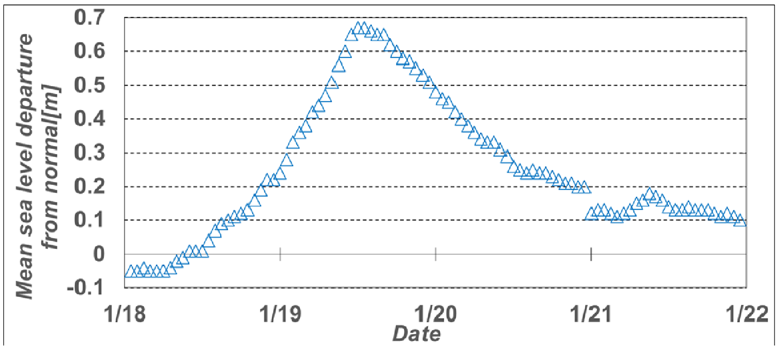

Figure 3. Observation values of mean sea level departure from normal at Nemuro.

3 NUMERICAL SIMULATOR

3.1 SWAN

Third-generation wave hindcasting model, Simulating Waves Nearshore (SWAN) which developed at the Delft University of Technology was used for wave estimation. It is the model for calculating wave propagation in time and space based on energy balance equation.

3.2 STOC-ML

A quasi-3-dimensional model, multi-layered static dynamics model (STOC-ML) which developed at PARI, was used for storm surge estimation. It is the model for calculating fluid dynamics that result from a tsunami by using hydrostatic approximation.

4 NUMERICAL CONDITION

4.1 Wind and atmospheric pressure Condition

GSM climate distribution data set by JMA was calculated by Global spectral model and applied objective analysis. About GSM data set and MSM data set are shown in Table 1 and Figure 4.

Table 1. Format of GSM and MSM data set.

Data set	GSM (Japan area)	MSM
Domain	10.0N-60N/110E-160.0E	22.4N-47.6N/120E-150E
Spatial Resolution	0.2°×0.25°	0.0625°×0.05°
Grid	251×201	481×505
Temporal Resolution	6hourly	3hourly (analysis) 1hourly (forecast)

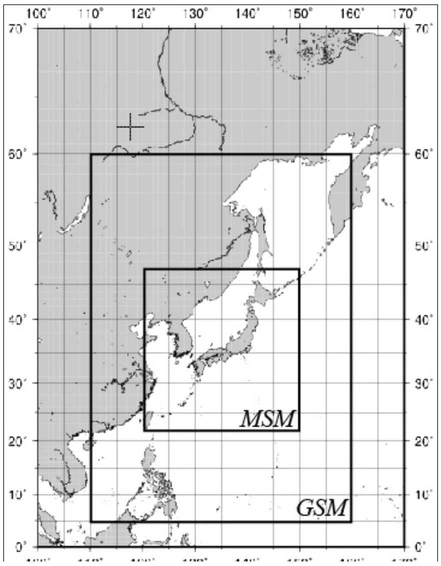

Figure 4. Domain of GSM and MSM data set.

Wind and atmospheric pressure condition for the wave and storm surge estimation is made by two ways. One way is that GSM data set is linearly interpolated while another is Myers method based on the data set.

The comparisons between observation and calculation for the time variations of mean wind speed, atmosphere pressure and wind direction at Shiraoi are shown in Figure 5. Maximum wind speed value by Myers method approximately matches the value of observation, but timing does not match. On the other hand, the value by linear interpolation is approximately equal to the observation speed. The explosive cyclone had two centers that the wind and atmospheric pressure condition by Myers method is poorly reproducible.

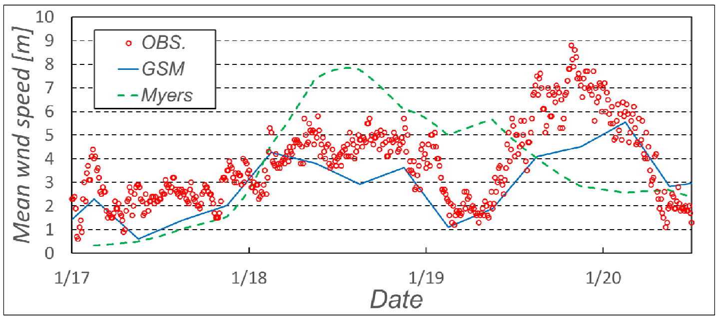

Figure 5. Observation and calculation values of mean wind speed, at Shiraoi.

4.2 Topography condition

Gridded bathymetry data by GEBCO (General Bathymetric Chart of the Ocean) is spatially interpolated linear to made topography condition.

4.3 Condition of wave estimation

Wave estimation is calculated by two step nested Domain. The calculation period is 2016/1/17 9:00 – 1/21 3:00. About conditions of the estimation are shown in Table 2. Domain of estimation and observation points are shown in Figure 6.

Table 2. Condition of wave estimation.

Domain	**1**	**2**	**3**	**4**
Lat./Lon.	135E-154E 32N-48N	138E-149E 36N-46N	139E-146E 40.5N-44.5N	140E-145E 37.5N-42.5N
Δx,Δy	6000m	2000m	1000m	1000m
Δt	360s	180s	60s	60s

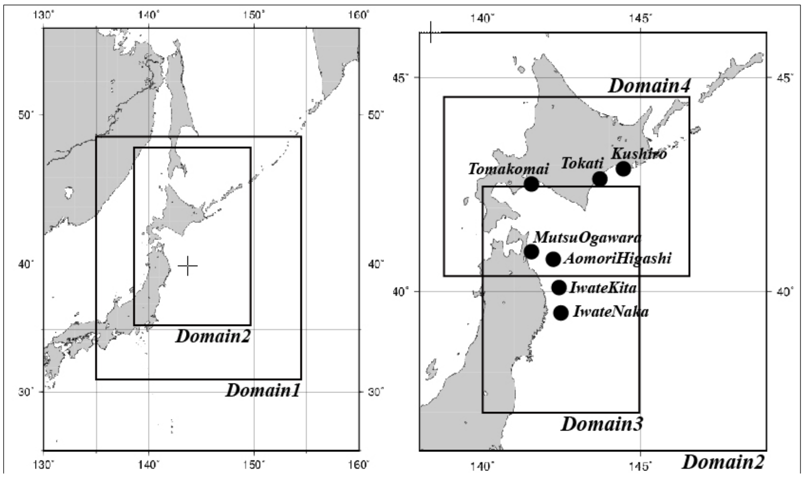

Figure 6. Domains of estimation and observation points.

4.4 Condition of storm surge estimation

Storm surge estimation is calculated one step nested Domain. The calculation period is 2016/1/17 9:00 – 1/21 3:00. About conditions of the estimation are shown in Table 3 Domain of estimation and observation points are shown in Figure 7.

Table 3. Condition of storm surge estimation.

Domain	**1**	**2**
Lat./Lon.	135.5E-151.5E 35.5N-47.5N	137E-147.5E 38N-45N
Δx,Δy	5000m	2000m
Δt	1s	1s

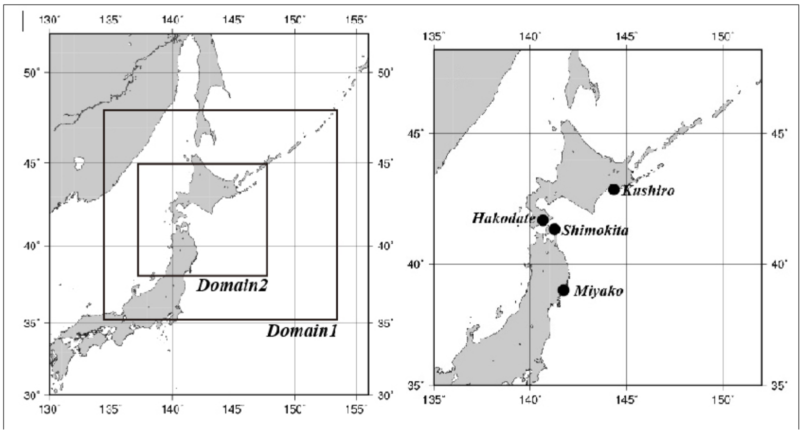

Figure 7. Domains of estimation and observation points.

5 RESULT

5.1 Verification of wave estimation

Comparison between calculation and observation for the time variations of significant wave height and mean wave period is conducted at observation points. The comparisons at Tomakomai are shown in Figure 8 and Figure 9.

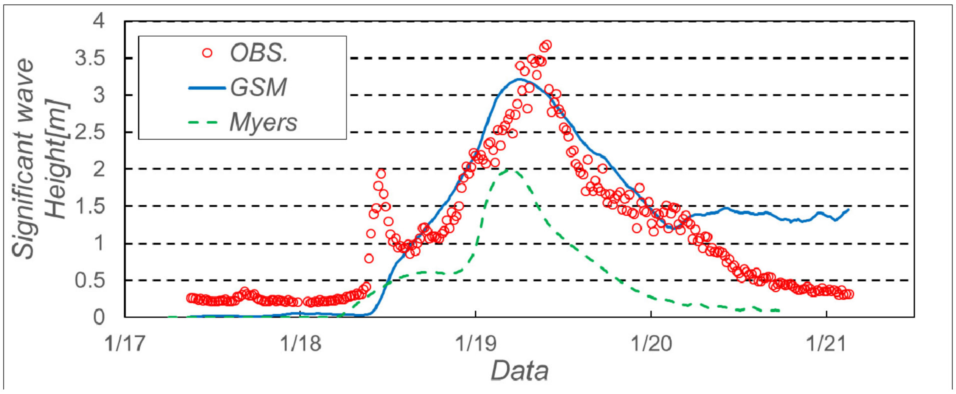

Figure 8. Calculation and observation of significant wave height at Tomakomai.

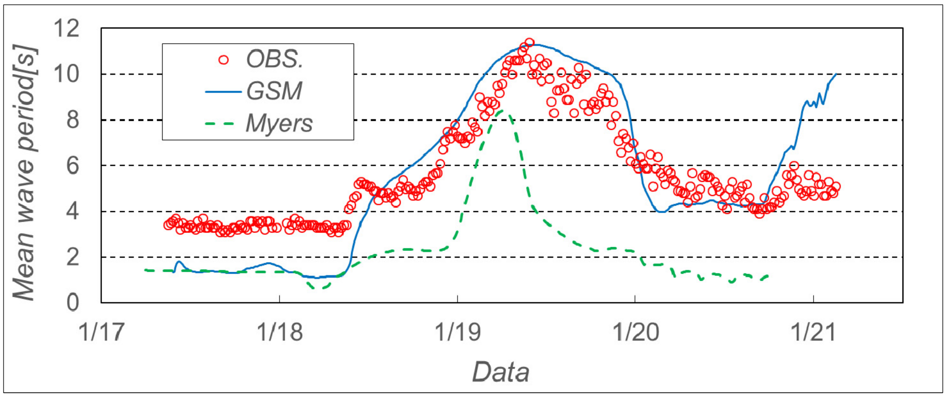

Figure 9. Calculation and observation of significant wave periodt at Tomakoma.

The fluctuation of calculation which use wind by linear interpolation approximately matches the fluctuation of observation, but the fluctuation of calculation which use wind by Myers method does not. Correlation of calculation and observation at 6 points are shown in Figure 10 and Figure 11. ρ is correlation coefficients. Correlation about maximum values are shown in Figure 12.

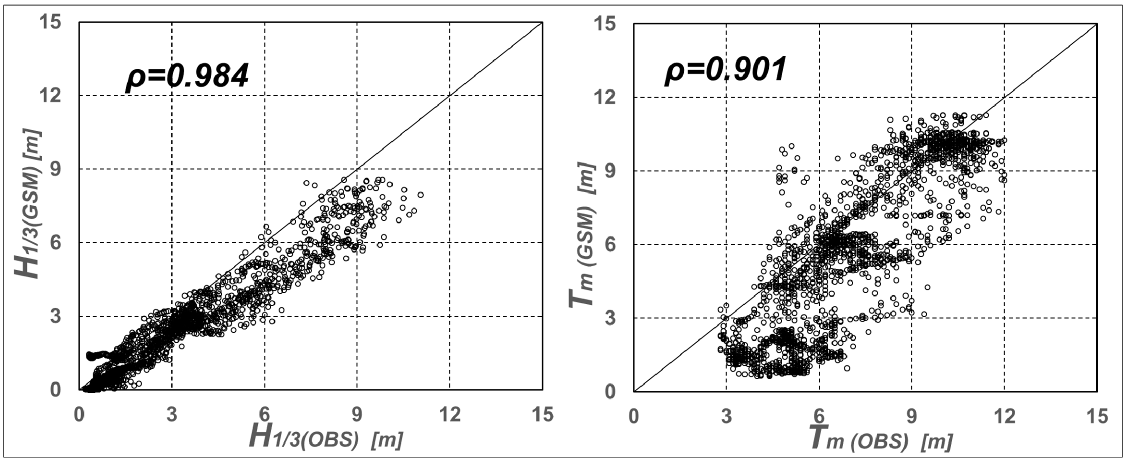

Figure 10. Correlation of calculation by linear interpolation and observation.

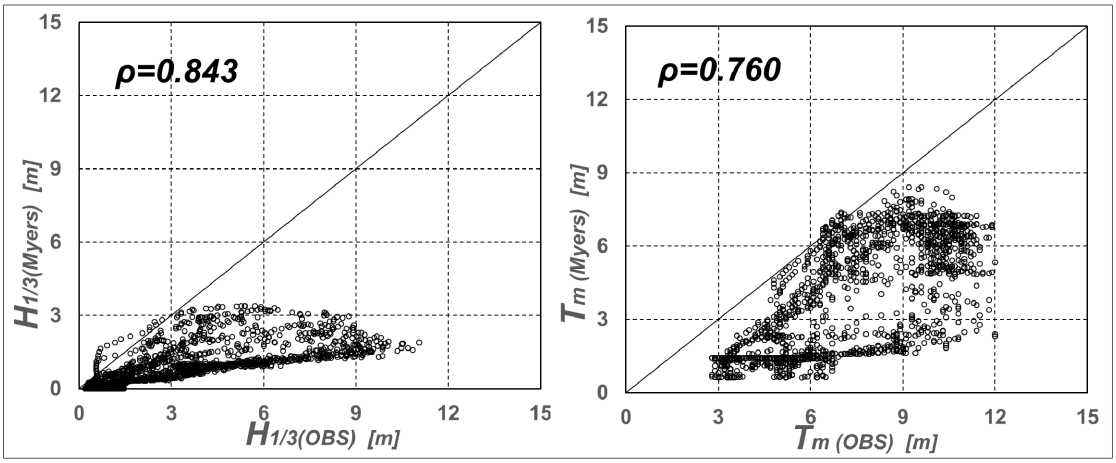

Figure 11. Correlation of calculation by Myers method and observation.

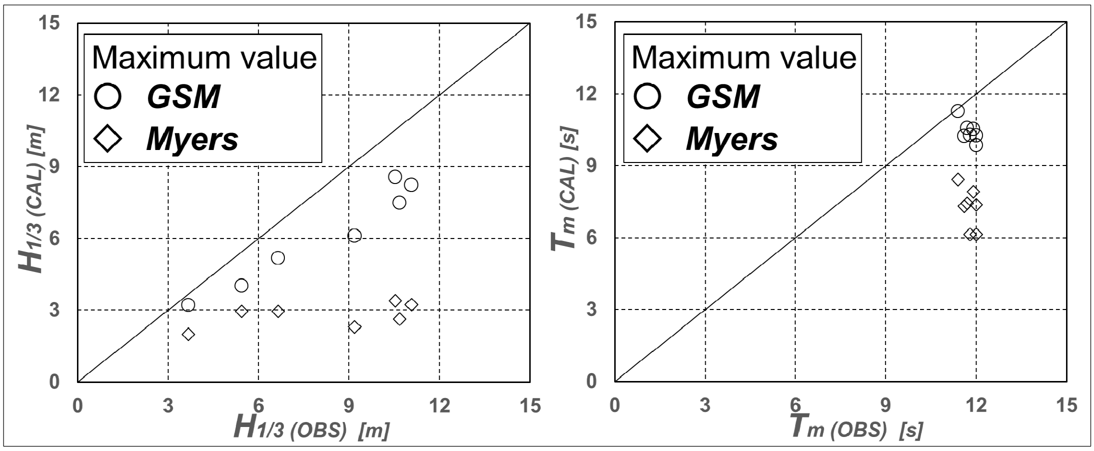

Figure 12. Correlation about maximum value of calculation and observation.

Wave values of calculation by Myers method are underestimated, and wave values of calculation by linear interpolation approximately equal to the value of observation. Maximum significant wave heights of calculation are a little underestimate and maximum mean wave periods approximately match.

5.2 Verification of storm surge estimation

Comparison between calculation and observation for the time variations of mean sea level departure from normal is conducted at observation points. The comparisons at Tomakomai are shown in Figure 13.

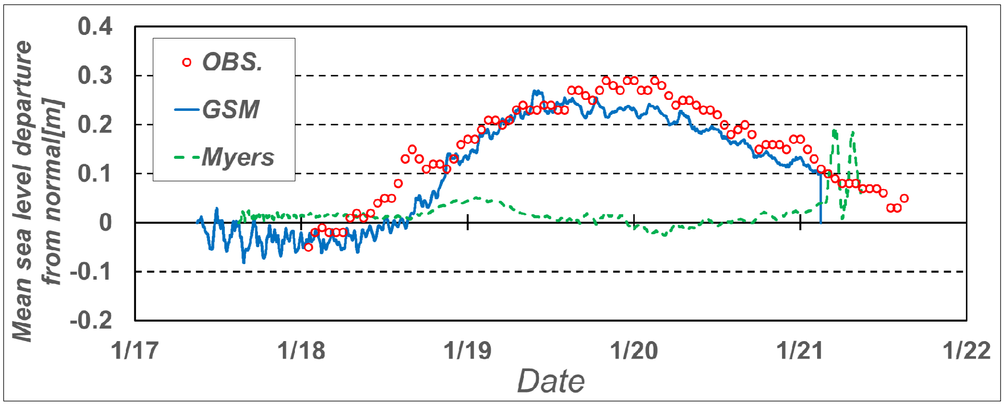

Figure 13. Calculation and observation of mean sea level departure from normal at Shimokita.

The fluctuation of calculation which use atmosphere pressure by linear interpolation approximately matches the fluctuation of observation, but the fluctuation of calculation which use wind by Myers method does not. Correlation of calculation and observation at 4 points are shown in Figure 14 and Figure 15. ρ is correlation coefficients. Correlation about maximum values are shown in Figure 16.

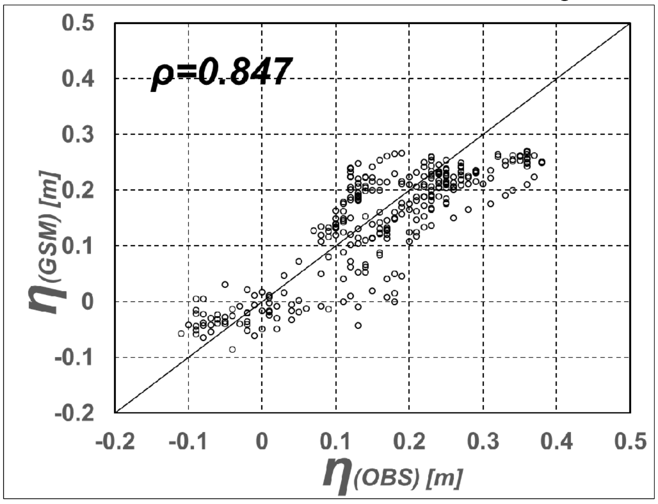

Figure 14. Correlation of calculation by linear interpolation and observation.

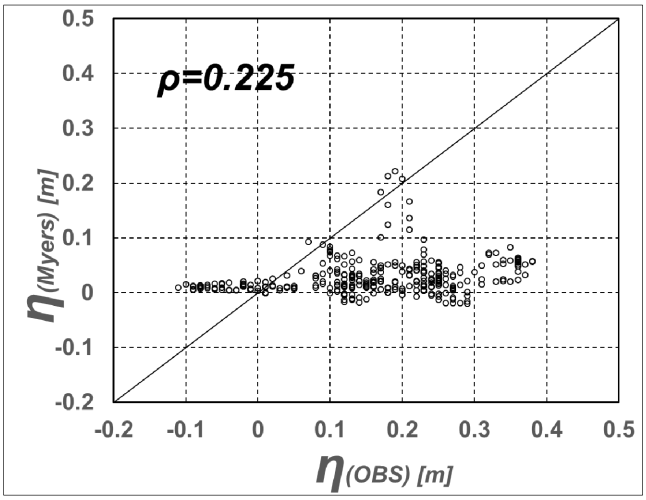

Figure 15. Correlation of calculation by linear interpolation and observation.

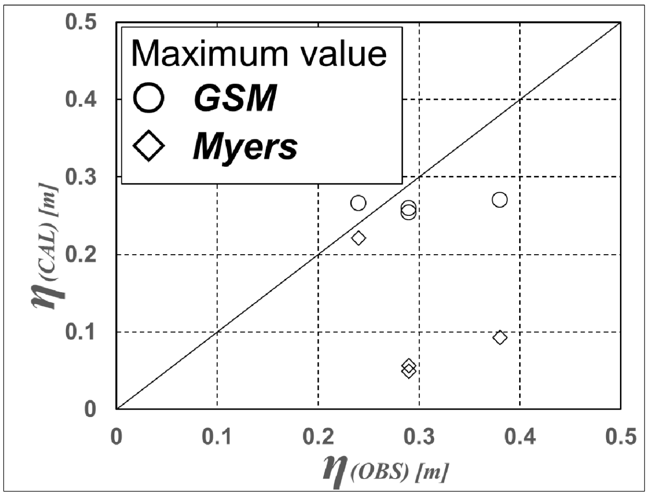

Figure 16. Correlation about maximum value of calculation and observation.

Value of calculation by Myers method are underestimate, and wave values of calculation by linear interpolation are approximately equal to the value of observation. Maximum values of calculation approximately match.

6 CONCLUSIONS

High wave and storm surge which is caused by explosive cyclone development, is rapid with strong wind and low pressure ranges is estimated by GSM data set as numerical condition. The applicability of the data set to wave and storm surge estimation is verified. The main results are summarized as follows:

(a) Maximum wind speed value by Myers method approximately matches the value of observation, but timing does not match. On the other hand, the fluctuation by liner interpolation is approximately equal to the observation fluctuation;

(b) Significant wave height, mean wave period and mean sea level departure from normal of calculation by Myers method are underestimated as compared with observation values;

(c) Significant wave height of calculation by linear interpolation is approximately equal to observation values, but the maximum values are a little underestimated. Mean wave period, mean sea level departure from normal and maximum them of calculation by linear interpolation are approximately equal to observation values.

ACKNOWLEDGEMENTS

The research reported herein is provided waves data set by Port and Airport Research Institute (PARI), sea levels data set by Japan Meteorological Agency (JMA) and winds data set by JMA. The authors would like to thank.

REFERENCES

Nonaka, H., Yamaguchi, M., Inouchi, K., Hino, M. & Hatada, Y. (2015). Verification of Applicability of JMA-MSM-Based Winds and SWAN-Based Wave Hindcasting System to the Japan Sea [in Japanese]. *Proceedings of coastal engineering, JSCE,* 71(2), 109-114.

Nonaka, H., Yamaguchi, M., Inouchi, K., Utsunomiya, Y., Hino, M. & Hatada, Y. (2016). Verification Tests of MSM Winds/SWAN-Based Wave Hindcasting System Using Measurement Wave Records by GPS Buoys Deployed Along Offshore Areas of the Japanese Pacific Coasts [in Japanese]. *Proceedings of coastal engineering, JSCE,* 72(2), 151-156.

Ris, R.C., Booij, N. & Holthuijsen, L.H. (1999). A Third-Generation Wave Model for Coastal Regions: Part II, Verification, *J. Geophys. Res*., 104(C4), 7667-7681.

Saruwatari, A. & Watanabe, Y. (2015). Mechanisms to Develop High Waves Induced by an Explosive Cyclogenesis Over the Japan Sea [in Japanese]. *Proceedings of coastal engineering, JSCE,* 71(2), 1537-1542.

Takashi, T. & Taro, K. (2005). Development of Numerical Simulator STOC for Storm Surge and Tsunami Considering Three Dimensionality of Seawater Flow and Application to Tsunami Analysis [in Japanese]. *Report of the Port and Airport Research Institute, PARI,* 44(2), 83-98, 2005-06.

EXPERT SYSTEM FOR CALIBRATION OF WATER SUPPLY NETWORK SIMULATION MODEL

TOMASZ BOCZAR(1), DARIUSZ ZMARZLY(2) & PAWEL FRACZ(3)

(1,2,3)Faculty of Electrical Engineering Automatic Control and Informatics, Opole University of Technology, Proszkowska 76, 45-011 Opole, Poland
t.boczar@po.opole.pl; d.zmarzly@po.opole.pl;p.fracz@po.opole.pl

ABSTRACT

The subject matter of this research work considers improvement of the leakage detection and localization in water supply networks. The proposed method involves an application of a simulation model, which in order to be applied successfully implemented has to be carefully calibrated. For the calibration process, an expert system was designed and implemented. The mentioned expert system and applied algorithms are presented in the paper. Furthermore, the paper presents the characteristics of the studied object, which is waterworks of the city Kedzierzyn-Kozle, Poland.

Keywords: Water Supply Network; modeling; simulation; calibration; genetic algorithm.

1 INTRODUCTION

Water supply networks (WSN) are one of the basic components of the technical infrastructure of towns and settlements. The necessitate to reduce the operational costs, especially due to loss of water, causes a continuous need to develop new methods for supporting monitoring and diagnosing of these objects. The most common damage of water supply infrastructures, beyond the extensions and strictures in pipes, the sludge causing changes of surface roughness, etc., is the occurrence of cracks that cause water leaks. Unfortunately, only part of the water outflow is manifested on the surface of the ground, the other part is invisible and difficult to locate. The problem arises in areas of those cities, where as a result of conducted exploitation of coal and calcium, which are located under the city. The occurrence of failure is more common and will be felt for a long time after the cessation of mining.

The well-known method for diagnosis of the WSN state is a phone accepting failure notification observed and reported by people (customers). On the emergency call the water supply is the only source of information about the so-called reported leaks. The leaks reported are part of all leaks, but there exist also leaks unreported, which are difficult to detect and which can, in the long term, cause much more damage. Despite the duty hours on the emergency all, the water supply is the method of diagnosis, used as primary source of knowledge about the state of the network. Frequently, in the cases of leakage, a leak location service is outsourced to an external company, which is provided with necessary equipment enabling diagnosis of auscultation and poses knowledge and skills of its application. But this service is payable in each case, thus in the event of minor leaks, it should be considered if the service cost is not higher than the possible losses resulting from WSN failure.

In the current exploitation of WSN, numerous solutions for the diagnosis are applied, with particular emphasis on the detection and location of leaks. The first group of solutions existing on the market is combination of network monitoring and expertise. In this embodiment, a well-designed measurement systems registers data are then presented in a SCADA (*Supervisory Control and Data Acquisition)* system (Piechurski, 2013; Urbaniak, 2007). An expert (employees) observes the network parameters and finds anomalies. Another group of solutions to diagnose the state of the WSN is the auscultation diagnostics. It is currently the most popular and most widely used solution, involving the location of leakage in the ground by finding anomalies in the sound waves accompanying the flow of water. Acoustic zonal loggers are applied in addition to the functionality of diagnostic auscultation equipment. Positioned in the most strategic parts of the network, they archive the emergency information based on the acoustic noise and allow further data analysis in a wider time window. The service of radio loggers is much more comfortable than of portable auscultation, because reading can be done remotely. Pressure loggers archive the momentary pressure value at predetermined time intervals. Representation of knowledge about the state of the network based only on the pressure, however, is very difficult to translate into knowledge about the state of installation, because a momentary pressure value depends on many factors that are not included in the record. Only after verification of this knowledge by an expert, it can be determined whether the measured pressure values are consistent with expectations, or evidence of failure. The last group addresses solutions which are most complex and technologically advanced and are based on simulation models of WSN. In this group is embodied implementation of a simulation model (through digitization or by GIS skeleton migration), and then fine tuning (calibration) of the model parameters.

It is possible to simulate the current day using incomplete data (prediction), as well as detection of the existence of leaks by the Night Minimum Flow (MNP), and in some systems by the Integrated Flow Measurement methods.

The existing methods for failure location in the WSN, which utilize listening devices, are less effective when PVC (polyvinyl chloride) and PE (polyethylene) pipes are included in the network infrastructure. Therefore, modern industry requires development of improved tools and mechanisms for signaling the appearance and location of the failure. The basic principles of the understanding, monitoring and control of leakages are renowned within the water industry and have not changed significantly in recent years. There is, however, the opportunity to introduce additional innovations in the strategy of reducing leaks and leak detection technology, supporting faster and more accurate decisions about leaks and leakages in the water supply infrastructure. These technologies have a major impact on the improvement of network performance and further reduction of water leakage, thereby on minimizing financial losses for both the suppliers and the recipients (Pieczyński et al., 2007).

Simulation models of water supply systems are nowadays commonly used by network operators (Schmid, 2001; Ulanicki et al., 1996; Jia et al., 2008). An important application of OFF-LINE WSN simulation models is the ability to analyze the effects of network expansion, connecting new clients (e.g. When determining the conditions for new investments), etc. In such cases, the calibration of the network model can be performed off-line in the cycle e.g. monthly or seasonal. The main limitation of OFF-LINE methods is the approximation of the unknown parameters of the water supply system using historical data. The calibration results may represent the state of the system in a short time and are not able to accurately represent the system state for a long period of time, due to the lack of stationarity of the water supply system. For water supplies the water demand can vary over a wide range, for economic reasons, demographic climate random events, and the like. It should be noted that the determination of flow in the water network comprising of thousands of nodes and sections of pipes of different sizes, and tens of thousands of recipients of water, based on a limited set of measurement data (several dozen) is impossible from the formal point of view (mathematical), due to the ill-conditioned/ill-posed problem. Determination of the network status in real time, with a certain time step allows the determination of the current water flows in the individual pipe sections and the pressure in the nodes of the network, which in turn allows carrying out diagnosis of leakages in the network. Network conditions are changing from hour to hour, as well as in a daily cycle, weekly and seasonal.

A diagnostic system working ON-LINE allows one to track current changes in the network. Due to the necessity to collect measurement data and to perform a set of complex calculations, cycle diagnostic system cannot be shorter than 15 minutes. However, the need to perform additional series of operations related to the diagnosis of leakage in the water supply system entails the necessity of lengthening the duty cycle of diagnostic system to about 1 hr. The computing power of today's PCs (4-core processor, RAM 4 GB) enables for to realize this task.

The authors’ research area considers development of a leakage signaling tool applied for WSN which is based on computer simulation. One of the main parts is a well-designed and carefully calibrated simulation model. In further chapters the object under study, the measurement system and the modeling and calibration procedure, which are performed by a specially designed expert system, are presented.

2 THE OBJECT UNDER STUDY

The object under study is a WSN of the city Kedzierzyn-Kozle (WSNKK), which includes the following elements:

- Two pumping stations: water treatment plant (WTP) and water treatment station (WTS);
- Two zonal pumping stations located in the towns: Slawiecice and Cisowa;
- Transmission pipelines with valves;
- Junction valves;
- The water recipients.

2.1 The WSN characteristics

The distributed system of pipelines, supplying water from the pumping station to the recipients, consists of buses and the backbone network, with a total length of about 153 km, and of junction valves of total length of about 74 km. The pipelines are mainly made from iron and PVC. Connections on the other hand are mostly galvanized steel or PE pipes. In recent years, more and more products are made from PE and all new connections, as well as the majority of the network is built using PEHD (high density polyethylene). The largest diameter of the pipe is 500 mm and the average diameter of buses is 200 mm, while the average diameter of the pipes is 100 mm. The total length of the pipe sections with diameters greater than 50 mm is more than 155 km.

The area covered by the network is in shape of a rectangle with dimensions of 6392 x 12322 m (excluding wholesale customers in the neighboring communities). The city has an area of 123.4 km^2 where about 64000 residents live. The city is situated in lowland, but there exists a difference of over 30 m in the levels within the network.

2.2 The pumping systems

The WTP pumping station serves as the main water supply system of the city Kedzierzyn-Kozle. It consists of six centrifugal pumps of type PJM that are powered by engines with a capacity of 3 x 45 kW and 3 x 75 kW, connected in a parallel arrangement. The overriding control system for WTP is a SCADA system, which has the additional function of data recorder. In Figure 1, example time courses of pressure *P* (Figure 1 left) and flow rate *Q* (Figure 1 right) measured in the WTP pump are depicted. The flow in the WTP reaches 400 m^3/h; the annual production of water reaches nearly 2 million m^3.

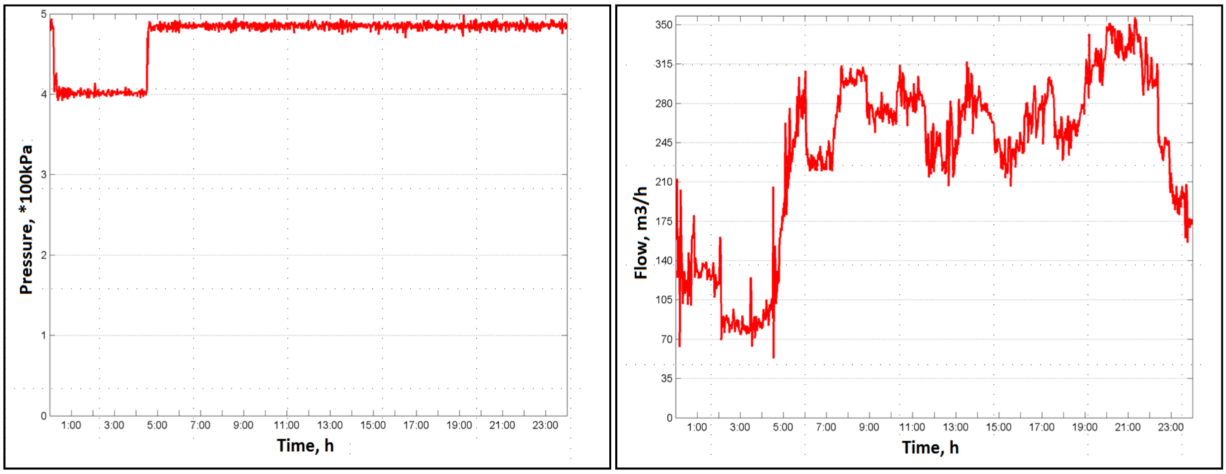

Figure 1. Example daily courses of pressure *P* (left) and flow rate *Q* (right) measured in the WTP.

In addition, the WSN is supplied with water from the WTS. It is made up of the five pumps powered by engines with a power of 5.5 kW. The pressure setting during the day is 475 kPa, while at night the pressure is lowered to 400 kPa. At night the WTS is completely switched off. The flow here reaches 300 m^3/h and the annual production reaches a size of nearly 1 million m^3 of water.

Apart from the mentioned WTS and WTP pumping systems, intermediate (zonal) pumping stations and hydrophores also operate in the system. The hydrophore pumps provide local solutions and may be defined in the simulation model as specific wholesale recipients; but the intermediate pumping stations are an important element of the network. For both of the zonal pumping stations, the pressure setting is 350 kPa; the flow reaches 35 and 45 m^3/h and the annual production exceeds 70 000 and 100 000 m^3 of water.

All registered measuring signals of flow and pressures in each of the four pumping stations (WTP, WTS, Cisowa, Sławiecice) are transferred via GPRS to a computer station located in the central control room in the WTP.

2.3 The measurements and data acquisition system

In order to obtain, during normal operation of the water supply system, a large number of measurement data, a distributed measurement system was designed and implemented. A PMS (Pressure Measurement System) is responsible for measuring and acquisition of analog signals, power failure control, and battery voltage control. The measured data is sent via the GSM network using GPRS data packets. The main element of the PMS is a microprocessor module - ePMS (economical PMS).

The main element of the data acquisition system is a server cooperating with a MySQL database, web server, providing data in the Internet, and with the diagnostic system. The server collects measurement data from the pumping stations and PMS devices.

3 MODELING AND CALIBRATION PROCEDURES

3.1 Computer model of the WSN

The WSN is a multi-node and multi-eyelet system, involving thousands of nodes that may be described by a system of nonlinear algebraic equations. The network model consists of the following: water sources, feed pumps, pumping stations and transmission pipelines of a specific topology and the water recipients, who determine a time-varying demand for water. Most of the parameters characterizing the WSN are strictly defined from the follwing: the network topology, length and diameter of pipes, water pressure in the supply stations, nodes, junctions, etc. In contrast, the water demand is the subject to stochastic daily, weekly, and seasonal fluctuations.

Epanet system is a widely used software package, developed by the US Environmental Protection Agency on behalf of the American Government. The software is made available under public domain license (USEP, 2013). Epanet al.ows to edit the parameters of the WSN and provides tools for solution of the algebraic equations systems. In addition, Epanet contains tools to calibrate the network model. The main advantage of Epanet, which is applied in the here presented expert system, is a library for using the available functions remotely, by e.g. MATLAB. The WSN simulation model must be subjected to tuning operation (calibration) using empirical data, obtained during measurements. Calibration is performed based on historical data, assuming that it has been recorded during a period when there were no leaks in the network. It is possible to calibrate three groups of parameters for all the pipes and the nodes:

- Roughness of a pipeline (link);
- Water losses in the various nodes, based on the natural leakage;
- Water demand in various nodes.

The roughness of a link depends significantly on the material from which it is made (cast iron, PVC), lifetime of the pipeline and the degree of water hardness. The roughness significantly affects the pressure drops in the individual sections of pipelines. It cannot be measured and further as it undergoes changes slowly in time. The numerical size of roughness is determined strictly, by defining the film thickness in mm, or relatively, by referencing the layer thickness to the diameter of the pipeline. As an example, for pipes made of PVC, the initial absolute value of roughness is assumed at approx. 0.02 mm, while by cast iron pipes it is approx. 2 mm.

Water losses in the individual network nodes take a small value. This parameter allows to fine-tune the flow in the individual sections of the network. In the first step of the model calibration, the same course of daily water demand $pattern_t$ is assumed for all nodes. In the second step, the calibration should take into account the different courses of $pattern_t$ in the individual network nodes due to the different nature of the water recipients (multi-family buildings, houses, offices, industrial plants, service companies, etc.). Generally, the method of network calibration can be grouped into three categories (Clark et al., 2006):
Iterative methods (trial and error)

- Iterative methods (trial and error);
- Direct methods (hydraulic models simulation);
- Optimization methods.

In each step of iterative algorithm parameters are determined and modified on the basis of the solution of the balance equations describing the water supply system. Iterative methods are characterized by a slow convergence and can be used for a small number of parameters tuned. Hydraulic models simulation methods are based on the solution of the balance equations describing the water supply system. The system of nonlinear equations is solved using an iterative method of Newton-Raphson. The number of determined parameters is limited to the number of available measurements. In the case of undetermined problem the calibrated parameters must be grouped. In this method measurement errors are not taken into account and it is impossible to determine the uncertainty of the designated parameters. Optimization methods combine the methods of hydraulic simulation with methods of determination of the extreme of functions of several variables. The algorithm for evaluation of the unknown parameters of the studies WSN is shown in Figure 2.

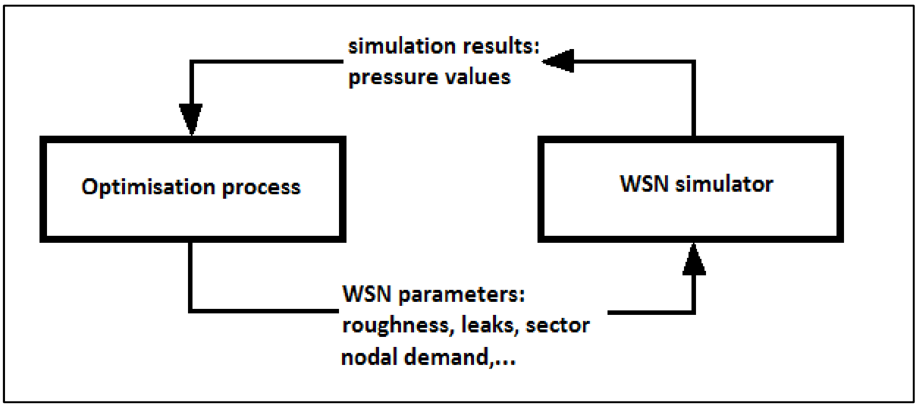

Figure 2. General state chart of the optimization algorithm applied for the WSN model parameters calibration.

The searching process, from the point of view of a particular criterion, which is the measure of the difference between the empirical and theoretical values, modifies the parameters and then passes them to the WSN simulation model, which in turn transfers it to the optimization process, which seeks the extreme of objective function (*OF*), Eq [1].

$$OF = \sum_{i=1}^{n} \|P_i - \bar{P}_i\| \qquad [1]$$

where, *n* - no of pressure measurement points P_i, $\bar{P}_i$ - the estimated (theoretical) pressure value.

For determining the minimum value of the objective function a whole range of gradient and non-gradient methods is applied (Savic et al., 2009). Due to the fact that the problem of parameters tuning is often characterized by a much larger number of unknown parameters rather than the number of measurement data, there exist no unique solution of the optimization task (Clark et al., 2006). The objective function is characterized by many local minima and determining the global minimum is practically impossible. The problem of tuning parameters of the water supply network is a non-convex problem (Clark et al., 2006), which means that there is no clear solution of a search for the minimum of the objective function. Currently, in order to determine the global minimum of the objective function, stochastic search algorithms are used, of which the main role is played by the evolutionary algorithms (Savic et al., 2009).

The evolutionary methodologies have a number of advantages over the other methods:

- Calibration using a genetic algorithm is conceptually very simple and does not require complex mathematical apparatus;
- Size of the problem to be solved can be very large;
- Easy to take into account a number of constraints for the searched parameter values;
- Can be applied for parallel computing by large problem sizes.

The evolutionary methodologies are also characterized by a number of drawbacks, which include:

- Genetic algorithms do not provide determination of the global optimum, and by each time the algorithm will start, from the principle of the appointment, a slightly different solution will be found;
- Running of a genetic algorithm requires a precise set a number of parameters individually for each task;
- Genetic algorithms are more efficient than traditional gradient algorithms.

Optimization methods for WSN parameters determination have been developed (Clark et al., 2006; Prais et al., 2011). Nevertheless, it can be stated that there are lack of works on specific practical applications and solutions.

3.2 Reduction of model complexity

For the WSNKK simulation model, which is implemented in the Epanet environment and containing more than 1000 nodes and a similar number of sections of the pipelines, it is impossible to calibrate all the network parameters with reasonable time. It becomes necessary to reduce the computational complexity of calibration tasks. There exist a number of methods to reduce the complexity WSN models, whose aim is to obtain a hydraulic model with a smaller number of elements than the original model. The reduced model must have the non-linear properties similar to the original model and be approximated well fitted to the original model.
Methods of reducing the complexity of WSN models can be divided into three groups (Perelman et al., 2013):

- Method creating a backbone network model;
- Methods for the elimination of variables;
- Grouping of network elements (clustering).

The backbone of water supply system includes only those components that are the most important for the network properties. The backbone enables replacement of several pipelines connected in parallel or serial with one link. For example, Saldarriaga et al. (2008) stated that under normal operating conditions, a number of the pipes can be removed from the model without any significant influence on the pressure values determined. In Figure 3, the WSN backbone (skeleton) implemented in Epanet is depicted.

Reduction methods involving the elimination of variables are based on mathematical formalism. The mathematical model of WSN is a set of nonlinear algebraic equations. Through several algebraic operations, some data can be eliminated from the model and thereby less complexity can be provided. In the WSNKK ten clusters (sectors) were extracted (see Figure 4) based on the following criteria:

- Separation of neighborhoods in the city, characterized by different nature of recipients (multi-family housing, single-family housing, offices and offices, industrial plants, buildings, rural, etc.). Due to the different nature of the water recipients, various sectors have a different course of daily water demand.
- Separation of relatively distinct parts in the WSN, where the specific sectors are connected only by the bus transmission pipes.

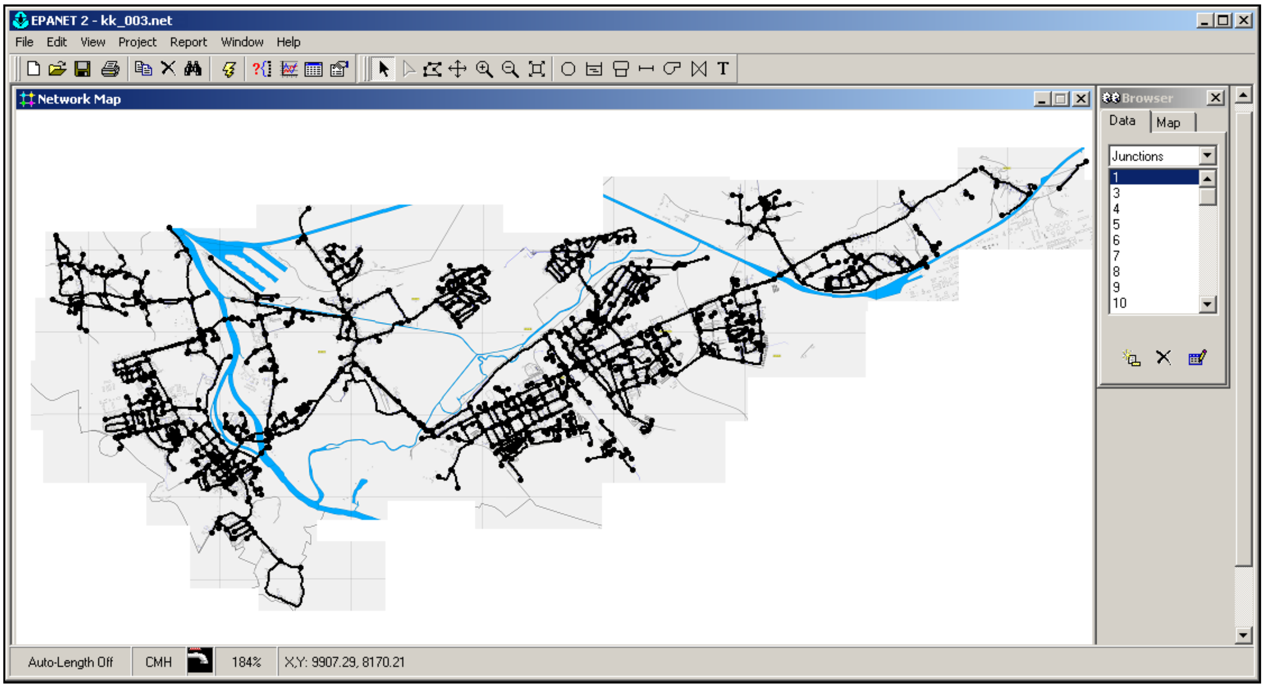

Figure 3. WSN skeleton created using the Epanet software (screenshot).

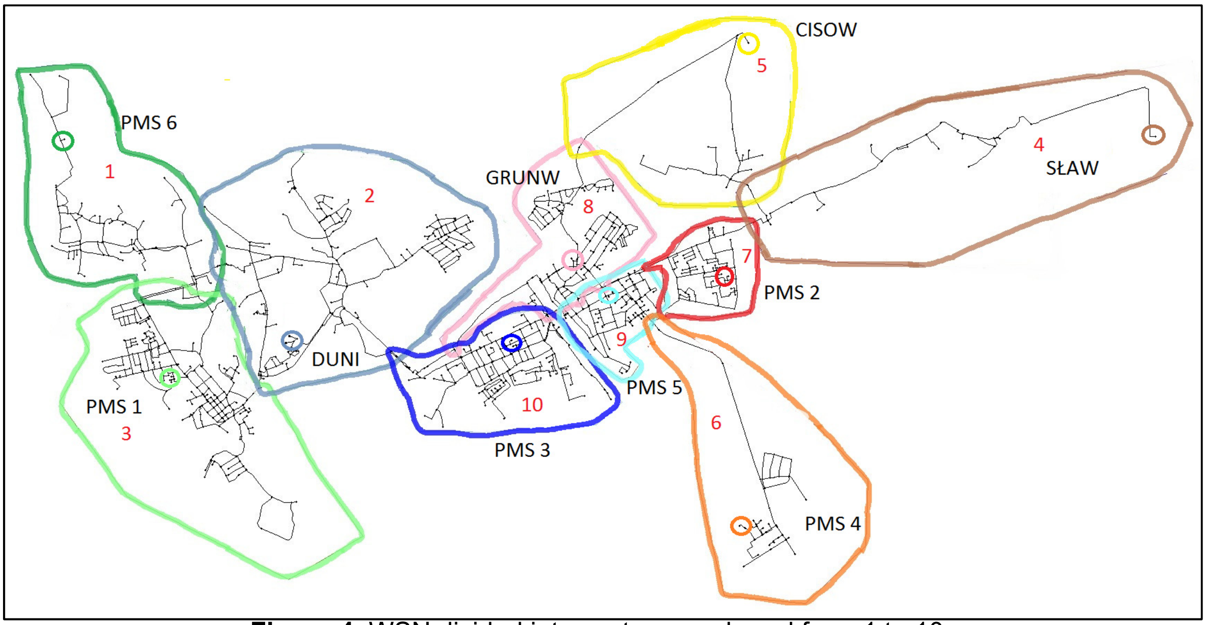

Figure 4. WSN divided into sectors numbered from 1 to 10.

The course of momentary demand for water in the *k*-sector in the network describes the parameter SND^k- Sector Nodal Demand. This parameter is analogous to the parameter *pattern*$_t$, however, it has an equal value for all nodes with the same sector. The current water demand in the *i*-node is given by Eq. [2].

$$AD_t^i = BD^i * SND_t^k \qquad [2]$$

where, AD_t^i - water demand in *i*-th node located in the sector k, BD^i-base demand in the *i*-th node, SND_t^k - the sector nodal demand in the k-th sector, *t*-hour.

Currently there is a whole range of implementations of evolutionary strategies to solve complex optimization tasks. In this study, two methods were applied:

- Evolutionary algorithm implemented in the Epanet ver. 2.0;
- Evolutionary strategies implemented in MATLAB.

  / ISSN 1562-6865 (Online) - ISSN 1063-7710 (Print)

Implementation of GA (Genetic Algorithm) in the Epanet software does not allow for a selection of all optimization parameters thus the results obtained are often unsatisfactory. These disadvantages are not present in the MATLAB. Due to the possibility of a detailed selection of any parameter of the GA algorithm, the gathered optimization results are much more favorable. Communication between MATLAB and Epanet is possible when using the epanet2.dll library.

The designed tool is applied for estimation of the optimal values of parameters: *roughness*^{k} and SND_t^k, by using the GA available in MATLAB. The operation was performed in two steps. First, rhe *roughness*^{k} was tuned, assuming that the values of SND_t^k are the same for all sectors of the network. The following parameters of GA were defined: the number of variables to search for: 10, population size: 50, fitness limit: 10^{-6}, start values: random, the search range: 10^{-4} - 60, stochastic uniform selection, Ladder scaling, Gauss mutation, scattered crossing, migration: forward direction every 20 generations, and 20% of the population. In Figure 5, example of the results of the one-day course calibration procedure of pressure, showing the before and after states for chosen pipe, are presented.

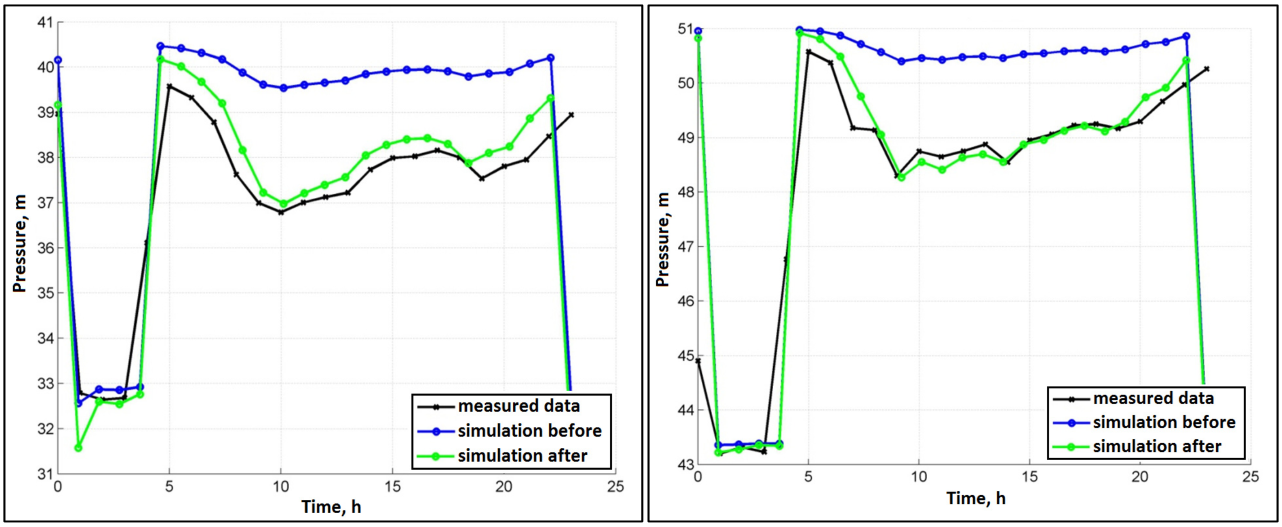

Figure 5 Example result of the calibration procedure, showing the before and after state for chosen pipe.

The pressure values in Figure 5, which were given prior in the model (before simulation), are marked in blue, the measured (empirical) pressure values are shown in black, and the calculated values (after *roughnees*^{k} calibration) are marked with green. The mentioned calibration procedure of the *roughness*^{k} parameters was performed for all nodes within the 10 defined sectors on the basis of empirical data obtained during 100 measurement days in the WSNKK network. In Figure 6, the calibration results are shown in blue while the mean values are depicted in red.

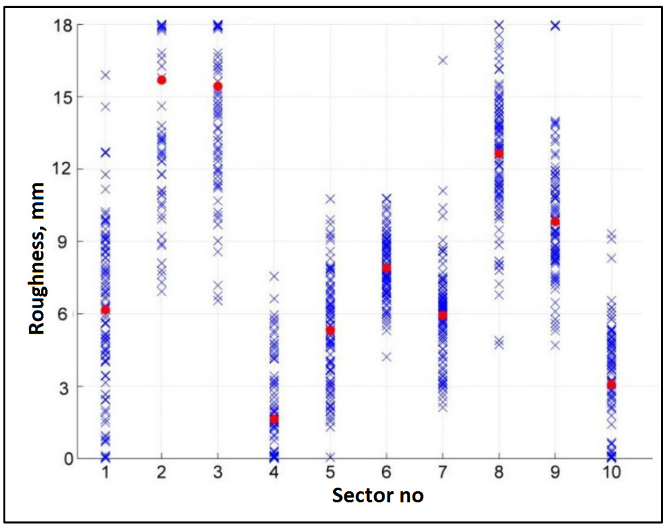

Figure 6 The estimated values of the roughness parameter for 100 selected measurement days.

4 THE STRUCTURE OF THE EXPERT SYSTEM

The main elements of the system are:

- User interface;
- WSN knowledge base;
- Inference engine;
- Explaining module.

The *user interface* is implemented in the editor of Epanet. It enables WSN and automatic control (AC) experts for the introduction of the specialized knowledge considering the backbone of water supply network, i.e. the number and localization of nodes (junctions), parameters of pipes, pumps, valves, reservoirs, and information concerning the rules used to control the value of the network pressure.

The *WSN knowledge base* includes rules and physical models, which are used by the *calculation module* to determine the value of the objective function, Eq. [1]. Within the *knowledge base* contained are the following: the skeleton of the WSN with rules for controlling the pressure at each node; information on sector nodal demand (*SND*), which is gathered from the real object in form of measurement data; and result from the inference engine, i.e. the *roughness*^{k} of pipelines in the *k* sectors of the WSN. In addition, the *knowledge base* contains information about eventual leakages *C*, which in further procedures, are detected and localized (the leakages detection and localization procedures are beyond the scope of this paper).

The *inference engine* is based on the calculations made using the GA, which takes into account: (1) the reference values gathered as measurement data from a server installed in the real object, and (2) the values calculated in the simulation model. The inference engine determines in an optimization process the value of roughness parameter, which corresponds to roughness of pipes in particular sectors in the WSN. The result of inference is stored in the form of a report and is transferred to the *explaining module*, which is then presented to the user.

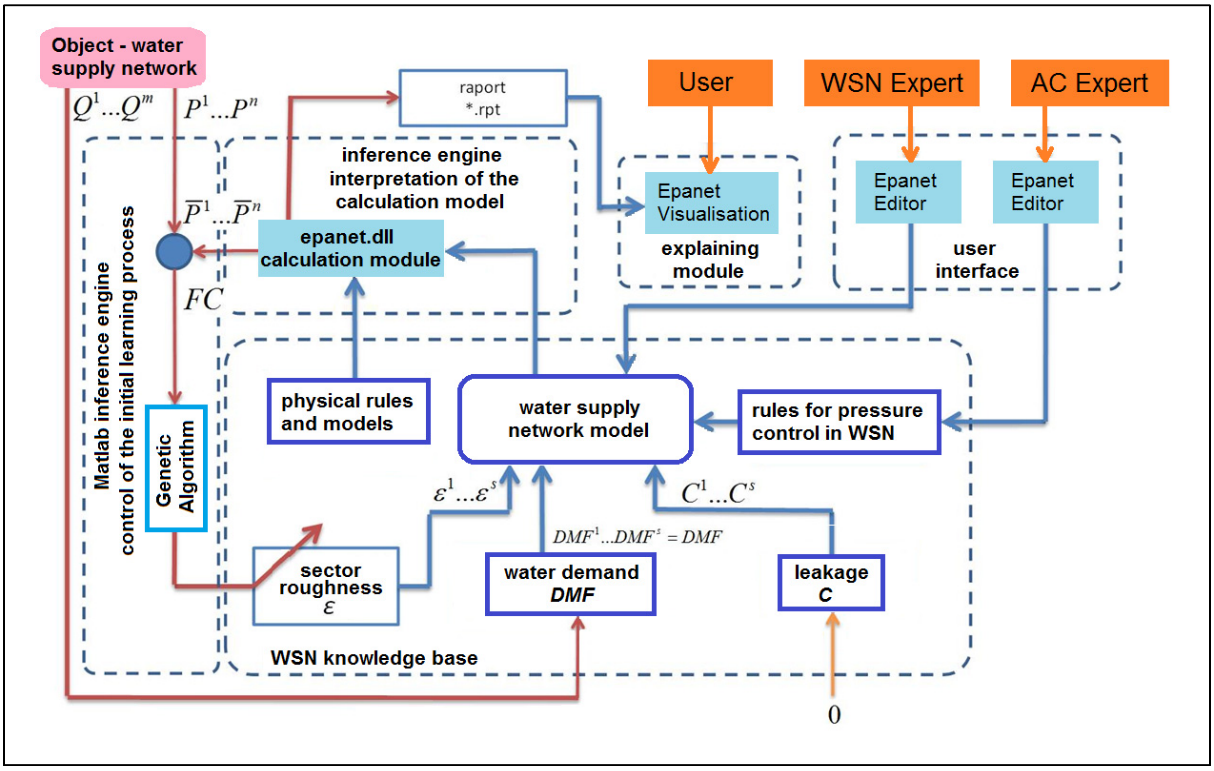

Figure 7 Functional diagram of the expert system for calibration of WSN parameters.

5 CONCLUSIONS

So far WSN simulations were based on theoretical estimates and were mainly focused on expert analysis of extreme situations that may arise during the operation of the network. Meanwhile, simulation models also allow the detection of so-called unreported leaks, which according to the literature account for up to 60% of all leaks. Creating a precise simulation model using measurements results carried out under industrial conditions translates directly into economic benefits for the network operator. It can greatly facilitate the strategic decisions made so far by experts, guided mainly by intuition on the location of the failure, which was confirmed by performing a series of measurements using the auscultatory (electro-acoustic) or infrared methods. In this paper, a method for determining the current state of the WSN in real time based on the measurement data was described. The WSN structure was given in the paper. Furthermore, it was shown how evolutionary algorithms are applied for to determine the distributions of pressure values in the individual network nodes and flows in the individual sections of pipelines. For calibration of chosen model parameters, an expert system was designed, which combines Epanet, a software for modeling of hydraulic and water quality behavior of water distribution piping systems, with MATLAB environment by using the epanet2.dll dynamic link library. Based on the calibration results, a very good fitting of the simulated values to the empirical data, which were recorded during measurements in the real WSN, was achieved. From the studies conducted, it follows that for proper operation of the diagnostic system, a precise measuring system, working in real time, is essential. Furthermore, it was stated that for the purposes of diagnostic system pressure measurements at various points in the water supply system and flows measurements in the supply points and points of water consumption by large wholesale customers is sufficient.

ACKNOWLEDGEMENTS

The work was co-financed by the Polish National Center for Science and Development within the project no PBS3/B3/33/2015.

REFERENCES

Clark, C. & Yi, W.Z. (2006). Integrated Hydraulic Model and Genetic Algorithm Optimization for Informed Analysis of Real Water System. *International Symposium on Water Distribution System Analysis*, 1-11.

Jia, H., Wei, W. & Xin, K. (2008). *Hydraulic Model for Multi - Sources Reclaimed Water Pipe Network Based on EPANET And It's Applications In Beijing, China.* Higher Education Press and Springer - Verlag.

Perelman, L. & Ostfeld, A. (2013). Water-Distribution Systems Simplifications through Clustering. *Journal of Water Resources Planning and Management,* 138(3), 218-229.

Piechurski, F.G. (2013). Wykorzystanie monitoringu sieci wodociągowej do obniżenia poziomu strat wody. *Napędy i sterowanie*, 2, 66-71. (In polish).

Pieczyński, A., Kowal, M. & Prętki, P. (2007). *Solving optimization tasks in the construction of diagnostic systems. Measurements models systems and design,* Ed. J. Korbiczr*,* Warszawa, 204-239 pp.

Prais, A. & Whittle, A.J. (2011). Efficient Hydraulic State Estimation Technique using Reduced Models of Urban Water Networks. *Journal of Water Resources Planning and Management*, 137(4), 343-351.

Schmid, R. (2002). Review of Modelling Software for Piped Distribution Networks. *Working papers on water supply and environmental sanitation*.

Saldarriaga, J.G., Ochoa, S., Rodríguez, D. & Arbeláez J. (2008). Water Distribution Network Skeletonization using the Resilience Concept. *In Water Distribution Systems Analysis,* 1-13.

Savic, D.A, Kapelan, Z.S. & Jonkergow, P.M. (2009). Quo vadis water distribution model calibration? Quo vadis water distribution model calibration? *Urban Water Journal*, 6(1), 3-22.

Ulanicki, B., Zehnpfund, A. & Martinez, F. (1996). Simplification of Water Distribution Network Models. *Proceeding 2nd Intl. Conf. on Hydroinformatics,* 493-500.

Urbaniak A. (2006). Monitorowanie i Sterowanie Procesami Wodociągowymi. *Wodociagi – Kanalizacja*, 39-41. (In polish).

USEP Agency. (2013). *Epanet System Software Package*, Developed By the US Environmental Protection Agency On Behalf of the American Government.

Proceedings of the 37th IAHR World Congress
August 13 – 18, 2017, Kuala Lumpur, Malaysia

NUMERICAL AND PHYSICAL MODELING OF WATER FLOW IN V-SHAPED STEPPED SPILLWAY

ZHAOLIANG BAI(1) & JIANMIN ZHANG(2)

(1,2) State Key Laboratory of Hydraulics and Mountain River Engineering, Chengdu, China,
baizhaoliang@hotmail.com; zhangjianmin@scu.edu.cn

ABSTRACT

V-shaped stepped spillway is a new type of stepped spillways, which has distinguished three-dimensional flow program and greater aerated characteristic. In this paper, the flow characteristics of V-shaped stepped spillway are systematically studied, including the flow pattern, velocity vectors, pressure distribution on step surfaces and energy dissipation rates by physical and numerical models. And through comparing with traditional stepped spillway, the unique flow field is analyzed. These results are useful when choosing V-shaped stepped spillway to use.

Keywords: V-shaped stepped spillway; flow characteristics; physical model; numerical model.

1 INTRODUCTION

Owing to the special structure in stepped spillways, the flow structure is changed and produces vortices of energy dissipation (Chen et al., 2002; Amador et al., 2006), which easily proceed the conversion of kinetic energy to turbulent kinetic energy and heat energy, effectively increasing the energy dissipation. Therefore, the applications of stepped spillway have been widely adopted (Chanson et al., 2001; Emiroglu et al., 2003).

Researches on stepped spillways are hot topics, including the flow pattern, velocity distribution, pressure distribution, energy dissipation rate, aerated characteristics with the factors of step size, the arrangement of steps, slope and so on. The flow pattern was studied (Chanson and Toombes, 2004; Ohtsu et al., 2004; Bung, 2011) for it can reflect the hydraulic characteristics of flow and it can be divided into: nappe flow, transition flow and skimming flow. Some researches focus on energy dissipation rates with factors of flow pattern, step roughness, step size and slope of stepped spillway (Christodoulou, 1993; Chinnarasri and Wongwises, 2006; Felder and Chanson, 2011; Shahheydari et al., 2015). There are also some researches on pressure distributions for negative pressure may lead to cavitation damage (Sánchez-Juny, 2007; Qian et al., 2009; Zhang et al., 2012; Daneshfaraz et al., 2016).

It can be seen that most researches are about traditional stepped spillway. Most studies were primarily focused on the step size and step arrangement, among other factors, but few studies investigated steps by changing the horizontal face angles of the steps. V-shaped stepped spillway as a new shaped stepped spillway by changing the horizontal face angles of the steps, there should be some different characteristics from traditional stepped spillway. In this paper, physical model and numerical model were performed to study the water flow of V-shaped stepped spillway. The flow pattern of V-shaped stepped spillway was observed through physical model in different flow regimes. The streamlines and velocity vectors were analyzed by numerical model to illustrate the unite flow pattern in skimming flow regime. Furthermore, pressure distribution and energy dissipation rate were studied. These results can provide support when choosing V-shaped stepped spillway.

2 MODEL SETUP

2.1 Physical and numerical model

In this paper, θ represents the horizontal face angle of the stepped spillways, as shown in Figure 1. When $\theta=120^o$, the stepped spillway is named as the V-shaped stepped spillway and when $\theta=180^o$, it is the traditional stepped spillway. The physical model consisted of an upper water tank, a press slope section, a smooth section, a stepped spillway, a tail water section, a measuring weir and a reservoir. The total model height was 5.4m, and the stepped spillway was made of organic glass to observe the flow pattern on the steps, as shown in Figure 2. In both models, the chute width was B = 0.4m; the height of the model inlet was h = 0.12m; the outlet of the press slope section was 0.08m; and the step section consisted of 56 steps. The first 28 steps were transitional steps to improve the flow regime, then was the uniform steps. The slope of the stepped spillway was 1V:2H.

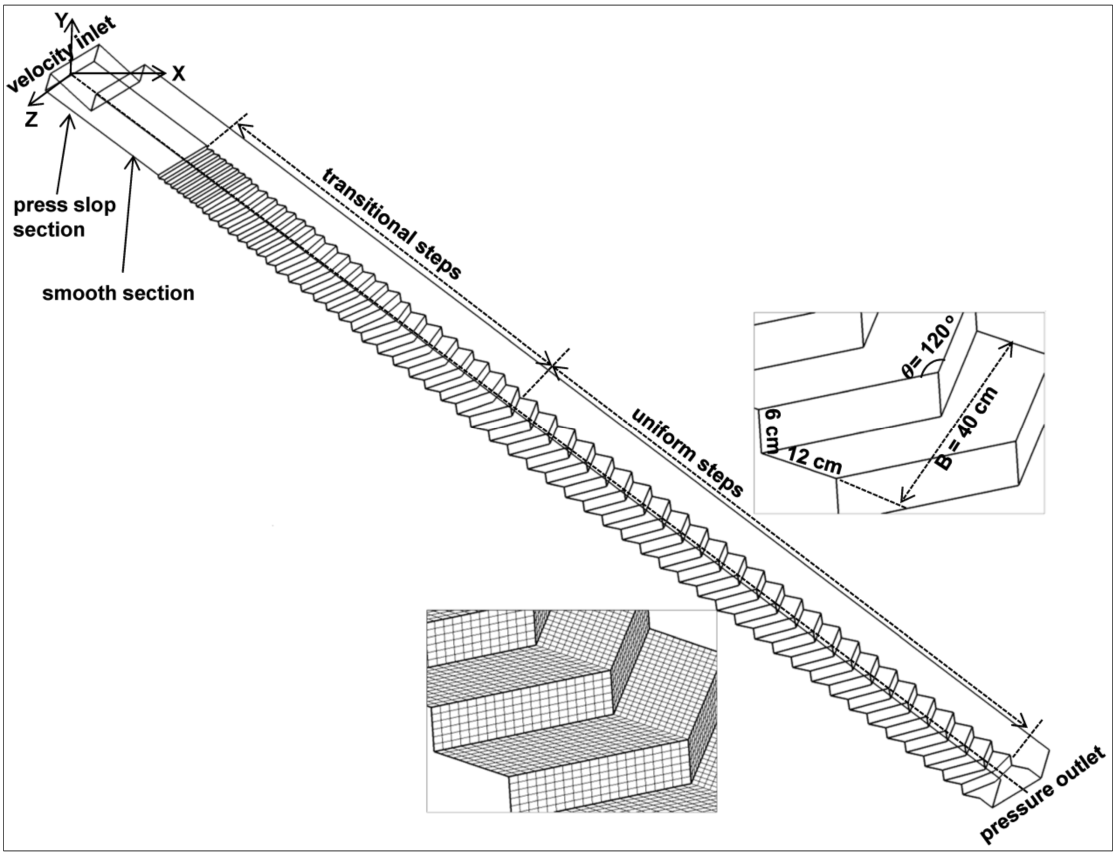

Figure 1. The numerical model layout.

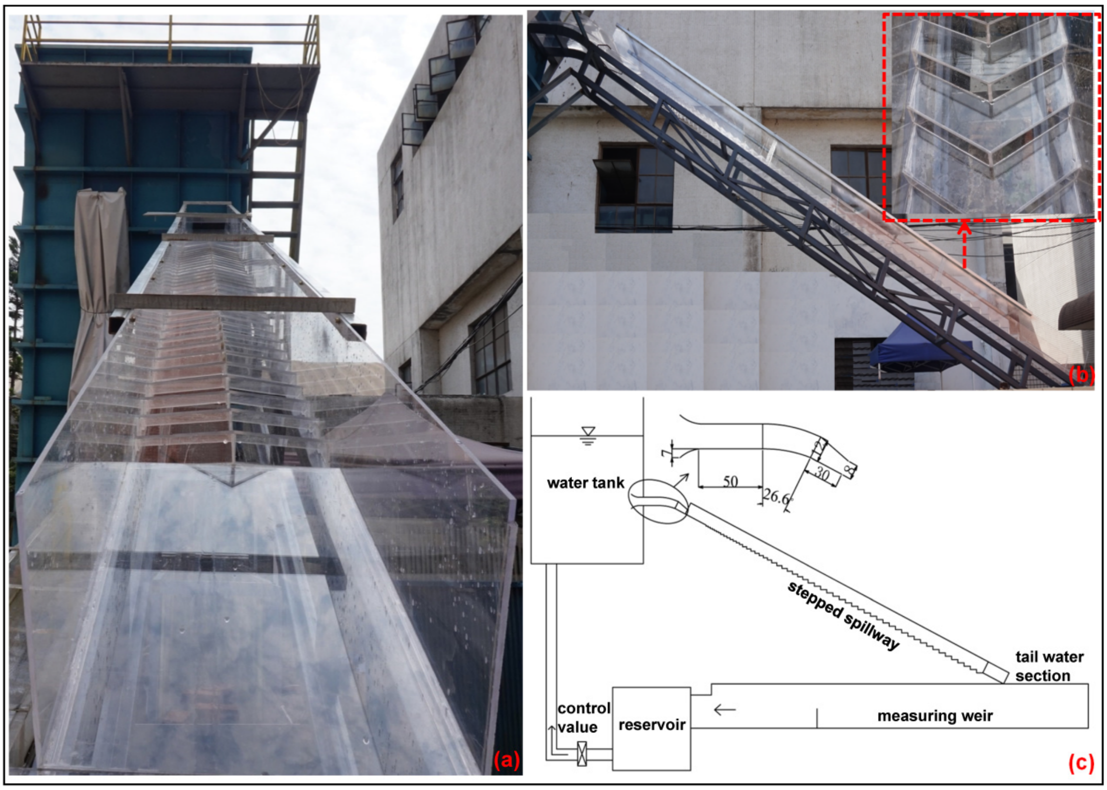

Figure 2. The physical model layout.

2.2 Turbulence model for the VOF model

The renormalization group (RNG) k–ε turbulence model was presented by Yakhot and Orszag (1986). And the volume of fluid (VOF) (Hirt and Nichols, 1981) method was used to track the air-water interface. The equations of turbulent kinetic energy, k, and its dissipation rate, ε, are as follows:

$$\frac{\partial(\rho k)}{\partial t}+\frac{\partial}{\partial x_i}(\rho u_i k)=\frac{\partial}{\partial x_i}\left[(\mu+\frac{\mu_t}{\sigma_k})\frac{\partial k}{\partial x_i}\right]+G_k-\rho \qquad [1]$$

$$\frac{\partial(\rho \varepsilon)}{\partial t}+\frac{\partial}{\partial x_i}(\rho u_i \varepsilon)=\frac{\partial}{\partial x_i}\left[(\mu+\frac{\mu_t}{\sigma_\varepsilon})\frac{\partial \varepsilon}{\partial x_i}\right]+C_{1\varepsilon}\rho\frac{\varepsilon}{k}G_k-C_{2\varepsilon}\rho\frac{\varepsilon^2}{k} \qquad [2]$$

$$\rho=\alpha_w\rho_w+\alpha_a\rho_a \qquad [3]$$

where α_a and α_w are the volume fraction of air and water, respectively; ρ_a and ρ_w are the density of air and water, respectively; ρ is the mean density; μ and μ_t are the molecule viscosity coefficient and turbulent viscosity coefficient, respectively; u_i is the mean velocity component in the ith direction; α_k, α_ε are the inverse effective Prandtl numbers; η_0, β, C_μ, $C_{1\varepsilon}$ and $C_{2\varepsilon}$ are empirical constants and the empirical constants are specified as follows: η_0=4.38, β=0.012, C_μ=0.0845, $C_{1\varepsilon}$=1.42, $C_{2\varepsilon}$=1.68.

2.3 Boundary conditions

The boundary conditions are as follows:

(1) Inlet boundary: the velocity inlet was used;
(2) Outlet boundary: pressure outlet; the normal gradient of all variables was 0;
(3) Wall boundary: no-slip velocity boundary condition; the method of standard wall function was used to analyze the near-wall regions;
(4) Free surface: pressure inlet; the pressure value was P=0.

3 RESULTS AND ANALYSIS

3.1 Flow pattern

Figure 3 is the flow pattern of nappe flow and transition flow in V-shaped stepped spillway. It can be seen that the flow pattern of nappe flow and transition flow in V-shaped stepped spillway is similar with that of in traditional stepped spillway. In nappe flow, when the water flow drops on the horizontal step surface and then travels in the downstream direction, there is an approximately triangular cavity between the step surface and the mainstream, and there is an approximately trapezoidal hydrostatic pool below the cavity. As the unit discharge increases, the water flow is in transition flow regime. In transition flow, in some steps, the flow pattern is similar with the flow in nappe flow, but the cavity is smaller; whereas in other steps, it is full of water where it is cavity in nappe flow and forms some vortices.

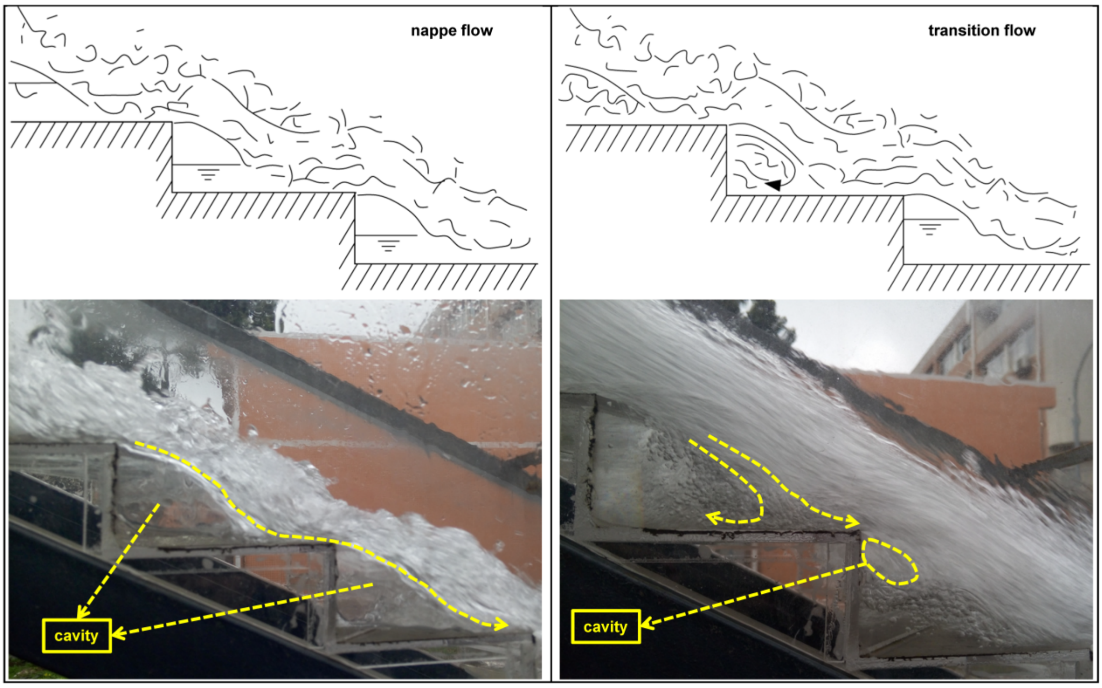

Figure 3. The flow pattern of nappe flow and transition flow in V-shaped stepped spillway.

As the unit discharge continues to increase, the water flow is in skimming flow regime, as shown in Figure 4. As we all know, in traditional stepped spillway, when the water flows from one step to the next step, the flow drops on the horizontal step surface, then part of the flow travels in the downstream direction, and the other part changes direction and forms vortices in skimming flow regime. Because there is no difference in the transverse section, the vortices parallel to the axial plane and the water free surface is nearly the same in different profiles along the cross section in traditional stepped spillway. But Figure 4 shows that the flow pattern of skimming flow in V-shaped stepped spillway is different from that of in traditional stepped spillway for the unique body type. Figure 4(c), (d) are the photo and numerical result of water free surface, respectively. All of them indicate that the water free surface changes along the cross section.

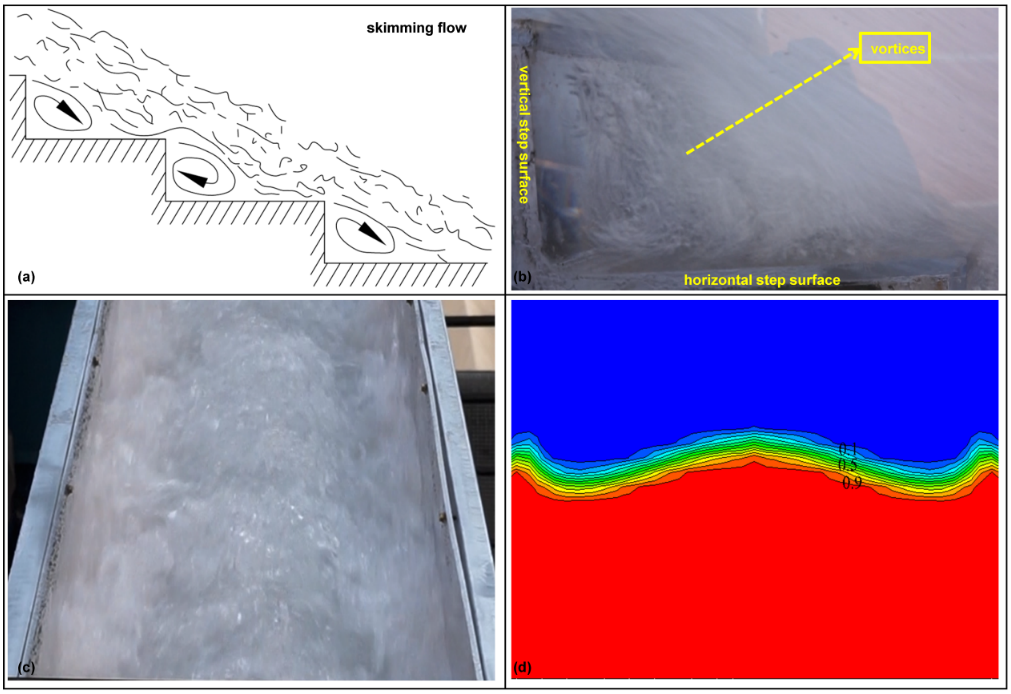

Figure 4. The water flow of skimming flow in V-shaped stepped spillway.

3.2 Velocity distribution of profile

Figure 5 shows the streamlines and velocity vectors of skimming flow in V-shaped stepped spillway. In order to show the spiral flow and downstream flow clearly, the streamlines are shown in different steps in Figure 5(a). Figure 5(a) shows that the streamlines are not parallel to axial plane and that there is transverse velocity, which is not like in traditional stepped spillway. Therefore, the vortices are not parallel to axial plane and the vortices decay from the sidewall to the axial plane, but there is little change from the profile of Z/B=0.5 to Z/B=0.25 and there are great changes from the profile of Z/B=0.25 to Z/B=0, as shown in Figures 5(b)-(d). Near the axial plane, the flow from the sidewalls to the axial plane makes collision and the mainstream is raised, so there is no vortex near the axial plane. Because of these flow characteristics, the unique flow pattern is formed in the skimming flow.

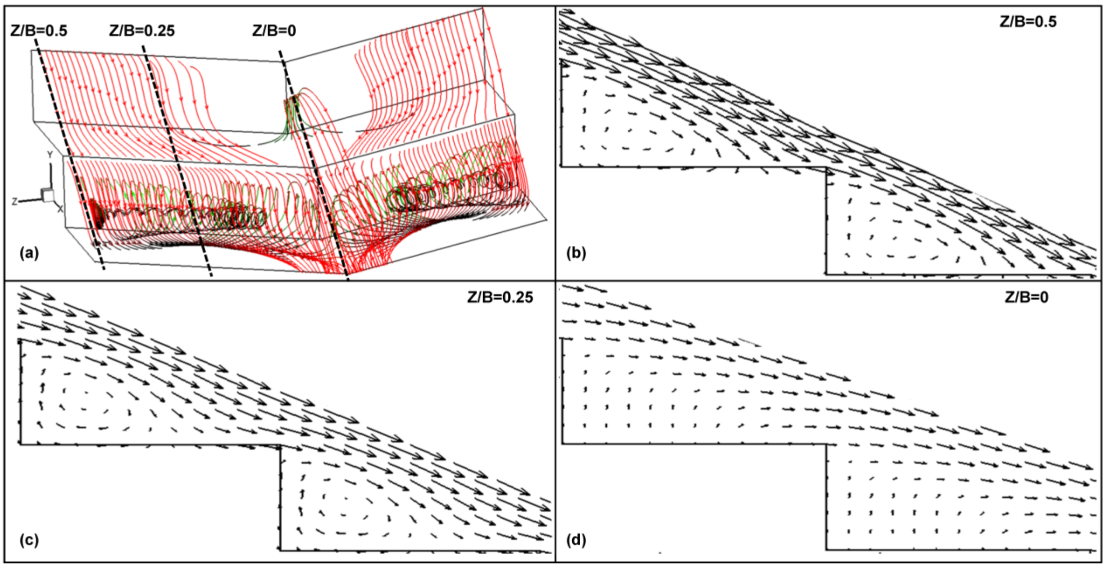

Figure 5. The streamlines and velocity vectors of skimming flow in V-shaped stepped spillway.

3.3 Pressure distribution

Figure 6 shows the pressure distribution on steps of transition flow and skimming flow, where L represents the width of the step and H represents the height of the step. It can be seen that: 1) as we all know that, the pressure distribution of traditional stepped spillway doesn't change along the cross section, but there are obvious differences in V-shaped stepped spillway; 2) pressure distribution changes along the cross section when the flow is in transition flow regime and skimming flow; 3) comparing the pressure distribution of transition flow and skimming flow, the location of the extreme pressure values is similar, but the fluctuation of pressure distribution is larger in skimming flow regime; 4) the maximum negative pressure occurs on the upper edge of vertical step surface near the sidewalls and the maximum pressure occurs on the outer edge of horizontal step surface near the sidewall profile.

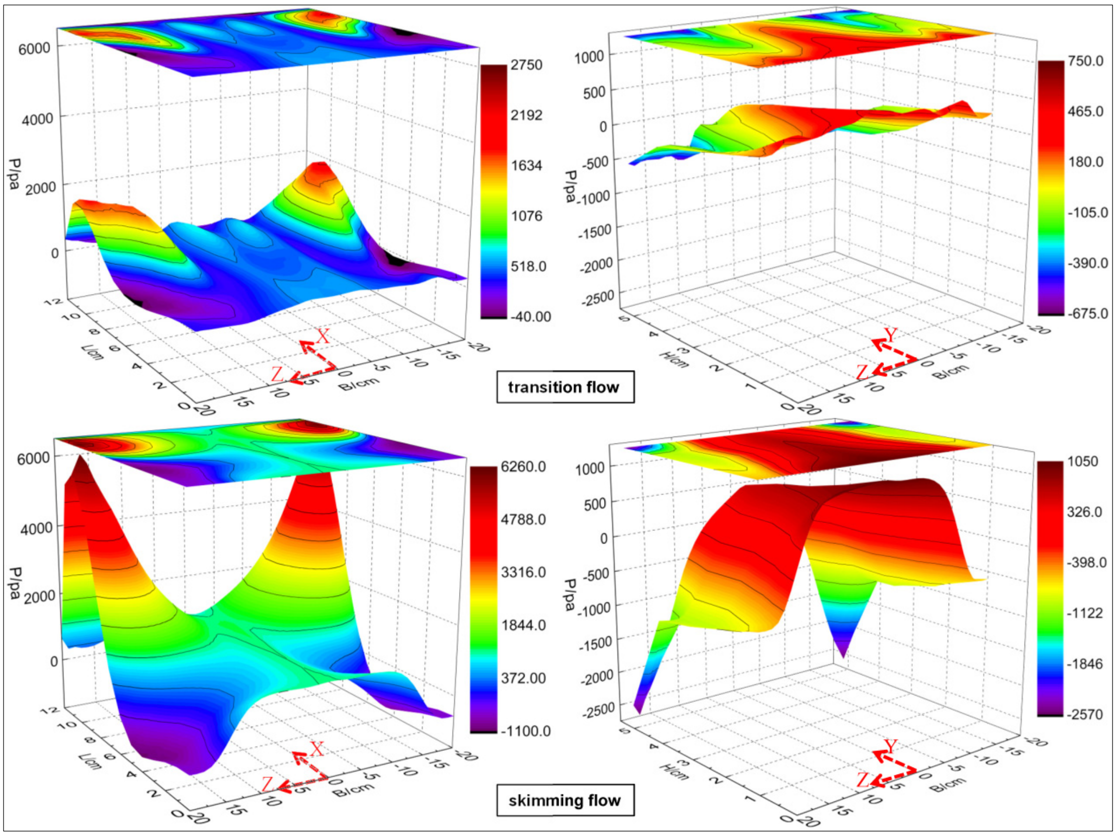

Figure 6. The pressure distribution on steps of different flow regimes.

3.4 Energy dissipation rate

The flow has three-dimensional characteristics and the flow field increases the turbulence intensity in V-shaped stepped spillway. So the energy dissipation rate was studied. In this paper, the comparison of energy dissipation rates in V-shaped and traditional stepped spillway was analyzed. The energy dissipation rate in traditional stepped spillway was calculated by numerical model and the model size was same as the V-shaped stepped spillway. And the energy dissipation rate is defined by the energy loss of upstream and downstream:

$$\eta = \frac{\Delta E}{E_1} \times 100\% = \frac{E_1 - E_2}{E_1} \times 100\% \qquad [4]$$

$$E_1 = \Delta h + v_1^2/(2g),\ E_2 = v_2^{\,2}/(2g) \qquad [5]$$

where E_1 and E_2 are the total energy in the first step section and the beginning section of tail water section, respectively; Δh is the difference in height between the two sections, and v_1 and v_2 are the mean velocities in the two sections, respectively.

Figure 7 is the ratio of energy dissipation rates in V-shaped and traditional stepped spillways corresponding to various unit discharges, where V_{edr} and T_{edr} represent the energy dissipation rates in V-shaped and traditional stepped spillways, respectively. The figure shows that: 1) the energy dissipation rate in V-shaped stepped spillway is larger than that of in traditional stepped spillway; 2) as the unit discharge increases, V-shaped stepped spillway has better energy dissipation rate than traditional stepped spillway.

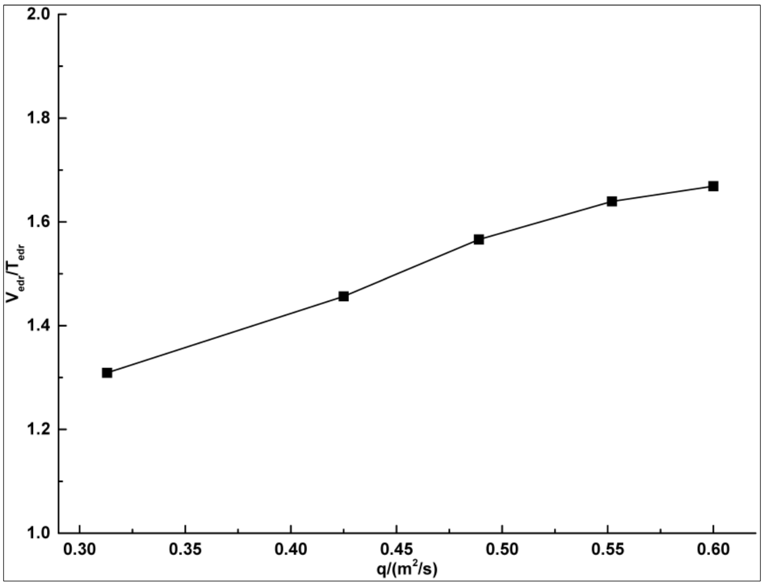

Figure7. The ratio of energy dissipation rates in V-shaped and traditional stepped spillways.

4 CONCLUSIONS

In this paper, the water flow characteristics of V-shaped stepped spillway was studied by physical and numerical model. The following conclusions can be drawn:

(1) There are also three flow patterns in V-shaped stepped spillway: nappe flow, transition flow, and skimming flow. Nappe flow and transition flow are similar with that of traditional stepped spillway, but the flow pattern in skimming flow regime is quite different from the traditional stepped spillway.

(2) The maximum negative pressure occurs on the upper edge near the sidewalls not on the hole cross section and V-shaped steps have better energy dissipation rate than traditional stepped spillway, but is more susceptible to erosion damage than traditional stepped spillway. Furthermore, three-dimensional flow characteristics will lead to better aerated properties. In ecological water conservancy and aeration tanks, the velocity is smaller, so we can make full use of its aerated properties, but avoid erosion damage. This will be studied in the future.

ACKNOWLEDGEMENTS

This project was supported by the National Natural Science Foundation of China (NO: 51579165) and the National Science Fund for Distinguished Young Scholars (NO: 51625901).

REFERENCES

Amador, A., Sanchez-Juny, M. & Dolz, J. (2006). Characterization of the Nonaerated Flow Region in a Stepped Spillway by PIV. *J. Fluid Eng.,* 128(6), 1266-1273.

Bung, D.B. (2011). Developing Flow in Skimming Flow Regime on Embankment Stepped Spillways. *J. Hydraul. Res.,* 49(5), 639-648.

Chanson, H. (2001). Historical Development of Stepped Cascades for the Dissipation of Hydraulic Energy. *Transactions Newcomen Society for the Study of the History of Engineering & Technology,* 72(2000-2001), 295-318.

Chanson, H. & Toombes, L. (2004). Hydraulics of Stepped Chutes: The Transition Flow. *J. Hydraul. Res.,* 42(1), 43-54.

Chen, Q., Dai, G.Q. & Liu, H.W. (2002). Volume of Fluid Model for Turbulence Numerical Simulation of Stepped Spillway Overflow. *J. Hydraul. Eng.,* 128(7), 683-688.

Chinnarasri, C. & Wongwises, S. (2006). Flow Patterns and Energy Dissipation Over Various Stepped Chutes. *Journal of Irrigation and Drainage Engineering,* 132(1), 70–76.

Christodoulou, G.C. (1993). Energy Dissipation on Stepped Spillways. *J. Hydraul. Eng.,* 119(5), 644- 650.

Daneshfaraz, R., Joudi, A.R., Ghahramanzadeh, A. & Ghaderi, A. (2016). Investigation of Flow Pressure Distribution Over a Stepped Spillway. *Advances and Applications in Fluid Mechanics,* 19(4), 805-822.

Emiroglu, M.E. & Baylar, A. (2003). An Investigation of Effect of Stepped Chutes with End Sill on Aeration Performance. *Water Quality Research Journal of Canada,* 38(3), 527–539.

Felder, S. & Chanson, H. (2011). Energy Dissipation Down a Stepped Spillway with Non-Uniform Step Heights. *J. Hydraul. Eng.,* 137(11), 1543-1548.

Hirt, C.W. & Nichols, B.D. (1981). Volume of Fluid for the Dynamics of Free Boundaries. *J. Comput. Phys.,* 39(1), 201-225.

Ohtsu, I., Yasuda, Y. & Takahashi, M. (2004). Flow Characteristics of Skimming Flows in Stepped Channels. *J. Hydraul. Eng.,* 130(9), 860-869.

Qian, Z.D., Hu, X.Q., Huai, W.X. & António, A. (2009). Numerical Simulation and Analysis of Water Flow Over Stepped Spillways. *Science China Technological Sciences,* 52(7), 1958-1965.

Sánchez-Juny, M., Bladé, E. & Dolz, J. (2007). Pressure on a Stepped Spillway. *J. Hydraulic Res.,* 45(4), 505-511.

Shahheydari, H., Nodoshan, E.J., Barati, R. & Moghadam, M.A. (2015). Discharge Coefficient and Energy Dissipation Over Stepped Spillway Under Skimming Flow Regime. *Journal of Civil Engineering,* 19(4), 1174-1182.

Yakhot, V. & Orszag, S.A. (1986). Renormalization Group Analysis of Turbulence: I. Basic Theory. *Journal of Scientific Computing,* 1(1), 3-51.

Zhang, J.M., Chen, J.G. & Wang, Y.R. (2012). Experimental Study on Time-Averaged Pressures in Stepped Spillway. *J. Hydraul. Res.,* 50(2): 236-240.

Proceedings of the 37th IAHR World Congress
August 13 – 18, 2017, Kuala Lumpur, Malaysia

THE NEW DEVELOPMENT OF FLUID-STRUCTURE INTERACTION IN STRUCTURE PHYSICAL BEHAVIOUR ANALYSIS

YANG TANG[1], JIJIAN LIAN[2] & CHUNLAI QU[3]

[1,2] State Key Laboratory of Hydraulic Engineering Simulation and Safety, Tianjin University, Tianjin, China,
sunny_1677@163.com; jjlian@tju.edu.cn

[3] School of Hydroelectricity, Hebei University of Engineering, Handan, China,
quchunlai@hebeu.edu.cn

ABSTRACT

Fluid-structure interaction (FSI) is an independent branch of mechanics which comprises of fluid mechanics and solid mechanics. The crux of the FSI problem is the interaction between the flow field and solid deformation field. When the field is overlapping and penetrative, the coupling can be realized by establishing the differential equations of constitutive equations which are different from the single-phase medium. However, when the field is contrary to the above one, the coupling takes effect by the interface force. In this paper, the current research status of fluid-solid coupling numerical simulation methods is discussed from the point of view of continuum mechanics and non-continuum mechanics, and the shortcomings of the numerical simulation methods of fluid-solid coupling are described. The result of this research has instructive significance relevant for the development of FSI numerical simulation methods and helps engineers make better choices for reliable simulation methods for the physical behaviour of materials.

Keywords: Fluid-structure interaction; numerical simulation; discrete element method; SPH.

1 INTRODUCTION

Along with the development and application of engineering technology, the research on fluid-structure interaction (FSI) has received widespread attention in the academic community since the 1980s. In general, the problem of FSI can divided into two types according to its coupling mechanism:

- The coupling action only occurs at the two-phase interface and the coupling equation is introduced by the equilibrium and coordination of the two-phase coupling surfaces, such as aero elastic, hydrodynamic, etc.;
- As the fluid and structure field overlap partially or completely and cannot be separated, the equations which describe the physical phenomena, especially the constitutive equation, must be built based on concrete physical phenomena, and its coupling effect is reflected by the differential equation of the problem.

For a long time, the research on FSI mainly focused on the macro research methods, such as using the rock and dam body as the research object. This working scale and research depth of FSI have undoubtedly been necessary and important in this area (Dullien, 1992). However, there are many problems, especially on the coupling mechanism, that cannot be addressed using only use the macro research methods. One feature of FSI is that the structural deformation not only lies on the load given by a moving fluid, but it also affects the motion of the fluid and then changes the load on the structure surface as a result. The solution to the FSI problem can divided into two types, which are unidirectional and bidirectional FSI.

The unidirectional FSI method is applicable for situations where the solid deformation change is small after the flow field affects the solid. However, the flow field boundary is also changed; the distribution of flow field also varies greatly. Two types of influences, the interaction between the flow field and stress of solid as well as how the solid deformation affects the flow field, must be considered to achieve balance. Thus, it is necessary to utilize the bidirectional FSI method (Xu, 2012).

In this paper, the current research status of fluid-solid coupling numerical simulation methods is discussed from the point of view of continuum mechanics and non-continuum mechanics, and the shortcomings of the numerical simulation methods of fluid-solid coupling are described. The result of this research has instructive significance relevant for the development of FSI numerical simulation methods and helps engineers make better choices for reliable computational methods for the physical behaviour of materials.

2 FSI IN CONTINUUM MECHANICS

When using existing finite element analytical software, only the coupling data exchange platform is needed, and the software can apply appropriate solution methods in both the fluid and solid domain (Wang and Yang, 2008; Deng, 2012). It is common for the finite element method for the Lagrangian description to be employed in the solid domain, since one of its features is that the computational grid is fixed on the solid and moves along with it. In other words, both the grid and material coordinates are always in the process of deformation or movement, so there is no relative motion between the material and grid. However, in regard to the problem of large deformations, the aberrant grid caused by the object's distortion can lead to the failure of the calculation.

For the fluid field, the finite difference method for the Eulerian description is often used. However, finding the solution of the moving surface on a solid requires very complex mathematical mapping which can also lead to significant error. Due to the influence of the material transfer item, the coefficient matrix of the system is asymmetric, which will sharply increase the solving difficulty.

To address this problem, a new method called the arbitrary Lagrangian-Eulerian (ALE) method, was presented, and it became a commonly used numerical method to solve the FSI problem. The ALE method, as its name implies, combines features of both the Lagrangian and Eulerian descriptions. Even though the computational grid and material coordinates are separated, the computational grid can be in arbitrary motion in space, and the material is transferred between the grids at different times. The method can track the existence of the boundary of the material structure effectively by processing structural motion boundaries, so it has this advantage over the Lagrangian description. Within the division of the internal grid, the grid is independent of the material, so that the calculation grid can adjust its position. This prevents significant distortion, so the ALE method also has this advantage over the Eulerian description.

When using the ALE method to solve FSI problems, the particles move with the corresponding nodes in solid grid, therefore, the ALE method has good treatment of the coordination problem of the coupling surface, and reflects the interaction between fluid and solid more realistically. However, when structures with irregular shape were used for numerical simulation with the ALE method, it becomes much more difficult, and the frequent grid updates is both complex and time consuming. Aiming at the problems of the ALE method to address FSI, the no unit method makes it possible to handle this problem. Yang (2011) improved the classical element free method, and introduced the no element method into the FSI problem. The combined application of the element free Galerkin method and the three orders distributed finite element method was proposed. This method uses velocity and pressure separation and the new algorithm is used to control the flow field governing equations of two-dimensional incompressible flow to obtain the discrete equations and solve them. Taking the V1V problem as an example shows that the algorithm is not dependent on the element information and can be applied to the FSI problem.

The above numerical analysis methods are mostly based on the mechanics of a continuous medium. Continuous medium methods use elastic-plastic mechanics and the discrete material is treated as a continuum medium. This method focuses on the mechanical behaviour of the whole object and ignores the individual properties of the element. It also depends on the constitutive equations of highly simplified and/or prescribed properties.

For bulk granular materials, it is generally not satisfactory to assume that the complexity of the dynamic behaviour is difficult to simulate using the traditional continuum mechanics. For example, the slope, rock fill, etc. (Figure.1 and Figure.2) are composed of granular material. Because it is composed of a large number of different shapes of discrete elements, its nature was between the solid and fluid. It can even flow under the action of an external force or flow. With the continuous development of modern mechanics, from the continuous medium to today's discontinuous, collective particle movement of the media is a major object of the current study of mechanics (Qian, 1984). The research on rock and soil and its engineering structures starts to develop from continuum mechanics and macro mechanics models and moves toward discrete mechanics of discontinuous media to explore the mechanism of micro mechanical behaviour (Zhang, 2008).

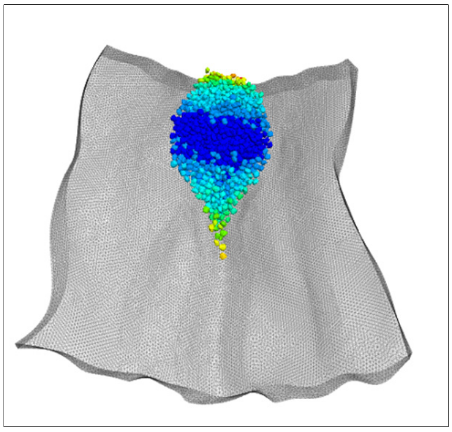

Figure 1. The slope model.

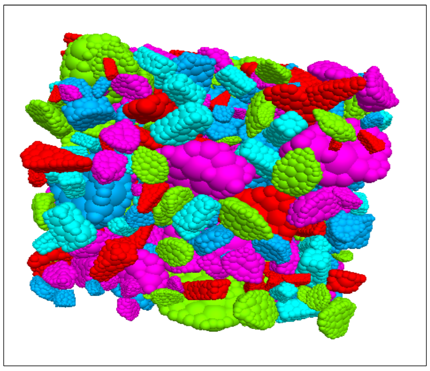

Figure 2. Rock fill.

3 THE NON-CONTINUUM MECHANICS OF FLUID-SOLID COUPLING

Terzaghi (1925) first put forward the concept of soil structure where the granular medium is treaded as a continuum and ignoring the discontinuous characteristics of the medium. The constitutive equation does not include the scaling parameter and cannot describe the characteristics of the scale of the mechanical properties (Yao and Hou, 2009). For nearly 20 years, researchers gradually began to pay attention to the fine mechanical behaviour of a granular material system. A large number of experimental observations and numerical simulations were carried out, and results showed that the particle system has a small effect on the nonlinear response and self-organization. Unique properties such as the static and dynamic behaviour cannot be described with the general theory of solid or fluid mechanics (Sun and Jin, 2009). In the study of soil mechanics, Terzaghi put forward the famous effective stress principle (Terzaghi, 1925) and established a one-dimensional consolidation model. After this, Biot (Biot, 1941; Biot and Willis, 1957), on the basis of some pioneering research, established a nearly perfect three-dimensional consolidation theory. Then, in 1984, Zienkeiwiez et al. (Zienkiewicz and Shiomi, 1984; Zienkiewicz et al., 1990), on the basis of Biot's three-dimensional consolidation theory, considered the material nonlinearity and geometrical nonlinearity of the soil and proposed the general Biot consolidation equation. Fredlud et al. (2012) considered the soil pore water and air coupling and established the constitutive equation of one dimensional consolidation of unsaturated soil structure. Bai et al. (1999) and Hudson et al. (2005) treated fissure medium equivalent as continuous for porous media to carry out the fluid-structure coupling calculation and analysis. Li et al. (2003) developed a mathematical model based on the effective stress principle of porous media saturated porous media seepage. Dong (2005) established a finite-element numerical model of fluid-solid coupling of fluid seepage based on deformable porous media. Chu et al. (2007) put forward a solid skeleton integral form of the equilibrium equation based on the theory generalized by Biot (1957), and combined with continuous equation of unsaturated seepage flow using the weighted residual method, deduced fluid-structure coupling equations of the finite element formulations. Liu et al. (2004) took sand and water seepage into accord with the two-dimensional Darcy's law and proposed the governing differential equations of unsteady seepage under the action of an anisotropic seepage field and stress field and used the finite element method to solve. Deng (2011) established a solid coupling mathematical model based on effective stress principle of porous media theory.

Since then, fluid-structure interaction theory research basically complies with the Biot three-dimensional consolidation theory which assumes that the constitutive relation of the porous medium of stress strain is different or makes the pore fluid assumption for the difference of multiphase fluid or single phase fluid. For many years, the particulate matter qualitative macro-mesoscopic research, grain contact force was deduced and spatial location associated with macroscopic stress and strain. Geometry provides a preliminary description of the force chain but also cannot link directly to the kinetic process of the system. Literature (Xia et al., 1995) provides a good reference of the research paradigm.

Cundall (1979) put forward the concept of particle discrete elements, which generated widespread interest into the related research. Britain's university of Aston and Swansea began the research work of discrete elements earlier and wrote the related calculation programme and software and promoted the progress of discrete element (Feng et al., 2009). Japanese scholars also began the study of discrete elements early. Tsuji of Osaka University has achieved fruitful results using discrete elements in the research of fluid-solid coupling. Oda A&M University in Tokyo promoted the positive role of the development of discrete elements in a number of studies. (Oda and Iwashita, 1999). In countries such as Australia, Canada, France and the Netherlands, scholars have also studied discrete elements in a large number of engineering applications. Our country started the research of discrete element relatively late. In the first session of the national conference of rock mechanics in 1986, Yongjia Wang, professor at north-eastern university presented the numerical calculation and models, domestically introducing Cundall's discrete element method (DEM) for the first time (Wang, 1986). Since then, Zhou jian, Ming-jing Jiang, Zhong-qi Yue and other scholars have researched the application of the discrete element method in geotechnical engineering, materials engineering, chemical engineering, mining engineering and agricultural engineering. Other fields continue to rapidly development applications of the method.

Discrete elements can effectively address solid phase particles, but it is difficult to solve the problem of the interaction between a fluid and particles. In 1999, Cundall (1999) proposed a simplified method. This type of method for as small number of particles is relatively easy to calculate, but in the case of a large number of particles, the calculation of pore volume becomes tedious. To solve this problem, some special algorithms for the calculation of fluid mechanics is introduced into the discrete element method, such as the computational fluid dynamic (CFD) method, the smooth particle hydrodynamics (SPH) method (Potapov et al., 2001), the lattice Boltzmann method (LBM) (Ladd, 1994), etc.

In 1993, Tsuji et al. (1993) combined the DEM and CFD methods to solve the soil seepage problem (Figure.3). The solid portion was treated as a collection of particles and the liquid portion of the mesoscopic scale treated according to the average Navier-Stokes equations. Considering the interaction between particles and fluid successfully simulates the seepage velocity of the fluid flow distribution and also obtains the particle migration stress distribution, etc. As a result, since this method consistently improves results, it has been widely used (Shimizu, 2006), but the CFD calculation method focuses on macro flow characteristics of the fluid.

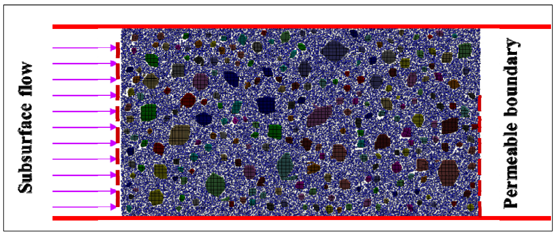

Figure 3. Distinct element method coupled with computational fluid dynamics calculation.

3.1 Particles discrete element PFC in the application of fluid-structure coupling model

The particle discrete element PFC2D method, introduced by Tsuji, deals with fluid in the discrete particle method, and performs very well. In the fixed coarse grid method fluid scheme (Shimizu, 2004), the whole flow field is divided into several fixed size fluid cells. Each unit contains dozens of particles (Figure. 4) used to numerically simulate the seepage flow velocity of fluid. Because of differences in the internal value of basic parameters such as permeability and porosity the particles of fluid within a cell are forced to produce change to simulate movement under the action of a fluid medium of particles.

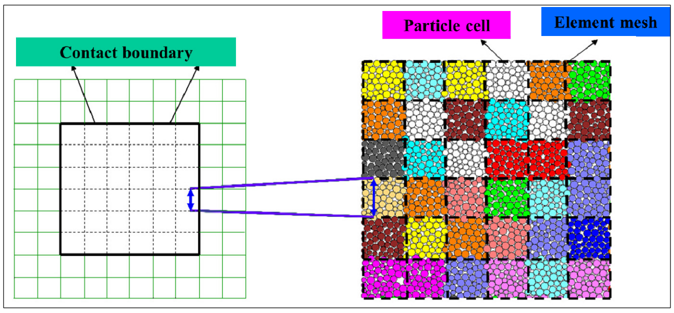

Figure 4. Fluid cell (2d).

3.2 The application of LBM in liquid-solid coupling model

Over the past 20 years, many scholars have studied the application of the LBM to the field of non-Newtonian fluids. Boek et al. (2003) simulated the flow of power-law fluid in a two-dimensional porous medium with the LBM. They found that at low Reynolds numbers, the flow was well satisfied by Darcy's law of permeability. Ginzburg (2002) simulated the free filling process of Bingham fluids using an improved Papanastasiou model. One important advantage of the LBM is that it can be fully coupled with a large number of moving particles; it can therefore successfully simulate multi-phase and multi-scale problems. Moreover, this method of liquid-solid coupling is easy to implement in both 2D and 3D cases, especially in porous media with complex boundary conditions, which can show its advantages compared to the traditional CFD method. The most commonly used fluid-solid coupling method is the coupling of LBM and DEM, in which the flow and evolution of the fluid phase is simulated with LBM, and the motion and collision of the solid phase is realized with DEM (Figure. 5). LBM and DEM are both mesoscale and have natural parallelism, which makes the coupling algorithm based on LBM-DEM very suitable for the study of fluid structure coupling mechanisms. The results showed that the LBM-DEM coupling method can address many complex fluid-solid coupling problems. For example, Nguyen and Feng et al. (Nguyen and Ladd, 2005; Feng and Michaelides, 2005) simulated the solid particle settlement problem with low Reynolds number. Cook et al. (2001; 2004) simulated the cementitious materials erosion problem. Feng et al. (2007; 2008) studied the transport of solid particles under the conditions of turbulent flow. Leonardi et al. (2012) simulated the process in mining engineering where fine particles through the gap between large stones and migrate towards the mouth of the mine. They used LBKG to simulate the liquid with a piecewise power-law rheological relationship and simulated the fine particles with DEM. They predicted the migration of fine particles and the relative movement of fine particles and large stones by 2D and 3D simulation, which provides a basis for the development of mining technology. The numerical model of soil with pressure was established by Shen et al. (2015) who used the LBM with the scale of REV. Qiu (2015) established the two-dimensional model of LBM-DEM to study the seepage characteristics of a porous medium. Zhang et al. (2014) simulated the particle motion in turbulent flow and the heat transfer between the particles by IMB-LBM-DEM.

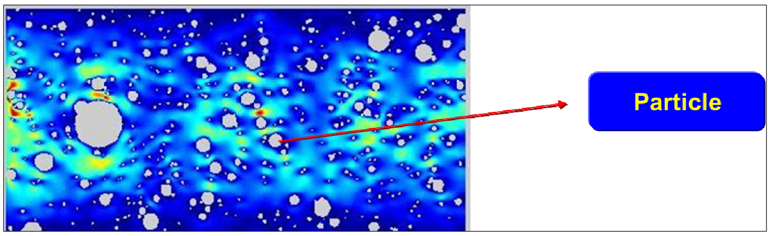

Figure 5. The coupling of DEM and LBM.

3.3 The application of SPH in liquid-solid coupling model

The smooth particle hydrodynamics (SPH) method is a meshless method which was the earliest successfully applied method in China. As early as 1996, Zhang (1996), a scientist from the Chinese academy, had begun to focus on the SPH method, and he published a review on the method. Monaghan et al. (2003) and Qiu (2008) investigated the process of the rectangular and triangular objects, respectively, falling on a sloped water surface. The free surface motion of an ellipsoidal object under the action of an asymmetric potential field was studied by Kajtar et al. (2008). Different responses of isosceles triangle shaped wedges falling into water was studied by Oger et al. (2006), who used the strategy of changing the smooth length. Omidvar et al. (2012) studied and simulated the interaction between cylinders and water waves during oscillation of the cylinder. However, the method of smoothing length changes with time and space, and involved complex processing. Therefore, for multiphase systems containing multiple or even a large number of solids (usually particles), the interaction between solids must be considered. The DEM is usually used to describe the interaction between solids. Based on the coupling of SPH and DEM (based on the linear contact model), the relationship between the shear stress and the Bagnold number of the model wall was studied by Potapov et al. (2011). Qiu (2013) simulated the settlement of cylindrical particles in liquid and the impact on the bottom surface of the container based on the nonlinear particle contact model (normal Hertz model and tangential Mindlin and Deresiewicz model). The SPH method has made great progress in the past ten years because of its unique advantages introduced by its meshless features. The study of the SPH method in complex flow was reviewed by Zhou et al. (2014). In addition, the SPH method has been extended to turbulent flow (Dalrymple and Rogers, 2006; Shao et al., 2006; Shi et al., 2012), heat transfer (Cleary, 1999; Szewc et al., 2011), mass transfer (Tartakovsky et al., 2007; Tartakovsky, 2010) and other fields. At the same time, open source SPH methods utilizing parallel computing for different problems are more and more common, such as GRADSPH (Vanaverbeke et al., 2009), JOSEPHINE (Cherfils et al., 2012), SPHYSICS (Gomez-Gesteira et al., 2012), etc. The emergence of these procedures will effectively promote the further development of the basic theory of SPH and its applications. However, there are still many deficiencies in the SPH method.

- Improvement of boundary treatment has proven difficult;
- SPH calculations are large, so its computational efficiency needs to be improved;
- The coupling of SPH with other methods (Liu, 2010);
- The SPH method has the problem of boundary particle deletion. To give full play to the advantages of the SPH method to describe large deformation while avoiding its shortcomings, the engineering practice usually combines the SPH method with the FEM to solve the fluid-solid coupling problem.

A coupling model of the SPH particles and the FEM unit is shown in Figure 6. In the coupled model, there is a transition element on the fluid-solid coupling surface. The transition element is not only a FE unit, which is involved in the calculation of the solid domain but also a SPH particle, which participates in the calculation of the fluid domain. To ensure that the fluid field has a uniform density, the mass of the SPH particles on the transition unit is calculated according to the properties of the fluid. At the same time, the field function of the SPH particles in the coupled surface is summed approximately by the SPH particles located in the compact support domain. FEM nodes are not involved in the SPH approximation in the particle compact support domain. The strain of the transitional cell on the coupling surface is determined by the SPH calculation in the fluid domain, but the nodal forces of the transition element are determined by the SPH calculation in the fluid domain and the FE calculation in the solid domain.

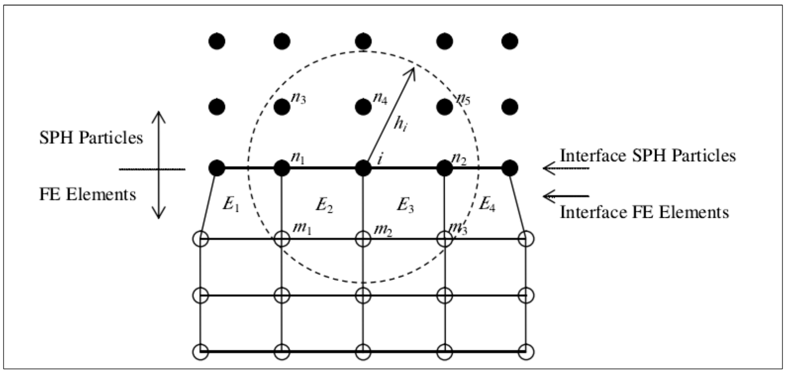

Figure 6. The coupling model of SPH particles and FEM elements.

4 CONCLUSIONS

In this paper, commonly used numerical simulation methods of fluid-solid coupling and their underlying calculation methods are summarized. There still exist a significant number of issues with the existing coupling algorithms that necessitate further improvement. Realizing accurate representations of the fluid-solid coupling mechanism is the key to the establishment of the macro-meso mechanics model. Improving the accuracy of boundary treatment and calculating coupling efficiency are of great significance to the accuracy of simplified algorithms that can satisfy this engineering problem with adequate precision. The mechanical behaviour of fluid-solid coupling in different environments is not the same and the coupling mechanism has always been a challenging subject. Therefore, the method and mechanism of fluid-solid coupling require further study. The author puts forward the following suggestions as a reference:

- Establish the model of thermal force fluid-solid coupling to further study the influence of thermal effects on the complexity of the fluid characteristics;
- Based on the mechanics of discontinuous granular media, develop algorithms that can simulate the real solid particle medium;
- Optimize the similar scale theory of the coupled macroscopic model and establish the exact similarity scale in accordance with the change of the spatial and temporal distribution;
- Establish a numerical model of the response of the macroscopic mechanical parameters and the corresponding relationship between the macro and micro parameters.

ACKNOWLEDGEMENTS

The authors would like to acknowledge the support received from the Science Fund for Creative Research Groups of the National Natural Science Foundation of China (Grant no. 51321065) and Funding research projects in Hebei education department (Grant no. QN2015157).

REFERENCES

Bai, M., Meng, F., Elsworth, D. & Roegiers, J.C. (1999). Analysis of Stress-Dependent Permeability in Nonorthogonal Flow and Deformation Fields. *Rock Mechanics and Rock Engineering*, 32(3), 195-219.

Biot, M.A. (1941). General Theory of Three-Dimensional Consolidation. *Journal of Applied Physics*, 12(2), 155-164.

Biot, M.A. & Willis, D.G. (1957). The Elastic Coefficients of the Theory of Consolidation. *J. Appl. Mech.*, 24, 594-601.

Boek, E.S., Chin, J. & Coveney, P.V. (2003). Lattice Boltzmann Simulation of the Flow of Non-Newtonian Fluids in Porous Media. *International Journal of Modern Physics* B, 17(01n02), 99-102.

Wang, B. & Yang, Q. (2008). The Realization and Application of Loosely Coupled Algorithm. *Engineering Mechanics*, 25(12), 48-52. (In Chinese)

Cherfils, J.M., Pinon, G. & Rivoalen, E. (2012). JOSEPHINE: A Parallel SPH Code for Free-Surface Flows. *Computer Physics Communications*, 183(7), 1468-1480.

Zhang, C.H. (2008). Discrete-Contact-Fracture Analysis of Rock and Concrete. *Chinese Journal of Rock Mechanics and Engineering*, 27(2), 217-235, (In Chinese).

Chu, W.J., Xu, W.Y. & Su, J.B. (2007). Study on Solid-Fluid-Coupled Model and Numerical Simulation for Deformation Porous Media. *Engineering Mechanics*, 9(24), 9, (In Chinese).

Cleary, P.W. & Monaghan, J.J. (1999). Conduction Modelling Using Smoothed Particle Hydrodynamics. *Journal of Computational Physics*, 148(1), 227-264.

Cook, B.K. (2001). A Numerical Framework for the Direct Simulation of Solid-Fluid Systems, *PhD Thesis*. Massachusetts Institute of Technology.

Cook, B.K., Noble, D.R. & Williams, J.R. (2004). A Direct Simulation Method for Particle-Fluid Systems. *Engineering Computations*, 21(2/3/4), 151-168.

Cundall, P.A. & Strack, O.D. (1979). A Discrete Numerical Model for Granular Assemblies. *Geotechnique*, 29(1), 47-65.

Cundall, P.A. & Strack, O.D.L. (1999). Particle Flow Code in 2 Dimensions. *Itasca Consulting Group*, Inc.

Dalrymple, R.A. & Rogers, B.D. (2006). Numerical Modeling of Water Waves with the SPH Method. *Coastal Engineering*, 53(2), 141-147.

Deng, C.H. (2011). The Algorithm Study of Weak Coupling in Fluid-Structure Interaction. *Huazhong University of Science and Technology Wuhan*, (In Chinese).

Deng, T., Wan, L. & Wei, Z.A. (2011). Stacking Model Test of Wenzhuang Tailings Reservoir and Its Stability Analysis. *Rock and Soil Mechanics*, 32(12), 3647-3652, (In Chinese).

Dong, P. (2005). Numerical Model of Fully Coupled Fluid-Solid Seepage in a Deformable Porous Medium and Its Applications. *Journal of Geomechanics,* 11(3), 273, (In Chinese).

Dullien, F.A. (2012). *Porous Media: Fluid Transport and Pore Structure*. Academic Press.

Feng, Y.T., Han, K., Owen, D.R.J. & Loughran, J. (2009). On Upscaling of Discrete Element Models: Similarity Principles. *Engineering Computations*, 26(6), 599-609.

Feng, Y.T., Han, K. & Owen, D.R.J. (2007). Coupled Lattice Boltzmann Method and Discrete Element Modelling of Particle Transport in Turbulent Fluid Flows: Computational Issues. *International Journal for Numerical Methods in Engineering*, 72(9), 1111-1134.

Feng, Y.T., Han, K. & Owen, D.R.J. (2010). Combined Three-Dimensional Lattice Boltzmann Method and Discrete Element Method for Modelling Fluid-Particle Interactions with Experimental Assessment. *International Journal for Numerical Methods in Engineering*, 81(2), 229.

Feng, Z.G. & Michaelides, E.E. (2005). Proteus: A Direct Forcing Method in the Simulations of Particulate Flows. *Journal of Computational Physics*, 202(1), 20-51.

Fredlund, D.G. (2006). Unsaturated Soil Mechanics in Engineering Practice. *Journal of Geotechnical and Geoenvironmental Engineering*, 132(3), 286-321.

Ginzburg, I. (2002). A free-Surface Lattice Boltzmann Method for Modelling the Filling of Expanding Cavities by Bingham Fluids*. Philosophical Transactions of the Royal Society of London A: Mathematical*, *Physical and Engineering Sciences*, 360(1792), 453-466.

Hudson, J.A., Stephansson, O. & Andersson, J. (2005). Guidance on Numerical Modelling of Thermo-Hydro-Mechanical Coupled Processes for Performance Assessment of Radioactive Waste Repositories. *International Journal of Rock Mechanics and Mining Sciences*, 42(5), 850-870.

Gomez-Gesteira, M., Rogers, B.D., Crespo, A.J., Dalrymple, R.A., Narayanaswamy, M. & Dominguez, J.M. (2012). SPHysics–Development of a Free-Surface Fluid Solver–Part 1: Theory and Formulations. *Computers & Geosciences*, 48, 289-299.

Liu, H.X., Li, N., Liao, X., Gong, J.L. & Fang, F.H. (2004). Unsteady Seepage Analysis of Tailings Dams Considering Coupling of Stress and Seepage Fields. *Chinese Journal of Rock Mechanics and Engineering*, 23(17), 2870-2875, (In Chinese).

Iwashita, K. & Oda, M. (1999). *Mechanics of Granular Materials: An Introduction*. CRC Press.

Kajtar, J. & Monaghan, J.J. (2008). SPH Simulations of Swimming Linked Bodies. *Journal of Computational Physics*, 227(19), 8568-8587.

Ladd, A.J. (1994). Numerical Simulations of Particulate Suspensions Via a Discretized Boltzmann Equation. Part 2. Numerical Results. *Journal of Fluid Mechanics*, 271, 311-339.

Leonardi, C.R., Owen, D.R.J. & Feng, Y.T. (2012). Simulation of Fines Migration Using a Non-Newtonian Lattice Boltzmann-Discrete Element Model: Part II: 3D Extension and Applications. *Engineering Computations*, 29(3-4), 392-418.

Leonardi, C.R., Owen, D.R.J. & Feng, Y.T. (2012). Simulation of Fines Migration Using a Non-Newtonian Lattice Boltzmann-Discrete Element Model: Part I: 2D Implementation Aspects. *Engineering Computations*, 29(4), 366-391.

Monaghan, J.J., Kos, A. & Issa, N. (2003). Fluid Motion Generated by Impact. *Journal of Waterway, Port, Coastal, and Ocean Engineering*, 129(6), 250-259.

Qian, W.C. (1984). Development Trend of Current Mechanics [J]. *Engineering Mechanics*, 1(01), 6-10, (In Chinese).

Liu, M.B. & Liu, G.R. (2010). Smoothed Particle Hydrodynamics (SPH): An Overview and Recent Developments. *Archives of Computational Methods in Engineering*, 17(1), 25-76.

Nguyen, N.Q. & Ladd, A.J. (2005). Sedimentation of Hard-Sphere Suspensions at Low Reynolds Number. *Journal of Fluid Mechanics*, 525, 73-104.

Oger, G., Doring, M., Alessandrini, B. & Ferrant, P. (2006). Two-Dimensional SPH Simulations of Wedge Water Entries. *Journal of Computational Physics*, 213(2), 803-822.

Omidvar, P., Stansby, P.K. & Rogers, B.D. (2012). Wave Body Interaction in 2D Using Smoothed Particle Hydrodynamics (SPH) with Variable Particle Mass. *International Journal for Numerical Methods in Fluids*, 68(6), 686-705.

Li, P.C., Kong, X.Y. & Lu, D.T. (2003). Mathematical Modeling of Flow in Saturated Porous Media on Account of Fluid-Structure Coupling Effect. *Journal of Hydrodynamics*, 18(4), 419-426, (In Chinese).

Potapov, A.V., Hunt, M.L. & Campbell, C.S. (2001). Liquid–Solid Flows Using Smoothed Particle Hydrodynamics and the Discrete Element Method. *Powder Technology*, 116(2), 204-213.

Shen, L.F., Wang, Z.L. & Li, S.J. (2015). Numerical Simulation for Mesoscopic Seepage Field of Soil Based on Lattice Boltzmann Method at REV Scale. *Rock and Soil Mechanics*, 36(S2), 689-694, (In Chinese).

Qiu, L.C. (2008). Two-Dimensional SPH Simulations of Landslide-Generated Water Waves. *Journal of Hydraulic Engineering*, 134(5), 668-671.

Qiu, L.C. (2013). Numerical Modeling of Liquid-Particle Flows by Combining SPH and DEM. *Industrial & Engineering Chemistry Research*, 52(33), 11313-11318.

Qiu, L.C. (2015). A Coupling Model of DEM and LBM for Fluid Flow Through Porous Media. *Procedia Engineering*, 102, 1520-1525.

Shao, S., Ji, C., Graham, D.I., Reeve, D.E., James, P.W. & Chadwick, A.J. (2006). Simulation of Wave Overtopping by an Incompressible SPH Model. *Coastal Engineering*, 53(9), 723-735.

Shimizu, Y. (2006). Three-Dimensional Simulation Using Fixed Coarse-Grid Thermal-Fluid Scheme and Conduction Heat Transfer Scheme in Distinct Element Method. *Powder Technology*, 165(3), 140-152.

Shimizu, Y. (2004). Fluid Coupling in PFC2D and PFC3D[C]//Numerical Modeling in Micromechanics Via Particle Methods, *Proc. of the 2nd International PFC Symposium*, Kyoto, Japan, 281-287.

Shi, Y., Ellero, M. & Adams, N.A. (2012). Analysis of Intermittency in Under-Resolved Smoothed-Particle-Hydrodynamics Direct Numerical Simulations of Forced Compressible Turbulence. *Physical Review E*, 85(3).

Sun, Q.C. & Jin, F. (2009). The Multiscale Structure of Granular Matter and Its Mechanics. *Physics*, 4, 225-232, (In Chinese).

Zhang, S.C. (1996). Smoothed Particle Hydrodynamics (SPH) Method (A Review) [J]. *Chinese Journal of Computation Physics*, 13(4), 385-397.

Szewc, K., Pozorski, J. & Taniere, A. (2011). Modeling of Natural Convection with Smoothed Particle Hydrodynamics: Non-Boussinesq Formulation. *International Journal of Heat and Mass Transfer*, 54(23), 4807-4816.

Tartakovsky, A.M., Meakin, P., Scheibe, T.D. & West, R.M.E. (2007). Simulations of Reactive Transport and Precipitation with Smoothed Particle Hydrodynamics. *Journal of Computational Physics*, 222(2), 654-672.

Tartakovsky, A.M. (2010). Langevin Model for Reactive Transport in Porous Media. *Physical Review E*, 82(2), 026302.

Tsuji, Y., Kawaguchi, T. & Tanaka, T. (1993). Discrete Particle Simulation of Two-Dimensional Fluidized Bed. *Powder Technology*, 77(1), 79-87.

Vanaverbeke, S., Keppens, R., Poedts, S. & Boffin, H. (2009). GRADSPH: A Parallel Smoothed Particle Hydrodynamics Code for Self-Gravitating Astrophysical Fluid Dynamics. *Computer Physics Communications*, 180(7), 1164-1182.

Wang, Y.J. (1986). Discrete Element Method a Numerical Method Suitable for Analysis in Jointed Rocks. *First National Rock Mechanics Numerical Calculation & Model Test Discuss Proceedings*, 32-37, (In Chinese).

Xia, M.F., Han, W.S., Ke, F.J. & Bai, Y.L. (1995). Statistical Meso-Scopic Damage Mechanics and Damage Evolution Induced Catastrophe. *Adv. Mech.*, 25(1), 1-40, (In Chinese).

Xu, Z.J. (2012). Based on the CFD Complex Tall Building Two-Way Flow-Solid Coupling Research, *MSc Thesis.* College of Civil Engineering of Chongqing University, (In Chinese).

Yang, L. (2011). Numerical Simulation Method Research of the Nonlinear Fluid-Solid Interaction Problems. *Ocean University of China*, (In Chinese).

Yao, Y.P. & Hou, W. (2009). Basic Mechanical Behavior of Soils and Their Elastoplastic Modeling. *Rock and Soil Mechanics*, 30(10), 2881-2902.

Zhang, H., Tan, Y., Shu, S., Niu, X., Trias, F.X., Yang, D. & Sheng, Y. (2014). Numerical Investigation on the Role of Discrete Element Method in Combined LBM–IBM–DEM Modeling. *Computers & Fluids*, 94, 37-48.

Zhou, G.Z. & Ge, W. (2014). Progress of Smoothed Particle Hydrodynamics in Complex Flows. *CIESC Journal*, 65(4), 1145-1161, (In Chinese).

Zienkiewicz, O.C., Xie, Y.M., Schrefler, B.A., Ledesma, A. & Bicanic, N. (1990). Static and Dynamic Behaviour of Soils: A Rational Approach to Quantitative Solutions. II. Semi-Saturated Problems. In *Proceedings of the Royal Society of London A: Mathematical, Physical and Engineering Sciences,* 429(1877), 311-321, The Royal Society.

Zienkiewicz, O.C. & Shiomi, T. (1984). Dynamic Behaviour of Saturated Porous Media; The Generalized Biot Formulation and Its Numerical Solution. *International Journal for Numerical and Analytical Methods in Geomechanics*, 8(1), 71-96.

